PB86-167160

Symposium on the Transfer and Utilization of Particulate Control Technology (5th). Volume 2

Research Triangle Inst.
Research Triangle Park, NC

Prepared for

Environmental Protection Agency
Research Triangle Park, NC

Feb 86

U.S. Department of Commerce
National Technical Information Service
NTIS

PB86-167160

EPA/600/9-86/008b
February 1986

Proceedings: Fifth Symposium on the Transfer and Utilization of Particulate Control Technology

Volume 2

Franklin A. Ayer, Compiler

Research Triangle Institute
P. O. Box 12194
Research Triangle Park, North Carolina 27709

EPA Cooperative Agreement CR810152

EPA Project Officer:
Dale L. Harmon
Air and Energy Engineering Research Laboratory
Research Triangle Park, NC 27711

EPRI Project Manager:
R. F. Altman
Air Quality Control Program
Coal Combustion Systems Division
Palo Alto, California 94304

Prepared for:

U.S. Environmental Protection Agency
Office of Research and Development
Washington, DC 2046

Electric Power Research Institute
412 Hillview Avenue
Alto, California 94304

REPRODUCED BY
NATIONAL TECHNICAL
INFORMATION SERVICE
U.S. DEPARTMENT OF COMMERCE
SPRINGFIELD, VA. 22161

AIR AND ENERGY ENGINEERING RESEARCH LABORATORY
OFFICE OF RESEARCH AND DEVELOPMENT
U.S. ENVIRONMENTAL PROTECTION AGENCY
RESEARCH TRIANGLE PARK, NC 27711

Title pg

TECHNICAL REPORT DATA

(Please read Instructions on the reverse before completing)

1. REPORT NO. EPA/600/9-86/008b	2.	3. RECIPIENT'S ACCESSION NO. PB86 167160/AS
4. TITLE AND SUBTITLE Proceedings: Fifth Symposium on the Transfer and Utilization of Particulate Control Technology; Volume 2		5. REPORT DATE February 1986
		6. PERFORMING ORGANIZATION CODE
7. AUTHOR(S) Franklin A. Ayer, Compiler		8. PERFORMING ORGANIZATION REPORT NO. EPRI CS-4404, V1-4
9. PERFORMING ORGANIZATION NAME AND ADDRESS Research Triangle Institute P.O. Box 12194 Research Triangle Park, North Carolina 27709		10. PROGRAM ELEMENT NO.
		11. CONTRACT/GRANT NO. CR810152
12. SPONSORING AGENCY NAME AND ADDRESS EPA, Office of Research and Development* Air and Energy Engineering Research Laboratory Research Triangle Park, NC 27711		13. TYPE OF REPORT AND PERIOD COVERED Proceedings; August 1984
		14. SPONSORING AGENCY CODE EPA/600/13

15. SUPPLEMENTARY NOTES AEERL project officer is Dale L. Harmon, Mail Drop 61, 919/541-2429. EPA-600/9-84-025a, b, and c were proceedings for the fourth symposium. (*) Cosponsored by EPRI.

16. ABSTRACT

The proceedings document the Fifth Symposium on the Transfer and Utilization of Particulate Control Technology, held August 27-30, 1984, in Kansas City, MO. The symposium was sponsored by EPA's Air and Energy Engineering Research Laboratory (formerly the Industrial and Environmental Research Laboratory), located in Research Triangle Park, NC, and EPRI's Coal Combustion Systems Division, in Palo Alto, CA. The symposium provided for the exchange of knowledge and to stimulate new ideas for particulate control with the goal of extending the technology and aiding its diffusion among designers, users, and educators. Fabric filters and ESPs received the major attention, but novel concepts and advanced technologies were also explored. Volume 1 covered the plenary session, advanced energy applications, economics, and novel concepts. Volume 2 was devoted to electrostatic precipitators. Volume 3 dealt with fabric filters. Volume 4 described fugitive emissions, dry SO2, and operation and maintenance.

17. KEY WORDS AND DOCUMENT ANALYSIS

a. DESCRIPTORS		b. IDENTIFIERS/OPEN ENDED TERMS	c. COSATI Field/Group	
Pollution	Economics	Pollution Control	13B	05C
Particles	Processing	Stationary Sources	14G	13H
Aerosols	Leakage	Particulate	07D	
Electrostatic Precipitators		Fabric Filters	13I	
Filtration		Fugitive Emissions		
Fabrics			11E	

18. DISTRIBUTION STATEMENT Release to Public	19. SECURITY CLASS *(This Report)* Unclassified	21. NO. OF PAGES 503
	20. SECURITY CLASS *(This page)* Unclassified	22. PRICE

EPA Form 2220-1 (9-73)

NOTICE

This document has been reviewed in accordance with U.S. Environmental Protection Agency policy and approved for publication. Mention of trade names or commercial products does not constitute endorsement or recommendation for use.

This article documents research that was conducted under the auspices of the U.S. Environmental Protection Agency (USEPA). As an arm of the government, the USEPA has a paid up, non-exclusive, irrevocable, worldwide license to reproduce, prepare derivative works, and distribute to the public all of the material contained herein, and to grant others acting on its behalf the right to do so. The USEPA grants to the National Technical Information Service, Department of Commerce, the right to act as its agent in the distribution of this material.

ORDERING INFORMATION

Requests for copies of this report should be directed to Research Reports Center (RRC), Box 50490, Palo Alto, CA 94303, (415) 965-4081. There is no charge for reports requested by EPRI member utilities and affiliates, U.S. utility associations, U.S. government agencies (federal, state, and local), media, and foreign organizations with which EPRI has an information exchange agreement.*

(*) Copies of this report are available to the public through the National Technical Information Service, Springfield, Virginia 22161.

Copyright © 1986, EPRI CS-4404, V1-4, "Proceedings: Fifth Symposium on the Transfer and Utilization of Particulate Control Technology, Volumes 1-4." Since this work was, in part, funded by the U.S. Government, the Government is vested with a royalty-free, non-exclusive, and irrevocable license to publish, translate, reproduce, and deliver that information and to authorize others to do so.

NOTICE

This report was prepared by the Electric Power Research Institute, Inc. (EPRI). Neither EPRI, members of EPRI, nor any person acting on their behalf: (a) makes any warranty, express or implied, with respect to the use of any information, apparatus, method, or process disclosed in this report or that such use may not infringe privately owned rights; or (b) assumes any liabilities with respect to the use of, or for damages resulting from the use of, any information, apparatus, method, or process disclosed in this report; or (c) is responsible for statements made or opinions expressed by individual authors.

ABSTRACT

These proceedings are of the Fifth Symposium on the Transfer and Utilization of Particulate Control Technology, held August 27 to 30, 1984, in Kansas City, Missouri. The symposium was sponsored by EPA's Air and Energy Engineering Research Laboratory (formerly Industrial Environmental Research Laboratory), located in Research Triangle Park, North Carolina, and the EPRI Coal Combustion Systems Division, located in Palo Alto, California.

The objective of the symposium was to provide for the exchange of knowledge and to stimulate new ideas for particulate control with the goal of extending the technology and aiding its diffusion among designers, users, and educators. Fabric filters and electrostatic precipitators were the major topics, but novel concepts and advanced technologies were also explored. The organization of sessions was as follows:

- Day 1
  - --Plenary session
  - --ESP: Performance Estimating (Modeling)
  - --FF: Practical Considerations
  - --Economics
  - --Novel Concepts
- Day 2
  - --ESP: Performance Enhancement I
  - --FF: Full-Scale Studies I (Coal-Fired Boilers)
  - --Fugitive Emissions I
  - --ESP: Performance Enhancement II
  - --FF: Full-Scale Studies II (Coal-Fired Boilers)
  - --Fugitive Emissions II
- Day 3
  - --ESP: Advanced Technology I
  - --FF: Fundamentals/Measurement Techniques

--Dry SO_2 Removal I

--ESP: Advanced Technology II

--FF: Advanced Concepts

--Dry SO_2 Removal II

- Day 4

--ESP: Fundamentals I

--FF: Pilot-Scale Studies (Coal-Fired Boilers)

--Operation and Maintenance I

--ESP: Fundamentals II

--Advanced Energy Applications

--Operations and Maintenance II

Volume 1 contains 19 papers presented at the Plenary, Advanced Energy Applications, Economics and Novel Concepts Sessions.

Volume 2 contains 33 papers presented at the ESP: Performance Estimating (Modeling), ESP: Performance Enhancement I and II, ESP: Advanced Technology I and II, and ESP: Fundamentals I and II Sessions, plus one unpresented paper.

Volume 3 contains 24 papers presented at the FF: Practical Considerations, FF: Full-Scale Studies I and II (Coal-Fired Boilers), FF: Fundamentals/Measuring Techniques, FF: Advanced Concepts, and FF: Pilot-Scale Studies (Coal-Fired Boilers) Sessions.

Volume 4 contains 29 papers presented at the Fugitive Emissions I and II, Dry SO_2 Removal I and II, and Operations Maintenance I and II.

PREFACE

These proceedings for the Fifth Symposium on the Transfer and Utilization of Particulate Control Technology constitute the final report submitted to EPA's Air and Energy Engineering Research Laboratory (AEERL), Research Triangle Park, North Carolina, and to the Coal Combustion Systems Division, EPRI, Palo Alto, California. The symposium was conducted at the Hyatt Regency Hotel at the Crown Center in Kansas City, Missouri, August 27-30, 1984.

This symposium (the first jointly sponsored by EPA and EPRI) was designed to provide a forum for the exchange of knowledge and to stimulate new ideas for particulate control with the goal of extending technology and aiding its diffusion among designers, users, educators, and researchers. In the opening session, an address was given on the regulatory framework for future particulate technology needs followed by a series of addresses on the impact of coming particulate requirements on the utility industry and the iron and steel industry as well as the viewpoint of large and small manufacturers. There were subsequent technical sessions on electrostatic precipitator performance estimating (modeling), ESP performance enhancement, ESP advanced technology, ESP fundamentals, practical considerations for fabric filters, fabric filter full-scale studies (coal-fired boilers), fabric filter fundamentals/measurement techniques, fabric filter pilot-scale studies (coal-fired boilers), fugitive emissions, dry SO_2 removal, operation and maintenance, and advanced energy applications. Participants represented electric utilities, equipment and process suppliers, state environmental agencies, coal and petroleum suppliers, EPA and other Federal agencies, educational institutions, and research organizations.

The following persons contributed their efforts to this symposium:

- Dale L. Harmon, Chemical Engineer, Particulate Technology Branch, Utilities and Industrial Power Division, U.S. EPA, AEERL, Research Triangle Park, North Carolina, was a symposium co-general chairman and EPA project officer.
- Ralph F. Altman, Ph.D., Project Manager, Coal Combustion Systems Division, EPRI, Chattanooga, Tennessee, was a co-general chairman and EPRI project manager.
- Franklin A. Ayer, Consultant, Research Triangle Institute, Research Triangle Park, North Carolina, was the overall symposium coordinator and compiler of the proceedings.

TABLE OF CONTENTS

VOLUME 1, PLENARY, ADVANCED ENERGY APPLICATIONS, ECONOMICS, AND NOVEL CONCEPTS

VOLUME 2, ELECTROSTATIC PRECIPITATION

VOLUME 3, FABRIC FILTRATION

VOLUME 4, FUGITIVE EMISSIONS, DRY SO_2, AND OPERATION AND MAINTENANCE

VOLUME 1
PLENARY, ADVANCED ENERGY APPLICATIONS, ECONOMICS, AND NOVEL CONCEPTS

Page

Session 1: PLENARY SESSION 1
Everett L. Plyler, Chairman

The Regulatory Framework for Future Particulate Technology Needs 2
Sheldon Meyers

The Impact of Coming Particulate Control Requirements on the Utility Industry 9
George T. Preston

The Impact of Coming Particulate Control Requirements on the Iron and Steel Industry. 16
Earle F. Young, Jr.

The Impact of Particulate Control Requirements: Large Manufacturer's Viewpoint 22
Herbert H. Braden
Paper presented by Gary R. Gawreluk

Future Particulate Regulations: The View of the Small Manufacturer 33
Sidney R. Orem

Session 2: ADVANCED ENERGY APPLICATIONS. 36
George A. Rinard, Chairman

Page

High-Temperature, High-Pressure Electrostatic Precipitation, Current Status 37
P. L. Feldman* and K. S. Kumar

Test Results of a Precipitator Operating at High-Temperature and High-Pressure Conditions 50
Donald E. Rugg*, George Rinard, Michael Durham, and James Armstrong

Evaluation and Development of Candidate High Temperature Filter Devices for Pressurized Fluidized Bed Combustion. . . . 64
T. E. Lippert*, D. F. Ciliberti, S. G. Drenker, and O. J. Tassicker

High Temperature Gas Filtration with Ceramic Filter Media: Problems and Solutions 79
Ramsay Chang

The Development and High Temperature Application of a Novel Method for Measuring Ash Deposits and Cake Removal on Filter Bags. 92
David F. Ciliberti*, Thomas E. Lippert, Owen J. Tassicker, and Steven Drenker

Session 3: ECONOMICS 107
John S. Lagarias, Chairman

Economics of Electrostatic Precipitators and Fabric Filters 108
Victor H. Belba*, Fay A. Horney, Robert C. Carr, and Walter Piulle

Estimating the Benefits of SO_3 Gas Conditioning on the Performance of Utility Precipitators When Burning U.S. Coals 126
Peter Gelfand

Microcomputer Models for Particulate Control 135
A. S. Viner*, D. S. Ensor, and L. E. Sparks

The Impact of Proposed Acid Rain Legislation on Power Plant Particulate Control Equipment. 142
William H. Cole

Session 4: NOVEL CONCEPTS. 158
Dale L. Harmon, Chairman

*Denotes speaker

Page

Particle Charging with an Electron Beam Precharger 159
J. S. Clements*, A. Mizuno, and R. H. Davis

Charging of Particulates by Evaporating Charged Water Droplets 175
G. S. P. Castle*, I. I. Inculet, and R. Littlewood

Role of Electrostatic Forces in High Velocity Particle Collection Devices 187
H. C. Wang, J. J. Stukel*, K. H. Leong, and P. K. Hopke

Hot-Gas Fabric Filtration 500° F - 1500° F, No Utopia but Reality. 201
Lutz Bergmann

The Prediction of Plume Opacity from Stationary Sources. . . . 211
David S. Ensor*, Ashok S. Damle, Philip A. Lawless, and Leslie E. Sparks

APPENDIX: Attendees 234

VOLUME 2
ELECTROSTATIC PRECIPITATION

Session 5: ESP: PERFORMANCE ESTIMATING (MODELING) 267
Leslie E. Sparks, Chairman

Microcomputer Programs for Precipitator Performance Estimates. 268
M. G. Faulkner*, J. L. DuBard, R. S. Dahlin, and Leslie E. Sparks

Analysis of Error in Precipitator Performance Estimates. . . . 283
J. L. DuBard* and R. F. Altman

Use of a Mobile Electrostatic Precipitator for Pilot Studies. 299
Robert R. Crynack* and John D. Sherow

Prediction of Voltage-Current Curves for Novel Electrodes--Arbitrary Wire Electrodes on Axis. 314
Phil A. Lawless* and L. E. Sparks

Numerical Computation of the Electrical Conditions in a Wire-Plate Electrostatic Precipitator Using the Finite Element Technique. 328
Gregory A. Kallio* and David E. Stock

*Denotes speaker

Page

Session 6: ESP: PERFORMANCE ENHANCEMENT I 345
Ralph F. Altman, Chairman

A Field Study of a Combined NH_3-SO_3 Conditioning System on a Cold-Side Fly Ash Precipitator at a Coal-Fired Power Plant. 346
Robert S. Dahlin*, John P. Gooch, Guillaume H. Marchant, Jr., Roy E. Bickelhaupt, D. Richard Sears, and Ralph F. Altman

Conditioning of Power Station Flue Gases to Improve Electrostatic Precipitator Efficiency. 362
Gernot Mayer-Schwinning* and J. D. Riley

Pilot-Scale Study of a New Method of Flue-Gas Conditioning with Ammonium Sulfate. 375
Edward B. Dismukes*, E. C. Landham, Jr., John P. Gooch, and Ralph F. Altman

Power Plant Plume Opacity Control. 390
J. Martin Hughes* and Kai-Tien Lee

Pulse Energization System of Electrostatic Precipitator for Retrofitting Application 404
Senichi Masuda* and Shunsuke Hosokawa

Session 7: ESP: PERFORMANCE ENHANCEMENT II. 419
B. G. McKinney, Chairman

Practical Implications of Pulse Energization of Electrostatic Precipitators. 420
H. Milde*, J. Ottesen, and C. Salisbury

Laboratory and Full-Scale Characteristics of Electrostatic Precipitators with Rigid Mast Electrodes 437
H. Krigmont*, R. Allan, R. Triscori, and H. W. Spencer, III

Full Scale Experience with Pulsed Energization of Electrostatic Precipitators. 458
K. Porle* and K. Bradburn

New Life for Old Weighted Wire Precipitators: Rebuilding with Rigid Electrodes. 479
Peter J. Aa* and Gary R. Gawreluk*

*Denotes speaker

Page

Pulsing on a Cold-Side Precipitator, Florida Power Corporation, Crystal River, Unit 1 495
Joseph W. Niemeyer*, Robert A. Wright, and Wayne Love

Session 8: ESP: ADVANCED TECHNOLOGY I 499
Norman Plaks, Chairman

Field Study of Multi-Stage Electrostatic Precipitators 500
Michael Durham, George Rinard, Donald Rugg, Theodore Carney, James Armstrong*, and Leslie E. Sparks

Optimizing the Collector Sections of Multi-Stage Electrostatic Precipitators. 513
George Rinard*, Michael Durham, Donald Rugg, and Leslie Sparks

Ceramic-Made Boxer-Charger for Precharging Applications. . . . 525
Senichi Masuda*, Shunsuke Hosokawa, and Shuzo Kaneko

Precipitator Performance Enhancement with Pulsed Energization 539
E. C. Landham, Jr.*, James L. DuBard, Walter R. Piulle, and Leslie Sparks

Aerosol Particle Charging in a Pulsed Corona Discharge 554
James L. DuBard* and Walter R. Piulle

Session 9: ESP: ADVANCED TECHNOLOGY II. 569
Walter R. Piulle, Chairman

Performance of Large-Diameter Wires as Discharge Electrodes in Electrostatic Precipitators. 570
P. Vann Bush*, Duane H. Pontius, and Leslie E. Sparks

Technical Evaluation of Plate Spacing Effects on Fly Ash Collection in Precipitators. 586
Ralph F. Altman*, Gerald W. Driggers, Ronald W. Gray, and James L. DuBard, and E. C. Landham, Jr.

Electrical Characteristics of Large-Diameter Discharge Electrodes in Electrostatic Precipitators. 599
Kenneth J. McLean* and Leslie E. Sparks

Laboratory Analysis of Corona Discharge Electrodes and Back Corona Phenomena. 610
P. Vann Bush* and Todd R. Snyder

*Denotes speaker

Page

Session 10: ESP: FUNDAMENTALS I 627
Grady B. Nichols, Chairman

The Onset of Electrical Breakdown in Dust Layers 628
Ronald P. Young*, James L. DuBard, and Leslie E. Sparks

Bipolar Current Probe for Diagnosing Full-Scale Precipitators. 643
Senichi Masuda*, Toshifumi Itagaki, Shigeyuki Nohso, Osamu Tanaka, Katsuji Hironaga, and Nobuhiko Fukushima

A Method for Predicting the Effective Volume Resistivity of a Sodium Depleted Fly Ash Layer 658
Roy E. Bickelhaupt* and Ralph F. Altman

Analysis of Air Heater-Fly Ash-Sulfuric Acid Vapor Interactions 676
Norman W. Frisch

Session 11: ESP: FUNDAMENTALS II. 698
Philip A. Lawless, Chairman

Experimental Studies of Space Charge Effects in an ESP 699
D. H. Pontius* and P. V. Bush

An Electrostatic Precipitator Facility for Turbulence Research 714
J. H. Davidson* and E. J. Shaughnessy

On the Static Field Strength in Wire-Plate Electrostatic Precipitators with Profiled Collecting Electrodes by an Experimental Method. 730
C. E. Akerlund

The Fluid Dynamics of Electrostatic Precipitators: Effects of Electrode Geometry. 741
E. J. Shaughnessy*, J. H. Davidson, and J. C. Hay

VOLUME 3
FABRIC FILTRATION

Session 12: FF: PRACTICAL CONSIDERATIONS. 751
Wallace B. Smith, Chairman

Fabric Screening Studies for Utility Baghouse Applications . . 752
Larry G. Felix* and Randy L. Merritt

*Denotes speaker

Page

Tensioning of Filter Bags in Reverse Air Fabric Filters. . . . 769
Robert W. Tisone* and Gregory L. Lear

Sound of Energy Savings. 784
N. D. Phillips* and J. A. Barabas

Solving the Pressure Drop Problem in Fabric Filter Bag Houses 797
Carl V. Leunig

Session 13: FF: FULL-SCALE STUDIES (COAL-FIRED BOILERS) 807
Robert P. Donovan, Chairman

Emission Reduction Performance and Operating Characteristics of a Baghouse Installed on a Coal-Fired Power Plant 808
David S. Beachler*, John W. Richardson, John D. McKenna, John C. Mycock, and Dale Harmon

Evaluation of Sonic-Assisted, Reverse-Gas Cleaning at Utility Baghouses 823
Kenneth M. Cushing*, Larry G. Felix, Anthony M. LaChance, and Stephen J. Christian

Sonic Horn Application in a Dry FGD System Baghouse. 839
Yang-Jen Chen*, Minh T. Quach, and H. W. Spencer III

Full Scale Operation and Performance of Two New Baghouse Installations 853
C. B. Barranger

Session 14: FF: FULL-SCALE STUDIES II (COAL-FIRED BOILERS). . . 867
Robert C. Carr, Chairman

Performance of Baghouses in the Electric Generating Industry 868
Wallace B. Smith* and Robert C. Carr

Flue Gas Filtration: Southwestern Public Service Company's Experience in Design, Construction, and Operation. 893
John Perry

Start-Up and Operation of a Reverse-Air Fabric Filter on a 550 MW Boiler 902
R. A. Winch and L. J. Pflug, Jr.*

*Denotes speaker

Page

Update on Australian Experience with Fabric Filters on Power Boilers 920
F. H. Walker

Session 15: FF: FUNDAMENTALS/MEASUREMENT TECHNIQUES 937
David S. Ensor, Chairman

Modeling Baghouse Performance. 938
David S. Ensor*, Douglas W. VanOsdell, Andrew S. Viner, Robert P. Donovan, and Louis S. Hovis

Measurement of the Spatial Distribution of Mass on a Filter 952
Andrew S. Viner*, R. P. Gardner, and L. S. Hovis

Laboratory Studies of the Effects of Sonic Energy on Removal of a Dust Cake from Fabrics. 964
B. E. Pyle*, S. Berg, and D. H. Pontius

Cleaning Fabric Filters. 981
G. E. R. Lamb

Session 16: FF: ADVANCED CONCEPTS 994
John K. McKenna, Chairman

Modeling Studies of Pressure Drop Reduction in Electrically Stimulated Fabric Filtration 995
Barry A. Morris*, George E. R. Lamb, and Dudley A. Saville

Flow Resistance Reduction Mechanisms for Electrostatically Augmented Filtration 1007
D. W. VanOsdell*, R. P. Donovan, and Louis S. Hovis

Laboratory Studies of Electrically Enhanced Fabric Filtration 1020
Louis S. Hovis*, Bobby E. Daniel, Yang-Jen Chen, and and R. P. Donovan

Pressure Drop for a Filter Bag Operating with a Lightning-Rod Precharger .1034
George E. R. Lamb* and Richard I. Jones

New High Performance Fabric for Hot Gas Filtration 1048
J. N. Shah
Paper presented by Peter E. Frankenburg

*Denotes speaker

Page

Session 17: FF: PILOT-SCALE STUDIES (COAL-FIRED BOILERS). . . .1059
Louis S. Hovis, Chairman

The Influence of Coal-Specific Fly Ash Properties Upon Baghouse Performance: A Comparison of Two Extreme Examples 1060
Stanley J. Miller* and D. Richard Sears

Top Inlet Baghouse Evaluation at Pilot Scale 1081
Gary P. Greiner* and Dale A. Furlong

Development of Woven Electrode Fabric and Preliminary Economics for Full-Scale Operation of Electrostatic Fabric Filtration. 1082
James J. Spivey*, Richard L. Chambers, and Dale L. Harmon

ESFF Pilot Plant Operation at Harrington Station 1101
Richard L. Chambers*, James J. Spivey, and Dale L. Harmon

VOLUME 4
FUGITIVE EMISSIONS, DRY SO_2, AND OPERATION AND MAINTENANCE

Session 18: FUGITIVE EMISSIONS I 1119
Chatten Cowherd, Jr., Chairman

Technical Manual on Hood Capture Systems to Control Process Fugitive Particulate Emissions 1120
E. R. Kashdan*, J. J. Spivey, D. W. Coy,
H. Goodfellow, T. Cesta, and D. L. Harmon

Pilot Demonstration of Air Curtain Control of Buoyant Fugitive Emissions 1132
Michael W. Duncan*, Shui-Chow Yung, Ronald G. Patterson,
William B. Kuykendal, and Dale L. Harmon

Characterization of Fugitive Particulate Emissions from Industrial Sites 1147
K. S. Basden

Evaluation of an Air Curtain Secondary Hooding System. 1161
John O. Burckle
Paper presented by William F. Kemner

*Denotes speaker

Page

Session 19: FUGITIVE EMISSIONS II. 1172
Michael J. Miller, Chairman

Technical Manual on the Identification, Assessment, and Control of Fugitive Emissions. 1173
Chatten Cowherd, Jr.*, John S. Kinsey, and William B. Kuykendal

Quantification of Roadway Fugitive Dust at a Large Midwestern Steel Mill. 1188
Keith D. Rosbury and William Kemner*

Evaluation of Street Sweeping as a Means of Controlling Urban Particulate. 1200
T. R. Hewitt

Windbreak Effectiveness for the Control of Fugitive-Dust Emissions from Storage Piles--A Wind Tunnel Study. 1210
Barbara J. Billman

Evaluation of Chemical Stabilizers and Windscreens for Wind Erosion Control of Uranium Mill Tailings. 1227
Monte R. Elmore* and James N. Hartley

Session 20: DRY SO_2 REMOVAL I. 1245
Richard G. Rhudy, Chairman

Modeling of SO_2 Removal in Spray-Dryer Flue Gas Desulfurization System 1246
Ashok S. Damle* and Leslie E. Sparks

Fabric Filter Operation Downstream of a Spray Dryer: Pilot and Full-Scale Results 1275
Richard G. Rhudy and Gary M. Blythe*

Novel Design Concepts for an 860 MW Fabric Filter Used with a Dry Flue Gas Desulfurization System. 1303
Michael F. Skinner, Steven H. Wolf, John M. Gustke*, and Donald O. Swenson

Start-Up and Operating Experience with a Reverse Air Fabric Filter as Part of the University of Minnesota Dry FGD System 1315
J. C. Buschmann*, J. Mills, and W. Soderberg

*Denotes speaker

Page

Spray Dryer/Baghouse Experiences on a 1000 ACFM Pilot Plant. 1325
Wayne T. Davis*, Gregory D. Reed, and Tom Lillestolen

Session 21: DRY SO_2 REMOVAL II 1337
Theodore G. Brna, Chairman

Design and Operation of the Baghouse at Holcomb Station, Unit No. 1. 1338
B. R. McLaughlin* and R. D. Emerson

An Update of Dry-Sodium Injection in Fabric Filters. 1357
Richard G. Hooper*, Robert C. Carr, G. P. Green, V. Bland, L. J. Muzio, and R. Keeth

Removal of Sulfur Dioxide and Particulate Using E-SOX. 1366
Leslie E. Sparks*, Geddes H. Ramsey, Richard E. Valentine, and Cynthia Bullock

Comparison of Dry Injection Systems at Normal and High Flue Gas Temperatures .1382
Robert M. Jensen*, William Dunlop, George C. Y. Lee, and Duane Folz

Acid Rain Control Options - Impact on Precipitator Performance. 1397
Victor H. Belba*, Fay A. Horney, and Donald M. Shattuck

Session 22: OPERATIONS AND MAINTENANCE I 1412
Richard D. McRanie, Chairman

Comparison of U.S. and Japanese Practices in the Specification and Operation and Maintenance of Electrostatic Precipitators. 1413
Michael F. Szabo*, Charles A. Altin, and William B. Kuykendal

Operation and Maintenance Manuals for Electrostatic Precipitators and Fabric Filters 1427
Michael F. Szabo*, Ronald D. Hawks, Fred D. Hall, and Gary L. Saunders

An Update of the Performance of the Cromby Station Fabric Filter. 1448
M. Gervasi*, J. R. Darrow, and J. E. Manogue

*Denotes speaker

Page

Critical Electrostatic Precipitator Purchasing Concepts. . . .1463
Charles A. Altin* and Ralph F. Altman

Reducing Electrostatic Precipitator Power Consumption. 1481
Joseph P. Landwehr* and George Burnett

Session 23: OPERATIONS AND MAINTENANCE II. 1494
Peter R. Goldbrunner, Chairman

Design Considerations to Avoid Common Fly Ash Conveying Problems 1495
Gus Monahu* and Walter Piulle

Feasibility of Using Parameter Monitoring as an Aid in Determining Continuing Compliance of Particulate Control Devices. 1510
Joseph Carvitti*, Michael F. Szabo, and William Kemner

Air Pollution Control: Maintenance Cost Savings from the Washing, Patching and Reuse of Bags Used in Fabric Filters. 1530
Frank L. Cross, Jr.
Paper presented by Lutz Bergmann

Optimizing the Performance of a Modern Electrostatic Precipitator by Design Refinements 1537
Donald H. Rullman* and Franz Neulinger

Weighted Discharge Electrodes - A Solution to Mechanical Fatigue Problems. 1567
John A. Knapik

PAPER PRESENTED AT THE FOURTH SYMPOSIUM ON THE TRANSFER AND UTILIZATION OF PARTICULATE CONTROL TECHNOLOGY BUT NOT PUBLISHED IN PROCEEDINGS

Measurement of the Electrokinetic Transport Properties of Particles in an Electrostatic Precipitator. 1584
Wallace T. Clark III*, Robert L. Bond, and Malay K. Mazumder

UNPRESENTED PAPER

Electrostatic Precipitator Bus Section Failure: Operation and Maintenance. 1596
Louis Theodore, Joseph Reynolds, Francis Taylor, Alan Filippi, and Steve Errico

*Denotes speaker

Session 5: ESP: PERFORMANCE ESTIMATING (MODELING)

Leslie E. Sparks, Chairman
U.S. Environmental Protection Agency
Air and Energy Engineering Research Laboratory
Research Triangle Park, NC

MICROCOMPUTER PROGRAMS FOR PRECIPITATOR PERFORMANCE ESTIMATES

by: M. G. Faulkner
J. L. DuBard
R. S. Dahlin
Southern Research Institute
Birmingham, Alabama 35255

L. E. Sparks
Industrial Environmental Research Laboratory
U.S. Environmental Protection Agency
Research Triangle Park, North Carolina 27711

ABSTRACT

The EPA/SRI mathematical model of electrostatic precipitation has been coded in FORTRAN for the Radio Shack TRS-80 Model III or 4 microcomputer. The TRS-80 model retains all essential features of the main-frame computer model, but omits several user options. The precipitator simulation is divided into four separate programs: a simplified data entry menu, a choice of a rigorous computation of ideal collection efficiency or a rapid estimation procedure, and approximate corrections for non-ideal gas flow and rapping reentrainment. A supplementary program can be used to estimate the electrical operating points that are required for the precipitator simulation. Given values of fly ash resistivity and precipitator plate spacing, this program estimates the electrical operating points by using average data from cold-side utility fly ash precipitators. Another supplementary program can be used to compute the plume opacity, given an optical path length and the particulate emissions computed by the precipitator simulation. All six microcomputer programs are included in Revision III of the main-frame computer model.

This paper has been reviewed in accordance with the U.S. Environmental Protection Agency's peer and administrative review policies and approved for presentation and publication.

INTRODUCTION

The Electrostatic Precipitator Performance Model (ESP Model) developed by Southern Research Institute for the Environmental Protection Agency was first released in 1975 (1). Since that time, the model and its revisions (2,3) have been widely used to study proposed and existing precipitators. Revision 3 of this model (4) features a faster algorithm and many new options, including calculation of plume opacity, V-I curve generation, flexible rapping schedule, metric input data, and a routine to check input data for errors. The FORTRAN code for this model requires 221,000 bytes of memory. This is well within the memory limits of a modern main-frame computer.

In order to make this program more widely available, a microcomputer version of it has been written. The microcomputer version uses the same algorithms as the main-frame version to compute collection efficiency and plume opacity, and to estimate operating voltages and currents if these quantities are not known. The system for which this program was developed is the Radio Shack Model III (or Model 4) computer with a minimum of 48 kilobytes of memory, two disk drives, and a line printer. Although some of the newest and largest microcomputers have enough memory for the entire main-frame program, at the time that this project was undertaken, 48 kilobytes was about the maximum available.

CALCULATION OF COLLECTION EFFICIENCY

Like the main-frame model, the microcomputer model performs a detailed mathematical simulation of the precipitation process along a single gas passage. For calculation purposes, the precipitator is divided into sections, permitting different electrical and gas conditions in each section, and then further divided into incremental lengths on the order of the precipitator wire-to-wire spacing. The efficiency calculation is performed sequentially on each incremental length to determine the total collection efficiency. The use of small length increments allows the calculation of the changing effects of space charge, electric fields, and particle concentrations throughout the precipitator. To compensate for the different charging and collecting rates of large and small particles, the input dust load is divided into particle size bands, each of which is handled separately in the efficiency calculation.

A flow chart for the ESP Model is shown in Figure 1. In the ESP Model the efficiency calculation is performed using the Deutsch-Anderson equation for each particle size band in each incremental length. The Deutsch-Anderson equation is given by

$$\eta = 1 - \exp(-A\omega/Q) \qquad (1)$$

where

η = the fractional collection efficiency,
A = the collection plate area,
ω = the migration velocity of the charged particles, and
Q = the gas volume flow rate.

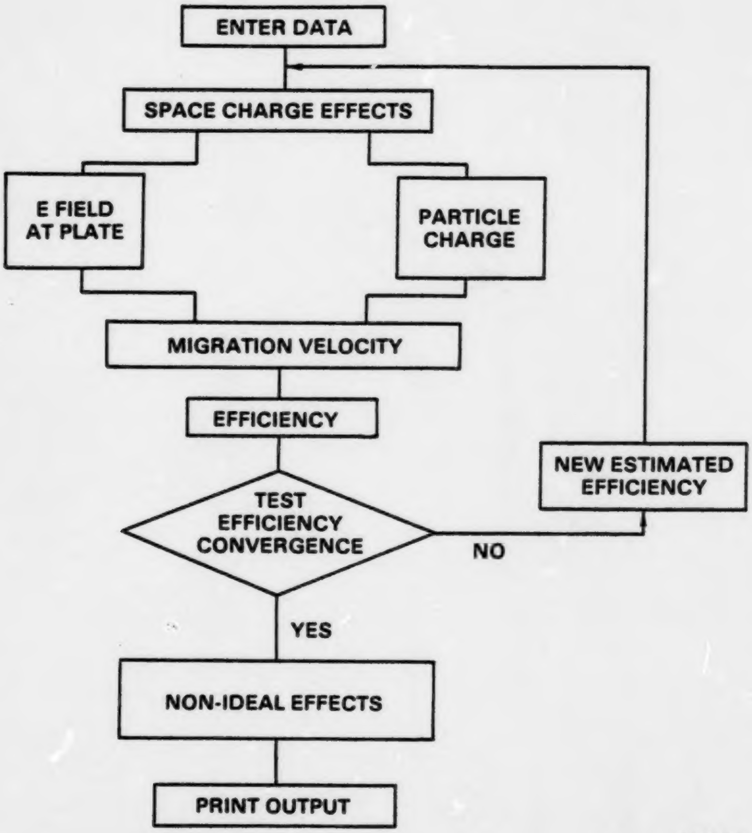

4877-182

Figure 1. Flow chart for the ESP Model.

The migration velocity is calculated from

$$\omega = qE_pC/6\pi au \qquad (2)$$

where

q = the charge of the particle,
E_p = the electric field at the plate,
C = the Cunningham slip correction factor,
a = the radius of the particle, and
u = the viscosity of the gas.

Thus, the calculation of collection efficiency requires the calculation of the charge for each particle size and of the electric field at the plate, in each incremental length. These quantities can be obtained quickly by estimation formulas or more rigorously by using a unipolar ionic charging theory (5) and a detailed analysis of the electric field in the interelectrode space of the precipitator.

In the particle charging calculation, the entire operating current density specified by the user is assumed to be useful for unipolar ionic charging. No allowance is made for back corona. In the rigorous charging calculation, the algorithm sums the time rates of charging for field charging (until the saturation limit is reached for a given particle size), charging by thermal diffusion of ions, and field-enhanced thermal diffusion charging. The algorithm calculates a fourth-order Runge-Kutta numerical solution to the differential equation for the charging rate. The charge acquired by an aerosol particle depends on the particle size, the density of ions, the exposure time, and the average electric field in the interelectrode space.

In the rigorous computation of the electric field at the plate, the ESP Model does not assume any explicit spatial distribution of suspended charged particles. Instead, the ESP Model performs a self-consistent iterative computation of the interelectrode space charge distribution in each computational length increment, including both ionic and particulate space charge. The algorithm simultaneously solves Poisson's equation and the current continuity equation in the interelectrode space. Starting with an estimate of space charge density at the corona electrode and the electrostatic potential distribution for wire-plate geometry, local values of electric potential and space charge density are computed alternately, one from the other, on a rectangular coordinate grid until convergence is obtained. The results at the boundary representing the collecting plate are then tested against the current density specified by the user. If the test fails, the estimate of space charge density at the corona electrode is adjusted and the whole procedure is repeated until the boundary condition is satisfied. This procedure requires the simplifying assumption that the average combined motions of ionic and particulate charge carriers can be described by a single effective mobility, reduced from the ionic mobility. The ESP Model is not sensitive to the geometrical details of different types of corona electrodes or different collecting plate baffles.

After the ideal collection efficiency is calculated, the ESP Model corrects the efficiency for various non-ideal effects. Corrections for gas sneakage and non-uniform gas velocity are applied by adjusting the migration velocity for each particle size band by a factor based on theoretical and experimental studies of a pilot-scale precipitator (6). Following this, the losses due to rapping reentrainment are calculated. This correction is based on the amount of mass collected in the last section of the precipitator. A fraction of the collected mass is fit to a log-normal size distribution and added by size bands to the dust penetration predicted by the ideal efficiency calculation. The collection efficiency is then recomputed based on the combined effluent. The log-normal size distribution used to describe the reentrained particles has default parameters of a 6 μm mass median diameter and a standard deviation of 2.5. Other size distribution data may be used in addition to these values if desired. However, the total mass of the reentrained particles is fixed by a relationship based on data derived from a study of rapping reentrainment in six utility fly ash precipitators (7).

In order to fit these calculations into a 48 kilobyte TRS-80, it was necessary to reduce the program in scope. A comparison of the features of the TRS-80 Model and Revision 3 of the main-frame model is presented in Table 1. Those functions which are included in the TRS-80 Model are divided into six programs. In addition, in order to fit the rigorous efficiency calculation into the TRS-80, it was necessary to reduce the sizes of some of the arrays, as shown in Table 2.

Four of the six programs apply directly to the collection efficiency calculation. These are shown in Figure 2. Three of these four programs must be used in order to calculate the efficiency. The programs are connected by data files stored on diskette, so that all of the programs need not be used in one session.

The first task in the use of the TRS-80 ESP Model is to enter data into the computer. The ESP Model requires a rather complete specification of the precipitator operating parameters. The necessary parameters are summarized in Table 3. These data are entered into the TRS-80 using the first program in the sequence, named DATA. This is an interactive data entry routine which prompts the user for data, displays the data on the screen, and allows the data to be easily changed. Figure 3 shows a sample data entry screen. This program also reads old data files so that the data can be updated. The final data from this routine is saved in a file for later use in the efficiency calculation.

As Figure 2 implies, the user has a choice of two routines for calculating the ideal collection efficiency. Program MAIN uses the rigorous calculations of electric field and particle charge. Program ESTIMATE calculates efficiency using much simpler estimations of field and charge. The difference in these routines is that the rigorous calculation is more accurate and takes much more time to run. Table 4 shows a comparison of calculation accuracy for one utility precipitator. The calculated results from the DEC 2020 computer are taken as the correct values. Note that in this case, the rigorous and estimated microcomputer calculations fall about equally on either side of the main-frame value. In other examples, the differences between the rigorous and estimated values have been much greater.

Table 5 shows the times required to run the data set used for Table 4. The rigorous run time is a factor of 16 greater than the estimation time for

TABLE 1. OPERATIONS PERFORMED BY TRS-80 ESP MODEL

Main-Frame Calculations	Availability in TRS-80
1. Inlet mass distribution	Yes
2. Charge on particles (estimation or rigorous)	Two separate programs
3. Field at plate (estimation or rigorous)	Two separate programs
4. Sneakage and non-uniform gas flow	Yes
5. Rapping reentrainment (empirical or dynamic)	Empirical only
6. Plume opacity	Separate program
7. Input data error check	No
8. Unknown electrical operating conditions	Separate program
9. Metric data	No

TABLE 2. ARRAY SIZES

Variable	TRS-80 Maximum	Main-Frame Maximum	Main-Frame Typical
Particle size bands	12	20	16
ESP electrical sections	5	10	4
ESP incremental lengths	30	99	40
Non-ideal conditions	5	15	3
Rapping data	2	10	1
Characters in title	45	80	40
Electric field calculation grid	8 x 8	15 x 15	10 x 10

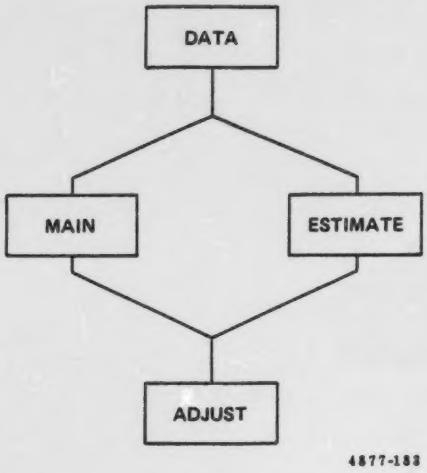

Figure 2. TRS-80 ESP Model program sequence.

TABLE 3. ESP MODEL INPUT PARAMETERS

1) Precipitator geometry in each gas passage of each electrical field.

2) Operating voltage and current in each electrical field.

3) Inlet aerosol parameters.
    - Gas temperature, pressure, viscosity
    - Gas velocity
    - Particle mass loading
    - Particle size distribution

4) Non-ideal correction parameters.
    - Number of baffled sections
    - Fractional gas sneakage past each baffled section
    - Normalized standard deviation of the gas velocity distribution

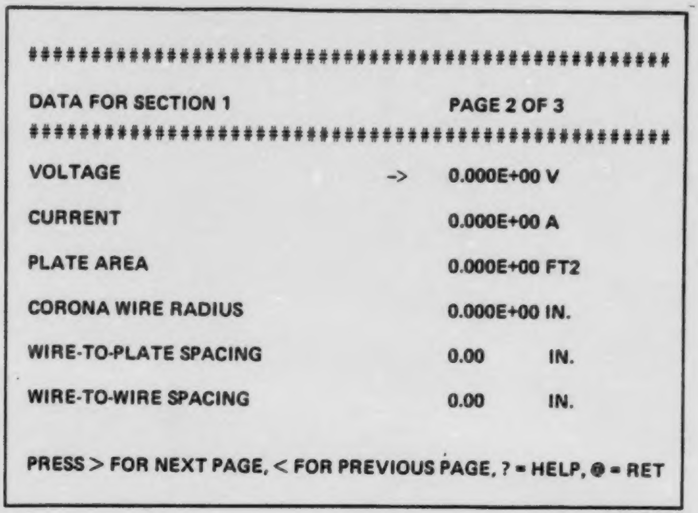

```
###################################################

DATA FOR SECTION 1                      PAGE 2 OF 3
###################################################
VOLTAGE                          ->     0.000E+00 V

CURRENT                                 0.000E+00 A

PLATE AREA                              0.000E+00 FT2

CORONA WIRE RADIUS                      0.000E+00 IN.

WIRE-TO-PLATE SPACING                   0.00      IN.

WIRE-TO-WIRE SPACING                    0.00      IN.

PRESS > FOR NEXT PAGE, < FOR PREVIOUS PAGE, ? = HELP, @ = RET
```

4877-184

Figure 3. Sample data screen for the TRS-80 ESP Model.

TABLE 4. CALCULATED RESULTS

Quantity	DEC 2020 Rigorous Calculation	TRS-80 Rigorous Calculation Value	TRS-80 Rigorous Calculation Error	TRS-80 Estimation Value	TRS-80 Estimation Error
No rap penetration, %	0.19	0.17	10	0.21	10
No rap efficiency, %	99.81	99.83	-	99.79	-
Penetration with rapping, %	0.32	0.30	6	0.35	9
Efficiency with rapping, %	99.68	99.70	-	99.65	-

TABLE 5. CALCULATION TIME COMPARISON

	DEC 2020	TRS-80
Rigorous calculation	3 min	3 hr
Estimation	11 sec	2 min

the DEC computer. But for the TRS-80, this difference is a factor of 90. In fact, the TRS-80 took about the same amount of time to run the estimation as the DEC did for the rigorous calculation. However, other factors inhibiting the use of a main-frame computer should be considered -- factors such as terminal availability, computer load, job priority, and job cost. Thus, in spite of the greater computer time, a microcomputer may be the instrument of choice. The choice of running a rigorous or estimated efficiency calculation must be determined on a case-by-case basis. Although the rigorous calculation is more accurate, there are many cases in which the accuracy difference is negligible. In such cases, the faster run time makes the estimation routine the procedure of choice.

The third routine in the program sequence shown in Figure 2 is ADJUST. This routine reads the data files produced by DATA and MAIN (or DATA and ESTIMATE). The data are then corrected for sneakage, non-uniform gas velocity, and rapping reentrainment. Finally the data are printed. ADJUST prints the full input data set, followed by particle charge data, precipitator outlet statistics by particle size band, and overall outlet statistics with and without rapping.

CALCULATION OF PLUME OPACITY

An additional program may be used to calculate plume opacity. This program, named OPAC, reads the data files created by DATA and MAIN (or DATA and ESTIMATE), makes the specified non-ideal corrections, and calculates opacity for each non-ideal data set. The only additional data needed are optical path length (stack diameter) and complex index of refraction (if different from the default value of 1.5 - 0.0i).

The mathematical relationships required to predict plume opacity were derived from the theory of light scattering and absorption by Gustov Mie in 1908 (8,9). These relationships, which are used in all opacity calculations, have been discussed in detail by Ensor (10). The equations have been tested against experimental data obtained under controlled laboratory conditions and found to be accurate to within a typical error of 5 percent in the total extinction coefficient. The major source of error in opacity calculations appears to be the accuracy of the particle size distribution used in the opacity calculation. Opacity is a sensitive function of particle size and concentration. Opacity calculations have been based on log-normal particle size distributions with varying degrees of accuracy. The present trend is to use a particle size histogram instead of a log-normal distribution, as precipitator effluents tend to deviate significantly from the log-normal curve. In this program, the plume opacity is calculated from the particle size histogram generated in the collection efficiency calculation.

Figure 4 compares calculated opacities with in-stack transmissometer readings made during field tests. These data are from tests of 11 pulverized-coal-fired power plants. To compare accuracy, opacities were calculated using both particle size histograms and log-normal curves. The particle size histograms were measured by cascade impactors during the field tests. Log-normal curves were then derived from the histograms. The opacity values calculated

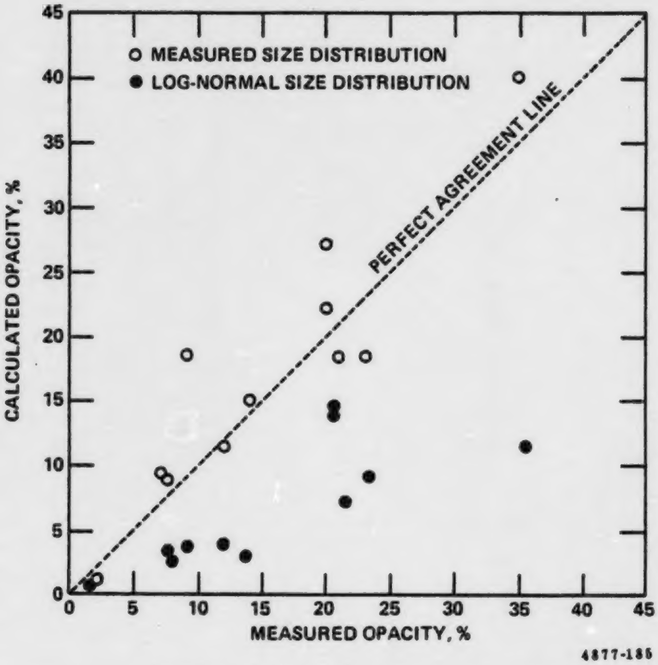

Figure 4. Calculated vs. measured opacity.

from the particle size histograms, shown by open circles in Figure 4, have an average error of 26 percent. The opacity values calculated from the log-normal curves, shown by closed circles in Figure 4, have an average error of 59 percent. The data comparison shown in Figure 4 clearly demonstrates the superiority of basing opacity calculations on particle size histograms.

ESTIMATION OF ELECTRICAL OPERATING CONDITIONS

Whenever possible, the electrical operating conditions used to model ESP efficiency should be based on field test data. However, for cases where this is not feasible, another program may be used to estimate the electrical operating points. The empirical approach used in this program is the result of a critical review and compilation of comprehensive field test data available to SRI, sponsored by the Electric Power Research Institute (11). The data on electrical operating conditions were restricted to cold-side fly ash precipitators. There were 17 complete data sets, obtained on 13 different precipitators at 12 different plant sites. The principal data consisted of V-I characteristic curves for each electrical section, the V-I operating point in each electrical section, and simultaneous in situ fly ash resistivity measurements. Fly ash resistivity was determined by the spark method, using the SRI point-plane resistivity probe. It should be emphasized that these data represent operating precipitators having a variety of electrode geometries, dirty electrodes, and particle-laden gases.

The relationship between the operating voltage and current density and the fly ash resistivity was developed by (1) obtaining a correlation between measured values of fly ash resistivity and estimated useful current density, and (2) obtaining a correlation between useful current density and operating voltage. The prediction of operating current density is based on a least-squares fit to the precipitator data for each electrical field. Figure 5 shows the data for the first electrical field. The solid line represents the least-squares fit. The dashed lines flanking the solid line represent the 90 percent confidence interval.

Empirical relations for useful current density, averaged over all electrical fields of a precipitator, have been given by H. J. Hall (12) and have been used to predict electrical operating points. The most conservative relation given by Hall corresponds to a restriction of the average electric field inside a fly ash layer on the collecting plate ($E = \rho J$) to less than 1 kV/cm. This line is superimposed on Figure 5. The more recent data show that this line is overly conservative for high-resistivity fly ash.

In the program named VI, the operating current densities are obtained from the specified ash resistivity and the least-squares fitted line for each field of the precipitator. Then another set of correlations is used to obtain the average interelectrode electric field in each precipitator field. The operating voltages are obtained by multiplying the average electric fields by the specified wire-to-plate spacing.

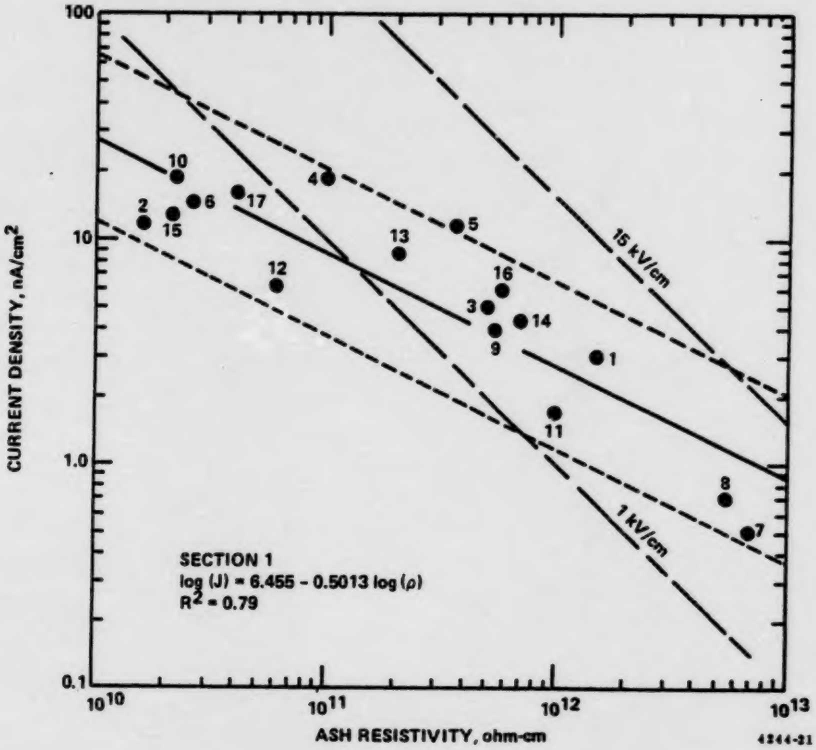

Figure 5. Current density vs. fly ash resistivity for section 1.

SUMMARY

The microcomputer programs described in this paper are written in FORTRAN specifically for the Radio Shack TRS-80 Model III or 4 computer. With the exception of program DATA, these programs may be used with any microcomputer which has a FORTRAN compiler. Program DATA uses routines which are specific to the TRS-80 computer. Transcribing this program to another computer would require extensive rewriting of the interactive screen portion of the program. An alternative approach would be to replace the interactive screen portion with statements which display the data in list form and ask for the number of the data item to be changed. This would be followed by an appropriate GO TO statement and prompt statements pertaining to that specific data item.

The functions of the six microcomputer programs described in this paper are included in the main-frame ESP Model. These functions are:

1. calculation of collection efficiency,
2. calculation of plume opacity, and
3. estimation of operating voltages and currents.

Table 6 summarizes the advantages and disadvantages of each of these calculations, as performed by the microcomputer. A major advantage is that these calculations have been successfully tested against field data. The accuracy of the collection efficiency calculation compared to measured efficiencies is discussed in the following paper (13). The accuracy of the opacity calculation is discussed in this paper and summarized in Figure 4. The V-I curve generator is an empirical relationship derived from fly ash precipitators operating under typical conditions with dirty electrodes and particle-laden gases. These programs allow a microcomputer user to simulate an existing or planned electrostatic precipitator under realistic operating conditions.

REFERENCES

1. Gooch, J. P., J. R. McDonald, and S. Oglesby, Jr. A Mathematical Model of Electrostatic Precipitation. EPA-650/2-75-037, U.S. EPA, IERL, Research Triangle Park, NC, 1975.

2. McDonald, J. R. A Mathematical Model of Electrostatic Precipitation (Revision 1): Volumes I and II. EPA-600/7-78-111a,b, U.S. EPA, IERL, Research Triangle Park, North Carolina, 1978.

3. Mosley, R. B., M. H. Anderson, and J. R. McDonald. A Mathematical Model of Electrostatic Precipitation (Revision 2). EPA-600/7-80-034, U.S. EPA, IERL, Research Triangle Park, NC, 1980.

4. Faulkner, M. G., and J. L. DuBard. A Mathematical Model of Electrostatic Precipitation (Revision 3): Volumes I, II, and Source Code Tape. EPA-600/7-84-069a,b,c. (NTIS PB84-212-679, PB84-212-687, PB84-232-990). U.S. EPA, IERL, Research Triangle Park, NC, 1982.

TABLE 6. PROGRAM ADVANTAGES AND DISADVANTAGES

EFFICIENCY MODEL
  Advantages
- Menu driven data entry
- Allows different electrical conditions in each ESP field
- Broken down into logical program blocks
- Accuracy tested against field test data

  Disadvantages
- Longer run time than main-frame version
- Limited memory size

OPACITY MODEL
  Advantages
- Very little input data (most data is generated by efficiency model)
- Accuracy tested against field test data

  Disadvantages
- Requires ESP efficiency model

V-I CURVE GENERATOR
  Advantages
- Derived from field test data
- Estimates electrical operating points in each ESP field

  Disadvantages
- Applies only to cold-side fly ash precipitators

5. Smith, W. B., and J. R. McDonald. Development of a Theory for the Charging of Particles by Unipolar Ions. J. Aerosol Sci., 7:151-166, 1976.

6. Preszler, L., and T. Lajos. Uniformity of the Velocity Distribution of a Flowing Gas Upon Entry into an Electrostatic Precipitator. Staub Reinhalt. Luft (in English), 32(11):1-7, 1972.

7. Gooch, J. P., and G. H. Marchant, Jr. Electrostatic Precipitator Rapping Reentrainment and Computer Model Studies. EPRI Report FP-792, Electric Power Research Institute, Palo Alto, CA, August 1978.

8. Mie, G. Beitrage zur Optik truber Medien, Speziell Kolloidaler Metallosunge. Ann. Physik. 25:377-455, 1908.

9. van der Hulst, H. C. Light Scattering by Small Particles. John Wiley and Sons, New York, 1957.

10. Ensor, D. S. Smoke Plume Opacity Related to the Properties of Air Pollutant Aerosols. Ph.D. Dissertation, University of Washington, 1972.

11. DuBard, J. L., and R. F. Altman. Prediction of Electrical Operating Points for Use in a Precipitator Sizing Procedure. EPRI Report CS-2908, Electric Power Research Institute, Palo Alto, CA, April 1983.

12. Hall, H. J. Trends in Electrical Energization of Electrostatic Precipitators. Electrostatic Precipitator Symposium, Birmingham, AL, February 23-25, 1971.

13. DuBard, J. L., and R. F. Altman. Analysis of Error in Precipitator Performance Estimates. The Fifth Symposium on the Transfer and Utilization of Particulate Control Technology, Kansas City, MO, August 27-30, 1984.

ANALYSIS OF ERROR IN PRECIPITATOR PERFORMANCE ESTIMATES

by: J. L. DuBard
Southern Research Institute
Birmingham, Alabama 35255

R. F. Altman
Electric Power Research Institute
Chattanooga, Tennessee 37411

ABSTRACT

The EPA/SRI mathematical model of electrostatic precipitation has been analyzed for the propagation of error in estimated input data and for the agreement between measured and computed collection efficiency, using both measured and estimated input data. The estimated aerosol data and electrical data are based on measurements performed at 33 utility boilers and 13 utility fly ash precipitators. The numerical parameters used to make approximate corrections for non-ideal gas flow are based on a comparison of 18 sets of measured and computed efficiency, obtained for precipitators of SCA from 135 to 745 ft^2/kACFM. Numerical confidence intervals in the efficiency computed using estimated input data are established for four test cases with fly ash resistivity of 5E10 and 1E12 ohm-cm and SCA of 250 and 500 ft^2/kACFM. In each case, the lower 90% confidence margin in computed collection efficiency requires an increase in SCA of approximately 125 ft^2/kACFM to attain the nominal collection efficiency.

INTRODUCTION

The electrostatic precipitator performance model (ESP MODEL) is described in documentation available from the National Technical Information Service (1). This paper describes an error analysis of the computation of fly ash collection efficiency. The numerical specification of error makes the ESP MODEL more reliable for users. The objectives of this work were to develop

1) a numerical procedure for estimating input data for the computation:

   - fly ash particle size distribution and inlet mass loading,
   - operating voltage and current in each electrical field,
   - non-ideal gas flow correction parameters, and

2) a numerical specification of the effect of error in estimated input data on the error in computed collection efficiency.

The first part of this paper describes tests of the intrinsic accuracy of the numerical simulation of electrostatic precipitation. The measured collection efficiencies from 18 field tests of utility fly ash precipitators are compared with ESP MODEL computations, using measured input data for fly ash aerosol parameters and electrical operating points. This comparison yields an objective determination of the parameters used by subroutine ADJUST to make approximate corrections for non-ideal gas flow.

The second part of this paper describes an analysis of the propagation of error from the input data to the computed collection efficiency. This procedure requires a means of estimating input data for fly ash aerosol parameters and electrical operating points, and a numerical determination of the uncertainty in those estimates. The error analysis is based on compilations and correlations of the precipitator data base available to Southern Research Institute. Finally, the input data are sorted into five groups that are approximately uncorrelated mathematically, in order to obtain a numerical estimate of the uncertainty in computed collection efficiency.

ESP MODEL COMPUTATIONS WITH MEASURED INPUT DATA

The precipitator performance data base is summarized in Table 1, in order of increasing specific collection area (SCA) of the precipitators. Table 1 presents 18 different tests of 14 different cold-side utility fly ash precipitators. Three of the precipitators were tested with and without flue gas conditioning. One precipitator was tested at both normal and reduced boiler load. Using measured input data for fly ash aerosol parameters and electrical operating points, and two different sets of correction parameters for non-ideal gas flow, the ESP MODEL was executed for each precipitator.

TABLE 1. DATA BASE FOR PRECIPITATOR COLLECTION EFFICIENCY

Test Number	Coal Type	Gas T °F	Resistivity ohm-cm	Duct Inches	SCA ft^2/kACFM	Efficiency percent
3	SB	260	5E11	9	135	77.
4	SB	260	1E11	9	135	97.5
22	B	260	2E9	9	150	95.5
21	B	260	2E9	9	155	99.7
27	L	370	1E10	9	165	98.5
7	SB	250	7E12	9	175	91.3
25	B	285	2E9	9	175	88.
26	B	260	2E9	9	220	99.3
2	B	315	2E10	11	245	99.6
10	B	315	2E10	10	255	99.8
11	SB	320	1E12	9	310	88.
12	SB	320	6E10	9	310	99.1
5	B	350	4E11	9	360	99.90
6	B	350	3E10	9	360	99.96
23	L	330	2E10	12	390	99.97
13	SB	300	2E11	12	570	99.92
9	SB	220	5E11	9.75	585	99.8
8	SB	300	6E12	12	745	99.7

A user of the ESP MODEL must specify the fractional gas sneakage (S) in each electrical field and the normalized standard deviation ($\sigma_{gas} = SD/v_{avg}$) of the inlet gas velocity distribution. Conservative values of those parameters have been estimated as S = 0.10 and $\sigma_{gas} = 0.25$. Figure 1 shows the comparison of measured and computed collection efficiency using those values. The horizontal error bars show the range of scatter, day-to-day, in the measurements of collection efficiency.

The performance of high-efficiency precipitators is consistently underestimated in Figure 1. The plants with measured collection efficiency less than about 97% are outliers, as well as Plant 9. Plants 3,7, 9, and 11 operated in severe back corona. Reduced values of useful voltage and current density (estimated from the measured V-I curves) were used in the mathematical modeling. However, the computed collection efficiency remained higher than the measured collection efficiency. Plant 4 is the same as Plant 3, and Plant 12 is the same as Plant 11, but tested with flue gas conditioning to eliminate the back corona problem. Plants 22 and 25 suffered from excessive reentrainment of collected fly ash. Plant 26 is the same as Plant 22, but tested under low-load conditions to eliminate the reentrainment problem. Figure 1 shows that when the operating difficulties with back corona and reentrainment were removed, the comparison between measured and computed collection efficiency became consistent with the general pattern of data.

Modern, high-efficiency precipitators may be designed to reduce the gas sneakage to as little as 5%, and a more typical measure of the inlet gas velocity distribution is about 15% normalized standard deviation. Figure 2 shows the comparison of measured and computed collection efficiency, using $S = 0.10$ and $\sigma_{gas} = 0.15$. (The vertical error bars in Figure 2 are the subject of the second part of this paper.) In this figure, the data points above 97% are scattered closely about the perfect agreement line. Below 97%, however, the precipitator performance is degraded by non-ideal operating conditions that are not well simulated in a routine execution of the ESP MODEL. This analysis of precipitator performance data leads to two conclusions.

1) The comparisons in Figures 1 and 2 give an indication of the intrinsic accuracy of the numerical simulation of electrostatic precipitation. With reliable input data, the ESP MODEL reliably computes the precipitator collection efficiency.

2) The numerical approximations in subroutine ADJUST give a reliable simulation of the degrading effects of non-ideal gas flow. The comparisons in Figures 1 and 2 give an objective estimate of appropriate numerical values of S and σ_{gas} that are consistent with typical gas flow in modern precipitators.

ESP MODEL COMPUTATIONS WITH ESTIMATED INPUT DATA

COMPILATION OF PRECIPITATOR DATA

The operating data that are most critical for a numerical simulation of electrostatic precipitation are the fly ash aerosol properties and the electrical operating points. The operating data available to Southern Research Institute have been described in detail in published EPRI conference proceedings (2,3). Measurements of fly ash particle size distribution and total mass loading were obtained at 33 pulverized-coal-fired utility boilers. The measurements were correlated with boiler operating parameters, ultimate coal analyses, and chemical analyses of the flue gas and fly ash. The T-R secondary operating voltage and current in each electrical field, and the V-I characteristic curves, were obtained in 17 tests of 13 cold-side utility fly ash precipitators. The electrical data were compared with simultaneous in situ measurements of fly ash resistivity, using a point-plane probe and the spark method.

The data for inlet mass loading are plotted in Figure 3 versus the percent ash in the coal. The data for inlet particle size distribution were reduced to the form of cumulative percent mass contained in particles of diameter less than 1, 2, 5, and 10 μm. The average values of cumulative percent mass are shown in Figure 4 for the two separate groups of fly ashes from bituminous and

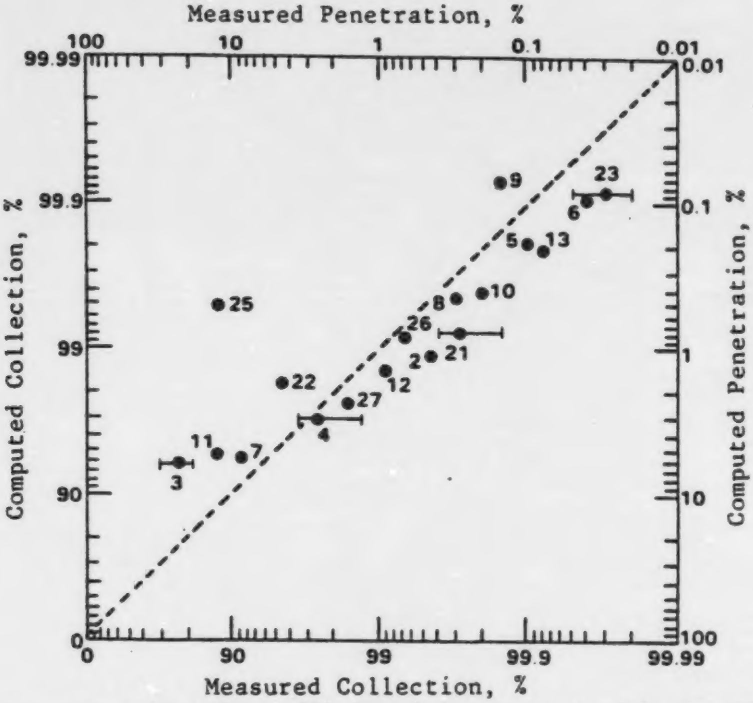

Figure 1. Measured collection efficiencies compared with the ESP MODEL, using measured input data, for 10% gas sneakage and σ_{gas} = 0.25.

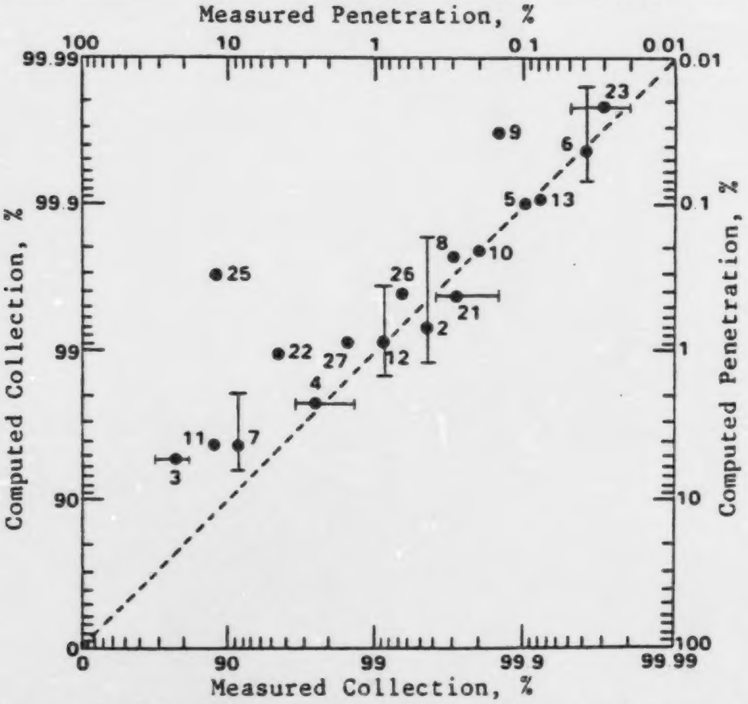

Figure 2. Measured collection efficiences compared with the ESP MODEL, using measured input data, for 5% gas sneakage and σ_{gas} = 0.15.

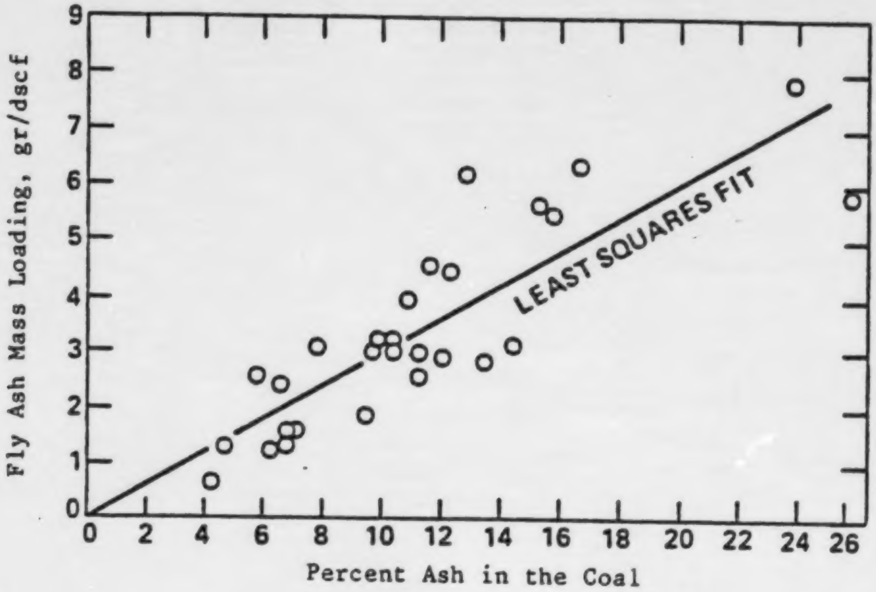

Figure 3. Fly ash mass loading versus percent ash in the coal.

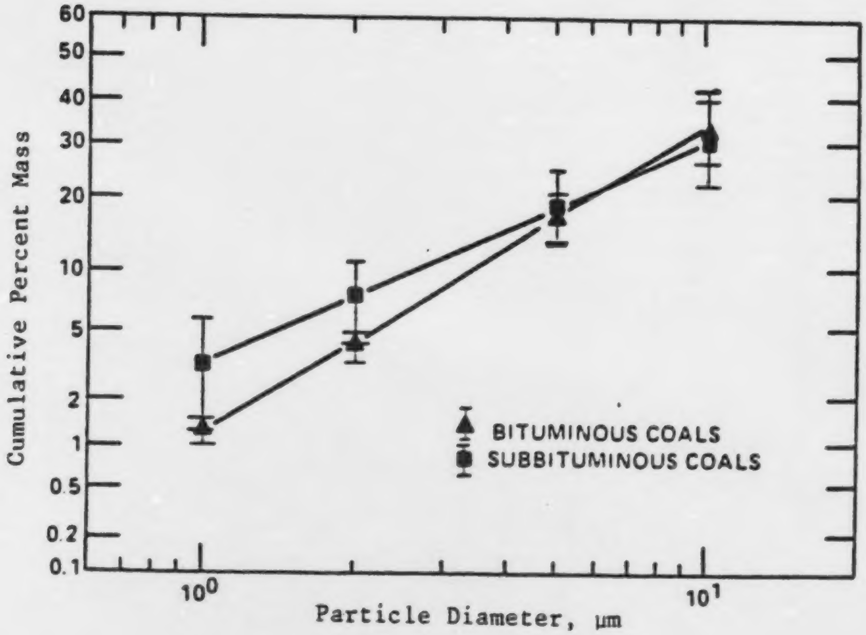

Figure 4. Fly ash particle size distributions for bituminous and subbituminous coals.

subbituminous coals. For each group, the average values of cumulative percent mass lie almost exactly along a log-normal straight line. However, there is a lot of scatter in the fly ash data from subbituminous coals, as shown by the wide error bars. These data are presented in more detail in Figure 7.

The values of useful current density in the inlet electrical field are shown in Figure 5 versus in situ fly ash resistivity. A least-squares-fitted straight line and its 90% confidence interval (given by 1.645 times the standard deviation of the fitted ordinate intercept) are superimposed on the data. The operating voltage in each electrical field was divided by the wire-plate spacing to obtain an average interelectrode electric field for the electrical data correlation. The data for the inlet electrical field are shown in Figure 6. Given a specification of precipitator wire-plate spacing, the fitted straight line in Figure 6 becomes in effect an average V-I characteristic curve for the inlet electrical field. With a further specification of fly ash resistivity, the fitted straight line in Figure 5 determines the operating point on that V-I curve. Data of the sort shown in Figures 5 and 6 form the basis of the estimation procedure for electrical operating points.

The field test data for fly ash aerosol properties and electrical operating points, and the correlations of data, have been described in detail (2,3). Correlations of the data provide a means of estimating input data for the ESP MODEL, and a means of estimating uncertainty in the input data. However, the estimation procedure is influenced by the mathematical method of the error analysis.

METHOD OF THE ERROR ANALYSIS

The penetration (P) of a fly ash precipitator, computed by the ESP MODEL, is a dependent function of the several input data,

$$P_i = f(x_i, y_i, z_i, ---),$$

where the subscript denotes the ith execution of the ESP MODEL. The variables $\{x, y, z, ---\}$ represent input data such as particle mass loading, electrical operating points, and gas temperature. A sample of N independent determinations of penetration is obtained (conceptually) by allowing random fluctuations about the point $\{\bar{x}, \bar{y}, \bar{z}, ---\}$ in the multi-dimensional coordinate space of the several input data. The probability of obtaining any particular result $P_i = f(x_i, y_i, z_i, ---)$ from a particular execution of the ESP MODEL is assumed to be governed by the "normal" or gaussian probability distribution. The same probability distribution is assumed to govern the random fluctuations in each of the several input data. The sample mean value of penetration is given approximately by $\bar{P} = f(\bar{x}, \bar{y}, \bar{z}, ---)$. The sample variance in penetration is given by

$$\sigma_P{}^2 = \frac{1}{N-1} \sum_{i=1}^{N} (P_i - \bar{P})^2 .$$

The fluctuations in P can be calculated approximately by writing a Taylor series expansion of P about the point $\{\bar{x}, \bar{y}, \bar{z}\ ---\}$.

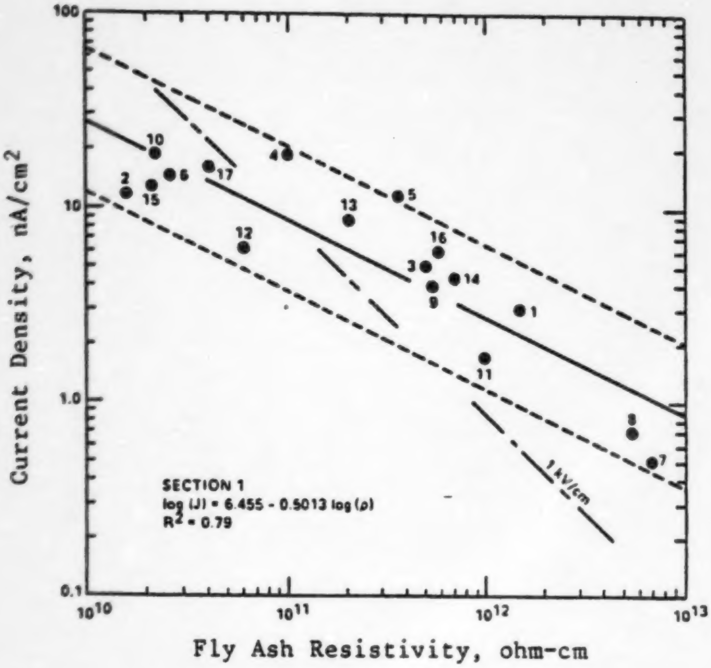

Figure 5. Current density versus the fly ash resistivity in the first electrical field.

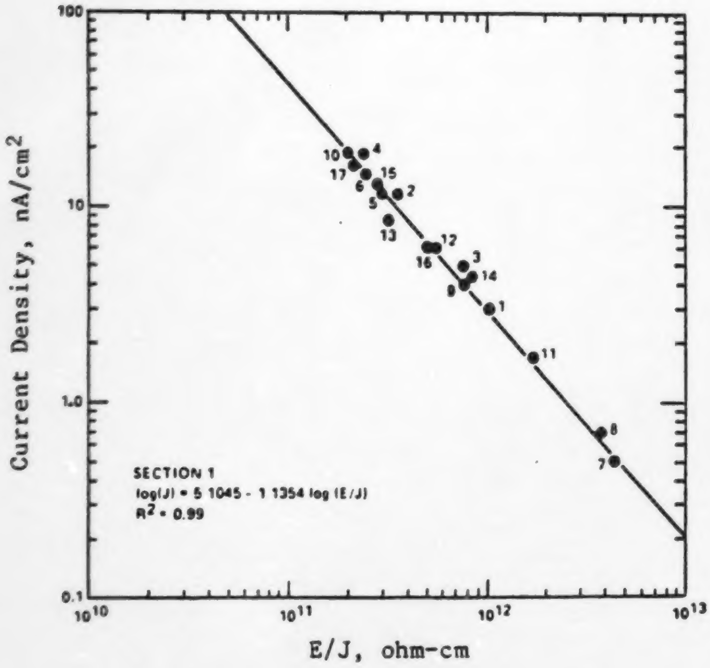

Figure 6. Current density versus the effective interelectrode ohm-cm of the first electrical field.

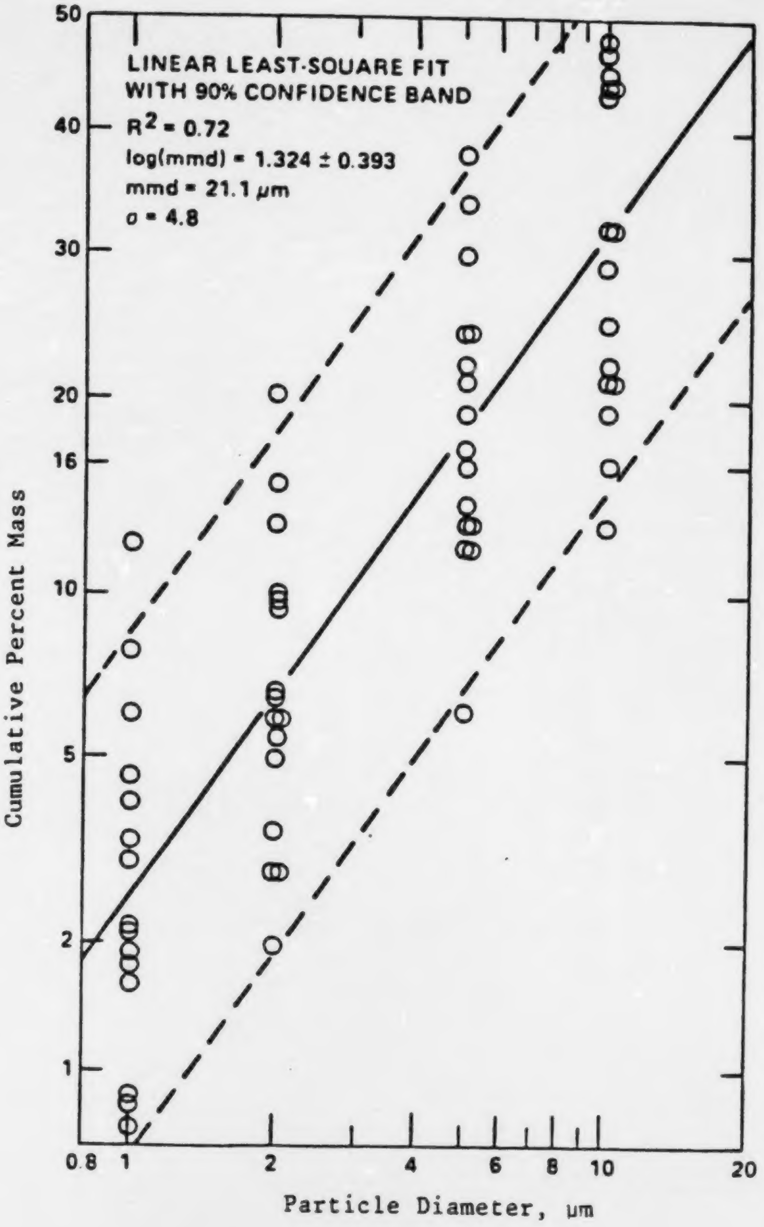

Figure 7. Particle size distributions for fly ashes from 16 subbituminous coals.

$$P_i - \bar{P} = (x_i - \bar{x}) \frac{\partial P}{\partial x} + (y_i - \bar{y}) \frac{\partial P}{\partial y} + (z_i - \bar{z}) \frac{\partial P}{\partial z} + ---,$$

where the partial derivatives are evaluated at $\{\bar{x}, \bar{y}, \bar{z}, ---\}$. This expression must be squared and summed in order to calculate the sample variance in penetration. The sample variance is assumed to be approximately the same as the square of the standard deviation appearing in the normal probability distribution of all determinations of penetration.

In the process of squaring and summing, terms involving $(x_i - \bar{x})^2$ are related to the sample variance in each ESP MODEL input parameter (each independent variable) as

$$\sigma_x{}^2 = \frac{1}{N-1} \sum_{i=1}^{N} (x_i - \bar{x})^2 .$$

If the independent variables are not correlated in their fluctuations, all cross-product terms vanish in the calculation of $\sigma_p{}^2$, and

$$\sigma_p{}^2 = \sigma_x{}^2 \left(\frac{\partial P}{\partial x}\right)^2 + \sigma_y{}^2 \left(\frac{\partial P}{\partial y}\right)^2 + \sigma_z{}^2 \left(\frac{\partial P}{\partial z}\right)^2 + ---.$$

Some input data to the ESP MODEL are obviously correlated -- for example, flue gas temperature and fly ash resistivity (which influences the electrical operating points.) Other input data, such as inlet particle mass loading and negative ion mobility, are obviously uncorrelated. The error analysis of the ESP MODEL proceeds by defining five groups of input data, each of which is approximately independent of the other groups in its effect on the computed penetration.

1) Inlet mass loading.
2) Negative ion mobility in the flue gas.
3) Inlet particle size distribution (mmd and σ of a log-normal distribution).
4) Flue gas temperature (with correlated fluctuations in fly ash resistivity, inlet mass loading, flue gas pressure and viscosity, negative ion mobility, and flue gas velocity).
5) Fly ash resistivity (with correlated fluctuations in operating voltage and current density in each electrical field).

With this approximation, the calculation of variance in the penetration is a simple sum of five numerical terms, each of the form $\sigma_x{}^2(\partial P/\partial x)^2$. Each partial derivative is evaluated at the nominal values of ESP MODEL input data $(\bar{x}, \bar{y}, \bar{z}, ---)$ for a specified test-case precipitator.

Four test-case precipitators were chosen to represent approximately most existing precipitator applications to pulverized-coal-fired utility boilers in the United States. The four cases are listed in Table 2. The four cases are listed in order of increasing value of the nominal collection efficiency $(100 - \bar{P})$ computed using nominal values $(\bar{x}, \bar{y}, \bar{z}, ---)$ of the ESP MODEL input data. The nominal input data are listed in Table 3. All four test cases represent cold-side precipitators with 9-inch plate spacing.

TABLE 2. TEST CASES FOR THE SENSITIVITY ANALYSIS OF THE ESP MODEL

Case	SCA (ft^2/kACFM)	Coal	Resistivity (ohm-cm)	Efficiency (%)
1	250	Subbituminous	1×10^{12}	95.6
2	250	Bituminous	5×10^{10}	99.1
3	500	Subbituminous	1×10^{12}	99.7
4	500	Bituminous	5×10^{10}	99.97

TABLE 3. NOMINAL INPUT DATA FOR THE SENSITIVITY ANALYSIS OF THE ESP MODEL

1. Mechanical Parameters		
Number of Electrical Sections	3(SCA 250 ft^2/kACFM) 6(SCA 500 ft^2/kACFM)	
Electrical Section Length	9 ft	
Collection Area per Section	33,333 ft^2	
Wire-Wire Spacing	6 in.	
Plate-Plate Spacing	9 in.	
2. Electrical Parameters		
Ash Resistivity, ohm-cm	5×10^{10}	1×10^{12}
Current Density, $\mu A/ft^2$		
Section 1	12	2.5
Section 2	17	3.5
Section 3	19	6.0
Operating Voltage, kV		
Section 1	41	34
Section 2	40	33
Section 3	38	33
3. Inlet Aerosol Parameters		
Gas Temperature	300°F	
Gas Velocity	5 ft/s	
Gas Flow	400,000 ACFM	
Inlet Mass Loading	3.0 gr/SCF (2.1 gr/ACF)	
Particle Size Distribution		
Ash from Bituminous Coals	MMD = 16.3 μm, $\sigma = 3.4$	
Ash from Subbituminous Coals	MMD = 21.1 μm, $\sigma = 4.8$	
4. Non-Ideal Correction Parameters		
Gas Sneakage per Electrical Section	$S = 0.10$	
Gas Velocity Distribution	$\sigma_{gas} = 0.25$	

Of the five terms in each of four calculations of variance in the penetration, an example is given here of the one term representing the inlet particle size distribution, for Case 3. This test case is a moderately large precipitator (500 ft^2/kACFM) collecting high-resistivity fly ash (1E12 ohm-cm) from a western subbituminous coal. The particle size distribution data from Figure 4 are shown in individual detail in Figure 7, along with the linear least-squares-fitted mean and 90% confidence interval.

The sensitivity of the ESP MODEL computation to the inlet mass loading of fine particles is illustrated in Figure 8. The large difference in the two curves in Figure 8 does not result entirely from the difference in particle size distribution, but rather mostly from the different nominal values of electrical operating point. That is, bituminous coal was associated with moderate-resistivity fly ash, 5E10 ohm-cm, and subbituminous coal with high-resistivity fly ash, 1E12 ohm-cm. Figure 8 shows the computed penetration versus the cumulative percent mass contained in particles of diameter less than 2 μm, only to illustrate the importance of the inlet particle size distribution. This set of curves was not actually used in the error analysis.

For the error analysis, the logarithm of the mass median diameter was treated as the independent mathematical variable. That is, the standard deviation of the log-normal particle size distribution was fixed at the fitted value of 4.8; while the log-normal distribution was allowed to fluctuate within the 90% confidence interval in log(MMD). This method fixed the slope of the solid line in Figure 7; while shifting the line sideways in the range between the dashed lines. From Figure 7, the 90% confidence interval in log(MMD) is ± 0.393, where the horizontal decade from 1 μm to 10 μm represents one unit in log(MMD). Thus, an estimate of the standard deviation in log(MMD) is 0.393/1.645 = 0.239. The variance is the square of this number.

A curve of computed penetration versus mass median diameter is shown in Figure 9. The penetration for fly ash from subbituminous coals is given along the right-hand vertical axis. The nominal value is about 0.003, corresponding to the collection efficiency of 99.7% listed for Case 3 in Table 2. The partial derivative required for this numerical example is given by the slope of a straight line drawn tangent to the curve at the nominal operating point marked by a triangle in Figure 9. The value of that slope is $\partial P/\partial \log(MMD) = -0.00895$. Thus, the numerical value of this one term in the calculation of the variance in penetration is $(0.239)^2(-0.00895)^2 = 4.58E-06$. This number appears in the summary of results for Case 3 in Table 4.

RESULTS OF THE ERROR ANALYSIS

The numerical components of overall error in the ESP MODEL computation are listed in Table 4. Errors arising from uncertainty in the estimated data for inlet mass loading and negative ion mobility were computed for only two cases. Table 4 shows that these two components contribute little to the overall error. Far more significant are the uncertainties in estimates of the inlet particle size distribution, the fly ash resistivity (as it affects the electrical operating points) and the flue gas temperature (as it affects the fly ash resistivity and electrical operating points.) These calculations demonstrate

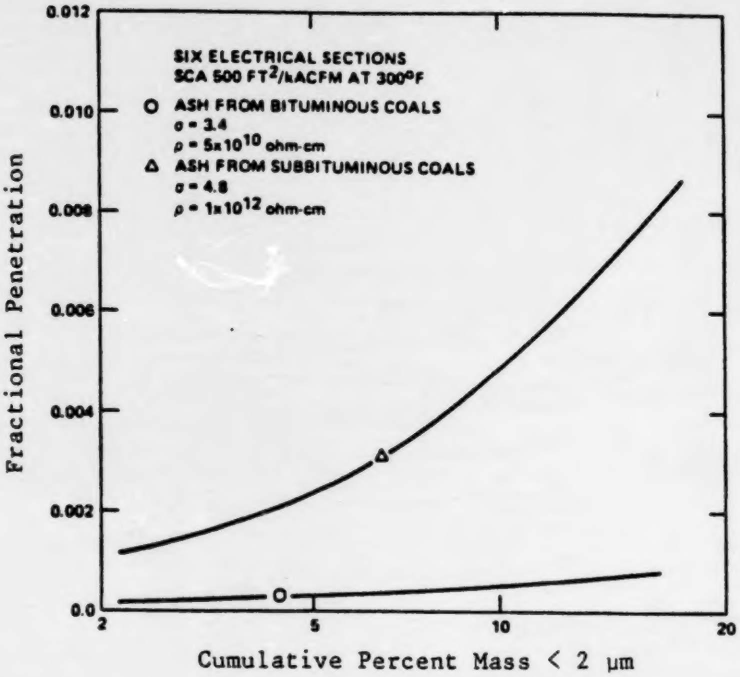

Figure 8. Fractional penetration in a test-case precipitator (500 ft^2/kACFM) versus cumulative percent mass < 2 µm.

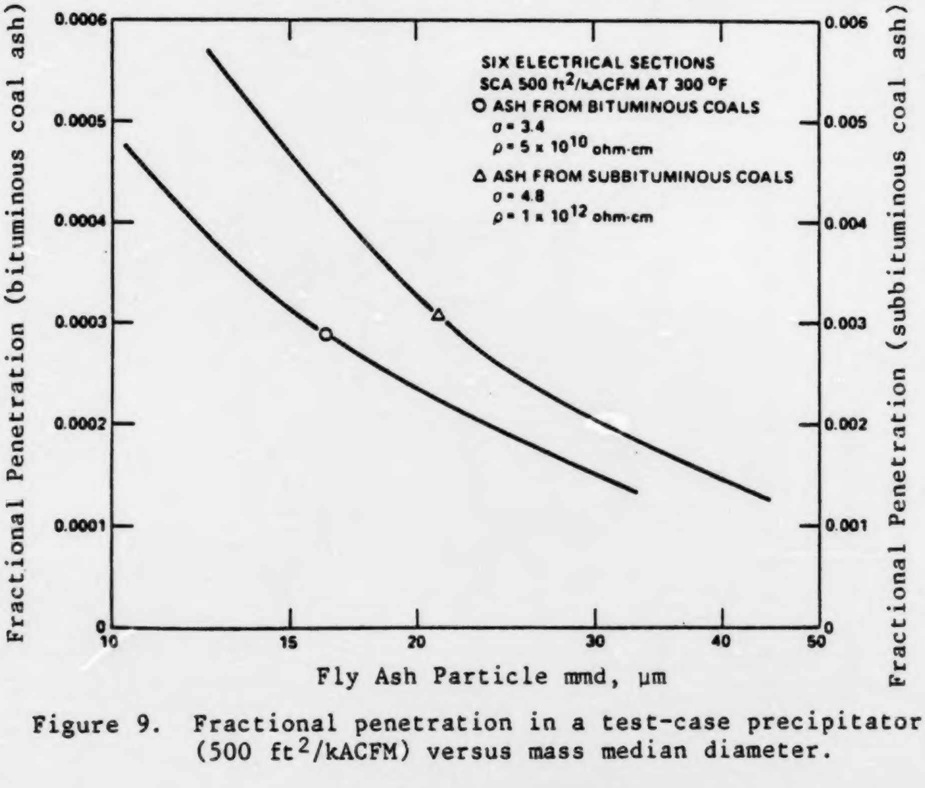

Figure 9. Fractional penetration in a test-case precipitator (500 ft^2/kACFM) versus mass median diameter.

TABLE 4. RESULTS OF THE ERROR ANALYSIS OF THE ESP MODEL

Case	1	2	3	4
SCA	250	250	500	500
Resistivity	1E12	5E10	1E12	5E10
	$\sigma_x^2 \ (\partial P/\partial x)^2$			
Inlet Mass Loading		1.03 E-7		1.80 E-10
Negative Ion Mobility		3.32 E-7		3.72 E-9
Inlet Particle Size	6.30 E-4	5.88 E-6	4.58 E-6	7.03 E-9
Gas Temperature	1.31 E-5	3.73 E-6	1.08 E-7	6.46 E-9
Ash Resistivity	5.69 E-4	5.18 E-5	5.33 E-6	1.40 E-7
$\sigma_p^2 = \sum \sigma_x^2 \ (\partial P/\partial x)^2$	1.21 E-3	6.19 E-5	1.00 E-5	1.57 E-7
Efficiency	95.6%	99.1%	99.7%	99.97%
Penetration	0.0441	0.0087	0.00309	0.00029
$0.6745\sigma_p$	0.0235	0.0053	0.00213	0.00027
$1.6449\sigma_p$	0.0573	0.0129	0.00521	0.00065

that the ESP MODEL computation of collection efficiency is not very sensitive to the value of inlet mass loading, within the range of fly ash data shown in Figure 3. That is, for fixed values of other data, the outlet mass loading will vary approximately in proportion to the inlet mass loading. However, much higher values of inlet mass loading (as, for example, from a cement kiln or Kraft recovery boiler) can have a very strong adverse effect on the electrical operating points.

The calculations of error for bituminous coal and moderate-resistivity fly ash (Cases 2 and 4) show that the variance in penetration is dominated by the uncertainty in the estimate of fly ash resistivity. The uncertainty in fly ash resistivity is due in part to an uncertainty in the effect of naturally occurring SO_3 vapor in the flue gas. This source of error does not enter into the calculations for Cases 1 and 3. The equilibrium concentration of SO_3 vapor is assumed to be zero in the flue gas from combustion of western subbituminous coals. In Cases 1 and 3, the three components of variance in the penetration are comparable within a factor of two.

Reading left-to-right across the calculated values of σ_p^2 in Table 4, the absolute magnitude of the variance decreases by four orders of magnitude. As the penetration decreases, the rate of change in penetration with changes in the ESP MODEL input data also decreases. In other words, these calculations demonstrate that more efficient precipitators have more certainty in a computation of their efficiency, using estimated precipitator operating data.

CONCLUSIONS

One conclusion from the error analysis can be illustrated with the vertical error bars superimposed on the data points in Figure 2. From a comparison of Tables 1 and 2, the measured data from precipitator Test #7 are fairly similar to the hypothetical data for Case 1 of the error analysis. Precipitator Tests #2 and #12 can be compared with Case 2, and precipitator Test #6 with Case 4. The variance in penetration of the test-case precipitators, computed from estimated operating parameters, can be applied to the penetration values in Figure 2 computed from measured operating parameters. This procedure yields the vertical error bars which show the probable error, or 50% confidence interval, in computed penetration. A comparison of vertical and horizontal error bars leads to the conclusion that the probable error in computing the precipitator collection efficiency, using estimated input data for the ESP MODEL, is comparable to the day-to-day scatter in measurements.

The results of the error analysis were used to estimate the additional plate area necessary to compensate for the uncertainty in the collection efficiency computed by the ESP MODEL. A utility fly ash precipitator was assumed to have been designed and built using estimated operating parameters. The measured emissions were assumed to exceed the designed emissions at the 90% confidence limit in computed penetration. This scenario was simulated with the ESP MODEL, for each of the four test-case precipitators, by using input data to represent higher-than-expected values of fly ash resistivity and fine particle concentration. Then, the SCA of each precipitator was increased until the designed performance level was recovered. For the two test cases with SCA 250 ft^2/kACFM constructed, a 45% increase in SCA was necessary to recover the designed performance level. For SCA 500 ft^2/kACFM constructed, 25% to 30% more SCA was necessary., Thus, in all four test cases, the estimated add-on SCA was about 125 ft^2/kACFM. For SCA 500 ft^2/kACFM, the computations are plotted in Figure 10. Figure 10 shows also how the Matts-Ohnfeldt approximation (using exponent $k = 0.5$) underestimates the increase in collection efficiency with large increases in SCA. The conclusion is that the lower 90% confidence limit in collection efficiency, computed from estimated precipitator operating parameters, corresponds to a design margin of approximately 125 ft^2/kACFM.

REFERENCES

1. Faulkner, M. G., and J. L. DuBard. A Mathematical Model of Electrostatic Precipitation (Revision 3): Volumes I, II, and Source Code Tape. NTIS PB84-212-679, PB84-212-687, and PB84-232-990. US EPA, IERL, Research Triangle Park, NC, 1982.

2. DuBard, J. L., and R. F. Altman. Prediction of Electrical Operating Points for Use in a Precipitator Sizing Procedure. EPRI Report CS-2908, Electric Power Research Institute, Palo Alto, CA, April 1983.

3. Dahlin, R. S., and R. F. Altman. Prediction of Mass Loading and Particle Size Distribution for Use in a Precipitator Sizing Procedure. Ibid.

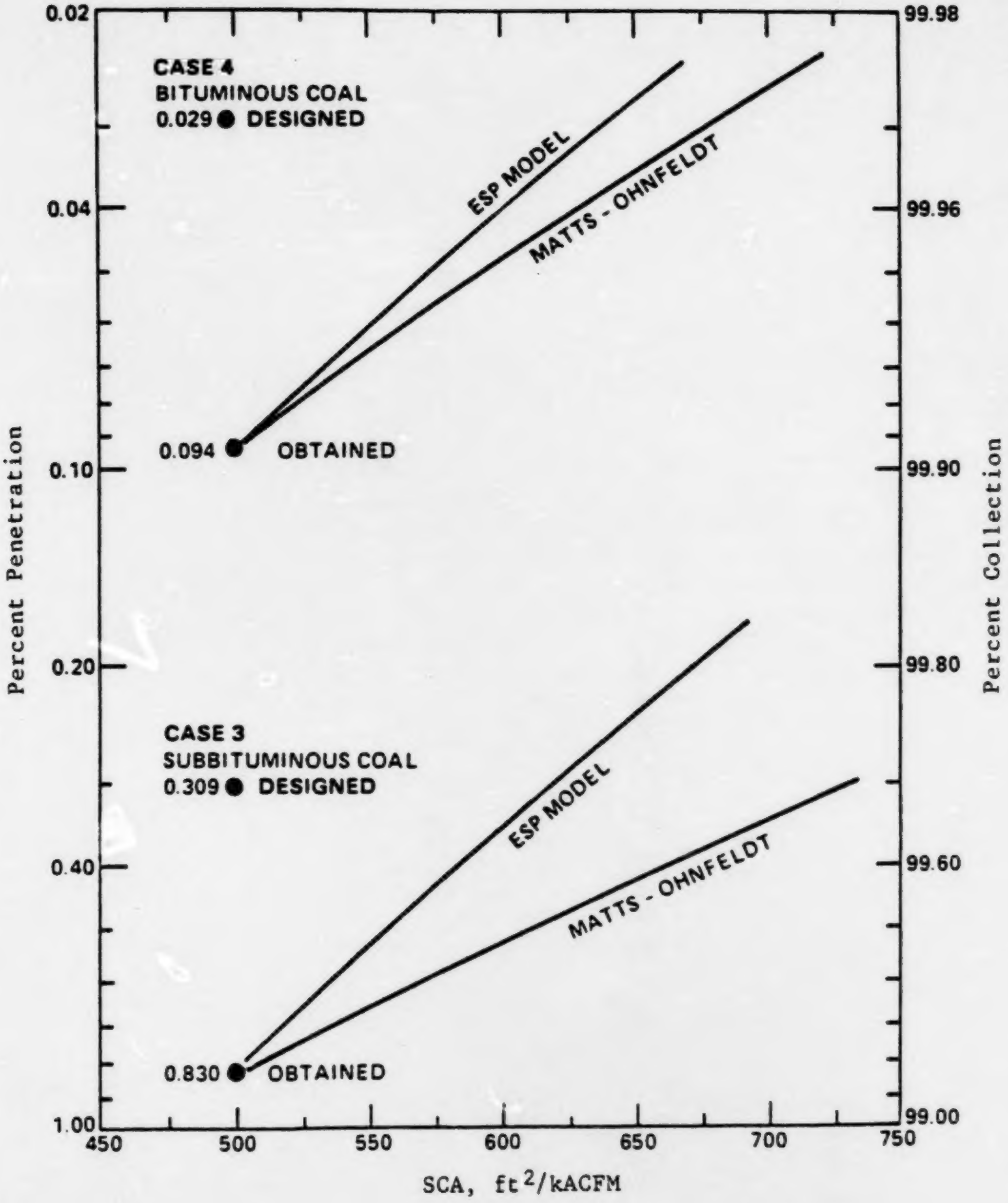

Figure 10. SCA added to correct measured emissions exceeding designed emissions at the 90% confidence limit.

USE OF A MOBILE ELECTROSTATIC PRECIPITATOR FOR PILOT STUDIES

by: Robert R. Crynack, John D. Sherow
Wheelabrator Air Pollution Control
One of the Signal Companies
5100 Casteel Drive
Coraopolis, PA 15108

ABSTRACT

This paper describes the use of a mobile electrostatic precipitator for pilot studies. The advantages and disadvantages of using and operating a pilot ESP are reviewed along with cost estimates. The paper includes a description and the features of the mobile ESP, which include variable plate spacing, three field operation, tapped transformers and reactors, automatic controls, and the ability to quickly change electrodes. Four case studies using the mobile ESP are discussed. The first study was to determine the scale factor between the pilot unit and a cold side, full scale unit and to compare the performance of various electrode configurations. The second study was to obtain performance data on a new fuel, solvent refined coal. The third study was to evaluate ESP performance where a conditioning agent was injected on a hot side, high resistivity application. The fourth study was the application of an ESP following a spray dryer operating under various conditions.

MOBILE ESP EQUIPMENT DESCRIPTION

The Wheelabrator Air Pollution Control (WAPC) mobile electrostatic precipitator (MESP) is a three field unit complete with automatic voltage controls, transformer/rectifier sets, rappers, hoppers and an induced draft fan. The MESP is mounted on a trailer 8 ft. wide by 54.5 ft. long by 13.5 ft. high, as shown in Figure 1. Each of the three fields consists of sets of discharge electrodes and collecting plates. Although almost any kind of discharge electrode or collecting plate may be installed in the MESP, the basic design is set up for normal WAPC discharge and collecting electrodes as shown in Figure 2 and Figure 3, respectively.

The collecting plate is 6.5 ft. high and consists of four interlocking strips, providing a length of 6.25 ft. for each field. The plate spacing can be varied to produce gas passage widths from 10 inches to 20 inches in 2 inch increments. The variable plate spacing results in varying numbers of gas passages and collecting areas. A summary of this information is provided in Table 1.

TABLE 1. NUMBER OF GAS PASSAGES AND COLLECTING AREA FOR VARIOUS PLATE SPACINGS

PLATE SPACING (INCHES)	GAS PASSAGES (#)	COLLECTING AREA (SQ.FT.)
10	5	1218
12	4	975
14	3	731
16	3	731
18	2	488
20	2	488

The standard discharge electrodes used in the MESP consist of pipe frames that are 5 ft. high, 6.25 ft. long, and have 12 wires per frame. Two standard wires are normally available in the pipe frame, a star-shaped and a spiked wire.

There are three large top access doors, which allow for removal and installation of internal components. Four smaller oval shaped man doors are provided on the side for inspection and maintenance.

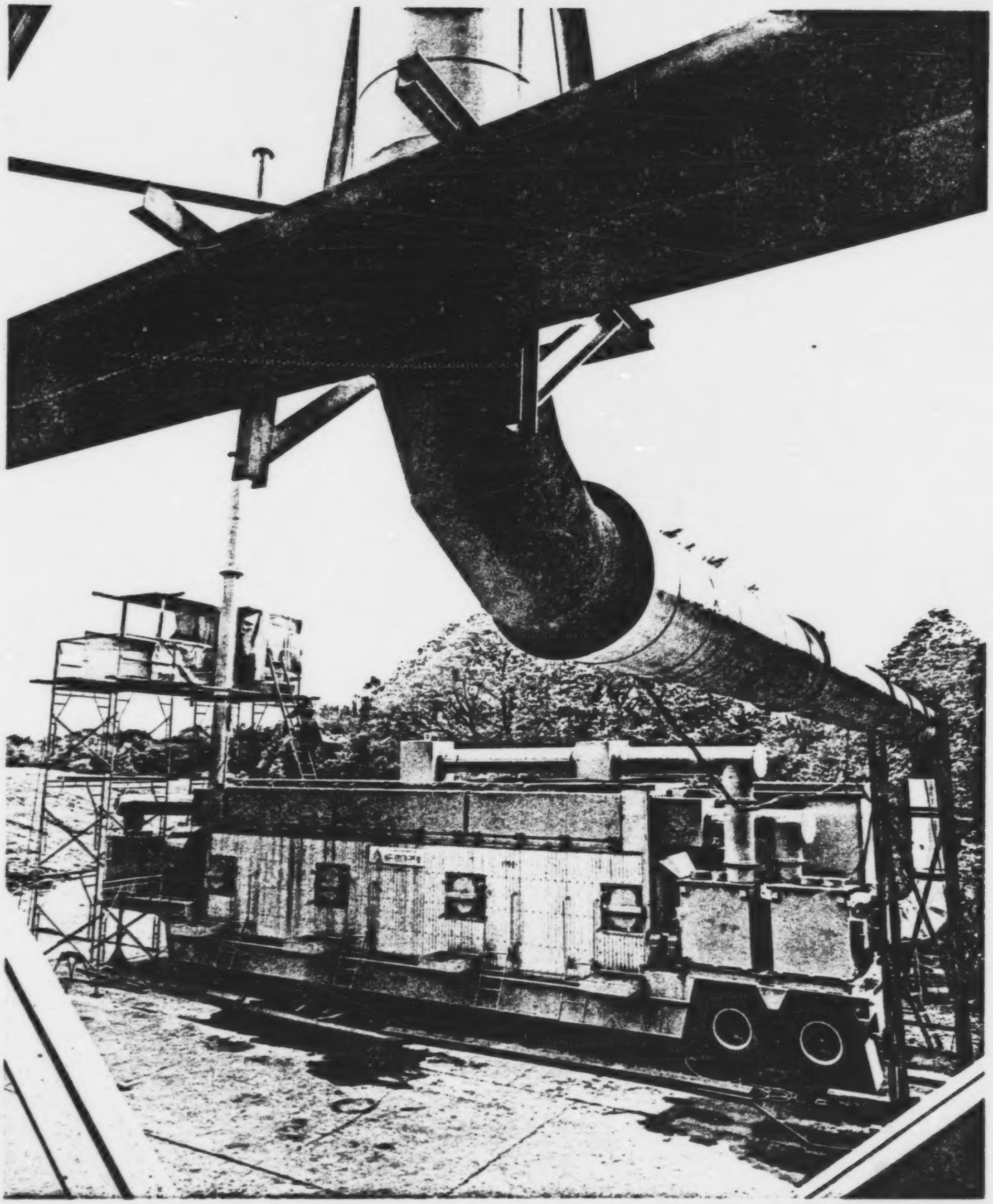

FIGURE 1. MOBILE ELECTROSTATIC PRECIPITATOR

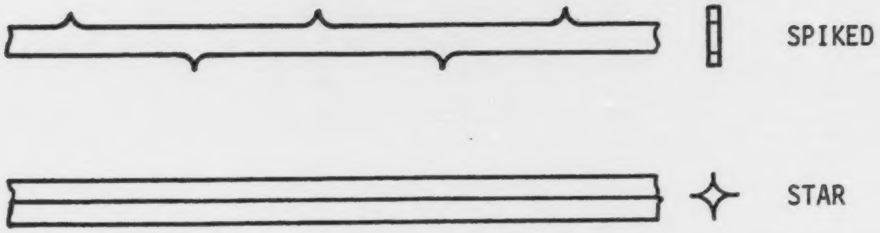

FIGURE 2. STANDARD DISCHARGE ELECTRODES

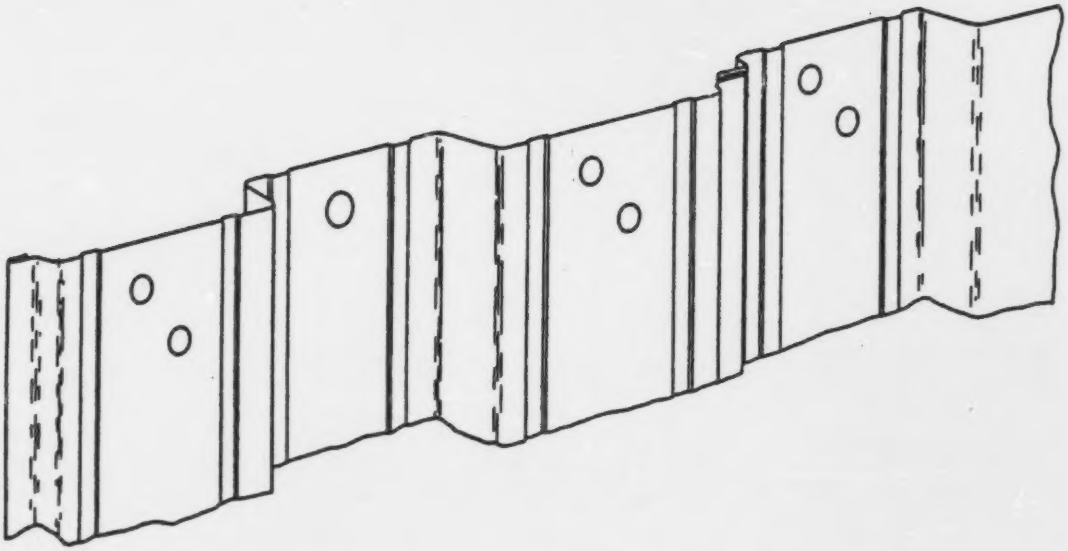

FIGURE 3. STANDARD COLLECTING ELECTRODE

Each collecting curtain is individually rapped at the bottom with a rotating, falling hammer. All the discharge electrodes and pipe frames in each field are cleaned with a side mounted vibrator. Both the plate rappers and the discharge electrode vibrators are manually controlled for each field.

The ash or dust removal system consists of two trough hoppers per field. Each trough hopper has a screw conveyor which empties into a pyramidal hopper at the end of the screw conveyor. The ash is then emptied into 55 gallon drums using an industrial vacuum system.

The induced draft fan is capable of drawing 9,000 acfm at 700°F. The volumetric flow rate is controlled by an opposed louver damper. The specific collecting area, SCA, (square feet per thousand acfm) for varying gas volumes and varying plate spacings are given in Table 2. Gas velocity as a function of gas flow and plate spacing is given in Table 3.

TABLE 2. SPECIFIC COLLECTING AREA* AS A FUNCTION OF GAS FLOW AND PLATE SPACING

FLOW RATE (ACFM)	PLATE SPACING (INCHES) 10	12	14	16	18	20
3000	406	325	244	244	163	163
5000	244	195	146	146	98	98
7000	174	139	104	104	70	70
9000	135	108	81	81	54	54

*SPECIFIC COLLECTING AREA IN FT^2/1000 ACFM

TABLE 3. GAS VELOCITY* AS A FUNCTION OF GAS FLOW AND PLATE SPACING

FLOW RATE (ACFM)	PLATE SPACING (INCHES) 10	12	14	16	18	20
3000	1.9	1.9	2.2	1.9	2.6	2.3
5000	3.1	3.2	3.7	3.2	4.3	3.9
7000	4.3	4.5	5.1	4.5	6.0	5.4
9000	5.5	5.8	6.6	5.8	7.7	6.9

*GAS VELOCITY IN FT/SEC

The MESP is equipped with automatic voltage controls and high voltage transformer/rectifier sets. Variable tap reactors are provided in the primary control circuit to produce an impedance of 30%, 50%, or 70%. Variable taps are also provided on the transformer/rectifier sets to provide a rated output of 45 KV, 60 KV, and 75 KV for the same primary voltage. A polarity switch provides for selection of positive or negative corona. The secondary current rating of the transformer/rectifier sets is 50 ma. With the maximum collecting area for five 10 inch gas passages, a current density of 0.12 ma/ft^2 can be obtained.

INSTALLATION OF MESP

Even though the MESP is a self-contained unit, installation and setup at the test site generally takes about one week. High voltage feedthrough insulators, insulator housings, hoppers, rappers, and vibrators are shipped separately and must be installed on the unit before operation. To provide access under the mobile ESP for installation of the pyramidal hoppers and to facilitate ash removal, the mobile ESP is normally raised off the ground an additional one to two feet. Inlet and outlet ductwork must be connected to the MESP along with 480 volt, three phase power. If the gases are to discharge into the atmosphere rather than being returned to the process ductwork, a stack must be erected. A support frame surrounding the fan is capable of sustaining the weight of five 10 ft. long sections of stack. Guy wires are used for stabilizing 30 to 50 ft. high stacks.

OPERATION AND TESTNG

Test coordination and operation of the MESP is handled by one engineer or technician. Normal operation of the MESP includes such tasks as (1) adjusting gas flow, (2) obtaining voltage-current curves, (3) adjusting and monitoring operating voltages and currents, (4) operating the manual rapping system, and (5) removing and disposing of ash.

The size of the test crew depends upon the types of testing to be conducted. For conducting particle mass concentration tests, standard EPA Method 5 or 17 is used. Only one person is required to set up and conduct these tests at each test location. If inlet and outlet tests are conducted, then a two man test crew is necessary. However, for expendency a third test crew member is valuable. If laboratory facilities are available on site, the third test crew member can process the samples and filters and provide results on the following day. Availability of immediate results of tests are important in determining test validity and in making decisions on how to proceed with the test program. This is an effective cost and manpower procedure that is beneficial for a successful field test program. Additionally, the third test crew member can assist the other two test crew members in their routine, time consuming activities.

The observed scatter of data on pilot test programs suggests that a minimum of six tests be conducted at any given condition. Normally a set of three emission tests are adequate for showing guarantee or compliance. However, for research purposes variations in performance that may be acceptable for guarantee or compliance purposes, are not acceptable in evaluating new process technologies or in making comparative studies of electrode geometries.

In pilot scale testing many factors must be considered to minimize their effect on the test results. Although temperature loss, sneakage, and in-leakage are of concern in a full-scale precipitator, they can be devastating in pilot ESP testing. Consider first the temperature loss due to the ductwork from the take-off point of the slip stream to the pilot ESP. Temperature loss in ductwork is primarily due to two affects, radiation and in-leakage. A 2 to 3 inch layer of thermal insulation covered by a waterproof covering such as sheet metal can provide adequate insulation to minimize heat loss due to radiation. By far the more difficult loss in gas temperature is due to in-leakage. This is particularly true of pilot studies where long runs of ductwork are required. Generally, small sections of ductwork are assembled to form the long duct runs. This produces many opportunities for in-leakage due to poor sealing at the joints of the sections. It is recommended that a heavy flange with a substantial number of bolts and a good gasket be used at each joint. Bolts must be torqued adequately to assure adequate compression of the gasket to minimize the in-leakage. All joints should be tested for in-leakage before insulation of the joints is made.

Temperature loss and in-leakage can also occur in the pilot unit itself. The three large doors, four man doors, and six pyramidal hoppers of the MESP provide ample opportunity for a significant amount of air in-leakage. Care was taken in the design of the door flanges and gasket seats. Gasket material must be resilient and acid resistant to minimize air in-leakage over an extended period of time.

Large industrial ESPs normally utilize purge air systems to prevent contamination of insulators. The amount of purge air relative to the large gas volume is small and does not have a significant effect on gas temperature or ESP performance. However, the percentage of purge air can be substantial with the smaller gas volumes in pilot units. For relatively high resistivity flyash, purge air of the insulators in a pilot unit can be minimized or even eliminated. However, low resistivity ashes, particularly those with a high carbon content, require a substantial amount of purge air. A substantial drop in temperature and the effect on pilot ESP performance can be observed if extensive purge air is required. In one of the pilot tests discussed later, in-leakage primarily due to purge air, was 15 to 20 percent.

The pilot ESP can be a significant source of heat radiation and heat loss due to a relatively large surface area. As with the ductwork, 3 inches of good thermal insulation is adequate to minimize heat loss when there is a reasonable gas flow through the mobile ESP to act as a continuous source of heat. In the case of the MESP this is around 4,000 acfm or more. In two uses of the mobile ESP only one or two gas passages were used. A single gas passage was used in one application where the gas flow was less than 1,000 acfm and two gas passages were used in another test program where the gas flow was approximately 2500 acfm. With the low gas flow the heat loss can be substantial and results in a substantial temperature drop across the pilot precipitator. To offset this heat loss, supplemental heaters were required.

Just as in a full-scale precipitator, the gas sneakage can be detrimental to the performance of a pilot ESP. With proper baffling at the top, bottom, and sides gas sneakage can be minimized. In the MESP the side baffling is made adjustable because of the potential change in the number of gas passages and the width of those gas passages.

In monitoring the operation of any pilot ESP, it is important to obtain voltage-current curves for each electrical section. For the mobile ESP voltage-curent curves are taken on a daily basis during normal operation. Additionally, airload voltage-current curves are obtained to verify clean insulators and good electrical clearances. In addition to voltage-current curves, power reaadings on all three fields are taken in 20 to 30 minute intervals. This verifies that the operation of the pilot ESP is steady. Any variation during a test of more than 2 KV raises concern about the operation of the precipitator or changes in the process.

For high efficiency full-scale precipitators, it has been shown that rapper reentrainment can account for a significant amount of particulate emissions. Because rapper acceleration levels and even the type of rapping may be different in a pilot unit as compared to a full-scale unit, it is difficult to account for the rapping reentrainment of full-scale unit from that determined in a pilot unit. During normal operation of the mobile ESP, testing is conducted without rapping. The rappers are manually operated before and after each test, but not during the test. Therefore, in analyzing the results and in predicting full-scale efficiency, some consideration has to be given to rapping reentrainment losses.

CASE STUDIES

The MESP has been used in four field test programs. The first study was to determine the scale factor between the pilot unit and a full-scale unit with a coal fired boiler and to compare the performance of various electrode configurations. The second study was to obtain ESP performance data on a new fuel, solvent refined coal. The third study was to evaluate ESP performance where a conditioning agent was injected on a hot-side, high resistivity application following a mini-combustor. The fourth study was the application of an ESP following a spray dryer operating under various conditions. Each of these four fields studies will be discussed briefly.

TEST PROGRAM #1

The purpose of this test program was (1) to determine a scale factor between the mobile ESP and a full-scale WAPC precipitator and (2) to evaluate the relative performance of several electrode configurations. Tests on these configurations were conducted at various gas volumes and corona power levels. Tests were conducted April through June of 1982.

Table 4 shows the performance based on migration velocity of four different electrode geometries, named A, B, C, and D. These tests were conducted at a gas volume of 6,000 acfm and specific corona powers of 200 and 350 watts per thousand acfm. For the higher specific corona power each of the four electrode configurations showed a higher migration velocity W_k (centimeters/second). In comparing the performance of the four electrode configurations, configurations A and B were the first and second ranked configurations for both high and low corona power levels. However, the ranking of C and D reverse for the two corona power levels.

TABLE 4. PERFORMANCE OF FOUR ELECTRODE GEOMETRIES AS A FUNCTION OF GAS FLOW AND CORONA POWER

GAS FLOW (acfm)	CORONA POWER (watts/1000 acfm)	ELECTRODE GEOMETRY	MIGRATION VELOCITY, W_k RELATIVE
6000	200	A	1.00
		B	0.94
		C	0.93
		D	0.93
6000	350	A	1.00
		B	0.92
		C	0.78
		D	0.84

Table 5 shows the results of varying gas volume for one electrode configuration. For gas volume flow rates of 4,000, 6,000, and 8,000 acfm the specific corona power was kept at 200 watts per thousand acfm. As the gas flow increased, the efficiency decreased while the residual and migration velocity increased.

TABLE 5. MESP PERFORMANCE FOR VARIOUS GAS FLOWS

GAS FLOW (acfm)	EFFICIENCY (%)	RESIDUAL (gr/acfm)	MIGRATION VELOCITY, W_k RELATIVE
4000	99.69	.0020	1.0
6000	99.40	.0035	1.1
8000	99.34	.0042	1.4

Tests were conducted to show the effect of corona power on the performance of an electrostatic precipitator. Using one configuration and gas volume flow of 6,000 acfm, the corona power was reduced from 311 to 103 watts per thousand acfm. Table 6 shows the efficiency, residual and migration velocity for the four values of specific corona power. The table shows good consistency of results, with both migration velocity and efficiency decreasing with decreasing corona power.

TABLE 6. ESP PERFORMANCE AS A FUNCTION OF SPECIFIC CORONA POWER

CORONA POWER (watts/1000 acfm)	EFFICIENCY (%)	RESIDUAL (gr/acfm)	MIGRATION VELOCITY, W_k RELATIVE
311	99.6	.0024	1.00
192	99.4	.0035	0.86
131	99.0	.0048	0.77
103	98.8	.0054	0.65

In order to use the mobile ESP effectively in pilot studies, it is important to establish a scale factor between the pilot ESP and the full-scale precipitator. This site has a full-scale WAPC electrostatic precipitator and provided an excellent opportunity to make such a comparison. Table 7 shows the comparison of parameters for the operation of the full-scale and the mobile ESP. It is impossible to operate a pilot ESP with all the same parameters as the full-scale ESP. In this study the gas velocity, current density and power density of the full-scale and mobile ESP were approximately the same. The results show that even though the efficiency of the full-scale precipitator was much higher and the residual much lower, the full-scale migration velocity was lower. In comparing the calculated migration velocities, the ratio of the mobile to full-scale values is 1.85. This would be defined as the scaling factor for these tests. The closer to unity the scaling factor is, the more confident one might be in sizing a full-scale ESP from pilot ESP test results.

TABLE 7. COMPARISON OF FULL-SCALE AND MOBILE ESP OPERATING PARAMETERS

PARAMETER	FULL-SCALE	MOBILE
PLATE SPACING (in)	12	12
NO. FIELDS	4	3
GAS FLOW (acfm)	436,500	6000
SCA (ft^2/1000 acfm)	513	163
GAS VELOCITY (ft/s)	3.7	3.8
CURRENT DENSIGY (ma/ft^2)	0.025	0.027
POWER DENSITY (watts/ft^2)	1.47	1.33
CORONA POWER (watts/1000 acfm)	756	200
INLET CONCENTRATION (gr/acf)	0.525	0.637
EFFICIENCY (%)	99.87	99.40
RESIDUAL (gr/acf)	0.00055	0.0035
MIGRATION VELOCITY,W_k (cm/s)	46.7	86.4

During this program the MESP was turned over to the host utility for their own evaluation of the program. The purpose, description, and results of this test program have been reported and will not be discussed in this paper. (1)

TEST PROGRAM #2

The International Coal Refining Company was under contract from the Department of Energy to study the technical feasibility and marketing potential of solvent refined coal (SRC) fuels for oil fired boiler applications. The technical aspects of the boiler fuel system conversion, combustion performance, and emission control system performance were studied through an SRC combustion test program. This program was conducted at the Pittsburgh Energy Technology Center (PETC). Testing was conducted on a 700 hp water tube industrial boiler, designed for oil firing. Baseline data was conducted by firing #6 fuel oil. Feasibility data were obtained by firing three types of SRC fuels: (1) pulverized SRC solids, (2) SRC residual oil, and (3) SRC - water slurry. (2)

WAPC was contracted to supply and operate the MESP and to perform mass emission tests. Tests were conducted between August 1982 and February 1983. Most tests were conducted with a gas volume of 5,000 acfm. Results for similar precipitator operating conditions for the four fuels that were burned are summarized in Table 8. The migration velocity varies slightly for the three SRC fuels, but all three are far above that of the #6 fuel oil. Part of the reason for the low migration velocity for the #6 fuel oil may be the low inlet mass concentration which results in low efficiency.

TABLE 8. SUMMARY OF TEST RESULTS FOR SOLVENT REFINED COAL

FUEL	INLET ESP ($lb/10^6 Btu$)	OUTLET ESP ($lb/10^6 Btu$)	EFFICIENCY (%)	RELATIVE MIGRATION VELOCITY, W_k
No. 6 FUEL OIL	0.050	0.004	92.35	1.0
SRC FUEL #1	0.959	0.005	99.46	4.3
SRC FUEL #2	0.208	0.002	99.08	3.3
SRC FUEL #3	0.960	0.006	99.34	4.2

TEST PROGRAM #3

This test program was conducted to evaluate the effect of a conditioning agent for a full-scale, hot side electrostatic precipitator. This hot side precipitator exhibits deterioration of performance similar to that reported many times in previous literature. The cause for the deterioration was assumed to be the sodium depletion as described by Bickelhaupt. (3)

The mobile ESP was used on a small combustor burning the same coal as in the full-scale unit at a rate of 125 lb. per hour. Just as with pilot precipitator tests, care must be taken with small scale combustor tests. The first phase of the test program was to modify the existing combustor to produce the same flyash as that of the full-scale unit. Only when this was completed could the evaluation of the performance of the mobile ESP be made. With a gas volume of less than 1,000 acfm, only one gas passage was used for this evaluation. As discussed previously, with small gas volumes the heat loss can be substantial.

Table 9 shows a summary of the operating voltages and currents of the precipitator with and without the conditioning agent. Due to a transformer problem that developed due to shipping of the mobile ESP, fields #2 and #3 were tied together and powered from one transformer/rectifier. It can be seen that the inlet field power changed very little, but the outlet two fields deteriorated significantly and then improved substantially with the addition of the conditioning agent.

TABLE 9. MESP POWER LEVELS FOR ESP CONDITIONING STUDY

CONDITION	KV_1	MA_1	$KV_{2,3}$	$MA_{2,3}$
INITIAL	32.0	1.5	35.0	4.5
AFTER DETERIORATION	28.0	0.5	31.0	3.5
AFTER CONDITIONING	29.0	1.0	38.0	7.0

TEST PROGRAM #4

WAPC and the U.S. Department of Energy jointly sponsored a program to evaluate the potential of retrofit applications of spray dryer flue gas desulfurization (FGD) systems to existing coal-fired furnaces using electrostatic precipitators for particulate emission control. The objective of this project was to characterize the emissions (SO_2, NO_x, and particulates) from a spray dryer FGD system while burning different types of coal, and to study the effectiveness of an electrostatic precipitator in reducing emissions. Three different coals (low, medium, and high sulfur) were burned in a 500 lb. per hour combustion facility. The flue gas was then treated by a rotary atomizer spray dryer and the MESP. For each type of fuel a three part test program was conducted, consisting of: (1) baseline ESP performance tests with no spray dryer operation to determine precipitator requirements for flyash collection only, (2) parametric tests defining SO_2 removal efficiency versus lime stoichiometric ratios for both the spray dryer and ESP at various spray dryer operating conditions, and (3) recycled tests in which particulate collected by the MESP was recycled into the spray dryer system. A summary of the data is presented in Table 10 for one coal.

TABLE 10. ESP PERFORMANCE FOR A SPRAY DRYER APPLICATION

CONDITION	SO_2 REMOVAL (%)	EFFICIENCY (%)	RESIDUAL (gr/acfm)
BASELINE	0	99.4	0.003
SPRAY DRYER	70	99.3	0.005
SPRAY DRYER	80	99.1	0.008
SPRAY DRYER	90	99.3	0.010

PILOT STUDY COST ESTIMATES

The cost of any pilot ESP test program is site specific and depends upon many factors. Because of the wide range of potential costs depending upon the length of the program, scope of the program, and location of the program, it is difficult to precisely estimate the cost of a pilot test program. Table 11 is an approximate cost estimate for a pilot ESP test program that would last four weeks. Most of the costs are fixed, and therefore, extending the program beyond the four weeks would primarily increase the testing and operating costs.

TABLE 11. COST ESTIMATE FOR A PILOT ESP TEST PROGRAM

TRANSPORTATION & INSTALLATION	5,000
FABRICATION OF DUCTWORK	10,000
INSTALLATION OF DUCTWORK	10,000
MISC. SUPPLIES	3,000
TESTING	40,000
PILOT OPERATOR/COORDINATOR	10,000
	$78,000

Transportation and installation costs range from $2,000 to $20,000 depending upon site location. The cost of hauling the MESP from Pittsburgh to California was $10,000 one way. However, a reasonable cost would be $5,000. Ductwork fabrication installation costs are also site specific and depend upon length and diameter. Approximate costs for 100 ft. of insulated ductwork, 16 in. in diameter and fabricated in 10 ft. sections with flanges on each end, would be approximately $10,000. Installation costs of the ductwork would probably be about the same. There are always a myriad of miscellaneous consumable supplies that are required on a pilot test program. These costs are estimated at $3,000. The cost of testing depends upon the scope of the testing that is to be conducted. A typical cost for a three man test crew that would conduct two to three efficiency tests per day would be approximately $10,000 per week. This would include testing, analysis, and reports. The cost of an operator and test coordinator would be an additional $10,000 for the four week program.

The estimated cost for this four week program would be $78,000. This cost estimate does not include the cost of man power associated with planning the test program, technical and administrative management of the program, data analysis, or report writing. It is again emphasized that the cost figures are rough estimates only, and are so site specific that it is difficult to produce an estimate with reasonable accuracy.

SUMMARY

The Wheelabrator Air Pollution Control mobile electrostatic precipitator is a fully self-contained unit, complete with fan, high voltage transformer/rectifier sets and controls. This three field unit was designed to readily change electrodes or gas passage spacing. Care must be taken in using a pilot ESP to minimize the effects of thermal loss, inleakage, sneakage, and purge air. Data from four case studies show a wide variety of test programs are possible using a pilot ESP. Although a scale factor between pilot and full scale ESP performance can be determined, care must be taken in using the data. The mobile ESP provides an excellent tool to obtain relative performance data for a variety of operating conditions.

The work described in this paper was not funded by the U.S. Environmental Protection Agency and therefore, the contents do not necessarily reflect the views of the Agency and no official endorsement should be inferred.

REFERENCES

1. Kisha, M., Goerss, E., Schwinn, M. Investigation of acidic matter emissions at the Niles Generating Station. Paper presented at the 1983 Annual Meeting of the Air Pollution Control Association, Atlanta, Georgia. June 19-24, 1983.

2. Harrison, W., Nicholson, J., Boyd, K., Lennon, D. SRC burn test. Southern Company Services. January, 1984.

3. Bickelhaupt, R. An interpretation of the deteriorative performance of hot-side precipitators. Journal of the Air Pollution Control Association . August, 1980. 882 pp.

PREDICTION OF VOLTAGE-CURRENT CURVES FOR NOVEL ELECTRODES
Arbitrary Wire Electrodes on Axis

by: Phil A. Lawless
Research Triangle Institute
P. O. Box 12194
Research Triangle Park, North Carolina 27709

L. E. Sparks
Industrial Environmental Research Laboratory
U. S. Environmental Protection Agency
Research Triangle Park, North Carolina 27711

ABSTRACT

Theoretical prediction of voltage-current characteristics for ESPs has been limited to single wires or infinite arrays of wires in the wire-plate geometry. As part of a program investigating the prediction for arbitrarily arranged electrodes, a model for wire electrodes has been developed that accurately predicts starting voltages and V-I curves for finite numbers of wires of mixed diameters and spacings. This model is implemented on a microcomputer, providing an interactive approach for investigating electrode arrangements. The accuracy of the model is demonstrated, and some of the implications for operating ESPs are explored.

This paper has been reviewed in accordance with the U. S. Environmental Protection Agency's peer and administrative review policies and approved for presentation and publication.

INTRODUCTION

The prediction of voltage-current (V-I) curves for operating electrostatic precipitators (ESPs) shows a large gap between the theory for smooth clean wires and the observations for dirty complex electrodes. This is because of the variety of unmodeled effects in the theory and the uncontrolled conditions under which operating ESPs can be observed.

The calculation of corona onset voltages and V-I curves in wire-duct precipitators, for an infinite series of wires, has been addressed theoretically by Cooperman.(1) In reality, the number of corona wires in any one electrical section is finite and may be quite small. The corona onset condition was experimentally determined by Peek(2) for smooth, clean wires--a condition that leads to a different type of corona from that encountered in ESPs. Particle space charge in operating units also shifts the characteristics of the corona in a way that is difficult to model, because it involves highly interacting effects of charging and collection as well. Back corona is another electrical effect that complicates the modeling.

The work to be described here is aimed toward the whole problem of predicting the operating point of a given ESP. It involves, at this stage, the prediction of corona onset voltages and V-I relations for round wires; the wires may be arranged conventionally or in unusual configurations. The effects of rusty/dirty wires will be included through a combination of theoretical and experimental relations for negative corona but will be reported elsewhere.

The eventual scope of the work will include the prediction of characteristics for rather arbitrarily shaped electrodes, the full space charge interactions, and the integration of the electrical model into a full ESP performance model. It will be aimed at evaluating the various aspects of design and testing that go into a proposed ESP installation.

The current model is built around the capabilities of an advanced personal computer, but the basic aspects of the model can be run on any of several popular microcomputers.

CALCULATION OF THE STARTING VOLTAGES

Starting Voltage Relation for Coaxial Geometry

In a coaxial ESP, the voltage on a round-wire electrode can be determined from the electric field at the wire surface, provided no space charge is present:

$$V_w = E_w \times r_w \times \ln(R/r_w), \qquad (1)$$

where V_w is the voltage, E_w is the electric field, r_w is the wire radius, and R is the radius of the outer electrode. It is generally assumed that the electric field at corona onset is not significantly different from the electrostatic field just below corona onset.

The corona onset field was first determined by Peek(2) in the coaxial geometry, among others, for a wide range of wire and tube radii and environmental conditions. The electric field so determined will be called the Peek field, E_c; when it is present at the surface of a clean smooth wire, corona will ensue.

Single Wire Between Planes

For a single wire located midway between two planes, a conformal mapping of cylindrical geometry onto the planes results in the following relation for the starting voltage:

$$V_c = E_c \times r_w \times \ln(d/r_w), \qquad (2)$$

where d is the equivalent cylinder radius, given by:

$$d = 4 \times b/\pi, \qquad (3)$$

where b is the wire-plate separation.(1)

This relation does assume that the electric field near the wire is unaffected by the relatively distant plates; but for wire diameters much smaller than the plate-plate spacing, this is not a major restriction.

This expression for the single wire lends itself to expression in an infinite series of wires, where the effects of all the other wires can be calculated.(1) When the wire-wire spacing in such a series becomes much larger than the wire-plate spacing, the terms in the series converge so rapidly that Equation 2 is accurate enough for most uses.

Effect of One Wire on the Starting Voltage of Another

A wire operating at a given voltage produces an electric field at all points in space at some distance from itself. If that electric field is integrated from the plate to the location of another wire, a potential difference arises. The resulting potential difference is a bias that must be added to the second wire's single-wire starting potential before the Peek field can be reached at the surface of the second wire. The integrated potential at the second wire, because of a potential on the first wire, is given by:

$$V_{12} = V_1 \times F_{12}, \tag{4}$$

where F_{12} is a purely geometrical factor, given by:

$$F_{12} = \frac{\ln\left[\dfrac{\cosh(\pi c_{12}/2b) - \cos(\pi r_2/2b)}{\cosh(\pi c_{12}/2b) + \cos(\pi r_2/2b)}\right]}{\ln\left[\dfrac{1 - \cos(\pi r_1/2b)}{1 + \cos(\pi r_1/2b)}\right]}, \tag{5}$$

where c_{12} is the distance between wires 1 and 2, r_1 and r_2 are the radii of wires 1 and 2, respectively, and b is the wire-plate spacing, as before.

Operation of All Wires at a Common Voltage

For a multi-wire ESP with all wires operating at a common voltage, a given wire will be at its corona threshold when the following relation is satisfied:

$$V_i = V_{ci} + \sum_{j \neq i} F_{ij} \times V_i, \tag{6}$$

where V_i is the corona threshold of the i-th wire in the presence of all the others; V_{ci} is the single-wire corona threshold voltage of the i-th wire, given by Equations 2 and 3; and the geometry factors, F_{ij}, are given by Equation 5, with i and j substituted for 1 and 2. V_i appears on both sides of Equation 6 because it assumes that all wires are at the same voltage.

In general, Equation 6 is most easily evaluated iteratively since the geometrical factors are usually much less than 1, giving a rapidly converging process:

First approximation:

$$V_{i1} = V_{ci} + \sum_{j \neq i} F_{ij} \times V_{ci}, \tag{7a}$$

second approximation:

$$V_{i2} = V_{ci} + \sum_{j \neq i} F_{ij} \times V_{i1}, \tag{7b}$$

n-th approximation:

$$V_{in} = V_{ci} + \sum_{j \neq i} F_{ij} \times V_{in-1}. \tag{7c}$$

When the wires are large in diameter or close together, the convergence of the approximations is slower and should be monitored by means of the changes between successive values.

Consequences and Limitations of the Interaction of Wires

One major point becomes apparent when calculating the starting voltages of an array of equally spaced wires of the same diameter: the first and last wires in the array have noticeably lower starting voltages than the central wires. This is the result of having fewer strong interactions with neighboring wires and becomes most apparent when the wire-wire spacing is less than the wire-plate spacing.

This difference in starting voltages means that attempts to raise the overall corona onset point by grouping wires close together will fail because the outermost wires of the grouping will have much lower starting voltages than all the others.

On the other hand, placing a large diameter wire near a small diameter wire will raise the threshold of the small wire considerably. This effect may be so large that wires near large diameter mast supports do not ever reach their corona threshold in normal operation.

The major limitation for applying the algorithm of Equations 6 and 7 is that it does not include the electric field effects due to the presence of the ionic space charge once a wire has begun corona generation. The ionic electric field would have the effect of raising the threshold of the others wires above that calculated electrostatically. The difference would be most apparent for wires of equal diameters, whose corona thresholds would otherwise be quite similar. The amount of the shift due to the ion-produced electric field depends on the current from each wire at the corona threshold being calculated, a consideration that requires knowledge of the V-I curve of each wire.

CALCULATION OF WIRE V-I RELATIONS

Uniform Electrical Conditions at the Wire

The V-I relation for a single wire between plates is based upon the solution for the similar case in the coaxial geometry. In the coaxial geometry, Poisson's equation for the ionic space charge can be solved if certain assumptions are made about the nature of the corona discharge.(3,4) These amount to knowing the electric field and ion density at the boundary of the corona. For both the negative glow and positive Hermstein glow(5), the corona region appears to be cylindrically uniform around the corona wire. If the diameter of the bipolar generation region is assumed to be approximately equal to the wire radius, then the governing differential equation can be solved analytically.

In the case of the wire-plane geometry, the electric field around the wire can be shown to be nearly uniform for small wire diameters; therefore, the ion generation should also be uniform. From Cooperman's solution for the potential around the wire, the ratio of the field directed parallel to the plate to the field directed toward the plate, at the wire's surface, is given by:

$$E_{\parallel}/E_{\perp} = \sin(\pi a_c/2b)/\sinh(\pi a_c/2b), \qquad (8)$$

where a_c is the wire radius and all other terms are as before. In the limit as a_c/b tends to zero, this ratio is unity; but for large diameter wires, the electric field from wire to plate is stronger than that directed parallel to the plates, as would be expected.

Provided a_c/b is kept to less than 0.1, the variation of E around the wire will be less than about 0.003. At this level, the corona generation should remain nearly uniform as well, although it is very sensitive to the electric field variation.

V-I Curve in Cylindrical Geometry

In the cylindrically symmetric coaxial ESP, the voltage can be computed for a given current/length of wire analytically.(3,4) Under the simplifying assumption that the wire diameter is much less than the tube diameter, an expression for the operating voltage is:

$$V = V_c + E_c \times a_c \left[(1 + B)^{1/2} - 1 - \ln\left\{[1 + (1 + B)^{1/2}]/2\right\}\right], \qquad (9)$$

where V_c is the corona starting voltage, B is a reduced current/length of wire, and the other terms are as before. The reduced current/meter is given by:

$$B = I/\ell \times b^2/[2\pi\varepsilon_0\mu(E_c \times a_c)^2], \qquad (10)$$

where I is the current, ℓ is the length of wire, ε_0 is the free-space permittivity, μ is the mobility, and the other terms are as before. The term $[b/(E_c \times a_c)]$ represents the electrostatic part of the electric field at the outer boundary. The current density at any point on the outer cylinder is related to the current/meter by:

$$j_0 = (I/\ell)/(2\pi b). \tag{11}$$

Of course, below the corona onset voltage, no current flows and Equation 9 is inapplicable.

Current Density in Wire-Plate Geometry for a Single Wire

The current density on the plate directly opposite the wire has almost the same value as in the cylindrical geometry for the same wire-plate spacing. This is a consequence of assuming a uniform generation of ions around the circumference of the corona wire, a uniform electric field around the circumference, and the fact that the ions must travel the same distance in the two cases. In those instances where the uniformity provisions no longer hold, then the current density will depart from the coaxial geometry value.

The implication is that the V-I density relation for points directly under the wire is a universal one, given by the relations in Equations 9 through 11. That is, if B is written as:

$$B = j_0 \times b^3 \times \pi/4/[\varepsilon_0 \mu (E_c \times a_c)^2], \tag{12}$$

then Equation 9 gives the voltage corresponding to that local current density.

To obtain the full current flowing from the wire, an auxiliary condition is needed, relating the current density under the wire to the current density at other positions. Such a relationship is being developed experimentally and theoretically(6), but most ESP applications can be given with sufficient accuracy by:

$$j(\theta)/j_0 = \cos^3(\theta) \ , \tag{13}$$

where $j(\theta)$ is the current density at a point on the plate at an angle θ, measured between a normal to the plate which passes through the wire and a plane passing through the wire and point of interest.

In more accurate terms, the power of the cosine is a function of current density, ranging from somewhat more than 2.5 at zero to about 4 at extremely high current densities. The choice of 3 as an average value gives good results over the conventional range.

The current/meter is obtained by integrating over the plate at angles for which current may flow from the wire:

$$I/\ell = 2 \int_{-\theta_1}^{\theta_2} j_0 b \cos(\theta)\, d\theta, \tag{14}$$

where θ_1 and θ_2 are the limiting angles. For the single wire case, both will be equal to $\pi/2$. For integral powers of the cosine function, the integral may be written explicitly, and for the cubic power is:

$$I/\ell = 2j_0 b\ [\sin(\theta_2) + \sin(\theta_1)]. \tag{15}$$

Thus, the V-I relation for the single wire is obtained on the basis of a 1 m length.

Current Density in Wire-Plate Geometry for Multiple Wires

For the multiple wire ESP, similar relations hold. The starting voltages for each wire have already been described. The normalized current densities, B, for each wire can be calculated according to Equation 12; no compensation for the increased electric field at the plate is needed, because of a cancellation in terms involving E_c.

The cosine power law has been found to remain a good representation of the distribution of current density, even though the currents flowing from adjacent wires do not overlap.(6) If the angles θ_1 and θ_2 are computed from the points on the plate midway between adjacent wires, then the total current from a given wire is adequately represented by Equation 15.

As was the case with the starting voltage, these relations do not take into account the effects of the ionic space charge on the currents flowing under adjacent wires. Nonetheless, experimental evidence does support the use of these relationships, even for tightly spaced wires.

COMPARISON OF STARTING VOLTAGES WITH THEORY

In addition to the electrode effects which are at the heart of this work, there are polarity effects for the corona starting voltage. Since the direction of movement of the ion-generating free electrons is different for positive and negative polarity, it is to be expected that there would be differences in the critical field for self-sustained ionization. Based on V-I curves measured in a small coaxial ESP, the following expressions for the critical fields have been derived. These are similar to the one determined by Peek but clearly distinguish between the positive and negative coronas.

Positive:

$$E_c = 3.126E06[d_r + 0.0266(d_r/a_c)^{1/2}]. \tag{16a}$$

Negative:

$$E_c = 3.126E06[d_r + 0.0301(d_r/a_c)^{1/2}]. \tag{16b}$$

Here d_r is the gas density relative to its value at normal temperature and pressure. The constants were chosen by least squares fits, requiring the leading constant, the critical field at infinite radius, to be the same for both polarities.

With these relations for the critical field, experimental values were compared with the predicted ones, and the results are in Table I. The measurements were made at the EPA's optical ESP at Research Triangle Park, North Carolina. It comprises a single-lane pilot-scale ESP, made of Plexiglas and operated at ambient temperature. The apparatus is constructed so that it can be easily disassembled in the quickest manner for adjustment or modification.

The plate spacing in the ESP is adjustable up to 30.5 cm (12 in.), and discharge wires can be inserted with any desired spacing. Air is circulated through the ESP in a closed loop at an adjustable velocity, but a portion of the flow is exhausted from the loop to prevent buildup of gaseous discharge products. For this work, only enough air flow was used to keep the gas in the discharge region fresh.

Each plate is 1.2 m (4 ft) square and is covered with aluminum strips isolated from one another so that the current to each can be measured. On one plate, the center strips are 1.27 cm (1/2-in.) wide for a distance in the direction of flow of 25.4 cm (10 in.); the remaining strips on that plate are 5.08 cm (2 in.) wide. On the opposite plate, all strips are 5.08 cm wide. The strips are used to measure the current from the corona wire (or wires) independently of one another.

Several different voltmeters were used during the measurements, because of limitations on the maximum voltage which could be applied to each. Pending a satisfactory calibration of all the meters used, it is assumed that the measured values are accurate to no better than 5 percent.

The predicted clean wire voltages in Table 1 are in good agreement with the measured values, mostly within the 5 percent limit. There does appear to be a systematic underprediction of the corona starting voltages, which may be due to a calibration problem. Nonetheless, both measured and predicted values show the same trends, with positive corona starting at lower voltages than negative corona, and center wires of an array having higher starting voltages than those at the ends of the array.

When it is possible to compare the starting voltage at the center and end of an array, the prediction is usually better for the end wire. This is a consequence of not including the ionic space charge effects of a given wire on another: the center wire should have a higher starting voltage due to the other wires' ion currents than the (electrostatic) calculation predicts.

It is also apparent that the discrepancies between theory and experiment increase as the wires become more closely spaced. This is partly due to the experimental difficulties in ensuring a smooth clean wire, and partly due to inadequacies in the theory, particularly with regard to the applicability of the Peek field criterion.

COMPARISON OF V-I CURVES WITH THEORY

For comparing the full V-I curves, polarity effects again intrude on the values of ionic mobility chosen. In air at room temperature, both positive

TABLE I. Comparison of Calculated and Experimental Starting Voltages

Setup	a_c (cm)	b (cm)	c (cm)	V_c		V_{exp}	
				(+kV)	(-kV)	(+kV)	(-kV)
A	0.159	15.2	—	+39.7	-41.7	+41.7	-43.8
A	0.159	11.4	--	+37.3	-39.2	+38.9	-40.0
A	0.308	11.4	--	+55.7	-58.1	+58.0	-59.2
A	0.159	7.62	—	+33.9	-35.7	+35.0	-37.0
B (center wire)	0.159	11.4	≈10.6	+38.8	-40.8	+41.7	-42.2
B (outer wire)	0.159	11.4	11.4	+38.0	-40.1	+40.5	-40.8
C (center wire)	0.159	11.4	8.89	+40.7	-42.8	+42.5	-43.0
C (outer wire)	0.159	11.4	8.89	+38.9	-41.0	+40.8	-41.0
D (center wire)	0.159	11.4	6.35	+45.9	-48.3	+46.6	-47.8
D (outer wire)	0.159	11.4	6.35	+41.2	-43.3	+42.6	-43.0
D (center wire)	0.159	11.4	5.08		-49.5		-53.0
D (outer wire)	0.159	11.4	5.08		-46.0		-46.0
D (outer wire)	0.159	11.4	3.81	+49.4	-52.0	+49.0	-50.0
E (center wire)	0.159	11.4	3.81	+70.6	-74.3	+60.0	-64.0
E (center wire)	0.159	11.4	5.08	+52.6		+53.0	
E (center wire)	0.159	11.4	6.35		-48.3		-49.6
F (center wire)	0.159	11.4	≈10.6	+38.9		+40.6	
F (center wire)	0.159	11.4	8.89	+40.7		+41.0	
G (outer wire)	0.159	11.4	6.35	+41.2	-43.3	+42.7	-44.0
H (outer wire)	0.159	15.2	—	+46.6		+47.0	
H (inner wire)	0.159	15.2	—	+65.4		+66.0	
H (outer wire)	0.159	11.4	—	+40.6		+41.0	
H (inner wire)	0.159	11.4	--	+51.3		+56.0	
J (outer wire)	0.159	11.4	--	+42.0		+42.5	
J (inner wire)	0.159	11.4	--	+51.6		+53.5	

A: Single wire between plates.
B: Five equal diameter wires spaced 20.3 - 22.9 - 22.9 - 20.3 cm apart.
C: Five equal diameter wires spaced equally.
D: Seven equal diameter wires spaced equally.
E: Seven wires--center wire 0.308 cm diameter, all others 0.616 cm diameter, spaced equally.
F: Five wires--center wire 0.308 cm diameter, all others 0.616 cm diameter, spaced 20.3 - 22.9 - 22.9 - 20.3 cm.
G: Four wires--one outer wire 0.308 cm diameter, all others 0.616 cm diameter, spaced equally.
H: Mast, 3.17 cm diameter; supporting 0.308-cm wires at 7.62 cm and 22.9 cm from center of mast.
J: Same mast as H, plus 0.616-cm wires at 41.9 cm from center of mast.

and negative ions have mobilities of about 1.8 cm^2/Vs, but they are dependent on the level of moisture. In flue gas atmospheres, the presence of electronegative gases (acid gases) can modify the mobility as much as temperature does. In the computer model used to obtain the present theoretical values, the relations of Lawless and Sparks(7) are used, but should be extrapolated to other conditions with suitable caution.

Three basic cases were used to test the quality of the prediction of the V-I algorithm: a small three-wire ESP(8), a pilot-scale ESP with five wires(9), and a high-voltage, high-current laboratory ESP.(10) In addition, V-I curves for a near-full-scale laboratory ESP section were available to check the general performance of the model, although the conditions of the wires did not correspond to the clean conditions required for the theory.(11)

The results of the comparisons of these experimental values with the model predictions are shown in Figures 1 through 3. The first V-I relation, from the three-wire ESP, was done with positive corona. The wires were all the same diameter; the central wire was made of brass and the outer wires of steel. This may explain the large difference in starting voltage observed experimentally. Figure 1 has two theoretical curves: one with corona starting voltages calculated as outlined above, and the other with the starting voltage of the center wire artificially raised to about 38 kV. This is a value corresponding to an inflection in the experimental curve, where the corona start was observed visually on the center wire.

Although the model does not accurately predict the starting voltages of all the wires, the V-I curve has the correct slope when corona is flowing from all the wires. The alteration of the starting voltage for the center wire brings the model into excellent agreement with the measurements.

Figure 2 shows data taken on the EPA pilot scale ESP, with all three sections configured identically: wire diameter 0.308 cm, plate-plate spacing 22.8 cm, and five wires spaced 22.8 cm apart. Special care was taken to smooth and clean the wires, resulting in nearly identical V-I curves. The theoretical model also is in excellent agreement from the starting voltage up to about 70 nA/cm^2, which covers the usual operating conditions of industrial ESPs. The growing discrepancy above that current density is due mainly to the approximation in Equation 12: it has been observed that the high current limit of the exponent of the cosine dependence is 4, which will be approached at voltages well above the starting voltage.

Figure 3 shows two experimental situations, a normal wire size and plate spacing, and a small wire size at larger-than-normal plate spacings. The exact arrangements were not clear from Reference 10, but the assumption was made that the data correspond to the central wire of an array. Even so, the starting voltages are not in agreement with the model.

For Figure 3a, the experimental starting voltage, 37 kV, corresponds to a single wire, while for five wires, the starting voltage for the center wire is 45 kV. Except for the starting voltage, the remainder of the curve is in excellent agreement with the data. For Figure 3b, the experimental starting voltage, 25 kV, cannot be obtained with a wire of diameter 1.78×10^{-2} cm, as

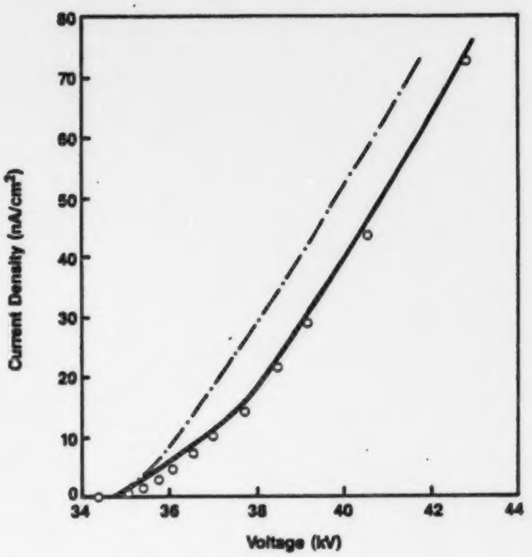

Figure 1. Laboratory ESP with three wires (diameter = 0.308 cm, plate-plate spacing = 15.2 cm, wire-wire spacing = 15.2 cm).

—•—•— Complete model prediction.

——— Model with adjusted starting voltage for center wire.

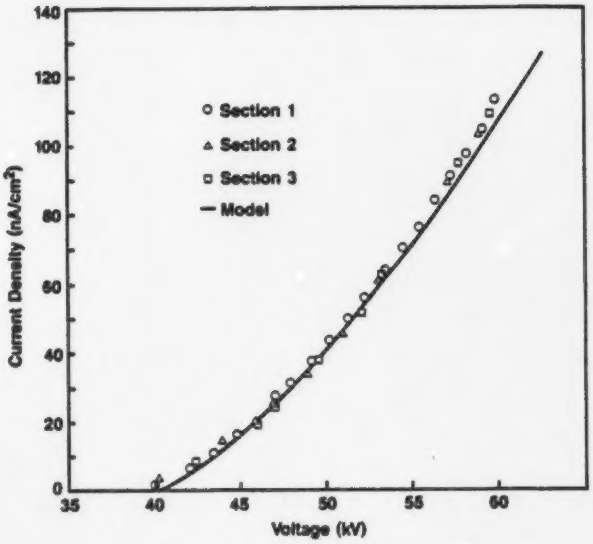

Figure 2. Pilot-scale section with five wires (diameter = 0.308 cm, plate-plate spacing = 22.8 cm, wire-wire spacing = 22.8 cm).

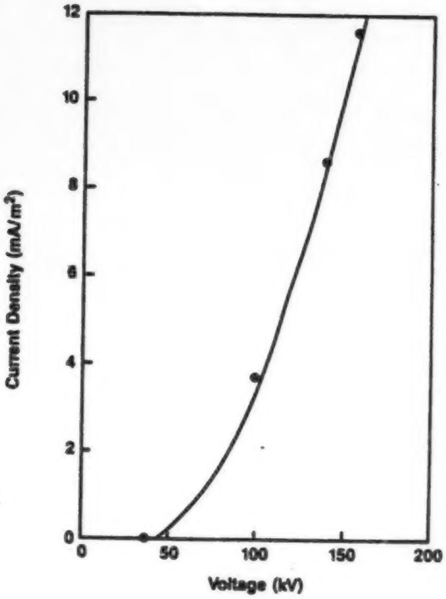

Figure 3a. Laboratory ESP (wire diameter = 0.277, plate-plate spacing = 30.5 cm, wire-wire spacing = 15.2 cm). Five wires assumed with model predicting current density of center wire.

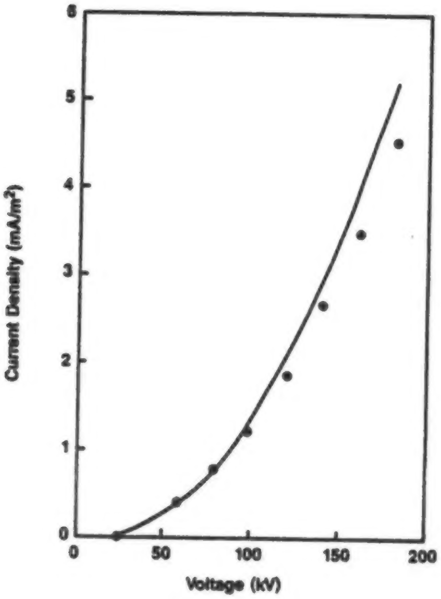

Figure 3b. Laboratory ESP [wire diameter = 1.78 × 10^{-2} cm, plate-plate spacing = 45.7 cm, wire-wire spacing = 22.9 cm]. Five wires assumed; model predicts current density of center wire; starting voltage of center wire adjusted to 25 kV.

given in Reference 10; the highest reasonable voltage is about 10 kV. The model was artificially adjusted to give the experimental starting voltage, producing a curve in good agreement with the data.

In spite of the difficulties with Reference 10, it is useful because of the extreme current densities and voltages found in the data. The model shows good agreement up 1000 nA/cm^2, far above the normal ESP range. The normally excellent predictions of starting voltage are so far in error that either the data or the description of equipment is suspect.

The model predictions and the near-full-scale V-I curves(11) were in good agreement only at voltages well above the smooth-wire corona-start voltage. The wire-wire spacing was large enough that the interactions between wires was barely noticeable, but the rough condition of the wires led to corona onset (both positive and negative) at voltages well below the smooth-wire value. It is useful to note that the smooth-wire V-I curve, as predicted by the model, is rapidly approached by the real curve above the smooth-wire starting voltage.

CONCLUSIONS

The results of the initial phases of this work have demonstrated that the theory for corona starting can be extended very well to wires of varying spacings and diameters, using Peek's criterion for the electric field at the surface of the wire. Such discrepancies as there are seem to be due to imperfections in the model relating to the influence of ions from wires where corona has started.

An important result of the starting voltage predictions is that arrays of wires of the same size may have very different starting voltages, depending on the wire's location within the array. This means that unusual electrode arrangements can have important consequences for the operation of the electrical section, in that some wires may fail to even reach the corona threshold before other electrical effects limit the applied voltage. Mast electrode supports were shown to have a very significant effect on the starting voltages of adjacent corona wires.

In addition to the starting voltage, the V-I curve of a wire follows a universal law in which the current density directly under the wire is determined by the equivalent current density in the coaxial geometry. For areas not under the wire, the current density is given by a simple cosine relation to the current density under the wire. This holds over a range of current densities normally encountered in ESPs and has been experimentally verified to much higher levels.

Although the model is strictly limited to uniform modes of corona, it has applicability wherever the smooth-wire corona threshold is exceeded. Further work on non-uniform corona is being addressed as part of this effort.

REFERENCES

1. Cooperman, P. A theory for space-charge-limited currents with application to electrical precipitation. AIEE Transactions. 79: 47-50, 1960.

2. Peek, F. W. Dielectric phenomena in high-voltage engineering. McGraw-Hill, New York, 1929.

3. Oglesby, S., Jr. and Nichols, G. B. Electrostatic precipitation. Marcel Dekker, New York, 1978.

4. Waters, R. T. and Stark, W. B. Characteristics of the stabilized glow discharge in air. Journal of Physics D: Applied Physics. 8: 416-426, 1975.

5. Loeb, Leonard B. Electrical coronas -- their basic physical mechanisms. University of California Press, Berkeley and Los Angeles, California, 1965.

6. Lawless, P. A., McLean, K. J., Sparks, L. E., and Ramsey, G. H. Work in progress.

7. Lawless, P. A. and Sparks, L. E. Measurement of ion mobilities in air and sulfur dioxide-air mixtures as a function of temperature. Atmospheric Environment. 14: 481-483, 1980.

8. Lawless, P. A., Damle, A. S., Viner, A. S., Shaughnessy, E. J., and Sparks, L. E. Laser doppler anemometer measurements of particle velocity in a laboratory precipitator. In: Third Symposium on the Transfer and Utilization of Particulate Control Technology, Vol II. Electrostatic Precipitators. EPA-600/9-82-005b (NTIS PB83-149591). U. S. Environmental Protection Agency, Research Triangle Park, North Carolina, 1982. p 25-34.

9. Lawless, P. A. and Sparks, L. E. A mathematical model for calculating effects of back corona in wire-duct electrostatic precipitators. J. Applied Physics. 51: 242-256, 1980.

10. Cooperman, G. A new current-voltage relation for duct precipitators valid for low and high current densities. IEEE Transactions on Industry Applications. IA-17: 236-239, 1981.

11. Davidson, J. H. Ph.D. Thesis, Duke University, 1984.

NUMERICAL COMPUTATION OF THE ELECTRICAL CONDITIONS IN A WIRE-PLATE ELECTROSTATIC PRECIPITATOR USING THE FINITE ELEMENT TECHNIQUE

by: Gregory A. Kallio and David E. Stock
Mechanical Engineering Department
Washington State University
Pullman, WA 99164-2920

ABSTRACT

The calculation of electrical conditions inside electrostatic precipitators is integral in the development of performance models and design of hardware. Specifically, accurate knowledge of the electric field strength and space charge density is needed to evaluate such processes as particle charging, coulombic drift, electric wind, and back corona. In the present paper, electrical conditions in a wire-plate ESP are computed by utilizing the finite element method to solve the governing electrostatic equations. This method offers distinct advantages in this geometry over conventional finite difference numerical techniques: i) nodal spacing can be selectively adjusted over the solution domain to optimize computational accuracy and economy; ii) curved boundaries are easily and accurately accommodated; iii) internodal solutions can be readily evaluated. The solution yields voltage-current characteristics in addition to space charge density, electric potential, and electric field distributions. The results are compared to finite difference solutions and existing experimental data.

INTRODUCTION

Accurate knowledge of the electric field and space charge density distributions inside electrostatic precipitators is vital to the modeling and analysis of device performance. These quantities play an important role in characterizing particle charging, coulombic particle drift, and the effects of electric wind. Past studies have determined electrical conditions inside wire-plate precipitators by numerically solving the governing partial differential equations (PDE's), namely, Poisson's and current continuity equations. Yabe, et al. (1), Yamamoto and Velkoff (2), and Ushimaru and Butler (3) have used finite difference techniques to solve the governing PDE's, but their models required experimentally measured current versus voltage data to establish the charge density boundary condition at the wire electrode. Leutert and Bohlen (4), McDonald, et al. (5), and Lawless and Sparks (6) employed finite difference solution methods without the reliance of empirically derived boundary conditions. The electrical model of McDonald, et al. has subsequently become an integral part of the well-known Southern Research Institute (SRI) electrostatic precipitator model which has been widely used for performance predictions (7). Felder and Arce-Medina (8) have recently suggested improvements to the SRI electrical model through the use of convergence acceleration methods to minimize computation time.

The finite difference method has an inherent weakness when applied to the solution of Poisson's equation over the domain of the wire-plate geometry due to the strong gradients in potential and electric field near the wire electrode. In order to obtain accurate solutions near the wire, grid size must be significantly smaller than the wire radius. Typical wire-plate geometries would then require grids of at least 200 x 200 points, and solving such finite difference grids would consume unreasonable amounts of computation time. Alternatively, a variable size grid system can be employed to reduce the number of computation points, but the difference equations become awkward to solve. The scheme of Lawless and Sparks (6) numerically solves the integral forms of the governing electrostatic equations to yield electric field and charge density solutions. The method appears to predict the gradients near the wire with a coarse grid, however, an ad hoc power law assumption with an arbitrary exponent is required to compute values within the wire grid cell. The SRI model overcomes the aforementioned problems by requiring solution accuracy only near the precipitator plate. A 10x10 grid is normally utilized which yields satisfactory electric field values near the plate and current-voltage characteristics. However, values of potential, electric field, and space charge density in the midsection of the precipitator generally are not accurate.

The finite element method is well-suited to the solution of elliptic PDE's such as Poisson's equation. The method is especially advantageous in the present application since grid (mesh) size can be continuously varied throughout the computational domain to accommodate large gradients in the solution. The potential and electric field solutions to the wire-plate precipitator are further complemented by the following properties of the finite element method: i) curved boundaries, e.g., at the wire electrode, are accurately accounted for; ii) the functional form of the solution allows direct evaluation of internodal values; iii) solution derivatives, e.g., the electric field, are easily evaluated by differentiation of the elemental solution functions.

The present scheme utilizes the finite element method to solve Poisson's equation in order to obtain more accurate potential and electric field values over the entire wire-plate domain. Triangular elements are employed with quadratic polynomials as basis functions. The nonlinear continuity equation is not amenable to standard finite element techniques, so it is solved using a backward difference method to yield the space charge density distribution. Since the charge density solution does not typically possess large gradients, a rather coarse finite difference grid is adequate. Aside from the finite element solution technique, the solution generally follows the procedure of the SRI computer model (subroutine EFLD2). The space charge is assumed to consist solely of corona-generated unipolar ions of constant mobility. The present computational technique is used to determine potential, electric field, and charge density distributions in addition to current-voltage characteristics. Comparisons are made with finite difference solutions in terms of accuracy and computation time.

THEORETICAL DEVELOPMENT

The electrical conditions inside an electrostatic precipitator are determined by the strongly-coupled applied electric field and corona-generated space charge (in the absence of particles). The corona, or glow, discharge is characterized as a stable process of ion emission from a highly-stressed electrode in a nonuniform electric field. This stable region typically occurs over a wide range of applied voltage, from a minimum threshold called "corona onset" to an eventual spark breakdown. The currents within this range are relatively small (a few milli-amperes at most) and they increase nearly proportional to voltage. This is referred to as the Ohm's law regime. The process is thus described by the steady-state Maxwell equations and a constitutive law relating current and voltage. With the assumption that the magnetic field due to the corona current is negligibly small, the governing electrostatic equations are

$$\nabla \cdot \bar{E} = \rho/\varepsilon_o \tag{1}$$

$$\nabla \cdot \bar{J} = 0 \tag{2}$$

$$\bar{J} = \rho b \bar{E} \tag{3}$$

Equation (1) is the point form of Gauss's law, Eq. (2) represents the continuity of steady currents, and Eq. (3) is the point form of Ohm's law, assuming isotropic conduction. In the present case, the charge carriers are singly-charged unipolar ions. Recent experimental measurements by Lawless and Sparks (9) show that negative ions have a mobility (b) of approximately $1.82\times10^{-4}\,m^2/V/s$ in simulated flue-gas conditions. Since the electric field is irrotational (conservative) in the region of interest, it is derivable from the gradient of a potential (V):

$$\bar{E} = -\nabla V \tag{4}$$

Equations (1) to (4) can be rearranged to yield governing forms for the two primary dependent variables, charge density and electric potential

$$\nabla^2 V = -\rho/\varepsilon_o \tag{5}$$

$$\rho^2 - \varepsilon_o \nabla V \cdot \nabla \rho = 0 \tag{6}$$

Equation (5) is the well-known Poisson's equation and Eq. (6) is a special form of the continuity equation. These two equations compose a coupled pair of PDEs, one of which is nonlinear. With appropriate boundary conditions and solution method, the scalar functions V and ρ can be numerically computed along with the vector fields $\bar{E}$ and $\bar{J}$ from Eqs. (4) and (3).

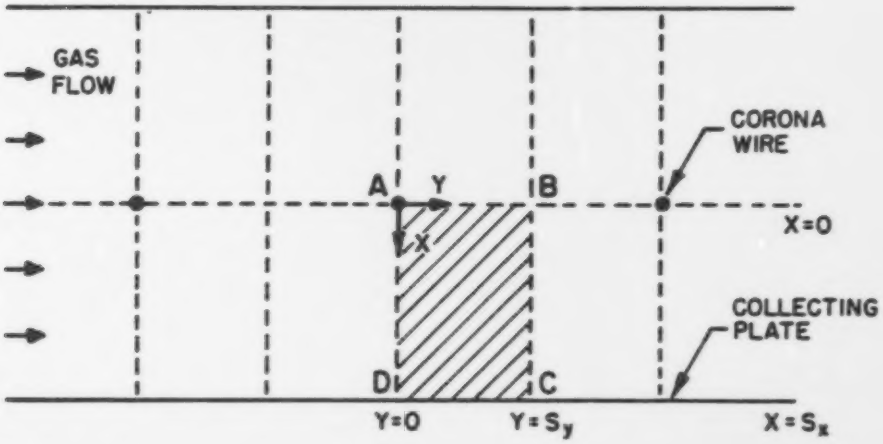

Figure 1. Numerical solution domain for the wire-plate electrostatic precipitator

The solution domain in the wire-plate precipitator geometry is shown in Figure 1. Due to the symmetry of the multi-wire precipitator, the domain consists solely of the rectangle ABCD. It is assumed that the solution will hold for all similar rectangles within the precipitator. The nomenclature and coordinate system are similar to those used by McDonald et al. The following boundary conditions are applied to the specified domain:

i) $E_x = 0$ along line AB;
ii) $E_y = 0$ along lines BC, CD, and AD;
iii) $V = 0$ along line CD;
iv) $V = V_o$ at point A.

Formulation of the boundary conditions near the discharge wire poses some difficulties. The corona discharge establishes an ionization region around the wire which is characterized by a radius (r_i). The ionization radius is typically the same order of magnitude as the wire radius (a). This radius separates the unipolar space charge (outer) region from the very complicated bipolar ion processes contained in the ionization region. This narrow ionized sheath around the wire is generally not modeled due to its complexity, so inner boundary conditions are placed at $r=r_i$ rather than $r=a$. Establishing values or expressions for voltage (V) and charge density (ρ) at $r=r_i$ is the crux of formulating an accurate electrostatic model. Past studies have often determined these boundary conditions from experimentally measured current versus voltage corona characteristics. This reliance on empirical data obviously weakens a theoretical model. The present study adopts the theoretical charge density condition of McDonald et al., who formulated the following expression from the observed constancy of the ion amplification factor

$$\rho_i = (0.002\ S_y J_p)/\pi ba\{31f[\delta+0.0308(\delta/a)^{\frac{1}{2}}]\} \tag{7}$$

where f is the wire roughness factor (f=1 for smooth wires), δ is the gas density normalized to STP, and J_p is the average current density at the collecting plate. The quantity $31f[\delta+0.308(\delta/a)^{\frac{1}{2}}]$ is the semi-empirical relation of Peek (10) for the corona onset electric field of a coaxial wire in a cylinder. All quantities are measured in mks units except wire radius (a), which is in cgs units. The onset ionization radius estimated by Cobine (11) is employed, which is thought to be nearly constant in the Ohm's law regime.

$$r_i \cong a + 0.3\sqrt{a} \tag{8}$$

where the wire radius (a) is again given in cgs units. McDonald et al. chose to use the applied wire voltage (V_o) as the appropriate value at $r=r_i$, however, it appears that a significant voltage drop can exist across the ionization region. A more accurate expression for V_i may be obtained by using the coaxial cylinder expression for potential near the wire (assuming that the ionization region contains no net space charge).

$$V_i = V_o\ \{\ [\ell n(r_i/a)]/[\ell n(r_c/a)]\ \} \tag{9}$$

where r_c is the effective radius of the collecting plate, which is very nearly equal to the wire-plate spacing (S_x).

METHOD OF SOLUTION

The governing equations (5) and (6) with boundary conditions are numerically solved in two dimensions using a combination of finite element (FE) and finite difference (FD) methods. The solution procedure is an iterative scheme similar to that of the SRI model, where an average current density is specified and the applied voltage adjusted until current density computed from $\bar{J}=\rho b\bar{E}$ at the plate agrees with the desired value. The computer code produces values of ρ, V, $\bar{E}$, and $\bar{J}$ at any point in the computational domain in addition to the current-voltage characteristics.

POISSON'S EQUATION

Poisson's equation (5) is solved using finite elements with the Galerkin method of weighted residuals (12). The desired electric potential solution, V(x,y), is replaced by a finite series approximation V(x,y) over each element,

$$\hat{V}(x,y) = \sum_{j=1}^{m} V_j\phi_j(x,y) \tag{10}$$

where ϕ_i are basis functions defined for each node of the element and V_i are undetermined coefficients. The basis functions are chosen to be quadratic polynomials,

$$\phi_j = a_j + b_jx + c_jy + d_jx^2 + e_jxy + f_jy^2,$$

which must allow $\hat{V}$ to meet the imposed boundary conditions and possess continuity across element boundaries. The Galerkin method requires that the integral of each node's residual, when weighted with the basis function, be equal to zero. In this way, the undetermined coefficients are selected to minimize the residual, or error. Imposing this requirement to Poisson's equation and applying Green's theorem yields a linear matrix equation of the form Kc=b where

$$K = \int\int \sum_{j=1}^{m} \left(\frac{\partial\phi_j}{\partial x}\frac{\partial\phi_i}{\partial x} + \frac{\partial\phi_j}{\partial y}\frac{\partial\phi_i}{\partial y}\right)dxdy,\ i=1,2\ \ldots\ m$$

$$b = 1/\varepsilon_o \int\int \rho_i\phi_i dxdy,\ i=1,2\ \ldots\ m$$

$$c = V_j,\ \ j=1,2,\ \ldots\ m.$$

Calculation of the above integrals is simplified by mapping each element onto a master element by an isoparametric transformation. This allows the use of elements with curved boundaries. The matrix equation is solved for c, which contains the approximate potential value at each node. Once solved, internodal potentials can be directly evaluated from Eq. (10). Furthermore, the electric field is determined by simply differentiating Eq. (10):

$$E_x(x,y) = -\sum_{j=1}^{m} V_j \frac{\partial\phi_j}{\partial x} \tag{11}$$

$$E_y(x,y) = -\sum_{j=1}^{m} V_j \frac{\partial\phi_j}{\partial y} \tag{12}$$

The present finite element scheme uses 52 triangular elements with a total of 111 nodes over the solution domain as shown in Figure 2. Each element has six nodes to accommodate the quadratic basis functions. The computer code automatically generates a mesh whose nodal arrangement depends upon a, S_x, and S_y. Near the wire, the mesh has circular symmetry where the radial positions progress as

$$r_n = (a/S_x)^{1-n/10} \quad n=1,\ 2,\ \ldots\ 8$$

This provides a high nodal density where the solution gradients are high. The elements have curved boundaries which match the wire radius exactly and also allow the nodal positions to diverge in a uniform fashion. Away from the wire, the nodal arrangement transforms into a rectangular pattern with seven equi-spaced nodes along lines BC and CD. The residual intergrals in the matrix equation are evaluated over the master element using a seven-point Gaussian quadrature scheme. Assembly of the integral terms yields a

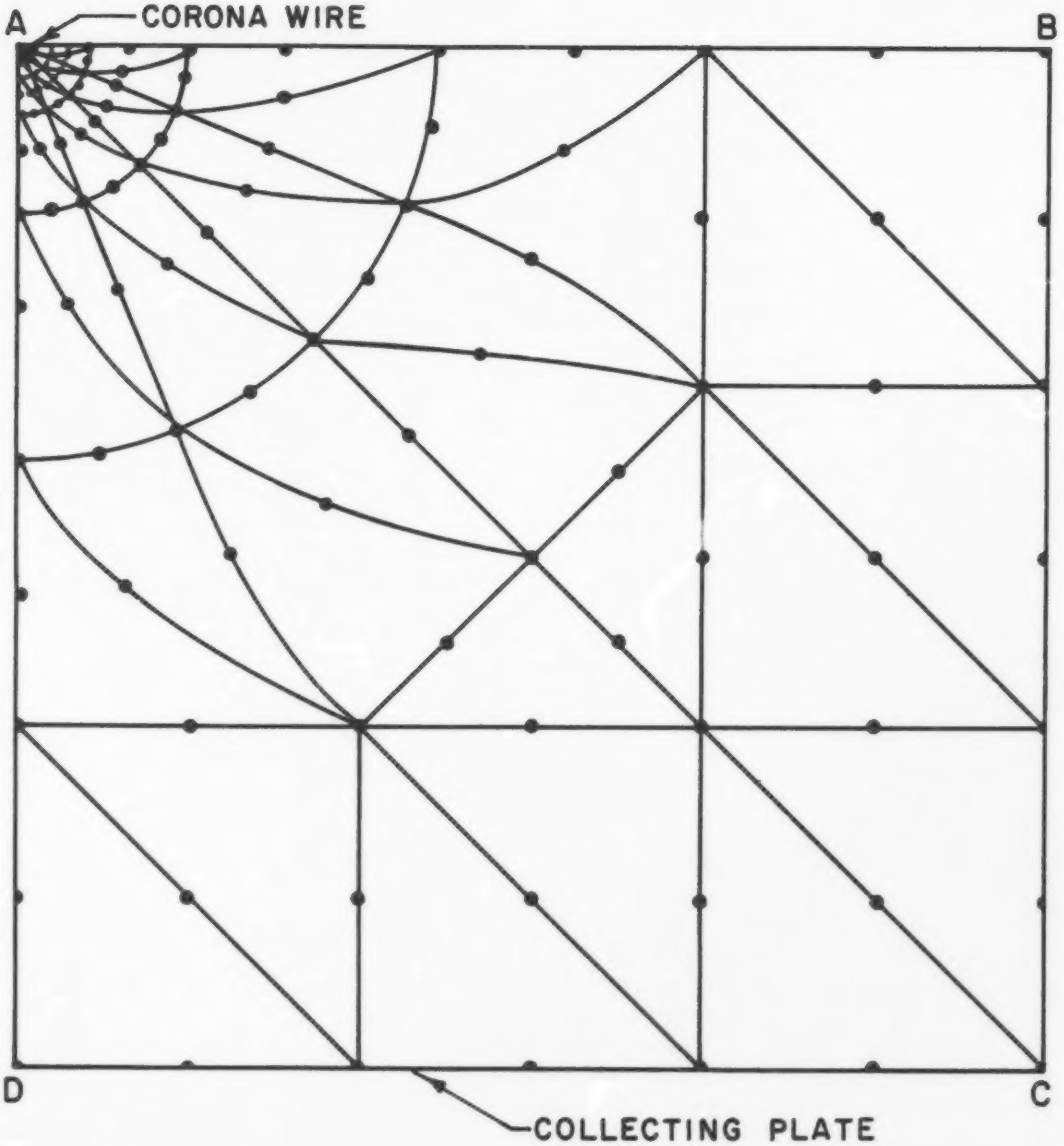

Figure 2. Finite element mesh arrangement

banded, positive definite matrix equation which is solved by a LINPACK subroutine. LINPACK is a package of machine independent Fortran subroutines which analyze and solve various systems of simultaneous linear algebraic equations (13).

CONTINUITY EQUATION

The special form of the continuity equation (6) is approximated by a finite difference formulation, based upon a constant-size rectangular grid. Using backward differences on $\nabla\rho$ and the notation of the SRI model, Eq. (6) becomes

$$\rho_o = -\alpha + (\alpha^2+\beta)^{\frac{1}{2}} \tag{13}$$

where $\alpha = \frac{1}{2}\varepsilon_o(a_y E_{xo} + a_x E_{yo})/a_x a_y$

$\beta = \varepsilon_o(a_y E_{xo}\rho_2 + a_x E_{yo}\rho_3)/a_x a_y$

The subscript "o" refers to the computational point of interest, while subscripts "2" and "3" refer to the "upstream" points in the x and y direction respectively. Values of ρ_o are successively computed at each grid point by progressing outward from the known condition (Eq. 7) at the wire electrode.

COMPUTATIONAL PROCEDURE

The solution procedure begins by specifying an average current density (J_{po}) at the collecting plate and a corresponding estimate (guess) of the applied wire voltage (V_o). The electric field at the FD grid points is initialized by using Cooperman's space charge-free analytic solution (14). Charge density is computed at all points from Eqs. (7) and (13). The values of ρ at the FE nodes are then interpolated from the FD point values using a bilinear approximation over each grid rectangle. This allows the FE computation of potential at all nodes from Poisson's equation. Next, charge density is recomputed from the FD equations using the new values of electric field found from Eqs. (11) and (12). Likewise, potential is recomputed using FE with new values of interpolated charge density. This computation cycle is repeated until changes in potential values become less than 0.1 percent. Average current density is then determined at the plate using the computed charge density and electric field values.

$$J_p = \frac{1}{N}\sum_{j=1}^{N} \rho_j b E_{xj} \tag{14}$$

where N is the number of equi-spaced grid points along the plate. The value of J_p calculated from Eq. (14) is compared to the specified value. If they do not agree to within 1 percent, the value of V_o is adjusted and the entire procedure repeated until J_p converges. The applied voltage is adjusted according to a power law relationship in order to speed convergence (8),

$$V_o^{(n)} = V_o^{(n-1)}(J_{po}/J_p^{(n-1)})^{\gamma}$$

where n refers to the present value and n-1 is the previous value.

The exponent γ is determined from the preceding two steps as

$$\gamma = \ell n(V_o^{(n-1)}/V_o^{(n-2)})/\ell n(J_p^{(n-1)}/J_p^{(n-2)})$$

When the voltage is first adjusted, an arbitrary value of $\gamma=0.9$ is used to initialize the sequence. This algorithm produces a significant decrease in convergence time over the SRI model, typically requiring only three iterations to satisfy the current density convergence criterion.

RESULTS

The finite element (FE) and finite difference (FD) solutions are compared in Figures 3 through 7 in terms of electric potential, electric field, space charge density, and current versus voltage characteristics. The FD model was run with a 10x10 grid (121 points) for all square domains, which is comparable to the 111 nodes used in the FE model. The computations represent standard gas (air) conditions ($\delta=1$) and discharge wires that are clean and polished ($f=1$). Figures 3(a) and 3(b) display the potential and electric field profiles, respectively, for zero space charge ($J_p=0$) along line AD between the wire and plate of a typical geometry. Accompanying the numerical solutions is Cooperman's analytic solution. As expected, the coarse-grid FD solution poorly approximates the exact solution due to the high gradients in potential near the wire. The FE solution closely follows the exact solution due to the high nodal density near the wire. Note that the FD electric field is discrepant near the plate, indicating that inaccuracies initiated near the wire tend to propagate throughout the computational domain. The discrepancy between the FD and FE (or exact) solutions lessens as the wire size is increased, however, even for a=1.27 mm, the error was found to be significant; FD potential solutions were approximately 15 percent higher over the entire profile while electric field values ranged from 15 to 75 percent high.

Figures 4(a) and 4(b) compare FD and FE solution profiles for a moderate and high average current density, $J_p=10^{-4}$ and $J_p=10^{-3}$ A/m². The presence of space charge tends to decrease the gradients in electric potential, however, the FD model still has difficulty predicting the potential and electric field profiles when $J_p=10^{-4}$ A/m². Again, note that the electric field values at the collecting plate are highly discrepant. At $J_p=10^{-3}$ A/m², the space charge is sufficient to reduce the gradients in potential over the entire wire-plate gap, except very near the wire. Consequently, the FD and FE solutions agree closely over most of the region.

Figure 5 displays space charge density profiles along line AD for both low and high current densities, $J_p=10^{-5}$ and $J_p=10^{-3}$ A/m². Note that both solution techniques show close agreement, which is expected since each model employs FD to solve the continuity (space charge) equation. Also note that low current density gives rise to a nearly uniform charge density distribution while high current density promotes a decreasing profile toward the plate, representing a space charge-limited current.

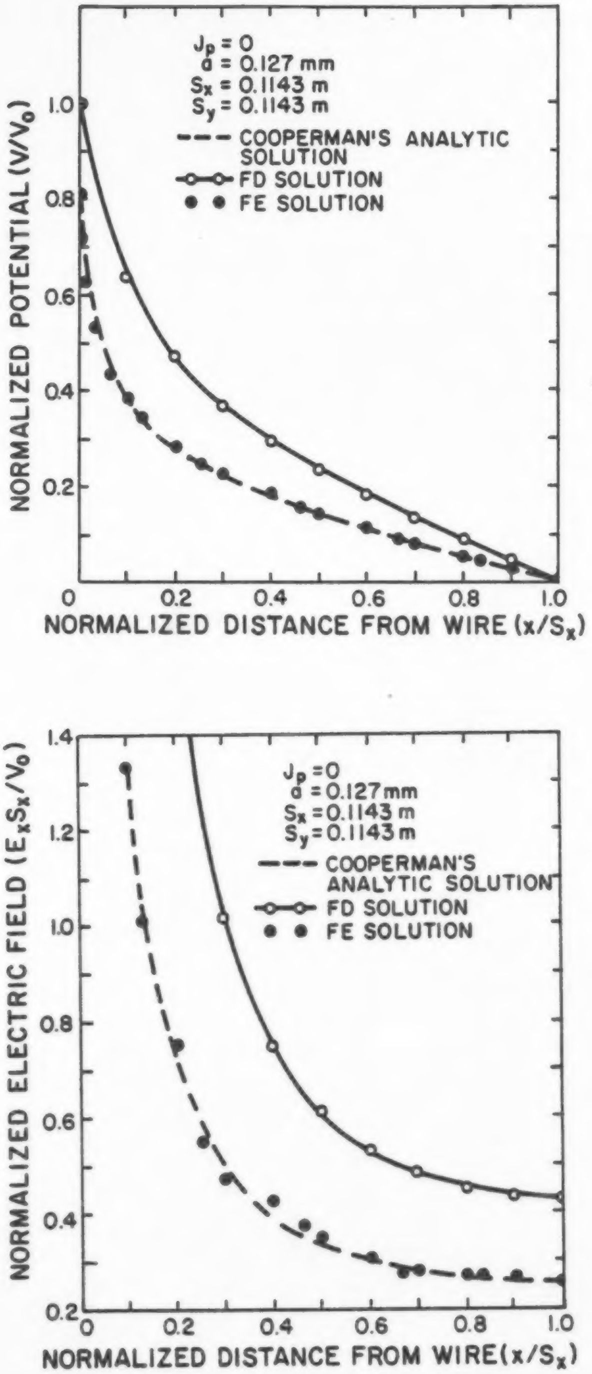

Figure 3. Electric potential (a) and electric field (b) distributions along line AD for zero space charge ($J_p = 0$)

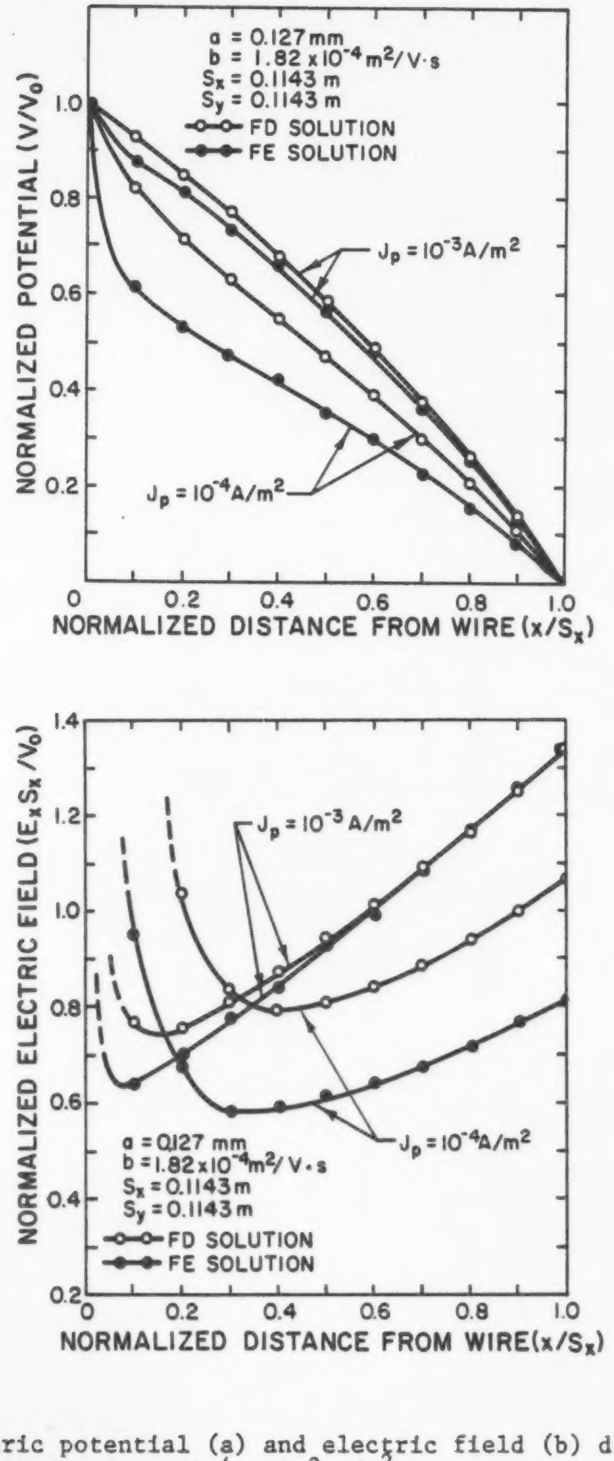

Figure 4. Electric potential (a) and electric field (b) distributions along line AD for $J_p = 10^{-4}$, 10^{-3} A/m^2

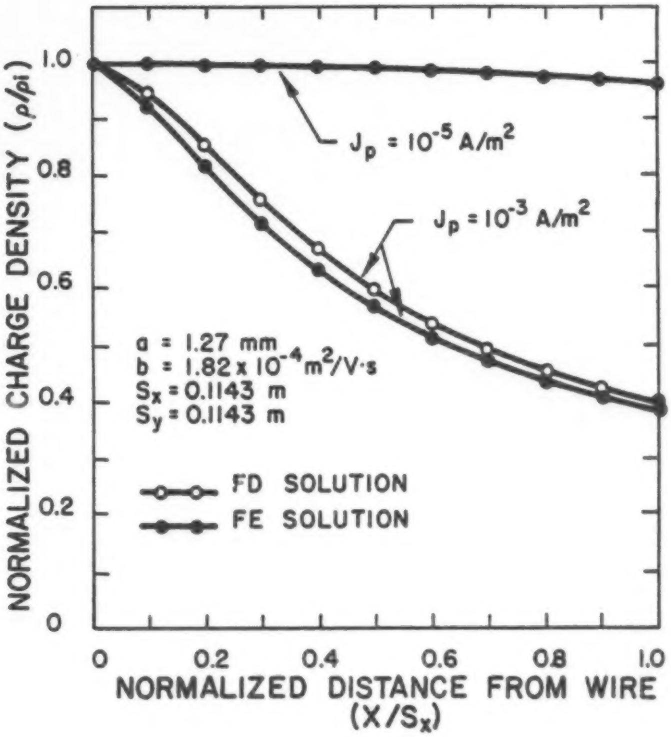

Figure 5. Space charge density distribution along line AD for $J_p=10^{-5}$, 10^{-3} A/m²

Figure 6 presents computed current versus voltage characteristics for two wire sizes, a=0.127 mm and a=1.27 mm. The FD results display a generally higher current density for a given applied voltage due to the higher electric field predicted at the plate. For a=0.127 mm, note that the FD and FE curves merge together at high current density ($J_p=10^{-3}$ A/m²) since the electric field solutions of the two methods become comparable for such conditions. Likewise, for a=1.27 mm, the current-voltage curves merge at approximately 115 kV for $J_p=10^{-2}$ A/m² (not shown on plot).

Figure 7 shows the electric potential profiles along BC, i.e., from the midpoint between wires to the plate. Experimental data from Penney and Matick (15) compared to the numerical solution predictions. These potential measurements were taken with a shielded fine-wire probe in which voltage was applied to the shield to overcome the excess potential of the wire probe due to the ionic charge transfer. The plots show good agreement over the entire region for both FD and FE predictions. Unfortunately, accurate experimental measurements of potential or electric field are not available in regions and geometries where the two numerical techniques give discrepant solutions.

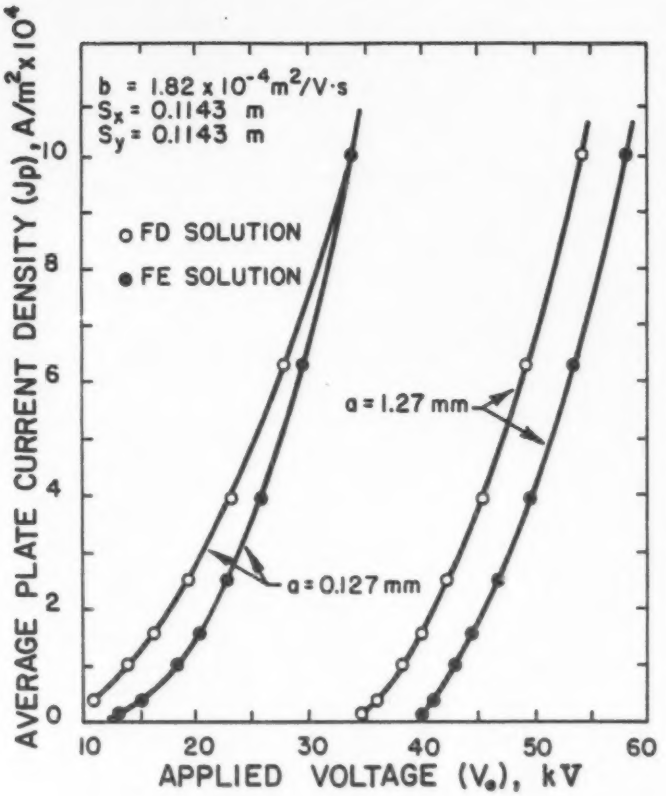

Figure 6. Current density versus applied voltage for a=0.127, 1.27 mm

CONCLUSIONS AND DISCUSSION

The prediction comparisons of the finite difference and finite element electrical models can be summarized as follows:

i) For low to moderate current densities, the FD potential and electric field solutions possess significant inaccuracies over the entire wire-plate region due to the high gradients in potential near the wire. For such conditions, the FE solution is suggested.

ii) For high current densities and large wire sizes, the discrepancies between the FD and FE predictions are minimal due to the lower potential gradients near the wire. Either solution method is adequate for these cases.

iii) The space charge predictions of each numerical model agree closely due to the similar treatment of the space charge PDE.

Of further interest is the accuracy and required computation time for each numerical model. Accuracy of FD methods is easily defined in terms of Taylor series expansions. In the SRI FD model, electric potential is second-order accurate due to center differencing, while the electric field

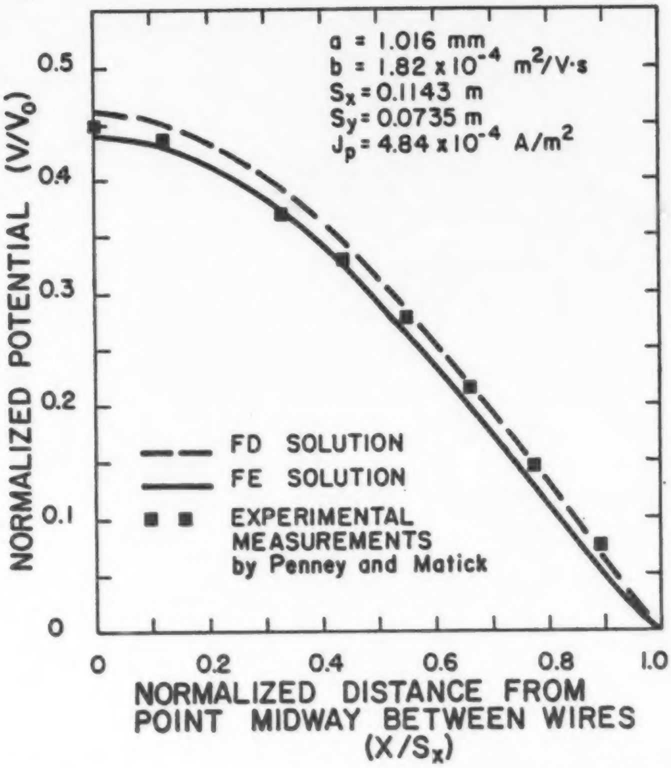

Figure 7. Comparison of electric potential predictions along line BC with experimental measurements of Penney and Matick

and space charge density solutions are first-order accurate from backward differencing. The accuracy of finite element techniques are somewhat difficult to characterize and compare due to their variable nodal spacing. Since the basis functions are quadratic, the accuracy of the potential solution is approximately second-order, while the electric field is approximately first-order accurate due to differentiation. However, the nodal spacing in the FE formulation is much smaller than the FD grid size in those regions where higher-order accuracy is needed (near the wire). Therefore, the relative accuracy of the two methods is best described by the ratio of FE nodal spacing to the FD grid spacing in the region of interest.

The improved accuracy of the FE technique is slightly offset by an increase in computation time. Even though the number of iterations between Poisson's equation and the continuity equation are drastically reduced by using the FE method, the time required to invert the K-matrix and solve the matrix equation is lengthy. In addition, the alternating conversion between FD and FE grid systems consumes a significant amount of time. As an example, computation of the potential and electric field profiles for a=0.127 mm (Figure 4) on a Prime 400 minicomputer yields the following:

	total iterations	CPU time
FD method	686	72 sec
FE method	13	206 sec

The accuracy and computational efficiency of the present finite element model could be further improved through several modifications. First, the use of Hermitian (cubic polynomial) basis functions in the FE approximation would provide third-order accurate potentials, but more importantly, it would also provide continuity in the first derivative (electric field) across element boundaries. The present quadratic approximation does not insure first derivative continuity, so electric field values at element boundaries are somewhat ambiguous. These small discontinuities are noticed in the slightly ragged appearance of the presented electric field profiles. Second, the required computation time of the model may be reduced by solving the continuity (space charge) PDE with the FE method rather than the FD method. This would eliminate the time consuming conversion between FE and FD grids and would provide second-order accurate space charge density solutions. However, the application of the Galerkin method to the hyperbolic, nonlinear continuity equation does not appear straightforward (12).

The work described in this paper was not funded by the U.S. Environmental Protection Agency and therefore the contents do not necessarily reflect the views of the Agency and no official endorsement should be inferred.

ACKNOWLEDGEMENTS

The authors wish to thank Associate Professor David S. Watkins for his helpful advice on utilizing the finite element technique, Jack R. McDonald for information about the SRI electrical model, and James R. Ferguson for providing general discussion of the numerical model.

In addition, the support from the U.S. Department of Energy in the form of a research fellowship is gratefully acknowledged.

NOMENCLATURE

a	radius of discharge wire
a_x	length of FD grid cell in x-direction
a_y	length of FD grid cell in y-direction
b	mobility of ionic charge carriers
$\bar{E}$	electric field strength
E_x	electric field component in x-direction
E_y	electric field component in y-direction
f	wire roughness factor
$\bar{J}$	current density
J_p	average current density at collecting plate
r	radial distance from wire
r_i	radius of ionized sheath
r_c	effective radius of collecting plate in a wire-cylinder geometry
S_x	wire-to-plate spacing
S_y	one-half wire-to-wire spacing
V	electric potential, or voltage
$\hat{V}$	FE approximation to electric potential
V_o	applied voltage at wire
V_i	voltage at ionization radius (r_i)
x	coordinate position toward collecting plate from center of wire
y	coordinate position parallel to collecting plate from center of wire
α	parameter used in Eq. (13)
β	parameter used in Eq. (13)
δ	relative density of gas
ε_o	permittivity of free space ($8.854\text{x}10^{-12}$ F/m)
γ	exponent in Eq. (15) x
ϕ_j	FE basis function associated with node j
ρ	space charge density
ρ_i	space charge density at ionization radius (r_i)

REFERENCES

1. Yabe, A., Mori, Y. and Hijikata, K. (1978), EHD study of the corona wind between wire and plate electrodes, AIAA Journal 16, 340-345.
2. Yamamoto, T. and Velkoff, H.R. (1981), Electrohydrodynamics in an electrostatic precipitator, J. Fluid Mech. 108, 1-18.
3. Ushimaru, K. and Butler, G.W. (1984), Numerical simulation of gas-solid flow in an electrostatic precipitator, Proceedings of the Symposium on Gas Solid Flows, 7th Annual Energy-Sources Technology Conference & Exhibition, February 12-16, 1984, New Orleans.
4. Leutert, G. and Bohlen, B. (1974), The spatial trend of electric field strength and space charge density in plate-type electrostatic precipitators, Staub 32, 27-33.
5. McDonald, J.R., Smith, W.B. and Spencer, H.W. (1977), A mathematical model for calculating electrical conditions in wire-duct electrostatic precipitation devices, J. Appl. Phys. 48, 2231-2243.
6. Lawless, P.A. and Sparks, L.E. (1980), A mathematical model for calculating effects of back corona in wire-plate electrostatic precipitators, J. Appl. Phys. 51, 242-256.
7. McDonald, J.R. (1978), A mathematical model of electrostatic precipitation, Vol. I, U.S. Environmental Protection Agency Report No. EPA-600/7-78-111A.
8. Felder, R.M. and Arce-Medina, E. (1984), Calculation of voltage and space charge distributions in a wire-plate electrostatic precipitator, J. Electrostatics 15, 3-13.
9. Lawless, P.A. and Sparks, L.E. (1980), Measurement of ion mobilities in air and sulfur dioxide-air mixtures as a function of temperature, Atmos. Environ. 14, 481-483.
10. Peek, F.W. Jr. (1924), Dielectric Phenomena in High Voltage Engineering, 3rd edition, McGraw-Hill, Inc., New York, 66.

Session 6: ESP: PERFORMANCE ENHANCEMENT I

Ralph F. Altman, Chairman
Electric Power Research Institute
Chattanooga, TN

A FIELD STUDY OF A COMBINED NH_3-SO_3 CONDITIONING SYSTEM ON A COLD-SIDE FLY ASH PRECIPITATOR AT A COAL-FIRED POWER PLANT

by: Robert S. Dahlin
John P. Gooch
Guillaume H. Marchant, Jr.
Southern Research Institute
Birmingham, Alabama 35255

Roy E. Bickelhaupt
Bickelhaupt Associates, Inc.
Carbondale, Illinois 62901

D. Richard Sears
University of North Dakota
Energy Research Center
Grand Forks, North Dakota 58202

Ralph F. Altman
Electric Power Research Institute
Chattanooga, Tennessee 37411

ABSTRACT

This paper presents the results of a field study of a combined NH_3-SO_3 conditioning system used to improve the performance of a cold-side electrostatic precipitator at a coal-fired power plant. The NH_3 was injected between the air heater and the precipitator at a rate of 5 ppm, and the SO_3 was injected ahead of the air heater at a rate of 9 ppm (in addition to 5 ppm of SO_3 produced naturally in the boiler). The measured concentrations of NH_3 and SO_3 just ahead of the precipitator were below 0.5 ppm, suggesting that the two agents were adsorbed on the fly ash and/or reacted together to form a sulfate particulate. Laboratory studies showed that the adsorption of these quantities of NH_3 and SO_3 on the ash produced a surface film that reduced the electrical resistivity of the ash by about one order of magnitude. The reduced resistivity was directly responsible for the excellent electrical operating conditions of the precipitator, which made it possible to achieve a collection efficiency of 98.5% with an SCA of only 166 ft^2/kacfm.

INTRODUCTION

This paper describes the results of a field study of a combined NH_3-SO_3 conditioning system used to improve the performance of a cold-side electrostatic precipitator at a large coal-fired power plant. The combined NH_3-SO_3 conditioning system was placed into continuous service after numerous tests by plant personnel showed that the combined NH_3-SO_3 system was more effective than the use of either NH_3 or SO_3 alone. In the tests by plant personnel, the effectiveness of various injection locations and injection rates of one or both agents was judged on the ability to maintain an acceptable stack opacity. The evaluations performed by plant personnel also included resistivity measurements, particle sizing, and emissions testing. Based on the results of these tests, the plant management selected a combined conditioning system in which NH_3 is injected between the air heater and the precipitator at a rate of 5 ppm, and SO_3 is injected ahead of the air heater at a rate of 9 ppm. This was in addition to 5 ppm of SO_3 that is produced naturally in the pulverized coal-fired boiler. In most applications of flue gas conditioning, the SO_3 is injected downstream of the air heater; however, it is believed that injection ahead of the air heater, as was done at this plant, may result in a more uniform distribution of the SO_3 in the flue gas and more effective utilization of the SO_3.

Although the tests by plant personnel were successful in identifying a conditioning system that would improve precipitator performance and reduce stack opacity to an acceptable level, the tests provided no information concerning the mechanisms involved, or why the combined NH_3-SO_3 system was more effective than either NH_3 or SO_3 alone. Thus, the present study was undertaken to obtain a more fundamental understanding of the combined NH_3-SO_3 conditioning process, and to hopefully learn what makes the combined process more effective than NH_3 or SO_3 alone. The present study provides some new understanding of the mechanisms, but it stops short of a definitive analysis. This is largely because field studies could not be done with one or both of the conditioning agents turned off. Nevertheless, laboratory studies have made it possible to infer significant information concerning the role of NH_3 and SO_3 in the combined conditioning process.

OBJECTIVES AND SCOPE

The work described in this paper was jointly sponsored by the Electric Power Research Institute (EPRI) and the Grand Forks Projects Office of the U. S. Department of Energy (DOE). The EPRI-sponsored portion of the work was primarily concerned with laboratory studies aimed at developing a better understanding of the effects of NH_3 and SO_3 on the electrical resistivity of the ash. The DOE-sponsored portion of the work was primarily concerned with field studies aimed at: evaluating the performance of the conditioned precipitator; obtaining data on the concentration, composition, and size distribution of the conditioned fly ash; defining the injected and residual levels of NH_3 and SO_3 in the flue gas and the levels of NH_4^+ and SO_4^{-2} on the fly ash; quantifying the overall and fractional collection efficiency of the precipitator; and collecting coal and size-fractionated ash samples for further characterization. Along with similar data from other field tests, the data listed above are being used by the Grand Forks Projects Office in the assessment of particulate control technologies for low-rank Western coals.

The scope of the test program encompassed the following elements:

(1) Determination of inlet and outlet mass loadings of fly ash and overall fly ash collection efficiency by EPA Method 17 (1),

(2) Measurement of inlet and outlet particle size distributions of fly ash and fractional collection efficiency using calibrated cascade impactors (2),

(3) Documentation of boiler and precipitator operating conditions during testing,

(4) Sampling and analysis of coal by ASTM methods (3),

(5) Sampling of fly ash in glass fiber thimbles and analysis of major elements by atomic absorption spectrometry (4),

(6) Analysis of the fly ash for NH_4^+ content by specific ion electrode (5) and for SO_4^{-2} content by ion chromatography (6),

(7) Measurement of injected and residual levels of NH_3 in the flue gas by collection in a 0.02 N H_2SO_4 solution,

(8) Measurement of injected and residual levels of SO_3 in the flue gas by the Cheney-Homolya method (7), and

(9) Laboratory resistivity studies with the conditioned ash and with ash in which the conditioning effect had been removed by thermal treatment.

Space limitations preclude a detailed presentation of all of the above; the interested reader is referred to the DOE report on this work (8).

SITE DESCRIPTION

PRECIPITATOR

The precipitator layout is illustrated in Figure 1. The flue gas stream leaving the boiler and economizer is split and passes through two air heaters and then through four separate precipitators in a double-chevron arrangement as shown in the layout. The precipitator designated ESP 2-1 was the subject of this testing. It is identical to the other precipitators: divided into two chambers, each with two electrical fields in the direction of gas flow. All fields are equipped with standard 0.109 in. weighted discharge wires and 9 ft by 30 ft collection plates spaced 9 in. apart. The precipitator is small by modern standards, with a specific collection area of only 166 ft^2/1000 acfm. This is the actual operating specific collection area which is slightly greater than the design value of 156 ft^2/kacfm. It is operated at a

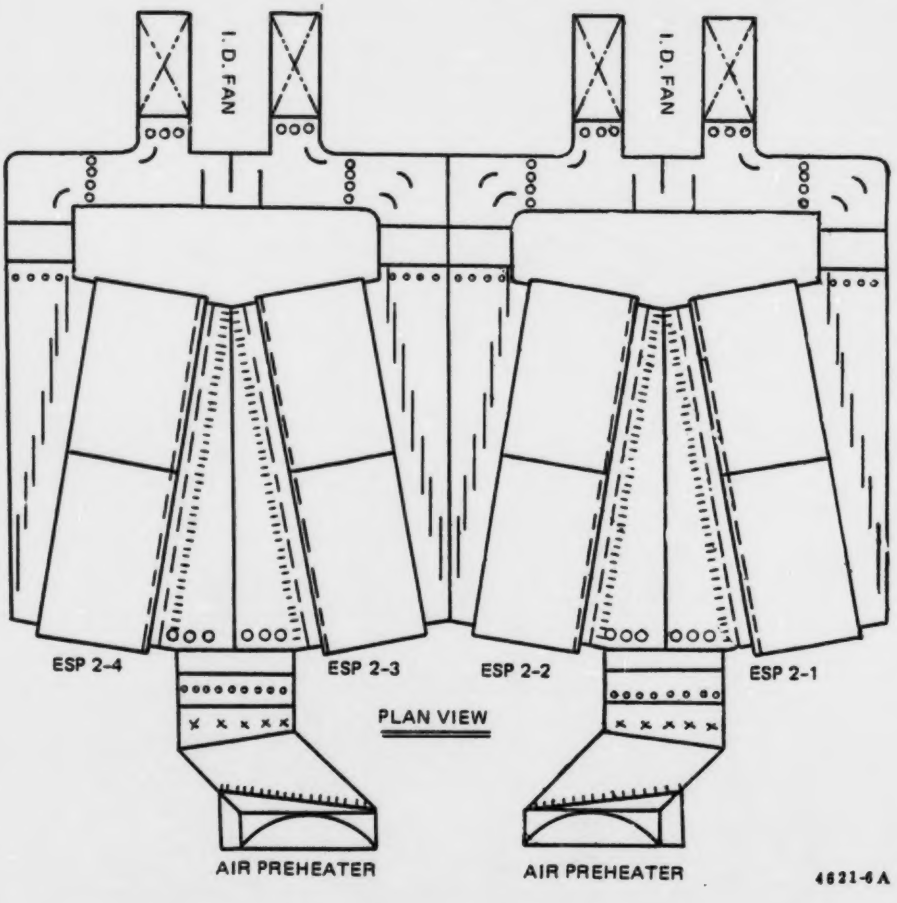

Figure 1. ESP layout.

fairly high temperature (~370°F) compared to most cold-side precipitators that normally operate at about 300°F. Both the small size and the high temperature are factors that contributed to poor precipitator performance before this was corrected by the use of the combined NH_3-SO_3 conditioning process.

BOILER

The steam generator that supplies the flue gas to ESP 2-1 is one of two identical units. Each unit is a tangentially-fired, dry-bottom boiler. Both units are normally base-loaded with a nominal generating capacity of 575 MW. During the testing, the unit of interest, designated Unit 2, was operated at a fairly constant load in the range of 566 to 580 MW with excess air in the range of 13 to 19%.

FUEL

Both generating units burn a Wilcox-group Texas lignite that is mined on site at the plant. Lignite samples taken from one of the Unit 2 feeders during the testing showed an average heating value of 7000 Btu/lb and an average ash content of 17% on an as-received basis. Daily samples showed considerable variability in the lignite composition. The results of several proximate and ultimate analyses are given in Table 1.

TEST PROCEDURES AND RESULTS

MASS LOADINGS AND OVERALL EFFICIENCY

Mass loadings were measured at the inlet and outlet of ESP 2-1 by EPA Method 17 (1). Each sampling location was traversed with mass trains equipped with in-stack filters. Isokinetic sampling was approximated as closely as possible at each sampling point. The measured mass loadings are given in Table 2. During this testing the boiler load was maintained fairly constant in the range of 566 to 580 MW, with excess air in the range of 13 to 19%. The stack opacity recorded by the plant transmissometer was between 26 and 32%.

During the test period the average operating SCA was 166 ft^2/1000 acfm, slightly higher than the design value. The average inlet and outlet mass loadings were 6.64 and 0.103 gr/dscf, yielding an average efficiency of 98.45%. Previous measurements made by plant personnel yielded efficiencies in excess of 99%, somewhat higher than the present data. The difference may be related to differences in coal composition, boiler operating conditions, and ESP operating conditions.

PARTICLE SIZE DISTRIBUTIONS AND FRACTIONAL EFFICIENCY

The inlet and outlet particle size distributions were determined from in-stack cascade impactor sampling (2) using modified Brink impactors at the inlet and University of Washington Mark III impactors at the outlet. Seven real impactor runs and one blank run were performed in separate sampling ports at the inlet, while six complete traverses of duct area were performed at the outlet with two blanks. Glass fiber substrates were used in the impactors. The blank runs did not reveal any appreciable substrate interference problems.

TABLE 1. PROXIMATE AND ULTIMATE COAL ANALYSES (AS-RECEIVED BASIS)[a]

	Sample 1	Sample 2	Sample 3
Proximate			
% Moisture	21.07	29.37	31.51
% Ash	14.41	23.05	12.91
% Volatile	42.21	22.42	50.45
% Fixed carbon	22.31	25.16	5.13
Btu/lb	8,671	5,978	6,452
% Sulfur	0.91	0.85	0.73
Ultimate			
% Moisture	21.07	29.37	31.51
% Carbon	51.49	35.22	39.50
% Hydrogen	2.81	2.39	2.68
% Nitrogen	1.12	0.71	0.64
% Chlorine	0.06	0.05	0.05
% Sulfur	0.91	0.85	0.73
% Ash	14.41	23.05	12.91
% Oxygen[b]	8.13	8.36	11.98

---

[a] Samples taken from Unit 2 feeder discharge.

[b] Oxygen determined by difference.

TABLE 2. MASS TRAIN DATA

Run No.	Load (MW)	Temp. (°F)	SCA (ft^2/kacfm)	Inlet loading (gr/dscf)	Inlet percent isokinetic	Outlet loading (gr/dscf)	Outlet percent isokinetic	Efficiency (%)	Opacity (%)
1	580	380	171	6.22	105.7	0.111	97.0	98.22	26.4
2	568	385	163	6.37	109.8	0.0783	99.4	98.77	27.5
3	566	385	165	7.32	109.9	0.120	99.1	98.36	31.8

Figure 2 shows the inlet and outlet particle size distributions determined from the impactor sampling. The curves shown were obtained by averaging the spline fits (9) to a number of impactor runs; the points do not represent the raw data, but rather the interpolated points generated by the spline fit.

The fractional efficiency curve derived from the inlet and outlet impactor measurements is shown in Figure 3. This apparently shows a minimum in the collection efficiency at just below 1 μm. The curve appears to be qualitatively consistent with theoretically predicted fractional efficiency curves in the range of 1 to 10 μm. The fractional efficiencies are also consistent with the measured overall efficiency if one considers that half of the mass is contained in particles larger than 14 μm. The cumulative efficiency for collection of sub-5-μm particles is 97%.

SO_3 AND NH_3 MEASUREMENTS

SO_3 samples were collected ahead of the air heater and downstream of the SO_3 injection system using the Cheney-Homolya sampling system (7). For SO_3 and NH_3 sampling at the ESP inlet and outlet locations, the probe and quartz filter temperature was reduced from ~550°F to the prevailing flue gas temperature. This modification of the sampling procedure was necessary to prevent thermal decomposition of the ammonium sulfate particulate assumed to be present in the flue gas at these locations. The system was further modified for NH_3 sampling by removing the condenser and substituting one of two Greenburg-Smith bubblers for a Greenburg-Smith impinger. A dilute (0.02 N) H_2SO_4 solution was used as the collection medium for all NH_3 samples.

SO_3 samples were analyzed by $Ba(ClO_4)_2$ titration with Thorin indicator (7); NH_3 samples with a specific ion electrode (5). The results indicate that about 5 ppm of natural SO_3 was present in the flue gas ahead of the air preheater. Downstream from the SO_3 injection probes about 14 ppm of H_2SO_4 was found. Therefore, it appears that approximately 9 ppm of H_2SO_4 was added to the flue gas by the injection system. Based on the flowmeters on the injection system, only 6.5 ppm of H_2SO_4 should have been added to the flue gas. It is possible that this difference is due to nonuniform distribution of the H_2SO_4 across the duct, since traverses of the entire duct area were not made.

Less than 0.5 ppm of both NH_3 and SO_3 were found at the precipitator inlet, presumably due to adsorption on fly ash and reaction to form a sulfate particulate. Based on the NH_3 injection rate of 5 ppm, 2.5 ppm of H_2SO_4 would have been consumed in the formation of ammonium sulfate, and the remaining 11.5 ppm adsorbed by the ash.

The adsorption of 5 ppm of NH_3 onto the fly ash particles having a mass loading of 6.64 gr/dscf (see Table 2) would be expected to produce an NH_4^+ concentration of 0.029% by weight in the ash, assuming complete adsorption. The mean measured NH_4^+ concentration in the inlet mass train samples was 0.022%, or 76% of the expected value. The adsorption of 14 ppm of SO_3 would be expected to produce a SO_4^{-2} concentration of 0.4% by weight in the ash, again assuming complete adsorption. However, the measured concentrations of SO_4^{-2} in the inlet mass train samples ranged from 0.84 to 1.2%. The most likely explanation appears to be that the ash adsorbed additional SO_3 while it resided in the mass train thimble and flue gas was passed through it.

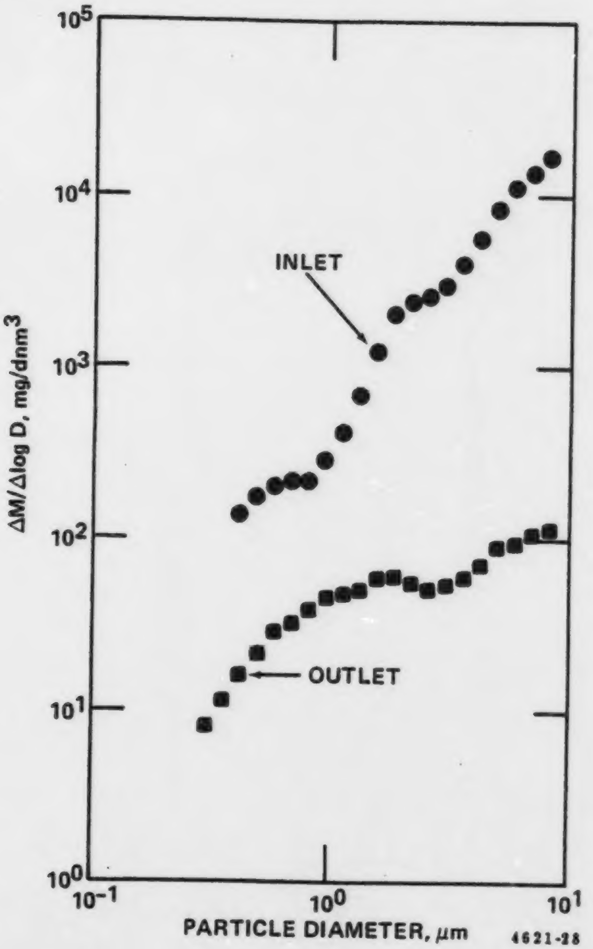

Figure 2. Differential mass distributions at inlet and outlet ESP.

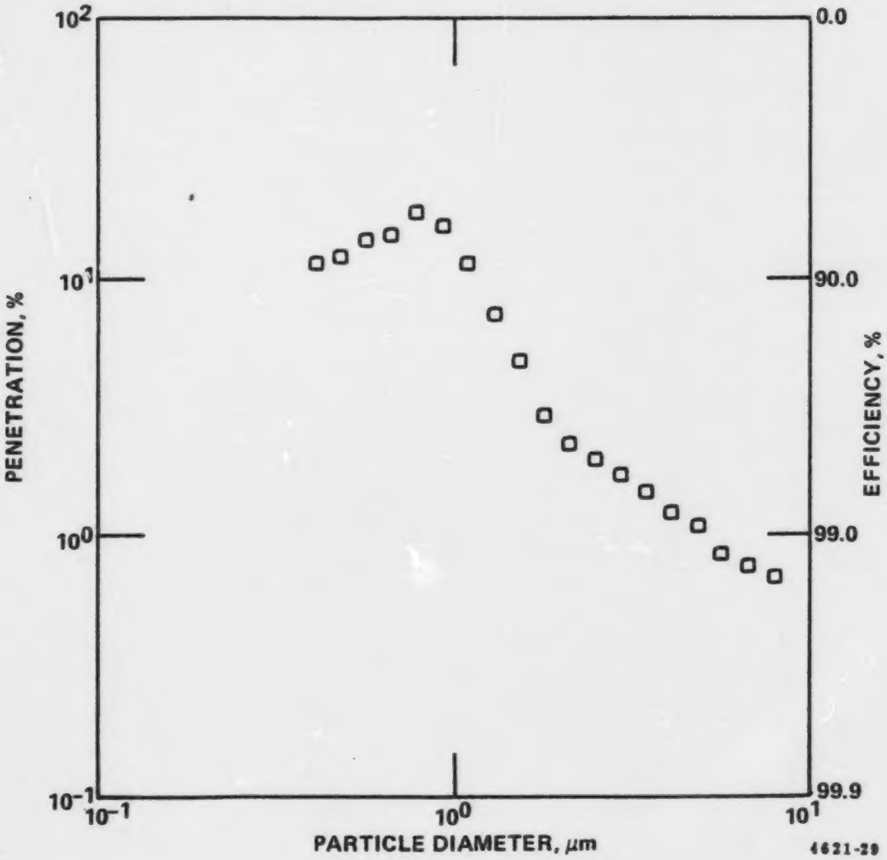

Figure 3. Fractional efficiency curve.

ELECTRICAL OPERATION OF ESP

Voltage-current curves were obtained for all of the ESP 2-1 transformer-rectifier sets. ESP 2-1 contains four fields: East inlet, West inlet, East outlet, and West outlet. Voltage-current curves for all four fields are shown in Figure 4. All of the curves are quite well behaved, indicating excellent electrical operating conditions are achievable. As will be shown later, this is a direct result of the low electrical resistivity of the conditioned ash.

LABORATORY RESISTIVITY STUDIES

These studies were done with a sample of fly ash taken from an outlet hopper of ESP 2-1. Normally, a composite sample from both inlet and outlet hoppers would be preferred for this work, but only the outlet hopper sample was available. It was, of course, biased toward fine particles (e.g., 12% of the sample by weight was smaller than 2 μm compared to the inlet impactor samples which showed only 2% smaller than 2 μm). This resulted in disproportionately high concentrations of NH_4^+ and SO_4^{-2} in the outlet hopper sample (e.g., 0.046% NH_4^+ and 1.54% SO_4^{-2} in the outlet hopper sample compared to 0.022% NH_4^+ and 1.01% SO_4^{-2} in the inlet mass train samples). This is to be expected since the finer particles have higher specific surface areas for adsorption of NH_3 and SO_3. Thus, the effects observed with this particular sample may be somewhat greater than the effects that would have been observed with a composite sample consisting of all particle sizes. Nevertheless, a composite sample should show the same trends.

In order to investigate the effect of the surface film that was assumed to be present on the ash as a result of the conditioning, the electrical resistivity was measured by two techniques: one in which the resistivity of the as-received ash was measured as a function of increasing temperature starting at 95°C, and one in which the ash was first heated to 450°C to destroy the surface film, with resistivity then being measured as a function of decreasing temperature starting at 450°C. The results are illustrated in Figure 5. It is obvious that the resistivity measured with increasing temperature is substantially lower than that measured with the decreasing temperature after the sample was heated to 450°C. This shift is apparently due to the destruction of the surface film deposited by the NH_3-SO_3 conditioning process.

Figure 5 also shows the predicted resistivity as a function of temperature. This curve was predicted from the ash composition, exclusive of NH_4^+ and SO_4^{-2}, using the technique of Bickelhaupt (10). The good agreement between the predicted curve and that measured with decreasing temperature suggests that there is no conditioning effect present in this case, or that the surface film has indeed been removed. Thus, at a temperature of 150°C, for example, the surface film appears to be responsible for reducing the resistivity by more than an order of magnitude.

It is important to note that the resistivity curves shown in Figure 5 were obtained without any NH_3 or SO_3 in the test environment. It would be desirable to make a resistivity measurement after the ash in the test cell had

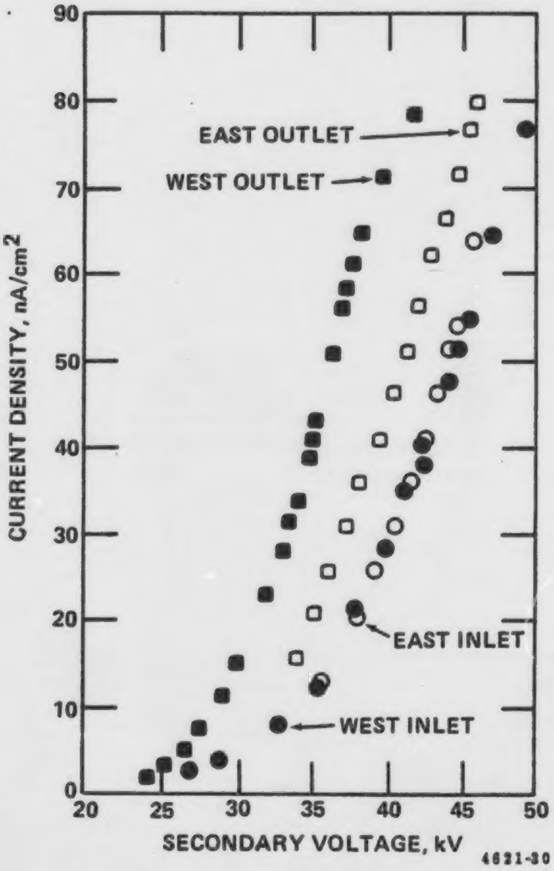

Figure 4. Voltage-current curves for ESP 2-1 T-R sets.

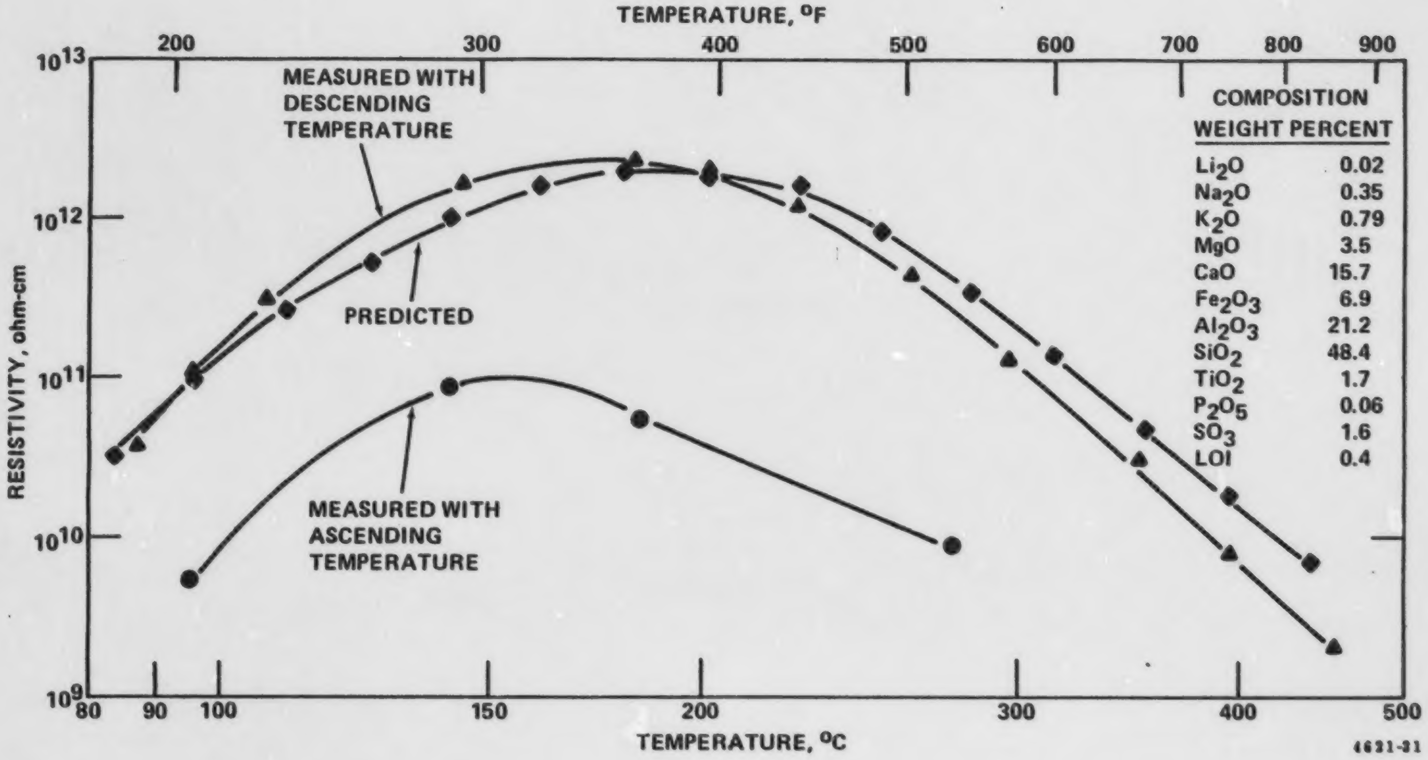

Figure 5. Resistivity measurements made with ascending and descending temperature and predicted resistivity as a function of temperature.

been allowed to equilibrate with the same levels of NH_3 and SO_3 found in the flue gas at the precipitator inlet. Unfortunately, however, the simultaneous use of NH_3 and SO_3 gases in the test cell is not recommended due to contamination of the apparatus with ultrafine $(NH_4)_2SO_4$ fume. Therefore, it was decided to make additional resistivity measurements with the ash equilibrated with SO_3 only. The results for the as-received ash and the ash that had been heated to 450°C (annealed) are indicated by the solid triangle and solid circle in Figure 6. The equilibration with SO_3 reduced the resistivity of the as-received ash to about 1×10^{10} ohm cm, compared to 5×10^{10} ohm cm for the annealed ash. The response of the as-received ash to the SO_3 was much greater than that predicted by the technique of Bickelhaupt (10) illustrated by the open symbols in Figure 6. For example, the predicted resistivity with 0.3 ppm of SO_3 is about 5×10^{11} ohm cm compared to the measured value of about 1×10^{10} ohm cm for the as-received ash with the same level of SO_3. Therefore, it is clear that the surface film has made the ash more responsive to SO_3 conditioning. An interpretation of this is that the NH_3 has been deposited on the ash surface as an NH_4^+ ion, which serves as an additional charge carrier that was not present in the case of SO_3 alone.

SUMMARY AND CONCLUSIONS

The surface film, which is believed to be deposited on the fly ash as a result of the NH_3-SO_3 conditioning process, appears to be contributing to the low resistivity of the ash. The hysteresis between the laboratory resistivity curves obtained with ascending and descending temperatures indicates at least an order of magnitude effect of the surface film on the resistivity (i.e., the descending curve was obtained after the ash had been heated to a temperature sufficient to decompose the surface film, and the resultant resistivity value at about 150°C was about an order of magnitude higher than the corresponding point on the ascending curve). The surface film also appears to have a synergistic effect with a small amount of adsorbed sulfuric acid (i.e., the resistivity of the as-received ash is attenuated by the equilibration with a given level of SO_3 to a greater degree than is the thermally annealed ash in which the surface film has been decomposed). The observations noted above suggest that the addition of NH_3 to the flue gas improved upon the efficacy of the SO_3 conditioning, probably by the contribution of an additional charge carrier, the NH_4^+ ion.

The voltage-current curves for ESP 2-1 showed good electrical operation in all of the fields. This is, of course, a direct result of the low resistivity of the conditioned ash. A resistivity of 1×10^{10} ohm cm was measured in the laboratory when the as-received ash was equilibrated with the level of SO_3 found to be present in the flue gas at the ESP inlet. This value of resistivity is a factor of 4 to 5 lower than in situ resistivity data obtained by plant personnel. This sort of difference between laboratory and in situ data is quite common. There may have been slight differences in ash chemistry, gas temperature, SO_3 levels, or other conditions as well. Equilibration with NH_3 was not possible due to possible contamination of the test cell, but, if anything, this would reduce the resistivity still further. As indicated previously in Figure 6, the resistivity would have been on the order of 10^{12} ohm cm in the absence of any NH_3 or SO_3.

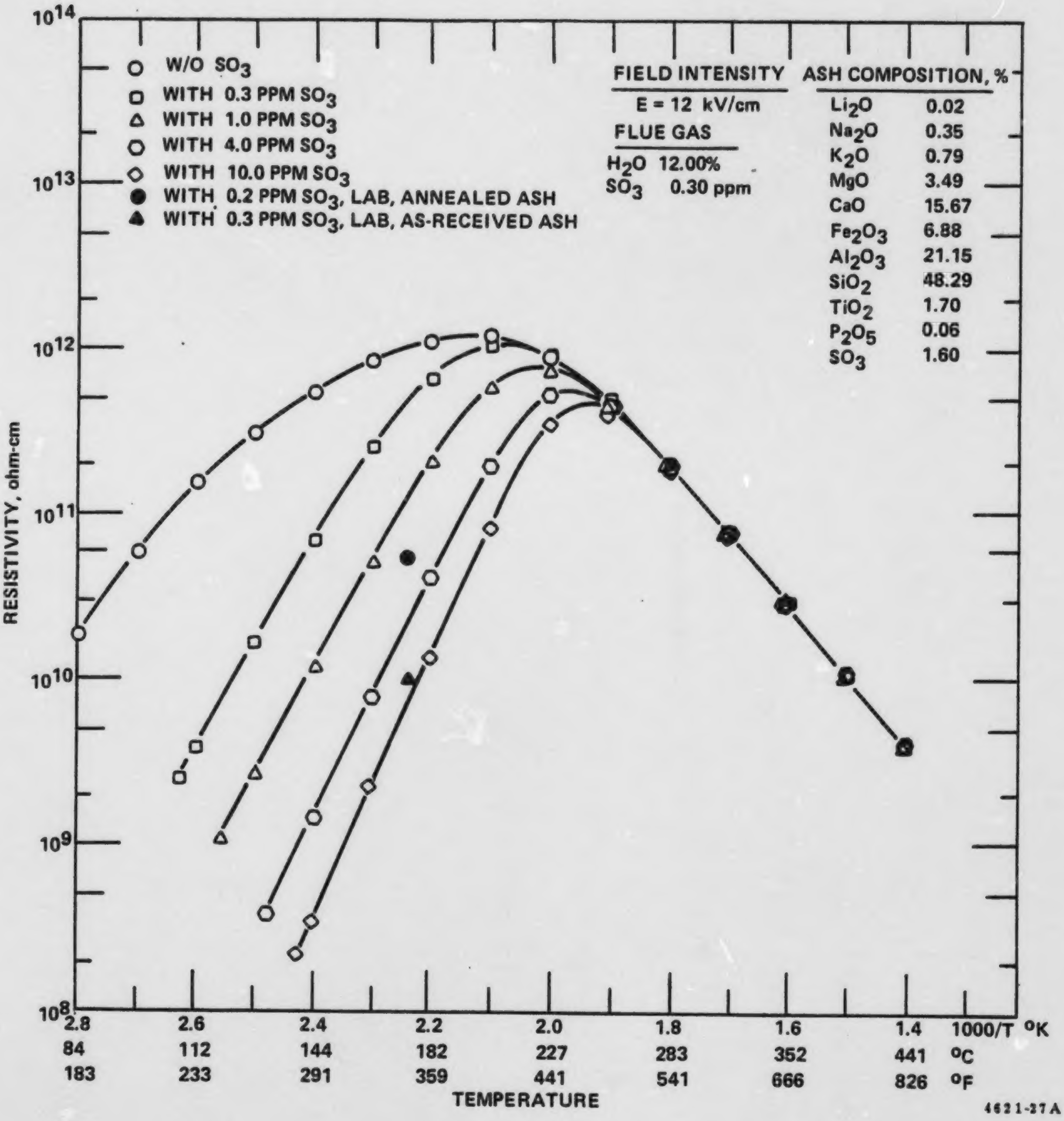

Figure 6. In situ and laboratory resistivity measurements with SO_3 and predicted resistivity for various SO_3 levels.

Considering the small size of the ESP (SCA = 166 ft^2/kacfm), its overall performance appears to be quite good. The overall mass collection efficiency for all particle sizes was found to be within the range of 98.22 to 98.77%, with a mean of 98.45%. The mean value is in good agreement with the overall collection efficiency predicted by a semi-empirical computer model of electrostatic precipitation (11), assuming that 10% of the flue gas bypasses the electrified regions of the ESP and that the standard deviation on the gas velocity profile is equal to 25% of the mean (rms) velocity. Without the resistivity attenuation afforded by the NH_3-SO_3 conditioning process, however, the predicted collection efficiency is well below 90%. This is based on a resistivity of 1×10^{12} ohm cm without any conditioning. In reality there would be some natural conditioning effect of the SO_3 formed in the boiler even with the injection systems turned off. Therefore, the collection efficiency with the conditioning systems turned off should be somewhat greater than 90%.

The combined NH_3-SO_3 conditioning process appears to be a feasible and useful method of maintaining acceptable performance levels in a cold-side electrostatic precipitator. Additional work is needed, however, to fully understand the mechanisms by which the NH_3 and SO_3 act together to condition the fly ash and affect precipitator performance. A more thorough investigation of the NH_3-SO_3 conditioning process is justified in view of the potential for improving ESP performance, or reducing the size of a new ESP. There is a need for field measurements to be made with and without NH_3, SO_3, and both agents injected ahead of the ESP. There is also a need for measurements of the effect of NH_3-SO_3 conditioning on rapping reentrainment. Further laboratory studies are also needed to elucidate the nature and chemical speciation of the ash surface film produced by the NH_3-SO_3 conditioning process.

The work described in this paper was not funded by the U.S. Environmental Protection Agency and therefore the contents do not necessarily reflect the views of the Agency and no official endorsement should be inferred.

ACKNOWLEDGMENTS

This work was supported by the U. S. Department of Energy under Contract No. DE-AC18-80FC10225 and the Electric Power Research Institute under Contract No. RP724-2. The DOE Project Manager was Dr. D. Richard Sears, and the EPRI Project Manager was Dr. Ralph F. Altman.

REFERENCES

1. 40 CFR 60, Appendix A, pp. 220-237.

2. D. B. Harris, "Procedures for Cascade Impactor Calibration and Operation in Process Streams." EPA-600/2-77-004, January 1977.

3. ASTM Standards D3172-73 and D3176-73 (Reapproved 1979), in Annual Book of ASTM Standards, Part 26, American Society for Testing and Materials, Philadelphia, PA (1982), pp. 392, 404-407.

4. ASTM Standard D3682-78, ibid., pp. 451-458.

5. M. L. Eagan and L. DuBois, "The Determination of Ammonium Ion in Airborne Particulates with Selective Electrodes." Anal. Chim. Acta 70, 157-167 (1974).

6. R. Steiber and R. Merrill, "Application of Ion Chromatography to the Analysis of Source Assessment Samples," in Ion Chromatographic Analysis of Environmental Pollutants, Vol. 2, J. D. Mulik and E. Sawicki, Eds., Ann Arbor Science, Ann Arbor, Michigan (1977), pp. 99-113.

7. J. L. Cheney and J. B. Homolya, "Sampling Parameters for Sulfate Measurement and Characterization," Environ. Sci. Technol. 13, 584-588 (1979).

8. R. S. Dahlin, R. E. Bickelhaupt, G. H. Marchant, and J. P. Gooch, "On-Site Field Tests for Study of Low-Rank Western Coal Fly Ash. Technical Summary Report, Field Test No. 3. Big Brown Station Electrostatic Precipitator." DOE/FC/10225-1584, February 1984.

9. J. W. Johnson, B. E. Pyle, and W. B. Smith, "Extending Precision in a Computer-Based Cascade Impactor Data Reduction System," in Proceedings of the Second Symposium on Advances in Particulate Sampling and Measurement, W. B. Smith, Ed., EPA-600/9-80-004, January 1980.

10. R. E. Bickelhaupt, "A Technique for Predicting Fly Ash Resistivity," EPA-600/7-79-204, August 1979.

11. J. R. McDonald, "A Mathematical Model of Electrostatic Precipitation," EPA-600/7-78-111, June 1978.

CONDITIONING OF POWER STATION FLUE GASES TO IMPROVE ELECTROSTATIC PRECIPITATOR EFFICIENCY

by: Gernot Mayer-Schwinning, Manager, Research & Development
Lurgi GmbH
Frankfurt, West Germany

J. D. Riley, Director, Pre-Contract Operations
Lurgi Corporation
River Edge, NJ 07661

ABSTRACT

Adverse collection conditions in electrostatic precipitators for cleaning flue gases from power stations can be improved by conditioning the flue gas. In many cases it is possible to lower the emission values from old plants or operate new plants at maximum efficiency. This paper will describe conditioning by the addition of SO_3 and conditioning with water in an evaporation cooler, the latter applied by Lurgi in a power station for the first time.

The work described in this paper was not funded by the U.S. Environmental Protection Agency and therefore the contents do not necessarily reflect the views of the Agency and no official endorsement should be inferred.

INTRODUCTION

Electrostatic precipitators have been used to dedust power station flue gases for many decades. By constantly improving their design and dimensioning them accordingly, they have been adapted to meet the prevailing pollution control standards, which are constantly becoming more stringent, all over the world. For example, the most recent laws in the Federal Republic of Germany require that all new plants must reduce emissions to 50mg/NM^3 (≈.02gr/SCF) and all old plants must be re-equipped by 1988 to meet emissions of 125 mg/NM^3 (≈.05gr/SCF).

In general terms, the following reasons may favour the use of conditioning units:

EXISTING PLANTS

The emission values originally established may no longer be attainable due to the use of different coal grades or a change in the boiler operating method.

Tighter pollution control legislation may force improvements in collection efficiency. A sufficient increase in precipitator size may be prevented by inadequate local conditions which could lead to considerable capital expenditure and undesirable shutdowns.

NEW PLANTS

If collection conditions are particularly difficult, the possibility of conditioning should also be looked at, even for new plants. It enables smaller precipitators to be installed, resulting in annual savings in capital and operating costs of typically 10 - 15%.

If, in new plants, the boiler is fired with various types of coal, it is possible to optimize the precipitator by constructing them smaller for the coals which permit easier dust collection and only conditioning the flue gas when the more problematical coals are being used. This becomes particularly attractive if the latter adverse situation only occurs relatively rarely.

CONDITIONING WITH SULFUR TRIOXIDE

Lurgi's experience with SO_3 conditioning dates back to the fifties and early sixties. At that time, hardly any flue gas cleaning plant was able to fulfill the required warranties in Australia, when low sulfur coal was fired.

The answer was the use of stabilized SO_3 imported from the United Kingdom, then available only within a narrow temperature range and impossible to evaporate without residues. These residues, once in place, were nearly impossible to remove.

In following years, up to 1973, further tests were occasionally run with SO_3, but owing to the problems in connection with the SO_3, they were never pursued to the stage of a technically viable solution.

The subject of SO_3 conditioning received renewed interest in 1973, when because of high dust resistivities, the guaranteed emission was not achieved at a 315 MW power plant in southwest Germany. After SO_3 conditioning tests were successfully completed at this plant in 1975, we designed our first industrial conditioning plant on the basis of sulphur combustion. This plant became the first one built in Europe and was very successful. Our biggest problem was to convince the government, who was concerned about SO_2 emissions, which we will discuss later in this paper.

This process was not new to Lurgi. It is based on the know-how of about 70 plants built for short-term sulphurization of washing-active substances and on the erection of approximately 110 plants for the production of SO_2, SO_3 and H_2SO_4.

These existing processes had to be simplified in most points on the way to becoming an SO_3 conditioning plant since the high demands as to gas quality, H_2O/SO_3 content and SO_3 conversion were not imposed.

Other agents were simultaneously tested for their effectiveness and economy as conditioning agents, but SO_3 from sulphur proved to be the most reliable and most economical of them all.

What is the experience gathered with conditioning plants between 1975 and 1984?

In an installation erected specifically for testing purposes, we have tested the flyashes of more than 35 coals from over 30 power plants with all significant firing methods.

Sixteen large-scale plants are now in operation or under construction (one of them on the basis of liquid SO_2 evaporation).

SO_3 CONDITIONING TECHNIQUE

The aim of conditioning with SO_3 or water is to reduce excessively high dust resistivities to ranges which do not impair the collection efficiency of the precipitator.

The conditioning effect of SO_3 is based on the conversion of the water present in the flue gas to sulphuric acid, the condensation of this acid in the pores of the dust particles and/or the adsorption of the sulphur trioxide onto the surface of the dust particles with formation of sulphates. While the flue gas temperature remains constant, the dust resistivity is reduced, in some cases considerably.

The raw material is liquid sulphur, which is burned to SO_2 in a furnace. The SO_2 gas is catalysed in a converter to SO_3, which is blown into the flue gas ducts upstream of the precipitator via a system of lances and nozzles, using hot air as the carrier. (See Figure 1.)

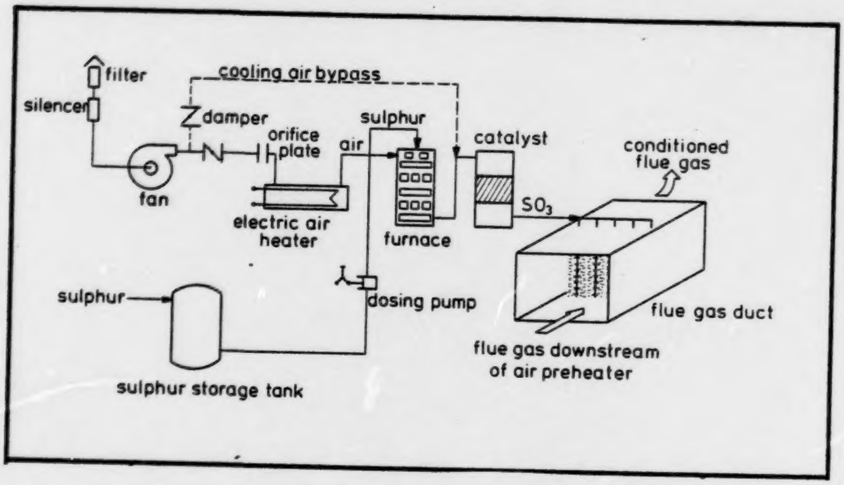

Figure 1. SO_3 Conditioning Plant (Sulphur Combustion)

It is also possible to use liquid SO_2, which is evaporated in a water bath and fed to the converter. This variant is considerably lighter in weight as there is no combustion furnace. It is recommended as a stationary system for smaller power station units or for dealing with occasional dust peaks in larger units. Mobile pilot plants also operate on this principle.

In larger boiler units, however, liquid sulphur should be used as it is 4 to 5 times cheaper than liquid SO_2. Also, it burns exothermically which means a saving of electric power which would otherwise be required for heating the carrier air and evaporating the SO_2.

Sulphur feeding is normally regulated in accordance with the boiler load; however, it can also be controlled according to other criteria, e.g. opacity, and integrated into the complete plant by means of micro-computer (e.g. "Precicontrol").

EFFECT OF CONDITIONING WITH SO_3 ON PRECIPITATOR PERFORMANCE

Lurgi's experience with approximately 30 boiler units can be summarized as follows:

- Dust resistivity can be reduced by 0.5 to 2 powers of ten. However, as the SO_3 dosing rate is increased, a state of saturation occurs, which is dependent on the boiler type and the properties of the dust such as chemical composition (basicity), specific surface area and particle geometry. (See examples in Figure 2.)

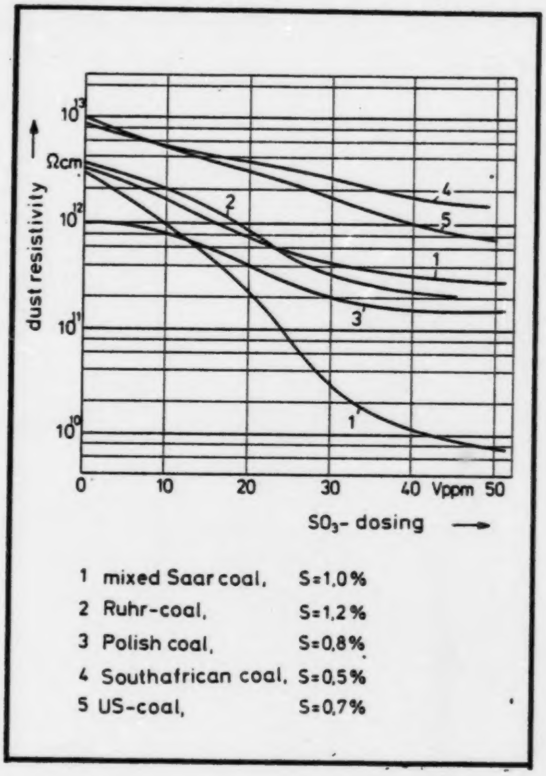

Figure 2. Dust resistivity vs. SO_3-dosing.

This contradicts the occasionally stated assumption that the dust resistivity can be reduced to any desired value.

- There is no measurable increase in the SO_3 concentration at the precipitator outlet, provided that saturation of the flyash is not reached.

- The voltage-current characteristics of the electrical fields provide significant information on the collection behaviour of flyash. If these have too steep a gradient or even slope backwards, back ionization is taking place. If the curve is too flat, the dust resistivity is also high and/or severe space-charge conditions are present. In both cases, the addition of SO_3 results in the characteristics being shifted into more favorable ranges. (See Figure 3.)

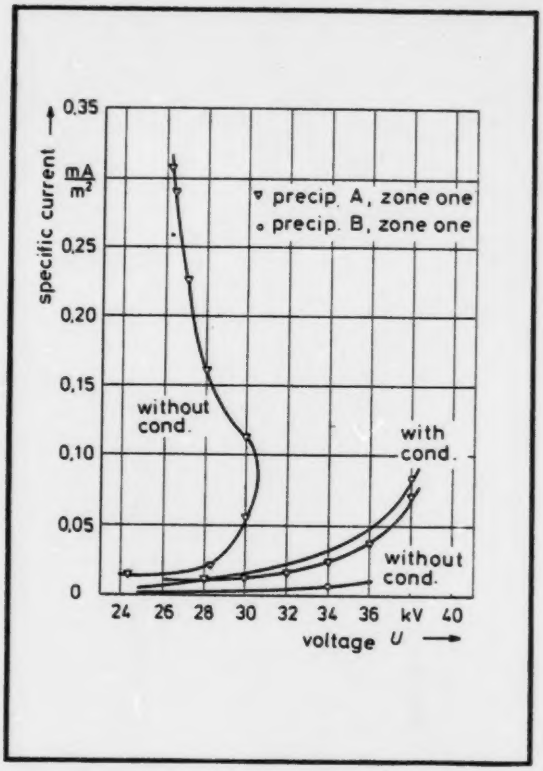

Figure 3. Current voltage characteristic with and without SO_3-dosing.

- The improvement in the collection efficiency by conditioning with SO_3 is dependent upon the situation without conditioning. The poorer the collection conditions, the higher the dust resistivity, the greater is the degree of improvement by conditioning with SO_3. This leads, as proved by the many tests performed, to the migration velocity behaviour shown in Figure 4.

The conditioning reduces the range of collectability of the flue dust considerably, leaving a relatively narrow range which depends less on the coal used than on the various boiler types.

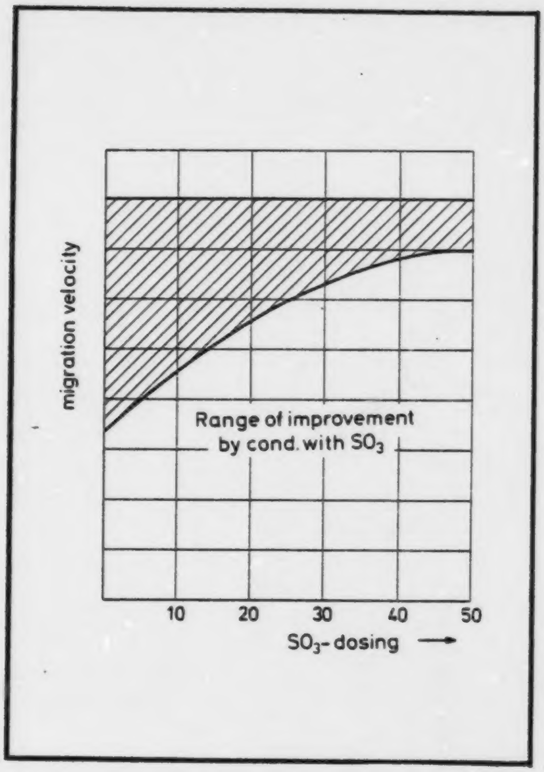

Figure 4. Migration velocity vs. SO_3 dosing.

As could be seen already from the compilation of some measuring results, w-value increases of up to 100% can be achieved by SO_3 conditioning although it should be admitted that these increases are dependent on the initial values and is only possible if there is a relatively low migration velocity initially.

This is demonstrated more clearly by Figure 5, where the w-value increases are plotted versus the initial value of the migration velocity in the unconditioned state.

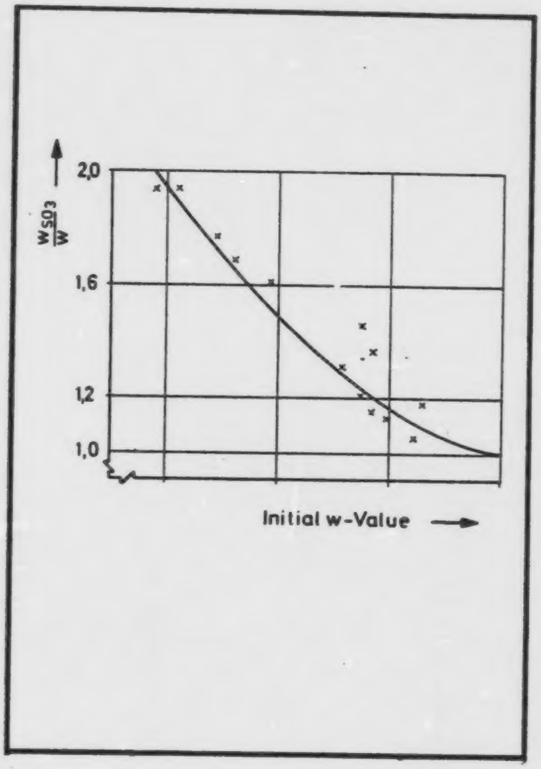

Figure 5. Improvement of w-Value vs. initial w-Value.

CHANGE OF SO_2/SO_3 EMISSIONS IN SO_3 CONDITIONING

The additional emissions of sulfur dioxide and sulfur trioxide in the waste gases during the conditioning remains to be a much discussed subject in the light of the official restrictions on the sulfur dioxide emissions of power plants. As pointed out before, however, the extra emissions are low and well within the range of measuring tolerances as evidenced by theoretical estimations as well as by actual tests.

This can be supported by an arithmetic example based on the following pessimistic assumptions:

- Assume a boiler with ash return (smelting chamber or cyclone boiler) where no flyash-bound SO_2 is withdrawn from the process as would be the case with a boiler with dry ash removal;
- Assume all chemical compounds of the ash constituents with injected SO_3 gas are separated again in the combustion chamber of the boiler and the gas volume corresponding approximately to the dosed SO_3 gas

quantity leaves the boiler as sulfur dioxide;

- Assume the SO_2 to SO_3 conversion rate of the catalyst is only 85% compared to the otherwise usual 90 - 95%.

This leads to a theoretical SO_2 increase as shown in Figure 6.

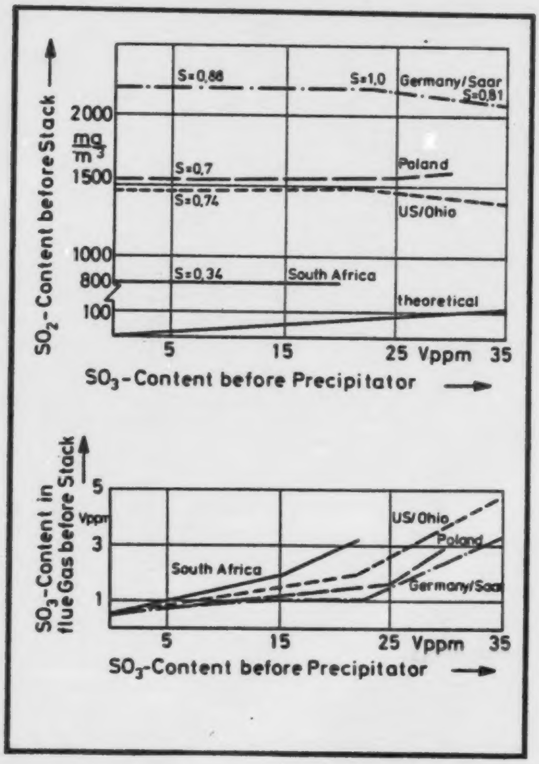

Figure 6. SO_2 and SO_3 content in flue gas vs. SO_3 dosing.

In collaboration with the appropriate authorities, Lurgi has now conducted a series of measurements at a power plant with the aforementioned less favorable type of firing.

The theoretical, calculated extra burden of SO_2 in the waste gas by the SO_3 conditioning as calculated according to the above-mentioned example is plotted in the upper graph. The pictures indicate clearly that the SO_2 emission depends exclusively on the type of coal charged. The shape of the curves show that an increase of the SO_2 emissions by conditioning cannot be detected or is within the range of measuring tolerances.

During the described measurements, the SO_3 content in the flue gas at the stack inlet with and without conditioning was also determined in addition to the inlet and outlet gas dust contents.

The determined sulfur trioxide contents in the flue gas are depicted in Figure 6, again according to the amount of SO_3 dosing. It must be emphasized here that the SO_3 measurements are generally very difficult and afflicted by a great factor of uncertainty, such that the represented values of measurement are rather to be considered as trend indications. However, it can be seen that the SO_3 emission rises in a low degree by about 2 to 4 Vppm up to values of approximately 3 to 5 Vppm SO_3, which are normally found in flue gases behind pit-coal fired steam generators.

On the other hand, the SO_3 conditioning achieves a substantial reduction of the clean gas dust contents down to ranges of 50 to 100 mg/NM^3 with three of the coal types charged.

FLUE GAS CONDITIONING BY EVAPORATION OF WATER

The concept of conditioning waste gases by evaporation of water is not new. It has been practiced in cement works downstream of preheater kilns since the early sixties, using evaporation coolers. The first industrial-scale system in a power station was constructed by Lurgi, with

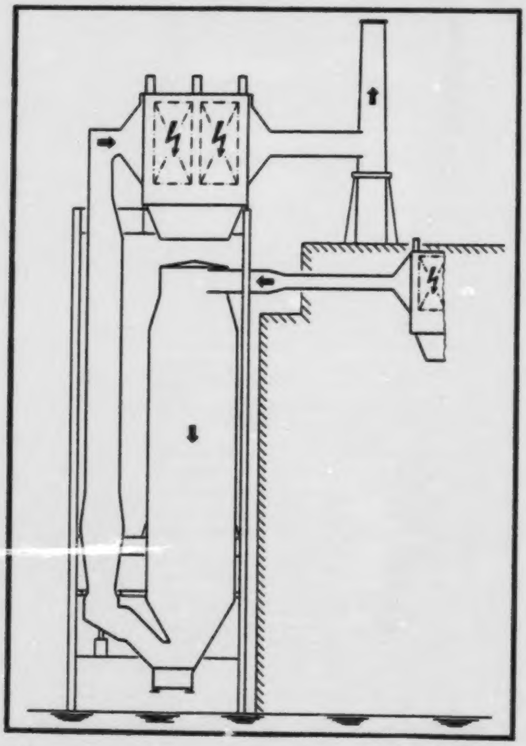

Figure 7. Flue gas dedusting precipitator with conditioning tower.

financial assistance from the Federal German Ministry of Research and Technology (BMFT), in the Mannheim superpower station downstream of a melting cyclone boiler with a capacity of 150 MW.

At the right of the diagram in Figure 7 is a prededusting precipitator in the power station building. Downstream of this precipitator is an evaporation cooler 10.5 m in diameter and 32.9 m high.

The fan is housed in the vertical duct at the left. The downstream precipitator is installed on a support structure above the evaporation cooler. This arrangement was selected of necessity due to existing jobsite conditions. In a new plant, the prededusting precipitator would naturally be dispensed with and the electrostatic precipitator constructed at ground level directly following the evaporation cooler.

The evaporation cooler is designed to cool the flue gases from 150°C to 90°C. Through the combination of the lowering of the temperature and the increase in the dewpoint of the waste gas, the dust resistivity is reduced by over two powers of ten. (See Figure 8.)

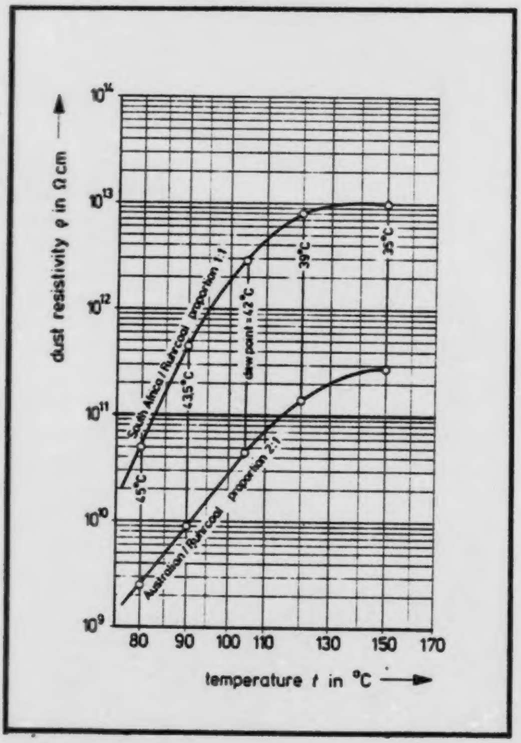

Figure 8. GKW-Mannheim Dust resistivity.

In addition to this effect, the breakthrough voltage of the gas increases, which permits a remarkably large rise in the corona voltage.

Conditioning with water thus results in a surprisingly large improvement in collection efficiency. Figure 9 shows the charts on the boiler switchboard in simplified form.

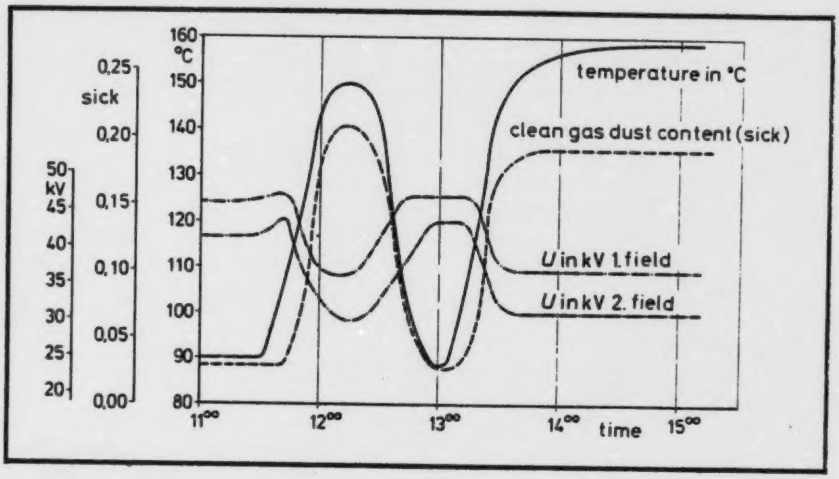

Figure 9. GKW-Mannheim Operational readings.

Recorded over time are:

- temperature downstream of the evaporation cooler (at precipitator inlet)
- opacity at the precipitator outlet (as a relative measure of the clean gas dust content)
- high voltages present in the 1st and 2nd fields of the precipitator

At about 11:30, the water injection system in the evaporation cooler is shut down: the temperature rises, the applicable high voltages fall and the clean gas dust content increases with a lag of about 10 minutes. At about 12:15, the evaporation cooler is brought back into operation: the temperature drops, the clean gas dust content improves immediately while the high voltages rise. At 13:00, the changes just described are repeated.

To demonstrate the true improvement, the complete prededusting precipitator and half of the downstream precipitator were shut down. Thus only 25% of the installed collection area was in use. Conditioning with water reduced the clean gas dust content from 600 mg/m^3 (NTP, dry) to 30 mg/m^3 (NTP, dry), while the high voltage rose from 40 kV to 60 kV. (See Figure 10.)

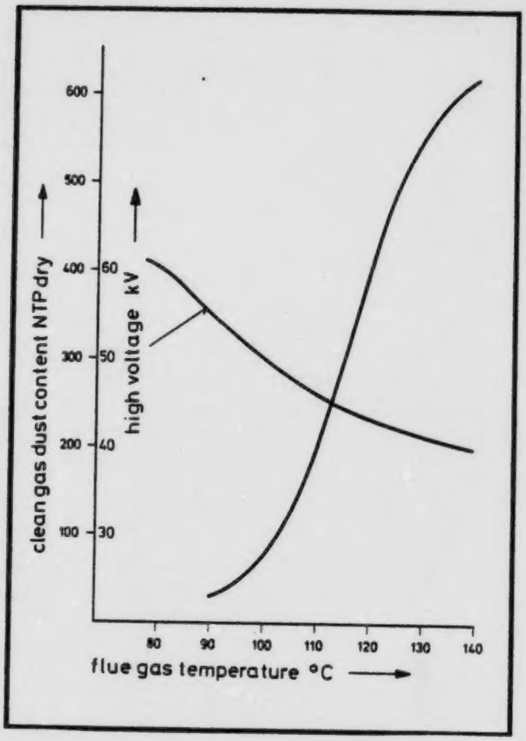

Figure 10. Clean gas dust content/high voltage vs. flue gas temperature.

The same improvements were achieved whatever the type of coal used, whether from Australia, South Africa or the Ruhr.

This plant has been in operation for almost 4 years without major problems occurring or effects of corrosion and condensation appearing.

As there is an evident trend in the power station field towards a single-pass boiler with dry ash removal, it would be entirely reasonable to imagine systems in which the vertical duct to the precipitator is designed as an evaporation cooler and used for gas conditioning with water and possibly for SO_2 removal with the addition of a reagent.

In conclusion, it can be said that conditioning with SO_3 and water is in many cases an attractive option from the point of view of cost. Furthermore - and this should be particularly emphasized in conclusion - the collection efficiency of the precipitator becomes largely independent of the coal being burnt.

PILOT-SCALE STUDY OF A NEW METHOD OF FLUE-GAS CONDITIONING WITH AMMONIUM SULFATE

by: Edward B. Dismukes,
E. C. Landham, Jr.,
John P. Gooch
Southern Research Institute
Birmingham, Alabama 35255

Ralph F. Altman
Electric Power Research Institute
Chattanooga, Tennessee 37411

ABSTRACT

A new process for flue-gas conditioning with ammonium sulfate was investigated on a pilot scale at EPRI's Arapahoe Test Facility. The agent is decomposed to ammonia and sulfur trioxide in a hot gas slipstream to simulate bypassing the air heater in a full-scale plant. The process thus avoids loss of sulfur trioxide (the effective chemical species) and corresponding plugging of the air heater, which occur when the agent is decomposed conventionally in the main flue-gas stream ahead of the air heater and the decomposition products recombine upon cooling in the air heater. Chemical aspects of the decomposition process were characterized on the pilot scale and compared with earlier laboratory data. Lowering of the electrical resistivity of ash from low-sulfur coal was demonstrated by (1) direct measurements of reduced resistivity in situ and (2) observations of electrical manifestations of suppressed back corona in an ESP. Comparable improvements in ash collection efficiency in the ESP, from about 98.6 to 99.6%, were observed with sulfur trioxide obtained by the decomposition of ammonium sulfate or by the vaporization of liquid sulfur trioxide.

The work described in this paper was not funded by the U.S. Environmental Protection Agency and therefore the contents do not necessarily reflect the views of the Agency and no official endorsement should be inferred.

BACKGROUND

The use of ammonium sulfate (formula: $(NH_4)_2SO_4$) for flue gas conditioning began to receive prominent attention some 15 years ago. Much of the original interest in the compound stemmed from the belief that it provided an optional source of the classical conditioning agent SO_3, which could be used without the hazards associated with other existing sources of SO_3. Generation of SO_3 from $(NH_4)_2SO_4$ was assumed to occur as the result of thermal decomposition when the compound was injected into a flue gas duct, either as the finely divided solid or as a spray of a concentrated aqueous solution. The thermal decomposition process can be written as follows:

$$(NH_4)_2SO_4(s) \rightarrow 2NH_3(g) + SO_3(g) + H_2O(g)$$

The earliest interest in $(NH_4)_2SO_4$ for flue gas conditioning was exhibited in Great Britain, and the earliest technical papers on the subject, from both practical and fundamental perspectives, were published by investigators of the CEGB (1,2,3,4). Application of the compound in the United States followed that in Britain and was promoted primarily by commercial interests (5,6). At the third of these symposia in Orlando in 1981 (7), staff members of Southern Research Institute presented the results of comprehensive studies of $(NH_4)_2SO_4$ conditioning at two U.S. power plants, which had been performed as part of a research project financed by the Electric Power Research Institute. Further details of this work have more recently appeared in an EPRI report (8).

A key finding by SRI investigators is that SO_3 resulting from the thermal decomposition process is the key to the conditioning process because of the usual effect of SO_3 on the electrical resistivity of fly ash. The Corette plant of Montana Power employed $(NH_4)_2SO_4$ successfully with the most common site of injection—in the backpasses of the furnace. The Gannon plant of Tampa Electric was able to use the compound with injection either before or after the air preheater. Success at Gannon with injection at the lower temperatures downstream from the air heater arose in large degree because these temperatures were well above 300°F and at least partial decomposition could still be effected.

Despite success at Corette with high temperature injection, the utility industry has encountered repeated difficulties with high temperature injection of $(NH_4)_2SO_4$ in the form of air heater pluggage. This phenomenon is a result of the reversal of the decomposition process on the relatively cool metal surfaces in an air heater. The frequency of this difficulty, plus the quite limited decomposition of $(NH_4)_2SO_4$ that occurs at prevailing air heater exit temperatures, led SRI and EPRI to the formulation of a new process for conditioning with $(NH_4)_2SO_4$—namely, injection of the compound in a slipstream of hot flue gas or hot combustion air that bypasses the air heater. This stream can be sufficiently high in temperature to give complete decomposition, while obviously avoiding the air heater pluggage problem.

The first step to implement this concept was a laboratory study at SRI supported by EPRI. The key findings in the laboratory were as follows:

- $(NH_4)_2SO_4$ injected as a concentrated aqueous solution can be completely volatilized in a gas stream at 700 to 900 °F with product concentrations up to 2000 ppm of NH_3 and 1000 ppm of SO_3. With an SO_3 concentration of this magnitude attainable, the slipstream need have a flow rate approximating only 1% of the gas stream to be treated, assuming a typical treatment level of 10 ppm.

- The decomposition process follows the desired course, rather than the thermodynamically favored process in which the products are N_2 and SO_2 rather than NH_3 and SO_3 (9). This merely means that the reaction follows a thermodynamically predicted course but not the course with the greatest release of energy (ΔF). The presumed explanation is that NH_3 and SO_3 are released by flash volatilization and the reactants required for N_2 and SO_2 production do not remain in contact.

- The decomposition process nears completion in a reaction time of about 2 sec in the stated temperature range, making for a practical length of the gas duct in a power plant where decomposition would be effected.

Certain major issues that could not be successfully resolved in the laboratory were addressed on a pilot scale at EPRI's Arapahoe Test Facility, where a pilot-scale ESP was available for study.

SCOPE OF THE PILOT-SCALE STUDY

The principal phases of the work in preparation for pilot-scale studies and execution of these studies at Arapahoe were as follows:

- Fabrication and installation of a decomposer that could provide up to 20 ppm of SO_3 in a flue gas stream having flow rates up to 5000 acfm at 300 °F.

- Exploratory studies with the apparatus to determine its performance capabilities with respect to:

  --achieving $(NH_4)_2SO_4$ decomposition efficiencies comparable to those in the laboratory,

  --accounting for the fate of the decomposition products following their injection into the flue gas duct,

  --determining the effect of the conditioning agent on fly ash resistivity, and

  --establishing the effect of the agent on the electrical behavior of a pilot-scale ESP.

- Exit temperature from the decomposer—minimum, 600 °F; maximum, 700 °F.

- Solution feed rate to the decomposer—minimum, 10 mL/min; maximum, 60 mL/min. The most commonly used feed rate was 30 mL/min, which delivered sufficient agent from a 20%-by-weight solution to produce 20 ppm of SO_3 at the typical flow rate of flue gas to the decomposer, 3500 acfm at 300 °F.

EXPLORATORY STUDIES[1]

A number of experiments were conducted to determine relative concentrations of NH_3 and SO_3 issuing from the decomposer outlet in the gaseous and particulate states. In most of these experiments, the rate of addition of $(NH_4)_2SO_4$ was selected to produce a concentration of 40 ppm of NH_3 and 20 ppm of SO_3 in the flue gas duct. The essential results from these experiments were as follows:

- The percentages of the total amounts of NH_3 and SO_3 collected in the particulate state were approximately 0.01% for NH_3 and 0.08% for SO_3. These results signified that the $(NH_4)_2SO_4$ was essentially all decomposed to the vapors. The somewhat higher value for SO_3 probably was a result of some vapor adsorption on the sampling filter. A typical distribution of the collected decomposition products is given in Table 1.

- Recoveries of both NH_3 and SO_3 were considered satisfactory in view of the handicap faced in the sampling operation. There could be no direct physical connection between the sampling line and the decomposer outlet; instead, the inlet of the sampling line had to be placed as close as possible to the outlet from the decomposition chamber, with the sheath air used as a shield against dilution by the flue gas. During injection of 40 ppm of NH_3 and 20 ppm of SO_3, the recoveries of both decomposition products averaged 83%. Further details are given in Table 2.

- No SO_2 from the decomposer was detected. Hence, the $(NH_4)_2SO_4$ decomposed exclusively to NH_3 and SO_3, as desired.

Another set of experiments was conducted to determine the fate of NH_3 and SO_3 from decomposed $(NH_4)_2SO_4$. Here, the sampling operation was at the inlet of the ESP; the results are given in Table 3. Total recoveries of NH_3

---

[1] Although the decomposer was designed for use with either air or flue gas as the transport medium in the decomposer, air was used at all times in the work discussed in this paper.

TABLE 1. DISTRIBUTION OF NH_3 AND SO_3 IN THE SAMPLING TRAIN AT THE DECOMPOSER OUTLET

Species collected	Component of the sampling train	Relative moles collected	
		NH_3	SO_3
Particulates	Instack filter	0.0002	0.0008
Gases	Probe	0.90	0.81
	Water bubbler	0.64	0.03
	Condenser	0.36	0.15
	Backup filter	0.04	0.01
	H_2SO_4 bubbler	0.06	-
		2.00	1.00

TABLE 2. RECOVERY OF NH_3 AND SO_3 AT THE DECOMPOSER OUTLET

Number of experiments	Feed solution		Calculated concentration as SO_3, ppm	Recovery, %	
	Wt %	ml/min		NH_3	SO_3
5	20	30	610-680	73-93	67-96
2	30	30	1060-1070	62-70	70-79
1	40	30	1480	42	56

TABLE 3. MATERIAL BALANCE AT THE ESP INLET

	Experiment			
	1	2	3	4
ppm $(NH_4)_2SO_4$ injected	12	11	21	22
ppm NH_3 found -				
particulate	16	12	20	18
gas	12	9	13	17
total(recovery, %)	28(115)	21(95)	33(79)	35(80)
ppm SO_3 found -				
particulate	13	10	18	13
gas	< 1	< 1	< 1	< 1
total(recovery, %)	13(108)	10(91)	18(86)	13(59)

- Determination quantitatively of the improvement in fly ash collection efficiency by this ESP unit upon treatment of the flue gas with $(NH_4)_2SO_4$ and comparison of the effect of $(NH_4)_2SO_4$ with that produced by SO_3 vapor from stabilized liquid SO_3 (that is, without the simultaneous addition of NH_3).

FABRICATION AND INSTALLATION OF THE DECOMPOSER

The decomposer was constructed from parts fabricated in the machine shop of SRI in Birmingham and certain other parts that were purchased from commercial sources. A schematic drawing of the apparatus is shown in Figure 1. The primary components were as follows:

- An inlet to allow either ambient air or flue gas from an existing duct at Arapahoe to be drawn into the system.
- A blower to force the air or flue gas to a heater capable of producing an exit air or gas temperature of 900 °F.
- A wye at the heater exit leading to two concentric vertical channels, with the inner channel to serve as a chamber for $(NH_4)_2SO_4$ decomposition and the surrounding annular channel to provide insulation.
- A spray nozzle for introducing $(NH_4)_2SO_4$ solution into the inner channel.
- A nozzle for directing the decomposition products into the flue gas duct, with the sheath gas providing a protective barrier between the inner stream of decomposition products and the surrounding flue gas, to allow gradual cooling of the decomposition products and gradual mixing with the flue gas.

The apparatus was mounted at Arapahoe above a duct having an inside diameter of 18 in., carrying flue gas from Unit 4 of the Arapahoe power station to the pilot-scale ESP. It was thus located some 56 ft from the entrance of the ESP and provided a residence time of about 1.5 sec between the decomposer outlet and the ESP inlet.

Performance characteristics of the decomposer in actual use were as follows:

- Air flow through the decomposer at a heater exit temperature of 900°F—minimum air flow, 90 acfm; maximum, 210 acfm.
- Gas residence time in the decomposer—minimum, 1.3 sec; maximum, 3.0 sec.

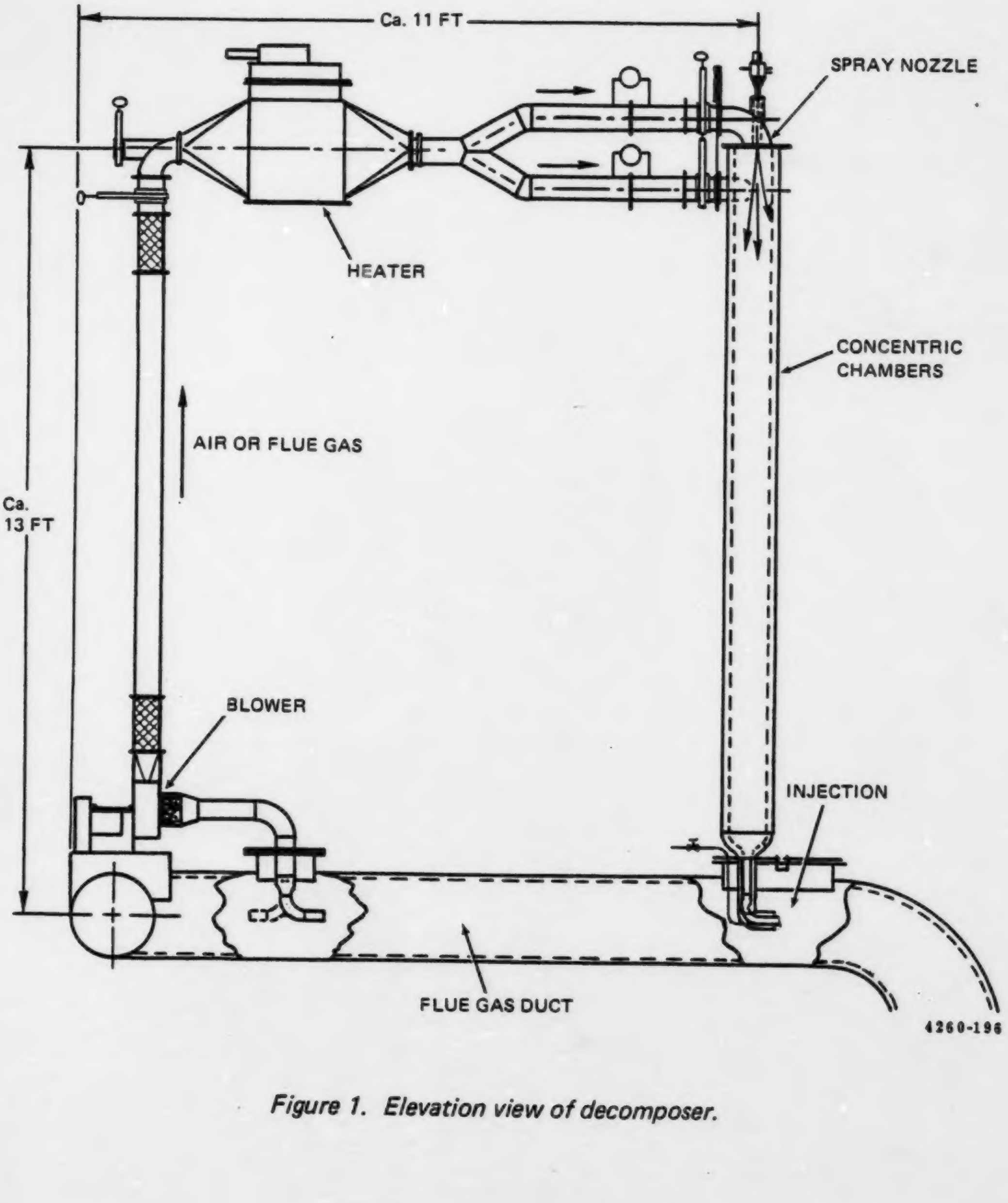

Figure 1. Elevation view of decomposer.

averaged 90% and of SO_3 84%. Approximately half of the NH_3 was found in the particulate phase and half in the gas phase. All of the SO_3 found, on the other hand, was in the particulate matter, indicating either partial recombination of NH_3 and SO_3 as NH_4HSO_4 particulate matter

$$NH_3(g) + SO_3(g) + H_2O(g) \rightarrow NH_4HSO_4(s \text{ or } l)$$

or selective adsorption of SO_3 by the fly ash.

Efforts to demonstrate the resistivity effect of NH_3 and SO_3 from decomposed $(NH_4)_2SO_4$ were handicapped by the absence of a consistent composition of the coal being burned in Unit 4. The resistivity of unconditioned ash ranged from 2×10^{11} to 3×10^{12} ohm cm. Part of this variation was attributed to observed variations in the Na_2O content of the fly ash; however, there were apparently other contributing factors not identified.

Figure 2 is the result of an effort to show the effects of conditioning in the face of large variations in the baseline ash. Here, the ratio of resistivity of conditioned ash to that of unconditioned ash is plotted versus the injected concentration of SO_3, the source material being either $(NH_4)_2SO_4$ or NH_4HSO_4. The effect appeared to have been most evident below 10 ppm of SO_3; the reduction was around one order of magnitude from 10 to 20 ppm of SO_3. The source compound, $(NH_4)_2SO_4$ or NH_4HSO_4, apparently had no bearing on the magnitude of the effect produced. NH_4HSO_4 (ammonium bisulfate) is an analog of $(NH_4)_2SO_4$, which decomposes similarly to produce a similar effect.

The effects on the ESP electrical conditions of $(NH_4)_2SO_4$ injected at a rate equivalent to 20 ppm of SO_3 are shown in Figure 3. Also shown for comparison are the effects of 10 ppm of SO_3 from the stabilized liquid SO_3 source material.[2] The plots of current density versus voltage without conditioning show clear evidence of back corona, and those with conditioning by either $(NH_4)_2SO_4$ or SO_3 show suppression of back corona. A difference between the effects of the two agents is higher voltages for given current densities with $(NH_4)_2SO_4$ than with SO_3; this may have been the result of a space-charge enhancement by the NH_4HSO_4 aerosol produced by partial recombination of NH_3 and SO_3, as mentioned above. There are other anomalies in these plots that cannot be explained on an unqualified basis. Even with conditioning, the maximum current densities that could be reached without sparking were low (<10 nA/cm^2). While this project was in progress, attempts to raise the attainable current density by cleaning of insulators, wires, and wire frames were unsuccessful; only later, after washing down the collection plates, did the limitation disappear.

ESP PERFORMANCE TESTS

Four series of tests were conducted to quantify the performance of the ESP with and without conditioning. Three series (referred to as Tests 1, 2, and 3) were conducted with the addition of $(NH_4)_2SO_4$ through the decomposer

---

[2] These data were from the performance tests subsequently described.

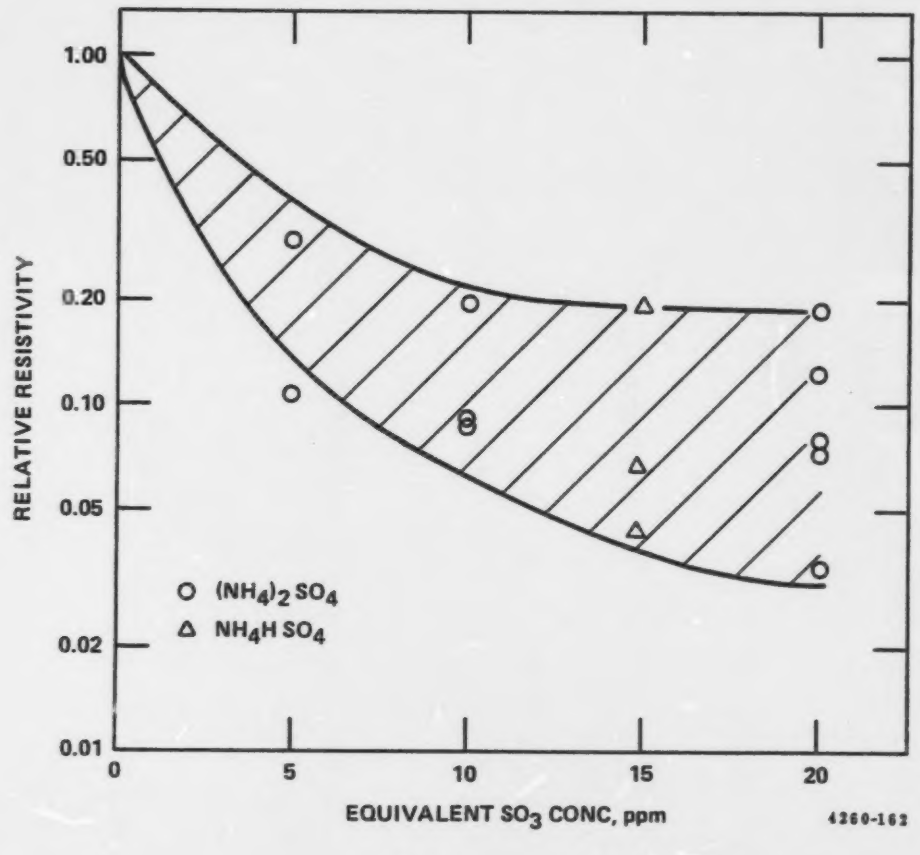

Figure 2. Effect of decomposed $(NH_4)_2SO_4$ and NH_4HSO_4 on fly ash resistivity.

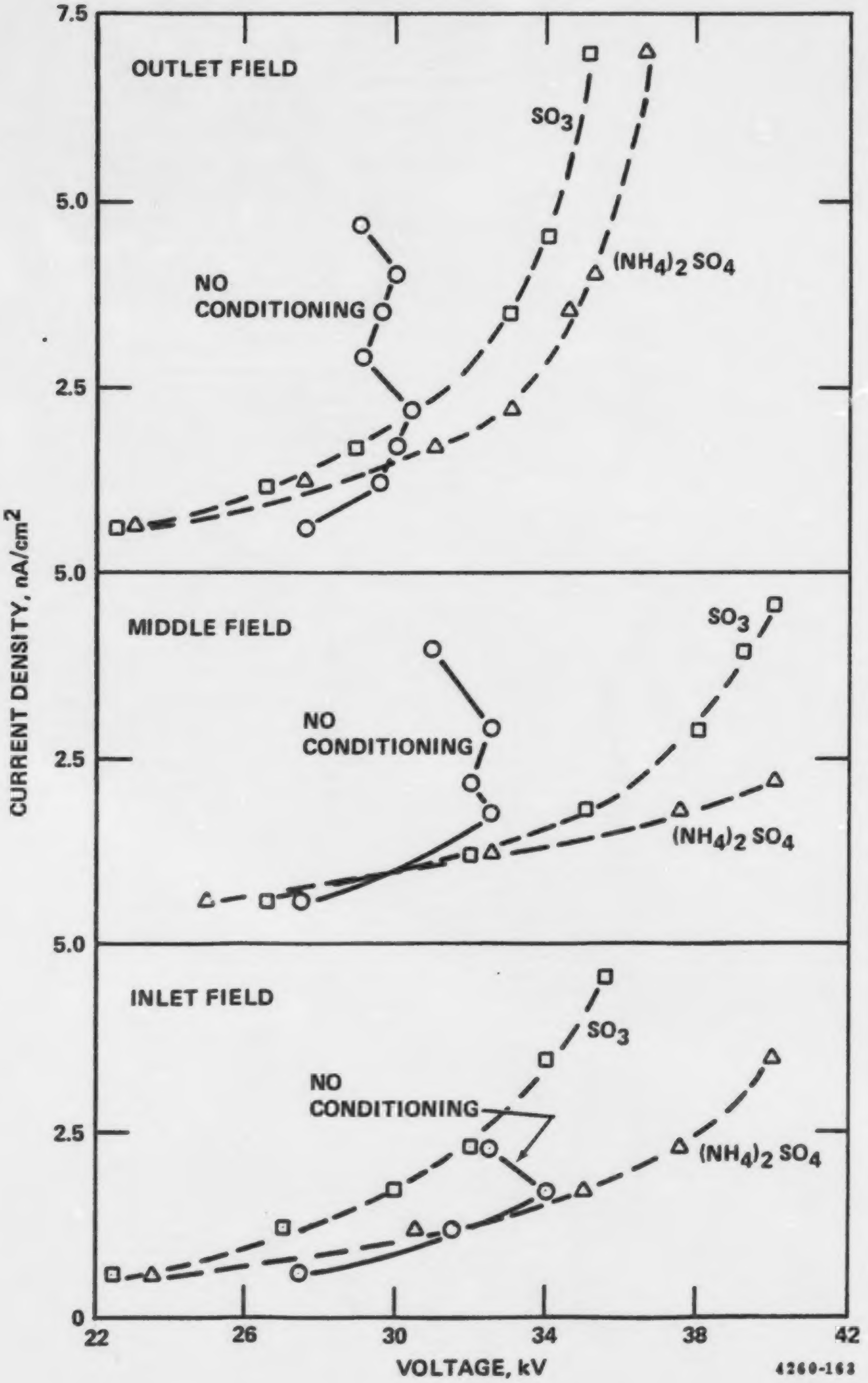

Figure 3. ESP electrical conditions without conditioning (circles) or with $(NH_4)_2SO_4$ conditioning (triangles) or SO_3 conditioning (squares).

at a rate equivalent to a nominal SO_3 concentration of 20 ppm. The fourth series (Test 4) was conducted with 10 ppm of SO_3 vapor from stabilized liquid SO_3. During Test 4, the SO_3 was vaporized by heating a drum of the liquid source material, and the vapor was fed through a flow meter and a pipe mounted at the top of the decomposition chamber in the decomposer with air as a carrier gas. The injected concentration of SO_3 from the source liquid, 10 ppm, was the maximum rate that could be maintained with this injection system. Parameters measured during the ESP performance tests included: inlet and outlet fly-ash concentrations, outlet opacity, electrical resistivity, ESP electrical conditions, and NH_3 and SO_3 concentrations.

So-called Energy coal was the customary fuel at the Arapahoe, but another coal referred to as Arco-Somerset was burned during one of the four tests. Both are subbituminous Western coals, typically with 0.6% sulfur. Analysis showed that the two coals differed somewhat in the composition of their ashes, as revealed by the results of analyses of hopper ash that are given in Table 4. The most important differences are in components that have an important bearing on electrical resistivity (Na_2O, K_2O, CaO, and Fe_2O_3). The higher sodium and potassium contents of the Arco-Somerset ash, in particular, lead to a lower predicted resistivity based on the Bickelhaupt model (10): for example, 2×10^{11} ohm•cm for Arco-Somerset versus 7×10^{11} ohm•cm for Energy (calculated for 300 °F, 8% water vapor, at 10 kV/cm).

Table 5 gives the results of measurements of the collection efficiency of the ESP with and without conditioning in each of the four test series. Except in Test 2, the reduction in penetration due to conditioning was around 60%; in Test 2, the reduction was only about 30%. There is no apparent reason why $(NH_4)_2SO_4$ performed so differently with Energy coal in Tests 1 and 2 although, as will be shown, data on the effect of the conditioning agent on the SO_3 content of the ash reveal an abnormally low recovery in Test 2.

Table 5 suggests that 20 ppm of $(NH_4)_2SO_4$ was capable of producing an improvement in ESP performance comparable to that observed with 10 ppm of SO_3. It should not be concluded that $(NH_4)_2SO_4$ will generally be required at higher concentrations than SO_3. To the extent that resistivity reduction determines the effectiveness of $(NH_4)_2SO_4$, one would expect that 10 or 20 ppm of this agent would produce equivalent effects (see Figure 2). It was unfortunate that a more comprehensive comparison of the two agents was not possible at Arapahoe. The unexpected limitation in the output of the SO_3 system, plus scheduling difficulties, forced postponement of more a definitive comparison until later.

Determination of the effects of $(NH_4)_2SO_4$ on the opacity of the flue gas at the ESP outlet revealed a significant suppression in both the time-average opacity (from about 16% to 8%) and the intensity of rapping puffs (from about 60% to 30% of the opacity scale). The latter effect, it might be argued, is a manifestation of increased cohesion of the ash deposits, an effect previously observed with NH_3 additive combined with naturally occurring SO_3 (11).

TABLE 4. COMPOSITIONS OF FLY ASH FROM ENERGY AND ARCO-SOMERSET COALS

	Weight percent in ash	
Component*	Energy	Arco-Somerset
Li_2O	0.03	0.03
Na_2O	0.52†	1.92†
K_2O	1.2†	1.5†
MgO	1.5	1.4
CaO	4.5†	5.2†
Al_2O_3	26.6	23.6
Fe_2O_3	3.5†	7.9†
SiO_2	57.0	54.6
TiO_2	1.2	0.95
P_2O_5	1.2	0.95
SO_3	0.45	0.70

*Determined after ignition of ash at 1380°F.
†Significant differences for components have a large impact on electrical resistivity.

TABLE 5. ESP MASS COLLECTION EFFICIENCIES

Test Series Coal	Agent*	SCA, ft^2/1000acfm	ESP efficiency,%	Relative penetration
1(Energy)	None	290	98.86	1.14
	$(NH_4)_2SO_4$	330	99.60	0.40
2(Energy)	None	324	98.44	1.56
	$(NH_4)_2SO_4$	320	98.93	1.07
3(Arco-Somerset)	None	367	95.60	4.30
	$(NH_4)_2SO_4$	367	98.14	1.86
4(Energy)	None	364	98.83	1.17
	SO_3	364	99.63	0.37

*$(NH_4)_2SO_4$, 20 ppm. SO_3, 10 ppm.

The results of measurements of ash resistivity are summarized in Table 6. The magnitudes of the effects of both agents on resistivity were comparable— reductions by one order of magnitude or more. The effects of both agents on voltage-current behavior of the ESP were also similar, as has been illustrated previously in Figure 3.

The results of determinations of NH_3 and SO_3 in the vapor state at the ESP inlet and determinations of these substances in the ash deposited in the ESP hoppers are summarized in Table 7. These experimental results are compared with the increments expected from the rates of injection as percentages recovered. Calculated recoveries of NH_3 and SO_3 are generally similar to those obtained in the preliminary studies, except in Test 2 when the recovery of SO_3 was abnormally low.

CONCLUSIONS

Ammonium sulfate can be thermally decomposed to NH_3 and SO_3 by spraying an aqueous solution into a hot gas stream. Product concentrations range upward to at least 2000 ppm of NH_3 and 1000 ppm of SO_3 in a residence time of 2 sec or less in the temperature range from 700 to 900 °F. Introduction of the product stream into a flue gas duct upstream from a cold-side ESP, in the ratio of about 1 volume part of product stream to 100 parts of flue gas, effectively lowers ash resistivity and produces corresponding improvements in the voltage-current performance of an ESP. The efficiency of ESP performance is correspondingly improved; reductions of ash penetration to the ESP outlet of 60% have been observed. The effect of ammonium sulfate conditioning on ESP performance approximates that by SO_3 introduced in the absence of NH_3.

TABLE 6. ASH RESISTIVITY DURING ESP PERFORMANCE TESTS

Test	Operating Mode*	Resistivity (ohm cm)	Relative Resistivity
1	Baseline	1.3×10^{12}	1.00
	Conditioning, $(NH_4)_2SO_4$	6.8×10^{10}	0.05
2	Baseline	3.0×10^{12}	1.00
	Conditioning, $(NH_4)_2SO_4$	8.9×10^{10}	0.03
3	Baseline	--†	--
	Conditioning, $(NH_4)_2SO_4$	3.4×10^{10}	—
4	Baseline	2.8×10^{12}	1.00
	Conditioning, SO_3	3.0×10^{11}	0.10

*Tests 1, 2, and 3 with 20 ppm of $(NH_4)_2SO_4$ or Test 4 with 10 ppm of SO_3.
†Not successfully determined.

TABLE 7. RECOVERIES OF NH_3 AND SO_3 DURING ESP PERFORMANCE TESTS

Test	Operating Mode	NH_3, ppm			SO_3, ppm		
		Vapor	Solid†	Recovery,%	Vapor	Solid†	Recovery,%
1	Baseline	1.4	0.1	-	0.9	8.7	-
	Conditioning	12.8	15.4	67	<0.1	17.6	40
2	Baseline	1.1	<0.1	-	0.8	6.8	-
	Conditioning	20.6	5.7	63	<1.0	9.2	10
3	Baseline	6.8	0.1	-	<1.0	5.4	-
	Conditioning	26.2	12.6	9.5	not det'd	13.3	40
4	Baseline	1.4	0.3	-	1.0	9.1	-
	Conditioning	0.6	0.1	-	4.3	12.0	60

*Recovery: total found for vapor and solid during conditioning less that for baseline operation, relative to injected value, 40 ppm of NH_3 or 20 ppm of SO_3.
†Calculated as the vapor concentration equivalent to that in the solid collected in the ESP hoppers.

REFERENCES

1. Lowe, H.J. Reduction of Emission of Pollutants - Recent Advances in Electrostatic Precipitators for Dust Removal. Phil. Trans. Roy. Soc. Ser. A. 265(1161):301, 1969.

2. Dalmon, J. and Tidy, D. A Comparison of Chemical Additives as Aids to the Electrostatic Precipitation of Fly Ash. Atmos. Environ. 6:721, 1972.

3. Halstead, W.D. Thermal Decomposition of Ammonium Sulfate. J. Appl. Chem. 20:129, 1970.

4. Dalmon, J. Research Division, Central Electricity Generating Board. Private communication, 1976.

5. Method of and Apparatus for Chemically Conditioning a Particle-Laden Gas Stream. U.S. Patent 3,665,676 (Assignee: Koppers Company, Inc.). 1972.

6. Method of Conditioning Flue Gas to Electrostatic Precipitator. U.S. Patent 4,043,768 (Assignee: Apollo Chemical Corporation). 1977.

7. Landham, E.C., Jr., Marchant, G.H., Jr., Gooch, J.P., and Altman, R.F. Field Evaluations of Ammonium Sulfate Conditioning for Improvement of Cold Side Electrostatic Precipitator Performance. In: EPA-600/9-82-005b. U.S. Environmental Protection Agency, Research Triangle Park, NC, 1982. p 237.

8. Gooch, J.P., Bickelhaupt, R.E., and Dismukes, E.B. Investigation of Ammonium Sulfate Conditioning for Cold-Side Electrostatic Precipitators. Volume 1: Field and Laboratory Studies. EPRI Report CS-3354, Volume 1, 1984. 59 pp.

9. Kelley, K.K., Shomate, C.H., Young, F.E., Naylor, B.F., Salo, A.E., and Huffman, E.H. Thermodynamic Properties of Ammonium and Potassium Alums an Related Substances, with Reference to Extraction of Alumina from Clay and Alunite. Technical Paper 688, Bureau of Mines, Washington, D.C., 1946. 104 pp.

10. Bickelhaupt, R.E. A Technique for Predicting Fly Ash Resistivity. EPA-600/7-79-204. U.S. Environmental Protection Agency, Research Triangle Park, NC, 1979. 15 pp.

11. Dismukes, E.B. Conditioning of Fly Ash with Sulfur Trioxide and Ammonia. EPA-600/2-75-015, U.S. Environmental Protection Agency, Research Triangle Park, NC, 1975. 155 pp.

POWER PLANT PLUME OPACITY CONTROL

J. Martin Hughes
Kai-Tien Lee

CIVIL ENGINEERING DEPARTMENT

Virginia Polytechnic Institute and State University

Blacksburg, Virginia 24061

ABSTRACT

Achieving compliance with plume opacity standards remains a significant problem in the electric utility industry. Even modern plants equipped with electrostatic precipitators and scrubbers emit plumes that do not comply with standards for visible emissions. The conversion in the presence of catalysts, of sulfur containing flue gases to sulfate aerosols is the major source of the problem. This paper deals with the control of plant operating parameters and the application of control equipment and/or chemical additives to bring about plume opacity compliance. In achieving compliance with opacity standards a reduction in plant particulate emissions will be achieved by the fact that particulate formation in the plume will be reduced.

INTRODUCTION

More than forty Class A1[1] SIP and NSPS Power plants operate with plume opacity in excess of opacity standards as measured by EPA Reference Method 9(1). Enforcement action against these plants consists of Federal Court Orders, Federal Consent Decrees, Administrative consent Orders and State Stipulation Agreements. The number of megawatts out of compliance due to these plants operating amounts to 29870(1).

Table 1 indicates overwhelmingly that ESP controlled plants generate the majority of the compliance problems. EPA Policy has been "... not to pursue visible emission violations where we believe it is probable that the source is in compliance with the mass standard"(2). Due to this EPA policy, almost no visible emission enforcement action has been instigated against coal fired power plants with FGD equipment.

Consultation with certified opacity observers in several states and Lidar operators indicated that a number of FGD type coal fired power plants do have plume opacity levels above the standards(4).

TABLE 1 ELECTRICAL UTILITY PLANT DATA*

Plants Operating #	Under Construction	Control Facilities	Collection Efficiency %	VE Violations Reported
59	41	FGD or ESP+FDG	45-99	4 (3)(4)
178		ESP	95-99+	41 (5)
31	11	FF	99.9	0 (6)

*	Plants Greater than 100 MWe Capacity
#	Reported number of utility power plants (not individual boiler units)
VE	Visible Emissions
FGD	Flue Gas Desulfurization
ESP	Electrostatic Precipitation
FF	Fabric Filter (Baghouse)

---

[1] Emissions of more than 100 TPY of criteria pollutant from plant with operating air pollution control equipment

Therefore, the four FGD plants indicated in Table 1 depict only a fraction of the FGD type plants with non-compliance status with reference to plume opacity (VE) standards. The number of these units experiencing problems in complying with plume opacity standards should be determined. Some plumes are subject to a no visible plume standard (5% opacity) and some a 10 or 20% standard for 3 minutes maximum depending on the state having jurisdiction and any applicable PSD or SIP designations.

The factors affecting plume opacity in reactive plumes were not well understood in 1977 when EPA promulgated NSPS for power plants(7). As a result the enforcement of regulations was such that the power plant opacity required by the standard could be overlooked after it had been demonstrated that mass emission limits were being met and that steps were taken to operate the source so as to minimize opacity emissions(8).

BACKGROUND

Oil fired power plants violating opacity standards typically comply with mass emission standards while coal fired plants typically violate VE standards when simultaneously violating mass emission standards(9). The investigation reported here focuses on the atypical case when in-situ transmissometer VE measurements show compliance but plume opacity as measured by Reference Method 9 or LIDAR exceeds opacity standards. This case comes about due to gas phase reactions that produce fine aerosols, vapor phase condensation and physical agglomeration of sub micron sized clusters and particles.

Stack sampling and monitoring facilities do not permit the determination of the composition and aerosol size distribution changes in plumes. Sampling of reactive plumes via ground based and airborne platforms presents challenging problems to be solved(10). Tethered balloons, helicopters and aircraft have been used with some success. The plume opacity control technology applicable to these aerosols which are created and/or grown in power plant plumes is the main topic of this paper.

Other topics that need to be investigated in more detail are

1. Particulate emissions inventory modification due to reactive plumes as related to receptor and dispersion modeling

2. The impact of near stack plume reactions on rain water quality

3. Modifications of ambient air quality levels resulting from plume reactions as related to existing ambient and proposed fine particulate standards

OIL FIRED POWER PLANTS

Over the past twenty years additives have been used for controlling sulfur compound levels in oil fired plant flue gases(11). Table 2 summarizes some results that relate to flue gas opacity control in that SO_3 at only a few PPM in flue gas is strongly related to plume opacity.

TABLE 2 TREATMENT OF FLUE GAS FROM RESIDUAL OIL(2-4.5%S) FIRED UNITS(11)

COMPANY	ADDITIVE	WT%	AS/IN	SO_3 % REDUCTION
Florida Power	Dolomite	0.1	Slurry/Fuel Oil	33
Florida Power	Dolomite	0.1	Dry Power/Flue Gas	42
Florida Power	Dolomite	0.2	Dry Powder/Flue Gas	50
English	Dolomite	0.2	Dry Powder/Flue Gas	80
English	$MgCO_3$	0.1	Dry Powder/Flue Gas	75
Long Island Lighting	MgO*	NS	NS	Significant
English	Mg(20-50 Mesh)	0.02	Dry Powder/Flue Gas	60-100#
Consolidated Edison	MMT**	NS	NS	45

* Low Excess Air (10% Range), Small Particle Size (10 Micrometer)
# Function of Injection Point
** Methyl Cyclopentadienyl Manganese Tricarbonyl
NS Not Specified

Recently Brookhaven National Laboratory conducted a study (12) of sulfate formation in oil-fired power plant plumes and produced the following empirical equation which the authors called a "somewhat speculative correlation".

$$TPO = 1.67[MSO_4] + 3([H_2SO_4] - 6) \qquad (1)$$

where

TPO is the total plume opacity in %

$[MSO_4]$ is the ppm on a molar basis of the metal sulfates in the flue gas

$[H_2SO_4]$ is the ppm on a volume basis of the sulfuric acid in the flue gas

The value of $[MSO_4]$ was predicted by

$$[MSO_4] = \frac{0.175}{(7.07 + 0.32[O_2])}\left(1 - \frac{ESP^{0.8}}{100}\right)\left\{[Na] + 0.38([V] + [Mg]) + 10[H_2SO_4]\right\} \qquad (2)$$

where

$[O_2]$ is the furnace oxygen in Vol. %

ESP is the ESP efficiency in %

[Na], [V], [Mg] are the ppm on a weight basis of sodium, vanadium, and magnesium in the fuel oil. Eq. (2) was reported to correlate with measured results with an overall relative standard deviation of 24%.

The sulfuric acid concentration in the flue gas was given by

$$[H_2SO_4] = \frac{1300\ L[O_2][S]}{(7.07 + 0.32[O_2])^2} \quad \frac{[V]}{([V] + [Mg] + [Na] + [M] + 1/2[C])} \qquad (3)$$

where

$[H_2SO_4]$ is the sulfuric acid concentration in ppmv in the flue gas

L is the operating fraction of full plant power output

[S] is the sulfur content of the fuel oil in wt. %

[M] is the wt. % of metal other than [V], [Mg], and [V] in the fuel

[C] is the unburned carbon in the fly ash as a fraction of carbon in the fuel oil, wt. ppm

Since this opacity correlation is based on sparse data from various sources with incomplete data sets, additional studies must be carried out to validate its range of applicability. For the Brookhaven data set the data ranges investigated are listed in Table 3.

Plume opacity exceeds in-stack opacity for the cases of (A) high emissions of sulfuric acid which condense (13,14) and (B) the presence in the plume of metal sulfate particles with sizes less than the visible size range (0.4-0.7 μm) (15-17) which grow into the visual size range by hydration in the plume as it cools.

TABLE 3 RANGE OF PARAMETERS INVESTIGATED

PARAMETER	PARAMETER RANGE MINIMUM	MAXIMUM
$[H_2SO_4]$, vol. ppm	0.1	39.5
L, fraction of full power	0.39	1.02
$[O_2]$, vol. %	0.1	2.9
[S], wt. %	0.31	2.59
[V], wt. ppm	4.0	463
[Mg], wt. ppm	11	841
[Na], wt. ppm	32	179
[M], wt. ppm*	50	100
[C], wt. ppm unburned	230	6100

*Other metals, M, in the fuel ash.

This plume opacity model and the field data from investigations which support it provide a composite picture of the significant factors that govern plume opacity in oil fired power plant plumes. They are:

1. Furnace oxygen
   Plume opacity increases almost linearly with furnace oxygen above the $[H_2SO_4]$ greater than 6 ppmV level up to 3% O_2 and then at a somewhat lesser rate for higher furnace oxygen concentrations. For a given furnace $[O_2]$ operating level the firing of fuel oil with a higher vanadium content will result in increased opacity levels.

2. Sulfur and Vanadium content of fuel oil
   To give an example of the effect of sulfur and vanadium content in fuel oil on plume opacity the data in Table 4 was used with Eq. (1). Note that for $[H_2SO_4]$ less than 6 the second term on the RHS of Eq. (1) is dropped. The plume opacity resulting from the operation of unit 1 was calculated by Eq. (1) to be more than 4 times greater than for unit 2 based on Table 4 data.

For [S] content of fuel oil below 2% the TPO is essentially all due to metal sulfate particulate. For [S] content of fuel at the 4% level TPO would be 36% with only 3% due to $[MSO_4]$ and the balance of 33% plume opacity would be due to $[H_2SO_4]$.

TABLE 4. EFFECTS OF FUEL OIL COMPOSITION ON PLUME OPACITY

Unit	[S]	[V]	[O_2]	[MSO_4]	[H_2SO_4]	TPO* %
1	2.10	390	2.0	12.3	19.5	61
2	0.33	5.0	3.6	8.1	0.07	14

*Calculated

3. Plant Load Level

The plant load, L, depicted in Eq. (3) was seen to be proportional to [H_2SO_4]. Below the 6 ppmV level [H_2SO_4] does not typically contribute to plume opacity. For these cases [MSO_4] levels determine TPO. Table 5 data was taken from a plant (12) which operated at 1/2 load (176 MW output) for 5 hours (1500-2000) on 6/12/78 and then at nearly full load (320 MW) for 2 1/2 hours (1330-1600) the next day with the same fuel oil with [S] = 0.75 wt. %.

From the point of view of steady state plant operation for the case examined in Table 5 doubling plant load will increase TPO by a factor ranging from three to seven.

TABLE 5 PLANT LOAD EFFECT ON PLUME OPACITY

Load MW	[MSO_4] ppmV	[H_2SO_4]	TSP mg/m^3	TPO* %
176	2.69-3.04	1.82-2.17	29-34	4.5-5.1
320	9.70-20.17	3.80-3.82	177-293	16-34

*Calculated

4. ESP Performance

Less than 5% of the total measured H_2SO_4 was found adsorbed on the fly ash (12). The concentrations of sulfuric acid vapor were measured at the inlet and outlet of an operating ESP and found, as expected, to be essentially the same (12). The ESP effect on TPO was indirect. As the furnace oxygen level was decreased, an increase in particulate carbon resulted. Therefore, for the more efficient ESP installations the furnace [O_2] can be reduced to a lower level to achieve lower levels of [H_2SO_4] in the flue gas and reduced plume opacity than would be the case with less efficient precipitator installations. For [H_2SO_4] greater than 6 ppmV this indirect effect is pronounced. For the case when [H_2SO_4] is less than 6ppmV the plume opacity would drop an insignificant amount (from 20% to 19%) when ESP efficiency was raised from 88% to 92% with an accompanying furnace [O_2] reduction from 2.7 to 1.0 vol %.

5. Combustion Conditions

The importance of good combustion achieved by efficient mixing of combustion air and fuel oil aerosol is illustrated by data from a study conducted at two units of an oil fired power plant (12). Measured results which were compiled over the July-December operating period are given in Table 6. Furnace oxygen concentrations were reduced in unit #3 in attempts to achieve compliance with TPO standards. The attempts failed and the TPO problem remained due to a flue gas sootiness resulting from poor combustion conditions. Only after air-fuel mixing and combustion was upgraded to that of unit #1 was TPO compliance achieved.

TABLE 6 COMBUSTION EFFICIENCY EFFECTS ON TPO

	UNIT #1	UNIT #3
[H_2SO_4] ppm	16 ± 6	2.1 ± 1.7
[O_2] %	1.3 ± 0.4 #	0.15 ± 0.09
COMBUSTION QUALITY	GOOD	POOR
[C]* mg/m^3	3.6 ± 17	45 ± 18
ESP, %	77 ± 13	65 ± 15
TPO, %**	0 - 15	30 - 50

#Higher furnace oxygen needed to control carbon build up in ESP

*At ESP inlet

**Estimated range (Unit 3 cited for TPO violation)

6. Chemical Additives

As seen in Table 2, Dolomite (a calcium magnesium carbonate), MgO, and MMT have been used to reduce acid corrosion and neutralize the acid gas fraction of flue gases from oil fired power plants. Liqui-Mag, a commercial additive containing MgO, has been used by direct addition to fuel oil at many power plants. Coaltrol M, a commercially available pulverized MgO additive marketed by the Basic Chemical Division of Combustion Engineering has been added in the economizer outlet area to scavenge H_2SO_4 by adsorption and/or reaction with subsequent removal of the dry material in the ESP. Calculations (12) indicated that the use of an additional 200 lbs/hr of Coaltrol at a typical oil fired power plant would reduce [H_2SO_4] by 26%. However, decreasing furnace [O_2] from 0.3 to 0.2% would reduce [H_2SO_4] by 33% at a lower cost.

For units firing high sulfur (2.5 wt %) and high vanadium (400 wt ppm) fuel oil the following set of recommendations have been given from the experience gained from an extensive study (12).

1. Maintain furnace O_2 no higher than 0.4 to 0.5%, preferably lower.
2. Add Liqui-Mag or other finely dispersed sub-micron MgO additive to the oil (front end addition) at 1.6 lbs Mg/lb V.
3. Provide efficient fuel and combustion air mixing (flue gas carbon at the ESP inlet should be less than 40 mg/m^3).
4. ESP efficiency should be 75% or higher.
5. Adjust fly ash recirculation injection location for minimum flue gas carbon.

COAL FIRED POWER PLANTS

Coal fired power plants have historically used ESPs for plume opacity control. ESPs normally achieved high removal efficiencies with relatively low power consumption. With the imposition of SO_2 emission standards in the early 1970's the shift to low (less than 1% S) sulfur coals began. ESP performance decreased and plume opacity increased. Coal fired power plants equipped with ESPs had a plume opacity problem to solve.

To burn the less costly high sulfur coals while meeting the stringent SO_2 emission standards required the use of flue gas desulfurization (FGD) units. Some of these units were found to emit plumes with high opacity levels. Nader and Conner (14), for example, reported plume opacities at FGD equipped plants as high as 70-90%. Some FGD equipped coal fired plants meeting NSPS particulate standards of 0.03 lb/MM Btu can still not meet plume opacity standards.

Since the late 1970's baghouses have been applied for the collection of particulate matter at coal fired power plants fueled by low-sulfur coal. No plume opacity problems have been experienced to date. As applications of baghouses to power plants firing high sulfur coal develop, opacity will become a problem. The bag filter cake coupled with flue gas conditioning may be a combination which will allow compliance with emission standards while firing coal with a moderate sulfur content.

Opacity Control With ESP Units

Properly operated and maintained ESP units produce plume opacity problems when fly ash bulk particle resistivity is above or below the 10^7-10^{10} ohm-cm resistivity range. The natural resistivity of the particle layer deposited on the ESP plates can be adjusted up or down to the 10^7-10^{10} ohm-cm range by (1) temperature change, (2) flue gas moisture change, (3) raising or lowering SO_3 concentration in flue gas, (4) selecting or spiking coal with higher or lower sodium content. Ammonia has been used as a conditioning agent but does not change resistivity. Ammonia brings about an increase in space charge within the ESP which can raise collection efficiency by increasing the electric field strength in the precipitation zone. Of these alternatives SO_3 has been used most successfully.

In one case a midwestern utility plant firing 3.5% sulfur coal to two 250-MW boilers was generating a detached "blue plume" of sulfuric acid aerosol at a 40-60% TPO level (18). The problem was low resistivity due to SO_3 levels of 30 ppmV entering the ESP. The opacity was reduced to the 15% level by spraying 224 lb/hr/unit of a Nalco chemical company liquid containing soluble sodium upstream from the ESP which chemically reduced the SO_3 concentration and raised the fly ash resistivity to approximately 10^9 ohm-cm.

AEP's ESP equipped Tanners Creek plant firing 3.8-4.2% S coal experienced a dense bluish-white plume with opacity exceeding the 20% standard (19). MMT was sprayed into the primary combustion zone at 20 gm/ton coal and did not reduce SO_3 enough to effect the TPO level of 30-40%. Injection of ammonia at 50 ppm just upstream from the ESP in conjunction with the MMT injection reduced TPO to a consistent 10-18%. It's hypothesized that the ESP efficiency increased in the sub micron size range resulting from the ammonia conditioning. In addition the MMT vaporized to molecular form and provided manganese molecules to form enough $[MSO_4]$ which was removed by the ESP to bring about the TPO drop. No testing with ammonia alone was reported.

To acquire the combined benefits of ammonia and sulfur trioxide conditioning Tampa Electric Company has injected ammonium-sulfate solution upstream of the ESP. Opacity was reduced for two high sulfur coal fired units at the Big Bend Station from 30% to 10% (20). Gannon Station Unit 6 (300 MWe) firing 1.3% sulfur 9% ash coal achieved ESP efficiencies of 99.9% with ammonium-sulfate conditioning (injection both before and after the air preheater). Prior to conditioning the high resistively of the low-sulfur-coal ash had caused high TPO due to high spark rates which burned charging wires and shorted out several ESP sections.

Opacity was reduced from 30% to 8% by sodium sulfate conditioning at Gulf Power Company's Lansing Smith Station (21). Ash was collected with a hot-side precipitator. ESPs are applied in this mode when used with boilers firing low sulfur coal. One gallon of sodium sulfate was added per ton of coal as a powder before the coal was pulverized.

In a study of plants burning high sulfur coal it was found that the number of ESP fields operating did not influence appreciably the sulfur composition of the ESP outlet flue gas (22). This was in contrast to concentrations of trace metals that decreased as more fields were energized. These results support the hypothesis that the submicron sulfate aerosols and thus the opacity are not effectively removed by ESP.

Opacity Control with FGD Units

The opacity problems encountered with high sulfur coal fired boiler emissions treated with combined ESP and FGD units are mainly due to sulfate emissions not fly ash. Concentrations of sulfate in combustion gases at scrubber outlets have been reported to exceed scrubber inlet sulfate values (23). It was found that on the average a wet limestone scrubber with venturi-absorber will remove [H_2SO_4] and [MSO_4] at the 29% efficiency level while scrubbing SO_2 at the 78% level.

This desparity in efficiency levels is explained by the fact that SO_2 absorption is effective with the typical low energy (pressure drop) scrubber operation whereas highly efficient removal of the submicron sulfate aerosol requires high energy (pressure drop) scrubber operation. After passing thru the scrubber the submicron sulfate aerosol is essentially unabated in its pass thru the mist eliminator and forms an aerosol plume with its characteristic bluish white hue. The submicron size range of the aerosol is such that plume opacity may be well above the 20% opacity standard even when mass emissions are at or below the 0.03 lb/MM Btu standard or lower.

A high sulfur (4% S) coal fired plant with two 240 MW units followed by an ESP and a FGD unit of the limestone spray tower type typically had residual plume opacity levels in the 30-50% range (24). Pilot (1MW) and full scale studies were conducted in order to make recommendations for solving the opacity problem among others. It was found that a venturi scrubber operating at a pressure drop in excess of 30" W.C. would be required to reduce the opacity to the required 20% level. The energy consumption to operate the venturi unit would be enormous.

A better solution was found. The basic idea for solving the opacity problem was to increase the size of the submicron sized sulfuric acid aerosol upstream of the ESP and FGD units. A quencher unit was used to provide the temperature and humidity conditions to promote growth in aerosol size. A FGD spray tower was operated immediately downstream of the quencher unit. Impactor measurements by Radian Corporation with low fly ash loadings indicated tremendous mass growth in suspended aerosol in the 0.2 to 0.7 μm range as the acid mist and fly ash passed thru the scrubber. In other words, a negative removal efficiency for submicron fly ash and sulfate particles. For high fly ash loadings the removal efficiency was generally positive for size ranges of 1/2 micrometer and larger. It was evident that no useful purpose was served by removing the fly ash prior to the acid aerosol. It was also evident that to control opacity with reasonable scrubber energy consumption that the submicron sulfate and fly ash particles must be collected with a unit downstream of the scrubber. A wet tubular precipitator (first used commercially some 75 years ago to control sulfuric acid mist from a sulfuric acid plant) was the obvious selection. It has the capability while operating at low power consumption levels to remove submicron aerosols at high efficiency. Its performance is virtually independent of coal sulfur content and collected fly ash resistivity. The mist eliminator was eliminated. By operating the WESP in the 50-60 KV range with specific collection areas (SCAs) of 20-30 ft^2/1000 acfm, plume opacity levels were found to be in compliance. The quencher pressure drop and the SCA of the WESP may be adjusted to meet the 5% plume opacity (no visible plume) that some state air quality agenices now require.

SUMMARY

Residual plume opacity results from sulfate and non-sulfate aerosols in the 0.4-0.7μm size range. To reduce non-sulfate plume constituents that cause opacity problems three means exist (1) maximize combustion efficiency by use of additives and excess air adjustment, (2) increase energy input to ESP and/or FGD units to reach peak efficiency, (3) replace ESP and/or wet FGD with baghouse units.

For sulfate plume opacity control, (1) reduce formation of sulfate, (2) increase sulfate aerosol size within the size distribution to enhance collection efficiency, (3) apply WESP. To reduce plume opacity caused by sulfate formation, use lower sulfur fuel containing less catalytic elements such as vanadium. Flue gas additives reduce sulfate aerosol formation in the plume by promoting the conversion of SO_3 to metal sulfates which are efficiently removed by collection equipment whereas the acid aerosols are not. Without additives SO_3 contributes to plume opacity by becoming acid sulfate in the plume of ESP or FGD controlled plants.

The plume opacity caused by sulfate aerosol is best controlled by hydration of the submicron sulfate aerosol in a quencher to increase aerosol size. Following the quencher, use a WESP to remove the aerosol from the flue gas prior to reheat and stack discharge.

The work described in this paper was not funded by the U.S. Environmental Protection Agency and therefore the contents do not necessarily reflect the views of the Agency and no official endorsement should be inferred.

REFERENCES

1. Director, Division of Stationary Source Enforcement Attachment I In: Compliance Analysis of Operating Class A SIP and NSPS Power Plants. Environmental Protection Agency, Washington D.C., August, 1983.

2. Bennett, K. M. Guidance on policy for enforcement of VE violations against sources which are meeting an applicable mass emission standard. U. S. Environmental Protection Agency, Washington D. C., May, 1982.

3. Edison Electric Institute, Location of FGD Systems in North America, Washington D. C., September, 1983.

4. Personal Communication with Certified Opacity Observers & Lidar Operators, 1984.

5. McDonald, J. R., and Dean A. H. Electrostatic Precipitor Manual, Noyes Data Corporation, Park Ridge, N. J., 1982 pp. 426-433,.

6. Carr, R. C. and Smith, W. B. Fabric Filter Technology for Utility Coal Fired Power Plants, Journal of the Air Pollution Control Association 34: 178-185, 1984.

7. Federal Register, 40 CFR 60.11(e), May, 1977.

8. Director, Division of Stationary Source Enforcement, Enforcement against opacity violations from power plants, U. S. Environmental Protection Agency, Washington D. C., June, 1981.

9. Lappan, J., Factors affecting plume opacity from power plants and associated enforcement problems. Environmental Protection Agency, Washington D. C., 1981.

10. Hughes, J. M., Aerosol Signatures For Receptor Modeling. DOE/PC/61254, U. S. Department of Energy, Pittsburgh, Pennsylvania, 1984, 40 pp.

11. Eliot, R. C. (ed.), Boiler fuel additives for pollution reduction and energy saving. Noyes Data Corp., Park Ridge, N.J., 1978.

12. Dietz, R.N. and Wieser, R.F., Sulfate Formation in Oil-Fired Power Plant Plumes. EPRI EA-3231, Vol. 1, Palo Alto, California, 127 pp. 1983.

13. Conner, W.D,, "A Comparison Between In-Stack and Plume Opacity Measurements at Oil-Fired Power Plants." Proceedings of Fourth Annual Conference on Energy and the Environment., Cinncinnati, Ohio, October 4-7, 1976.

14. Nader, J.S. and Conner, W.D., "Impact of Sulfuric Acid Emissions on Plume Opacity", In Workshop Proceedings on Primary Sulfate Emissions from Combustion Sources, EPA-600/9-78-0206, August 1978, pp. 121-135.

15. E.P. Parry, A Study of Stack Effluents at an Oil Fired Utility Station, Thousand Oaks, California: North American Rockwell, 1972.

16. R.B. Engdahl, E.J. Schulz, and J.A. Gieseke, Summary Report on Characteristics of Stack Effluents from the Northport Plant, Columbus, Ohio: Batelle Memorial Institute, 1969.

17. K.T. Knapp, W.D. Conner, and R.L. Bennett, "Physical Characterization of Particulate Emissions from Oil-Fired Power Plants", Proceedings of Fouth Annual Conference on Energy and the Environment, Cincinnati, Ohio, October 4-7, 1976.

18. Albanese, V., "Additive aids precipitator performance when fly ash resistivity is too low", Electric Light and Power, 1982.

19. Gray, M., "The Effects of a Volatile Fireside Manganese Additive on Coal-Fired Utility Boiler Operation." In: Workshop Proceedings: Applications of Fireside Additives to Utility Boilers, EPRI WS-80-127, Palo Alto, California, 1981, pp. 3-1, 3-13.

20. Hudson, J.L., "Flue Gas Conditioning Experience at Tampa Electric Company." In: Workshop Proceedings: Applications of Fireside Additives to Utility Boilers, EPRI WS-80-127, Palo Alto, California, 1981, pp 3-16, 3-28.

21. Altman, R.F., "Fly-Ash Conditioning", In: Workshop Proceedings: Applications of Fireside Additives to Utility Boilers, EPRI WS-80-127, Palo Alto, California, 1981 pp 3-29, 3-40.

22. Bennett, R.L. and Knapp, K.T., "Sulfur and Trace Metal Particulate Emissions from Combustion Sources", In: Workshop Proceedins on Primary Sulfate Emissions from Combustion Sources, Vol. II, EPA PB-287 437, Research Triangle Park, N.C., 1978, pp 165-183.

23. Homolya, J.B. and Cheney, J.L., "A Study of Primary Sulfate Emissions from a Coal-Fired Boiler with FGD", JAPCA 29:1000-1004, 1979.

24. Laslo, D., Bakke, E., and Chisholm, E. "Limestone/Adipic Acid FGD and Stack Opacity Reduction Pilot Plant Tests at Big Rivers Electric Corporation",In: Proceedings 77th Annual Meeting of the Air Pollution Control Association, San Francisco, California, 84-97.4, 1984.

PULSE ENERGIZATION SYSTEM OF ELECTROSTATIC PRECIPITATOR FOR RETROFITTING APPLICATION

By: Senichi MASUDA and Shunsuke HOSOKAWA
Department of Electrical Engineering,
University of Tokyo
7-3-1, Hongo, Bunkyo-ku, Tokyo, Japan 113

ABSTRACT

A cassette type pulser module has been developed for electrostatic precipitators for upgrading the performance of existing plants. The module is to be inserted between the existing dc power supply and corona electrodes. No coupling means like a pulse transformer or a coupling condenser are used. A saw-teeth voltage appears on the corona electrodes at a desired frequency, which includes at its leading edge a transient LC oscillation with its very sharp first peak and its amplitude decaying rapidly. The first peak behaves as a submicrosecond pulse and produces very active negative streamers uniformly distributed along the entire length of existing corona wires of the conventional construction. The average of the saw-teeth voltage produces a dc collection field between the corona and the collecting elctrodes. This "direct-coupled pulse energization" indicated in our laboratory test exactly the same collection performance as the hitherto most effective submicrosecond pulse energization using a coupling capacitor and a dc bias voltage. A specific feature of the present pulse energization system is its simplicity in construction and low initial and operating costs.

INTRODUCTION

The authors investigated the use of travelling wave coronas for pulse energization (1). They recognized that this system could produce an ideal uniformity in current distribution to produce a very high collection performance. The pulse generator with a phase-controlled rotating spark gap and a ceramic capacitor bank proved to be quite cost-effective and reliable (2). Moreover, this travelling wave scheme allows the use of pulse-peaking (1) to regenerate the corona-eroded pulse peak voltage, enabling the exploitation of the pulse energy to the full. The only problem which remained was the necessity of a dc-biased long corona transmission line of either a twin-electrode (wire-to-duct) or a tri-electrode (wire-third electrode-duct) type which must be replaced to the existing corona electrodes.

The present pulse generator produces a high-frequency LC oscillation when it is connected to the corona electrode of the conventional construction as a lumped constant load. It produces a very active plasma at its first peak over the entire length of the corona electrode. The saw-teeth like voltage appears between the corona and collecting electrode at a switching frequency, and a very sharp peak of the LC oscillation at its leading edge to act as the submicrosecond pulse. The average of the saw-teeth voltage provides a dc bias voltage. A very uniform current distribution could be produced with a concurrent improvement of collection performance just as good as that obtained by the travelling wave coronas.

The present direct-coupled pulse energization enables the use of the existing dc power supply and corona electrodes, so that it can be applied in the retrofitting applications for upgrading the existing precipitators. Pilot plant test of the present pulser module will be carried out soon. In this paper are reported the results of our laboratory tests made for developing this pulser system.

CONCEPT OF PULSER MODULE

Fig. 1 shows the concept of the present cassette type pulser module. It consists of a tank condenser C_0 to be charged by the existing dc power supply, voltage-doubling LC oscillation circuit with a thyrister switch T_h, and inductance L, a pulse forming capacitor C_p, and a rotating spark gap for producing a sharp rising narrow pulse. The module is inserted between the dc power supply and corona electrode of existing plants. C_p is charged up to $V_0 = 2V_{C0} - V_1$ from C_0 with the aid of a switching LC oscillation in the voltage-doubling circuit, where V_{C0} represents the voltage of C_0 and V_1 the remaining voltage of C_p just before T_h is switched. Then, after T_h recovered its interruption ability, the rotary spark gap fires to connect C_p to the corona electrode. The pulse repetition frequency can be changed in the range of 10 - 200 Hz by the controller which controls the servo motor and the gate circuit of T_h.

EXPERIMENTAL APPARATUS

TEST PULSER

The test pulser used throughout the present investigation is shown in Fig. 2 where the voltage-doubling circuit is removed. L_s in Fig. 2 represents the overall circuit inductance of the connecting wires and spark channel of the gap. The pulse rise time, T_r, is altered by inserting a coil, L_i, in series to the gap. The phase of rotation of the spark gap is adjusted so as to close the gap in the blocking half-cycle of the diode, D. Charging of C_p is made by an ac voltage, which makes the charging efficiency very high. A pulse repetition frequency, f_p, is 50 Hz throughout the present investigations where a twin-contact roter is used in the spark gap at a speed of 1500 rpm.

coronas, and the current density becomes very large on the opposit of these corona spots (Fig. 5(c) and Fig. 6(c)). Looking at the current distribution in Figs. 6(a) and (b) the direct-coupled pulse energization is anticipated to produce the same level of effect of back corona correction and performance enhancement as the condenser-coupled travelling pulse energization.

PULSE WAVE FORM AND EQUIVALENT CIRCUIT

The appearing voltage on the corona electrode is of a saw-teeth form as shown in Fig. 7(a). At its leading edge, it has a transient oscillation as shown in Figs. 7(b) and (c). When the spark gap fires, the LC oscillation starts to occur, and the voltage takes its first maximum, V_M, at $t = T_r$. The oscillation decays quickly and stops at $t = T_d$ when the spark channel is opened to disconnect C_p from the corona electrode. Approximate characteristics of the oscillation can be considered in consideration of an equivalent circuit as shown in Fig. 8(a). The oscillation phase lasts for some tens to hundreds microseconds, whereas the main negative streamers are produced only in its first half cycle (4). The oscillation decays quickly by the losses in the circuit, spark channel, and ion oscillation in corona plasmas. Then, we get the following expression for the damped oscillation:

$$V_{EP}(t) = V_R + k\,(V_0 - V_R)\,\frac{C_p}{C_p + C_{EP}}\,(1 - e^{-\alpha t}\cos \omega t) \qquad 0 \leqq t \leqq T_d \tag{1}$$

where

k : loss factor, $0.8 \leqq k \leqq 1$

V_R : residual voltage

$\alpha = r/2L$, r: equivalent overall loss

$\omega \simeq 1 / \sqrt{LC}$, $C = C_p\, C_{EP} / (C_p + C_{EP})$

and the equivalent pulse rise time, T_r, is given by

$$T_r \simeq T / 2 = \pi / \omega = \pi\sqrt{LC} \tag{2}$$

In the oscillation period, the ion migration towards collecting electrodes is negligible and R_{EP} is included in the loss factor of K, which represents the streamer formation loss.

Finally, the spark channel turns off at $t = T_d$ as shown in Fig. 7(b), and the decay phase of the saw-teeth starts. It consists of a first rapid decay (decay phase I) and the second slower one (decay phase II). The initial voltage of the decay phase I, V_D, will be :

$$V_D = V_R + k\,\frac{C_p}{C_p + C_{EP}}\,(V_0 - V_R) \tag{3}$$

and the voltage decay in the phases I and II will follow the equations below, derived from the equivalent circuit of Fig. 8(b),

$$\text{Phase I}: V_{EP} = V_D\, e^{-t/\tau_I} \qquad \tau_I = (R_{EP})_I\, C_{EP} \tag{4}$$

$$\text{Phase II}: V_{EP} = V_D\, e^{-T_I/\tau_I}\, e^{-(t-T_I)/\tau_{II}} \qquad \tau_{II} = (R_{EP})_{II} C_{EP} \tag{5}$$

Fig. 9 shows the ionic current wave form measured on the collecting electrode with one of the ionic current probes (Fig. 3). It can be seen that the ionic convection current lasts as long as several milliseconds. This time corresponds to the duration time of the decay phase I (Fig. 4(a)). A substantial fraction of energy stored in the inter-electrode capacity is consumed by the ion convection current flowing in the decay phase I with a concurrent sharp decay of V_{EP}. In the decay phase II, V_{EP} drops much more slowly because the pulse-induced plasma has been depleted and only leakage current and, in some cases, dc coronas are existing.

FACTORS AFFECTING VOLTAGE WAVE FORM

It is observed that among the factors affecting the overall voltage wave form in the present pulse energization the following three are the most dominant : the magnitude of the pulse peak voltage, V_M; pulse rise time, T_r; and occurence of back corona.

Pulse Peak Voltage, V_M:

Figs. 10(a) and (b) indicate the effect of V_M measured under a back corona free condition with the test electrode as shown in Fig. 3. A higher V_M produces a sharp drop of the voltage in the phase I to the dc residual voltage which remains almost constant in phase II and is substantially lower than that obtained at a lower magnitude of V_M (Fig. 10(b)). Whereas the use of lower V_M produces a much less voltage drop in the phase I and a long lasting gradual drop in the phase II (Fig. 10(a)).

This difference may be explained by the difference in the carrier production in the pulse-induced corona plasmas. The lower peak voltage will produce less carriers available for the discharge of the inter-electrode capacity, resulting in a smaller voltage drop in the phase I, which will, however, produce the dc corona current, small in magnitude, and a concurrently slower, but long lasting voltage drop in the phase II. Contrarily, the higher peak voltage, V_M, will produce enough carriers to discharge the inter-electrode capacity down to a level below the corona starting threshold in the phase I.

Pulse Rise Time, T_r:

Figs. 10(b) and (c) show the effect of T_r, which is identical to that of V_M. The use of a shorter T_r produces the same effect as that of a higher V_M. The difference may again be understood when the difference in carrier production in the corona plasma is considered. A shorter rise time produces a much more uniform and intense coronas with a greatly enhanced carrier production. But it also results in a decreased level of the average dc field.

Back Corona

Fig. 11 indicates the difference between the pulse waves with and without back corona. The wave form without back corona (Fig. 11(a)) is essentially the same as those (Fig. 10) observed with clean electrode system of Fig. 3. But it indicates a drastic change when back corona takes place (Fig. 11(b)). The voltage continues to drop during an entire period of a pulse cycle, and the difference between the phase I produced by the convection of pulse induced ions and phase II after depletion of these initial ions disappears. Positive ions by back corona contribute to the continuous discharge of the inter-electrode voltage in this particular case of extremely high dust resistivity. Concurrently, the final voltage, V_R, and the average level of the dc field take much lower values to produce a performance degradation, aside from charge degradation of dust.

DESIGN PARAMETERS

As already indicated in the previous section, the production of ions by a pulse voltage is enhanced by the use of a larger V_M and a smaller T_r. V_M can be changed by C_p and V_0 of the pulse forming capacitor. Assuming $K = 1$ and $r = 0$ in Eq. (1), we get

$$V_M / V_0 = V_R / V_0 + (1 - V_R/V_0) \frac{2 (C_p/C_{EP})}{1 + (C_p/C_{EP})} \qquad (6)$$

Fig. 12 indicates the calculated value of V_M/V_0 as a function of C_p/C_{EP} for various values of V_R/V_0 assumed. It can be seen that C_p/C_{EP} has to be increased to increase the magnitude of V_M, whereas its increasing rate becomes diminished beyond $C_p/C_{EP} = 1$. Hence, in consideration of the cost of the pulse forming condenser, the value of C_p should be restricted in the range $C_{EP} \leqq C_p \leqq 1.5\ C_{EP}$.

Fig. 13 shows the effect of V_0 on the distribution of ionic current density measured with the center probes (Fig. 3). In this particular case of $C_p = 2.99$ nF and $T_r = 200$ ns, $|V_0| > 80$ kV is needed to get an uniform current distribution. Thus it is imperative in the present pulse energization system to use a sufficiently high V_0 to obtain a satisfactory uniformity in current distribution.

Fig. 14 shows the effect of T_r on the ionic current density, again, measured with the center probes (Fig. 3). A smaller T_r gives a better uniformity in the current distribution with its magnitude also increased. T_r is reduced by lowering L and C in Eq. (2). However, it is difficult to reduce the overall circuit inductance, L_s (spark channel, feeding wires, etc.), below a certain level. Hence, the magnitude of C_{EP}, i.e. the number of parallel ducts, to be energized with a single pulse power supply should be limited so as to keep T_r at a desired level.

CORONA MEASUREMENTS

Various kinds of corona measurements are made using a wire-to-duct system of full scale dimensions as shown in Fig. 3. The corona electrode is of a conventional construction consisting 25 square wires, each having a 5 mm x 5 mm cross section. The pulser output is directly connected to a bottom corner of the corona electrode, and both ionic current density and its wave form are measured using 39 probes attached on the collecting electrode. Each probe is on the opposite of a corona wire, and has a 10 cm x 20 cm area. The capacitance between the corona electrode and two plates is measured with a LCR meter (KOKUYO ELECTRIC CO., LTD. Type KC-534), and its value is C_{EP} = 3.17 nF.

MEASUREMENT OF PERFORMANCE ENHANCEMENT

Fig. 4 illustrates a laboratory test precipitator in a race-track gas circuit used for measuring the performance enhancement produced by the present pulse energization. For the purpose of comparison tests are also made with a conventional dc-energization and a condenser-coupled submicrosecond pulse energization applied on top of a dc-bias voltage. Two flyash samples are used and their resistivity altered in the range of 5 x 10^{11} - 1 x 10^{13} ohm-cm by changing gas temperature.

Three collection fields are energized with a common power supply. Each field consists of 2 parallel ducts, each being spaced at 0.3 m, 0.76 m high, and 0.5 m long in the gas flow direction. The total duct cross-section is 0.46 m^2, and the total collection area of a single field is 1.52 m^2 with SCA = 4.03 $m^2/(m^3/s)$ at 0.82 m/s standard gas velocity. Three corona wires with 3 mm in diameter are installed in each duct with a 80 mm wire-to-wire spacing. The carrier gas is air, and its temperature can be raised by an electric heater up to 200 °C. The inlet dust mass loading, W_i, is kept constant by using a constant dust feeder, monitored by a dustmeter (Konitest) based on tribo-electrification. The dust mass-loading is measured at the outlet, W_0, by a sampling filter.

Back corona sevirity, expressed in terms of a ratio of the positive ionic current density to the negative one, I_+/I_-, is measured by the bi-polar current probe (3).

EXPERIMENTAL RESULTS

IONIC CURRENT DENSITY DISTRIBUTION

Fig. 5 shows the light activity of coronas in the full scale duct. Fig. 5(a) is for the present direct-coupled pulse energization. For the purpose of comparison, the cases of the condenser-coupled travelling pulse energization and the conventional dc energization are shown in Figs. 5(b) and (c), respectively. In the pulse energization of both types ((a) and (b)) the uniformity in the light activity is satisfactory, resulting an uniform ionic current density distribution on the collecting electrode as shown in Figs. 6(a) and (b). On the other hand, the dc energization produces spotty

Under these constrictions the average current density on the collecting electrode, a parameter determining the avoidance of back corona, can be altered only by changing the pulse frequency, f_p.

TESTS OF COLLECTION PERFORMANCE

The collection performance by the present pulse energization is tested in the laboratory precipitator (Fig. 4) at T_r = 800 ns using a high resitivity fly-ash sample, and compared with the test results obtained with a conventional dc-energization and a condenser-coupled submicrosecond pulse-energization applied on top of the dc bias voltage. The test conditions are indicated in Table 1. The collection performance, expressed by both the mass-based collection efficiency, η, and the Deutsch migration velocity, w, are shown in Table 2. The back corona severity, I_+/I_-, measured with the bipolar current probe is also indicated.

As can be seen from I_+/I_-, the dc-energization causes back corona at all of the three resistivity levels, and the back corona severity in terms of I_+/I_- becomes larger, and the collection performance lower with the increase in dust resistivity. The collection performance in the dc energization is the worst among all of the three energization modes. On the other hand, a distinct improvement is produced by both modes of the pulse energization. However, practically no difference exists between the two pulse-energization modes in the dust resistivity range tested. The performance enhancement factor defined in terms Deutsch migration velocity becomes H = 1.45, 1.35, and 1.1 at $\rho d = 5 \times 10^{11}$, 2×10^{12}, and 1×10^{13} ohm-cm, respectively. The performance enhancement is pronounced in the first two cases where back corona can be corrected by pulse energization. In contrast back corona can not be corrected by any mode of the two pulse energization in the case when $\rho d = 1 \times 10^{13}$ ohm-cm, and the performance enhancement is only H = 1.1. It should be added that the use of a precharger (Boxer-Charger) in combination with the pulsed collection fields produces a substantial performance improvement even at $\rho d = 1 \times 10^{13}$ ohm-cm (5).

Once back corona occurs, V_R, drops drastically in the present direct coupled pulse-energization as shown in Table 1 (from -30 kV at $\rho d = 5 \times 10^{11}$ ohm-cm to -9 kV at $\rho d = 1 \times 10^{13}$). The back corona extinguishing voltage, V_e, is found to be so low when $\rho d = 1 \times 10^{13}$ ohm-cm that back corona can be hardly interrupted and even tends to propagate in the lateral direction to cover the wide area of the collection electrode. Hence, a careful control of corona current is required at this extremely high resistivity level so as not to initiate back corona.

CONCLUSION

(1). The pulser module comprizing a voltage-doubling circuit, pulse forming condenser, and a rotating spark gap can be inserted between the existing dc high voltage power supply and the corona electrodes of the conventional construction.

(2). A very uniform distribution of ionic current density is produced by the present direct-coupled pulse energization, as good as that obtained by the condenser-coupled travelling pulse energization.

(3). A transient LC oscillation occurs when the spark gap fires, and its sharp first peak acts as a fast rising narrow pulse voltage, producing streamer coronas at its first rising phase. This LC oscillation decays rapidly to disappear when the gap is off. At this instance there remains a sufficiently high voltage between the corona and the collecting electrodes, to separate negative ions form the corona plasmas and drive them toward the collecting electrodes. The ion convection current lasts several milliseconds, with a concurrent rapid decay in the voltage. This fast decay of the voltage is succeeded by a much slower decay due to leakage and dc corona current. As a result, a saw-teeth like voltage wave form is obtained.

(4) The decay pattern is affected by V_0 and T_r, through the difference in carrier production, and also by the occurrence of back corona which produces positive ionic current.

(5). The optimum value of C_p lies in the range $C_{EP} \leq C_p \leq 1.5\ C_{EP}$. As the uniformity in corona current distribution is secured only by keeping a smaller T_r, the overall inductance of the pulse and feeder circuits must be kept as low as possible. In addition, the number of parallel ducts to be energized by a single pulser should be restricted. The level of average current density should be controlled primarily by changing pulse frequency, f_p.

(6). The present direct-coupled pulse energization shows the same collection performance for high resistivity fly-ash as the condenser-coupled submicrosecond pulse energization applied on top of a dc bias voltage. The performance enhancement factor in terms of Duetsch migration velocity is the same in these two pulse-energization modes, which are $H = 1.45$, 1.35, and 1.1 at dust resistivities of 5×10^{11}, 2×10^{12}, and 1×10^{13} ohm-cm respectively. At an extremely high dust resistivity of $\rho d = 1 \times 10^{13}$ ohm-cm back corona can not be corrected even with any of the two pulse energization modes operated at $f_p = 50$ Hz, with a concurrently decreased performance enhancement of $H = 1.1$.

In conclusion, the pulser module and the present direct-coupled pulse energization system are expected to provide useful and economical means of back corona correction, in particular for retrofitting applications.

The work described in this paper was not funded
by the U.S. Environmental Protection Agency and
therefore the contents do not neccessarily reflect
the views of the Agency and no official endorsement
should be inferred.

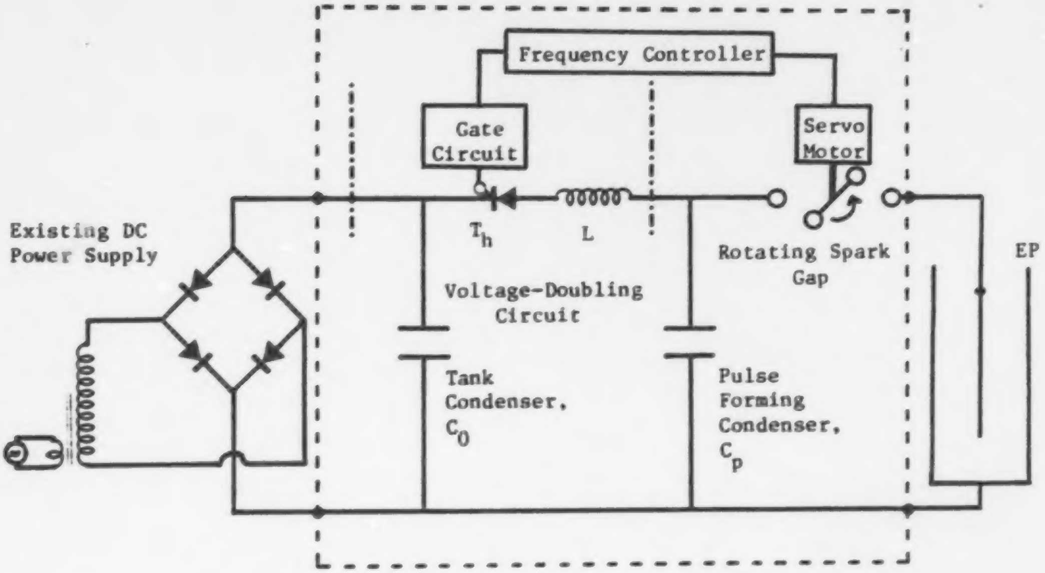

Fig. 1 Concept of Direct-Coupled Pulse Energization

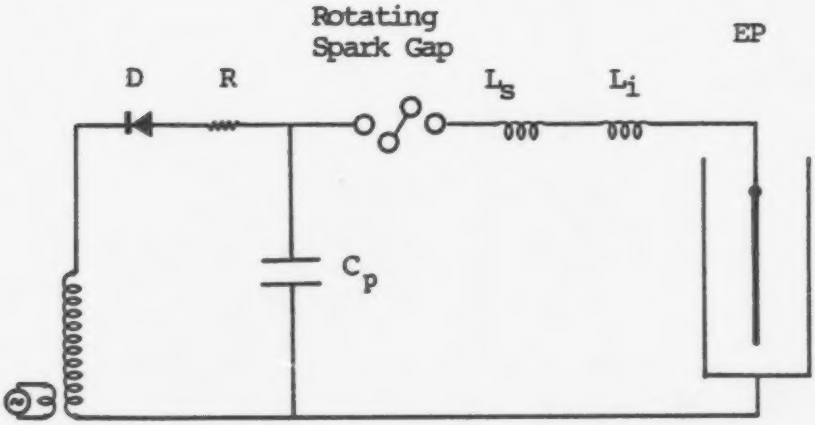

D : diode
C_0 : pulse forming capacitor
L_s : overall circuit inductance of connecting wires and spak channel
L_i : inductance of inserted coil

Fig. 2 Pulse Power Supply

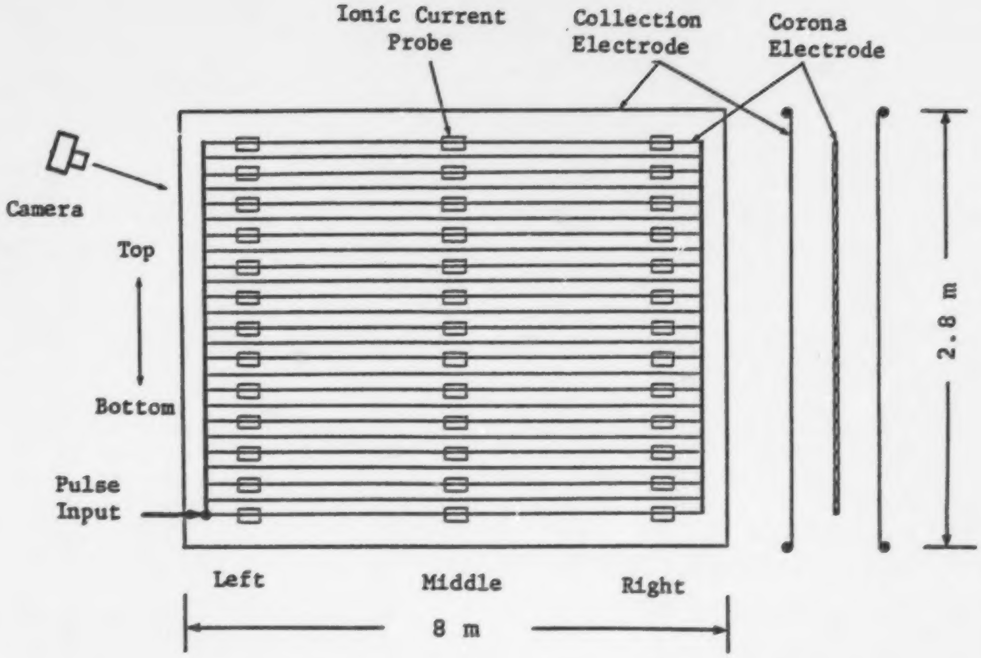

duct spacing : 250 mm ; wire-to-wire spacing : 100 mm
corona electrode : 25 wires ; wire : 5 x 5 mm cross section

Fig. 3 Single Duct Test Electrode System

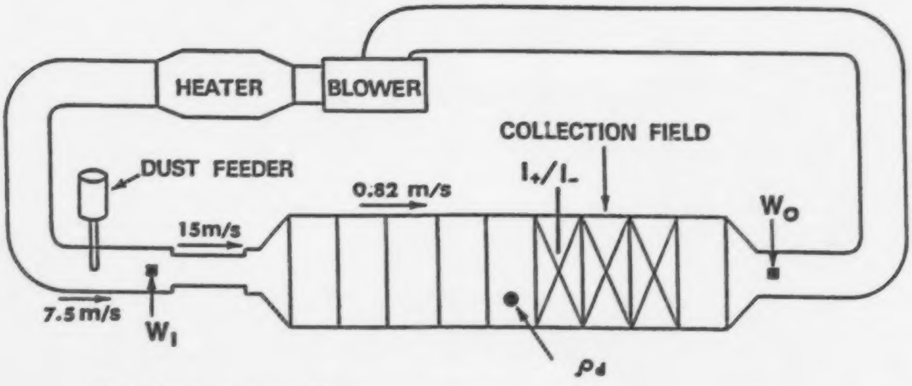

W_I : inlet dust loading
W_O : outlet dust loading
I_+/I_- : back corona sevirity measured by bi-polar ion current probe
ρ_d : dust resistivity

Fig. 4 Test Precipitator in Race-Track System

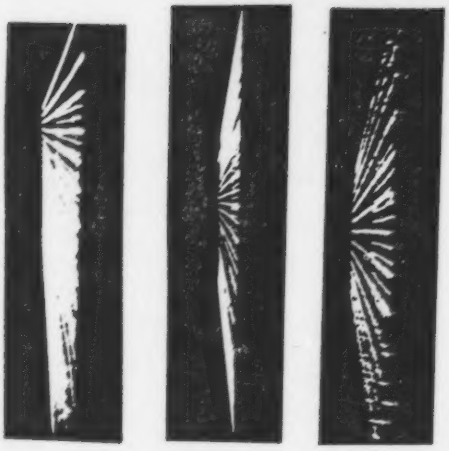

(a) (b) (c)

(a) Direct-Coupled Pulse Energization; T_r = 200 ns, T_h = 280 ns, V_0 = -70 kV

(b) Condenser-Coupled Travelling Pulse Energization; V_b = -25 kV, E_{dc} = -2.0 kV/cm, V_p = -50 kV

(c) DC-Energization; V_{dc} = -50 kV, E_{dc} = -2.5 kV/cm

Fig. 5 Light Activity of Coronas

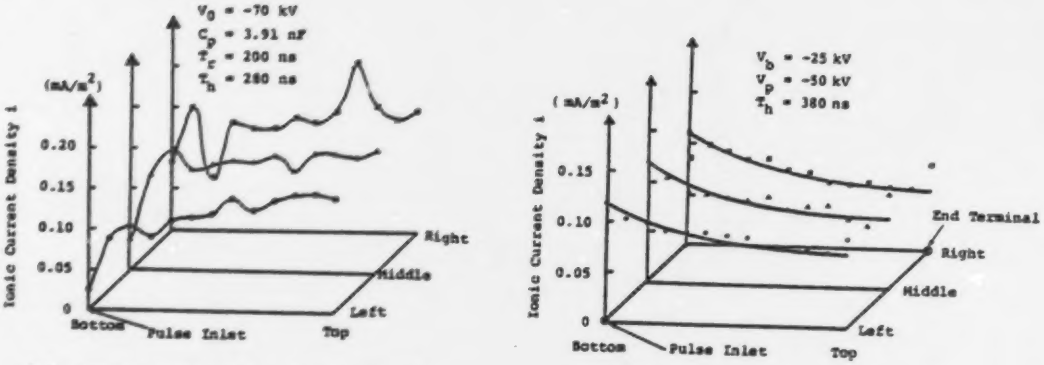

(a) Direct-Coupled Pulse Energization (sharp rising submicrosecond pulse)

(b) Condenser-Coupled Travelling Pulse Energization (L = 200 m)

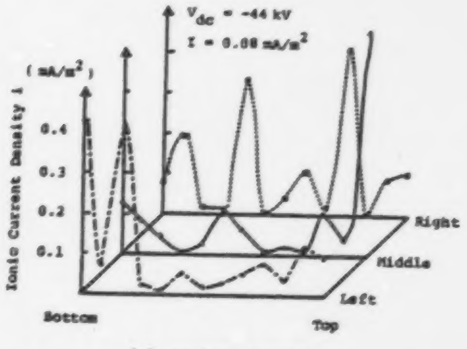

(c) DC-Energization

Fig. 6 Distribution of Ionic Current Density on Collecting Electrode

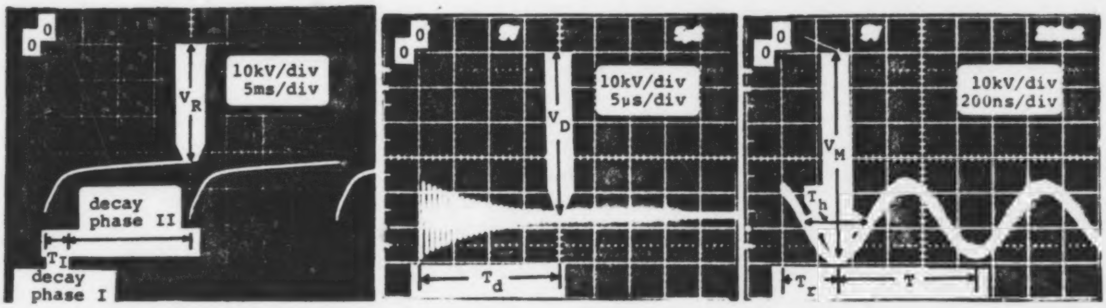

(a) Saw-Teeth Like Pulsating Wave with Sharp Initial Peaks

(b) Transient LC Oscillation

(c) Magnified Oscillating Part

Fig. 7 Voltage Wave Form, V_{EP}, Measured at the Inlet Terminal of Discharge Electrode (see Fig. 3)

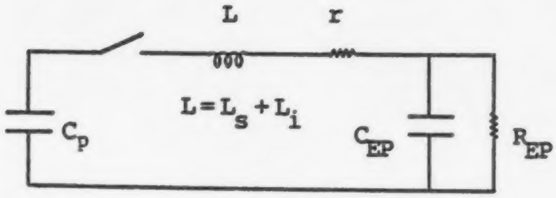

(a) Oscillation Phase

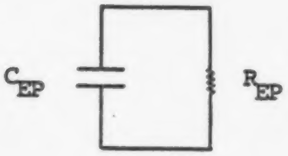

(b) Decay Phase

Fig. 8 Equivallent Circuit

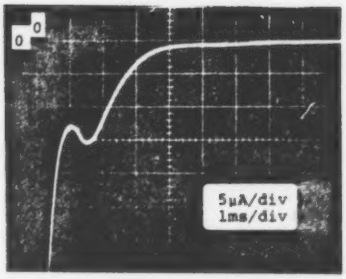

Fig. 9 Wave Form of Ionic Current Measured at Collection Electrode

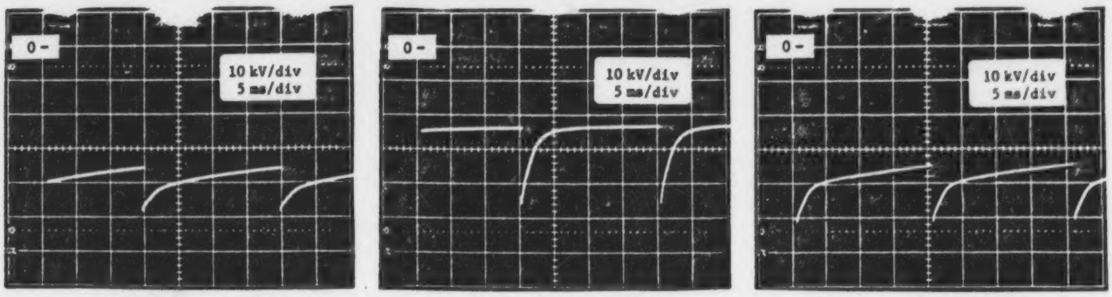

V_M = -58 kV V_0 = -60 kV
V_P = -22 kV T_r = 200 ns
V_R = -36 kV T_h = 250 ns

(a) V_M = -58 kV

V_M = -61 kV V_0 = -70 kV
V_P = -37.5 kV T_r = 200 ns
V_R = -23.5 kV T_h = 280 ns

(b) V_M = -61 kV
T_r = 200 ns

V_M = -64 kV V_0 = -70 kV
V_P = -29.5 kV T_r = 2.0 μs
V_R = -34.5 kV T_h = 2.7 μs

(c) T_r = 2.0 μs

Fig. 10 Effects of V_M and T_r on Pulse Voltage Wave Form (clean electrodes; see Fig. 3)

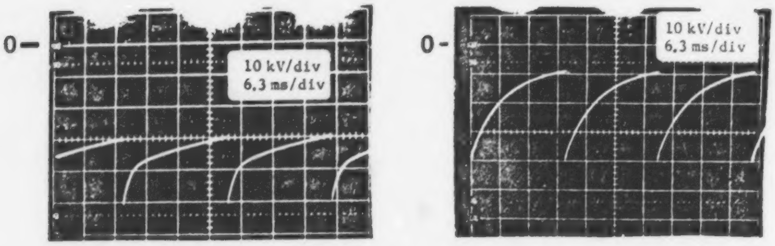

V_M = -60 kV V_0 = -60 kV
V_P = -30 kV T_r = 700 ns
V_R = -30 kV T_h = 900 ns

(a) Without Back Corona
($\rho d = 5 \times 10^{11}$ ohm-cm)

V_M = -62 kV V_0 = -50 kV
V_P = -53 kV T_r = 700 ns
V_R = - 9 kV T_h = 900 ns

(b) With Back Corona
($\rho d = 1 \times 10^{13}$ ohm-cm)

Fig. 11
Effect of Back Corona on Pulse Voltage Wave Form

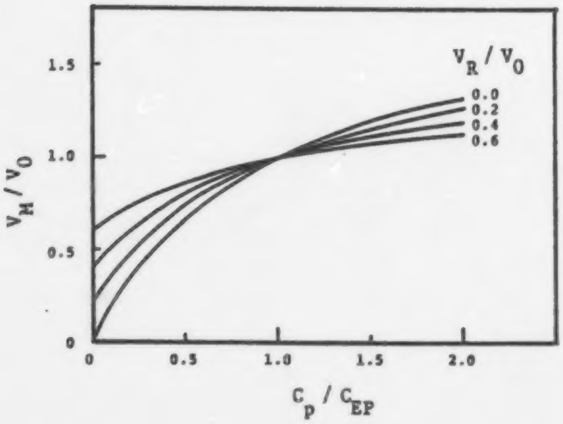

Fig. 12 V_M / V_0 v.s. C_p / C_{EP}

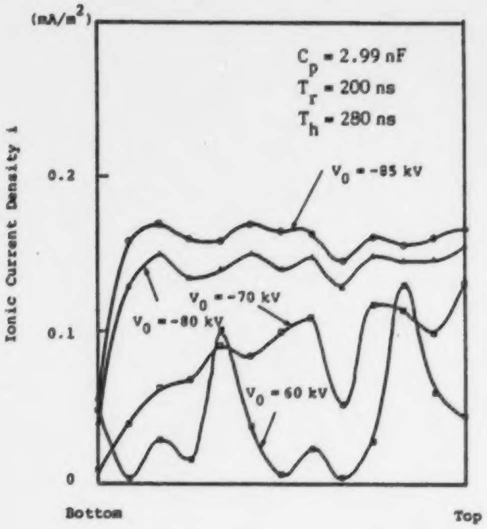

Fig. 13 Effects of V_0 on Distribution of Ionic Current Density Measured with the Center Probes (see Fig. 3)

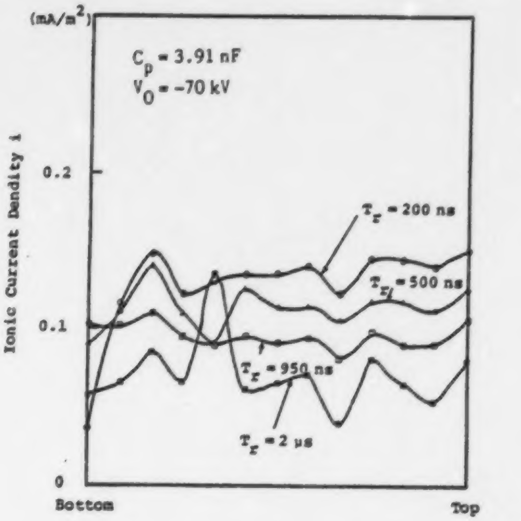

Fig. 14 Effects of T_r on Distribution of Ionic Current Density Measured with the Center Probes (see Fig. 3)

Table 1 Test Conditions

Dust Resistivity	DC-Energization	Condenser-Coupled (a) Submicrosecond Pulse Energization	Direct-Coupled (b) Pulse Energization
5×10^{11} ohm-cm (T = 130 °C)	V_{DC} = -42 kV I = 0.2 mA/m^2	V_b = -35 kV V_p = -20 kV I = 0.06 mA/m^2	V_0 = -60 kV V_M = -59 kV V_R = -30 kV I = 0.09 mA/m^2
2×10^{12} ohm-cm (T = 50 °C)	V_{DC} = -38 kV I = 0.2 mA/m^2	V_b = -30 kV V_p = -32 kV I = 0.04 mA/m^2	V_0 = -56 kV V_M = -65 kV V_R = -20 kV I = 0.09 mA/m^2
1×10^{13} ohm-cm (T = 100 °C)	V_{DC} = -32 kV I = 0.2 mA/m^2	V_b = -22 kV V_p = -32 kV I = 0.04 mA	V_0 = -50 kV V_M = -62 kV V_R = - 9 kV I = 0.08 mA/m^2

(a) T_r = 40 ns, T_h = 180 ns, f_p = 50 Hz

(b) T_r = 800 ns, T_h = 900 ns, f_p = 50 Hz

Table 2. Back Corona Sevirity and Collection Performance

Dust Resistivity	DC-Energization		Condenser-Coupled Submicrosecond Pulse Energization		Direct-Coupled Pulse Energization		Enhancement Facter
	Back Corona Sevirity (I_+/I_-)	Collection Performance	Back Corona Sevirity (I_+/I_-)	Collection Performance	Back Corona Sevirity (I_+/I_-)	Collection Performance	
5×10^{11} ohm-cm (T = 130 °C)	8.2 %	$\eta = 85.5$ % $w_{dc} = 12.4$ cm/s	0 %	$\eta = 92.6$ % $w_{pt} = 18$ cm/s	0 %	$\eta = 92.6$ % ($w_{pd} = 18$ cm/s)	H = 1.45
2×10^{12} ohm-cm (T = 50 °C)	2 - 15 %	$\eta = 84$ % $w_{dc} = 8.6$ cm/s	0 - 2 %	$\eta = 89$ % $w_{pt} = 11.6$ cm/s	0 - 2 %	$\eta = 89$ % ($w_{pd} = 11.8$ cm/s)	H = 1.35
1×10^{13} ohm-cm (T = 100 °C)	27 %	$\eta = 73$ % $w_{dc} = 6.6$ cm/s	24 %	$\eta = 76$ % $w_{pt} = 7.6$ cm/s	25 %	$\eta = 75$ % ($w_{pd} = 7.2$ cm/s)	H = 1.1

REFERENCES

1. Masuda, S., Hosokawa, S., and Nakatani, H. Corona Transmission Line Energized by Very Short Pulse Voltage as Applied in Electrostatic Precipitators, Record of IEEE/IAS 1983 Annual Conf. p.966 (Oct. 1983)
2. Nakatani, H. Doctoral Dissertation, University of Tokyo, 1983
3. Masuda, S., Itagaki, T., Nohso, S., Tanaka, O., and Hirinaga, K., Bipolar Current Probe for Diagnosing Full-Scale Precipitators, to be presented at the 5th EPA-EPRI Symp. on Transfer and Utilization of Particulate Control Technology (Aug. 27-30, 1984, in Kansas City)
4. Masuda, S. and Hosokawa, S. Pulse Energization System of Electrostatic Precipitator for Rectrofitting Application, to be presented at IEEE/IAS 1984 Annual Conf. (Oct. 1984)
5. Masuda, S., Hosokawa, S., and Kaneko, S., Ceramic-Made Boxer-Charger for Precharging Applications, to be presented at the 5th EPA-EPRI Symp. on Transfer and Utilization of Particulate Control Technology (Aug. 27-30, 1984, in Kansas City)

Session 7: ESP: PERFORMANCE ENHANCEMENT II

B. G. McKinney, Chairman
Electric Power Research Institute
Chattanooga, TN

PRACTICAL IMPLICATIONS OF PULSE ENERGIZATION OF ELECTROSTATIC PRECIPITATORS

By:
H. Milde, J. Ottesen, C. Salisbury
Ion Physics Company
A Division of High Voltage Engineering Corporation
Burlington, Massachusetts 01803

ABSTRACT

In a conventional electrostatic precipitator an applied dc voltage produces negative ions, charges particles and provides the electrical field needed to transport particles to collecting plates. In the case of high resistivity dust or fly ash, high dc voltages at the collecting plate produce positive ions in a back corona discharge. This positive current effectively reduces the negative charge on particles which reduces collecting efficiency. Pulse energization, which consists of superimposing narrow high voltage pulses onto a base dc voltage offers a way to improve collection efficiencies. Independent control of pulse amplitude and pulse frequency allows for separate control of negative ion generation and charging on the one hand and particle transport fields on the other. Techniques for applying pulses and the pragmatic significance of pulse energization are discussed along with benefits such as increased collection efficiency at low SCA and improved control. Operating results and cost data from coal-fired boiler installations are presented.

INTRODUCTION

While ESP's operate, in most cases, very efficiently and reliably, the collection of dust with a specific resistivity $\rho > 10^{11}$ Ωcm poses very severe problems. In such cases the product of current density J and resistivity ρ can reach values in excess of the electrical breakdown strength of the dust layer. The resulting breakdown produces, among other constituents, positive ions which will travel towards the negatively charged particulates and thus partially offset the negative charge on the particles. This phenomenon, called back corona, is especially prevalent in ESP's at coal burning power plants using coal with a sulfur content below 1%, since low sulfur coal usually produces a high resistivity dust layer.

When back corona conditions exist, it is necessary to lower the base voltage until the condition is under control. This reduction in voltage results in a nonuniform or spotty corona emission along the wire electrodes, insufficient current, and control difficulties, which in turn lead to poor collection efficiencies.

Pulse energization, however, is an attractive solution to precipitator problems stemming from high-resistivity dust. The frequent short high voltage pulses provide the high electric fields needed to produce corona current while the lower base voltage provides the collecting field. The relationship of pulse voltages to the base voltage is shown in Figure 1. Pulse energization systems work in like fashion to correct precipitator problems arising from warped collecting plates and dust encrusted wires; and can be easily retrofitted onto existing precipitators with little or no modification.

BACKGROUND

The origins of pulse energization of ESPs reach back as far as 1931, when R. Heinrich et al (1) applied for a U.S. patent in which the application of sharp electrical impulses to a precipitator is described.

In 1952, H. J. White and H. J. Hall (2) performed the first full scale field tests. During the tests high voltage pulses of approximately 100 μs duration were applied to a wire-plate type precipitator. The pulses were applied by the action of a rotary spark gap, a pulse transformer, and blocking diode which prevented the current from flowing back to the pulse generator.

In 1967, J. E. Luthi (3,4) described a three electrode arrangement whereby the charge carriers were produced by a pulse voltage between the third electrode and the anode. A more sophisticaed three-electrode arrangement has been discussed by Penny and Gelfand (5), whereby the potential on the third

PULSE ENERGIZATION CONCEPT

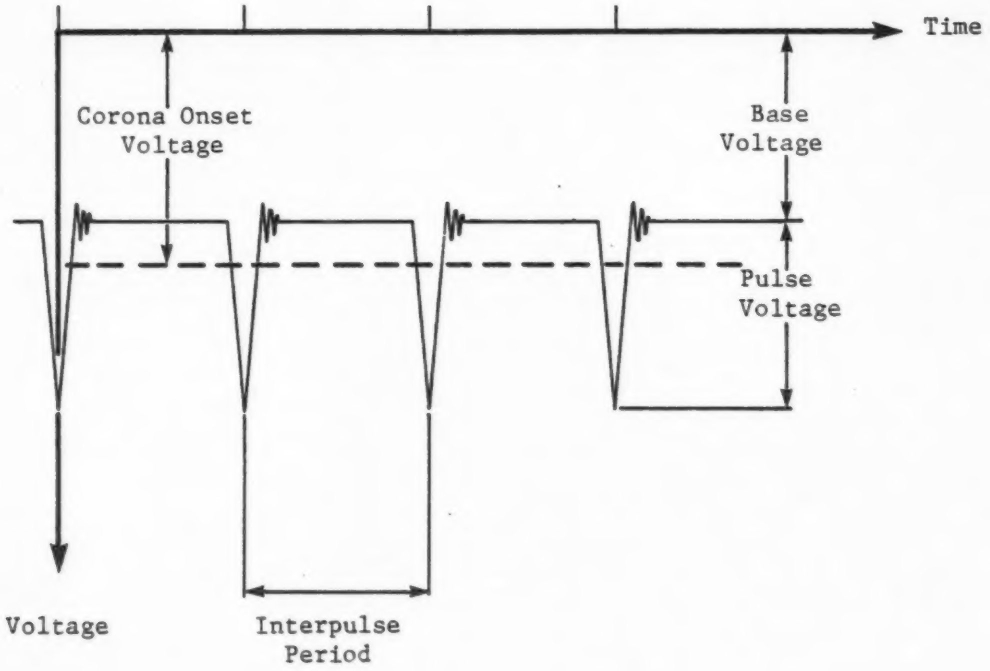

Figure 1. Voltage-time characteristics of pulse energization system.

electrode was reduced at the same time that a pulse voltage was applied to the corona wire. This method requires, however, handling of rather large displacement currents.

A unique pulse energization system nicknamed "Boxer Charger" was described by Masuda et al (6,7). The system operates as a precharger to an ESP. In the latest version the electrodes consist of double-helices energized by a pulse propagated along the double-helix. A separate charging field is provided by an alternating voltage applied to adjacent double-helical arrangements.

Full-scale commercial pulse energization systems for the standard wire-plate arrangement have been developed (8,9,19) and are beginning to find application.

Ion Physics has been developing pulse systems since the early 1970's and has recently introduced a second generation model, the PES-2000. The new system is a compact, energy efficient, highly reliable, and inexpensive unit designed to produce very short, rapid risetime pulses.

A schematic diagram of the IPC pulse energization system is shown in Figure 2. It consists of two separate arms, the conventional base supply with additional protection devices on one side and the pulse generating equipment on the other side. The pulse generator consists of a high voltage pulse capacitor, transfer switch and transformer as well as low voltage pulse circuitry. The pulse is applied to the precipitator by initiating switch closure at the time the pulse capacitor has been charged to its desired pulse voltage. The IPC system is designed to produce bursts of heavily damped sinusoidal signals with a period of approximately 1 microsecond and a repetition rate on the order of 150 pulses per second. The pulse repetition rate is controlled by varying the dead time before recharging.

TECHNICAL FEATURES

For the following discussion it was assumed that narrow pulses were superposed over a dc base voltage at a frequency of approximately 100 to 300 pulses per second (pps), as indicated in Figure 1.

INDEPENDENT CONTROL OF VOLTAGE AND CURRENT

In standard precipitators, the applied dc field is responsible for ion production, particle charging, and particle transport. Performing these three functions in a fixed geometry can lead to severe inefficiencies, especially under back corona conditions where the current density must be limited. Pulse energization offers here a unique advantage by allowing independent control of voltage and current. The base voltage is adjusted for minimum spark rate ($\sim$ 1 spark/minute) while the corona current is controlled by the pulse repetition frequency and pulse amplitude.

CIRCUIT DIAGRAM

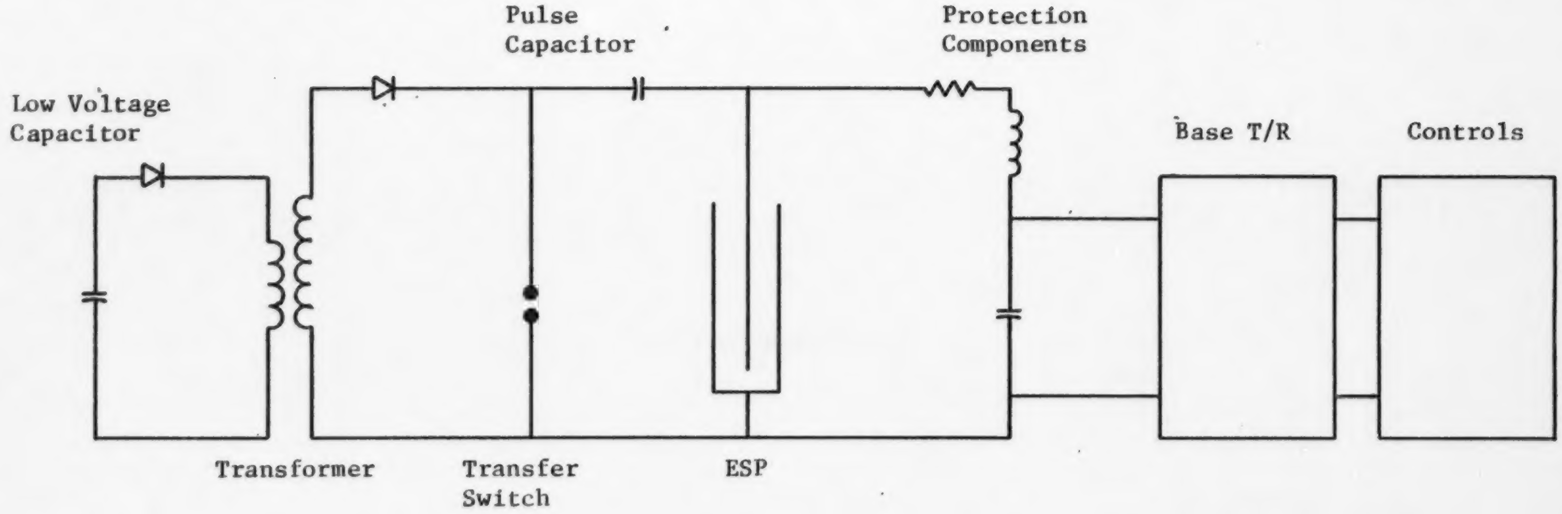

Figure 2. Schematic diagram of IPC pulse energization system.

UNIFORM PRODUCTION OF CORONA CURRENT

Since the electric field is far in excess of the corona onset voltage during the pulse period, a bright uniform corona is produced over the entire length of the corona wires during pulse application. This is in stark contrast to the spotty corona observed for low voltage dc corona.

Recent measurements on current distribution on the collector plates, under high-resistivity conditions, by D.E. Rugg et al (11) have verified our own findings and revealed that for dc energization and an average current density of 5 nA/cm2 there was no current on ninety percent of the collector plate area and high current densities on a few cells.

Uniform production of corona by pulse energization allows each precipitator section to contribute equally towards particle collection. Pulse energization also overcomes minor localized wire contamination, since the electric field during pulse application is high enough to produce corona even around a contaminated wire.

INCREASED CHARGING AND COLLECTION FIELD BY THE USE OF CORONA WIRES OF LARGER DIAMETER

Because very high electric fields are produced around corona wires during pulsing, it is possible to utilize corona wires of larger diameter and still obtain adequate corona current. This fact can be utilized to produce a higher and more uniform electric field in the proximity of the anode (12), where it is most beneficial for particle transport and consequently, collection efficiency. A conventionally energized precipitator, in contrast, requires a strong field concentration around the corona wire to provide adequate corona current without sparking.

LOWER SPARKING RATES

When pulse energization is added to the base precipitator the base TR voltage is adjusted so that sparking frequency is minimized. Pulse systems work best at spark rates of around one per minute versus several tens of sparks per minute with dc operation alone. These low spark rates lead to improved precipitator performance and reduce wire erosion thereby increasing the lifetime of discharge electrodes.

REDUCED CHARGING TIME

Due to its high instantaneous charge density, pulse energization is capable of charging particles in a much shorter time and consequently, in a shorter travel time (13,14). This feature of pulse energization is especially advantageous in precipitators suffering from reentrainment or precipitators which have a short overall length in the direction of gas flow. Additionally, it has been shown that pulse energization increases the effectiveness of sections near the precipitator inlet thereby increasing the contributions of these sections to overall collection efficiency.

BENEFITS OF SHORT PULSES

Short pulses offer some inherent advantages, partly because of the time dependent character of corona emission (15,16), strong space charge bunching, reduced severity of back corona at high resistivities and increased breakdown strength of gases for short pulse voltages.

TIME DEPENDENT CHARACTER OF CORONA EMISSION

Very early in our experimental effort we determined that emitted charge per pulse was only moderately determined by pulse width (17). This finding, which was recently confirmed by Professor Masuda et al (18), provided the basis for selecting pulses of very short duration.

Besides allowing the production of ample current, the time dependent character of corona emission also provides a means of converting nearly all the energy stored in the pulse capacitor into corona energy. On the other hand, for longer pulses it is reported (10) that the voltage on the precipitator is returned to the base value by special circuitry which recovers some of the stored energy in the precipitator and returns it to the pulse capacitor.

SEVERITY OF BACK CORONA IS INCREASED WITH LONG PULSES FOR HIGH RESISTIVITY ASH

Extensive back corona studies by Professor Masuda et al (19) revealed that for high resistivity ash the severity of back corona, i.e. the ratio of the positive ion current to negative ion current (i_+/i_-), increases with increasing pulse width for equal overall current. Masuda et al speculated that this pulse width dependence relates to the ratio of the ion transit times across the electrode gap. However, Masuda varied the pulse width only between 50 µsec and 1 msec and did not include data for a pulse width of 1 µsec.

NARROW PULSES MORE SUITABLE TO LARGE DIAMETER CORONA WIRES

In order to realize the benefit of a larger diameter corona wire it is necessary to apply very high voltages to the corona wires to overcome the less favorable emission geometry. Since the electrical breakdown strength of gases is strongly influenced by the pulse width, narrow pulses have a distinct advantage in providing ample corona current without excessive sparking.

OVERCOMES EFFECTS OF WIRE BUILDUP

Relatively high allowable pulse voltages attainable with short pulses increase the effectiveness of overcoming wire buildup. High pulse voltages produce more corona current than lower voltage pulses with both clean and dirty discharge wires. During laboratory tests of pulsers on a small ESP with dirty .156" diameter wires the PES system raised the efficiency from 75.38% without pulsing to 98.86% with pulsing. No pulse operation with clean wires gave 95.7% versus 98.9% with pulsing. With clean .25" wires and no pulsing the efficiency was 94.3% and 98.3% with pulsing. Dirty .25" wires caused the efficiency to drop to 92.7% with conventional energization while pulsing brought the efficiency back to 98.2% under identical dirty wire conditions. Both sets of data strongly suggest that short pulses are very capable of nullifying the negative effects of thick ash deposits on discharge electrodes.

SIMPLIFIED CONTROL CIRCUITRY

Very narrow pulses can be applied randomly at any point on the TR voltage waveform without initiating sparking. Complicated control circuitry to synchronize pulse application is therefore not needed. Initially the base TR voltage is set to a minimum spark rate (typically one spark/minute) and the pulse voltage and frequency are then set to optimize precipitator performance. Changes in pulse voltage and frequency alter the TR voltage only slightly as shown in Figure 3. As the voltage and frequency are increased with short pulses the base TR voltage remains nearly constant thereby providing an optimum collecting field with very high corona producing pulse voltages.

Since the application of pulse voltages has only a modest effect on the operation of the base supply it is, in most cases, possible in a retrofit application to retain the existing base TR controls.

PRACTICAL BENEFITS

IMPROVED COLLECTION EFFICIENCY

Collection efficiency of an electrostatic precipitator can be expressed by the modified Deutsch equation

$$\eta = 1 - \exp\left[-(w_k A/V)^m\right] \qquad (1)$$

where η is the collection efficiency, w_k the modified migration velocity in ft/min, A the collection area in ft^2 V the gas flow in acfm, and m an exponent dependent on inlet particle size distribution (typically between 0.5 and 1).

From numerous measurements it was found that the ratio (frequently referred to as enhancement factor) of migration velocities for pulsed versus dc energization varied between 1.3 and 2 depending on resistivity of the collected fly ash, as shown in Table 1.

TABLE 1

Enhancement as a Function of Ash Resistivity

Resistivity - ohm cm	10^{11}	10^{12}	10^{13}
Enhancement H	1.3	1.6	2

An increase in migration velocity is of great economic significance, since according to Equation (1) an increase in migration velocity is equivalent to a corresponding increase in collection area. Consequently, an increase of w_k

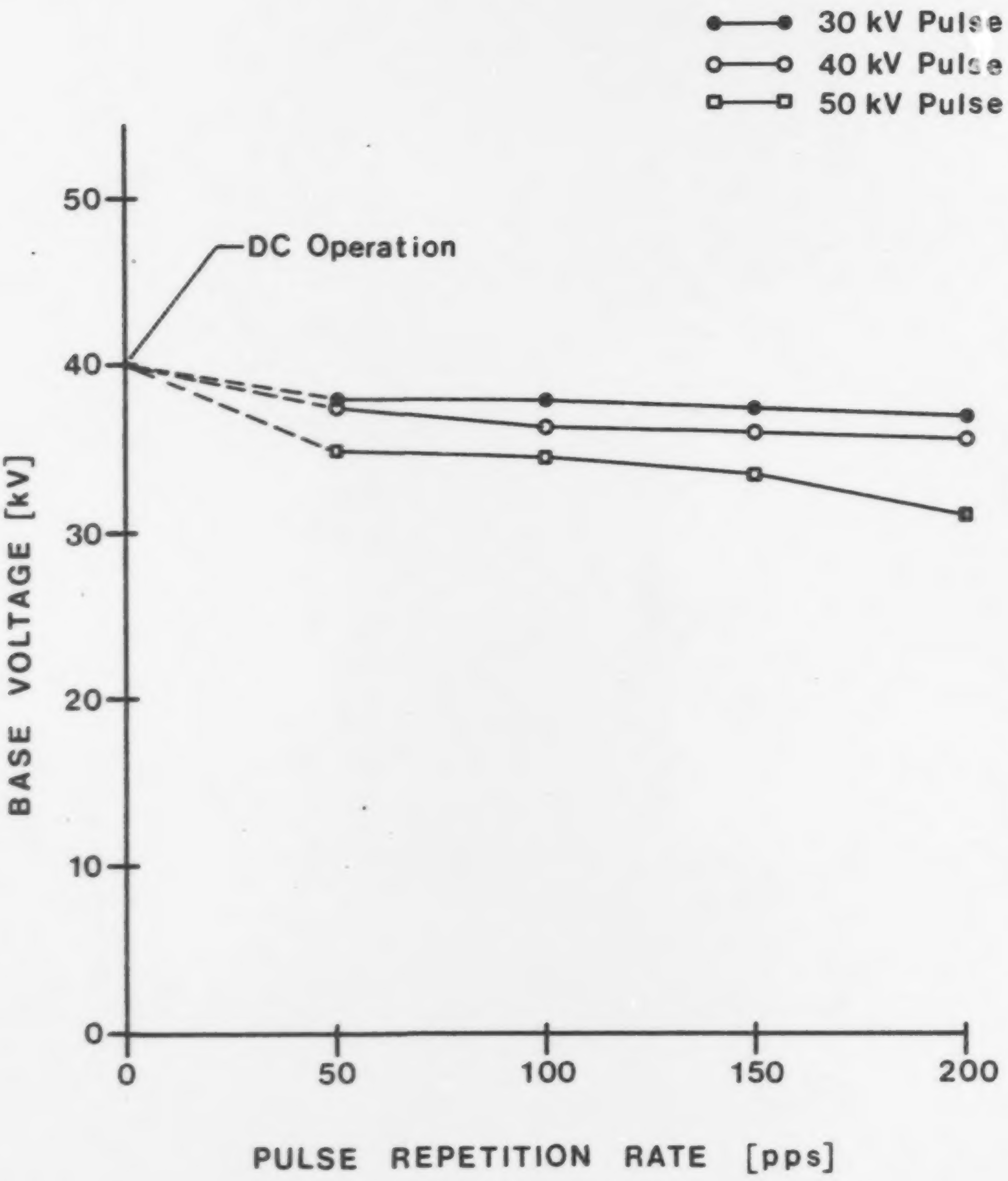

Figure 3. Base TR voltage as a function of pulse repetition frequency.

by a factor of two due to pulse energization has the same performance impact as increasing a dc energized precipitator's size by a factor of two. An enhancement of 1.5 typically implies a reduction in output loading by more than a factor of two as can be seen from Figure 4. For the conditions tested up to date a 4.5 fold reduction of outlet loading has been our best performance on a full scale installation, since the efficiency of the unpulsed precipitator was always below 99%. If outlet reduction in excess of 4.5 can be achieved as Figure 4 would indicate for high unpulsed efficiencies is still an open question.

FUEL SWITCHING AND FUEL FLEXIBILITY

Since pulse energization has the effect of increasing precipitator size for high resistivity dusts a relatively small older precipitator can be upgraded by addition of PES-2000 to collect fly ash from a lower sulfur coal than was originally burned while still allowing the boiler to meet emission standards. Furthermore, pulsing normalizes fly ash resistivity differences and treats dust from all fuels at near optimum precipitation conditions. Boiler operators are thus able to avoid costly fuel management procedures or switch to a low sulfur coal while maintaining high collection efficiencies without resorting to chemical conditioners or additional collecting area. Pulse energization also permits the use of higher ash content coal while maintaining emission standards through enhanced collection efficiencies. Such a step could potentially provide a substantial savings to the utility since higher ash content coal is generally less expensive. For example, if pulse energization would allow a cost reduction of one dollar per ton of coal, a payback period of less than one year could be achieved for the pulser.

EASY TO RETROFIT

The IPC PES-2000 is a compact modular roof mounted system compatible with all standard precipitators. Installation can be accomplished with a minimum of boiler outage, usually a day or less. All pulse energization system components are external to the base precipitator hence no internal modifications are required during installation. Controls for the PES-2000 are independent allowing the base TR sets to operate when the pulse system is turned off. Alternatively independent pulser units can be turned off while the remainder are left in an operating mode. Pulser modules are designed to pulse precipitator sections of any size up to 50,000 sq ft permitting existing sectionalization schemes to remain intact. Pulsers can be added to both cold and hot-side precipitators to improve performance.

ALL-ELECTRIC APPROACH TO PERFORMANCE IMPROVEMENT

The all-electric nature of pulse energization systems means no unusual peripheral services are required to make the PES-2000 system functional. Performance improvements are obtained via improvement in dust charging phenomenon which does not rely on the injection of costly chemicals and the attendant high operating costs.

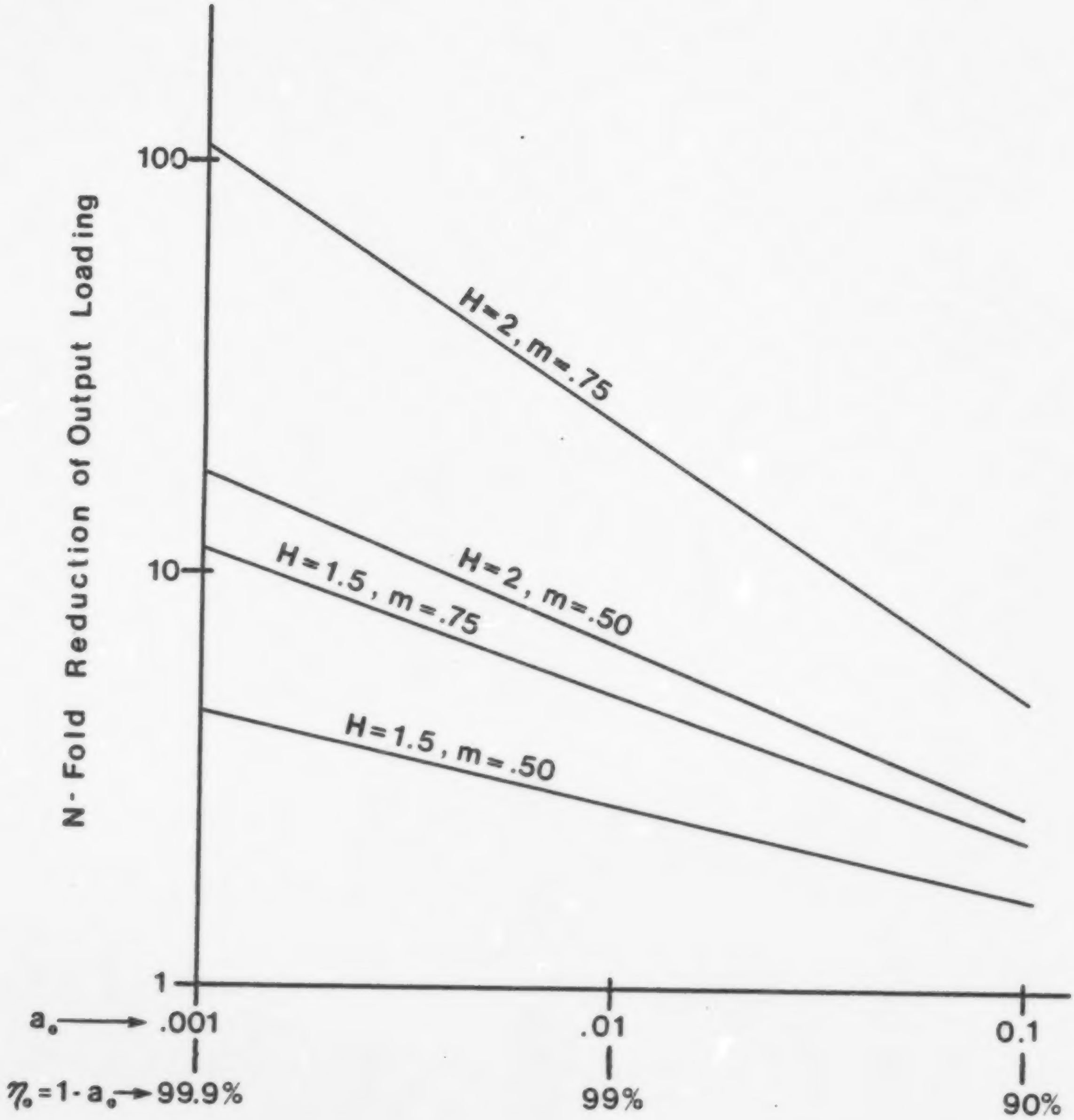

Figure 4. Reduction in outlet loading as a function of unpulsed efficiency for various pulsed enhancement factors.

LOWER MAINTENANCE COSTS

Optimal operating conditions for the PES-2000 occur when base TR voltages are adjusted for minimum sparking rates. Low sparking rates dramatically decrease wire erosion and as a result, extend discharge wire lifetimes. The high voltages associated with the pulse system also permit use of larger diameter wires. The two factors singly or in combination lead to reduced downtime and maintenance costs caused by broken wires. The high reliability of the pulser sytem, as demonstrated by over 500,000 hours of pulser module operation at full scale commercial installations, also leads to reduced maintenance costs. Pulse systems work even if discharge wires become encrusted with dirt or collecting plates become warped.

REDUCED CAPITAL COST

By taking advantage of enhancement factors associated with pulse energization new precipitators can be designed at relatively low SCA thereby, drastically reducing the size of the new precipitator and hence installation costs. The PES-2000 can be added to a large precipitator for as little as $1.47 per sq ft. The comparable charge for increasing the size of a precipitator by 50% which corresponds to an enhancement factor of 1.5 would be about $6.00 per sq ft of base precipitator area. For large sized facilities requiring millions of square feet of collecting area the capital savings can be substantial. The same is true for retrofit applications where adding more collecting plates is one proposed solution to poor collection efficiency. Addition of pulse systems is much cheaper than adding new precipitator sections. In many cases, increasing the size of existing precipitators is either impossible or extremely expensive due to space limitations.

LOWER OPERATING COSTS

The highly energy efficient PES-2000 converts nearly all the pulse energy into corona energy. The short pulses negate the requirements for expensive energy recovery circuitry and elimination of all energy dissipative components from the charging system ensures a high energy conversion efficiency. Typically, the PES-2000 system uses 5kW of electrical power per 15,000 sq ft of collecting area. However, total energy requirements for a pulse energized precipitator are generally slightly less than those of a well-energized conventional precipitator. Since PES-2000 operates on electricity only, there are no operating costs for chemicals or chemical storage facilities.

ON-SITE DEMONSTRATIONS

The modular compact nature of the PES-2000 allows for on-site demonstrations of the effectiveness of pulse energization. Connections are non-disruptive and require no intenal precipitator modifications or elaborate interfaces with existing equipment. Base TR sets are uneffected and sectionalization remains intact.

OPERATING RESULTS

Pulse systems manufactured by IPC have been tested at various demonstration sites and at full-scale commercial installations. Table 2 is a summary of results from various installations. In all cases, the observed enhancement factors equalled or exceeded expectations based on laboratory data. The results cover a range of resistivities from 5×10^{10} to 10^{13} Ωcm. In all cases, outlet loadings were reduced by a factor of 2.0 or more when pulse energization was added to the basic precipitator. Most of the units were cold-side precipitators. One site, however, was a hot-side precipitator using .7% Na conditioning; pulsing achieved a 50% reduction in outlet loading which corresponded to an enhancement factor of 1.46. These results illustrate and underscore the effectiveness of pulse energization as a technique for dramatically improving precipitator performance.

COSTS

The installed costs of PES-2000 depend strongly on the size of the ESP sections being pulsed. This feature is shown in Figure 5 where costs are stated in $/ sq ft of total ESP collecting area. If the entire ESP is pulse energized costs vary from about $6.00/sq ft of total area for very small sections to about $2.50/sq ft for large sections. In many cases, ESP performance goals can be achieved by pulsing only a fraction of the total ESP. The lower curve in Figure 5 shows the costs when only 50% of the total precipitator is pulse energized. The installed costs shown in Figure 5 are only good approximations since in actuality costs would also depend on total number of sections, total size of the ESP and particulars associated with installing the pulser at a specific site.

Pulser costs can be compared to costs for increasing collecting area to achieve equivalent collection efficiencies. Retrofitting collecting area costs about $20-25./sq ft of new area, while new ESP's cost about $15-20/sq ft. Consequently, adding pulse energization systems is significantly less costly than adding additional collecting area.

TABLE 2

SUMMARY OF PULSER PERFORMANCE AT VARIOUS SITES

Site Data	Operation	$ft^2/1000$ SCFM	ρ Ω cm	Precipitator Efficiency	Inlet Loading gm/m^3	Outlet Loading gm/m^3	Opacity	H
30 MW Boiler-Cold Side Precipitator Coal 1.09%-1.16% Sulfur	Not Pulsed	353	$5x10^{11}$	94.7%	6.548	.343	26%	1.52
	Pulsed	370		97.8%	6.82	.145	16.5%	
35 MW Boiler-Cold Side Precipitator Coal .58-.77% Sulfur	Not Pulsed	173	$5x10^{10}$	96.19	10.40	.407	33.2%	1.51
	Pulsed	173		98.53	10.48	.154	16.8%	
420 MW Boiler-Cold Side Precipitator 1000 hr. Test 1.12% Suflur Coal	Not Pulsed	280	$5x10^{10}$	97.67	7.98	.186	43%	1.50
	Pulsed	282		99.02	7.81	.076	31%	
4th Field Not Energized 5000 hr. Test .57% Sulfur Coal	Not Pulsed	270	$1x10^{13}$	85.42	11.69	1.703	84.5%	2.03
	Pulsed	272		93.65	12.18	.773	68.8%	
200 MW Boiler-Hot Side Precipitator Coal .85% Sulfur No Sodium Conditioning	Not Pulsed	326		96.67	15.781	.526	53.5%	1.49
	Pulsed	316		98.43	16.227	.255	37%	
.7% Sodium Conditioning	Not Pulsed	300		98.24	15.472	.272		1.46
	Pulsed	307		99.24	16.341	.124		

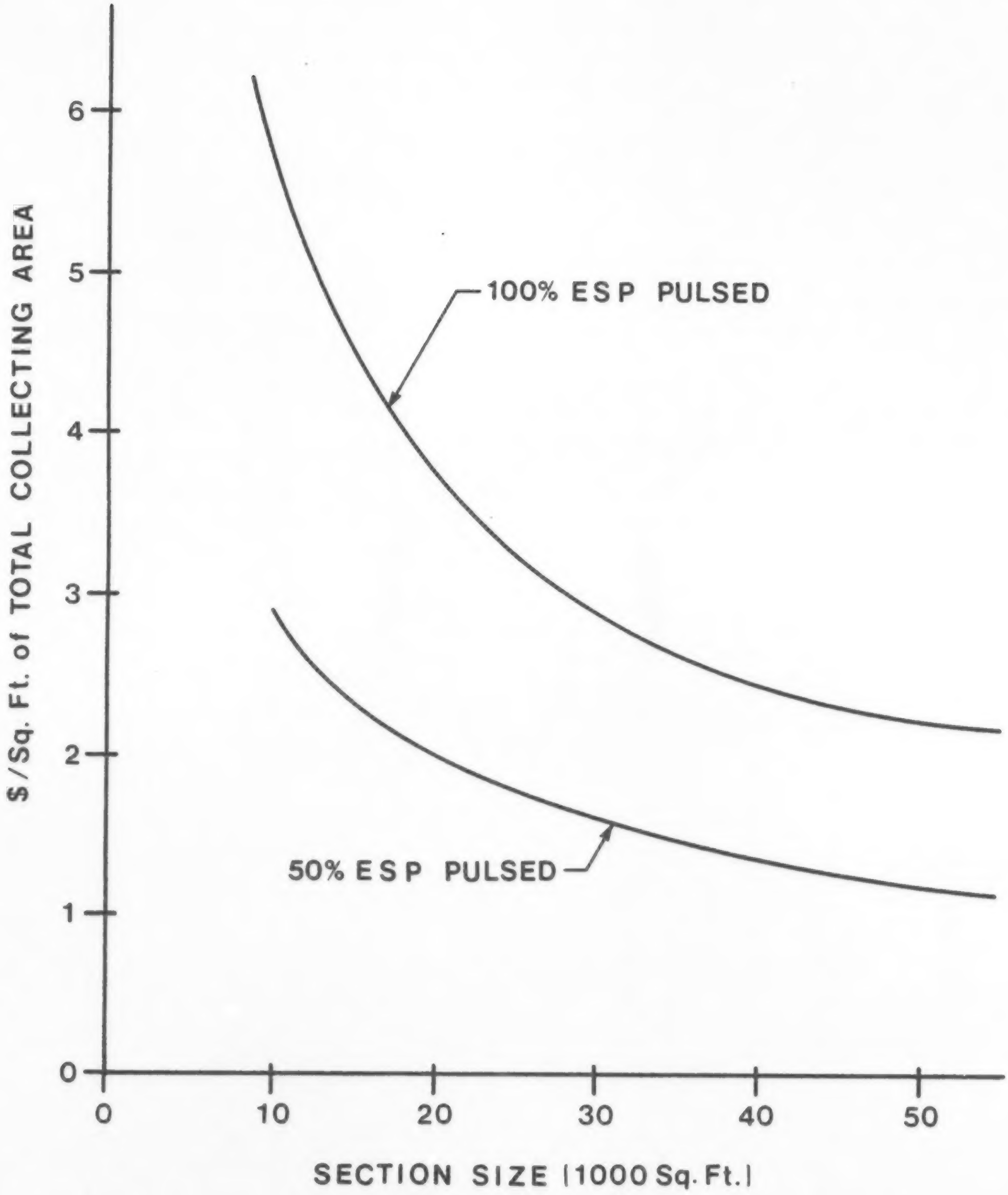

Figure 5. Approximate installed costs for PES-2000

REFERENCES

[1] R. Heinrich, W. Feldmann, Electrical Cleaning of Fluids, U.S. Patent 2,000,017, Applied April 4, 1931, granted May 7, 1935.

[2] H. J. White, A Pulse Method for Supplying High Voltage Power for Electrostatic Precipitation. Trans, AIEE, Nov. 1952, p. 326-329.

[3] J. E. Luthi, Grundlagen zur elektrostatischen Abscheidung von hochohmigen Stauben, Diss. Nr. 3924 ETH Zurich 1967, Prof. A. Guyer

[4] B. Bohlen, J. Luthi, A. Guyer, Neues Verfahren zur elektrostatischen Gasentstaubung, Chemie-Ing. -Techn. 39 (1967) Heft 15 910-913.

[5] G. W. Penney, P. C. Gelfand, The Trielectrode Electrostatic Precipitator for Collecting High Resistivity Dust, JAPCA, Jan. 1978, Vol. 28, 53-55.

[6] S. Masuda, D. Akutsu, Boxer Charger - A Novel Charging Device for High Resistivity Powders, Conf. Record of IEEE/IAS Annual Mtg., 1978, 16-22.

[7] S. Masuda, A. Mizuna, H. Nakatani, H. Kawahara, Application of Boxer Charger in Pulsed Electrostatic Precipitators, Conf. Record of IEEE/IAS Annual Mtg. 1980, 904-911.

[8] H. I. Milde, P. L. Feldman, Pulse Energization of Electrostatic Precipitators, IEEE/IAS (1978) Annual Mtg., Conf. Record, p. 66-70.

[9] P. L. Feldman, P. Aa, Operating Results from the First Commercial Pulse Energization System to Enhance Electrostatic Precipitator Performance, Conf. Records, American Power Conference, Chicago, April 1981.

[10] P. Lausen, H. Henriksen, H. M. Petersen, Energy Conserving Pulse Energization of Precipitators, IEEE/IAS 1979 Annual Mtg., Conf. Record, 163-171.

[11] D. E. Rugg, M. D. Durham, G. A. Rinard, L. E. Sparks, An Experimental Study of Electrostatic Precipitator Performance with Pulse Excitation, Atmospheric Environment, Vol. 16, No. 5, 1251-1256 (1982).

[12] H. I. Milde, Electrostatic Precipitation, U. S. Patent 4,183,736, Applied August 1972, granted January 1980.

[13] H. I. Milde, Pulse Corona Discharge in Electrostatic Precipitators IEEE Transactions on Electrical Insulation Vol. EI-17, No. 2, April 1982, 179-186.

[14] L. N. Menegozzi, P. L. Feldman, The Physics of Pulse Energization of Electrostatic Precipitators, Presented at Third EPA Sponsored Symposium on Transfer and Utilization of Particulate Control Technology - Orlando, March 1981.

[15] J. B. Thomas, T. R. Williams, Pulsed Corona Discharges, 1962 Gas Discharge and the Supply Industry, London: Butterworth, p. 202-208.

[16] D. B. Miller, S. E. Collier, J. L. Maitten, J. M. Niziolek, P. J. Phillips, Measurements of Pulsed Corona in Coaxial Electrode Structures, IEEE/IAS 1978, Conf. Records, Annual Mtg. 128-135.

[17] H. I. Milde, Reduced Power Input for Improved Electrostatic Precipitation Systems, U. S. Patent 4,133,649, Applied December 1973, granted January 9, 1979.

[18] S. Masuda, H. Nakatani, K. Yamada, M. Arikawa, A. Mizuno, Production of Monopolar Ions by Travelling Wave Corona Discharge, IEEE/IAS 1981 Conf. Records, Annual Mtg. 1066-1073.

[19] S. Masuda, Y. Nonogaki, Bi-ionized Structure of Back Discharge Field in an Electrostatic Precipitator, Record of IEEE/IAS Annual Meeting 1981, p. 1111-1119 (Oct. 1981, Philadelphia).

LABORATORY AND FULL-SCALE CHARACTERISTICS OF ELECTROSTATIC PRECIPITATORS WITH RIGID MAST ELECTRODES

By: H. Krigmont, R. Allan, R. Triscori and H.W. Spencer, III
Western Precipitation Division
Joy Industrial Equipment Company
Los Angeles, California 90039

ABSTRACT

There was an increase in development activities on rigid discharge electrodes in the mid-seventies. Since that time, JOY Manufacturing Company has carried out tests on a patented rigid mast electrode in the laboratory and on full-scale retrofitted and new units. JOY's mast electrodes are now in operation in 29 units around the world. The use of this electrode has improved precipitator reliability while maintaining particulate performance equal to or greater than that of conventional weighted-wire designs. This paper describes the electrode and its characteristics in various applications.

1. INTRODUCTION

JOY has a number of on-going development programs concerning ways and means of improving electrostatic precipitator performance and reliability.

This paper discusses one of these programs, discharge electrode design, the results of which have shown that significant improvement in electrostatic precipitator reliability can be achieved while maintaining or improving performance.

The summary of various development projects carried out under this program are discussed. The results have led to the development of a rigid mast electrode design that is rugged, durable and exhibits electrical characteristics that surpass those of traditional wire electrodes.

The discharge electrode discussed in this paper was described in the patent as "an improved discharge electrode having a stiffener centrally of planar side and corona edges in an electrostatic precipitator."(1) In more simplified terms, the electrode consists of a single sheet that is stiffened by means of a S-shaped profile. Corona points are created along the length by providing notches of a size and spacing selected to generate desired corona characteristics. This discharge electrode is unique in that it is of unitized construction and fabricated by a process that involves roll-forming and treating, to insure straightness and to eliminate critical stress concentrations. The electrode, in its most recent form, is shown in Figure 1.

Units are operating around the world that employ varied plate spacing, plate height, field lengths and methods of rapping utilizing this rigid mast electrode.

2. DEVELOPMENT OF THE MAST ELECTRODE

2.1 PRELIMINARY LABORATORY INVESTIGATIONS

The JOY patented mast discharge electrode has been under development since 1974. The mast electrode as developed replaces two wire electrodes in North American electrostatic precipitator design. Initial configurations tested consisted of flat sheets with saw-toothed edges, notched edges and flared edges. These tests were conducted with center support tubes with flat plates attached. Prototype mast electrodes are shown in Figures 2 and 3.

It was determined during these early studies that a notched plate could be used to simulate electrical characteristics of two wire electrodes. As shown in Table 1, it was possible to control corona characteristics by adjusting the separation of spacing between slots and the notch geometry.(2)

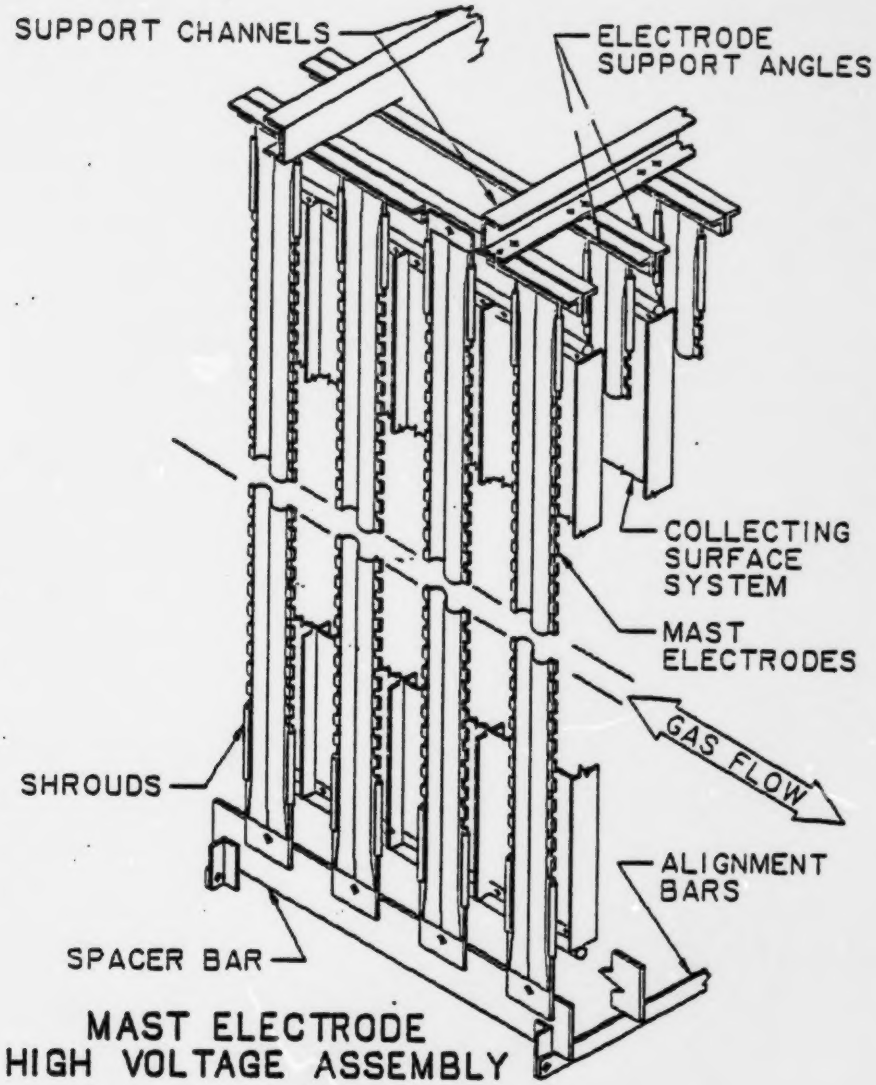
SUPPORT CHANNELS
ELECTRODE SUPPORT ANGLES
COLLECTING SURFACE SYSTEM
MAST ELECTRODES
GAS FLOW
SHROUDS
ALIGNMENT BARS
SPACER BAR
MAST ELECTRODE HIGH VOLTAGE ASSEMBLY

FIG. 1

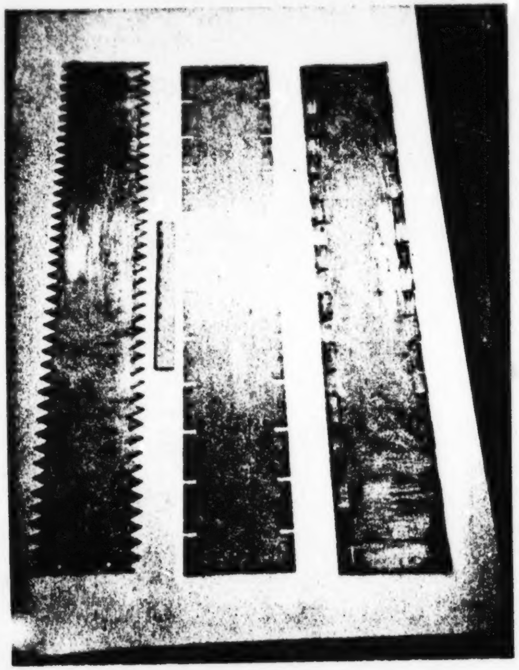

Figure 2.
Prototype Mast Electrodes

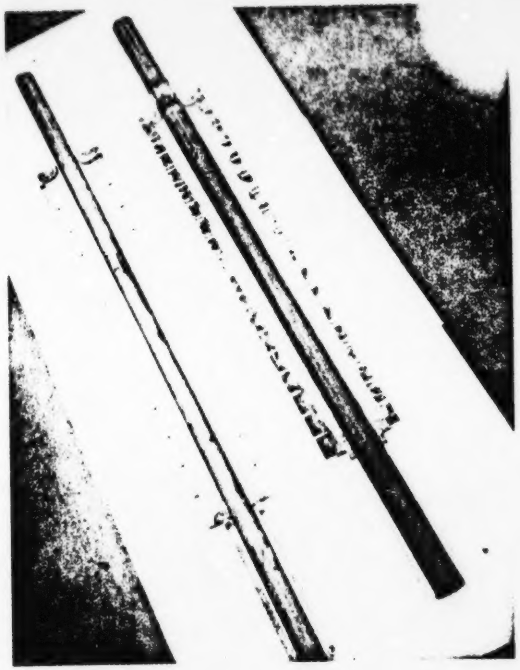

Figure 3.
Prototype Mast Electrodes

TABLE 1

Center-to-Center Spacing (Inches)	No. of Emitting Points per Foot per Side	Notch Opening (Inches)	Normalized Milliamps*
2-1/4	5.34	0	1.00
		1/4	1.56
		1/2	2.16
3	4.0	0	1.00
		1/4	1.56
		1/2	1.90
		3/4	2.00
3-1/2	3.43	0	1.00
		1/4	1.22
		1/2	1.60
		3/4	1.87

*Normalized to 3" Center-to-Center at Four Emitting Points/Ft. and 40 kV.

During these early studies, various member sizes were investigated and moments calculated to minimize deflections under different loads.

Flow investigations were also carried out at various velocities to determine if vibration would occur. It was found the frequency of shedded vortices did not correspond to the natural or primary harmonic frequency of the mast. In short, flow induced vibration did not occur.

The next development of the mast electrode was to replace the tubular member with a S-shape form. Electrical characteristics of this profile were extensively tested in the laboratory and a high-bay test facility used to evaluate 37-foot masts. Voltage current characteristics were obtained and compared to those of wires in a 9-inch duct, typical values of which are presented in Figure 4.

This figure shows that the mast electrode exhibited characteristics superior to those of wires in that the onset of corona occurred at lower voltages and lower current was provided at higher voltages in normal operating ranges. Higher sparkover voltages were also achieved with the mast electrode.

A special heat chamber was constructed to maintain constant differential temperatures, and movements of the mast electrode were measured with the aid of a laser beam. It was determined during these tests that the mast had excellent thermal stability. It maintained straightness within suitable tolerances at those differential and elevated temperatures which could be expected under adverse conditions in most applications.(3)

The electrostatic stability of the mast electrode was also investigated. The configuration of electrostatic forces considered for rotation of the mast electrode is shown in Figure 6. This investigation confirmed that the built-in stability was more than sufficient to account for the electromechanical forces exerted.

2.2 SUMMARY OF PILOT SCALE STUDIES

Pilot investigations of the mast electrode were conducted by Sumitomo Heavy Industries, JOY's licensee in Japan.(4) (5) Electrical characteristics and performance studies were conducted with cement finish mill dust for temperatures up to 350° C. A comparison of normalized effective migration velocity for various inlet dust concentration is presented in Figure 5.

Further studies of heat distortion, stability and voltage current characteristics were also completed verifying laboratory data.

TYPICAL LABORATORY V-I CURVES

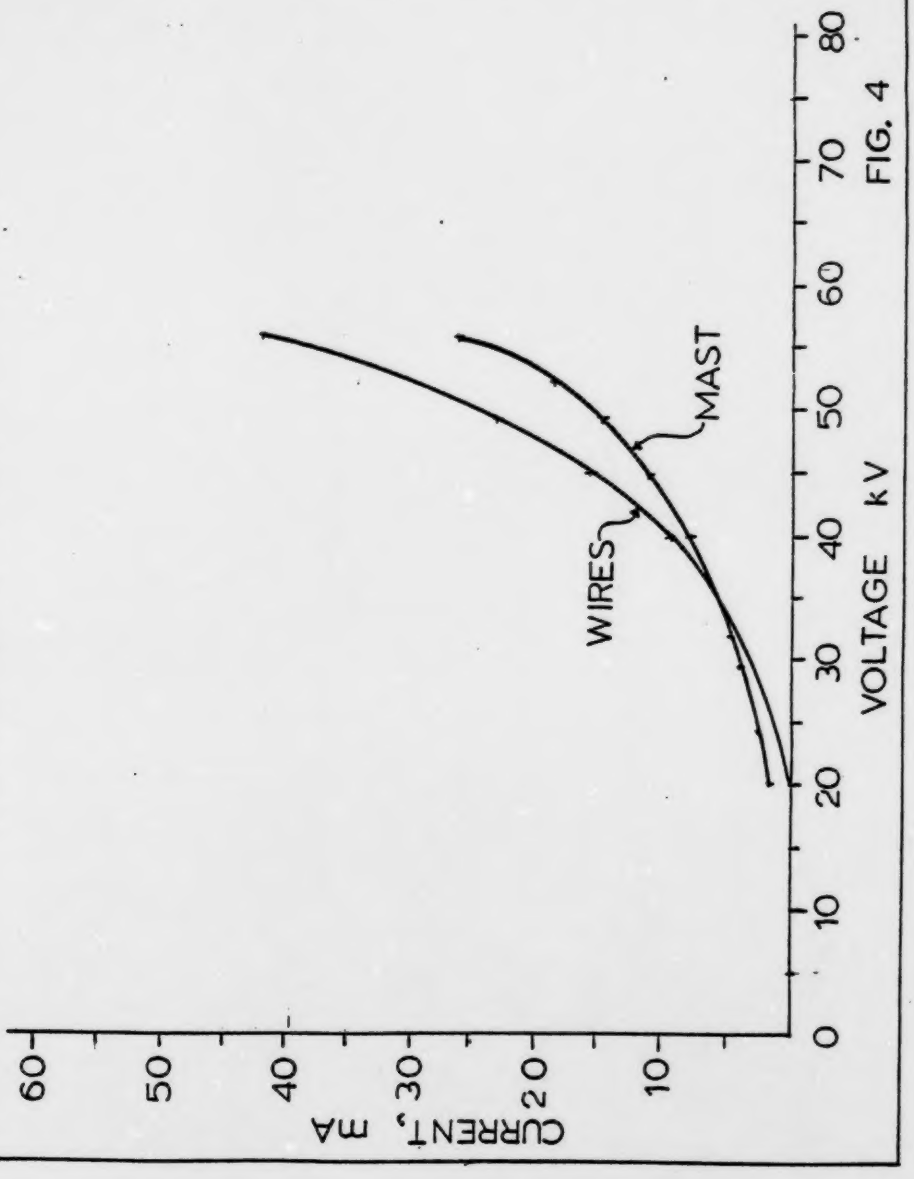

FIG. 4

FIG. 5

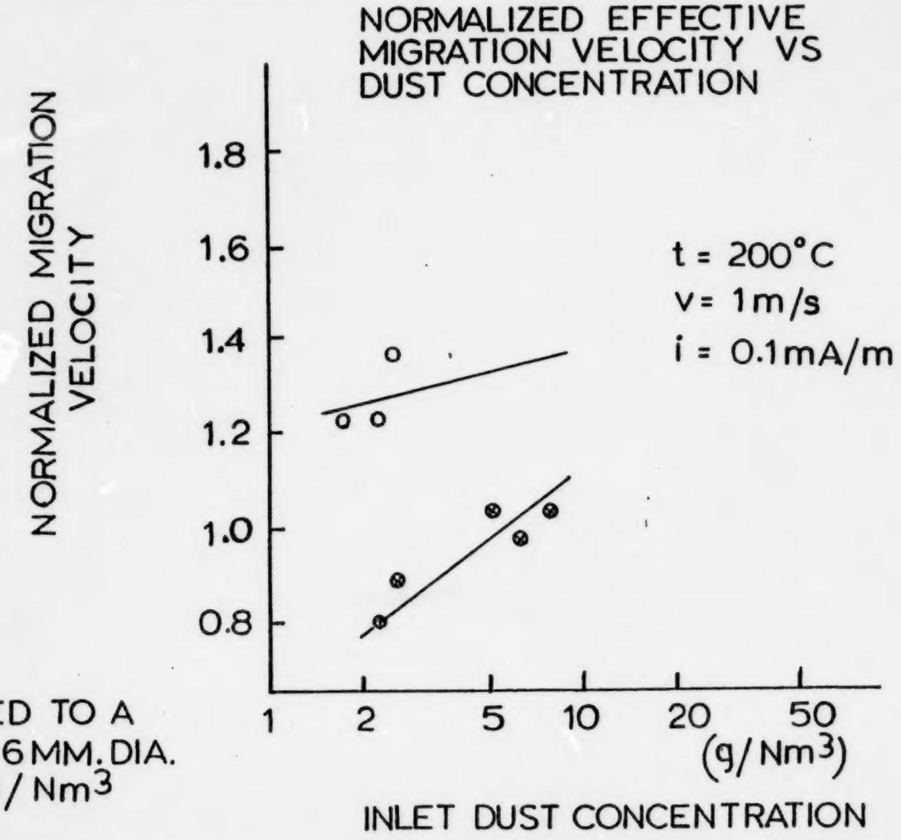

* NORMALIZED TO A WIRE OF 2.6 MM. DIA. AT 5 GRAM / Nm^3

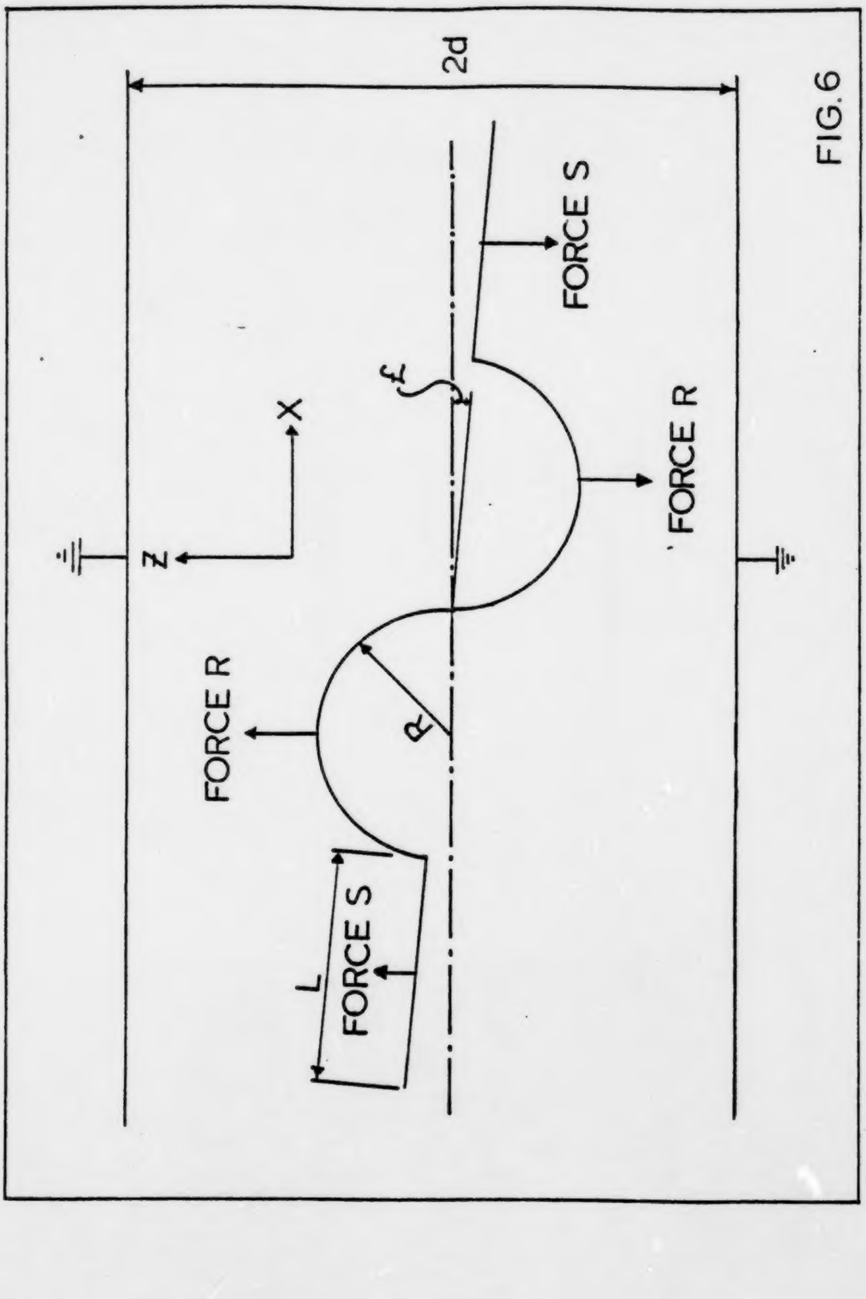

FIG.6

2.3 FULL-SCALE INVESTIGATIONS

Based on the laboratory and pilot studies, it was decided that full-scale operating experience was required. Two existing weighted-wire precipitators collecting flyash from a coal-fired boiler were partially retrofitted with mast electrodes.(6) Air load and operating voltage-current data were consistent with laboratory and pilot results as shown in Figures 7 and 8. Performance results were inconclusive, however, considerable knowledge was gained as to how fabrication and construction techniques might be improved.

Based on the information obtained, continued studies were undertaken in both the high-bay test facility and the field. Acceleration measurements were obtained in conjunction with development of improved methods of fabrication and installation.

Subsequently, a considerable number of new and rebuilt precipitators were supplied worldwide using the mast electrode in various applications.

3. OPERATING EXPERIENCE

Thirty-seven (37) installations incorporating mast electrodes are in operation or final design around the world on a variety of applications. These include the following:

- Coal Flyash
- Recovery Boilers (Direct and Non-Contact)
- Cement (Dry Kiln, Wet Kiln, Cooler or Finish Mill and Preheat Kilns)
- Potash Dryer
- Wood-Waste Boilers
- Coal Drying

Two non-flyash applications are described and the results of detailed studies on a flyash application are presented in the following case studies:

3.1 CEMENT INDUSTRY

A two-field, two-chamber conventional weighted-wire JOY electrostatic precipitator was installed after the dry process cement kiln at the Genstar plant in Regina, Saskatchewan in 1960.

This unit maintained or exceeded the design efficiency of 97.5% in all performance tests conducted between 1960 and 1980. However, due to increasingly stringent emission regulations and increased dust loadings due to kiln modifications, improved performance was required.

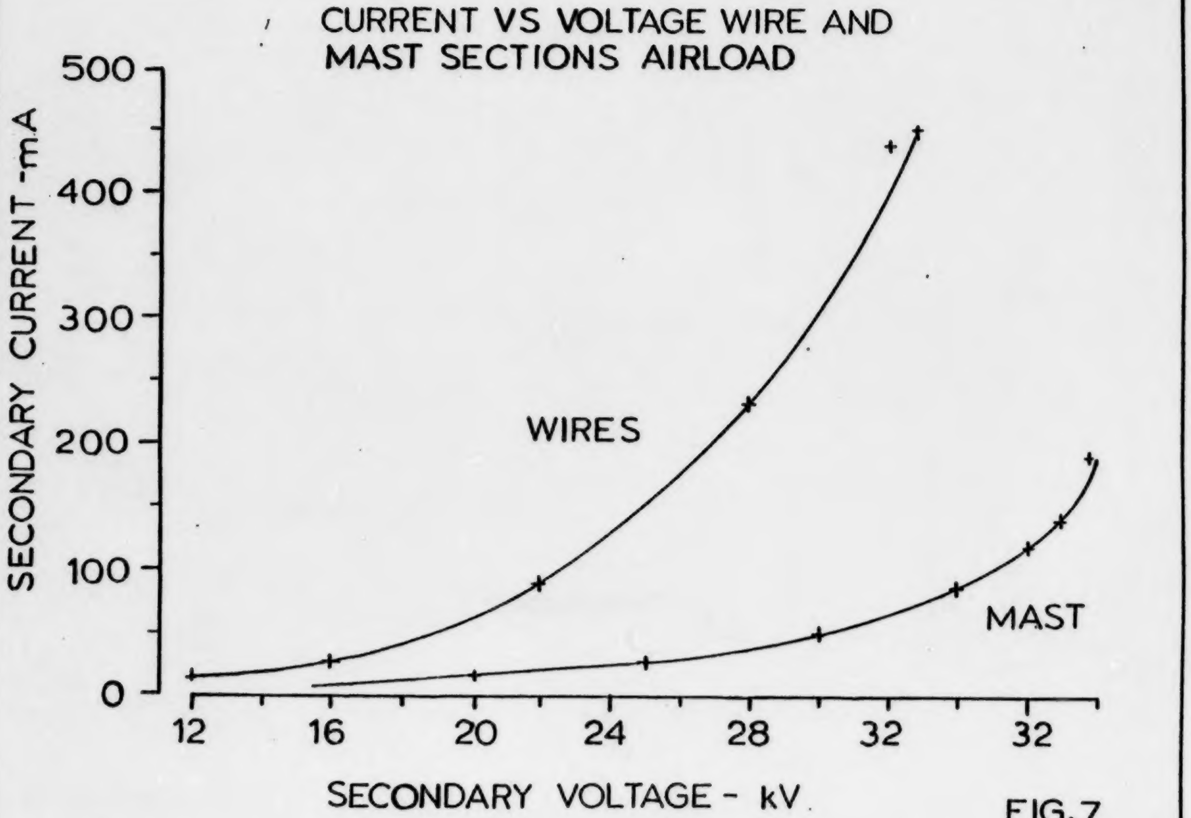
CURRENT VS VOLTAGE WIRE AND MAST SECTIONS AIRLOAD
SECONDARY CURRENT -mA
500
400
300
200
100
0
12
16
20
24
28
32
32
SECONDARY VOLTAGE - kV
WIRES
MAST

FIG.7

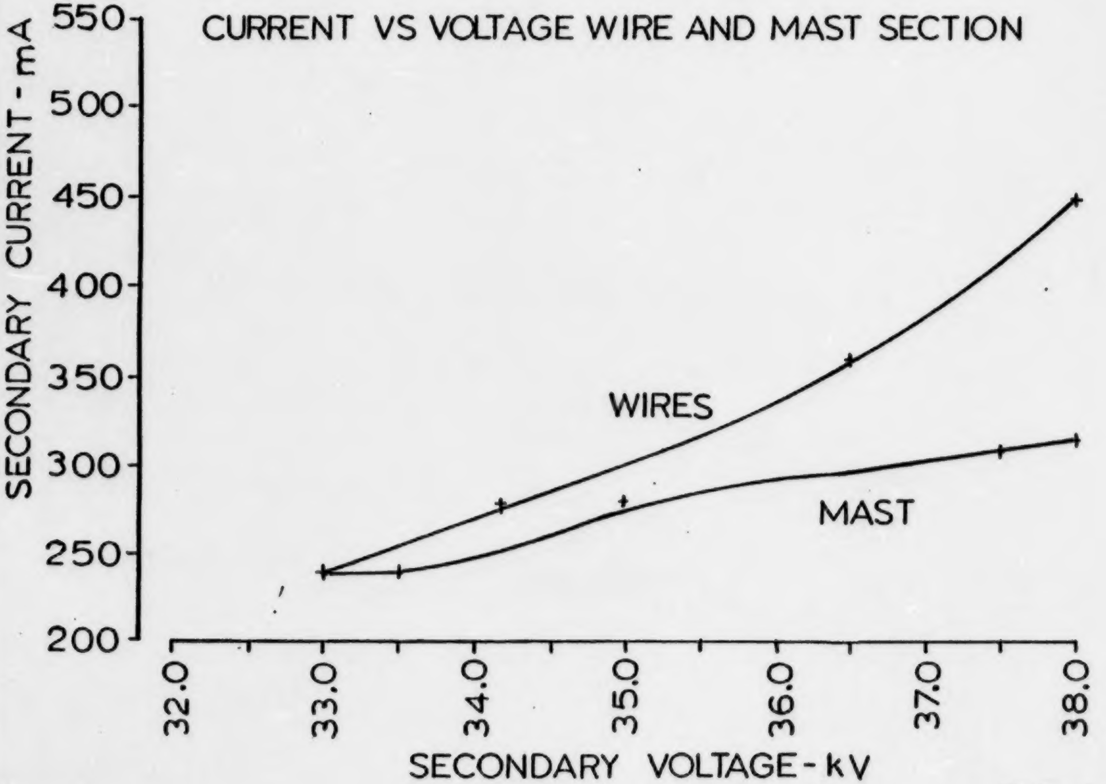
CURRENT VS VOLTAGE WIRE AND MAST SECTION
SECONDARY CURRENT - mA
550
500
450
400
350
300
250
200
32.0
33.0
34.0
35.0
36.0
37.0
38.0
SECONDARY VOLTAGE - kV
WIRES
MAST

FIG. 8

JOY was awarded a contract in 1980 to replace the discharge system of the existing installation (primary unit) and supply a new two-chamber precipitator in series (secondary unit) using the rigid mast electrode design. The complete installation was designed for 99.87% while handling 145,000 ACFM at 625° F.

The primary and secondary units were placed in service in November 1980 and June 1981 respectively. Since commissioning, the installation has equaled or exceeded performance requirements. During testing, the average gas inlet temperature was 716° F and excursions in excess of 800° have been experienced without adverse effect on mast alignment.

According to plant records, the primary unit operates at increased voltage and reduced current compared to the original configuration, and precipitator availability has improved dramatically.

3.2 SALT CAKE RECOVERY BOILER

There were existing weighted-wire electrostatic precipitators installed after Georgia Pacific's direct contact recovery boilers at the Woodland, Maine plant. These units were initially installed in 1964, each of which was designed to handle 180,000 ACFM at 98% efficiency. Although the units performed satisfactorily, deterioration due to corrosion necessitated major retrofit of both precipitator installations.

The client specified rigid discharge electrodes, anticipating improved long-term reliability while maintaining performance equal to or greater than that of conventional wire weight design.

In December of 1981, JOY was awarded the contract for materials and engineering to rebuild both units utilizing the rigid mast electrode design. Erection was scheduled such that the two separate casings on each boiler were retrofitted sequentially so as not to interfere with plant production. The first rebuilt chamber was placed on line June 1982, and the entire project was completed early in October 1982.

Subsequent performance testing resulted in emissions well within design and state requirements on both units. Since start-up the units have maintained performance with nearly 100% availability.

3.3 COAL-FIRED BOILERS

In 1970, two JOY weighted-wire electrostatic precipitators were installed after coal-fired boilers at a midwest location. Since that time, the performance of these units had become marginal due to changes in fuel and in state emissions standards.

Discussions were held and the operating conditions reviewed to determine if precipitator performance could be improved. Studies were undertaken to evaluate the influence of changes in discharge electrode design, plate spacing and sectionalization using computer modelling. The results of this investigation have been presented in Table 2.

It was decided that the precipitator would be rebuilt utilizing Alternate No. 5 from Table 2. The rebuild included split first field, collecting surfaces, mast electrodes, rapper attachments and the addition of transformer-rectifier sets and controls for the first field.

In March 1984, a comprehensive test program was undertaken in conjunction with compliance testing. The purpose of this program was to enable a better understanding of variables affecting precipitator performance using the mast electrode, and the data could be used to evaluate computer-generated predictions.

A summary of the significant observations and trends for Boiler No. 1 is as follows:

- Modified Migration Velocity versus SCA, Figure 9
- Modified Migration Velocity versus Power Consumption, Figure 11
- ESP Efficiency Measured versus Computer Prediction, Table 3
- Stack Opacity Measured versus Computer Prediction, Table 4

A summary of a regression analysis of performance data obtained for Boiler No. 1 is presented in Figure 9. During the tests, in situ resistivities were measured and these varied due to changes in the fuel composition, soot blowing and other factors. It was found values approaching 10^{12} ohm/cm were experienced, and further evaluations were carried out at these elevated resistivity levels at which back corona was clearly occurring (see Figure 10).

Modified migration velocity versus power input has been plotted in Figure 11 for those tests in which the unit was operating well into back corona region. It can be seen that the characteristics of the mast electrode are at a minimum consistent with those of wire electrodes operating in this region. Increased power does not improve performance and, in fact, contributes to marginal deterioration.

JOY's modified computer model was used to simulate performance of the precipitator using measured applied voltage and current, inlet particle size distribution and dust loading as input data. Predicted performance was obtained and demonstrated that this computer model can be used to predict performance of full-scale units with a high degree of confidence.

TABLE 2.

ESP COMPUTER MODEL PREDICTIONS. SUMMARY.

CONDITION (ARRANGEMENT) D.E., TYPE SPACING ITEM	EXISTING PPTR. (9'/6'/6') W/WIRE @ 9" SP 31 G.P.			EXISTING PPTR. (9'/6'/6') "MAST" @ 9" SP 31 G.P.			EXISTING PPRT. (9'/6'/6') "MAST" @ 10" SP 27 G.P.			EXISTING PPTR. (9'/6'/6') "MAST" @ 11" SP 25 G.P.			* SPLIT FIRST FLD. (4.5'/4.5'/6'/6') "MAST" @ 9" SP 31 G.P.			* SPLIT FIRST FLD. (4.5'/4.5'/6'/6') "MAST" @ 10' SP 27 G.P.			* SPLIT FIRST FLD. (4.5'/4.5'/6'/6') "MAST" @ 11" SP 25 G.P.		
	1			2			3			4			5			6			7		
FLUE GAS FLOW, KACFM	167	167	167	167	167	167	167	167	167	167	167	167	167	167	167	167	167	167	167	167	167
FACE VELOCITY, FT/S	5.	5.	5.	5.	5.	5.	5.	5.	5.	5.	5.	5.	5.	5.	5.	5.	5.	5.	5.	5.	5.
SCA, SQ. FT./KACFM	187	187	187	187	187	187	163	163	163	151	151	151	187	187	187	163	163	163	151	151	151
RESISTIVITY OHM/CM (Assumed)	$2*10^9$	$2*10^{10}$	$2*10^{11}$	$2*10^9$	$2*10^{10}$	$2*10^{11}$	$2*10^9$	$2*10^{10}$	$2*10^{11}$	$2*10^9$	$2*10^{10}$	$2*10^{11}$	$2*10^9$	$2*10^{10}$	$2*10^{11}$	$2*10^9$	$2*10^{10}$	$2*10^{11}$	10^9	10^{10}	10^{11}
EFF., %	97	94.8	90.7	98.6	97.6	94.75	97.6	96.6	92.6	97.6	96.17	91.96	99.05	98.	95.56	98.22	96.8	92.16	98.2	97.	92.26
MIGRATION VEL., W, CM/S	9.53	8.03	6.45	11.6	10.1	8.	11.6	10.54	7.99	12.55	10.98	8.48	12.65	10.63	8.46	12.56	10.73	7.94	13.5	11.8	8.6
AVG. APPL. VOLTAGE, kV	35.5	27	23.5	43.	37.8	28.7	44.5	40	30	46.67	40.33	31.37	42.33	36.33	27.87	44.33	38.5	28.42	44.83	39.5	29.25
AVG. CURR. DEN mA/FT²	36.	23	19	36	29.	19.5	38.7	36	20	39.8	36.67	19.75	37.5	32.17	19.81	37.8	30.2	29.9	38.02	32.47	20.1

*Split fields are both mechanical & electrical.

**Assumed MMD = 12 μm microns and σ = 2.5

TABLE 3

ESP COMPUTER MODEL EVALUATION OF SELECTED TEST RESULTS

Test	SCA	Inlet Loadings	Measured Efficiency	Predicted Efficiency	Average Current Density	Average Applied Voltage
No.	Sq.Ft./ KACFM	GR/ACF	%	%	mA/K Sq.Ft.	kV
13	214	1.92	99.30	99.26	22.13	34.41
14	224	1.85	99.31	99.38	21.29	34.02
15	225	1.92	99.24	99.35	21.14	33.71
16	243	1.74	99.30	99.3	32.	27.87
17	257	1.97	99.34	99.26	32.08	28.53
18	232	1.76	99.14	99.1	33.	28.72
23	245	2.46	99.28	99.35	17.30	30.13

TABLE 4

Opacity Model Evaluation of the Test Results

Test No.	ESP Eff., %	Outlet Loading GR/ACF	Outlet Particle Size Distribution		Opacity %		
			MMD		Measured (Avg.)	Visually Observed	Computer Predicted
01	97.66	.0611	9.	3.75	18.27	-	19.54
03	97.02	.065	10.	3.85	21.86	0-25	19.32
04	92.88	.228	22.	3.79	42.5	20-75	30.96
05	93.78	.1792	17.	3.15	31.6	-	25.30
06	95.88	.1252	7.6	2.38	27.25	-	27.74
08	99.15	.013	4.6	2.88	3.	-	6.8
10	98.74	.0193	13.	3.42	1.5	-	3.4
11	99.62	.006	2.	3.75	1.5	-	1.01
13	99.3	.015	12.	4.29	4.4	-	4.5
16	99.3	.0134	6.8	2.83	5.4	-	4.67
17	99.34	.014	7.8	3.9	6.1	0-10	5.69
18	99.14	.0167	6.6	3.14	6.68	-	6.68
19	98.77	.0226	10.	3.33	7.75	-	6.23
20	99.1	.0186	9.1	3.37	8.88	-	5.73
21	99.14	.0177	6.6	2.93	9.5	-	6.54
22	99.12	.024	11.	3.06	11.5	5.	6.03
23	99.29	.019	7.	2.69	10.5	-	6.03
24	99.30	.018	10.	2.78	11.5	-	4.10

SPECIFIC COLLECTION AREA (SCA) VS. MIGRATION VELOCITY (W, W_k)

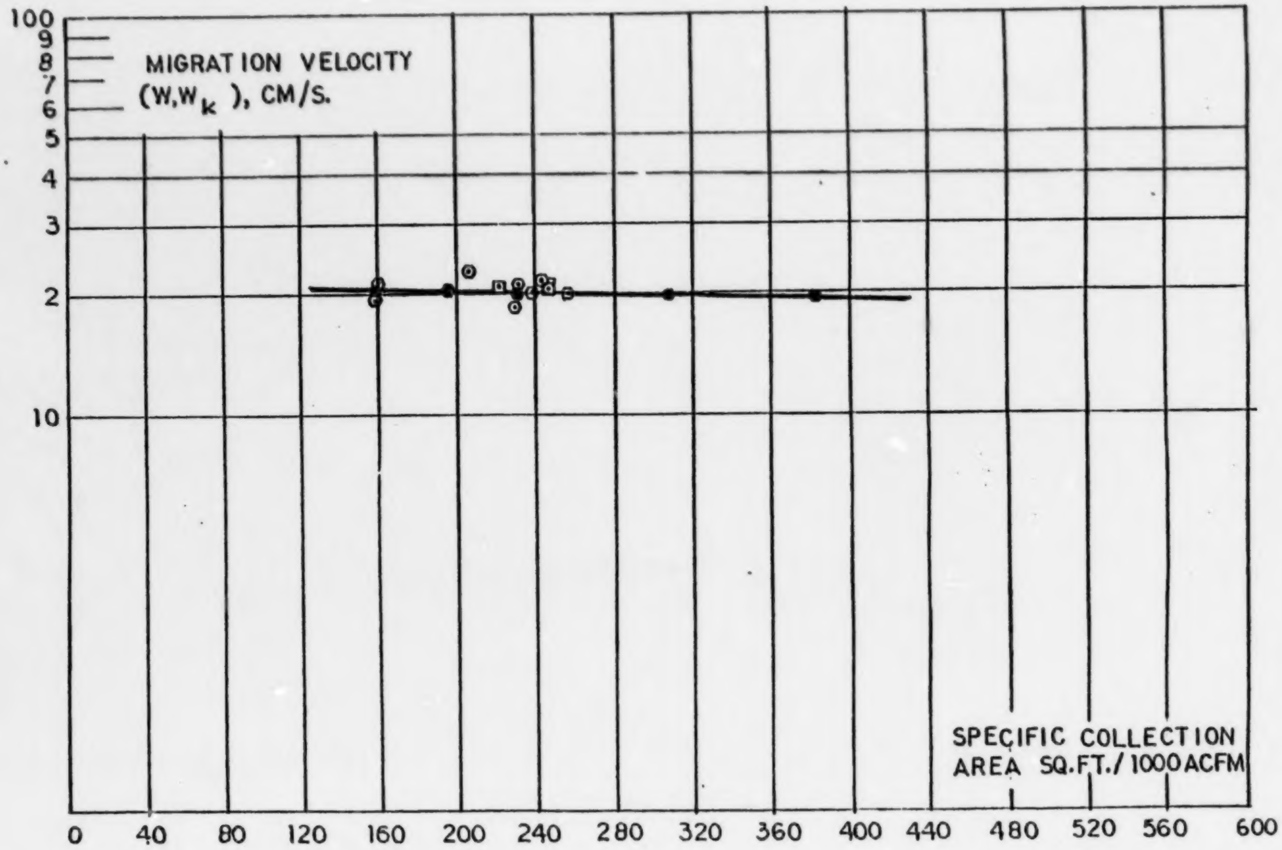

FIG. 9

TYPICAL V-1 CHARACTERISTICS, BLR1, 300,000#/HR

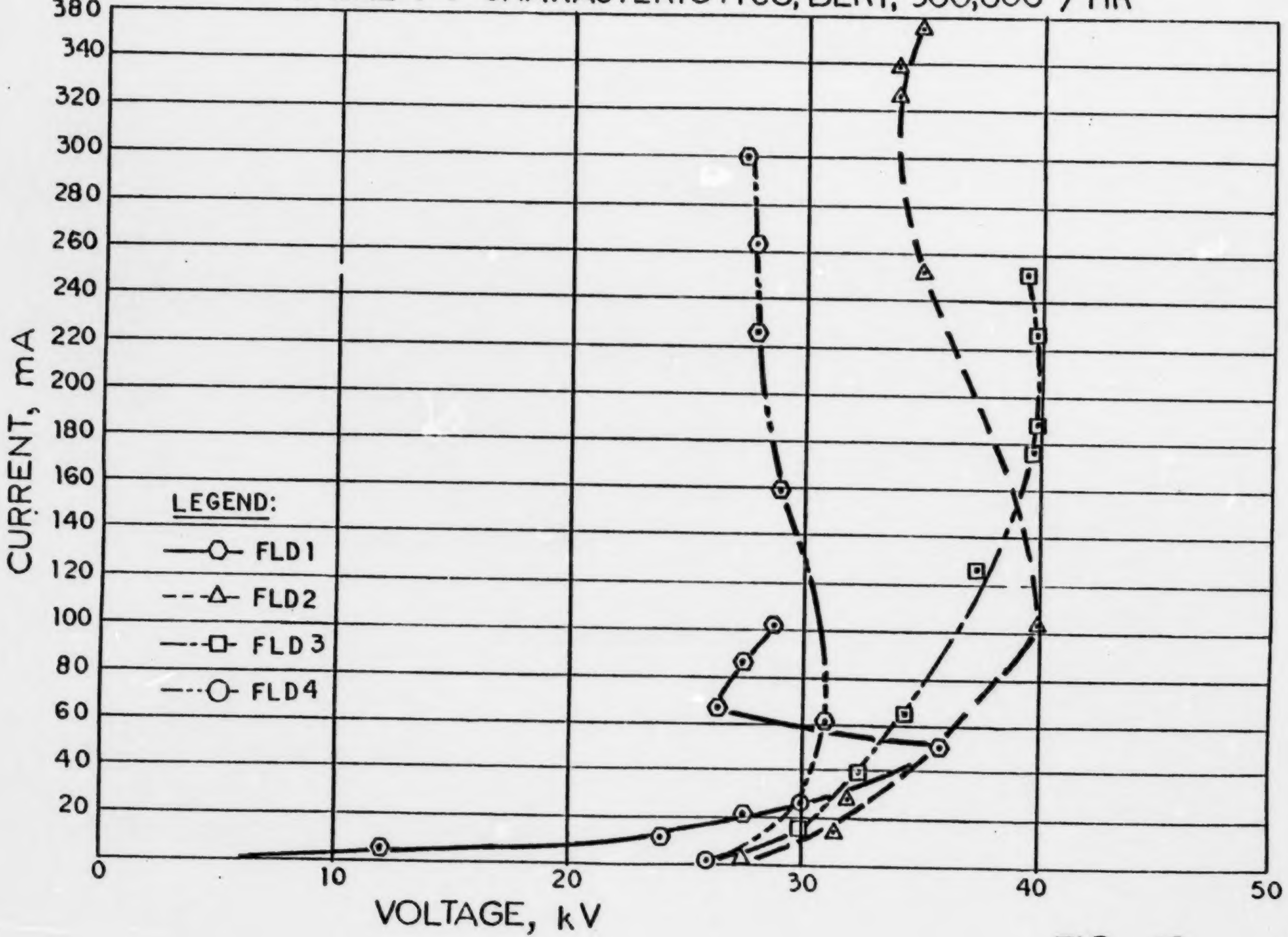

FIG. 10

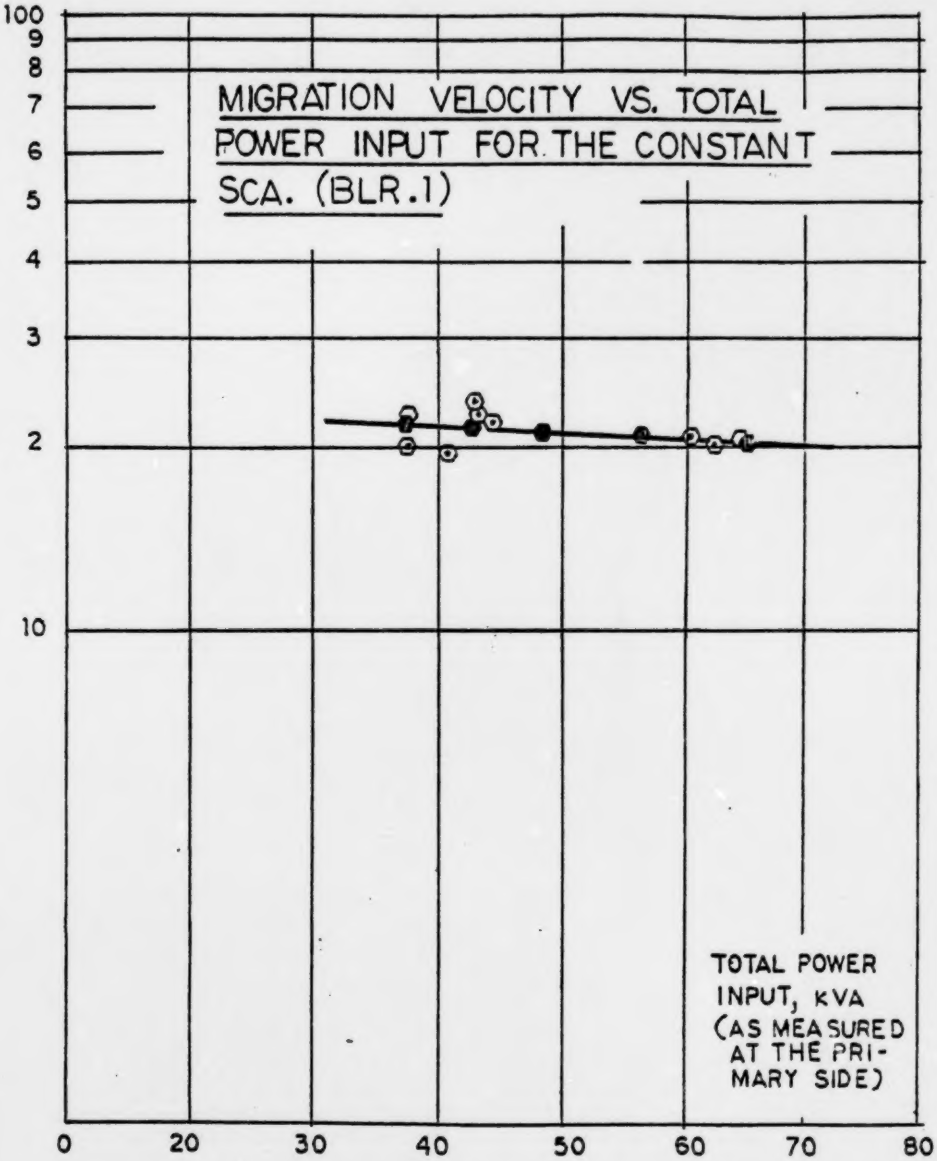

MIGRATION VELOCITY VS. TOTAL POWER INPUT FOR THE CONSTANT SCA. (BLR.1)
100
9
8
7
6
5
4
3
2
10
0
20
30
40
50
60
70
80
TOTAL POWER INPUT, KVA (AS MEASURED AT THE PRIMARY SIDE)

FIG. 11

The results of the efficiency test data as measured and as predicted by the computer model are presented in Table 3. The computer predicted efficiencies were adjusted to correspond to measured results by adjusting non-ideal factors. The differences in the non-ideal factors can be explained by the differences in particle size distribution, gas temperature, slight changes in sneakage and gas velocity distribution and variation of the rapping losses.

In addition, the results of the computer model predicted opacity are presented in Table 4 and are compared with the measured and visually observed opacities. It can be seen that the measured and calculated opacities are in agreement.

4. CONCLUSION

We have discussed the development of the rigid mast electrode.

It has been demonstrated that electrostatic precipitator reliability is improved and performance equal to or greater than that of a wire electrode can be achieved.

Additionally, field data were used to verify computer prediction models for determining electrostatic precipitator performance and in-stack opacity.

BIBLIOGRAPHY

1. U.S. Patent No. 4,303,418.
2. Merrill, S., R & D Report R-146, December 1974.
3. Goland, Y., "High Voltage Mast Electrode - Additional "Investigations, Engineering Report E-37, April 1978.
4. Spencer, H.W., Interoffice Memorandum Dated April 2, 1977.
5. Sumitomo Heavy Industries, R & D Internal Report.
6. Wennerholm, R., Jr., "Current Developments in Conventional Electrostatic Precipitation Concepts", CSIRO Conference, August 1978.

FULL SCALE EXPERIENCE WITH PULSED ENERGIZATION OF ELECTROSTATIC PRECIPITATORS

K. PORLE
TECHNICAL MANAGER, AIR POLLUTION CONTROL TECHNOLOGY
FLAKT INDUSTRI AB
VAXJO, SWEDEN

K. BRADBURN
MANAGER, PRE-CONTRACTS
FLAKT, INC., ENVIRONMENTAL SYSTEMS DIVISION
KNOXVILLE, TENNESSEE

ABSTRACT

One of the most promising new technologies for Electrostatic Precipitators is pulsed energization. Extensive research and development during the last 10 years has introduced several different concepts.

Reduced outlet emissions have up to now been emphazised but research by Flakt shows that remarkable power savings can be obtained by using suitable pulse concepts.

This paper presents test results from full-scale installations where up to 90% of the power has been saved in combination with reduced emission compared to conventionally energized ESP's.

Two different technologies have been used. A special T/R-set has been developed for the multiple pulse charging concept where thyristors are incorporated in the high voltage circuit thus avoiding any pulse transformer. Low energy losses are obtained and the pulse widths are in the microsecond range.

The semi pulse charging concept uses modified conventional T/R-set controls and produces pulse widths in the millisecond range. Plants with both technologies are today in operation worldwide and the equipment has shown excellent reliability and availability.

INTRODUCTION

Recently developed high voltage thyristors have made the concept of pulse energization a commercial reality. The transition from the laboratory to successful application on operating precipitators has been made in an economically viable manner. Flakt pulsing systems, and others, are now operating on precipitator installations in many parts of the world.

The ability of pulse energization to give improved precipitator collection efficiency offers an alternative to extremely large precipitators which are required when high resistivity ash associated with low sulphur coal must be collected. In addition, when upgrading existing precipitators to comply with new emission regulations or to accommodate more difficult ashes pulse energization becomes a particularly attractive option. An alternative of adding additional fields to the precipitator requires plant space which may not be available, pulse energization does not. Flue gas conditioning is also an option, but has both a chemical and operating cost over the life of unit. Pulse energization offers a reduction in the power consumed by the precipitator yielding an operating savings to the owner.

In addition, pulse energization can be installed with minimal precipitator downtime and requires no more maintenance or supervision when installed than conventional systems.

It must be understood that pulse energization is not a panacea for precipitator problems. The full benefits of pulse energization will only be realized if the ash is of medium high or high resistivity and the precipitator is in good condition.

Today, we can note the development of three generations of equipment for microsecond pulsing:

1. The spark-gap method, which requires a high degree of maintenance. The spark gap has to be contained in a gas-filled chamber.

2. Low-voltage thyristors and a pulse-transformer which require an extra base T/R set. The pulse-transformer is also a very costly piece of equipment.

3. High-voltage thyristors without a pulse-transformer which supply base DC voltage as well as pulses (the Flakt method).

Years of research and development, together with test programs on numerous precipitators installations, has culminated in Flakt's development of two distinct pulsing systems.

1. The MultiPulse Concept (MPC)*: bursts of 50 to 100 microsecond pulses at 3 to 100 millisecond intervals.

2. The SemiPulse Concept (SPC): power-line half-waves at 30 to 150 millisecond intervals.

The MPC system does not require an additional conventional transformer-rectifier coupled in parallel since it inherently provides a DC base voltage. This makes the equipment physically compact and cost effective when increased precipitator performance is required with highly resistive ashes.

The SPC system is a software feature incorporated into the Flakt microprocessor transformer-rectifier controller (EPIC). The EPIC controller with SPC is physically the same size, if not smaller than many controllers in use today, and can be incorporated into existing control panels with little difficulty and at minimal expense. The SPC, therefore, provides an opportunity to increase precipitator efficiency when operating on medium to high resistive ash, for a cost not significantly higher than that required to upgrade older transformer rectifier controllers with basic microprocessor controls.

Tests on commercial precipitators in many parts of the world operating on different types of fly ash have demonstrated that these pulsing systems cut energy consumption to such a dramatic extent that they are a viable economic alternative even if only minor improvement in preciipitator efficiency is achieved.

Monitored operation of precipitators of different designs equipped with MPC and SPC systems has shown energy consumption in some cases can be reduced by up to 90 percent and stack emissions up to 75 percent.

BACKGROUND TO PULSED ENERGIZATION

Good precipitator performance requires that the corona current must be evenly distributed over the entire collecting electrode surface. Ash build-up, temperature stratification in the flue gas, misaligned electrodes, etc., are examples of many causes of uneven current distribution. Experience shows that a certain minimum current is needed to ensure at least some flow to the most quiescent surface areas.

Each ash layer exerts a resistance to the flow of electrical current. According to Ohm's law, the voltage drop caused by this resistance across the dust layer is proportional to the magnitude of the current. Many ashes have very high electrical resistivity yielding a very high voltage -- so high, that local breakdown occurs in the ash layer. This is called back corona. It is a very critical factor in precipitator performance. In order to lower the voltage drop to make the back corona disappear, it is necessary to reduce the current or change the ash resistivity by means of gas conditioning (NH_3, SO_3, moisture, etc.). The first method is, of course, very simple but results in the loss of current in some areas of the precipitator lowering performance.

---

*Developed in close cooperation with Kraftelektronik AB Surte, Sweden.

The precipitator designer has to study the current distribution both in microscale (by detailed studies of electrode geometry) and in macroscale (distribution between front and rear surface areas of the precipitator).

Poor current distribution and back corona conditions can be overcome to a certain extent by pulsed operation. Let us first examine the electrical capacitance of the ash layer on collecting plates. If the resistivity of the ash is R (ohmm), and the relative dielectric constant is E, then the time constant is: $T=8.85*E*R*10^{-12}$ sec. This is a measure of the "electrical inertia" of the ash layer. For a resistive ash (for example, $R=10^{11}$ ohmm, E=2, T=1.8 sec.), T is in the second range, which is a long time even compared to the 10 millisecond half cycle of the power line. This also implies that the critical current density, i_{crit}, where back corona starts in the ash layer, is very nearly equal to the time-average current density. Thus, high peak currents from the discharge electrode normally have little effect on back corona -- only the average value does; it is possible to momentarily increase the power for good current distribution at regular intervals. By selecting peak power for good current distribution, as well as interval length for a low average current, the risk of back corona is minimized.

The quantitative improvement obtained by pulsed operation cannot be evaluated theoretically. Extensive testing in actual operation is therefore required. Since the current produced under pulsed operation is more efficiently used, we obtain the double advantage of performance improvements and power savings.

THE MULTIPULSE CONCEPT (MPC)

Figure 1 shows the principal circuit diagram of the Flakt pulsed power supply. A capacitor after the high-voltage rectifier is charged. By means of thyristors on the high-voltage side, the energy is transferred to the precipitator through inductance to form an oscillating circuit. The energy swings back and forth until an essential part has been utilized. The thyristor switching is carried out via transformers from ground potential. Since there is no need for a pulse-transformer, internal energy losses are low. The conventional base rectifier is not needed for DC since the pulse unit is designed to supply an inherent base voltage which automatically tracks the corona onset -- a salient feature of the MPC system. Since third-generation electronic components are utilized, the unit is small, lightweight and cost-effective.

If a base rectifier is still used as a standby unit to provide extra current for low-resistivity dust, a coupling capacitor is not required.

Figure 2 shows the high-voltage waveform for the MPC system. Before each burst, the required pulse energy is stored in a capacitor. When this energy is released, the first pulse in the burst is generated

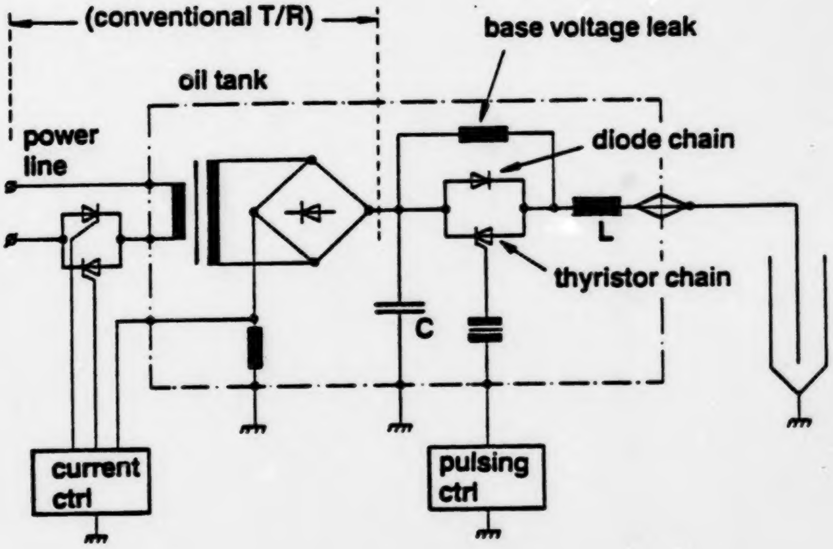

Figure 1. Multi-Pulse Power Set.

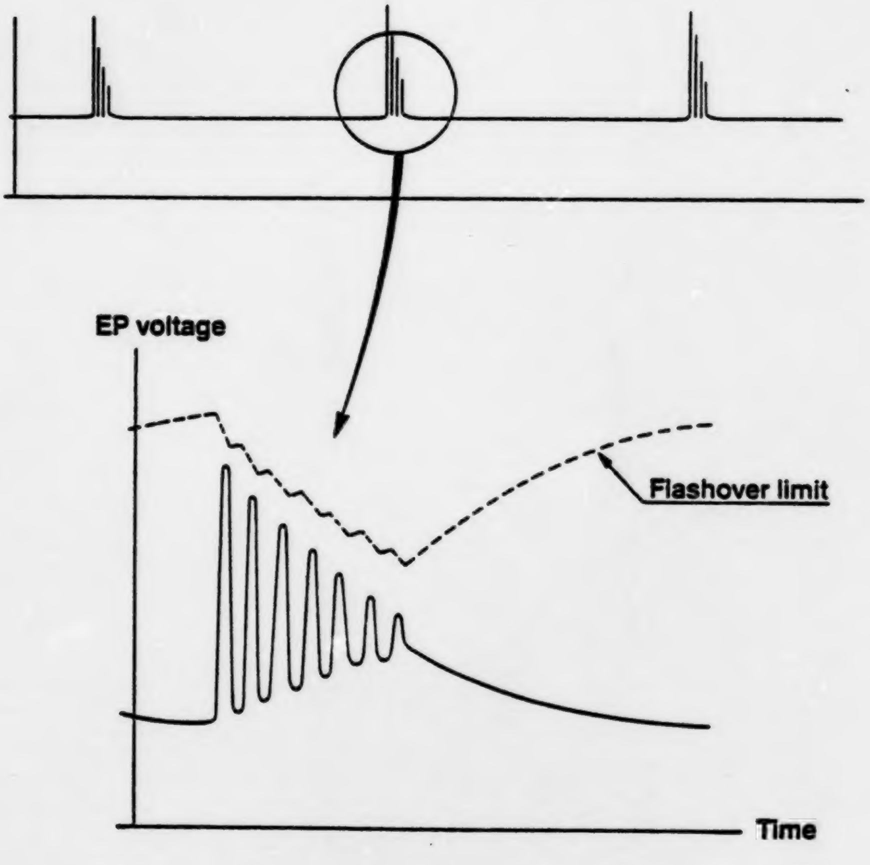

Figure 2. Multi-Pulse HV Wave Forms.

and the energy is then free to oscillate between the capacitor and the EP and through the inductance. While the oscillation proceeds, the pulse amplitude will decline, since capacitor energy is progressively used to form the corona in the precipitator. A train of pulse bursts is created. Each burst consists of closely spaced multiple pulses which decrease in size. Hence, the name "multipulse concept."

A precipitator becomes more prone to sparking as the corona forms. Compared to DC, this tendency towards sparking decreases as the pulses shorten. It takes some time before the precipitator's original sparking sensitivity is restore. The time between two pulses within a burst is not sufficient for full recovery but by decreasing the pulses in size, we avoid provoking the precipitator and causing it to spark.

In the MPC system, energy is very efficiently utilized in the precipitator. The favorable effect on current distribution from the ion cloud produced by the first pulse in each burst will remain during practically the entire duration of the burst. The average current can be controlled by varying the burst repetition frequency and/or pulse amplitude.

THE SEMIPULSE CONCEPT (SPC)

Figure 3 shows current and voltage from a conventional T/R set. Here, the controlling thyristors are fired each half cycle of the line power. Now it is possible to control the firing of the thyristors by still using the same standard T/R set. This is accomplished in such a way that only each third half wave is allowed to pass, resulting in the waveforms shown in Figure 4.

By maintaining the same amplitude on each half wave, the average current decreases to one-third the original. The voltage waveform in Figure 4 has a more pronounced ripple than in Figure 3. It is obviously possible to block any number of the half waves to make the ripple even more pronounced. The voltage curve form now becomes a DC base level with "pulses" superimposed on it. These pulses are of a much longer duration -- 3 to 5 milliseconds -- compared to those previously described in the MPC. We call this semipulsing.

The total number of unblocked pulses in relation to the total number of half cycles is called the charging ratio (CR). Since semipulsing is achieved by means of software programmed into the already powerful EPIC microprocessor unit, it represents a very minor investment offering major benefits. Field tests have shown that power consumption can be reduced substantially -- and in many cases, the outlet emission can also be lowered -- without any modification to the standard T/R set system other than the installation of the EPIC control units.

REVIEW OF OPERATING EXPERIENCES

Flakt pulse energization systems have been installed and tested for

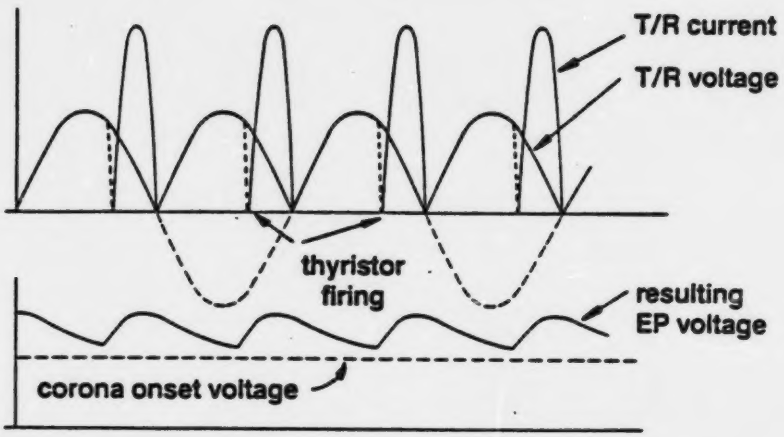

Figure 3. Conventional Full Wave T/R Operation.

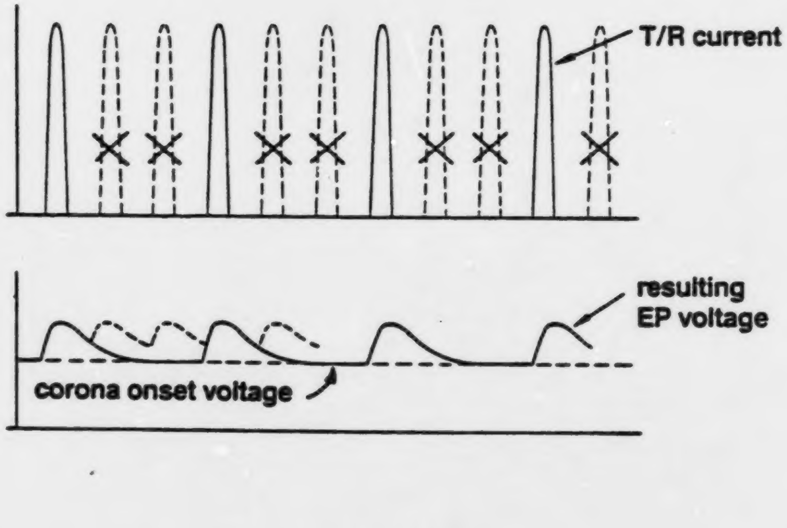

Figure 4. Semi-Pulsed T/R Operation.

various precipitator applications in the United States, Sweden, Belgium, Denmark, Japan, Taiwan, Finland, Australia, and South Africa.

In the United States, new Flakt precipitators are being installed with SPC as part of the microprocessor transformer rectifier controllers (EPIC). The first of these controllers installed in the U.S. were supplied on Flakt precipitators on a small (29 MW) boiler firing 1% sulphur coal. Performance tests conducted in conjunction with compliance testing demonstrated that emission levels, as measured with conventional charging, could be maintained with SPC while only consuming 15% of the transformer rectifier power normally required. Figure 12.

SPC test work has also been conducted on a large pilot precipitator installation in the U.S. operating on high resistivity ash. Tests were conducted with two different electrode systems with change ratios ranging from 1:1 to 1:9. Despite some data scatter normally associated with pilot test work, it was shown that significant power savings and reductions emissions were achieved over the range of charge ratio's tested.

Figure 5 summarizes the data for precipitators operating on flyash presented in Figures 6 through 14. Flakt data confirms the findings of others that the efficiency of pulsed operation increases the higher the resistivity of the ash and the shorter the pulse width.

With a precipitator collecting high-resistivity ash, we have the following options:

1. Particulate emissions exceed the required limit. The main interest is now to decrease emissions. We can expect to achieve a reduction of approximately 50% with SPC and 75% with MPC. Power consumption is also reduced.

2. Particulate emissions comply with the required limit since a very large precipitator was installed. The correspondingly large power consumption -- 1000 kW is the order of magnitude for a 500 MW boiler -- can be reduced 50 to 90% without affecting EP performance. The capitalized cost for power evaluated against equipment suppliers is usually U.S. $3,000 to 6,000/kW. A saving of 500 kW is thus worth $1.5 to $3 million.

The corresponding expectation for medium-resistivity ash is:

1. A reduction of 10 to 20% in emissions.
2. A reduction of 50% in power.

Operating results are uncertain when MPC or SPC is used in connection with low-resistivity ash.

MPC and SPC have also been tested in other applications (metallurgical, cement, recovery boilers). Similar results were obtained. The higher the resistivity of the dust, the greater the improvement in EP performance when pulsed energization is used.

CONCLUSION

Flakt's world wide testing has demonstrated that both the Multipulse and Semipulse concepts are viable economic means to reduce both precipitator emissions and energy consumption.

Pulsing permits the selection of smaller new precipitators for high resistivity ash and offers significantly lower transformer rectifier power consumption.

Existing precipitators required to operate with high resistivity ash and meet new stringent emission regulations can be fitted with pulse energisation. Both emissions and power consumption can be drastically reduced. Additional plant space is not required and retrofitting can be made with minimal unit downtime. No chemical additives or associated operating costs are required.

Both MPC and SPC have their place in precipitator systems. The choice of which system to install must be fully evaluated considering all aspects of each specific project.

Pulsed energisation has been demonstrated to be both viable and reliable technology for application to electrostatic precipitators.

The work described in this paper was not funded by the U.S. Environmental Protection Agency and therefore the contents do not necessarily reflect the views of the Agency and no official endorsement should be inferred.

REFERENCES

Lausen, P. and Lind, H. Application of Pulse Energization on Fly Ash Precipitators. Tiz-Fachberichte, Vol. 106, No. 12, 1982.

Petersen, H. Hoegh. An Energy Conserving Pulse Energization System. EPRI Conference on Electrostatic Precipitator Technology for Coal-Fired Power Plants. Nashville, Tennessee, July 1982.

Feldman, P. L., AA, P. J., and Thanh, L. C. Present Status of Research-Cottrell Pulse Energization Technology. EPRI Converence on EP Technology for Coal-Fired Power Plants, Nashville, Tennessee, July 1982.

Masuda, S. Novel Particulate Control Technology. 4th EPA-Symposium on Transfer and Utilization of Particulate Control Technology, Houston, Texas.

Stomberg, H. and Lundquist, S. Pulsed Radio Frequency Resonance Operation of Electrostatic Precipitators. Inst. Phys. Conference Ser. No. 66: Session VI. Paper presented at Electrostatics, 1983, Oxford.

Lundquist, S. and Sekar, S. An Investigation of Continous and Pulsed High Frequency Corona with Application to Electrostatic Precipitation. University of Uppsala, Sweden, Uurie 140-81 (December 1981).

White, H. J. Industrial Electrostatic Precipitation. Addison-Wesley Publishing Company, Inc. (1963).

100% = performance with pulse unit off.

Plant		Outlet emission %	Power consumption %	Dust resistivity
A	AUSTRALIA 66 MW	28	30	high
B	DENMARK 60 MW	34	50	high
		50	50	medium
C	AUSTRALIA 660 MW	50	100	medium
		100	50	medium
		50	50	high
D	DENMARK 600 MW	65	10	high
		100	25	medium — low
E	TAIWAN 140 MW	45	20	high
F	U.S. 29 MW	100	15	medium–low

Figure 5. Summary of Present Experience Regarding Pulsed Operation of EPs for Coal-Fired Boilers.

Dust emissions for different energization methods CC (conventional), MPC (multipulse), SPC (semipulse).

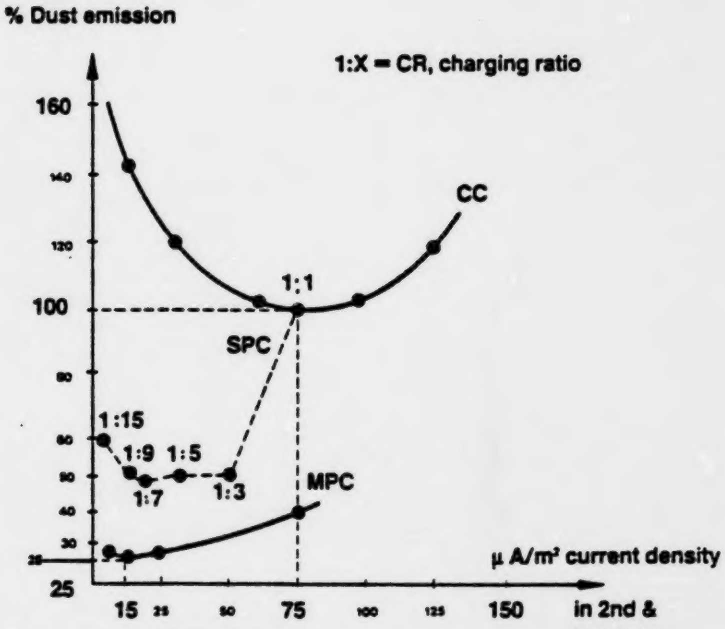

Arrangement of T/R-sets.

Case	Field 1st	2nd	3rd
A	CC	CC	CC
B	CC	SPC	SPC
C	CC	MPC	MPC
current density	always 150	varied	

At 15 µ A/m² a primary kWh-meter gave a power consumption of 1 W per m² collecting area with MPC.

Figure 6. Plant A--Coal-Fired Boiler, 65 MW, Australia.

Comparing outlet emissions for different energization methods. The emission for conventional operation at medium resistivity is set = 100%.

Values shown = (emission %)/(emission enhancement).

Operating mode			**Dust resistivity**
100	**70/1.42**	**50/2.00**	**medium**
276	**193/1.43**	**95/2.91**	**high**
conv.	*SPC*	*MPC*	

Plant configuration: 2 EP's, 2 fields each.
Pulsed operation in rear fields only.
Pulsed operation in front fields less effective.

Figure 7. Plant B--Coal-Fired Boiler, 60 MW, Denmark.

Medium dust resistivity, long term testing.

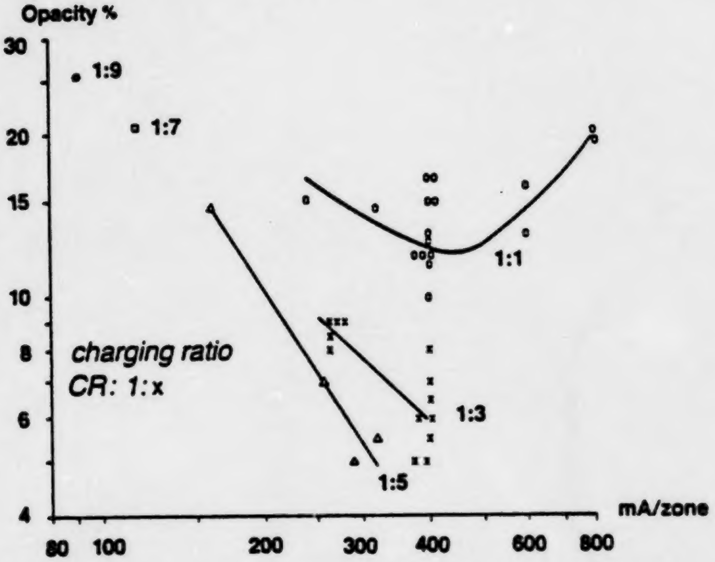

Data obtained from opacity meter recordings.

The table shows estimated power consumption based on the opacity being kept constant = 13%.

System	Current mA/bus sect.	Power kW	Energy saving %
Conventional	600-800	565	0
EPIC w. peakseeker	430	305	46
EPIC w. peakseeker and semipulse	160	128	77

Figure 8. Plant C--Coal-Fired Boiler, 660 MW, Australia.

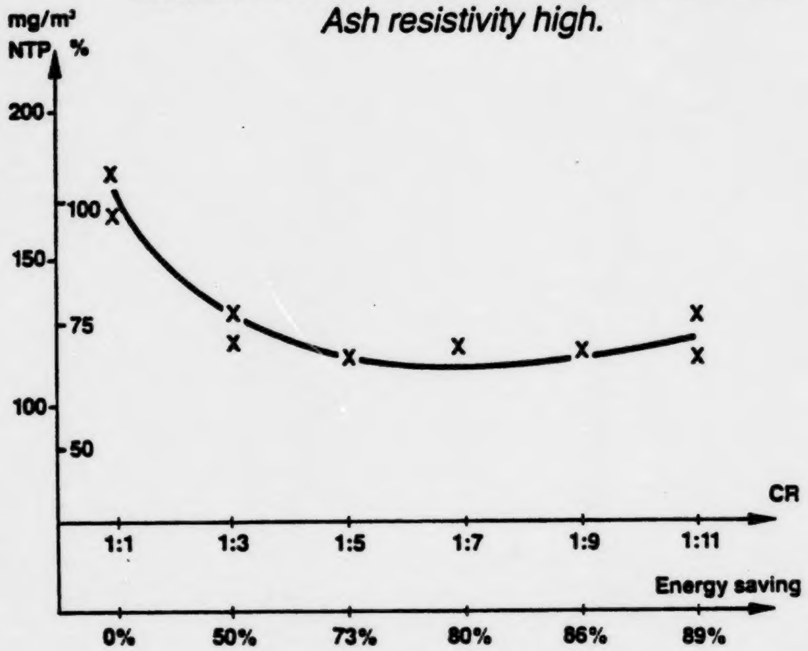

Blended S. African and Australian coals fired.
Ash resistivity high.

CR = charging ratio (1:1 = conventional)
Outlet emission measured by gravimetric sampling.

Plant configurations: 4 cells, 5 fields = 20 bus sections.
20 T/R sets all with EPIC controls.

Figure 9. Plant D--Coal-Fired Boiler, 600 MW, Denmark.

Ash resistivity low.

Semipulse mode	Current density µ A/m²	%	Pwr consumpt. kW	%	Emission mg/m³ NTP
1:1	276	100	1066	100	58
1:3	90	32	350	33	47
1:5	55	20	211	20	50
1:9	33	12	126	12	69
"Normal"	65	24	269	25	54

The power consumption measured with kWh-meter and includes T/R-set losses. Note that pwr. cons. is prop. to current density.

"Normal": CR = 1:3 for 1., 2. and 3. fields.
CR = 1:5 for 4. and 5. fields.

Plant configuration see fig 9.

Figure 10. Plant D--Coal-Fired Boiler, 600 MW, Denmark.

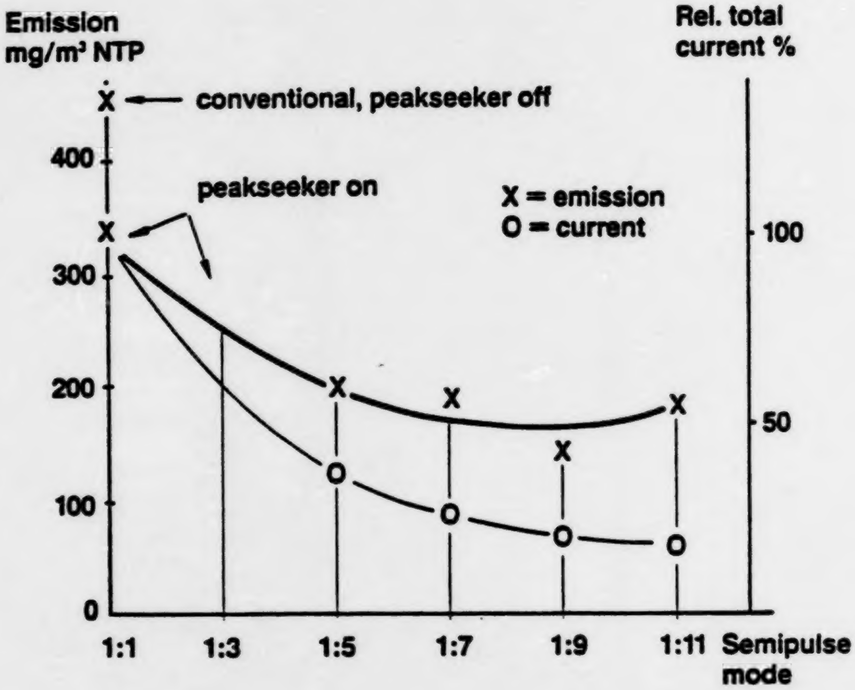
Australian coals, resistivity high.

Plant configuration: 3 fields, 3 T/R-sets.
All T/R-sets have EPIC controls.

Figure 11. Plant E--Coal-Fired Boiler, 40 MW, Taiwan.

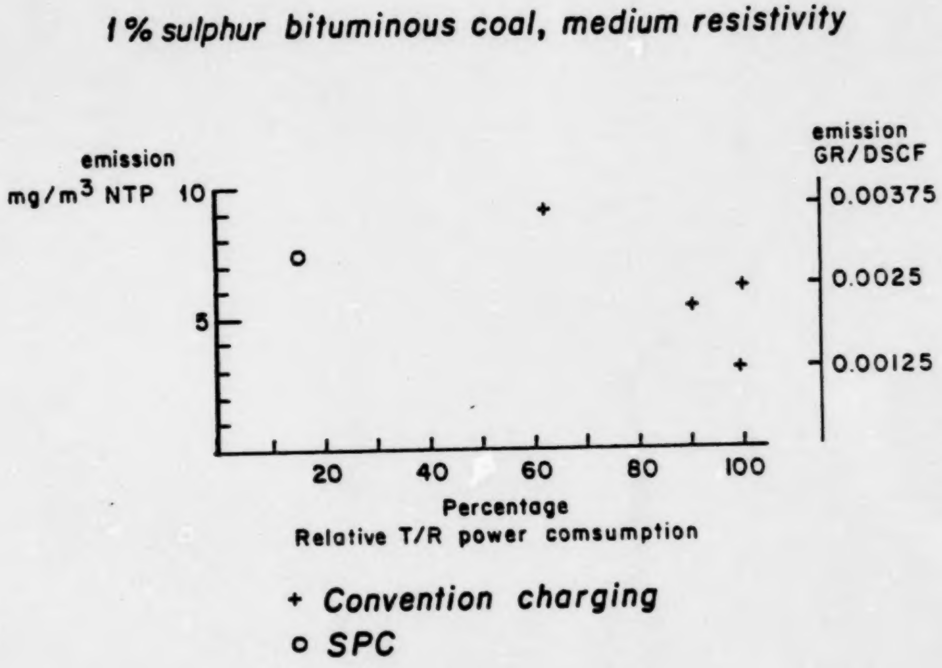

No visible emission for any test.

Data spread within accuracy of testing measurement.

Figure 12. Plant F--Coal-Fired Boiler, 29 MW, U.S.A.

Low sulphur bituminous coal, high resistivity

Electrode A

Relative Emission (%)

	Charge ratio					
test series	1:1	1:3	1:5	1:7	1:9	temp °C
1	100	82				120
2	100	90	68			120
3	100	99	80	75	54	120
4	100	77			79	120
5	100			62		120
6	100	98		95		160
7	100	75		71		160

Relative Current (%)

1	100	45				120
2	100	35	19			120
3	100	33	18	16	12	120
4	100	33			8	120
5	100	33		12		120
6	100	38	14			160
7	100	33		11		160

Figure 13. Plant G--Coal-Fired Boiler, Large Pilot Precipitator.

Low sulphur bituminous coal, high resistivity

Electrode B

Relative Emission (%)

	Charge ratio					
test series	1:1	1:3	1:5	1:7	1:9	temp °C
1	100	91				120
2	100				110	120
3	100			54		120

Relative Current (%)

1	100	30				120
2	100				7	120
3	100			12		120

Figure 14. Plant G--Coal-Fired Boiler, Large Pilot Precipitator.

NEW LIFE FOR OLD WEIGHTED WIRE PRECIPITATORS: REBUILDING WITH RIGID ELECTRODES

by: Peter J. Aa
Product Manager - Electronics
Maintenance & Service Division
Research-Cottrell, Inc.

Gary R. Gawreluk
Product Manager - Precipitators
Air Pollution Control Division
Research-Cottrell, Inc.

ABSTRACT

There are literally thousands of weighted wire precipitators currently operating in the United States. Most of these units were designed in the 50's, 60's and early 70's. Since that time pollution control requirements have become more stringent and electrostatic precipitator technology has advanced considerably.

This paper will discuss how vintage weighted wire precipitators may be upgraded to state-of-the-art rigid electrode designs while improving performance, enhancing reliability and avoiding costly equipment replacement.

Three case histories are examined where rigid electrode upgrades have been undertaken.

- o A black liquor recovery boiler
- o An industrial power boiler
- o A major utility generating station

Special attention is paid to major design modifications made and final operating results. Also discussed are modifications made to electrical control equipment in order to improve performance and reliability.

INTRODUCTION

A recent article in the Journal of the Air Pollution Control Association estimates that there were roughly 1400 electrostatic precipitators in operation on U.S. coal-fired power plants as of 1980(1). Further, it may be conservatively estimated that there are at least two or three times that many ESP's on line in various other applications including pulp and paper, petrochemical, rock products, and iron and steel.

Considerable numbers of these precipitators were designed and installed in the timeframe prior to 1970. In the utility industry alone this figure respresents more than 800 units, nearly all of which are weighted-wire design. What this points to is that any program that a utility or industrial user may be considering with regard to plant betterment or life extension would be remiss if it did not consider upgrade of its electrostatic precipitators. Rebuilding these older, vintage weighted-wire units, specifically rebuilding with state-of-the-art rigid electrode designs, is one option that many users are currently exercising in order to extend life, improve performance, enhance reliability, and minimize maintenance requirements.

WHY REBUILD?

Rebuilding an electrostatic precipitator is not an easy task nor is it inexpensive. In many cases, however, it may represent the most technically viable and cost effective approach to achieve the desired results.

There are many reasons why a user may wish to consider a rebuild option, a number of which are interrelated:

- Fire/explosion - The useful life of a set of precipitator internals can come to an abrupt end as a result of poor combustion efficiency or a boiler flame-out. High LOI combined with lengthy hopper storage and air inleakage have caused numerous damaging ESP fires (2). Explosions have also been known to occur where a boiler trip has sent large quantities of raw fuel and oxygen into the ESP, being ignited with a single spark.

- Corrosion - The thin gauge electrodes in an electrostatic precipitator are normally the first components to experience problems in a corrosion prone unit. Typical causes of corrosion include frequent start-ups/shutdowns, continuous operation below the acid dew point, and cool insulator purge air. Oftentimes the process gas by itself is inherently corrosive as in the case of recovery boilers for the paper industry. In a recent survey of owners of precipitators on recovery boilers, for example, 30% reported experiencing severe corrosion problems(3).

- Availability - Thin element discharge electrodes, whether weighted wire or supported in a rigid framework, have relatively small mass. As a result they are susceptible to failure from electrical arc erosion when subjected to high sparking rates, close electrical clearances, and ash build-ups. Some earlier designs had inherent failure modes due to poor shroud designs or electrode attachments. On precipitators with limited sectionalization a number of broken electrodes could have a negative impact on a plant's availability. In a survey in the mid-70's of 174 ESP users, discharge electrode problems were cited as the principle source of precipitator malfunction(4).

- Emissions - Precipitator deficiencies which result in emissions in excess of original design are well documented in the literature. Rebuilds can frequently address these deficiencies by improving rapping effectiveness, increasing electrical sectionalization, and correcting gas distribution. Additionally, when newer, more stringent emission requirements, fuel switches, or process changes cause a unit to fall out of compliance, a rebuild offers the potential for improving performance through an increase in collecting area, lower gas velocity, longer treatment time, and higher migration velocities.

- Life extension - In the power industry in particular, many utilities are considering comprehensive life extension programs rather than contend with the problems, demands, and uncertainties regarding new plant construction. Typical goals being set look for adding another 20-30 years on top of a plant that is already more than a quarter century old. A precipitator rebuild can provide the means of achieving these goals by providing the latest technology in an existing casing while avoiding the expense of a new unit.

There is no one single type of rebuild. Each new rebuild opportunity must be examined independently for what the client is trying to accomplish and what the site-specific conditions will permit. In the past, the most common type of rebuilds involved replacing the precipitator internals in kind, essentially duplicating what was initially supplied. More recently we are observing owners of weighted wire precipitators opting for rebuilds incorporating new rigid electrodes.

A rebuild with Research-Cottrell's rigid electrodes generally involves converting the original design from 9" gas passages to 12" gas passages in order to accommodate the larger mass of the electrode with regard to electrical clearances, as well as to take advantage of its higher operating voltage potential and attendent higher migration velocities. This increase in the interelectrode spacing permits some interesting things to be done with component selection and resulting precipitator configuration. The following discussion highlights a few of the more significant rebuild aspects and addresses the benefits to be derived.

RIGID DISCHARGE ELECTRODES

The most obvious modification made in a rebuild involving rigid discharge electrodes is the RDE itself. Compared to the thin diameter emitters characteristic of weighted wire and European style rigid frame designs its mass is many times greater (Figure 1). This yields an electrode that, for all intents and purposes, will not break from electrical arc erosion.

Research-Cottrell's Dura-Trode rigid electrode design (Figure 2) was commercialized in 1978 after a 6-year-long research and development program. Each electrode is shop fabricated of steel sheet at least as thick as the collecting electrodes. Its roll-formed body provides the desired section moment for structural rigidity and electrical stability in addition to enhancing the electrical field strength. The scalloped edges serve to establish corona generation at discrete points ensuring an even corona distribution along its entire length. This feature is especially beneficial on high resistivity applications since it reduces the potential for highly localized current densities which intensify back corona. Additionally, the design is based upon a single-pin top connection with a swaged end (which acts like a hinge) affording a self-aligning feature in both planes.

At first glance it would seem that there might be a significant weight differential involved in substituting rigid electrodes for weighted wires but this is not normally the case since:

1) One Dura-Trode replaces two weighted wires,

2) the heavy cast iron weights are eliminated, and

3) wider plate spacing actually reduces the total lineal feet of electrode required with no compromise in particulate removal efficiency.

On a typical 9'-wide by 36'-long field, for example, the total additional weight for the Dura-Trode electrodes represents only about a 15% increase. After adding in the reduction in collecting area due to the wider plate spacing, an overall decrease in weight is actually realized.

The benefits to be derived from utilizing rigid electrodes in a weighted wire rebuild are not solely attributed to the improved reliability and availability inherent in a virtually unbreakable electrode. A few other points deserve mention:

- Lower power consumption - Past sizing practice for transformer-rectifiers on weighted wire precipitators typically called for relatively large current ratings in order to drive up the voltage high enough to achieve desired space charge effects. The geometry of the Dura-Trode electrode, however, results in considerably higher voltages and consequently higher field strengths when operating at comparable weighted-wire output currents in equivalent gas passage widths (Figure 3). This means that in most applications power consumption may be reduced with Dura-Trode electrodes with no negative impact on outlet emissions.

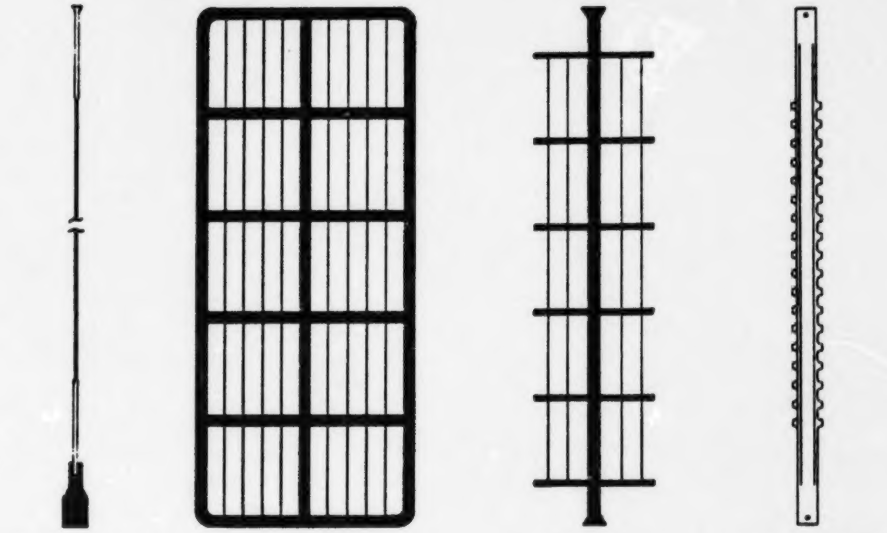

Weighted Wire (shrouded)

Rigid Frame (bedspring)

Rigid Frame (strung mast)

Rigid Electrode (Dura-Trode™)

Figure 1. DISCHARGE ELECTRODE TYPES.

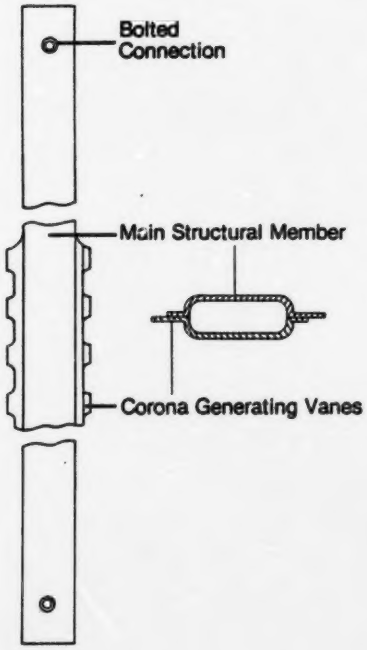

Figure 2. DURA-TRODE™ RIGID ELECTRODE.

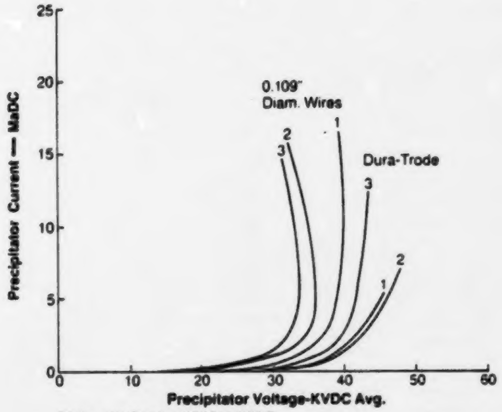

Note: (1) Gas load 330 to 360°F
(2) No's. by curves denote precipitator section

Figure 3. DURA-TRODE™ AND 0.109" DIAMETER WIRES IN 12" GAS PASSAGES.

- Improved cleanability - One of the major headaches plaguing numbers of weighted wire units has been keeping the wires free of ash build-up. The difficulty of setting up a standing wave in a wire that's part of a large bus section has been compounded by the loose connection of wire to supporting frame. Dura-Trode electrodes, however, behave more like a collecting electrode than a discharge electrode with respect to rapping response. Each electrode is firmly secured to its support frame with a Huck™ bolt fastener (Figure 4). A consistent clamping force of 20,000 pounds is applied to each electrode insuring both an excellent mechanical as well as electrical connection. Additionally, design changes that have been incorporated in the rapping assembly have improved system energy transfer by as much as an order of magnitude compared to assemblies in use on older weighted wire units.

- Longer electrodes - Older weighted wire units were typically designed with electrodes no longer than 36 feet, the majority of which were in the 24 to 30 foot range. In addition, many units were designed with gas treatment velocities in excess of 6 feet per second which was in line with the design practice of the times. Rebuilds with rigid electrodes, however, afford the opportunity to consider extending electrode length to as much as 48 feet. This increase in height would serve to bring down the gas velocity in line with current sizing practices as well as to increase both collecting area and treatment time. The bonus is that these performance benefits may be realized within the confines of the original equipment boundry limits (Figure 5).

COLLECTING ELECTRODES

Since a rebuild with rigid electrodes normally requires a widening of plate spacing, it is appropriate to examine the replacement of the collecting electrodes as well. More often than not, serious problems with the collecting electrodes themselves initially launch the client into investigating a full scale rebuild in the first place. The benefits to be derived from replacing the collecting surfaces are both reliability and performance oriented due to changes that have been made in their design in the past decade.

Barring the catastrophic, typical reliability-related failure modes are corrosion and metal fatigue. Considering the relatively large numbers of collecting electrodes involved on any given job, materials of construction are typically limited to mild steel or high strength, low alloys in order to be cost effective. Good control of the boiler or process goes a long way in minimizing corrosion problems.

Metal fatigue, on the other hand, should be the responsibility of the equipment manufacturer and is specifically related to the design of his collecting electrode system and the manner in which rapping forces are introduced into it. This issue is also very closely related to overall performance when one considers the responsiveness of the collecting electrodes as a function of rapping input energy. A relatively "dead" system may require high input energy or multiple level rapping in order to effect good plate cleaning, and the harder and more frequent that a plate is hit the more attention must be paid to addressing potential structural failures.

As a result of a trend towards increasingly taller precipitators as well as a desire to improve further the performance and reliability of its current product, Research-Cottrell launched a major R&D effort in the mid-70's aimed at collecting electrode redesign. The end product is a plate that, on the surface, looks very similar to the original Opzel™ design but upon closer examination contains some very significant design modifications. These include;

1) a rigid 10 gauge "stiff-back" which serves as a support for the thinner gauge collecting surface,

2) hyperbolically tapered mounting pads designed through finite element analysis to gradually introduce rapping stresses into the plate, and

3) a new approach to roll-forming plate elements which, when assembled, greatly enhances the dynamic responsiveness of the plate surface.

This new collecting electrode design, tradenamed G-Opzel™ (Figure 6), can take considerably more abuse than its Opzel predecessor but yet in comparative testing it has demonstrated superior response to rapping forces, requiring roughly one half the input energy to achieve equivalent "G" levels as compared to the earlier design. More than 35,000 of these plates have been installed in over 75 precipitators since being introduced in 1977. An excellent performance record has been established with not a single plate failure reported to date.

This same electrode that is used in all new equipment offerings is also well suited for most weighted-wire rebuild applications due to the similarity in overall dimensions and method of support.

RAPPERS & CONTROLS

Both the rigid electrodes and collecting plates are typically cleaned with a single impact rapping device (Figure 7). This affords the opportunity to replace any electromagnetic vibrating devices and consolidate control requirements and spare parts inventory.

Research-Cottrell's single impact rapper design employs two fundamental principles: electromagnetics and gravity. A low voltage D.C. pulse is applied to the rapper coil causing electromagnetic lift of a solid steel rod. Gravity causes the rod to drop as the coil is de-energized, imparting as much as 24 foot-pounds of energy to the electrodes below. No springs are used in the rapper as in a number of other top-mounted designs.

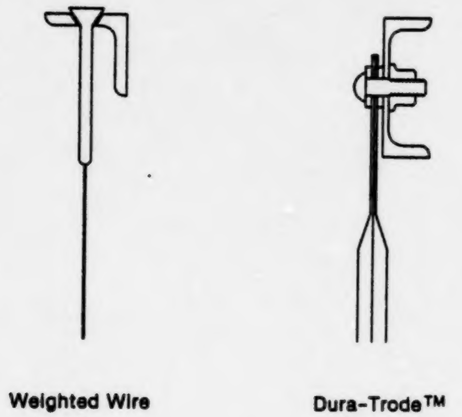

Figure 4. DISCHARGE ELECTRODE CONNECTIONS.

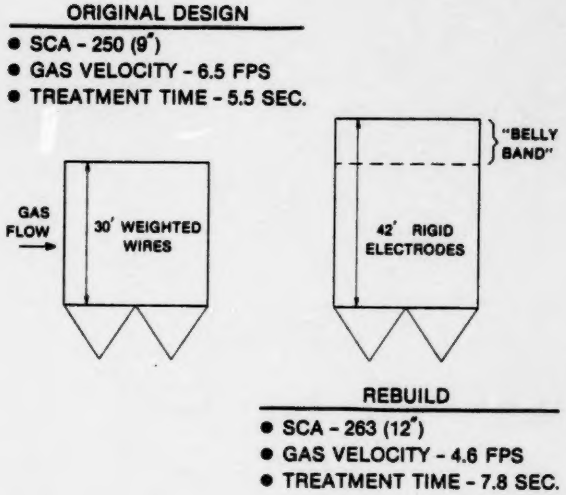

Figure 5. IMPACT ON EXTENDING CASING TO UTILIZE LONGER ELECTRODE.

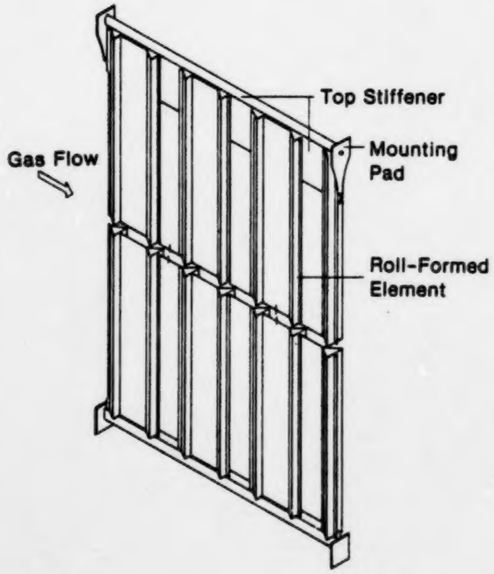

Figure 6. G-OPZEL™ COLLECTING ELECTRODE.

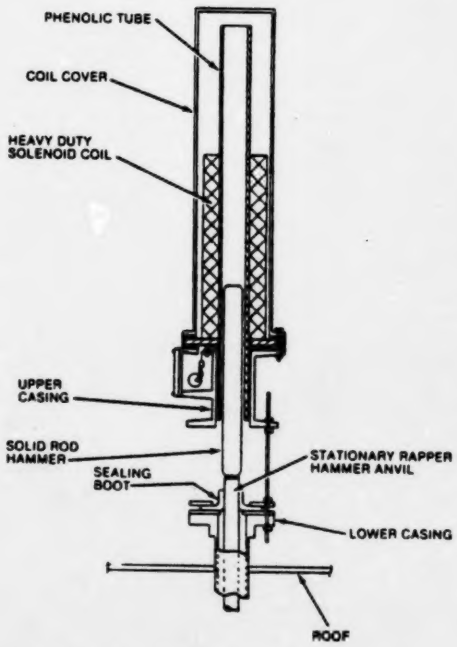

Figure 7. MIGI™ RAPPER ASSEMBLY.

Aside from the high reliability inherent in a rapper of such simple design, rebuild situations can realize performance enhancements through the addition of state-of-the-art microprocessor-based rapper controls. A typical control used on many vintage weighted wire units tied all rappers together on a single, motor-driven distributor switch. Turning at a constant speed the switch would fire consecutive rappers at identical time intervals, regardless of their location in the precipitator. Cycle times of two minutes were standard practice on many of these units. Although this may be satisfactory on inlet fields that build up quickly from high dust loadings, the outlet fields suffer: the lower loadings coupled with the fast rapping cycle typically result in higher than necessary outlet emissions due to excessive rapping re-entrainment losses. Modern controls can optimize cycle time on each field in the precipitator in order to minimize these losses. Further optimization may be achieved through fine-tuning individual rapping intensities at the control.

TRANSFORMER-RECTIFIERS & CONTROLS

As mentioned previously, rebuilding a weighted wire unit with rigid electrodes normally involves changing the original gas passage spacing from 9" to 12". In order to take advantage of the performance advantage of the wider gas passages an upgrade of the high voltage power supplies is often necessary. Typically this involves replacing the existing 70 KVp transformer-rectifiers with units rated at 85 KVp output. Depending upon the application, however, impact on plant load centers and field wiring may be negligible. This is due to the lower current draw of the Dura-Trode electrodes and whatever sizing conservatism which may have been built into the original T-R size selection.

The benefits derived from going to wider plate spacing are generally well recognized by most major suppliers and specifiers of electrostatic precipitators. The primary motivation has been the reduced cost of precipitator internals. On many applications SCA reductions proportional to the increase in spacing have been achieved while maintaining or improving design performance levels. This is widely attributed, for the most part, to the improvement in migration velocity due to the higher voltage and enhanced space charge effects.

With regard to transformer-rectifier controls, significant advancements have been made in the last 5 years, let alone the past couple of decades. Improvements in fundamental control functions such as spark sensing, quenching and recovery have resulted in faster system response and higher average power levels into the precipitator. Additionally, the introduction of microprocessor-based control systems has permitted the introduction of new integrated control strategies aimed at improving performance, reducing power consumption, and assisting in equipment troubleshooting and maintenance. It would be appropriate to say that any unit purchased more than 10 years ago, whether a rebuild candidate or not, should consider and investigate the benefits that may be derived from a control upgrade.

CASE HISTORIES

The foregoing discussion has outlined some of the basic modifications involved in rebuilding a precipitator with rigid electrodes and their impact on unit performance, reliability and maintainability. What follows are a few case histories of actual installations where rebuilds have taken place.

CASE HISTORY #1 - CONVENTIONAL RECOVERY BOILER

It is well known that conventional recovery boiler precipitators are prone to internal corrosion. The first internal component to be affected by this corrosion is usually the discharge electrode wire. Corrosion of these wires causes them to break which results in grounded electrical frames. Typically, when an electrical frame is grounded, the firing rate of the boiler is reduced in order to maintain acceptable stack emissions, resulting in reduced productivity.

Case History #1 is an example of an 8 year old recovery boiler precipitator where the internals were corroded and needed replacement. The customer chose to rebuild with Dura-Trode electrodes to increase the overall reliability and availability of the precipitator.

The support steel and shell of the precipitator did not require any replacement or repair. And since there was no change in operating conditions, the rebuild was done within the confines of the existing shell without any increase in plate height or treatment length.

As stated previously, the use of Dura-Trode electrodes necessitates the use of 12" gas passage spacing and higher voltage transformer-rectifiers (T-R's). Since the existing T-R's were the Askarel (PCB) filled type, replacing them with oil filled 85 KVp T-R's was an added benefit of the rebuild.

Due to the low current operating characteristic of Dura-Trode electrodes, the new T-R's were sized substantially lower in current rating than the old T-R's. The installed KW of the new T-R's is less than half that of the old T-R's.

In addition to the T-R replacement, the out-of-date T-R controls and rapper controls were also modernized with Powertrac™ T-R controls and microprocessor rapper controls to improve the overall performance of the precipitator.

Precipitator design conditions before and after the rebuild are exactly the same since neither the boiler operation nor the necessary precipitator efficiency required any changes (Table 1).

Table 2 highlights some of the precipitator design features before and after the rebuild. Due to the increase in gas passage spacing from 9" to 12", the number of gas passages was reduced from 41 to 31 per chamber. This gas passage reduction had a negligible impact on both gas velocity and treatment time as would be expected from an internal rebuild within the confines of the existing shell. The SCA reduction reflects the fewer number of collecting plates used with 12" gas passage spacing and is compensated for by the increased migration velocity achieved with wide plate spacing and higher field strength. A substantial reduction in the number of rappers was achieved through the use of G-Opzel collecting plates which are highly responsive and require only leading edge rapping.

As of the writing of this paper, only one half of this unitized precipitator had been rebuilt. However, the customer was operating at 75% of normal boiler firing rate with all gases passing through the rebuilt half of the precipitator and was maintaining a 30 to 35% opacity. This opacity level is slightly less than that achieved under the same conditions with the original internals. Based upon this observed performance, there is every reason to believe that the unit will perform as expected when both chambers are treating full gas volume.

CASE HISTORY #2 -INDUSTRIAL BOILER

Case History #2 represents a rebuild on a 12 year old precipitator serving a pulverized coal fired boiler for an industrial user. The primary reason for the rebuild was corroded internals, however, the plant also desired to switch to a coal that produced ash which was more difficult to collect than its present coal. Also, the plant wanted to update their saturable reactor T-R controls to silicon controlled rectifier (SCR) controls, and wanted to install a more reliable and flexible rapping system.

Except for the change in coal specification, the design conditions before and after the rebuild did not significantly change (Table 3). The guaranteed outlet emissions ranged from .01 to .025 grains, depending on the sulfur-to-ash ratio.

High reliability and consistent emission levels were high priorities of this customer. To satisfy the customer's concerns, Research-Cottrell recommended rebuilding with Dura-Trode electrodes and G-Opzel collecting plates. Since the structural steel and shell were in good shape, the rebuild involved replacing internals within the confines of the existing shell without increasing plate height or treatment length.

Table 4 shows the before and after rebuild precipitator design. The number of gas passages was reduced from 23 to 17 due to the increased gas passage spacing. Remaining within the confines of the existing shell caused a slight increase in gas velocity with a corresponding decrease in treatment time. These changes were considered to be insignificant due to the increased migration velocity produced by the higher field strength. This increased migration velocity also compensates for the reduction in SCA from 361 to 249.

As part of the rebuild the electrical sectionalization was increased. Due to the relatively low dust loading and moderate resistivity, Research-Cottrell was able to reuse the three existing T-R's that had energized the original five bus sections. These three 70 KVp T-R's were placed on the

TABLE 1. CASE HISTORY #1 - CONVENTIONAL RECOVERY BOILER, DESIGN CONDITIONS

	Before Rebuild (WW)	After Rebuild (RDE)
Gas Volume (ACFM)	430,000	430,000
Temperature (°F)	300	300
Inlet Loading (GR/DSCF)	6.6	6.6
Efficiency (%)	99.7	99.7

TABLE 2. CASE HISOTRY #1 - CONVENTIONAL RECOVERY BOILER, ESP DESIGN

	Before Rebuild (WW)	After Rebuild (RDE)
Gas Passages (Total)	82	62
Gas Passage Width (in.)	9	12
Gas Velocity (FPS)	3.88	3.85
Treatment Time (sec.)	9.28	9.35
SCA	412	311
T/R Controls	Outdated analog	State-of-the-art analog
Rapper Controls	Cam Switch Type	Microprocessor
No. of Rappers	146	100

TABLE 3. CASE HISTORY #2 - INDUSTRIAL BOILER, DESIGN CONDITIONS

	Before Rebuild (WW)	After Rebuild (RDE)
Gas Volume (ACFM)	110,000	110,000
Temperature (°F)	325	350
Inlet Loading (GR/ACF)	2.8	2.8
Outlet Loading (GR/ACF)	?	0.01 - 0.025(1)

(1) Depending on Sulfur/Ash Ratio

last three bus sections and two new 85 KVp T-R's were placed on the first two bus sections. Each of the five fields now has its own dedicated T-R. The three old T-R controls were also reused and were converted from saturable reactor controls to SCR-type with microprocessor control. The two new T-R controls were SCR-type microprocessor controls.

The collecting and discharge electrode rapping system was replaced with MIGI rappers and microprocessor rapper controller.

The rebuilt precipitator was brought into service in September 1983. Unit performance to date has exceeded guarantee requirements with average outlet emissions of 0.006 GR/ACF at design gas volume as compared to the corrected guaranteed level of 0.025 GR/ACF.

CASE HISTORY #3 - UTILITY PULVERIZED COAL FIRED BOILER

The third case history is a little more involved than the previous two. This 17 year old precipitator installation which was originally designed for high sulfur coal had experienced severe corrosion of its internals. Additionally the utility was also planning a switch to low sulfur coal. The fuel switch would result in a 21% increase in volume to the precipitator and the plant was contemplating a change from forced draft system to a balanced draft system. Lastly, the T-R and rapper controls were outdated.

Typically the above requirements would dictate that a new precipitator be built. Preliminary investigations, however, showed that the requirements could also be met with a rebuild plus SO_3 flue gas conditioning. An economic evaluation was performed and Table 5 shows the highlights. Even with the gas conditioning system, the cost of rebuilding was less than a new precipitator. And the turn-around time to complete the rebuild with conditioning was roughly one-third the turn-around time for a new precipitator. In addition, a new unconditioned precipitator would have taken two to three times the real estate of the rebuilt precipitator.

The design conditions before and after rebuild are shown in Table 6. The gas volume increased by 21%, the operating pressure changed from +5 H_2O to ± 25 H_2O, the inlet grain loading increased by 75%, the fuel sulfur content decreased from 3% to 0.6%, and the outlet loading guarantee was set at 0.10 lbs/MBTU.

Overall, the new precipitator design resulted in a reduction in gas passages from 200 to 150 due to an increase in plate spacing from 9" to 12" (Table 7). If was obvious, however, that rebuilding without further increasing the collecting area would not meet the utility's requirements. In order to place additional collecting area within the confines of the existing precipitator shell, the new collecting plates were made twelve (12) feet taller than the existing collecting plates. This modification served to reduce gas velocity by 14%, helping to minimize the re-entrainment losses, as well as to increase treatment time by 17%. Even though plate height was increased, total SCA was still less than originally installed due to the increase in gas volume.

TABLE 4. CASE HISTORY #2 - INDUSTRIAL BOILER, ESP DESIGN

	Before Rebuild (WW)	After Rebuild (RDE)
Gas Passages (Total)	23	17
Gas Passage Width (in.)	9	12
Gas Velocity (FPS)	4.43	4.69
Treatment Time (sec)	8.13	7.46
SCA	361	249
No. of Fields (Mech.)	5	5
(Elect.)	3	5
T/R Controls	Saturable Reactor	Microprocessor
Rapper Control	Motorized Switch Type	Microprocessor

Note: Original ESP was designed by Western Precipitation

TABLE 5. CASE HISTORY #3 - UTILITY P-C FIRED BOILER, EVALUATION FACTORS

	New ESP (W/O Cond.)	Rebuild ESP (W/Cond.)
Cost	\$15M	\$12M
Schedule (P.O. to startup)	92 weeks	34 weeks
Space Constraints	2-3 times more real estate	Existing real estate

TABLE 6. CASE HISTORY #3 - UTILITY P-C FIRED BOILER, DESIGN CONDITIONS

	Before Rebuild (WW)	After Rebuild (RDE)
Gas Volume (ACFM)	1,900,000	2,300,000
Temperature (^{o}F)	250-300	250-300
Pressure (in. W.C.)	+5	±25
Inlet Loading (GR/ACF)	2	3.5
Fuel Sulfur Content (%)	3	.60 - 1.3
Outlet Loading	0.01 GR/ACF	0.10 LBS/MBTU

TABLE 7. CASE HISTORY #3 - UTILITY P-C FIRED BOILER, ESP DESIGN

	Before Rebuild (WW)	After Rebuild (RDE)
Gas Passages (Total)	200	150
Gas Passage Width (in.)	9	12
Collecting Plate Height (ft.)	30	42
Gas Velocity (FPS)	7.0	6.0
Treatment Time (sec.)	4.3	5.0
SCA	190	167
No. of Fields (Mech.)	4	4
(Elect.)	4	6
No. of Rappers	244	448

The electrical sectionalization of each precipitator was also increased during the rebuild. The ten existing Askarel (PCB) filled, 70 KVp T-R's per precipitator were replaced with twelve oil filled 85 KVp T-R's. The four existing electrical fields were replaced with six new electrical fields to increase reliability, produce more stable precipitator operation, and improve power input.

Obsolete saturable core reactor type T-R controls and rotary distribution switch type rapper controls were replaced with microprocessor controls. Microprocessor energy management systems and a remote data logger were also supplied with the rebuild to optimize power consumption and provide a permanent automatic record of precipitator electrical operation.

Although outlet emission tests have not yet been performed, the station has run at full load conditions with less than eight percent opacity which is well below the 20% opacity limit that was guaranteed.

CONCLUSION

Experience to date with more than 8 precipitators has shown that rebuilding old weighted wire units with state-of-the-art rigid electrodes often represents a technically viable as well as cost-effective alternative to replacement with a new precipitator. Rigid electrodes have demonstrated both higher reliability and improved performance as compared to wire type electrodes. Further improvements in both reliability and performance may be realized by including more responsive collecting surfaces, more flexible rapping systems, and more effective transformer-rectifier controls.

Whether precipitator upgrade is being considered due to corrosion, poor performance, catastrophic failure, or simply as a key element in a plant betterment/life extension program, the rebuild potential of the existing equipment should be carefully examined before a new equipment purchase commitment is made.

The work described in this paper was not funded by the U.S. Environmental Protection Agency and therefore the contents do not necessarily reflect the views of the Agency and no official endorsement should be inferred.

REFERENCES

1. Lagarias, J.S., McDonald, J.R., Giovanni, D.V. Assessment of the commercial potential for the high intensity ionizer in the electric utility industry. Journal of the Air Pollution Control Association 31 (11): 1221-1227, November, 1981.

2. Bump, R.L. Fires in electrostatic precipitators - survey results, discussions and recommendations. Paper presented at the Joint ASME/IEEE Power Generation Conference, St. Louis, Missouri, October 4-8, 1981.

3. Henderson, J.S. Final survey results for direct contact evaporator recovery boiler electrostatic precipitators. TAPPI 65 (3): 91-94, March, 1982.

4. Bump, R.L. Electrostatic precipitator maintenance survey. Paper presented at APCA Specialty Conference on Operation and Maintenance of Electrostatic Precipitators, Dearborn, Michigan. April 10-12, 1978.

PULSING ON A COLD-SIDE PRECIPITATOR
FLORIDA POWER CORPORATION, CRYSTAL RIVER, UNIT 1

by: Joseph W. Niemeyer and Robert A. Wright
Lucidyne, Inc.
4235 Ponderosa Avenue
San Diego, California 92123

and

Wayne Love
Florida Power Corporation
3201 34th Street, South
St. Petersburg, Florida 33733

ABSTRACT

Lucidyne, Inc. and Florida Power Corporation conducted a pulser feasibility study on the Unit 1 precipitator at Crystal River Station. The test was to demonstrate pulsing as a viable means of enhancing precipitator performance.

Unit 1 Crystal River precipitator is a cold-side Buell design which was expected to operate below specification due to switching to low sulfur coal. Testing was done in one outermost cell of six cells across gas flow. Lucidyne's pulsers were installed on the first five fields in the direction of gas flow, the third field was grounded, reducing the number of pulsers to four in series.

Testing unpulsed with one field shorted resulted in an efficiency of 96.7%. Adjusting for power level and plate area provided an unpulsed base efficiency of 98.1%.

TEST RESULTS:

One pulser; enhancement factor = 1.09

Two pulsers; enhancement factor = 1.22

Three pulsers; enhancement factor 1.26

Four pulsers in series did not provide significant improvement.

PULSING ON A COLD-SIDE PRECIPITATOR
FLORIDA POWER CORPORATION, CRYSTAL RIVER, UNIT 1

In July and August of 1983, Florida Power Corporation and Lucidyne, Inc. conducted a pulser feasibility test on the Unit 1 precipitator at Crystal River Station. The test was one element of a precipitator enhancement study performed as a part of a Florida Power Corporation plan to allow burning of low sulfur coal in the unit. Compliance with emission standards would become a concern when Florida Power began to burn low sulfur fuel in Unit 1. A fuel switch is required to lower the SO_2 emission limits. This is an existing regulatory requirement to take effect prior to commercial operation of a new unit at the same site (CR-5). The precipitator was not designed for low sulfur fuel, and without modification was not expected to meet the particulate emission limit of 0.1 lb/MBTU. The pulser test was to determine if Lucidyne's pulsing system was a viable means of providing the required enhanced precipitator performance. Other means of enhancement were tested, but this paper is concerned only with the pulsing.

Crystal River Unit 1 is served by a 1978, cold-side Buell precipitator designed to meet particulate emission limits of 0.1 lb/MBTU and less than 20% opacity with the unit firing high sulfur coal. The precipitator has two chambers with three cells each. There are seven fields: three fields each six feet long followed by four fields each three feet long. Twenty one transformer/rectifier (T/R) sets are used in a double-halfwave each powering two side-by-side cells. The first three fields are powered by T/R's rated at 45 kVDC and 1400 mA. The remaining fields employ units rated at 45 kVDC and 1100 mA.

Lucidyne's pulsers were installed on the first five fields on the outermost cell of the eastside chamber. A broken wire eliminated the third field in the tested cell, thereby reducing the effective collection area and the number of pulsed fields to four.

The T/R sets associated with the pulsers were converted to fullwave operation for the test. The remaining T/R sets were left in double-halfwave configuration. To simplify installation, cable was used for the connecting bus work. The pulsers were connected in series with the T/R's by inserting the pulser high voltage terminals into the buses which connect the T/R outputs to the precipitator discharge electrode terminals.

Unit 1 has a rated capacity of 400 MW, but to prevent boiler tube leaks and provide reliability output was reduced to 370 MW. Soot blowing was scheduled to minimize impact on particulate testing. During testing, Unit 1's pulverized-coal-fired boiler burned coal rated typically at 1.0% sulfur, 9-10% ash and 12,000 BTU/lb.

Particulate testing consisted of gathering inlet and outlet samples over three separate runs. The data samples for each set of inlet and outlet measurements were averaged for use in calculating unadjusted efficiencies.

Initial testing with no pulsers energized established a base efficiency for normal operating conditions. Pulser testing began with four pulsers energized. As each particulate sampling set was completed, one pulser was de-energized, sequentially reducing the number of pulsers in use to zero. The affected pulser was de-energized at the end of the sampling set and the new configuration was operated overnight to condition the system prior to collecting the next set of data. Upon completion of the sequential reduction testing, a check was made to verify the results by retesting at two selected points. One of the two selected data points was with two pulsers on line, and the other with no pulsers.

The effect of pulsing on the precipitator is presented in terms of an enhancement factor which represents the precipitator size increase that would achieve the same performance improvement. Pulsing produces an increase in the average migration velocity and consequently in the collecting performance of the precipitator. The enhancement factor is defined as the ratio of the migration velocity after the addition of pulsing to the migration velocity before.

There are two commonly used methods of determining migration velocities and enhancement factors to ascertain improvement in performance levels. The Deutsch-Anderson equation is an industry standard which does not take into account variation in particle size. Since large particles are easier to collect than small, as the ash laden gas stream proceeds down the length of the precipitator a greater and greater percentage of the remaining particles are small and therefore harder to collect. A modified form of the Deutsch-Anderson equation takes particle size variation into account. Therefore, enhancement factors derived from the modified Deutsch-Anderson equation more accurately represent the real world, and are normally used to evaluate the performance of pulsing.

The unpulsed base efficiency was determined to be 97.4% at full boiler load and with all precipitator cells operating. The efficiency was calculated from the measured data. Then, since the data was taken at 92.5% load (370 MW instead of 400 MW) and with 20% of the tested cell inoperable (one six-foot field shorted out of a total of 30 feet), the efficiency was adjusted to reflect normal operation at full load.

Pulsing increased collection efficiency to 99.01%. The modified Deutsch-Anderson equation was used to adjust the data and to calculate the migration velocities corresponding to the two efficiencies. The resultant enhancement factor of 1.57 shows that pulsing produced improvement equivalent to increasing the size of the precipitator by 57%.

There was no significant difference in enhancement between pulsing three and four fields. Both configurations provided an enhancement factor of 1.57. With two pulsers energized the enhancement factor was 1.49. With one pulser it was 1.18. As previously mentioned, a cross check was performed. The resulting pulsed efficiency of 99.13% indicates that the quoted pulsing enhancement factors are conservative.

A useful method of viewing performance is in relation to precipitator penetration. Penetration is a measure of the particulate which exits the precipitator. It represents system loss and is a measure of the pollutant of concern. In this test pulsing three fields reduced penetration by a factor of 2.6 (outlet grain loading by 61.5%).

The tests conducted at Florida Power Corporation's Crystal River Station Unit 1 show that pulsing was reliable and significantly improved the performance of the electrostatic precipitator. It was agreed (by Florida Power Corporation and Lucidyne) that the enhanced precipitator performance provided by pulsing would bring the Unit 1 precipitator up to the required performance level.

The pulser tests were carried out concurrently with flue gas conditioning tests. The pulsers were tested of one cell on the eastside chamber while the flue gas conditioning tests were conducted on the west side.

The testing allowed Florida Power Corporation to estimate the equipment needed for the required precipitator enhancement and to fine tune the potential capital and operating costs of each acceptable method. It was found that less enhancement was required than first expected. For the enhancement methods studied, this tended to make the systems with lower first cost and higher operating costs more attractive economically than systems with higher first cost and lower operating cost. Lucidyne's pulsing system represented the latter. Florida Power Corporation ultimately chose a 15 ppm capacity SO_3 flue gas conditioning system based on the precipitator requiring approximately 2 ppm SO_3 injection rate. The system is due to come on-line in mid-1984.

The work described in this paper was not funded by the U.S. Environmental Protection Agency and therefore the contents do not necessarily reflect the views of the Agency and no official endorsement should be inferred.

Session 8: ESP: ADVANCED TECHNOLOGY I

Norman Plaks, Chairman
U.S. Environmental Protection Agency
Air and Energy Engineering Research Laboratory
Research Triangle Park, NC

FIELD STUDY OF MULTI-STAGE ELECTROSTATIC PRECIPITATORS

by

Michael Durham, George Rinard, Donald Rugg,
Theodore Carney*, and James Armstrong
Denver Research Institute
Denver, Colorado 80208
and
Leslie Sparks
Industrial Environmental Research Laboratory
Environmental Protection Agency
Research Triangle Park, North Carolina

ABSTRACT

A multi-stage electrostatic precipitator (ESP) utilizes a configuration of charging and collecting devices to provide optimum performance for a particular set of operating conditions. Each component of the ESP can then be designed to cope with the dust loading, particle size distribution, and dust resistivity encountered. This technology is applicable for improving ESP collection of fine, high resistivity dust from such sources as low sulfur power plant flue gas, cement kilns, and metallurgical processes.

This paper describes the results to date of field tests on a multi-stage ESP at the EPA/DRI Valmont Electrostatic Precipitator Test Facility in Boulder, Colorado. The ESP utilizes alternate stages of Temperature-Controlled Electrode Prechargers (TCEP) and parallel plate collectors. The precharger consists of corona wires suspended between anodes that are cooled by 38-43°C (100-110°F) water which reduces the resistivity of the dust collected in the precharger, allowing operation at very high field strengths, greater than 5 kV/cm. The mean flue gas temperature is reduced by only 1.7°C (3°F) by the precharger.

Tests were performed using different combinations of chargers and collectors. Collection efficiencies as high as 99.4% were obtained on an ESP with an SCA of 46 s/m (235 ft^2/1000 acfm). However, the collector sections experienced problems with non-rapping reentrainment, requiring operation at a velocity below 1 m/s (3 ft/s). The results are summarized and discussed in terms of further application of the precharger as a retrofit device on conventional ESPs.

This paper has been reviewed in accordance with the U.S. Environmental Protection Agency's peer and administrative review policies and approved for presentation and publication.

---

* Currently with S-Cubed in Albuquerque, New Mexico

INTRODUCTION

The multi-stage ESP is an extension of the two-stage ESP concept in that particle charging is performed in a separate section from particle collection. The multi-stage ESP is produced by putting two or more two-stage ESPs in series. This allows for the recharging and collection of particles exiting the upstream stages and reducing the effects of reentrainment which has limited the effectiveness of two-stage systems in the past. The multi-stage ESP concept offers a solution for the problems involved with collecting high-resistivity particles.

The problems produced by high-resistivity particles in an ESP have been the subject of numerous research programs. When the electrical resistivity of flyash is greater than 10^{11} ohm-cm, the collected dust layer on the plate resists the flow of electrical charges to the grounded plates. This leads to a buildup of very high electric fields within the dust layer, resulting in a breakdown of the dust layer producing a phenomenon known as back ionization. Back ionization leads to lower electrical operating voltages, poor particle charging, and subsequently greatly reduced particle collection.

This paper describes the field evaluation of the Temperature-Controlled Electrode Precharger (Rinard and Durham, 1984) that was developed as part of an EPA funded program to provide cost effective particulate control technology for sources of high-resistivity dusts. Results of laboratory tests and small scale field tests indicated that this concept warranted further evaluation. A near full scale evaluation of the Cooled-Electrode Precharger was performed at the 7.1 m^3/s (15,000 acfm) EPA/DRI Valmont ESP Test Facility. The results of this evaluation are presented here to demonstrate the potential of this concept. It has the capability to greatly reduce the size of an ESP required for high-resistivity dusts and, because of its small size, it can easily be retrofit into existing ESPs.

BACKGROUND

TEMPERATURE-CONTROLLED ELECTRODES

The use of temperature-controlled anodes is a concept that was first investigated in the 50's by Penney (1962) and White (1974). With this technique, back ionization is controlled by taking advantage of the relationship between resistivity and temperature. The resistivity of flyash peaks at about $150^{\circ}C$ ($300^{\circ}F$) and decreases at higher and lower temperatures. Therefore, the resistivity can be reduced and back ionization controlled by heating or cooling the flyash on the collector electrodes.

It should be noted that the purpose of cooling the anode is not to cool the gas stream and reduce the resistivity of the particles entrained in the gas, but to cool only the dust collected on the surface of the anode. It is only the dust on the anodes that causes the detrimental effects in an ESP. Therefore, by cooling the anodes, the resistivity of the collected dust is reduced which allows corona current to flow freely through the dust layer, eliminating the effects of back ionization.

Water-cooled electrodes have recently been successfully demonstrated in Japan (Drehmel, et al., 1979), where the entire collector plate is cooled. The collected dust is then removed from the collection surfaces by means of mechanical scrapers. The DRI Cooled-Electrode Precharger also uses water to cool the surface of the anode, but applies the concept in a precharger configuration. This wire-pipe precharger configuration has several advantages.

In the first place it minimizes the surface area to be cooled. This not only reduces the total amount of equipment needed to cool and circulate the water, but it minimizes the effect of the cooled anode on the gas stream temperature. With this precharger design, it is possible to reduce the temperature of the dust layer by 56-83°C (100-150°F) and yet only decrease the mean gas temperature by 2.7 °C (5°F). In addition, the precharger requires only about 0.3 m (1 ft) of space for installation, which provides a design that could be easily retrofit into an existing ESP. Also the wire-pipe precharger design can be rapped by conventional means and does not require a scraper system. As an added advantage, the wire-cylinder geometry produces higher field strengths at the surface of the cylinder than the wire-plate geometry which enhances particle collection.

The initial tests with temperature-controlled electrodes, using heated electrodes, showed that back ionization could indeed be eliminated by thermally controlling the resistivity on a small collector surface area (Rinard, et al., 1981a; Durham, et al., 1982). Cooled electrodes were then tested because cooling would be much more energy efficient. In addition, the cooled electrodes would operate in a region of surface-controlled resistivity, rather than bulk resistivity; therefore, the electrical characteristics would be controlled more by the components of the gas stream than by the elemental material in the flyash. This would prevent the deterioration in performance that occurs in hot-side ESPs (Gooch, 1979). Besides these advantages, the cooled electrodes operated at a higher field strength due to the higher gas density near the surface of the anode.

Laboratory experiments showed that, in addition to producing very high particle charge levels, a single 6 cm (2-3/8 in.) cooled-pipe precharger operating at an electric field strength of greater than 6 kV/cm had a collection efficiency on the order of 50% (Durham, et al., 1982). To validate the laboratory experiments, a small test device was built to evaluate the concept on a power plant flue gas stream. This device demonstrated at two power plants that back ionization could be controlled by cooling the anode. The next step in the evaluation was the evaluation of the precharger in a two-stage configuration at the EPA/DRI Valmont ESP Test Facility.

THE EPA/DRI ELECTROSTATIC PRECIPITATOR TEST FACILITY

The tests were performed at a pilot ESP test facility located at the Public Service Company of Colorado Valmont Station in Boulder, Colorado (Rinard, et al., 1981b). The test facility was designed for use in evaluating novel ESP concepts on an actual source of high-resistivity flyash. The facility operates on a slipstream of approximately 7.1 m^3/s (15,000 acfm) of stack gas from the 180 MW boiler burning pulverized low sulfur Western coal. This particular location was chosen because the high-resistivity ash produced by the boiler is so difficult to collect that the existing plant ESP was just replaced by a new baghouse.

The ESP itself was designed specifically for testing a number of novel concepts. It is constructed with alternate sections that can be used for charging and collecting the dust. Thus it is ideal for evaluating two-stage ESP concepts; however, the design is such that other concepts, including conventional ESPs, can be tested. The ESP has doors on the collector sections that can be opened to allow easy removal of internal components. Racks are provided so that these components may be easily rolled in and out of the ESP. The test unit was built to a scale so that its performance would be representative of a full scale unit.

Besides the test unit, the facility includes the following auxiliary equipment: an air-cooled heat exchanger for controlling the gas temperature to the unit; a fan, valving, and venturi for measurement and control of the flow rate of the flue gas; an instrumentation trailer housing a computerized data processing system and high voltage controls; a gas sampling trailer containing an automated gas sampling and analysis system; and a sampling house providing access to the inlet and outlet ducts for analysis of flue gas volume and temperature, mass concentration, particle size distribution, flyash resistivity, particle charge, opacity, gas composition (H_2O, O_2, N_2, CO_2, CO, SO_2, NO_x, and SO_3), and acid dew point.

TEMPERATURE-CONTROLLED ELECTRODE PRECHARGER

Figure 1 is a schematic of the Temperature-Controlled Electrode Precharger design used in the pilot scale evaluation. As can be seen, it is a very simple system consisting of a manifold of welded 6 cm (2.375 in.) pipe, with water entering the bottom header, rising through the vertical pipes, and exiting the ESP through the upper header. Corona is produced on wires which are suspended between adjacent pipes by a hanger system. Rapping is performed by means of a single-impact pneumatic rapper connected to the bottom header.

Cooling water is circulated through the prechargers in a closed loop system. The circulation system consists of the following components: a pump with a bypass to control flow; a water-to-water plate heat exchanger cooled by plant water; and an automatic valve on a bypass of the heat exchanger to control the inlet temperature to the prechargers. Each precharger has a flow meter, thermocouples, and valves to monitor and control the flow through the manifold. The closed loop system is used because it provides an easy means of controlling the water quality within the pipes. Since corrosion or fouling on the inside of the pipes would hamper heat transfer, water treatment could be provided in the closed loop. This is probably the design that would be used in a full scale ESP. It is estimated that the cooling water required from the plant for a full scale ESP with four prechargers added would be below 1% of the total plant cooling water flow rate, and therefore would not appreciably impact the cooling tower heat rejection capacity.

Four cooled-pipe manifolds similar to the one shown in Figure 1 were constructed for the ESP at Valmont. The vertical pipes were 6 cm (2.375 in.) in diameter and spaced 22.9 cm (9 in.) center to center which made six gas passages and a total width of 1.43 m (4.70 ft). The height of the vertical pipes was 3.66 m (12 ft) and the cooled area of collecting surface in each precharger was 4.16 m^2 (44.8 ft^2). The 3.2 mm (0.125 in.) diameter corona wires were 3.5 m (11.5 ft) long and centered in each of the six gas passages.

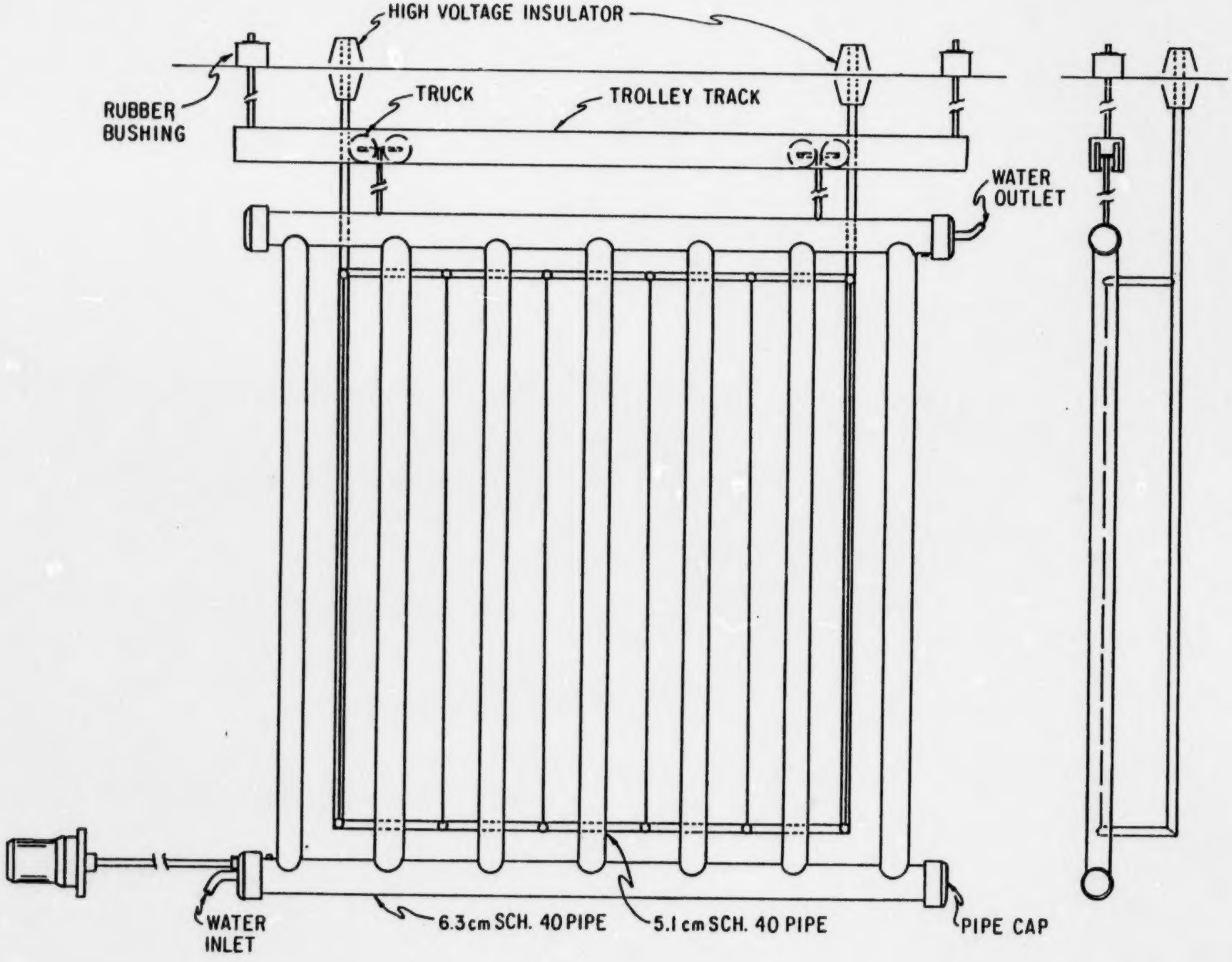

FIGURE 1. SCHEMATIC OF TEMPERATURE-CONTROLLED ELECTRODE PRECHARGER USED IN PILOT SCALE EVALUATION

In each precharger, the total corona wire length was 21.0 m (69 ft). The minimum corona-wire-to-cooled-pipe distance was 8.4 cm (3.31 in.) and the minimum distance from pipe to pipe was 16.8 cm (6.625 in.). The gas velocity at the center line of the pipes is 1.36 times the velocity of the average flow through the ESP. Two of the pipe manifolds were manufactured of stainless steel, while the other two were made of carbon steel to determine the effect of pipe material on corrosion and performance.

Four Cooled-Electrode Prechargers were installed in the first four precharging sections of the ESP and were each followed by parallel plate collectors. Grounded plates, 1.83 m (6 ft) x 3.67 m (12 ft), were spaced 22.9 cm (9 in.) apart forming six passages. The high voltage electrodes also were plates of the same size placed midway between the grounded plates and parallel to them. The parallel plate collectors were selected for the tests because they avoid any problems with the high-resistivity ash by operating at an electric field strength high enough to collect the precharged particles, but lower that that required to produce corona current. The prechargers and collectors were alternated so that particles that were reentrained could be recharged and then collected again.

RESULTS

COAL, FLYASH, AND FLUE GAS ANALYSES

During the evaluation of the Cooled-Electrode Prechargers at Valmont, coal and ash samples were collected daily and then combined and analyzed on a weekly basis. Oxygen and carbon dioxide were measured daily using a Fyrite analysis. Sulfur dioxide was measured continuously using a Thermo Electron Co. pulsed fluorescence unit. Water vapor concentration was determined from the condenser catches obtained during the mass concentration measurements. The resistivity of the flyash was measured in-situ using the DRI Field Resistivity Unit. The average of all the analyses during this test period are presented in Table 1.

TABLE 1 SUMMARY OF COAL, FLYASH, AND FLUE GAS ANALYSES

Coal Analysis		Ash Analysis		Gas Analysis	
H_2O	10.8%	SiO_2	61.44%	O_2	10.3%
Ash	8.3%	Al_2O_3	24.36%	CO_2	10.0%
Volatile	34.1%	TiO_2	0.66%	H_2O	6.8%
Fixed Carbon	46.8%	Fe_2O_3	3.72%	SO_2	150 ppm
Sulfur	0.6%	CaO	4.43%		
Heat Content	11299 Btu/lb	MgO	0.90%	Resistivity @ $350^{o}F$	4.2×10^{12} ohm-cm
		Na_2O	0.94%		
		K_2O	1.51%		
		P_2O_5	0.83%		
		SO_3	0.22%		

ELECTRICAL CHARACTERISTICS AND PARTICLE CHARGE MEASUREMENTS

Electrical characteristics and particle charge were measured at temperatures of 38, 43, and 56°C (101, 110, and 132°F) to determine the operating range of the Cooled-Electrode Precharger. The V-I curves for 38°C and 43°C were essentially the same except sparking occurred at a lower current level for the 43°C temperature. This shows that the resistivity of the dust on the surface of the cooled electrodes increased as the cooling water temperature increased. For a cooling water temperature of 56°C, sparking occurred at a current level of only 2 mA, which shows a further increase in dust resistivity. However, the resistivity was not high enough to produce stable back corona. The electrical characteristics were essentially the same for all four prechargers, except that the first precharger had lower currents than the three downstream prechargers. Since the first precharger experiences the higher particle loading, this indicates a space charge corona suppression. This was confirmed by measurements using the second precharger with and without the first precharger energized.

Charge measurements made using a screen probe showed that the maximum charging level occurred at the lowest water temperature, although there was not much difference between the results at 38°C and 43°C. The measurements show that, at low corona current levels, the charge levels were the same for the three temperatures, which indicates that back corona was not established. In all three cases, the charge level increased as the current increased until light sparking occurred. Any attempt to increase voltage and current further resulted in heavier sparking and reduced charge levels.

Charge measurements were made using the DRI In-Stack Charge/Mass (Q/M) Probe at an ESP temperature of 150°C (300°F) and a gas volume flow rate of 7.1 m^3/sec (15,000 acfm). The overall measured Q/M ratio was 4.1 uC/g at a current level of 2mA at 38 kV. At a current level of 5 mA at 44 kV, the Q/M ratio increased to an average of 8.6 uC/g. However, the average Q/M ratio was only 5.1 uC/g at a current level of 7 mA. The lower Q/M ratio at the higher current indicates that the precharger was operating in a heavier sparking mode. This is also indicated by the variation from 40 to 45 kV in the recorded voltages.

Additional charge measurements were made at various locations within the ESP using an electrically isolated impactor stage to determine the charge on particles 1.1 to 2.6 um in diameter. The ESP temperature was 150°C (300°F) and in one series of measurements the gas flow rate was 4.7 m^3/s (10,000 acfm) providing a gas velocity of 0.94 m/s (3.1 ft/s). In the other series, the flow rate was 7.1 m^3/s (15,000 acfm) and the gas velocity was 1.4 m/s (4.6 ft/s). A summary of the results, presented in Table 2, shows that the particles were charged by the inlet precharger and recharged by the following prechargers. The charging at both gas velocities appears to be about the same. As the particles exit a collector section, the Q/M ratio for the 1.1 to 2.6 um particles was about 8 uC/g or about 70% of the charge level out of the previous prechargers. The test at the higher flow rate after the first collector was an exception, with a Q/M ratio at the outlet of only 2.7 uC/g.

The theoretical Q/M ratio for 1.1 to 2.6 um diameter particles was calculated using 43.5 kV, which produces an average field strength of 5.2 kV/cm across the charging region. The current density on the pipes is 120 nA/cm^2 for 5 mA corona current. The treatment time is about 0.05 s for a volume flow rate of 7.1 m^3/s (15000 acfm). The calculated theoretical Q/M ratio was 14 uC/g compared to the measured value of about 12 uC/g. The cooled-pipe precharger charged the particles to 85 to 90% of the theoretical unipolar ion charging level. This indicates that the prechargers are charging with unipolar current.

TABLE 2
SUMMARY OF RESULTS OF CHARGE MEASUREMENTS

Probe Type: MRI impactor with isolated 4th stage.
Stack Temperature: 150°C (300°F)

Flow, m^3/s (acfm)	7.1 (15,000) Q/M (uC/g)	4.7 (10,000) Q/M (uC/g)
Precharger 1	14.38	9.11
Collector 1	2.68	8.35
Precharger 2	12.97	14.08
Collector 2	8.22	8.42
Precharger 3	17.71	20.67

COLLECTION EFFICIENCY

During most tests, the current in each precharger was 7 mA and the current density on the cooled-pipe surface was 160 nA/cm^2. The voltage for the first precharger was about 45 kV for a field strength of 5.3 kV/cm, and 39 kV or 4.6 kV/cm for the other three prechargers. The parallel plate collectors operated at about 33 kV, and the field strength was 2.9 kV/cm.

The water temperature at the inlet of the prechargers was about 39°C (102°F). The average flow rate through each manifold was 44 l/min (11.6 gal./min) and the average temperature increase of the water was 2.7°C (4.8°F). Using this data the heat removed from the flue gas was calculated to be 500,000 J/min (465 Btu/min) which, at a gas velocity of 1.4 m/s (4.6 ft/s), would lower the gas temperature 1.7°C (3°F) through each precharger.

The measured average temperature drop from the ESP inlet to outlet was 18°C (33°F) with four cooled-pipe prechargers and 10°C (18°F) without the prechargers. Therefore, the gas was cooled about 2°C (2.6°F) by each precharger, which is in close agreement with the temperature loss of 1.7°C (3°F) calculated from the cooling water flow rate and temperature increase.

Table 3 shows a summary of the results of the performance of the Temperature-Controlled Electrode Prechargers. All of the results in Table 3 represent averages of three or four runs. In Test 1 only one precharger and one collector section were energized. The penetration was 12.4% for an SCA of 12 s/m (60 ft^2/1000 acfm). In Test 2, another precharger and collector section were energized. For an SCA of 23 s/m (115 ft^2/1000 acfm), the penetration was 2.9%. The results of Tests 1 and 2 were about the values expected considering the particle charging levels being achieved.

TABLE 3

TEST RESULTS WITH THE COOLED-ELECTRODE PRECHARGERS
WITH PARALLEL PLATE COLLECTORS

Test No.	1	2	3	4	2A	3A	4A	2B	4B
Prechargers	1	2	2	4	2	2	4	2	4
Collectors	1	2	4	4	2	4	4	2	4
Baffles	no	no	no	no	yes	yes	yes	yes	yes
Velocity (m/s)	1.4	1.4	1.4	1.4	1.4	1.4	1.4	0.7	0.9
SCA (s/m)	12	22	46	46	23	46	46	46	67
Inlet (g/dscm)	4.6	4.7	4.8	5.4	3.8	4.1	4.7	3.6	4.3
Outlet (g/dscm)	0.57	0.13	0.11	0.10	0.12	0.085	0.055	0.023	0.018
Penetration (%)	12.4	2.9	2.5	1.9	3.2	2.5	1.2	0.6	0.5
Efficiency (%)	87.6	97.1	97.5	98.1	96.8	97.5	98.8	99.4	99.5

In Test 3, the first and third prechargers were energized as in Test 2 and all four collector sections were energized, increasing the SCA to 46 s/m (235 ft^2/1000 acfm). The penetration was 2.5% which was about the same value as in Test 2. This showed that additional parallel plate collector sections following a precharger do not improve collection. This effect had been encountered in previous precharger tests using parallel plate collectors.

The test results are plotted in Figure 2. The two-precharger ESP line, determined by Tests 2 and 3, shows the effect of increasing SCA in an ESP containing two prechargers. The one-precharger ESP line shows the projected effect of increasing SCA in an ESP with one precharger at the inlet. Curve A shows the decrease in penetration when the SCA was increased by adding a precharger with each additional parallel-plate collector section. Curve B shows the penetration decrease when a precharger was added for every two collector sections.

In Test 4 all four prechargers and collector sections were energized. In comparison to Test 3, the two additional prechargers reduced the penetration from 2.5% to 1.9%. Considering the results of Tests 1 and 2, the penetration in Test 4 was considerably higher than expected. This is apparent from the abrupt break in the slope of Curve A of Figure 2.

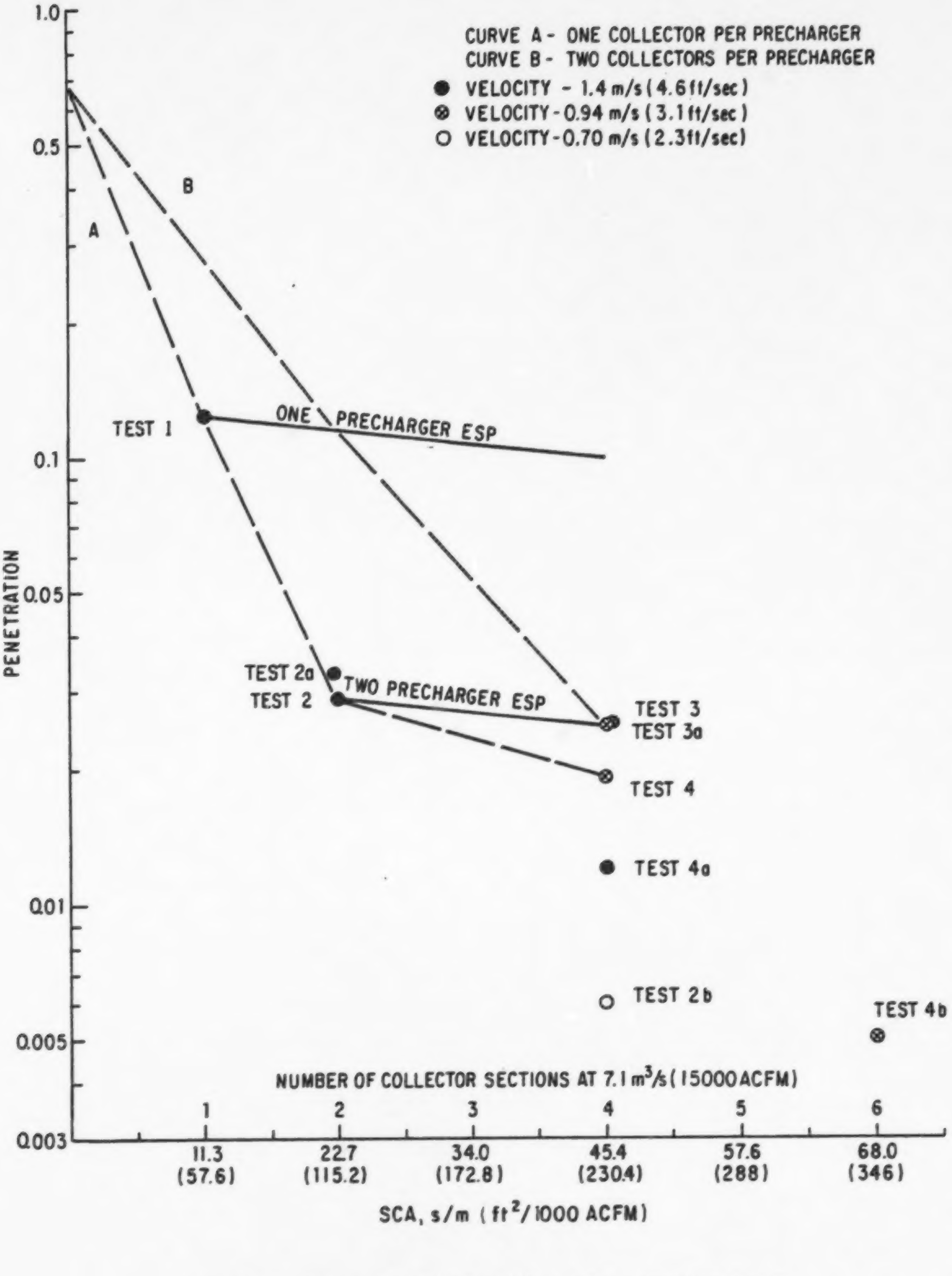

FIGURE 2. EFFICIENCIES OF VARIOUS ESP CONFIGURATIONS

One possible reason for the lack of improvement in performance was leakage around the prechargers. Baffles were added to prevent gas flow between the wall of the ESP and the outer pipes of the cooled-pipe manifold. Tests 2a, 3a, and 4a were repeats of Tests 2, 3, and 4, respectively, except for the added baffles. The results for Tests 2a and 3a were essentially the same as for Tests 2 and 3, showing that sneakage was not a problem at the penetration levels for these ESP configurations. Although the penetration in Test 4a was 1.2%, which was lower than in Test 4, it was still higher than expected based upon the projection of Tests 1 and 2 results shown in Figure 2.

Reentrainment from the parallel-plate-collector sections appeared to be the most probable factor that was limiting performance in Tests 4 and 4a. Since reentrainment is a function of gas velocity, two tests were performed at reduced gas velocities to determine if penetration would decrease as velocity decreased. In Test 4b, all prechargers and collectors were energized. The gas velocity was reduced to 0.94 m/s (3.0 ft/s) and the SCA was 67 s/m (350 ft^2/1000 acfm). The penetration was 0.005 which was considerably lower than the level that could have been achieved by adding two additional parallel-plate collector sections and keeping the velocity at 1.4 m/s (4.6 ft/s). The velocity was reduced to 0.7 m/s (2.2 ft/s) during Test 2b and only two prechargers and two collectors were energized, so the SCA was 46 s/m (235 ft^2/1000 acfm) which was essentially the same as in Tests 3, 4, and 4a. The penetration was measured to be 0.006 and is plotted in Figure 2 for comparison with the other test results. It is apparent that penetration decreased as velocity decreased, which indicated that performance was being limited by reentrainment from the parallel-plate collector sections.

The best example of the effects of velocity on reentrainment can be demonstrated by combaring Tests 2b and 3. Both configurations contain two prechargers and the identical plate area per volume of flow. The only difference is that in Test 2b, the velocity is reduced. Data in Table 2 shows that the reduced velocity does not significantly affect charging, so any differences in the results would be due to the effect of velocity on reentrainment from the plates. As can be seen from Table 3, the lower velocity resulted in a decrease in emissions by a factor of 4.

DISCUSSION

The test results provide a considerable amount of information on two-stage ESPs. The V-I curves for the cooled-pipe prechargers showed that back corona was eliminated when the cooling water temperature into the cooled-pipe manifold was 43°C (110°F) or less. The temperature of the water was increased about 2.7°C (4.8°F), and the temperature decrease of the flue gas was about 2°C (3.6°F). Without back corona, field strengths of 5 kV/cm could be maintained in the charging region of the precharger, and the current density on the cooled surfaces was 160 nA/cm^2. Q/M ratio measurements for particles in the 1 to 2 um diameter size range showed that the particles were charged to about 85% or 90% of the theoretical unipolar ion charging level. Again, this showed the effectiveness of the cooled-pipe precharger in eliminating back corona when charging dust which had resistivity of 4×10^{12} ohm-cm.

Performance measurements on several two-stage ESP configurations revealed the limitations of the parallel-plate collector sections. The two-precharger and two-collector configuration had a penetration of about 3%. For the four-precharger and four-collector configuration the penetration was reduced to 1.9% which showed that the additional prechargers and collectors had little effect upon performance.

The problem appeared to be caused by some non-ideal effect such as rapping or non-rapping reentrainment or sneakage. The frequency of rapping prechargers and collectors was varied and the resulting change in penetration was not measureable. This indicated that rapping reentrainment was not the limiting factor. Baffles were added to eliminate sneakage around the cooled-pipe prechargers. The penetration was reduced to 1.2% for the four-precharger and four-collector configurations but was unchanged in the other configurations tested. This indicated that sneakage was not the main factor that was limiting performance.

Non-rapping reentrainment from the parallel-plate collector sections appeared to be the main factor limiting performance. This was indicated by Q/M ratio measurements which showed that particles lost charge as they passed through a collector section. Cascade impactor measurements which showed a considerable amount of large particles at the ESP outlet also indicated reentrainment. Since non-rapping reentrainment is dependent upon gas velocity, performance tests were made at reduced flow rates which verified that performance was limited by reentrainment.

In the two-precharger and two-collector configuration, the velocity was reduced by a factor of 2 which made the SCA 46 s/m (235 ft^2/1000 acfm). The penetration was 0.6% compared to 1.2% measured in the four-precharger and four-collector configuration at just over twice the velocity and approximately the same SCA. Again, this indicated that non-rapping reentrainment was the main factor limiting performance.

The non-rapping reentrainment was not entirely unexpected. Without current in the collector sections, there is no force holding the particles onto the plate, other than adhesion. This is similar to the situation when a conventional ESP is operating on a dust with very low resistivity, such as the case of many stoker boilers with high carbon carryover. This problem of non-rapping reentrainment can be solved by designing the ESP to operate at a velocity below 1 m/s (3 ft/s).

CONCLUSIONS

Although the performance was limited by non-rapping reentrainment from the parallel-plate collectors, the test results showed that two-stage precipitators can meet the 43 ng/J (0.1 lb/10^6 Btu) emission level or the New Source Performance Standard of 13 ng/J (0.03 lb/10^6 Btu). The coal analysis showed that a penetration of 1.9% would meet the 43 ng/J (0.1 lb/10^6 Btu) emission level, and 0.6% penetration would meet New Source Performance Standard. The four-precharger and four-collector configuration with an SCA of 45 s/m (230 ft^2/1000 acfm) at a gas velocity of 1.4 m/s (4.6 ft/s) met the 43 ng/J (0.1 lb/10^6 Btu) requirement. The two-precharger and two-collector configuration with an SCA of 45 s/m (230 ft^2/1000 acfm) at a gas velocity of 0.7 m/s (2.3 ft/s) met the 13 ng/J (0.03 lb/10^6 Btu) requirements.

Lower penetration with an SCA of 45 s/m (230 ft^2/1000 acfm) at a gas velocity of 1.4 m/s (4.6 ft/s) could be achieved if reentrainment from the collector sections is reduced. It is expected that this can be provided by interfacing the Cooled-Electrode Precharger with a conventional wire-plate ESP. The wire-plate sections would be operated at current levels below that required to produce back ionization but sufficient to hold the collected dust on the plate. If this is not possible with dc energization, then pulsed energization could be applied.

The Temperature-Controlled Electrode Precharger has potential as a retrofit device on an existing ESP that is not performing as designed or at an installation that has undergone a process change that resulted in higher resistivity particles than the ESP was designed for. Examples of applications of the latter case would include changes resulting from acid rain mitigation strategies such as coal switching, coal washing, Limestone Injection with Multistage Burners (LIMB), and dry injection. The precharger can be installed in less than 0.3 m (1 ft) of space and provides high collection efficiencies even for extremely high resistivity dust. An economic analysis has shown that it can be installed at half the cost of an SO_3 conditioning system. The precharger will be tested in the near future at the Valmont Test Facility using the retrofit configuration.

REFERENCES

Drehmel, D.C., C.H. Gooding, and G.B. Nichols (1979). "Particulate Control Highlights: Recent Developments in Japan," EPA-600/8-79-031a (NTIS PB 80-148802), November.

Durham, M.D., G.A. Rinard, D.E. Rugg, and L.E. Sparks (1982). "The Development of a Charging/Collecting Device for High Resistivity Dust Using Cooled Electrodes;" J. Air Pollution Control Association, Vol. 32, No. 11, pp 1132-1136, November.

Gooch, J.P. (1979). "Electrostatic Precipitator Performance," In: Symposium on the Transfer and Utilization of Particulate Control Technology, Volume 1, EPA-600/7-79-044a (NTIS PB 295226), pp 1-17, February.

Penney, G.W. (1962). "Industrial Precipitator with Temperature-Controlled Electrodes," U.S. Patent 3,026,964, March 27.

Rinard, G.A., M.D. Durham, D.E. Rugg, and L.E. Sparks (1981a). "The Use of Heated and Cooled Electrodes for Charging and Collecting High-Resistivity Dust;" 74th Annual Meeting of the Air Pollution Control Association, Paper 81-63.3; Philadelphia, PA; June 21-26.

Rinard, G.A., M.D. Durham, J.A. Armstrong, D.E. Rugg, and L.E. Sparks (1981b). "The EPA/DRI Valmont Electrostatic Precipitator Test Facility;" J. Air Pollution Control Association, Vol. 31, No. 8, pp 908-911; August.

Rinard, G.A. and M.D. Durham (1984). "Electrostatic Precipitator using a Temperature Controlled Electrode Collector," U.S. Patent 4,431,434, February 14.

White, H.J. (1974). "Resistivity Problems in Electrostatic Precipitation," J. Air Pollution Control Association, Vol. 24, No. 4, April.

OPTIMIZING THE COLLECTOR SECTIONS OF MULTI-STAGE ELECTROSTATIC PRECIPITATORS

by

George Rinard, Michael Durham, and Donald Rugg
Denver Research Institute
Denver, Colorado 80208

and

Leslie Sparks
Industrial Environmental Research Laboratory
Environmental Protection Agency
Research Triangle Park, North Carolina 27711

ABSTRACT

A companion paper, "Field Study of Multi-Stage Electrostatic Precipitators," describes tests of parallel plate-plate collectors in multi-stage ESPs. The tests described in that paper showed that with this configuration the gas velocity must be reduced to avoid excessive non-rapping reentrainment. The present paper describes further tests that were performed at EPA laboratories in Research Triangle Park, North Carolina, utilizing conventional wire plate collectors in a multi-stage ESP. The ESP had cooled pipe chargers and conventional collectors in alternating sections. Both conventional and pulsed excitation were performed utilizing 0.32 and 0.95 cm (1/8- and 3/8-in.) diameter rod electrodes.

The results indicate that good collection efficiencies are possible in a multi-stage ESP, with high resistivity dust using conventional wire plate collectors. A particularly important application is for retrofitting an existing ESP on power plants utilizing coal switching, dry scrubbers, or the LIMB process to reduce sulfur emissions. In these cases the higher grain loading and higher dust resistivity produced by the sorbent material may cause a conventional ESP to no longer meet compliance. The use of the multi-stage technology can potentially improve the cost effectiveness of these strategies for mitigating acid precipitation caused by power plant sulfur emissions.

This paper has been reviewed in accordance with the U. S. Environmental Protection Agency's peer and adminstrative review policies and approved for presentation and publication.

INTRODUCTION

A number of electrostatic precipitators (ESPs), on electric power plants, are on the borderline of non-compliance. Often, because of these ESPs, plant operators are required to reduce load to maintain particulate emission standards. There are number of different causes for these poor performing ESPs. In the case of plants firing low sulfur coals, the predominate problem is high resistivity fly ash which produces back ionization and greatly reduces ESP performance. In the cases where high sulfur coals are utilized, ESPs may have problems which are due to undersizing, poor gas distribution, high gas velocity, or other detrimental causes. The Temperature Controlled Electrode Precharger (TCEP) has been investigated as one means of solving these problems. Tests on this device were performed at the EPA/DRI Valmont ESP Test Facility in Boulder, Colorado.

The TCEP is attractive because of its simplicity and ease with which it may be retrofit into an existing ESP. The major component of the device is a manifold of 6.1 cm (2 in.) pipes with inner-spaced corona electrodes. The precharger is installed upstream of one or more electrical sections of the ESP with the pipe manifold normal to the gas flow. It requires as little as 30.5 cm (1 ft) of space between eletrical sections for installation. Coolant may be passed through the pipes to cool the surface of the collecting electrodes to a temperature sufficiently low to prevent back corona. All the coolant is contained in the pipes; therefore, there is no mixing of the coolant and fly ash. The temperature of the pipe is always above the dew point so the fly ash remains dry. The precharger produces a high electrostatic field and high current density which charges the particles to a level which is higher than is possible in a conventional ESP. The result of the higher charge level is an increased migration velocity in the ESP with the net effect of increasing the effective specific collection area (SCA).

This device has been tested as the precharger in a two-stage ESP (Durham et al., 1984). In these tests, the precharger was installed upstream of parallel plate-plate collectors. The results of these tests showed that a higher collection efficiency could be obtained with this SCA than could normally be achieved with the 10^{12} ohm-cm resistivity fly ash that was being collected. However, there is an upper limit to the efficiency obtainable with even higher SCAs and higher efficiencies could be obtained only by lowering the gas velocity.

To find a more optimum collector, which would be effective at conventional gas velocities, the TCEP was tested as a retrofit device for a conventional wire plate ESP. These tests were performed in the pilot scale ESP at the Environmental Protection Agency's Industrial Environmental Research Laboratory, Research Triangle Park, North Carolina. In addition, tests were performed with the wires replaced with 0.95 cm (3/8-in.) diameter corona electrodes. Since the TCEP provides nearly all particle charging, anything that can provide higher field strength in the collector and still produce sufficient corona current should also improve ESP performance. This is the role of the large diameter corona wires. This is important for high resistivity applications since in this case very little corona current is necessary. SoRI recently reported good results with large diameter electrodes in a two-stage ESP (Bush et al., 1984).

TEST AT A TWO-STAGE ESP AT VALMONT TEST FACILITY

The TCEP was tested as the precharger in a two-stage ESP at the Valmont Test Facility in Boulder, Colorado (Durham, et al.,1984). In the collectors of the ESP, the corona electrodes were replaced with flat plates resulting in parallel plate-plate collectors. This configuration was used since it was desired to produce a high electric field and to completely eliminate corona current in the collector sections. The results of these tests are given in Figure 1 which shows the penetration (1-efficiency) plotted on a logarithmic scale as a function of the SCA. The numbers next to each data point represent, respectively, the number of charger sections, the number of collector sections, and the total gas flow in cubic feet per minute. The penetration was reduced significantly in going from one charger and one collector to two chargers and two collectors at 7 m^3/sec (15,000 acfm). The projected efficiency from these two data points would be greater than 99% when using four chargers and four collectors. However, as can be seen, the penetration was not significantly reduced when going to four chargers and four collectors at 7 m^3/sec (15,000 acfm). Further testing showed that, if the gas flow was reduced to 3.5 m^3/sec (7,500 acfm), the penetration was significantly reduced, and 99+% efficiency was obtained. The gas velocity for the reduced flow was 0.7 m/sec (2.3 ft/sec).

The results shown in Figure 1 and further testing verified that the primary cause of the inability of the two-stage ESP to obtain high collection efficiencies at the higher gas flow was caused by non-rapping reentrainment of the ash collected on the plates. In the case of the flat plate-plate collector, reentrainment is caused by insufficient corona current to provide the necessary clamping forces on the collected ash layer.

The testing at Valmont on the two-stage ESP showed that the TCEP functioned well. Even with the flat plate-plate collectors, the two-stage ESP was able to obtain 99.4% collection efficiency with an SCA of 45.5 sec/m (230 ft^2/1000 acfm) when collecting fly ash with an electrical resistivity of 10^{12} ohm-cm. Sufficient base line data were obtained on the TCEP to show that it charged and collected the high resistivity fly ash as expected. However, further work was needed to find a collector that would work efficiently at the higher velocities normally found in conventional ESPs.

TEST ON TCEP AS A RETROFIT FOR A CONVENTIONAL ESP

The tests were performed in EPA's Industrial Environmental Research Laboratory (IERL), Research Triangle Park, North Carolina. The ESP has four electrical sections of wire plate collectors each 4 ft long with 0.32 cm (1/8-in.) wires spaced 22.9 cm (9 in.) apart. The wires were removed from the first and third sections of the ESP. The corona support was used in these sections to power TCEP sections which were installed in the spaces between the first and second sections and the third

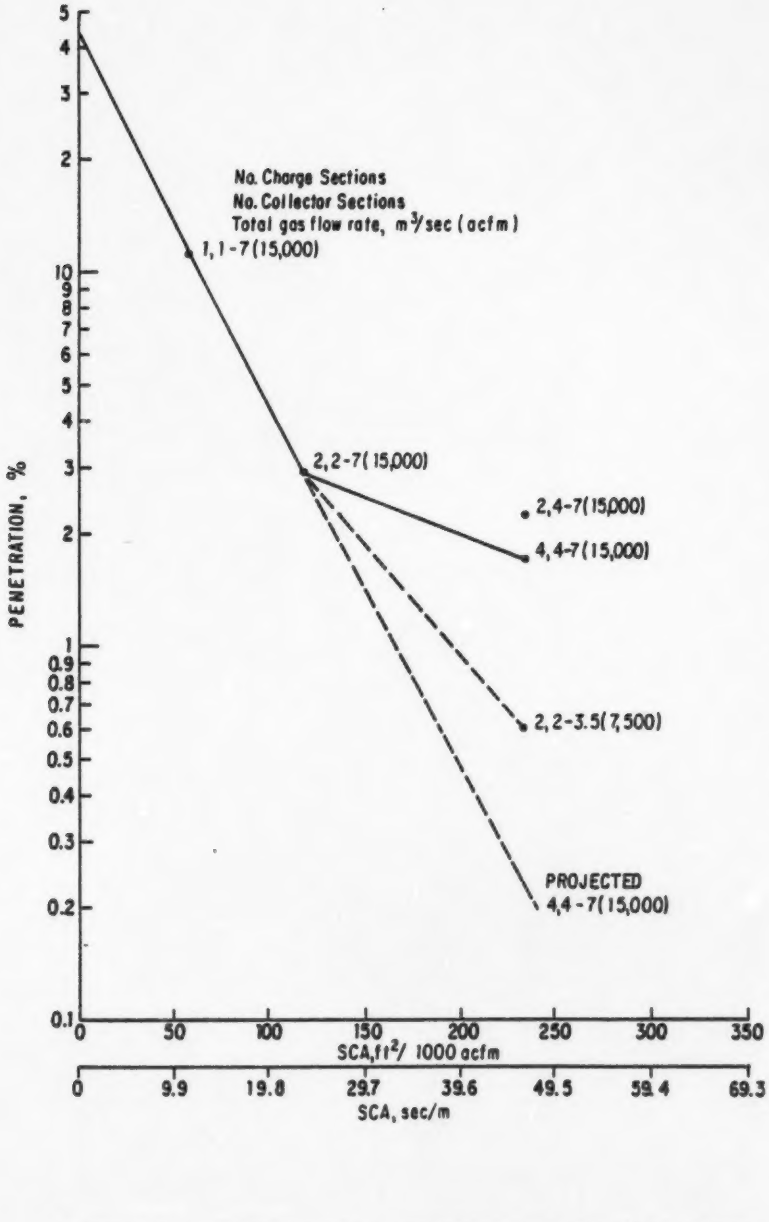

FIGURE 1. PENETRATION MEASURED IN VALMONT TESTS

and fourth sections. In the second series of tests, the corona electrodes were replaced with 0.95 cm (3/8-in.) rods. The test conditions and ESP configuration are summarized in Table 1. The TCEP installation is shown in Figure 2. This figure shows the ease with which the TCEP is installed between sections of the ESP.

TABLE 1. TCEP TESTS WITH CONVENTIONAL ESP AT EPA LABORATORY

TEST CONDITIONS

Temperature	148.9°C (300°F)
Gas Flow	0.47 m^3/sec (1000 acfm)
Moisture	4% volume
Ash Resistivity	9 x 10^{11} ohm-cm

ESP CONFIGURATION

Channels of Flow	One
Plate Spacing	25.4 cm (10 in.)
Wire Spacing	22.9 cm (9 in.)
Wire Size	0.32 cm (1/8-in.) 0.95 cm (3/8-in.)
Gas Velocity	1.5 m/sec (5 ft/sec)
Number of TCEPs	Two
ESP SCA	12.7 sec/m (64 ft^2/1000 acfm)

The ESP operating conditions and penetration measurements are shown in Table 2. As can be seen from this table, with very low current (~10μ A) in the wire plate sections of the ESP, the collection efficiency was approximately 96%. For the direct current tests with an average current of 610μ A, the average efficiency increased to 97%. When the two collector sections were pulsed (750 μA average current), the average collection efficiency increased to 98%. When the prechargers were both turned off and the ESP operated under pulse conditions, the collection efficiency dropped to 91%. The results with 0.95 cm (3/8-in.) corona electrodes show that even higher efficiencies are possible because of the resulting higher field produced by these electrodes.

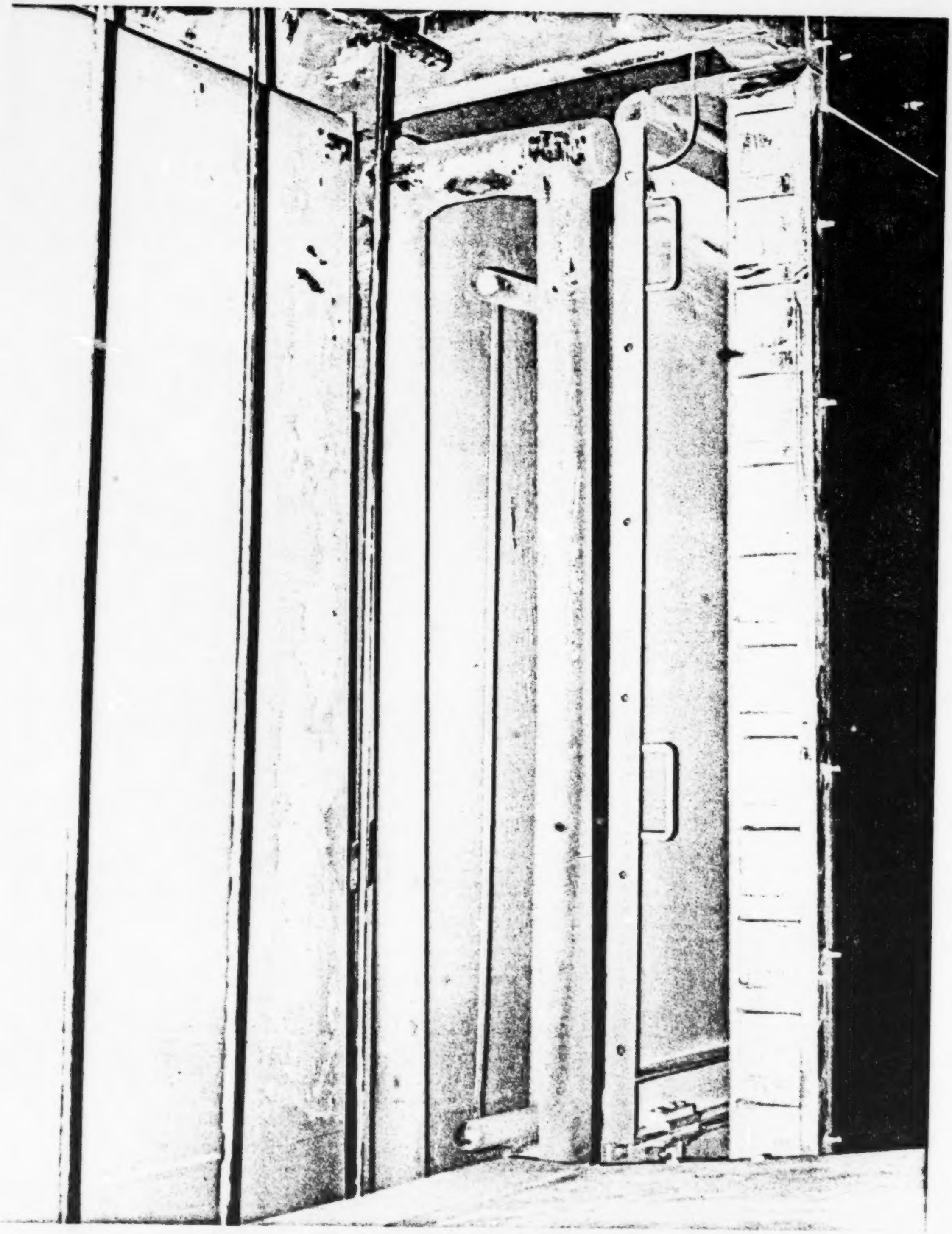

FIGURE 2. TCEP INSTALLATION AT EPA LABORATORY

TABLE 2. RESULTS OF TCEP AND CONVENTIONAL ESP TESTS AT EPA LABORATORY

Tests with 0.32 cm (1/8-in.) Discharge Electrodes
in the Collector Sections

	Direct Current		Pulsed
No. Tests	5	9	9
Ave. Collector Voltage, kV	32	35	32
Ave. Collector Current, μA	~10	610	750
Penetration	0.042	0.031	0.017
Efficiency, %	95.8	96.9	98.3
Penetration with TCEP off	---	---	0.093
Efficiency with TCEP off, %	---	---	90.7

Tests with 0.95 cm (3/8-in.) Discharge Electrodes
in the Collector Sections

No. Tests	4	4	---
Ave. Collector Voltage, kV	32	38	---
Ave. Collector Current, μA	~10	200	---
Penetration	0.016	0.008	---
Efficiency, %	98.4	99.2	---

The nature of the dust deposited on the collector plates of the last section during high efficiency operation is of interest. This is shown in Figure 3. The dust deposit was smooth and densely packed. As can be seen from Figure 3, rapping removed the dust in patches. These patches evidently separated from the plate in flake-like layers with little dust reentrainment. It appears that one role of corona current is to produce forces that help pack the deposited dust into a dense layer. When flat plate-plate collectors were used, the dust was more loosely deposited on the plate and reentrainment was more noticeable.

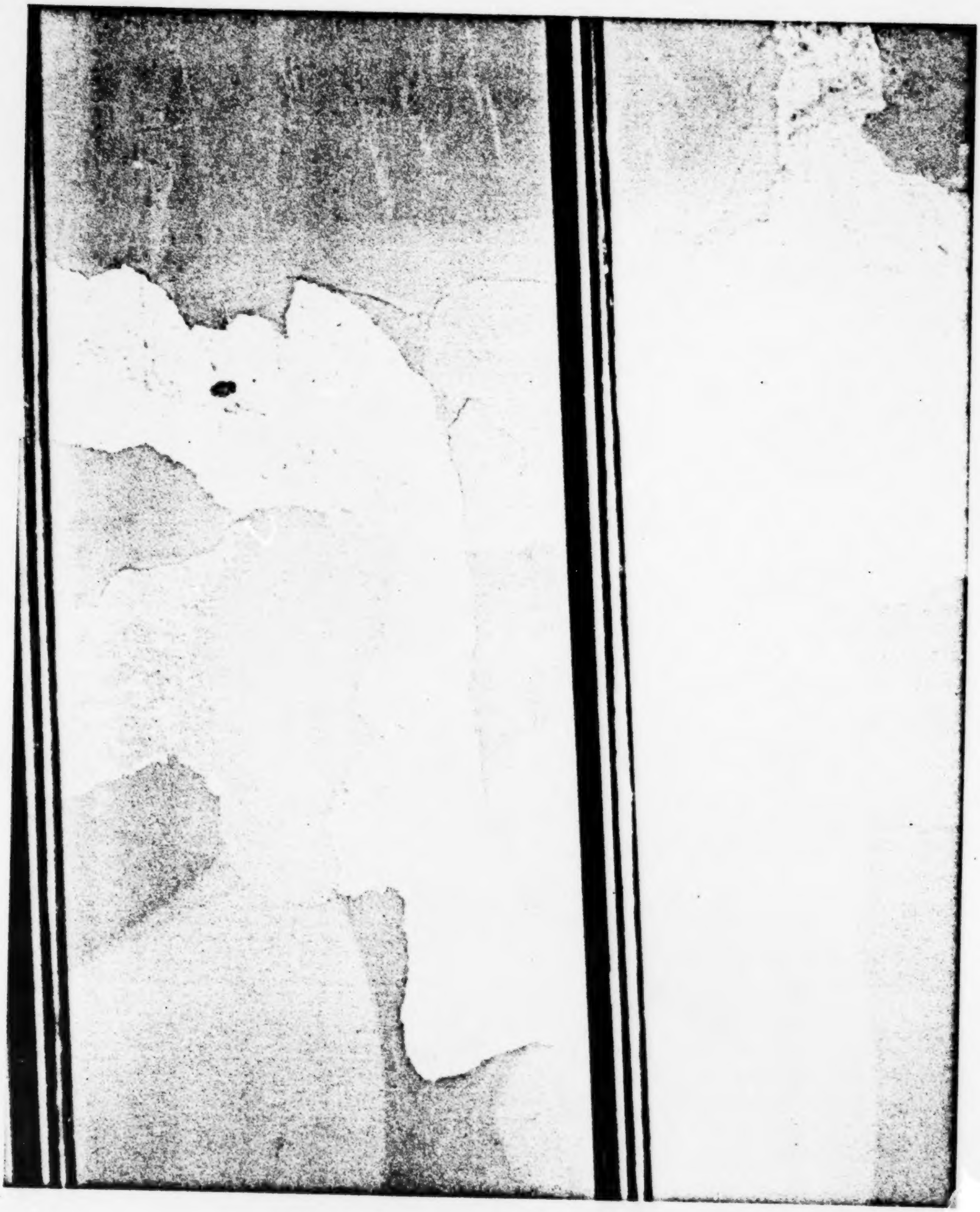

FIGURE 3. DUST DEPOSIT IN LAST STAGE OF ESP

ANALYSIS OF TEST RESULTS

The tests at Valmont, in the two-stage ESP utilizing flat plate-plate collectors, indicate that with high resistivity ash very little current is necessary to provide good clamping forces for the ash on the plates. This is indicated by the fact that 97% efficiency was obtained with a 120 SCA collector when utilizing two TCEPs. The clamping force in this case was provided solely by the charge on the particles themselves. This current is less than that found in a conventional ESP by two orders of magnitude. However, the ash resistivity is two orders of magnitude higher than that which is normally considered to be precipitable. Since the holding force is a function of the product of current density and ash resistivity, this very low current is sufficient for the high resistivity ash. However, as the dust is collected in the ESP, the current carried by the charged particles drops by another order of magnitude because of the lower dust concentration near the outlet section of the ESP. In the latter stages of the ESP, dust no longer carries sufficient current to provide the necessary clamping forces. These results show, that if the TCEP is used as a retrofit on a conventional wire plate ESP, a very low corona current needs to be maintained to provide good collection. In most cases this current can be provided without producing back corona; therefore, the TCEP followed by a conventional wire plate ESP should be very efficient at collecting high resistivity fly ash.

The tests at EPA utilizing a TCEP as a retrofit in a conventional ESP verify the predictions based on the Valmont test. The following calculations were made using the modified Duetsch equation that is used to size conventional ESPs for power plant applications:

$$\text{Eff} = 1 - e^{-(w\ A/V)^{1/2}} \qquad (1)$$

where: Eff = Efficiency
w = Migration velocity, m/sec
A = Collector area, m^2
V = Volume of gas treated, m^3/sec.

It is convenient to discuss the penetration, or amount of ash that exits the ESP, rather than the efficiency of the amount collected. Therefore, it is customary to define penetration as

$$P = 1 - \text{Eff} = e^{-(w\ A/V)^{1/2}} \qquad (2)$$

The 1/2 power in the exponent is used to account for different particle sizes and other non-ideal effects. The migration velocity is proportional to the charge on a particle and the electric field strength:

$$w \propto qE \tag{3}$$

where: w = Migration velocity, m/sec
q = Charge, C
E = Electric Field, V/m.

The predominate means of charging particles is due to a process which is also proportional to the electric field strength:

$$q \propto E. \tag{4}$$

In a conventional ESP, the field which produces charging is the same field that forces the charges to the plate. When a TCEP is retrofit into an ESP, two things are different than in a conventional ESP: first, the TCEP acts like an ESP and collects a portion of the ash; and second, the TCEP charges the particles which are then collected in the wire plate part of the ESP. Because the field in the TCEP is higher than that in the wire plate section, there is an increase in migration velocity as given by Equation (3). The net result is enhanced collection over that possible in the conventional wire-plate ESP. Table 3 summarizes the net effect of this enhanced collection for the operating conditions which were obtained at EPA. In this table "Wire-plate ESP following TCEP" refers to the collector section of the two-stage ESP in which collection is enhanced because the incoming particles are already charged.

TABLE 3

	SCA		E	w	Eff.
	sec/m	(ft^2/1000 acfm)	kV/cm	cm/sec	%
Unenergized ESP	12.7	64	—	—	50.0
Conventional Wire-plate ESP	12.7	64	2.76	45	90.7
TCEP Alone (2 sections)	1	5	5.16	157	71.0
Wire-plate ESP Following TCEP	12.7	64	2.76	84	96.1
Combination of TCEP and ESP	13.7	69	—	—	98.9
Conventional ESP Required for Above Efficiency	45.5	230	—	—	98.9

The higher field in the TCEP is due to the higher operating voltage and closer spacing of electrodes. The higher fields result in higher migration velocities, both in the TCEP and in the rest of the ESP. With the TCEPs, the collection efficiency of the wire-plate section is increased from 90.7% to 96.1%. The TCEPs themselves account for 71% collection. The combined efficiency after retrofit is one minus the product of the corresponding penetrations. The result is 98.9%. This is very close to that actually measured, as shown in Table 2. The results are consistent with ESP theory. The last line gives the SCA of a conventional ESP that would be required to obtain the same collection efficiency as the retrofit ESP. Thus, it can be seen that approximately one-third as much collector plate area is required in the retrofit ESP as would be required for the conventional wire-plate ESP without the TCEPs.

The test results to date are for high resistivity fly ash. Similar migration velocity enhancement can be expected for normal ash resistivity. In this case, the TCEPs may or may not require cooling, depending on the SO_3 level in the gas. Other operational problems such as poor rapping can reduce the enhancement obtainable in practice. However, it is clear that the TCEP offers the potential for relieving many of the problems that are presently experienced with poorly performing ESPs.

CONCLUDING REMARKS

The temperature-controlled electrode precharger (TCEP) has been referred to in previous articles as the Cooled Pipe Precharger or the Cooled Pipe Charger/Collector. These names were used to emphasize the main geometric features of the device and also to emphasize that, not only does the device charge particles but due to the high electric fields and high current densities, it is also a good collector. The new term TCEP was chosen because the temperature of the collector electrodes may be either above, the same as, or below that of the gas stream, depending on the application.

Figure 4 shows the means for retrofitting the TCEP in a conventional ESP. The pipe manifold is mounted in the space between electrical sections. Nearly all ESPs have sufficient space between sections for installing the manifold. The pipes are suspended from the top of the ESP, and appropriate high voltage feedthroughs are provided for suspending the corona electrode. The TCEP is installed through an opening which is cut into the side wall of the ESP so that the pipe manifold can be inserted between collector sections. When cooling is required, coolant is pumped through the pipes. A simple throttle valve maintains proper flow, and the coolant can be passed through the plant's evaporative cooling tower. The added heat load on the cooler is a fraction of 1%. No modifications need to be made on the rest of the ESP in many applications. However, additional enhancement of the effective SCA of the ESP may be obtained in many cases by using larger rod electrodes in the collector section. This is particularly true when collecting high resistivity fly ash.

REFERENCES

1984, Bush, P.V., Pontius, D.H. and Sparks, L.E., "Performance of Large-Diameter Wires as Discharge Electrodes in Electrostatic Precipitators," The Fifth Symposium on the Transfer and Utilization of Particulate Control Technology, Kansas City, MO, August 27-30.

1984, Durham, M.D., Rinard, G.A., Rugg, D.E. Carney, T., Armstrong, J., and Sparks, L.E., "Field Study of Multi-Stage Electrostatic Precipitators," The Fifth Symposium on the Transfer and Utilization of Particulate Control Technology, Kansas City, MO, August 27-30.

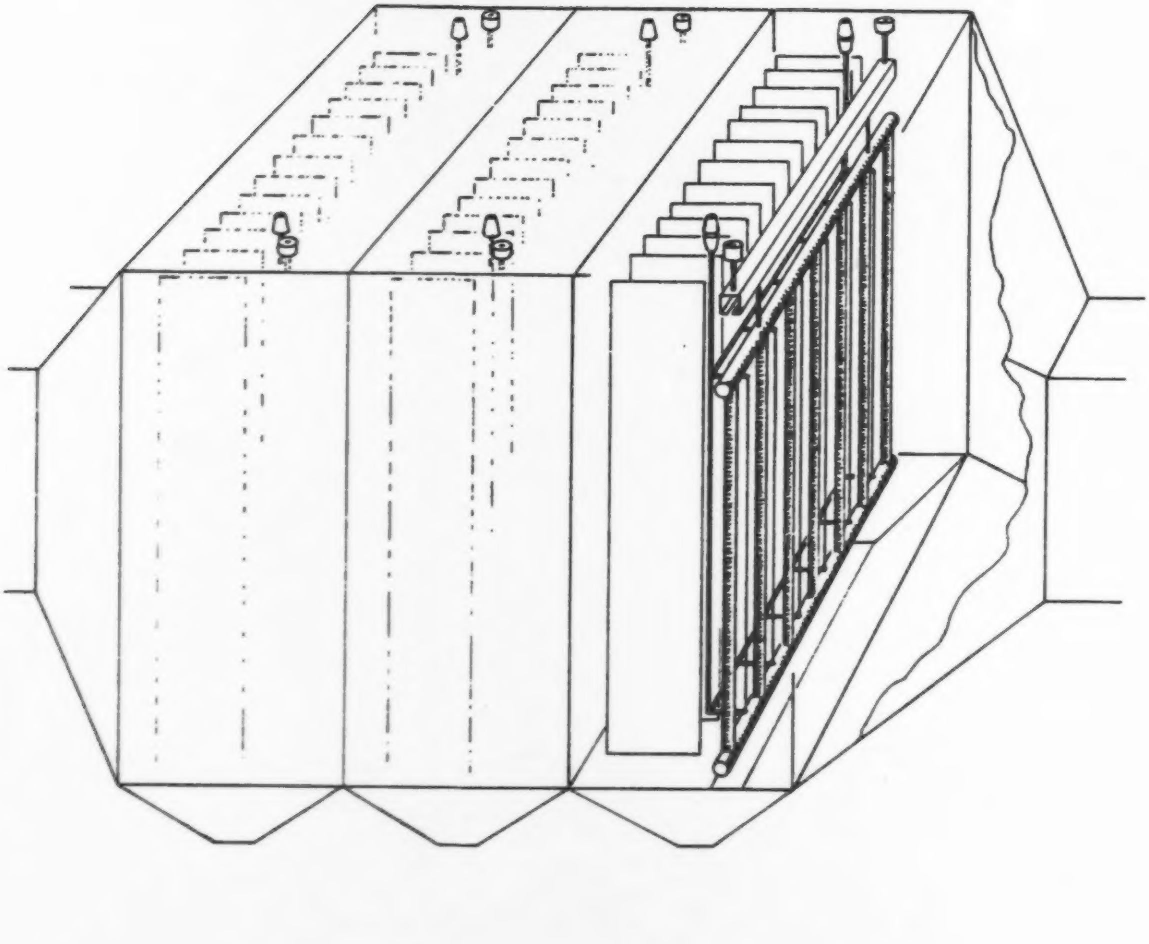

FIGURE 4. PROPOSED FULL SCALE TCEP RETROFIT

CERAMIC-MADE BOXER-CHARGER FOR PRECHARGING APPLICATIONS

by: Senichi Masuda, Shunsuke Hosokawa, and Shuzo Kaneko
Department of Electrical Engineering,
University of Tokyo
7-3-1, Hongo, Bunkyo-ku, Tokyo, Japan 113

ABSTRACT

A Boxer-Charger comprizing ceramic-made, high-performance, and compact-size ionizer units has been developed for back corona free percharging of high resistivity dust in electrostatic precipitation and electrostatic augmentation of fablic filters. The ionizer units consist of high purity alumina plates with tungsten corona electrodes on their surface and a tungsten-film induction electrodes embedded inside the plates (IS-panel ; ion source panel). A sharp pulse voltage with 200 - 500 ns duration time and -4 - -7 kV peak voltage produces very active surface streamers on the ceramic plates as an active plane-like ion source. The cost of a power supply for ion generation is greatly reduced owing to a reduced pulse voltage required, and yet a very satisfactory charging performance can be obtained.

The basic characteristics of ion generation and charging efficiency are confirmed to be very satisfactory for percharging applications. Tests are made in a laboratory precipitator with high resistivity flyash with up to 1.4 x 10^{13} ohm-cm resistivity. Their performance enhancement is especially remarkable in the two stage type precipitator when the ceramic-made Boxer-Charger is combined with the pulse-energized collection fields where no back corona takes place in the collection fields up to 2 x 10^{12} ohm-cm.

INTRODUCTION

The authors developed Boxer-Charger (1-4) for back corona free precharging of high resistivity dust, and novel ionizer panels made of high purity alumina (IS-panel ; ion source panel) (5). These two technology are combined to provide an improved type of Boxer-Charger. A pair of IS-panel ionizer units is spaced at 150 mm across the charging zone, and supplied with an a.c. low frequency voltage to produce a charging field. In synchronous to this a.c. voltage, a pulse voltage with 200 - 500 ns duration time and -4 - -7 kV peak voltage is alternately applied to one of these ionizer units between its corona and induction electrodes at an instant when the ionizer unit takes the negative crest of the a.c. voltage. Then the surface streamers are induced to produce an active plane-like ion source on the surface of the ionizer unit, from which copious negative ions are supplied. Thus, particles are charged in an a.c. field with negative ions from both sides, alternately. No back corona takes place as the negative charge accumulated on the dust deposit is eliminated by the streamer plasmas produced each cycle of the a.c. voltage. The thickness of the alumina layer between the corona and induction electrodes is only 0.5 - 1.0 mm. Hence the required pulse voltage for streamer generation is only -4 - -7 kV compared to -40 kV required in the double-helix type Boxer-Charger (3). Moreover, the surface streamers have a cleaning effect to keep the active surface of the ceramic plates free of dust contamination. As the result, a stable and satisfactory charging performance is obtained up to the dust resistivity as high as $r_d = 10^{13}$ ohm-cm. A two stage type laboratory precipitator comprizing this ceramic-made Boxer-Charger is tested, where comparison is made between the d.c. and pulse energization in the collection fields. A remarkable enhancement of the collection performance is obtained by the present Boxer-Charger as far as the pulse-energized collection field is used so that no back corona takes place. In this paper are reported these test results.

BASIC CHARACTERISTICS OF CERAMIC-MADE BOXER-CHARGER

IS-PANEL

Three different types of ceramic made IS-Panels as shown in Fig. 1 are used in this experiment. A high purity alumina ceramic sheet (92% purity) with only 0.5 - 1.0 mm thickness can provide enough electrical strength between the corona and the induction electrode even at an elevated temperature. Types I and II have fence-like corona electrodes. The capacitance between the corona and induction elctrodes are 300 pF (Type I) and 200 pF (Type II) in the non-corona condition. Type III has a zig-zag shaped corona electrode with 825 mm length, forming a transmission line against the film-like induction electrode with a surge impedance of approximately $Z_0 = 60$ ohm. But Z_0 differs very widely with the discharge condition.

Fig. 2 shows the light activity of pulse-induced surface streamers of these IS-Panels. A very uniform surface discharge occurs from the both sides of the strip-like thin corona electrode.

CIRCUIT DIAGRAM AND PULSE VOLTAGE WAVE FORM

Fig. 3 shows the circuit diagram of the ceramic-made Boxer-Charger. An a.c. main voltage, V_m, is applied between the two ionizer units, facing each other and spaced at $d = 15$ cm, and pulse voltage, V_p, is applied alternately to each unit between its corona and induction electrodes at an instance 1 ms ahead of its negative crest of V_m. This timing gives the best charging performance.

Fig. 4 shows the wave forms of the pulse voltage at the input of the IS-

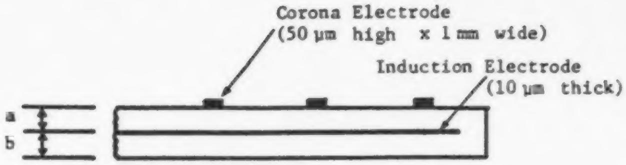

(a) Cross Section of IS-Panel
Type I and III : $a = 0.5$ mm, $b = 0.5$ mm
Type II : $a = 1.0$ mm, $b = 1.0$ mm

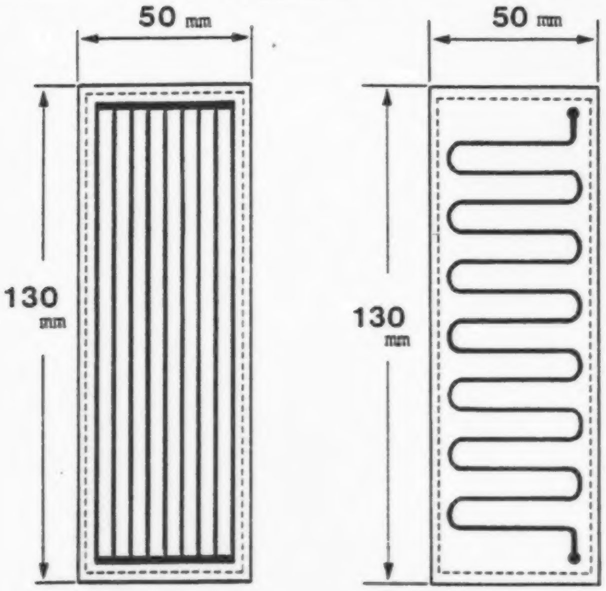

(b) Corona Electrode of Type I and II

(c) Corona Electrode of Type III

Fig. 1 IS-Panels Used

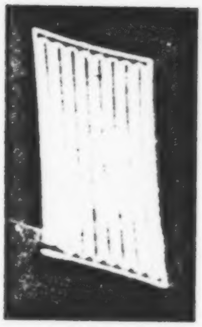

(a) Type I and II

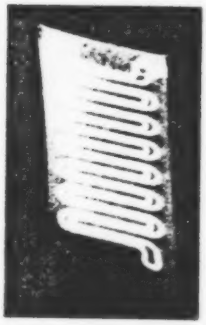

(b) Type III

Fig. 2
Light Activity of Surface Streamers

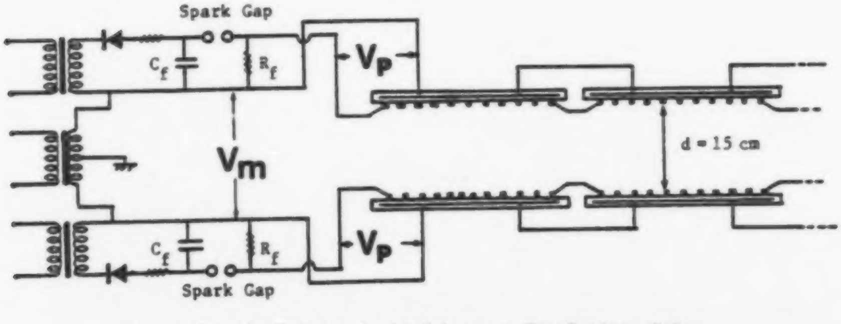

V_m : A.C. Main Voltage Applied between Two Ionizer Units
V_p : Pulse Voltage Applied between Corona and Induction Electrodes
C_f : Pulse Forming Capacitor
R_f : Pulse Forming Resistor

Fig. 3 Circuit Diagram of Ceramic-Made Boxer-Charger

panel and the light signal from the surface streamers detected by a photomultiplier. In Fig. 4(a) only a single IS-panel of Type I is used and the pulse voltage obtained is in a form of a triangle. This light signal starts at an instant when the pulse voltage reaches -3.6 kV. The light signal has a long tail due to the after glow of plasma. In Fig. 4(b), 6 IS-panels of Type I are used in series and the oscillating is enhanced in the voltage wave forms. The decay speed of the voltage oscillation can be altered by a pulse forming resistor, R_f, shown in Fig. 3. An intense light pulse in the rising phase of the first voltage wave is followed by three successive voltage waves. The surface streamer produced in the first voltage rise will stop when the local field at its front becomes too small to maintain its propagation. The successive weak streamers will be triggered at each phase of voltage change when the field induced by the accumulated charge and external field becomes strong enough to produce electron avalanche. At any rate the first streamer plays an essential role in producing enough ions (6).

IONIC CURRENT DENSITY

The ability of ionic current supply of the ceramic-made Boxer-Charger is measured at 50 Hz of the a.c. voltage using an apparatus of Fig. 5(a) which comprizes one IS-panel of Type I and represents one of the two ionizer units. The results obtained are shown in Fig. 5(b) where the ionic current density J, is plotted as a function of the space-averaged charging field strength, at its crest field strength, $E_0 = V_{m,max} / d$. The ionic current density obtained is about one-half of that obtained with the double-helix ionizer unit (3), with a concurrently longer charging time constant. But, it is still adequate for practical charging applications. The current density can be increased easily by using either a higher frequency of the a.c. voltage or multiple pulses instead of a single pulse at each half cycle.

SATURATION CHARGE

The saturation charge is measured using a steel ball with 3 mm in diameter suspended by an insulating string in the charging field between two IS-panels of a Boxer-Charger spaced at 15 cm. Measurement is made in room air with clean IS-panels, so that no back corona takes place. The steel ball after charging is brought into inside of a Faraday cage and its saturation charge, Q_{oo}, is measured. Fig. 6 shows the magnitude of Q_{oo} as a function of the average field strength at its crest E_0. Figs. 6(a), (b), and (c) are for the Types I, II, and III of IS-panels, respectively. The Pauthenier's theoretical curve is also depicted. The steel ball is located at the center and near one of the IS-panels (about 10 mm apart from its surface). It can be seen that the magnitude of Q_{oo} near the panel is always greater than the one at the center. This is because the local field near the IS-panel surface is enhanced by the ionic space charge. The saturation charge, Q_{oo}, follows the theoretical curve up to about $E_0 = 3.2 - 4$ kV/cm, but it indicates a sharp drop beyond this threshold. Fig. 7 shows the light activity of the pulse-energized IS-panel of Type I operated at $E_0 = 4$ kV/cm. Many bright spots are seen to appear at the edges of the panel. These are the positive parasitic coronas caused by the a.c. inter-electrode field in a half-cycle when this IS-panel is not excited by the pulse. Copious positive ions are emitted from these spots into the charging zone to neutralize the negative

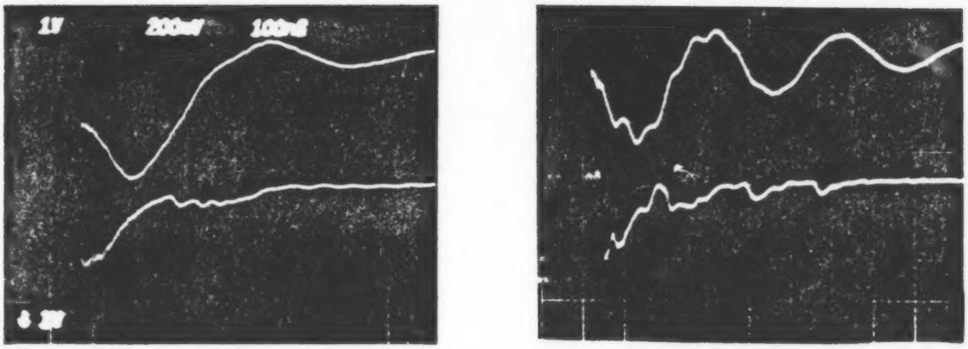

(a) 1 IS-Panel of Type I
(Triangle Pulse Voltage Wave Form)

(b) 6 IS-Panels of Type I
(Oscillating Pulse Voltage Wave Form
with Slow Decay)

Fig. 4 Pulse Voltage Wave Form and Light Signal Induced by Surface Streamers

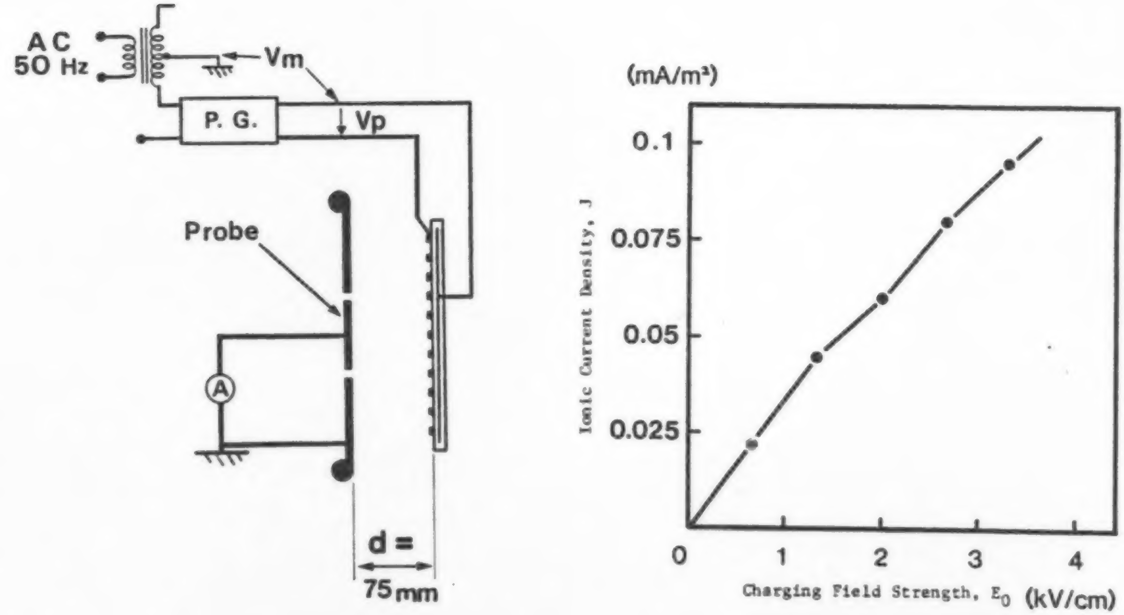

(a) Ionic Current Measuring System

(b) Effect of E_0 on Ionic Current Density

Fig. 5 Ionic Current Density of Ceramic-Made Boxer-Charger Comprizing a Single IS-Panel (Type I)

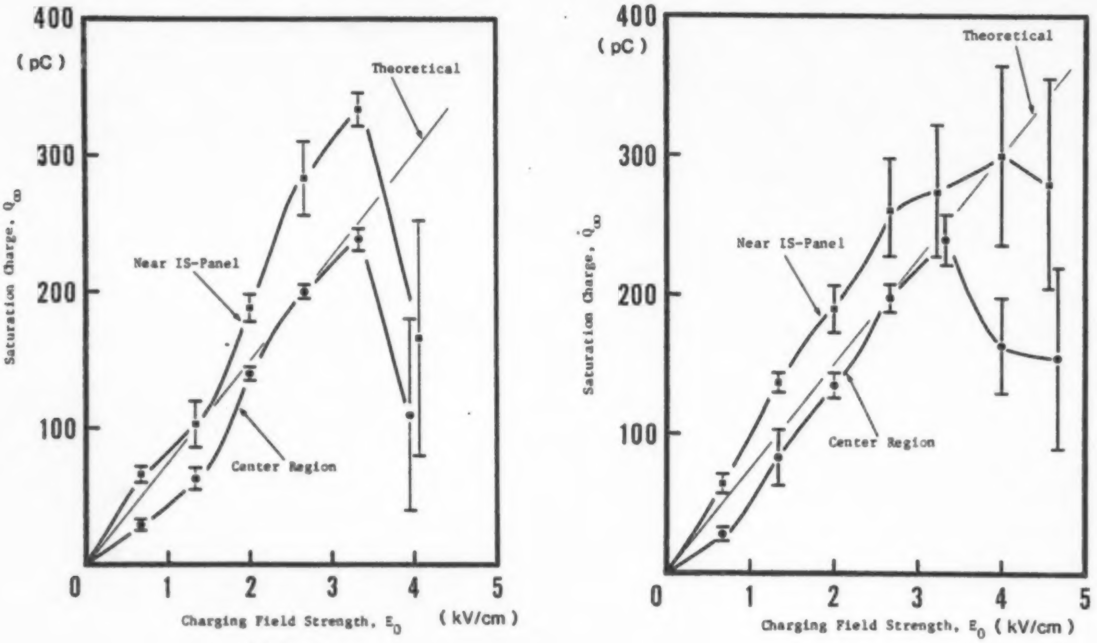

(a) Type I

(b) Type II

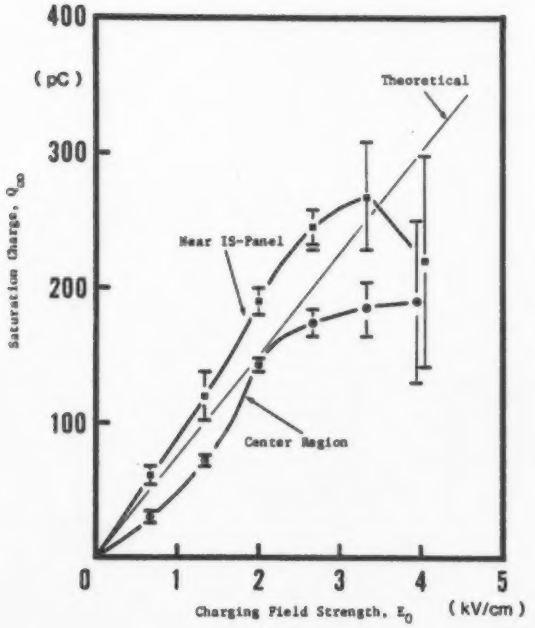

(c) Type III

Fig. 6
Effect of E_0 on Saturation
Charge of 3 mm Steel Ball

charge of the ball. The IS-panel of Type I with a thin ceramic plate and sharp edges of the corona electrode at its corners easily subjects to this charge limitting effect than the Types II and III. Hence, precautions are needed to avoid these parasitic coronas in the design of the IS-panel itself and the method of its assembly to form an ionizer unit.

It is discovered that the effective capacity between the corona and induction electrodes increases from its original value when streamers propagate as the effective area of the corona electrode increases. Hence, the inter-electrode capacity indicates a complicated time-dependent variation. In addition, the discharge produces a loss represented by a non-liner parallel resistance. Concurrently, Types I and II are the lumped constant pulse-loads with a non-liner capacitance and a non-liner discharge resistance. Type III is a distributed constant pulse-load with a non-liner surge impedance, and it allows the application of the pulse peaking technique (7) for a better exploitation of pulse energy. In this sense, Type III may have an inherent advantage as the ionizer unit of the pulse-excited Boxer-charger.

TESTS IN LABORATORY PRECIPITATOR

LABORATORY PRECIPITATOR

Fig. 8 shows the laboratory test precipitator in a race-track system used to test the charging performance of the ceramic-made Boxer-Charger for high resistivity flyash and its effect in enhancing an overall collection performance. The precipitator has the Boxer-Charger in two ducts (Fig. 9) and three two-duct collection fields. The carrier gas circulated is air and heated up to 150 °C. Two flyash samples I and II are used and their resistivity changed in the range of $9 \times 10^9 - 1.4 \times 10^{13}$ ohm-cm by changing gas temparature. The charge-to-mass ratio, Q/M, of the flyash sample is measured at the downstream of the Boxer-Charger by a suction type Faraday cage. The dust mass loading at the precipitator inlet, M_i, and the outlet, M_o, are also measured. Each collection field has 0.3 m in plate-to-plate spacing, 0.76 m in height, and 0.5 m in length in the gas flow direction. The total duct cross section is $0.46\ m^2$, and the total collection area of a single collection field is $1.52\ m^2$ with SCA = $4.03\ m^2/(m^3/s)$ at 0.82 m/s standard gas velocity. Each duct has three corona wires with 3 mm in diameter and 110 mm wire-to-wire spacing. The effective length of collection field is altered by energizing the first, the first and the second, and all of the three fields successively. Tests are made with two different energization modes of the collection fields : one being the dc-energization and another the pulse-energization on top of the dc bias voltage through a coupling condenser. The back corona severity in the collection fields are detected by bi-polar current probe (8), and expressed in term of a ratio of the back-corona-induced positive ionic current density to the negative one.

BOXER-CHARGER INSTALLED

Fig. 9 shows the ceramic-made Boxer-Charger in two ducts with 4 ionizer units in total, each having 6 IS-panels of Type II. The ionizer unit is carefully assembled to avoid the parasitic coronas. The light of the pulse-

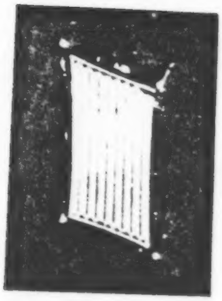

Fig. 7
Parasitic Coronas
at the Panel Edges

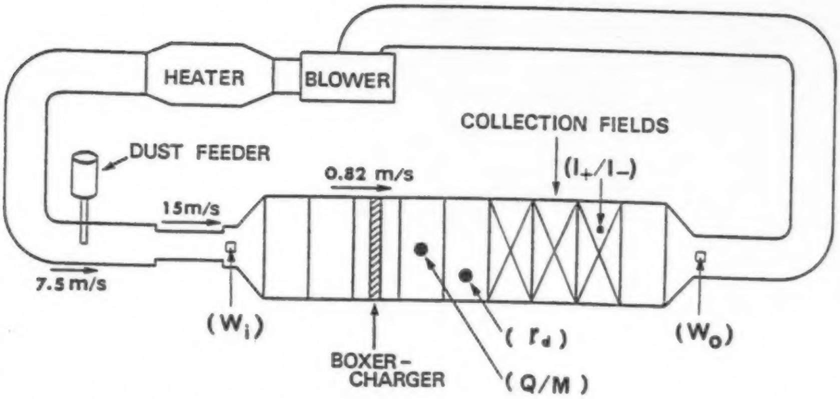

W_i : inlet dust loading, W_o : outlet dust loading
Q/M : charge-to-mass ratio of flyash
r_d : dust resistivity
I_-/I_+ : back corona severity measured by a bi-polar ion probe

Fig. 8 Race-Track System of Test Precipitator

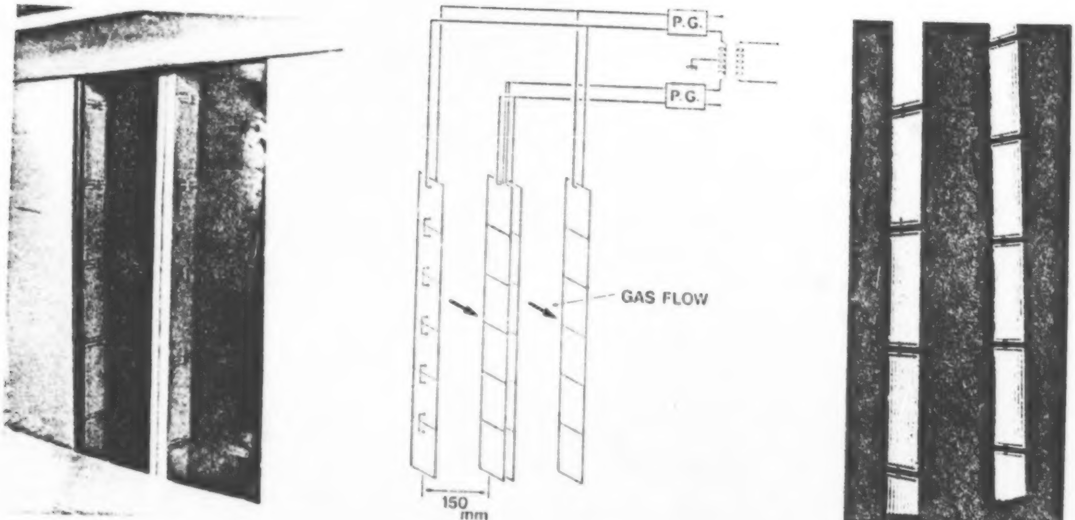

(a) Boxer-Charger (b) Arrangement of Ionizer Units (c) Light Activity

Fig. 9 Ceramic-Made Boxer-Charger Instrolled in front of Collection Fields

induced surface discharge is very uniform on all of the panels, as shown in Fig. 9(c).

Fig. 10 shows the charging performance of the Boxer-Charger measured at three different dust resistivity levels, $r_d = 9 \times 10^9$, 1×10^{12}, and 1.4×10^{13} ohm-cm obtained at T = 25, 80, 150 °C, respectively. The magnitude of Q/M rises at first proportionally with E_0, following the same curve independent of r_d. However, a sharp drop in Q/M begins to occur at $E_0 = 2.7$ kV/cm at T = 150 °C and $r_d = 1.4 \times 10^{13}$, and at $E_0 = 3.4$ kV/cm at T = 80 °C and $r_d = 1 \times 10^{12}$ ohm-cm. No back corona is observed to occur on the ionizer units even at T = 150 °C and $r_d = 1.4 \times 10^{13}$ ohm-cm, in contrast to the double-helix type Boxer-Charger. Hence, the drop in Q/M in the ceramic-made Boxer-Charger should be due to the temperature-enhanced parasitic coronas, and it could be corrected by an improved design of the panels to be reported separately.

Fig. 11 shows the dust contaminated surface of the IS-panels after a couple of hours operation without rapping or scraping. The dust deposit is remaining on the corona electrodes, but not on the region of the ceramic surface exposed to the surface streamers. This is because the surface streamers wipe off the dust deposit to keep the active region always clean.

PRECHARGING EFFECTS ON COLLECTION PERFORMANCE

Fig. 12 shows the collection performance in terms of dust penetration measured as a function of the effective length of collection field (number of series fields energized). The detailed test conditions are given in Table 1. The test results of collection performance in terms of Deutsch migration velocity, w, performance enhancement factor $H = w / w_0$ (w_0 = base line value with dc-energization alone), and back corona severity, I_+/I_- are tabulated in Table 2.

In Fig. 12(a) for $r_d = 5 \times 10^{11}$ ohm-cm the curve A represents the baseline data with the collection fields dc-energized, and the precharger off. Back corona is observed to occur in the collection fields with its severity $I_+/I_- = 8.2$ %, and the collection performance is the worst ($w_0 = 12.1$ cm/s). Back corona disappears by the pulse-energization of the collection fields, with a concurrent performance enhancement as shown by curve B (H = 1.5). The precharging in combination with the dc-energized collection fields produces an enhancement as shown by curve A', where the Boxer-Charger is operated at $E_0 = 2.7$ kV/cm and $V_p = -7$ kV with no parasitic coronas being produced and the collection fields with $V_{DC} = -42$ kV. The enhancement is remarkable in the first field ((B) in Table 2 ; H = 2.0), but it is lost in the succeeding fields with curve A' becoming parallel to curve A as a result of back corona ((A) in Table 2 ; H = 1.4). It can be seen that the combination of a single precharging with the dc-energized fields produces almost the same enhancement as that obtained by the pulse-energization alone. The highest performance enhancement can be obtained by the combination of the precharging and the pulse-energization of the fields (curve B' ; H = 2.0), where the enhanced charge of the particles are preserved, not subjecting to back corona. A very high enhancement obtainable in the first collection field ((B) in Table 2 ; H = 2.7) suggests the effectiveness of a successive use of the prechargers at every collection field. It should be noted that the repeat

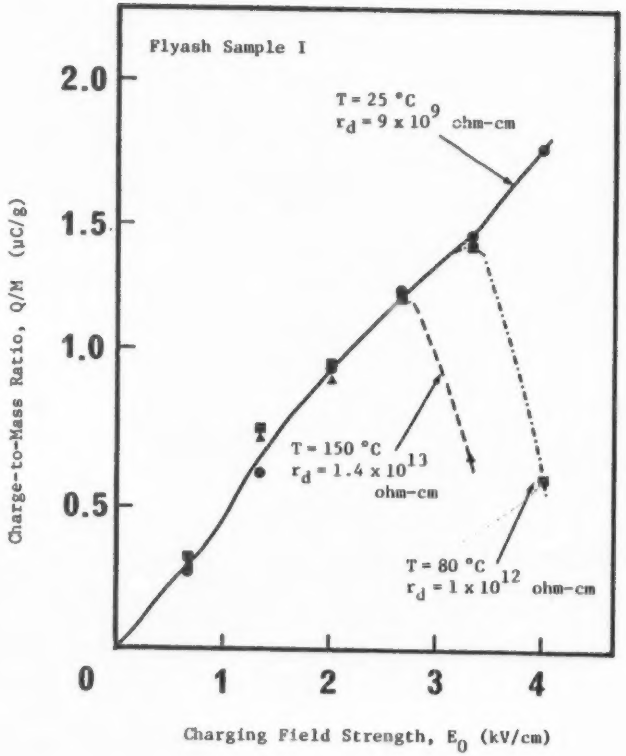

Fig. 10 Effect of E_0 on Charge-to-Mass Ratio of Flyash

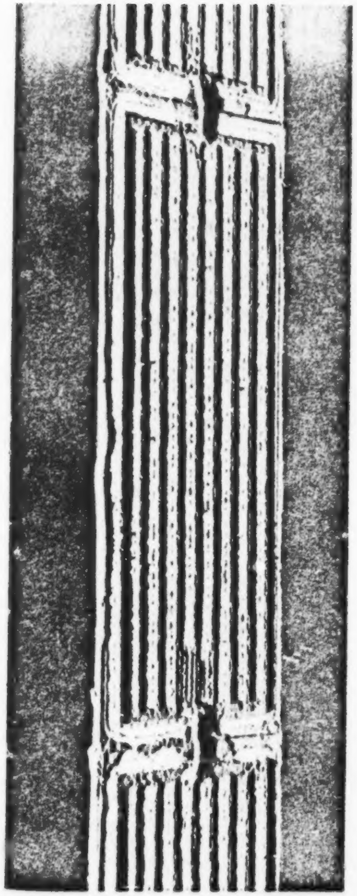

Fig. 11 Dust Diposition on IS-Panels

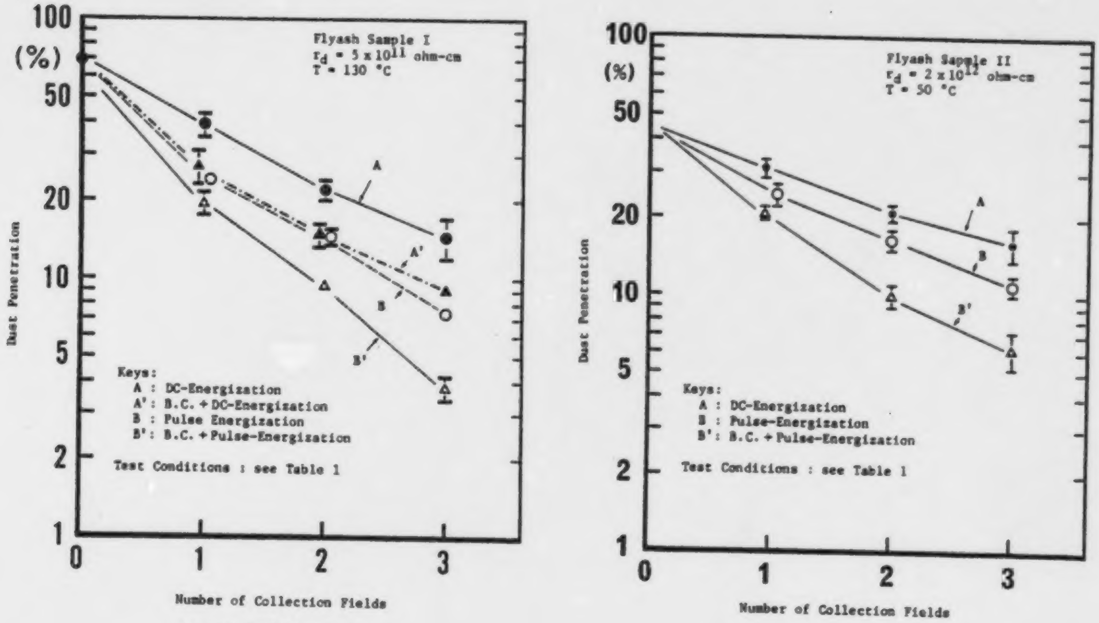

(a) High Resistivity Flyash

(b) Very High Resistivity Flyash

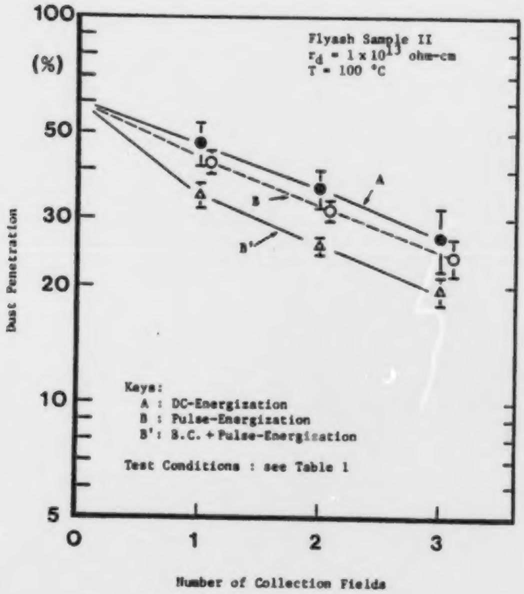

(c) Extremely High Resistivity Flyash

Fig. 12
Effects of Precharging on
Collection Performance

Table 1 Test Conditions

Dust Resistivity	DC-Energization	Pulse-Energization*
5×10^{11} ohm-cm (T = 130 °C)	$V_{DC} = -42$ kV $I = 0.2$ mA/m^2	$V_b = -35$ kV $V_p = -20$ kV $I = 0.06$ mA/m^2
2×10^{12} ohm-cm (T = 50 °C)	$V_{DC} = -38$ kV $I = 0.2$ mA/m^2	$V_b = -30$ kV $V_p = -32$ kV $I = 0.04$ mA/m^2
1×10^{13} ohm-cm (T = 100 °C)	$V_{DC} = -32$ kV $I = 0.2$ mA/m^2	$V_b = -22$ kV $V_p = -32$ kV $I = 0.04$ mA/m^2

* Pulse Voltage : rise time = 40 ns
half-tail = 180 ns
pulse repetion frequency = 50 Hz
Pulse voltage is superposed on top of a dc base voltage, V_b.

Table 2 Tests Results

Dust Resistivity (ohm-cm)	Operation Mode	Deutsch Migration Velocity			Back Corona Severity I_+/I_- (%)
		without B.C. (cm/s)	$^{(A)}$with B.C. (cm/s)	$^{(B)}$with B.C. (cm/s)	
5×10^{11} (T = 130 °C)	DC-Energization	$w_0 = 12.1$	17.0 (H = 1.4)	23.6 (H = 2.0)	8.2
	Pulse Energization	18.0 (H = 1.5)	24.1 (H = 2.0)	32.4 (H = 2.7)	0
2×10^{12} (T = 50°C)	DC-Energization	$w_0 = 8.6$	-------------	------------	2 - 15
	Pulse-Energization	11.6 (H = 1.4)	16.5 (H = 1.9)	19.5 (H = 2.3)	0 - 2
1×10^{13} (T = 100 °C)	DC-Energization	$w_0 = 6.6$	-------------	------------	27
	Pulse-Enwegization	7.6 (H = 1.2)	9.5 (H = 1.4)	14.1 (H = 2.1)	24

w_0 : base line Deutsch migration velocity in the dc-energized fields
H : enhancement factor in terms of w_0
(A) : overall Deutsch migration velocity enhanced by B.C.
(B) : Deutsch migration velocity in the first collection field enhanced by B.C.

Table 3 Performance Enhancement by Double-Helix Type Boxer-Charger

Dust Resistivity (ohm-cm)	Operation Mode	Deutsch Migration Velocity		
		without B.C. (cm/s)	$^{(A)}$with B.C. (cm/s)	$^{(B)}$with B.C. (cm/s)
$10^{11} - 10^{12}$ (T = 100 °C)	DC-Energization	$w_0 = 11.7$	18.0 (H = 1.5)	28.6 (H = 2.4)
	Pulse-Energization	19.1 (H = 1.6)	26.9 (H = 2.3)	34.1 (H = 2.9)

mode of precharging in the dc-energized collection fields and a single precharging mode in the pulse-energized fields provide the same enhancement factor (H = 2.0).

When $r_d = 2 \times 10^{12}$ ohm-cm (Fig. 12(b)), a weak back corona ($I_+/I_- = 0 - 2$ %) takes place even in the pulse-energized fields. Concurrently, the performance enhancement by the pulse energization becomes diminished (curve B ; H = 1.4). However, a combination of the Boxer-Charger produces a great improvement (curve B'; H = 1.9) which is about the same as in case of $r_d = 5 \times 10^{11}$ ohm-cm.. The performance by pulse-energization alone is not good in this case (w = 11.6 cm/s). However, when combined with precharging, the magnitude of w in the first collection field becomes as high as 19.5 cm/s ((B) in Table 2 ; H = 2.3).

In the case of an extremely high resistivity, $r_d = 1 \times 10^{13}$ ohm-cm (Fig. 12(c)), a severe back corona occurs not only in the dc-energized fields, ($I_+/I_- = 27$ %), but also in the pulse-energized ones ($I_+/I_- = 24$ %). As a result curves A and B come close to each other. Again in this case, the ceramic-made Boxer-Charger produces a substantial enhancement in the first collection field when combined with pulse-energization (curve B' ; H = 2.1). However this is lost in the second and the third fields. The overall enhancement is H = 1.4. The precharger must be inserted in front of each pulse-energized field in the case when a performance comparable to the base line w_0 of $r_d = 5 \times 10^{11}$ ohm-cm is required in this extremely high resistivity region.

The performance enhancement by the double-helix type Boxer-Charger is given in table 3 (2).It can be seen that the enhanacement obtained by the ceramic-made Boxer-Charger is the same as that by the double-helix one is achieved in the dust resistivity range of $r_d = 10^{11} - 10^{12}$ ohm-cm.

CONCLUSION

(1) A ceramic-made IS-panel (ion source panel) excited by a submicrosecond pulse with -4 - -7 kV peak voltage can be used as a satisfactory ionizer. The cost of the pulse generator is greatly reduced by the low pulse voltage required.

(2) The surface streamers take place at an instant when the pulse voltage reaches a certain threashold, and produce copious monopolar ions.

(3) The saturation charge given by the ceramic-made Boxer-Charger follows the Pauthenier's theory up to the a.c. field level when positive parasitic coronas begin to occur from the panel edges. They provide positive ions to the charging zone to greatly degrade the charging performance.

(4) No back corona is observed to occur even at $r_d = 1.4 \times 10^{13}$ ohm-cm. The performance degradation is only due to the parasitic coronas which occurs at a lower a.c. field level with increasing temperature.

(5) A dust deposition occurs only on the corona electrode, but not on the

active surface region subjecting to the surface streamers. As a result, this region is self-cleaned to maintain the discharge activity.

(6) A single-stage ceramic-made Boxer-Charger can provide the dc-energized precipitator with as good performance enhancement ($H = 1.4$) as the pulse-energization ($H = 1.5$) in the case when $r_d = 5 \times 10^{11}$ ohm-cm and back corona severity at dc-energization is less than $I_+/I_- = 10\ \%$. In the case when $r_d = 2 \times 10^{12}$ ohm-cm with the medium level back corona severity ($I_+/I_- = 2 - 15\ \%$ for dc-energization), a substantial performance enhancement ($H = 1.9$) occurs by the combination of the present Boxer-charger with the pulse-energized collection fields where $I_+/I_- = 0 - 2\ \%$. In the case of an extremely high dust resistivity level of $r_d = 1 \times 10^{13}$ ohm-cm, performance improvement is very small by the pulse-energization alone ($H = 1.2$). Even in this case, the present Boxer-Charger combined with the pulse-energized fields produces a substantial performance improvement ($H = 1.4$), especially in the first collection field ($H = 2.1$), but its effect becomes lost in the succeeding fields.

The work described in this paper was not funded by the U.S. Environmental Protection Agency and therefore the contents do not necessarily reflect the views of the Agency and no official endorsement should be inferred.

REFERENCE

1. Masuda, S., Mizuno, A., and Nakatani, H. Application of Boxer Charger in Electrostatic Precipitators, Conf. Rec. IEEE/IAS Annual Meet. 1979, pp.131-138
2. Masuda, S., Mizuno, A., Nakatani, H., and Kawahara, H. Application of Boxer-Charger in Pulsed Electrostatic Precipitator, Conf. Rec. IEEE/IAS Annual Meet. 1980, pp904-911
3. Masuda, S., Nakatani, H., Yamada, K., Arikawa, M., and Mizuno, A. Production of Monopolar Ions by Travelling Wave Corona Discharge, Conf. Rec. IEEE/IAS Annual Meet. 1981, pp.1066-1073
4. Masuda, S., and Nakatani, H. Distortion of Pulse Voltage Wave Form on Corona Wires due to Corona Discharge, Journal of Electrostatics 14(1983) pp.319-337
5. Masuda, S., and Kiss, E. Ceramic-Made Electric Curtain Devices and Their Applications, Invited Talk, Int. Conf. on Industrial Electrostatics (May 17 - 18, 1984. in Budapest, Hungary.)
6. Kaneko, S. Master Thesis, University of Tokyo, 1984.
7. Masuda, S., Hosokawa, S., and Nakatani, H. Corona Transmission Line Energized by Very Short Pulse Voltages as Applied in Electrostatic Precipitors, Conf. Rec. IEEE/IAS Annual Meet. 1983, pp.966-972
8. Masuda, S., Itagaki, T., Nohso, S., Tanaka, O., Hironaga, K., and Fukushima, N. Bipolar Current Probe for Diagnosing Full-Scale Precipitators, to be presented at EPA-EPRI 5th Symp. on Transfer and Utilization of Particulate Control Technology

PRECIPITATOR PERFORMANCE ENHANCEMENT WITH PULSED ENERGIZATION

by: E. C. Landham, Jr.
J. L. DuBard
Southern Research Institute
Birmingham, Alabama 35255

W. Piulle
Electric Power Research Institute
Palo Alto, California 94303

L. E. Sparks
Industrial Environmental Research Laboratory
U.S. Environmental Protection Agency
Research Triangle Park, North Carolina 27711

ABSTRACT

Research type pulsers were installed on each of three electrical fields of the EPRI pilot-scale precipitator at the Arapahoe Test Facility. Either fast risetime (1.5 μs) pulses or longer duration (140 μs) pulses of -25 kV amplitude could be superimposed on -50 kVDC at variable repetition rate up to 200 Hz. The precipitator collection efficiency, with and without pulsing during a single day, was measured on 35 days over a period of 3 months at both 9-inch* and 12-inch plate spacing. The fly ash resistivity was varied in the range of 5E10 to 5E12 ohm-cm. Omega-k enhancement factors for fly ash precipitators of SCA from 150 to 400 ft^2/kACFM, both full-scale and pilot-scale, correlate more closely with the baseline collection efficiency than with fly ash resistivity.

---

*Readers more familiar with metric units are asked to use the conversion factors at the end of this paper.

This paper has been reviewed in accordance with the U.S. Environmental Protection Agency's peer and administrative review policies and approved for presentation and publication.

INTRODUCTION

A number of techniques exist for improving electrostatic precipitator (ESP) performance when collecting high-resistivity fly ash. The options include modification of ash resistivity by chemical means, enlarging the size of the ESP, and the use of an unconventional ESP energization scheme. The last of these options is potentially the most convenient and cost effective but is also the least well understood.

One of the ESP electrical energization systems of interest at the present time is termed pulse energization. This technique involves superimposing a high voltage pulse on top of the conventional DC voltage waveform. Improved performance of utility fly ash precipitators with pulse energization has been demonstrated by several equipment manufacturers. In a retrofit application, the installation of pulse power supplies requires minimal time off line. The continuous operation of the pulse power supplies requires minimal supervision and maintenance. The attractive features of this new technology have been shadowed, however, by a limited ability to predict the performance of any particular ESP. Therefore, an independent study of precipitator pulsing has been sponsored by the Electric Power Research Institute and the U.S. Environmental Protection Agency.

Southern Research Institute was commissioned to design and construct pulse power supplies, and to test the effects of pulsing a pilot-scale ESP at the EPRI Arapahoe Test Facility in Denver, CO. The tests were designed to acquire systematic data on the effects of ESP pulsing, with wide variations in the fly ash resistivity and wide variations in the pulse power supply operation. A large quantity of pilot-scale ESP performance data are summarized and interpreted in this paper, and compared with a small quantity of full-scale ESP performance data.

EXPERIMENTAL FACILITIES

Commercial high voltage pulse power supplies fall into two categories. One type of pulse power supply uses spark gap switching in the high voltage circuit and produces a narrow pulse with a fast risetime. The other type uses a string of thyristors to switch the pulse and produces a wide sinusoidal pulse waveform. One of the project objectives was to test both types of commercial pulse waveforms. The pulse power supply that was constructed for the pilot-scale precipitator at the Arapahoe Test Facility uses a thyratron switch in the high voltage circuit. In a research application, this circuit design has the advantage of a widely variable pulse waveform (by switching resistors and inductors in the pulse-forming network) in order to simulate the physical effects of both types of commercial pulse waveforms. The research pulse power supply can produce a narrow pulse with a fast risetime (1.5 μs) or a slower pulse of longer duration (140 μs). Pulses of -25 kV maximum amplitude can be superimposed on a maximum DC voltage of -50 kV, at pulse repetition rates continuously variable up to 200 Hz. A separate pulse power supply was installed on each of the three identical electrical fields of the pilot-scale precipitator. The pulse waveforms were recorded with calibrated, frequency-compensated voltage dividers and a digital oscilloscope.

The pilot-scale precipitator receives flue gas at about 300°F from Arapahoe Unit 4 of the Colorado Public Service Company. The precipitator handles a nominal gas flow of about 3500 ACFM, at a nominal specific collecting plate area (SCA) of 400 ft^2/kACFM with 9-inch plate spacing. The collecting plates can be set at 9-inch spacing with four parallel gas passages, or at 12-inch spacing with three parallel gas passages. Both configurations were tested. The discharge electrodes were 0.115-inch diameter wires at 9-inch spacing on a harp frame.

Various low-sulfur western subbituminous coals were burned in Arapahoe Unit 4 on varying schedules during the test program. Therefore, the precipitator collection efficiency was measured both with and without pulsing on each of 35 test days over a period of three months. The precipitator electrodes were not rapped during tests. Measurements of collection efficiency were correlated with in situ measurements of fly ash resistivity and with the precipitator electrical operating points. In addition to continuous monitoring of the outlet flue gas opacity, the inlet and outlet mass loadings were measured with mass trains and with cascade impactors. A point-plane probe was used for in situ measurements of the fly ash resistivity by the spark method. An SO_3 injection system was installed on the inlet flue gas duct in order to vary the fly ash resistivity over the range of 5E10 to 5E12 ohm-cm.

PULSER OPTIMIZATION

Some controversy exists over the optimum DC voltage level for pulsed operation. One theory holds that a DC voltage which is below corona onset may serve to reduce back corona and improve ESP performance. As a test of this theory, the ESP outlet opacity was used as a measure of ESP performance while the pulse rate was varied for two levels of DC energization. The results are displayed in Figure 1. In this case, the high DC level performed much better than the low. For the low level, the DC voltage was set immediately below corona onset; while for the high level, the DC voltage was adjusted to the maximum value without sparking. All performance tests of the ESP were performed with a high DC level to maximize the ESP collection efficiency.

Further measurements of the outlet opacity were used to evaluate the optimum pulse rate for both pulse types. The results, displayed in Figures 2 and 3, indicate that the best ESP performance with both high and moderate resistivity fly ash occurred at repetition rates below about 50 Hz. The ESP performance either degraded or did not improve beyond that frequency. The figures also demonstrate that there was no apparent difference in the effect of the two pulse types, with either high or moderate resistivity ash.

Outlet opacity was measured again to determine if a relationship existed between the location in the ESP of the pulsed electrical field and the pulse rate at which optimum ESP performance was obtained. Figure 4 shows the results of a test where the pulse rate in only one field (either inlet or outlet) was varied, while the other fields were pulsed at 50 Hz. The data suggest that a higher pulse rate in the inlet field and a lower rate toward the outlet might be advisable. Since the range of optimum pulse rates for both inlet and outlet fields coincided at 50 Hz in the pilot-scale ESP, the performance tests were conducted with that rate in all three fields. Although high DC voltage levels and fairly low pulse rates produced the best performance at Arapahoe, these parameters should be optimized for each installation.

ESP PERFORMANCE

Extensive tests of the performance of the ESP with and without pulsing were performed at the optimum operating conditions. The tests were conducted with several coals and several levels of ash resistivity to simulate various coal types and levels of ESP performance degradation.

OPACITY

The most dramatic illustration of the effects of pulse energization is observed with the outlet opacity measurements. Figure 5 shows the result of pulsing when the baseline ESP performance was very poor. The ash resistivity at this time was 2.8E12 ohm-cm, and the baseline efficiency of the ESP was 82.7%. When the ash resistivity was reduced and the baseline efficiency was improved with SO_3 conditioning, the results were significant but less impressive. Figure 6, taken with 3.3 ppm SO_3 added, indicates that some improvement was gained with an ash resistivity of 2E11 ohm-cm and a baseline efficiency of 97.1%. When the ash resistivity was reduced to 2E10 ohm-cm with the addition of 15 ppm SO_3, no change in opacity or efficiency was observed due to pulsing.

COLLECTION EFFICIENCY

The primary method of evaluating the change in ESP performance due to pulsing was measurement of the total mass collection efficiency. The measurements were made by sampling simultaneously at the ESP inlet and outlet with EPA Method 17 mass trains. Measurements were performed at various levels of ash resistivity and baseline collection efficiency. The data have been averaged into six groups according to the baseline efficiency, as shown in Table 1. Comparison of the collection efficiency data with and without pulsing suggests a trend. As the baseline efficiency drops, the pulsed efficiency drops as well, but the improvement in performance due to pulsing increases. In order to interpret the ESP performance, the data are analyzed with the Matts-Ohnfeldt equation.

The Matts-Ohnfeldt equation provides a simple empirical method of describing the performance of an ESP. The equation takes the form

$$P = 100 \exp [-(\omega_k \ SCA)^k], \qquad (1)$$

where

P = ESP total mass penetration (%)
ω_k = effective migration velocity (m/s)
SCA = A/V ($m^2/m^3/s$)
k = 0.4 to 0.6 (assumed to be 0.5 here)
V = gas volume flow (m^3/s)
A = total ESP plate area (m^2)

From (1) the effective migration velocity can be calculated. This provides a measure of the ESP performance that is approximately independent of ESP size.

$$\omega_k = (V/A)[\ln (100/P)]^{1/k} \quad (2)$$

The performance improvement due to pulsing can be expressed as a ratio of the effective migration velocities with and without pulsing. This is termed the effective migration velocity enhancement, or omega-k enhancement, given by

$$\omega_k(\text{pulsed})/\omega_k(\text{baseline}). \quad (3)$$

Application of this technique to the ESP performance data can be seen in the last column of Table 1. From this analysis it is apparent that, as the baseline efficiency decreases, the omega-k enhancement due to pulsing increases.

It would be desirable to develop a relationship between the resistivity of the fly ash being collected and the omega-k enhancement expected with pulsing. An attempt to do this is illustrated in Figure 7, which plots the omega-k enhancement against the measured values of fly ash resistivity. Several problems are observed with this presentation of the data. The scatter in the data increases rapidly with increasing resistivity, and the data obtained at 12-inch plate spacing lie in a separate group. Furthermore, the fitted curve, Correlation A, does not reflect the fact that the ESP performance improvement due to pulsing approaches zero at fly ash resistivities in the 2E10 ohm-cm range. It appears that factors other than the in situ fly ash resistivity must be taken into account.

A tighter and simpler correlation of the mass train data is found upon plotting the omega-k enhancement against the baseline percent penetration. The pilot-scale data are plotted in this way as the solid symbols in Figure 8. In this method of data correlation there are no systematic differences between the data obtained at 9-inch and 12-inch plate spacing, nor between the data obtained with a fast pulse and a long pulse. A linear least-squares fit and its 90% confidence interval are superimposed on the pilot-scale ESP data. The fitted line is denoted Correlation B.

The open symbols in Figure 8 represent full-scale precipitator performance data gleaned from the literature. The full-scale data come from tests of the pulse power supplies of several different commercial manufacturers in the United States, over a time period of 7 years. Each of 17 full-scale data points is detailed in Table 2. The calculations of omega-k and the omega-k ratio, in Table 2, use k = 0.5 in the Matts-Öhnfeldt equation. It is apparent that the full-scale data exhibit a simple correlation with baseline percent penetration similar to that of the pilot-scale data, but with a lower slope. A least-squares fit to the full-scale data is denoted Correlation C.

Correlation B (Pilot-Scale Data)

$$\omega_k/\omega_{k,dc} = (1.34 \pm 0.32) + 1.25 \log_{10} P_{dc}. \qquad (4)$$

Correlation C (Full-Scale Data)

$$\omega_k/\omega_{k,dc} = (1.14 \pm 0.13) + 0.78 \log_{10} P_{dc}. \qquad (5)$$

The lower slope for the full-scale data correlation probably results from rapping reentrainment and a variety of electrical and mechanical defects that are likely to exist in a full-scale precipitator -- defects which pulsing cannot fix. By comparison, the pilot-scale precipitator was put in good operating condition for this project, and the electrodes were not rapped during tests.

Another relationship between pulsed and baseline ESP performance can be seen in Figure 9. In this figure the baseline penetration is plotted versus the pulsed penetration (reduced penetration). Careful inspection of the full-scale data indicates that, at baseline efficiencies below 98%, pulsing should be expected, on the average, to produce a factor of 2 reduction in the penetration. This assumes, of course, that the only problem with the ESP performance is poor electrical operating conditions due to high-resistivity fly ash. In using Figure 9, care should be exercised to note the upper 90% confidence limit when estimating the improvement in performance of a particular ESP.

ESP ELECTRICAL CHARACTERISTICS

For an electrical energization technique to modify collection efficiency, it should change the electrical conditions in the ESP. With AC coupling, the pulses provide no time-average electrical power input to the ESP. Therefore, the influence of the pulser is observed primarily in its effect on the relationship between the DC voltage and current. Figure 10 illustrates how the ESP secondary voltage and current change with varying pulse rate. As the pulse rate is increased, higher currents are observed at the same voltage. This effect could allow the voltage and current values to be customized to a particular application. However, this is not believed to be the cause of the improved ESP performance. Other data from this study indicate that the primary mechanism of performance improvement with pulsing is improved distribution of corona power. More uniform distribution of the ESP current tends to reduce the "hot spots" of high current density which produce intense back corona sites in a high-resistivity ash layer. Support for this explanation is obtained from Figure 11, a pair of voltage-current curves taken with and without pulsing during operation with high-resistivity ash. The curve obtained without pulsing indicates that back corona began around 0.5 nA/cm^2. The corona current input to the ESP above that level probably did not contribute greatly to improved performance. In comparison, the curve measured with pulsing indicates that severe back corona was not present, and that all the current input was useful in charging and collecting particles. Even though the average voltage was reduced somewhat during pulsing, the increase in useful current density more than compensated for that fact. Precipitator performance data obtained at the same time as the V-I curves in Figure 11 showed that the collection efficiency increased from 93.8% to 98.1% with pulsing. The outlet flue gas opacity dropped from 40% to 21%.

CONCLUSIONS

Pulse energization improved the performance of all precipitators studied, with the exception of the pilot-scale ESP when using high levels of SO_3 conditioning. The performance improvement appears to be related to the baseline efficiency of the ESP, with more benefit gained at lower baseline performance (< 98%). However, it does not appear that pulsing can improve efficiency more than other techniques such as SO_3 conditioning. The evidence is that the use of a pulser in addition to flue gas conditioning would not be appropriate. In fact, pulsing cannot improve many conditions which may limit the performance of a full-scale ESP. Use of pulsing should be based on a clear understanding that an ESP is in good mechanical condition, and that the major limitation to the performance of the ESP is degraded electrical operation caused by high-resistivity fly ash.

The data on both pilot-scale and full-scale fly ash precipitators that have been studied in this project indicate that the primary mechanism of precipitator performance improvement with pulsing is simply the more uniform corona discharge. The technology appears to be equally effective on both cold-side and hot-side precipitators and at both 9-inch and 12-inch plate spacing. The two pulse waveforms tested on the pilot-scale ESP were equally effective. No systematic differences were observed between the performance of the various commercial pulsers on the full-scale precipitators.

METRIC EQUIVALENTS

Readers more familiar with metric units may use the following to convert to that system.

Nonmetric	Multiplied By	Yields Metric
°F	5/9 (°F-32)	°C
ft^2	0.0929	m^2
ft^3	28.32	liters
in.	2.54	cm

TABLE 1. BASELINE AND PULSED ESP PERFORMANCE AVERAGED INTO SIX RANGES

Baseline Efficiency Range	Baseline Efficiency %	Pulsed Efficiency %	Omega-k Enhancement
99+	99.49	99.61	1.09
98 - 99	98.45	99.51	1.65
97 - 98	97.45	99.25	1.80
95 - 97	96.10	99.16	2.21
90 - 95	93.01	98.40	2.43
80 - 90	84.79	97.55	3.88

TABLE 2. PERFORMANCE TESTS OF FLY ASH PRECIPITATORS WITH COMMERCIAL PULSE POWER SUPPLIES

Test Date	Pulse Type	SCA, ft^2/ kACFM	Fly Ash ohm-cm	Baseline P_{dc}, %	Omega-k, dc, ft/s	Ratio $\omega_k/\omega_{k,dc}$
1976[a]	Fast	370	5E11	4.30	0.45	1.65
1979[b]	Fast	183	5E10	3.00	1.12	1.50
	Fast	176	5E10	3.39	1.08	1.70
1980[c]	Fast	272	1E13	13.68	0.24	1.99
	Fast	270	1E13	15.40	0.22	2.11
1980[d]	Fast	326		3.33	0.59	1.49
	Fast	312		1.76	0.87	1.46
	Fast	329		1.82	0.81	1.23
	Fast	304		0.80	1.28	1.05
1980[d]	Long	347		3.67	0.52	1.53
	Long	336		0.88	1.11	1.18
	Long	330		2.25	0.73	1.41
	Long	347		1.88	0.76	1.29
	Long	339		2.01	0.75	1.26
1983[e]	Long	230	1E12	3.43	0.82	1.49
	Long	230	1E12	3.43	0.82	1.62
	Long	230	1E12	3.43	0.82	1.61

a) P. L. Feldman and H. I. Milde. Pulsed Energization for Enhanced Electrostatic Precipitation in High-Resistivity Applications. In: Symposium on the Transfer and Utilization of Particulate Control Technology. Volume I. EPA-600/7-79-044a (NTIS PB295226). February 1979.

b) K. S. Kumar, P. L. Feldman, H. I. Milde, and C. Schubert. The Results of First Full-Scale Utility Demonstration of Pulsed Precipitation. IEEE/IAS Annual Meeting. Cleveland, OH, 1979.

c) P. L. Feldman and P. Aa. Operating Results from the First Commercial Pulse Energization System to Enhance Electrostatic Precipitator Performance. American Power Conference. Chicago, IL, 1981.

d) J. P. Gooch, G. H. Marchant, Jr., J. L. DuBard, and J. R. McDonald. An Evaluation of Pulse Energization on a Hot-Side Precipitator. EPRI CS-2634. Final Report of Project 1868-2. November 1982.

e) Private communication from Florida Power Corporation.

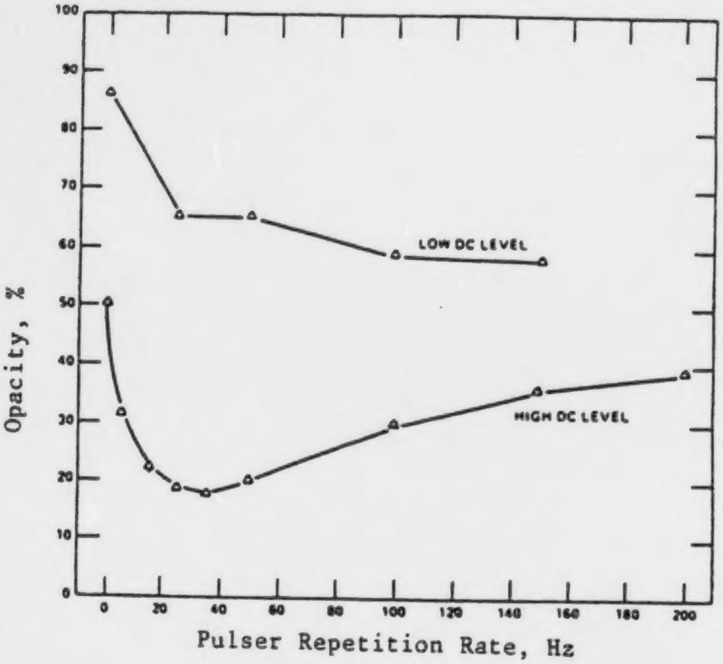

Figure 1. Outlet flue gas opacity, measured with 9-inch plate spacing and fly ash resistivity about 2E12 ohm-cm, using fast pulses with high and low dc voltage levels.

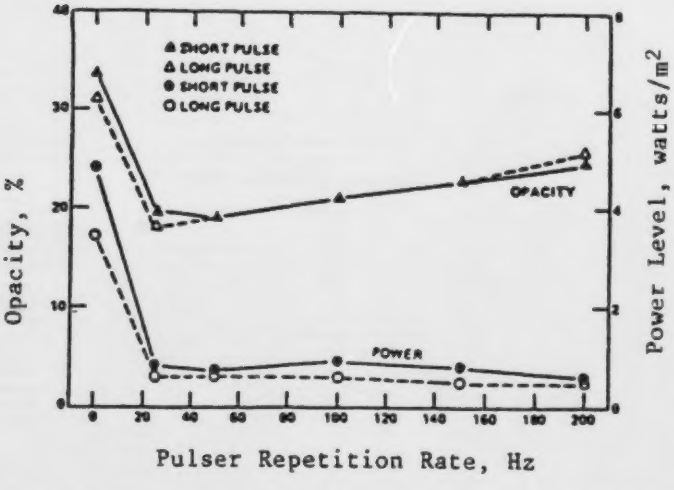

Figure 2. Time-average electrical power input and outlet flue gas opacity, measured with 9-inch plate spacing and fly ash resistivity about 2E12 ohm-cm.

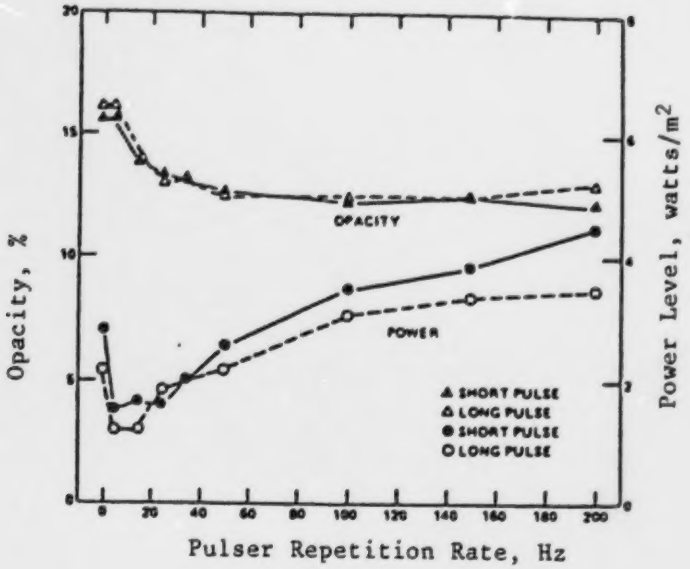

Figure 3. Time-average electrical power input and outlet flue gas opacity, measured with 9-inch plate spacing and fly ash resistivity about 2E11 ohm-cm.

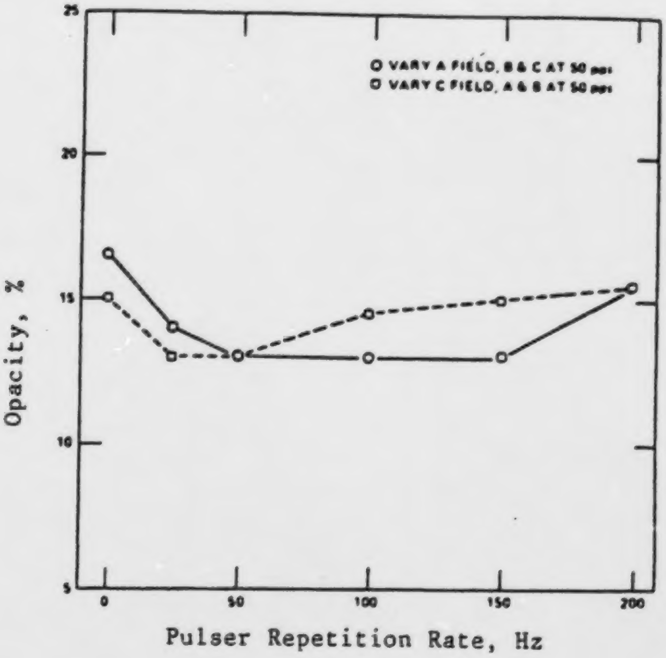

Figure 4. The variation in outlet flue gas opacity with varying pulse rate in the inlet field and in the outlet field.

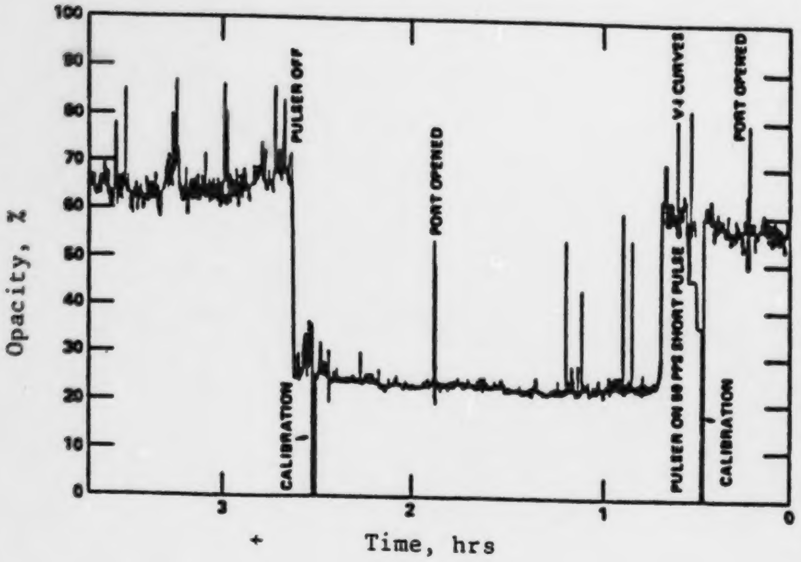

Figure 5. Chart recorder trace of outlet opacity, with and without pulsing, with no SO_3.

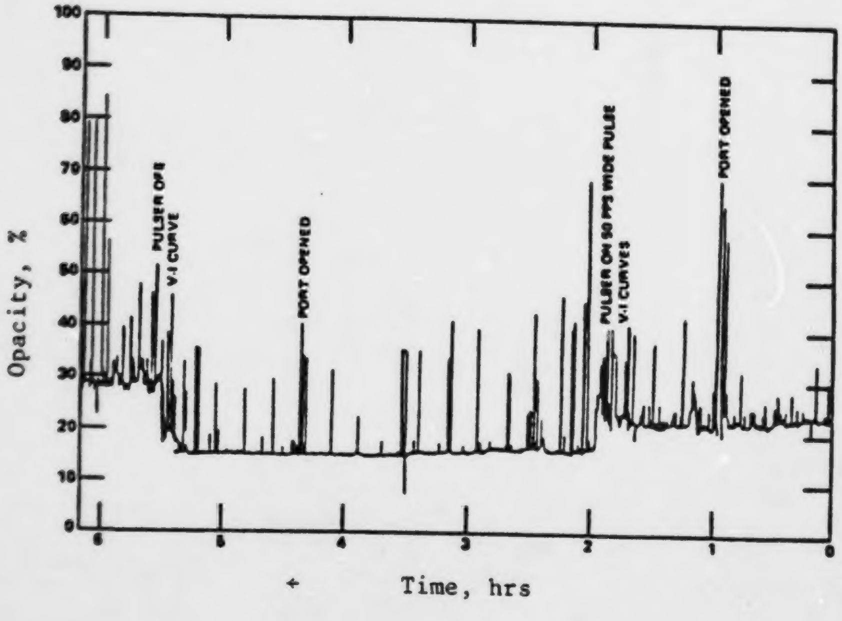

Figure 6. Chart recorder trace of outlet opacity, with and without pulsing, with 3.3 ppm SO_3 injected.

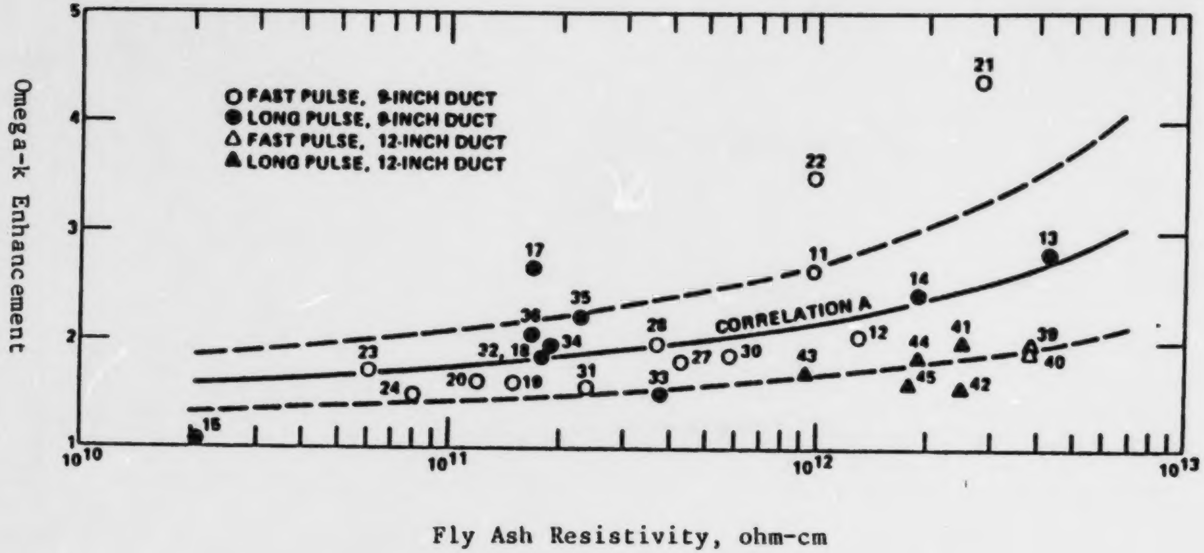

Figure 7. Calculated omega-k enhancement (k = 0.5) versus resistivity.

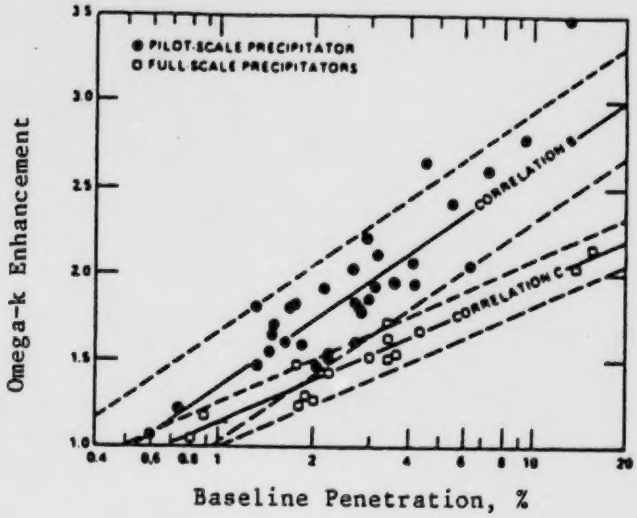

Figure 8. Omega-k enhancement, calculated using k = 0.5, versus baseline penetration of the pilot-scale precipitator and six full-scale fly ash precipitators.

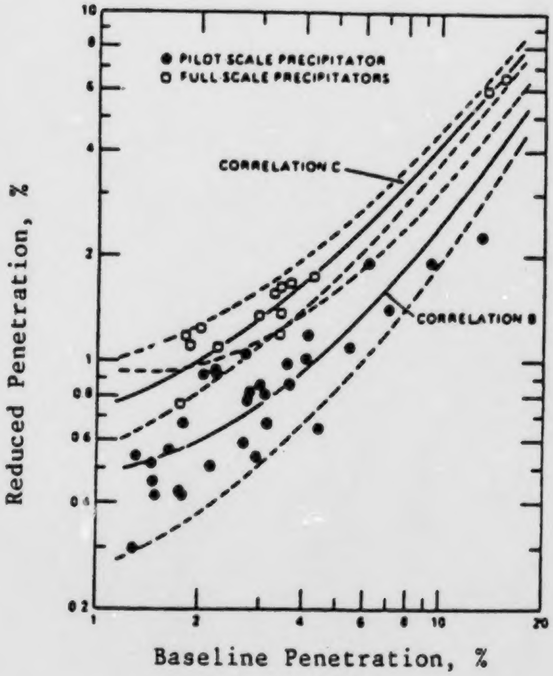

Figure 9. Baseline penetration and reduced penetration of the pilot-scale precipitator and six full-scale fly ash precipitators.

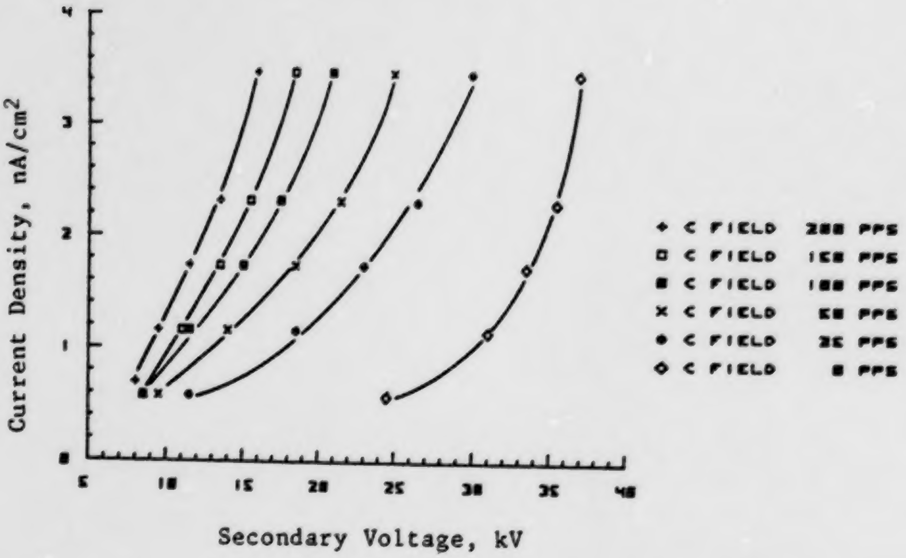

Figure 10. Change in the V-I curves for C Field, at 9-inch plate spacing and with 3.5 ppm SO_3 injection, with different repetition rates of 25 kV long pulses.

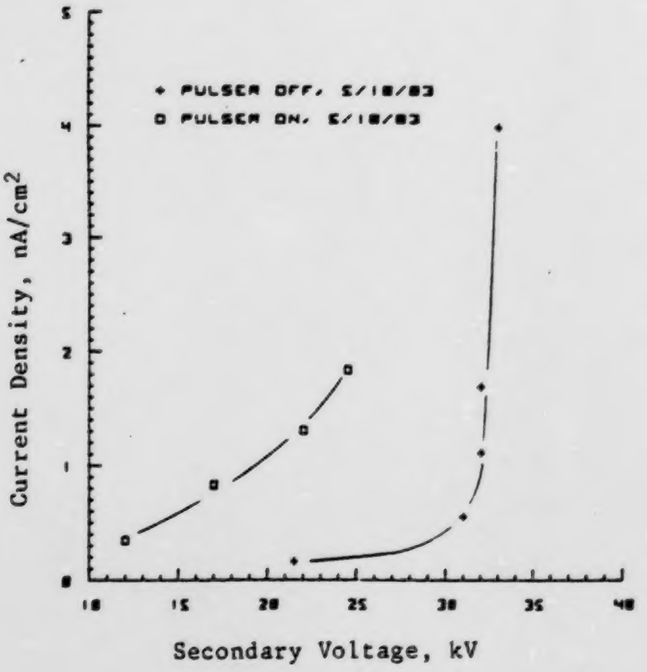

Figure 11. V-I curves for C Field, with no SO_3, with and without pulsing.

AEROSOL PARTICLE CHARGING IN A PULSED CORONA DISCHARGE

by: J. L. DuBard
Southern Research Institute
Birmingham, Alabama 35255

W. R. Piulle
Electric Power Research Institute
Palo Alto, California 94303

ABSTRACT

The charge acquired by individual aerosol particles, in both steady and pulsed negative corona, has been measured with a Millikan cell. Measurements have been performed on a pilot-scale fly ash precipitator and a wire-cylinder laboratory precipitator. The laboratory experiments were designed to isolate the particle charging mechanism from other electrical mechanisms that might be affected by pulse energization. The laboratory data were compared with particle charging computations, using a numerical simulation of the variations in space and time of the electric field and ion density. The laboratory measurements and computations showed that the periodic increases in electric field and ion density occur too briefly for particle charging to be a dominant mechanism of precipitator performance improvement. During tests of the pilot-scale precipitator with pulse energization, omega-k enhancements of 1.7 to 1.9 were observed when the Millikan data showed no increase in fine particle charge.

INTRODUCTION

Tests of aerosol particle charging in a pulsed corona discharge have been sponsored by the Electric Power Research Institute. This work was carried out in conjunction with pilot-scale precipitator performance tests at the Arapahoe Test Facility. One objective of the investigation of pulse energization was to determine the way in which pulsing works to improve precipitator performance. This paper describes the interpretation of data leading to the conclusion that the improved uniformity of the corona discharge is the dominant mechanism of performance improvement.

The precipitation process can be improved by increasing the charge on individual dust particles and by increasing the interelectrode electric field. Both experimental and theoretical determinations of particle charge values have been thoroughly tested in recent years (1,2). Therefore, the investigation of pulse energization included extensive tests of the hypothesis of increased particle charge. The tests were performed on the pilot-scale precipitator at the Arapahoe Test Facility and in the Birmingham laboratories of Southern Research Institute. The laboratory tests were designed to isolate the particle charging mechanism from other interactive electrical mechanisms in a precipitator.

LABORATORY INVESTIGATIONS

EXPERIMENTAL APPARATUS

A wire-cylinder precipitator was used for the laboratory investigations of particle charging. The discharge electrode was an 8-32 threaded steel rod, along the axis of an aluminum pipe 8.125 inch (20.7 cm) inner diameter. The active length of the corona discharge was 41.5 inches (105.4 cm). The total length of the cylinder was about 70 inches. Laboratory air was pulled through the cylinder at a velocity of 5.0 ft/s; so the aerosol treatment time in the precipitator was 0.69s.

A threaded discharge electrode was used to achieve uniform spacing of the tufts of the negative DC corona discharge. A liquid drop aerosol was used to avoid any electrical effects of a high-resistivity dust layer on the collecting cylinder. An artist's air brush was used to generate an aerosol of di-(2-ethylhexyl)-sebacate, a light-weight, non-volatile oil. The aerosol included fine particles that spanned the entire size range (0.5 to 2.5 μm diameter) that could be measured in a Millikan cell. In each experiment, the air brush was adjusted to limit the aerosol particle concentration so that there was no measurable effect of particulate space charge. The size and charge of individual fine particles escaping the precipitator were measured in a Millikan cell.

The DC high voltage corona threshold in the precipitator was about -29 kV. All laboratory measurements and computations of particle charging in a pulsed corona discharge were performed with the DC voltage set at -29 kV. There was no steady corona discharge. However, the time-average current with pulsing was read from the ammeter of the DC power supply. For a given pulse height, the time-average current was strictly proportional to the pulse repetition rate. The same behavior was observed for the AC-coupled pulse power supplies installed on the pilot-scale precipitator at the Arapahoe Test Facility when the DC voltage was set below corona threshold. The high voltage pulse acted as a switch to turn on a momentary corona discharge.

The laboratory pulse power supply was AC-coupled to the DC power supply and to the discharge electrode through a specially designed and fabricated LC network. The maximum pulse height was about -13.5 kV. The pulse risetime was about 0.9 μs, and the width was about 2 μs. A fast pulse was used in order to simulate one of the two pulse waveforms tested on the pilot-scale precipitator and to simplify the computations of particle charging.

The pulse repetition rate was continuously variable up to a few kilohertz, but limited to 200 Hz during the experiments in order to have a single burst of ionic space charge within the cylinder at any time. Both the pulse height and the pulse repetition rate were monitored with an oscilloscope, using a frequency-compensated voltage divider. Because the pulse width was negligible in comparison with the ion transit time of a few milliseconds, the only significant electrical parameter in the measurements and computations of particle charging was the total ionic space charge (per unit length of the cylinder) created by each high voltage pulse. That parameter was determined by the ratio of time-average current to pulse repetition rate.

PARTICLE CHARGING IN STEADY CORONA

A series of experiments with ordinary DC energization of the precipitator was performed to test the reproducibility of particle charge measurements and to test the mathematical simulation of particle charging in cylindrical geometry. Figures 1 and 2 show Millikan data obtained with two slightly different electrical operating points, chosen to give current density values that could be achieved with pulsed corona and no steady corona. The two electrical operating points were (34.5 kV, 89 μA, 13.0 nA/cm^2) and (35.5 kV, 134 μA, 19.5 nA/cm^2).

The dashed curve shown on each figure was computed using a conventional theory of unipolar ionic charging in a steady corona discharge (1). The computation assumed that fine particles were uniformly distributed over any cross-sectional area of the cylinder, due to fully-developed small-scale turbulence. The effect of turbulence on particle charging and particle sampling was simulated by averaging the charge values computed for particles moving through the precipitator at the area-median radii of seven equal increments of cross-sectional area. In spite of the typically large scatter in the Millikan data, the theoretical curves agree well with the mean values of measured particle charge. Furthermore, a close comparison of Figures 1 and 2 shows that both measured and computed particle charge values are slightly different for the two different electrical operating points.

PARTICLE CHARGING IN PULSED CORONA

A second series of experiments was performed with a pulsed corona discharge and no steady corona. Three data sets are shown in Figures 3, 4, and 5. The data in Figures 3 and 4 were obtained with different values of pulse repetition rate and time-average current density, but the same ratio of those two parameters. The ratio gives a total ionic space charge per pulse of 0.42 μC/m. The data in Figure 5 were obtained with 2/3 that ionic space charge, 0.28 μC/m.

A mathematical model of particle charging in a pulsed corona discharge was developed to assist in the interpretation of data. The model performs a detailed numerical simulation of the variation in space and time of local values of electric field and ion space charge density. The model is simplified by the cylindrical geometry, the narrow pulse width, and the absence of steady corona in the precipitator.

The computation begins with the experimental value of total ionic space charge created by each high voltage pulse. The initial radial distribution of charge is estimated from a numerical simulation of the electron attachment in laboratory air. Then, working with a specified initial charge distribution, eN(r), Gauss' law in cylindrical geometry gives

$$\varepsilon_0 E(r)\, 2\pi r = Q_{wire} + \int_{R_1}^{r} eN(x)dx.$$

The unknown value of charge on the corona wire, Q_{wire}, is determined by substituting the expression for E(r) into the radial path integral

$$V_{wire} = \int_{R_1}^{R_2} E(r)\, dr.$$

Finally, the values of Q_{wire} and eN(r) are substituted back into Gauss' law to determine the electric field E(r). Then, time is incremented, and the radial coordinate of each increment of space charge is changed by ($B\ E(r)\ \Delta t$) where B is the ion mobility. A new space charge distribution is calculated, and the entire procedure is repeated until all molecular ions reach the cylinder.

Because of the dense space charge around the corona wire after each high voltage pulse, there are large local variations in the electric field. The space charge cloud moves very fast in the first few hundred microseconds and actually blows itself apart into two bunches, as illustrated in Figure 7. Figure 7 shows the computation of eN(r) at 0.3, 0.6, and 1.2 ms after the high voltage pulse, for total ionic space charge of 0.42 μC/m. By way of comparison, the ionic space charge density in a steady corona with the same current density is of the order of 0.05×10^{-4} μC/m. This number would be barely visible on the vertical scale of Figure 7.

Figure 8 shows the corresponding electric field enhancement in front of the expanding space charge cloud. Local values of E(r) are plotted in proportion to the electrostatic field for 29 kV on the corona wire. That ratio is constant before and after each space charge cloud. As time elapses after each high voltage pulse, the negative charge on the corona wire increases to the value that the DC power supply maintains between pulses, and the electric field at the corona wire increases to the electrostatic field.

Given the detailed numerical map of eN(r,t) and E(r,t), the model computes the accumulation of charge on aerosol particles at seven area-median radii in the cylinder. The average charge value for each particle size gives the solid theoretical curves superimposed on the data in Figures 3, 4, and 5. The mean values of measured particle charge agree well with the results of the numerical simulation. A close comparison of the three figures shows that theory and experiment give the same result for the two tests with 0.42 μC/m, Figures 3 and 4. However, the results are clearly different for the test with 0.28 μC/m, shown in Figure 5. Figure 6 is the same as Figure 4, but with the addition of the dashed theoretical curve from Figure 1. The data sets for particle charge acquired in steady corona and in pulsed corona are comparable only in regard to the same current density, 13.0 nA/cm^2. However, Figure 6 illustrates that, within the range of Millikan data, the computed difference in particle charge with steady corona or pulsed corona is much less than the scatter in the data.

The model was used to compute trends in the charging of particles outside the range of Millikan data. Table 1 shows the computed data for 0.2s exposure time, or one foot of travel into the laboratory precipitator. In a pulsed corona discharge with no underlying steady corona, submicron particles have reduced charge levels. In spite of enhanced values of electric field and ionic

TABLE 1. COMPUTED PARTICLE CHARGING IN THE LABORATORY PRECIPITATOR

Particle Diameter	Saturation Charge Units	Accumulated Charge 0.2s Exposure	Q/QSAT 0.2s Exposure
Steady Corona 34.5 kV on the wire 13.0 nA/cm^2 on the cylinder			
0.2	3	9	3.0
0.6	19	47	2.5
1.3	82	163	2.0
2.8	366	603	1.6
6.1	1715	2399	1.4
Pulsed Corona (200 Hz) 0.4227 μC/m per pulse 13.0 nA/cm^2 on the cylinder			
0.2	0	0	-
0.6	26	27	1.0
1.3	113	154	1.4
2.8	508	652	1.3
6.1	2378	2751	1.2

space charge density, the charging of submicron particles by thermal diffusion of molecular ions is restricted by the brief exposure time during each burst of ionic space charge. This behavior is illustrated by the numbers in the right-hand column of Table 1. Q/QSAT is a measure of continued particle charging by thermal diffusion. This behavior is illustrated also by the intersecting theoretical curves in Figure 6, where the crossover point of higher particle charge with pulsing (and 0.69s exposure time) occurs at about 1.7 µm diameter. Particles larger than a few microns can be charged to higher values in a pulsed corona discharge, by bombardment of ions driven by the electric field. The momentary increase in local values of electric field leads to higher values of saturation charge.

PILOT-SCALE PRECIPITATOR TESTS

PARTICLE CHARGE MEASUREMENTS

A Millikan cell was set up at the pilot-scale precipitator outlet during performance tests at 9-inch plate spacing. The Millikan cell was used to determine the size and charge of individual fly ash particles escaping the precipitator. The charge data were acquired during 4 to 5 ppm SO_3 injection, when the fly ash resistivity was measured in situ to be 2E11 to 4E11 ohm-cm.

Typical Millikan data, obtained during precipitator operation with ordinary DC energization, are shown in Figure 9. The mean measured particle charge and its standard deviation are shown in Figures 10, 11, and 12, for precipitator operation with DC energization, fast pulses, and long pulses, respectively. The same theoretical curve is shown on each figure, to guide the eye. That curve is the computed particle charge for DC energization of the precipitator. During all tests with pulse energization, the DC voltage was set at spark limit in each field. The pulsed corona discharge was superimposed on a steady corona discharge.

The Millikan data show no statistically significant increase in the charge on fine fly ash particles with pulse energization. These data are consistent with the Millikan data obtained during tests of full-scale, pilot-scale, and laboratory precipitators (3,4,5). A large variety of DC and pulse energization parameters have been used in the various tests, but the Millikan data are unanimous: no statistically significant increase in the charge on individual particles in the diameter range 0.5 µm to 2.5 µm. Nevertheless, during the particle charge measurements compared in Figures 10 and 11, the precipitator collection efficiency increased from 97.2% to 99.1% with pulsing, and the outlet flue gas opacity dropped from 27% to 18%.

FRACTIONAL EFFICIENCY MEASUREMENTS

The pilot-scale precipitator collection efficiency, as a function of particle size, was measured with cascade impactors. Data are shown in Figure 13, with and without fast pulses at 50 Hz. These data were obtained simultaneously with the Millikan data compared in Figures 10 and 11. Similar cascade impactor data were obtained with and without long pulses at 50 Hz.

Across the entire particle size range, the collection efficiency increased with pulsing.

The effective migration velocity (ω) for particles in a small size band can be calculated from the cascade impactor data, using the Deutsch-Anderson equation (6),

$$\text{PERCENT EFFICIENCY} = 100\ (1 - e^{-\omega A/V}).$$

A/V is the specific collection area (SCA) given by the ratio of precipitator plate area to volume gas flow. The simple difference in values of migration velocity with and without pulsing (calculated from pairs of curves as shown in Figure 13) is shown in Figure 14. The two data sets in Figure 14 suggest that the long pulse worked better than the fast pulse. However, the difference is well within the scatter of all of the precipitator performance improvement data.

The experimental values of effective migration velocity can be compared with the theoretical migration velocity for particles of diameter D,

$$\omega = (\text{constant})\ QE/D,$$

where Q is the particle charge and E is the interelectrode electric field at the collecting plate (6). The theoretical increase in migration velocity with pulsing can be written as

$$\Delta\omega = (\text{constant})\ \Delta(QE),$$

for particles of a given diameter.

The left-hand side of Figure 14 covers the same particle size range as the Millikan data. Since the Millikan data show that $\Delta Q = 0$, it follows that the nearly uniform increase in migration velocity of particles smaller than about 2 μm results from an increase in the plate-area-average value of collecting electric field. In a typical fly ash precipitator, the collecting electric field is controlled more strongly by the interelectrode space charge than by the discharge electrode voltage. It follows that the increase in migration velocity of fine particles is caused by a more uniform distribution (over the plate area) of interelectrode space charge.

The Deutsch-Anderson collection efficiency equation assumes ideal electrical and aerodynamic operating conditions in the precipitator. In particular, the equation does not account for the reentrainment of collected dust. The right-hand side of Figure 14 covers the size range of most reentrained particles. The pilot-scale precipitator performance tests were conducted without rapping the electrodes. Therefore, the increase in migration velocity of particles larger than about 2 μm results from a suppression of non-rapping reentrainment, as well as increased values of Q and E. The suppression of reentrainment is caused by an increase in the plate-area-average value of the electrical holding force on the collected dust. This increase is caused by a more uniform deposition of ionic charge on the surface of the collected dust. The suppression of reentrainment is assisted by the rapid recharging of reentrained particles larger than about 2 μm.

CONCLUSIONS

The data from the investigation of precipitator pulsed energization indicate that the effects of a more uniform negative corona discharge fully explain the improved precipitator performance obtained with pulsing. The improved plate-area-average uniformity of the negative corona in a pulsed precipitator has several important effects. The effects can be summarized in terms of 1) improvements in the charging and collecting of dust particles, and 2) suppression of non-ideal precipitator operating conditions.

1) A uniform, controlled corona discharge leads to a uniform interelectrode ionic space charge, which causes
- increased average collecting electric field, and
- increased initial rate of particle charging.

The data indicate that pulsing has little effect on the primary charging of fine particles, but is more effective in the rapid recharging of large reentrained particles.

2) A uniform deposition of ions on the collected dust layer leads to a uniform electric field within the dust layer, which causes
- suppression of back discharge, and
- suppression of reentrainment.

The data indicate that pulsing is most effective in suppressing the conditions of back discharge and reentrainment that degrade precipitator performance.

REFERENCES

1. McDonald, J. R., M. H. Anderson, and R. B. Mosley. Charge Measurements of Particles Exiting Electrostatic Precipitators. Report EPA-600/7-80-077. U.S. Environmental Protection Agency. Research Triangle Park, NC. April 1980.

2. Anderson, M. H., J. R. McDonald, and R. B. Mosley. Particle Charge Measurements. International Conference On Electrostatic Precipitation. Monterey, CA, October 1981. APCA. Pittsburgh, PA, 1982.

3. Sparks, L. E., G. H. Ramsey, and R. E. Valentine. Comparison of Electrostatic Precipitator Performance With Pulse And DC Energization. Ibid.

4. Sparks, L. E., G. H. Ramsey, R. E. Valentine, and J. H. Abbott. Particle Charging in an Electrostatic Precipitator by Pulse and DC Voltages. EPA Third Symposium on the Transfer and Utilization of Particulate Control Technology. Orlando, FL, March 1981.

5. Gooch, J. P., G. H. Marchant, Jr., J. L. DuBard, and J. R. McDonald. An Evaluation of Pulse Energization on a Hot-Side Electrostatic Precipitator. EPRI Report CS-2634. Palo Alto, CA, November 1982.

6. White, H. J. Industrial Electrostatic Precipitation. Addison-Wesley Publishing Co. Reading, MA, 1963.

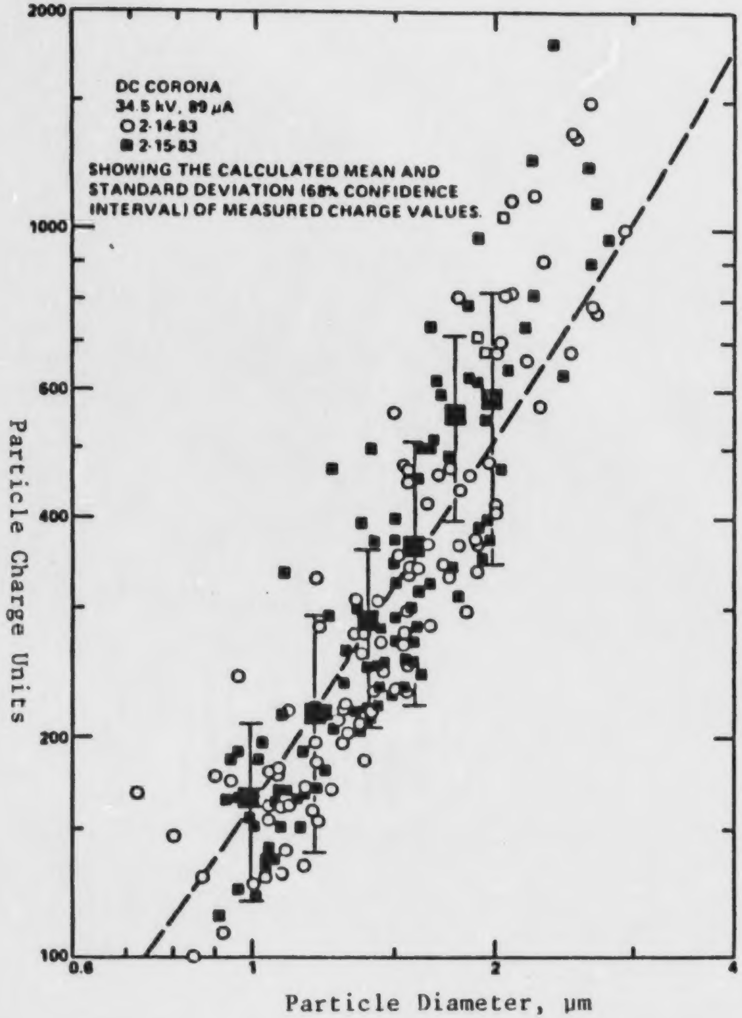

Figure 1. Mean values of particle charge acquired in steady corona at 34.5 kV and 13.0 nA/cm^2.

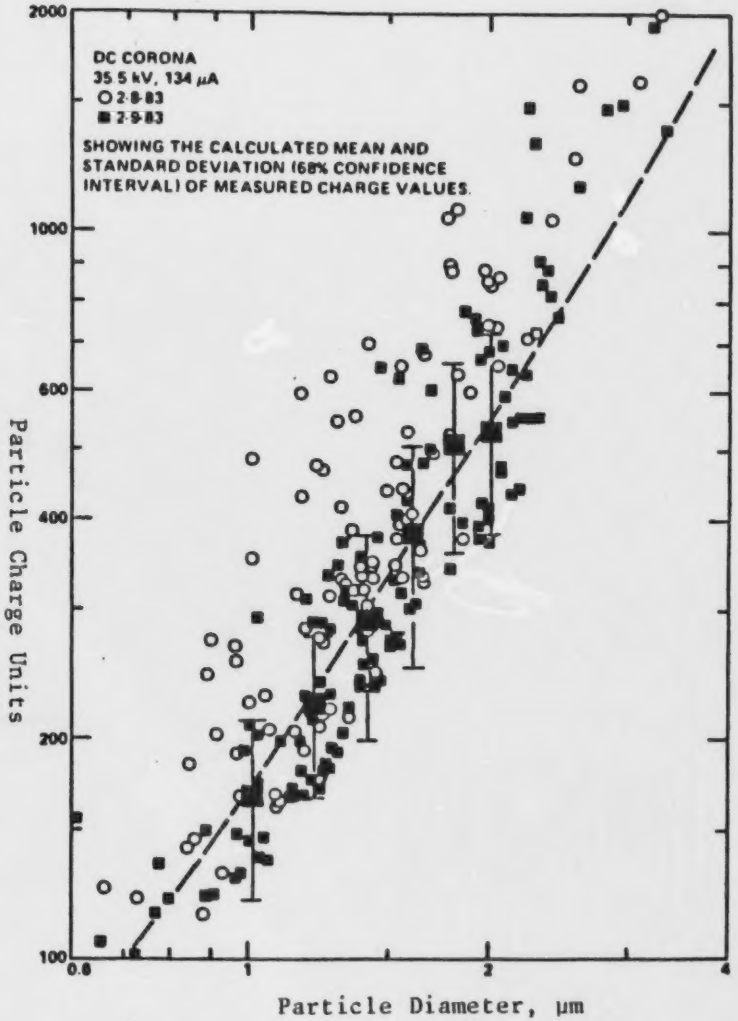

Figure 2. Mean values of particle charge acquired in steady corona at 35.5 kV and 19.5 nA/cm^2.

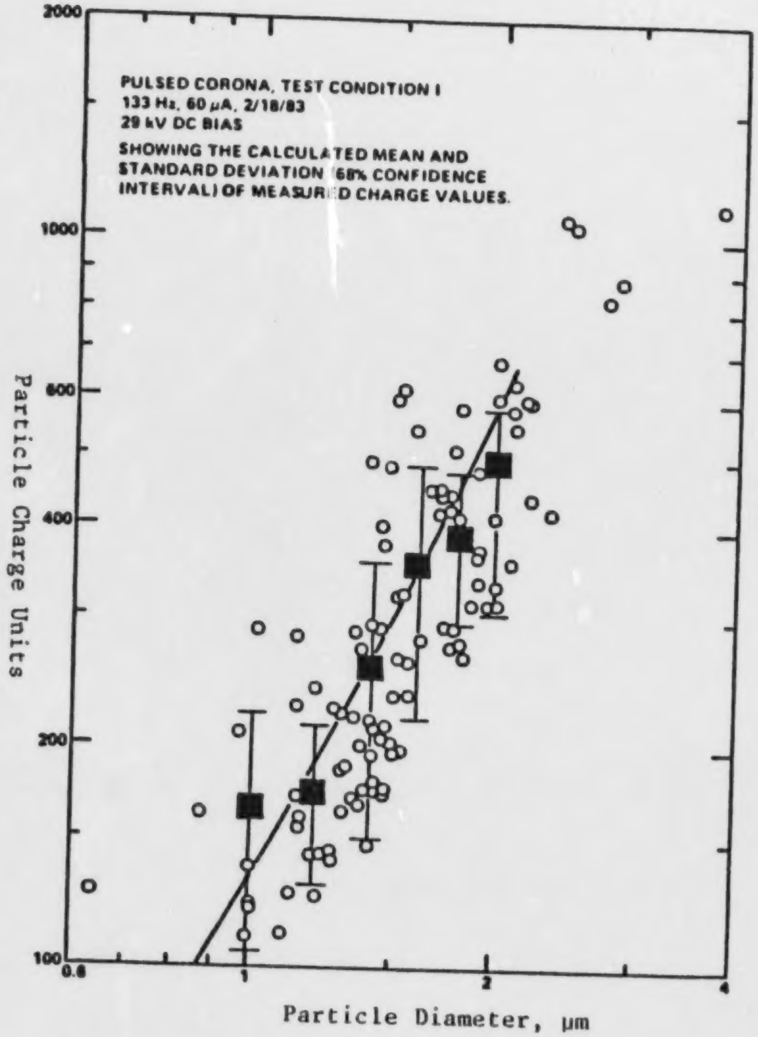

Figure 3. DES particle charging in pulser test I at 133 Hz and 8.67 nA/cm^2.

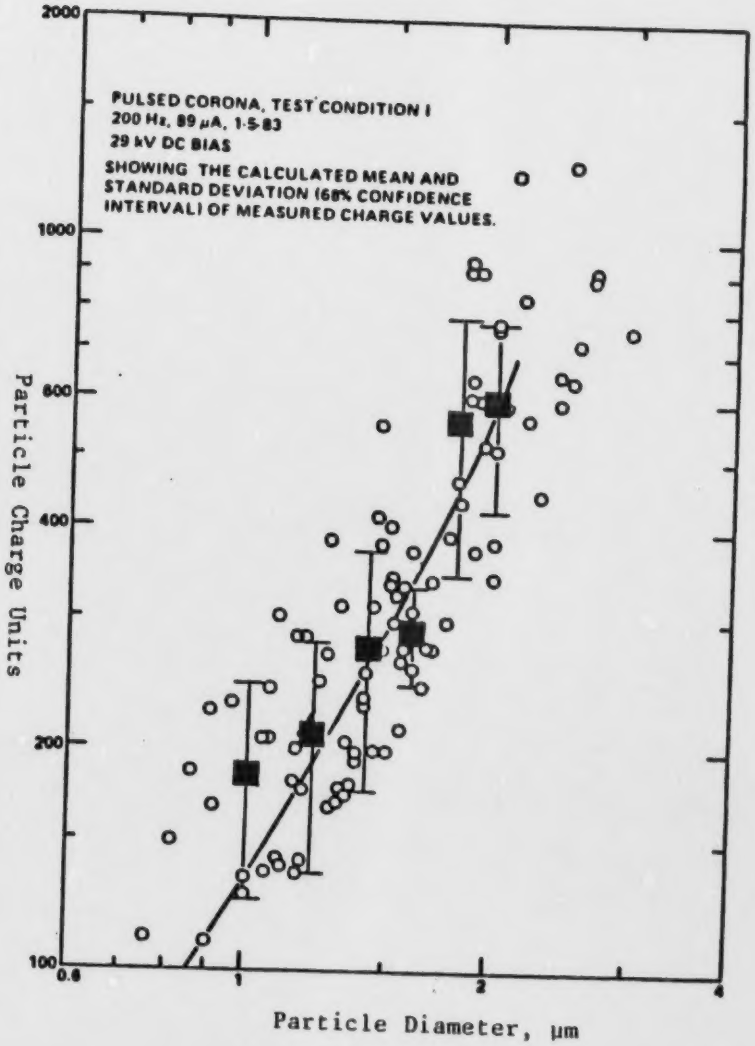

Figure 4. DES particle charging in pulser test I at 200 Hz and 13.0 nA/cm^2.

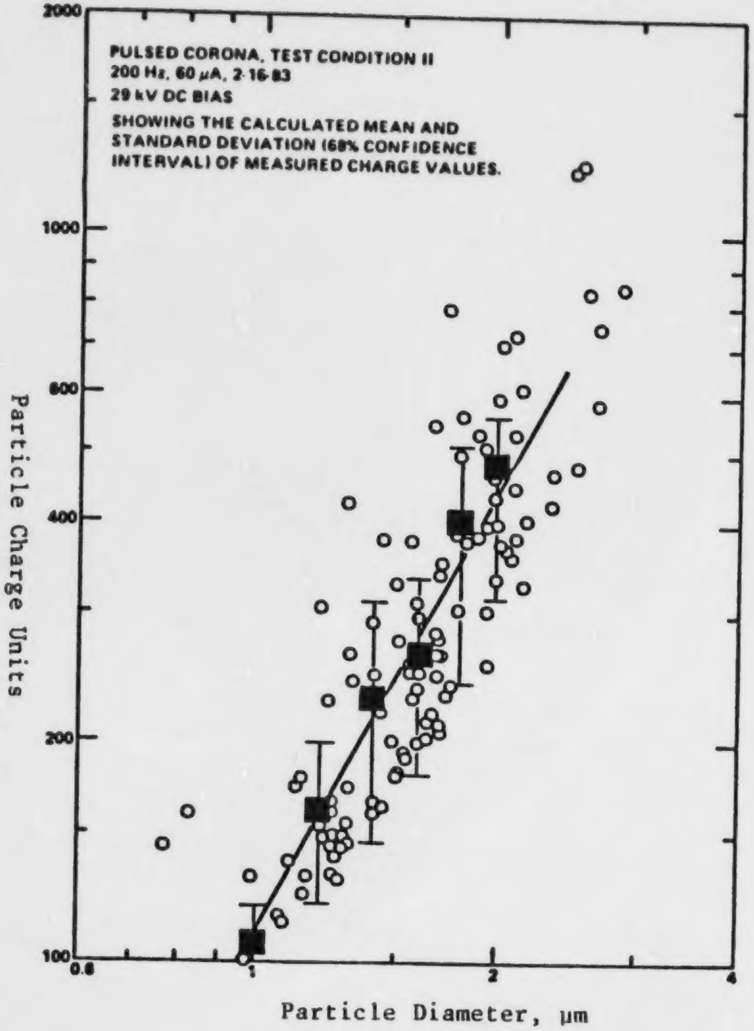

Figure 5. DES particle charging in pulser test II at 200 Hz and 8.67 nA/cm^2.

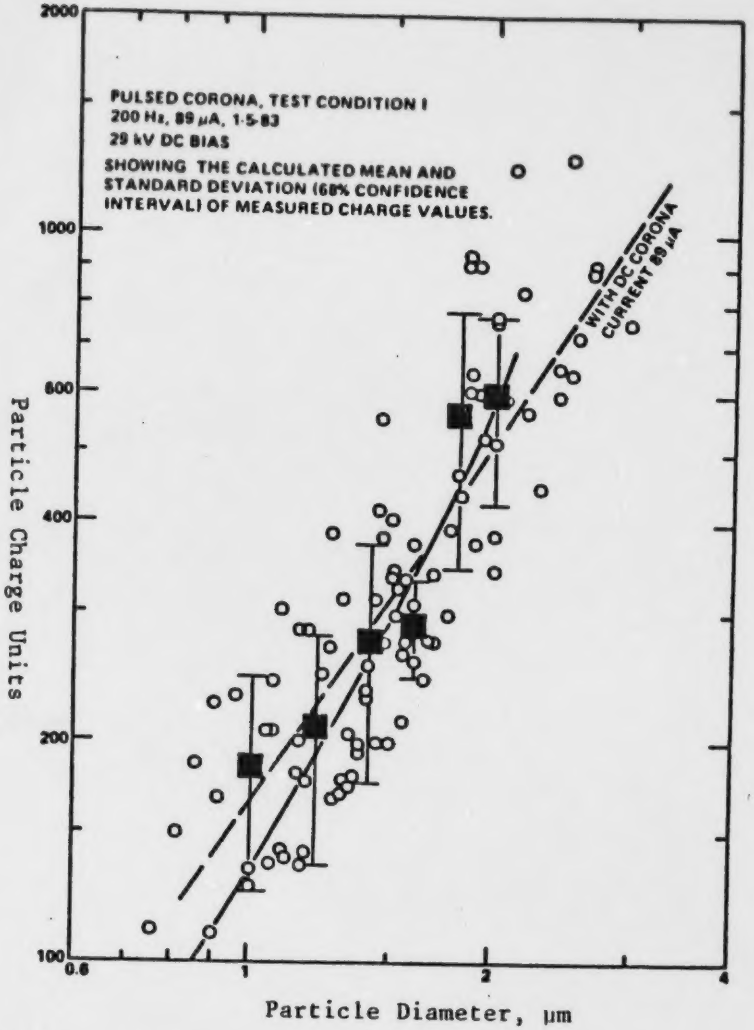

Figure 6. DES particle charging in pulser test I at 200 Hz and 13.0 nA/cm^2.

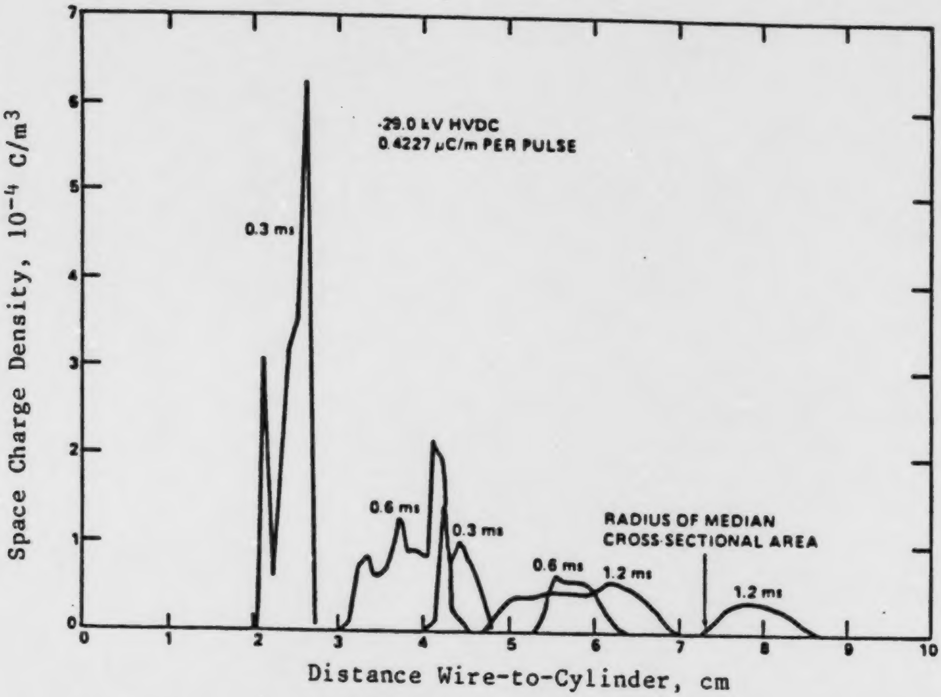

Figure 7. Local values of ionic space charge density, after an instantaneous corona discharge.

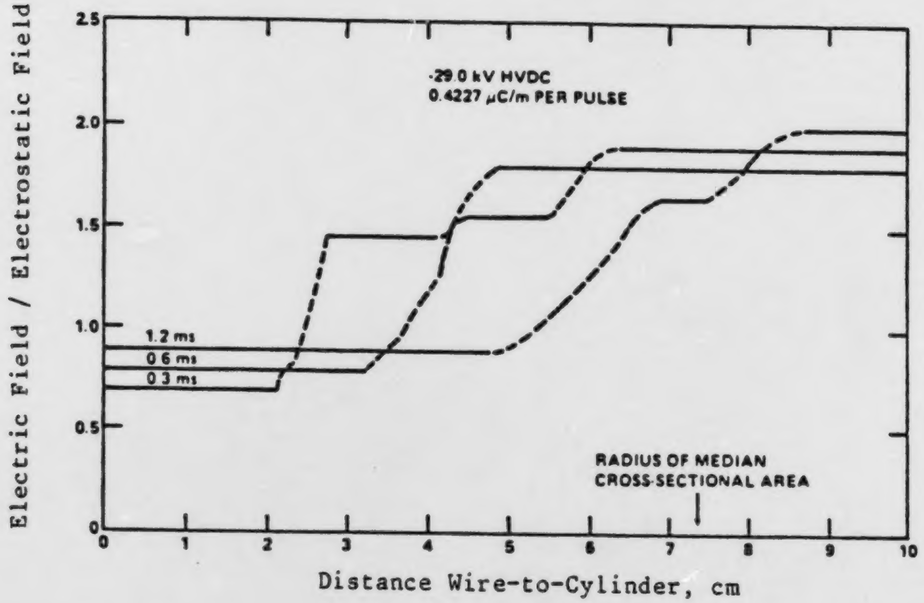

Figure 8. Local values of electric field enhancement, after an instantaneous corona discharge.

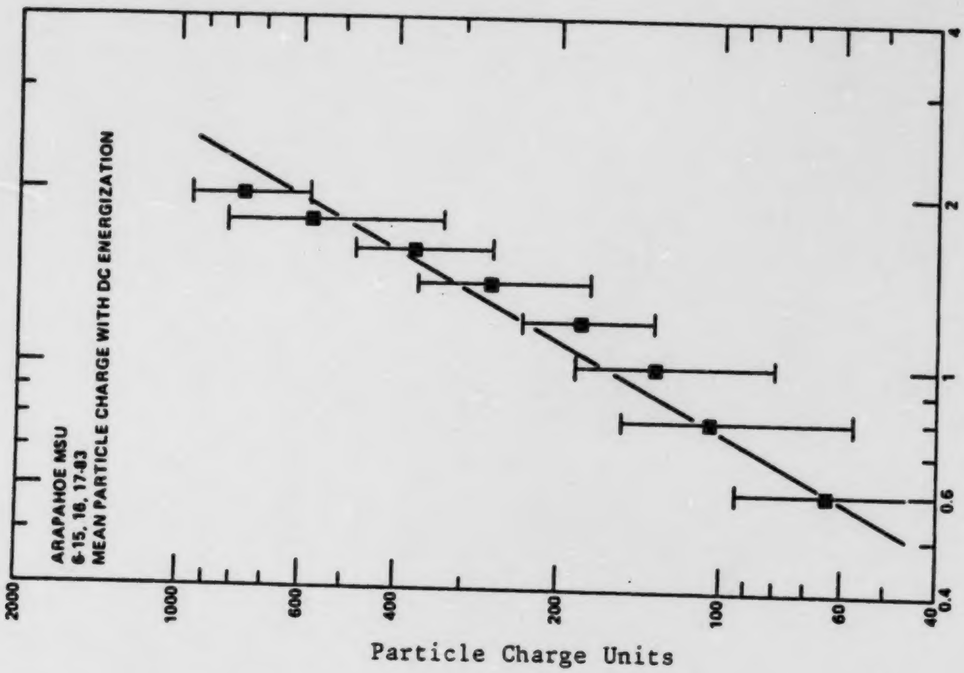

Figure 10. Measured mean charge and standard deviation, with DC energization.

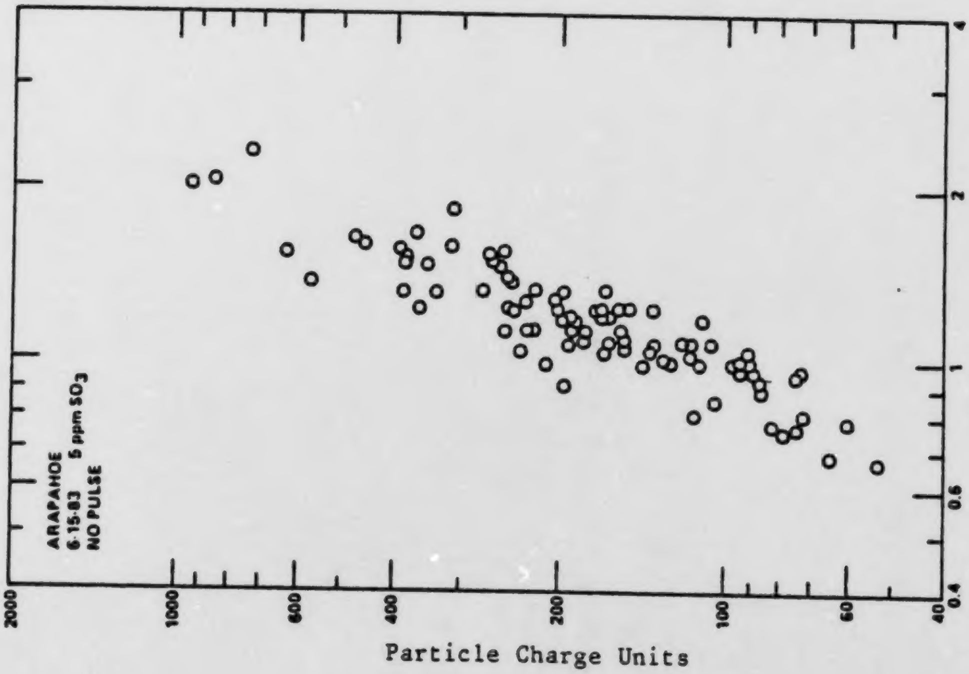

Figure 9. Measured particle charge data, with DC energization.

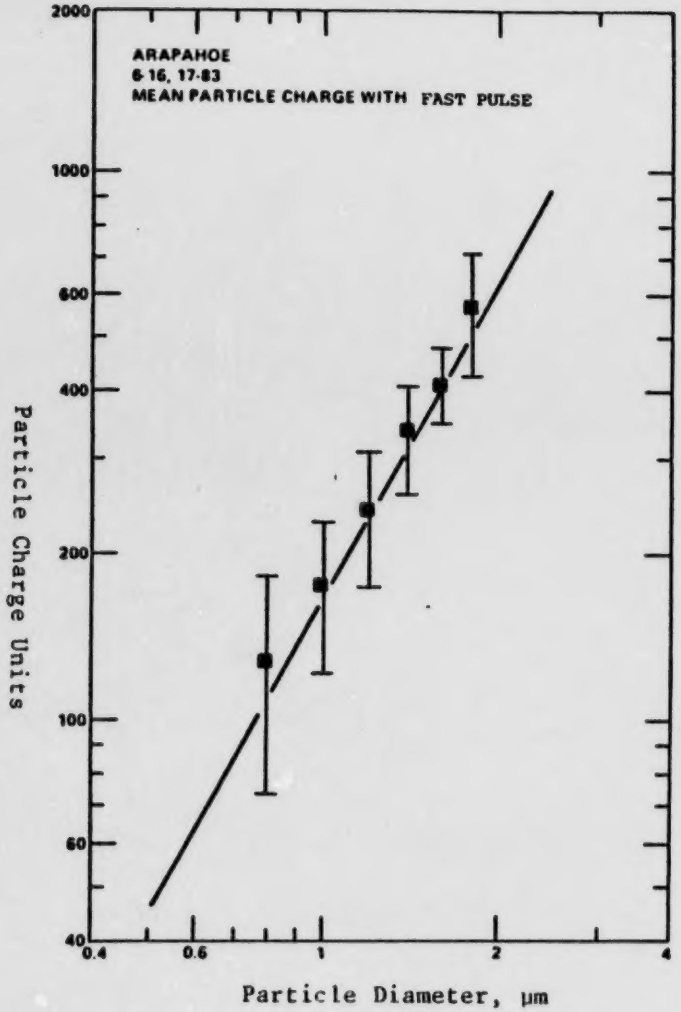

Figure 11. Measured mean charge and standard deviation, with fast pulses at 50 Hz.

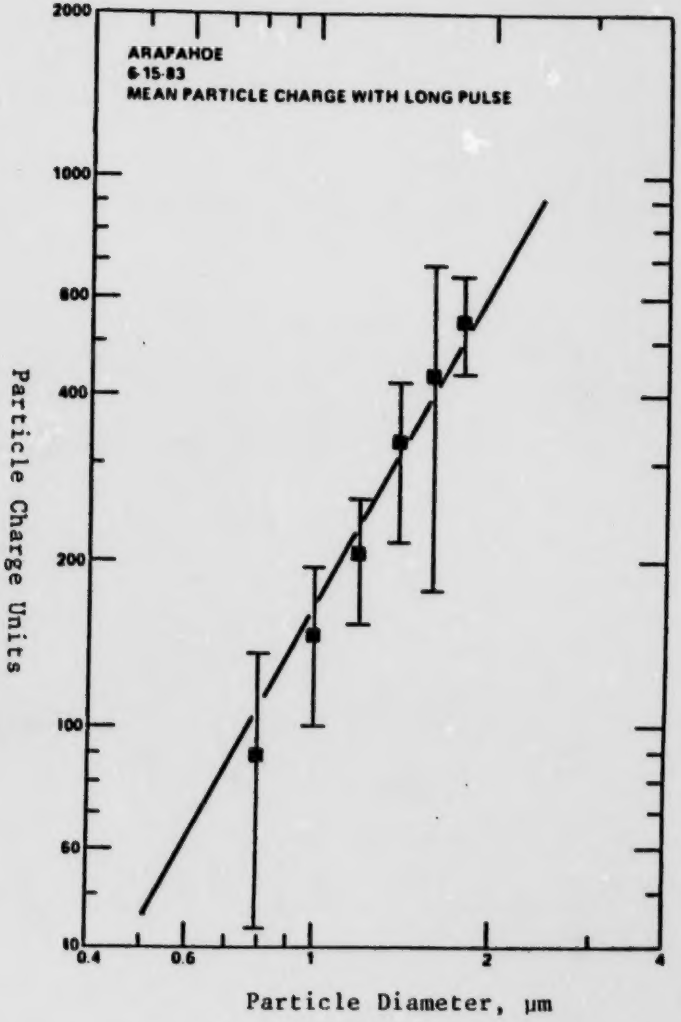

Figure 12. Measured mean charge and standard deviation, with long pulses at 50 Hz.

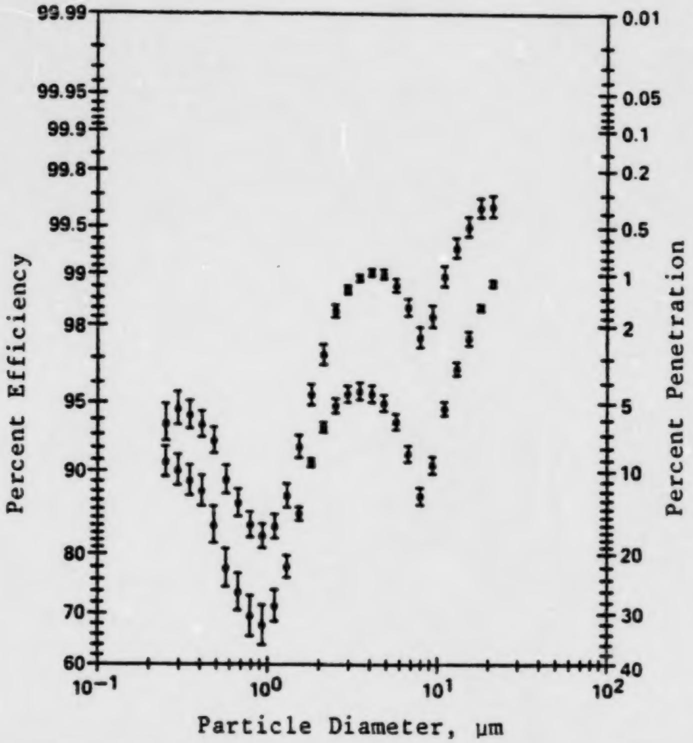

Figure 13. Size-fractional collection efficiency, with and without fast pulses at 50 Hz.

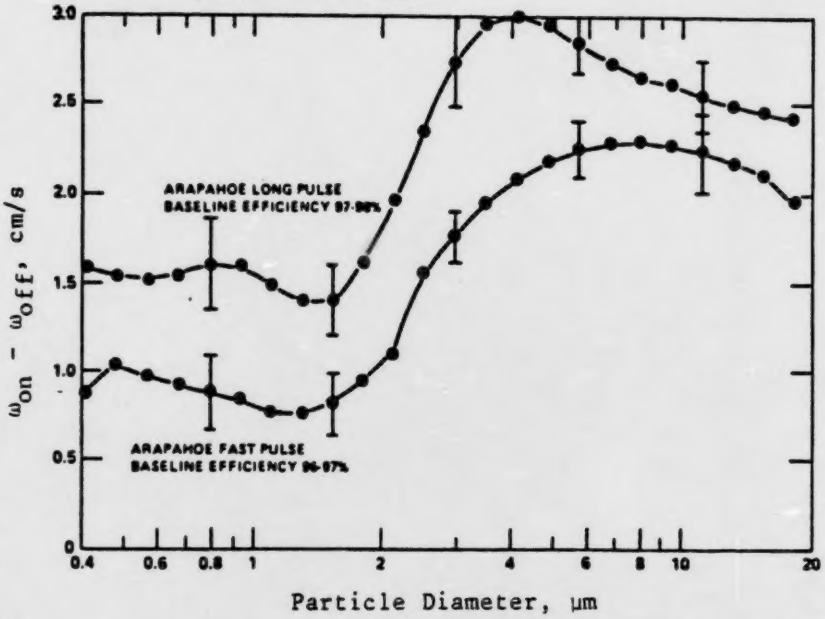

Figure 14. The difference in effective particle migration velocity, with and without pulsing.

Session 9: ESP: ADVANCED TECHNOLOGY II

Walter R. Piulle, Chairman
Electric Power Research Institute
Palo Alto, CA

PERFORMANCE OF LARGE-DIAMETER WIRES AS DISCHARGE ELECTRODES IN ELECTROSTATIC PRECIPITATORS

by: P. Vann Bush and Duane H. Pontius
Southern Research Institute
Birmingham, Alabama 35255-5305

and

Leslie E. Sparks
Industrial Environmental Research Laboratory
U.S. Environmental Protection Agency
Research Triangle Park, North Carolina 27711

ABSTRACT

Conventional practice in the design of corona discharge electrodes for electrostatic precipitators (ESP's) tends toward those having a relatively low corona inception voltage. The theory indicates that maximal electric field strength is of more importance to the precipitation process than is corona current, since it is beneficial to both charging and collection of particles. Only those particles smaller than about 0.2 micrometer diameter are more readily charged by increasing the ion current density instead of the electric field strength. Laboratory tests of a small pilot ESP (1 000 acfm*) and field tests of a large pilot system (30,000 acfm) comparing the performance of 3/8-inch diameter wires with more nearly conventional 1/8-inch wires have borne out the theory and resulted in substantially superior performance for the larger electrodes.

This paper has been reviewed in accordance with the U.S. Environmental Protection Agency's peer and administrative review policies and approved for presentation and publication.

---

*To convert to metric equivalents, please use the factors provided at the end of this paper.

INTRODUCTION

The first successful implementation of electrostatic precipitators (ESP's) in a commercial application is credited to Frederick Cottrell in 1907. The capacity of the mechanical rectifiers limited operating voltages to 10-15 kV. This limitation forced Cottrell to adopt an electrode which would develop corona discharge at these relatively low voltages. His choice was a wire coated with cotton filaments which produced a uniform corona discharge at these conditions. It was W.A. Schmidt who introduced the innovation of a fine wire to produce a vigorous corona discharge at the available voltage levels. The advances in transformer-rectifier capacity were rapid and, long before Deutsch produced a mathematical expression describing particle collection in ESP's (1922), voltages in excess of 100 kV were attainable (1).

In spite of the implications of the Deutsch model (discussed in the following section) and advances in ESP energization methods, the philosophy which led Schmidt to choose a fine wire for the corona discharge electrode has persisted in ESP design practice. It is true that a broad variety of discharge electrodes have been applied in commercial installations. Among these are weighted wires, wires on frames or masts, barbed wires, and rigid electrodes. Small radii of curvature and sharp edges or projections are commonplace (1,2). Endemic to this set is the design philosophy of Schmidt: the discharge electrode must be capable of producing a very dense ion current for particle charging. Certainly other criteria are included in the selection of electrode design, such as ruggedness, electric field strength, and corona current distribution.

It is known prima facie that a fine wire will produce a more vigorous discharge at a given voltage than a wire having a larger diameter. The larger diameter wire would have to operate at higher voltages to produce the same level of ion generation. The assumption that ion production is of foremost importance has led designers to overlook or constrain other criteria, such as electric field strength. The theoretical description of particle charging and collection indicates that a modest level of ion density is adequate, and an increase in the electric field strength yields substantially improved charging and collection. In practice, the ion current density in an ESP must be limited if the electrical resistivity of the dust is high so that performance will not be degraded by back corona. This is not an uncommon condition.

There are other considerations which favor fine wires over wires of larger diameter. The discharge from fine wires is relatively uniformly distributed over the length of the wire. The degree of uniformity at a given total ion flux diminishes as the wire diameter increases (3). This permits a larger number of particles to pass the wire without encountering ions for charging. Also, the operating range between corona inception and sparkover diminishes as the wire diameter increases. These are serious considerations. Laboratory and field experience with wires of different diameter have revealed that the larger diameter wires can provide superior performance in spite of these features. Tests indicate that the degree of performance benefit is equal to the predicted enhancements to particle collection which result from higher electric field strengths.

THEORETICAL CONSIDERATIONS

Two charging mechanisms are incorporated in theories describing particle charging: 1) particles are bombarded by ions which are driven by the force of the electric field; and 2) ions are attached to the particles by ion diffusion. For the first mechanism, Field Charging, the saturation charge level of the particle is directly proportional to the electric field strength. In Diffusion Charging the rate of charge acquisition depends on the thermal energy of the ions and the exposure time. It is only for particles less than ~0.2 μm diameter that ion diffusion becomes the dominant charging mechanism (4). Typically, this size range of particles constitutes less than 0.5% of the mass of the fly ash entering an ESP. The electric field strength has a dominant role in charging 99.5% of the mass entering the precipitator.

The Deutsch-Anderson equation has been shown to provide a reasonable estimate of ESP collection performance. It is especially useful as a tool for comparing the effects of changes in the operating parameters of an ESP. A simple form of the equation is

$$P = \exp\,(-wA/V) \tag{1}$$

where P is the overall penetration of the ESP (P = 1 - collection efficiency), w is the precipitation rate parameter, A is the total collecting surface area, and V is the gas volume flow rate. The precipitation rate parameter for particles of radius a is of the form

$$w = aE^2/2\pi\delta \tag{2}$$

where E is the average electric field strength and δ is the gas viscosity.

Combining Equations (1) and (2) and taking the logarithm results in

$$\ell nP = aAE^2/2\pi V\delta \quad . \tag{3}$$

If we wish to determine the effect of variations in any of the parameters we may use Equation (3). Specifically, the effect that changing the electric field strength from E_0 to E produces in the penetration P_0, with all other parameters constant, can be derived easily from the result

$$\ell nP/\ell nP_0 = (E/E_0)^2 \quad .$$

Solving for P,

$$P = \exp\left[(E/E_0)^2 \ell nP_0\right] \quad . \tag{4}$$

A family of curves resulting from this expression is shown in Figure 1.

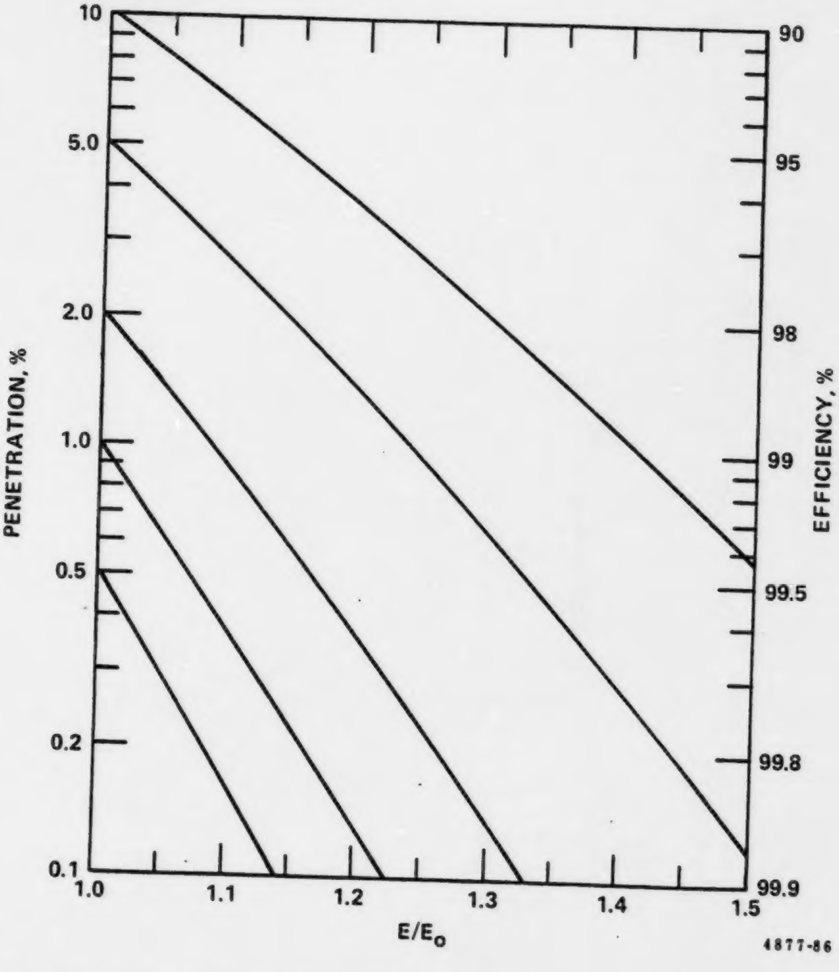

Figure 1. Theoretical predictions of the effect of electric field strength variations on penetration.

Of more interest than the values of penetration presented in Figure 1 are the trends that are indicated. Relatively small increases in the electric field strength result in a notable penetration reduction.

FIELD TEST RESULTS

The advantage of high electric field strength for collection of charged particles led to the selection of large diameter wires as discharge electrodes in the EPA/SoRI large pilot demonstration ESP. The pilot ESP was constructed to demonstrate two-stage ESP technology for high resistivity fly ash collection. The system was designed for 30,000 acfm of flue gas capacity. The collector stage of the two-stage system consisted of four electrical sections of commercial ESP design with the exception of the discharge electrodes. The total specific collection area (SCA) as tested was 287 ft^2/kacfm. Three-eighth inch diameter wires were installed in the Lodge-Cottrell mast suspension. The wires were mounted 3-3/4 inches apart. There were a total of 60 wires (10 masts) in each of the 13 lanes of the collector. The lanes were 10 inches wide by 10 feet-3 inches high. Other details of the pilot ESP design have been presented elsewhere (5,6).

The specific diameter of the discharge wires was selected based on limited tests in the EPA small pilot ESP at Research Triangle Park, North Carolina. The criteria for selection were combined high electric field strength and low current operating regime, and feasibility of implementation. These criteria were applied to the selection because the electrodes were intended to be used in a collector stage downsteam of a particle charging device. In this application it was expected that the absence of current uniformity and low total current levels could be tolerated.

TEST CONDITIONS

The large pilot ESP was evaluated over a period of 2-1/2 years. For the first two years of study the principal objective was to evaluate the two-stage technology with the 3/8-inch diameter discharge electrodes in the collector stage. The final phase of tests conducted in the pilot demonstration program evaluated the precharger as a retrofit to existing ESP's. For this study the collector stage was fitted with 1/8-inch diameter wires in the Lodge-Cottrell mast suspension. Measurements of particle penetration of the collector stage alone were made routinely, as baseline performance data. These data permit direct comparisons to be made between the two discharge electrodes under identical conditions.

The tests were conducted at a flue gas temperature of 325°F. This provided an ash resistivity of $2\text{-}4 \times 10^{12}$ ohm-cm. Inlet fly ash mass loadings for the tests were ~4.6 gr/acf. The mass median diameter of the ash was ~20 μm.

RESULTS OF COMPARATIVE TESTS

Voltage-current (V-I) characteristics for the 3/8-inch diameter wires at the test conditions are shown in Figure 2. The operating range between onset of corona and the onset of sparking and back corona was from 41 to 49 kV applied voltage (3.2 to 3.9 kV/cm average electric field strength), and up to 7 μA/ft^2 current density. During the tests which were used for the comparisons, the ESP with 3/8-inch diameter wires operated with applied voltages in the range 42 to 48 kV, producing average electric field strengths of 3.3 to 3.8 kV/cm. The average current density was 4.7 μA/ft^2. This corresponds to a total power consumption of ~1700 watts.

The V-I curves for the 1/8-inch wires are presented in Figure 3. The voltage range attainable for these electrodes was 36 to 41 kV, giving an average electric field strength of 2.8 to 3.2 kV/cm. The corresponding average current density was 6.8 μA/ft^2, giving a total power consumption of ~2100 watts.

The electrical operating conditions and resulting collection efficiencies for the two electrode tests are summarized in Table I. For the 3/8-inch diameter wires the average of total mass collection efficiency measurements was 99.64%. This high efficiency was typical of the performance of these electrodes for all tests at these conditions. The average total mass collection efficiency for the 1/8-inch diameter wires was 98.58%. The difference in penetration for the two cases was a factor of four (.0036 to .0142).

TABLE I. ESP PERFORMANCE

	3/8-inch wires	1/8-inch wires
Electric field strength, kV/cm	3.3-3.8	3.0-3.2
Current density, μA/ft^2	4.7	6.8
Power consumption, watts	1700	2100
Collection efficiency, %	99.64	98.58

The magnitude of the difference in collection efficiency for the two wire diameters is great when compared to the differences in electrical operating modes. The larger wires functioned with 30% less current density, 20% less power consumption, and 14% greater average electric field strength. The difference in penetration is plotted in Figure 4, superimposed on the theoretical projections which were shown in Figure 1. The data points fit the theoretical relationship between penetration and electric field strength. This confirms the argument that electric field strength plays the dominant role in ESP performance, and small changes in the strength of the electric field have a large effect on the penetration.

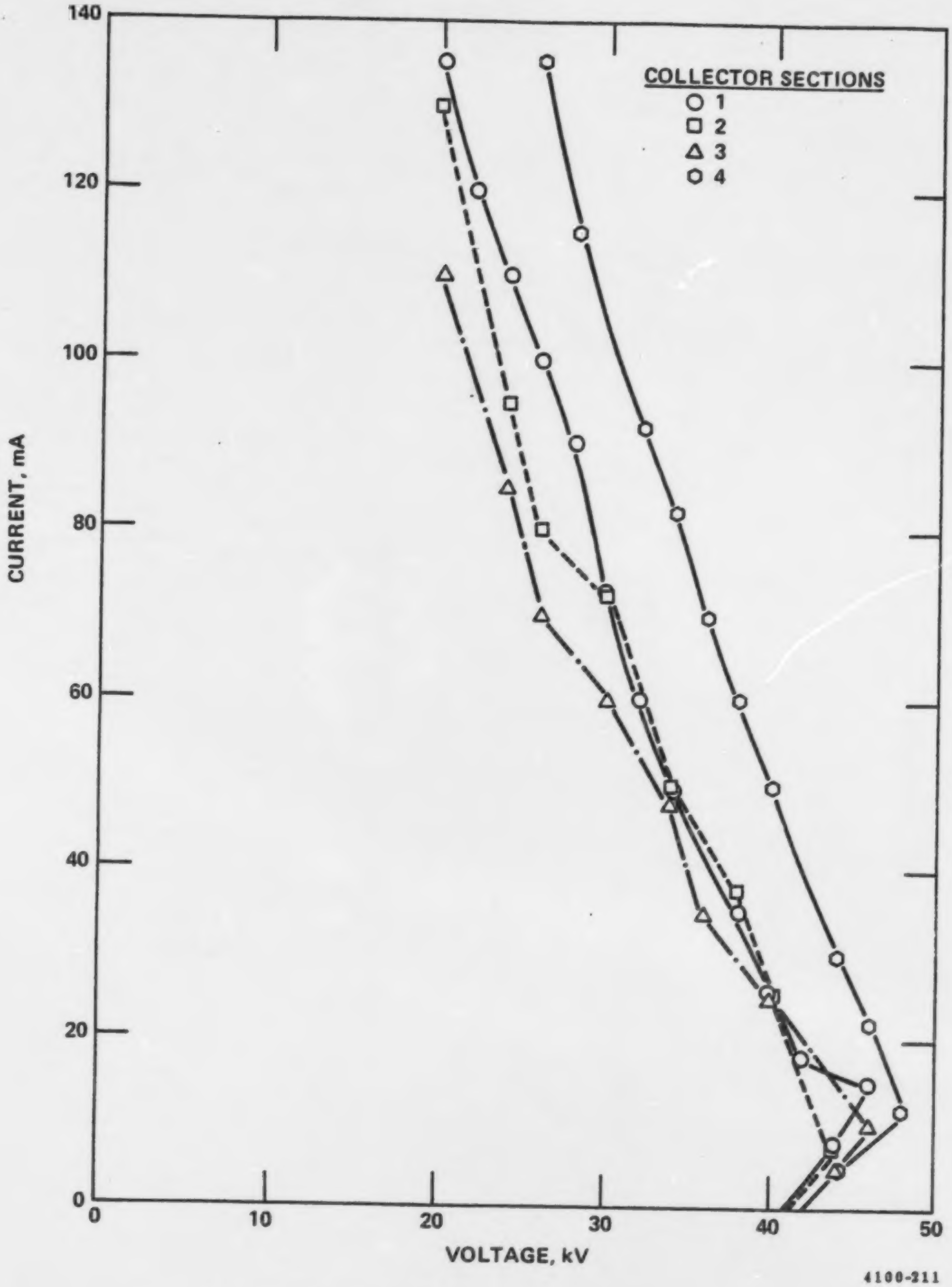

Figure 2. Voltage-current curves for 3/8-inch diameter wires at 325° F.

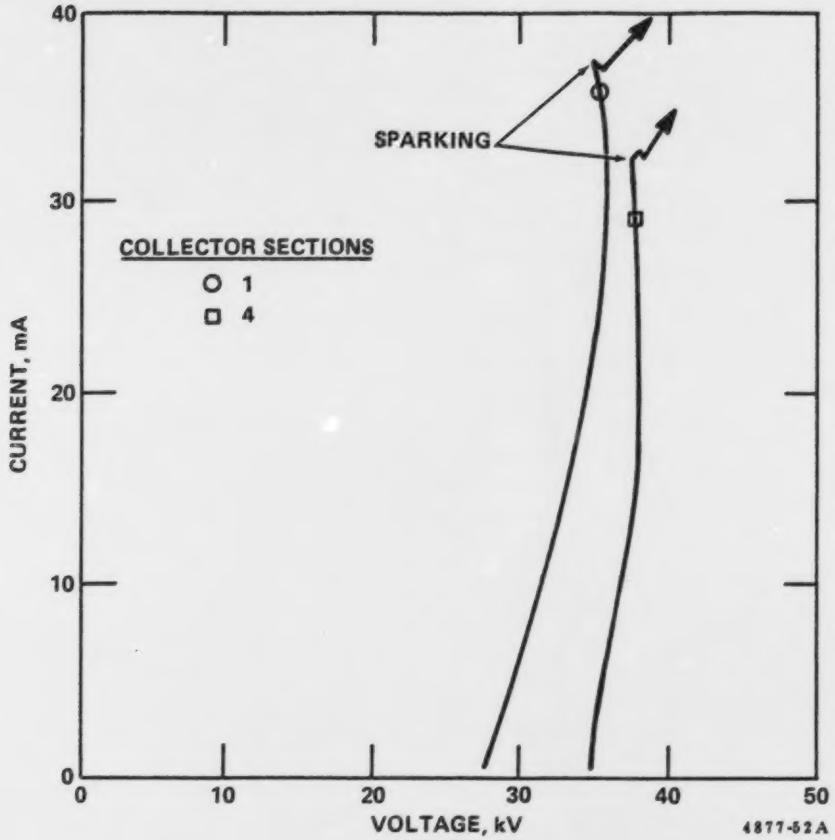

Figure 3. Voltage-current curves of 1/8-inch diameter wires at 325°F.

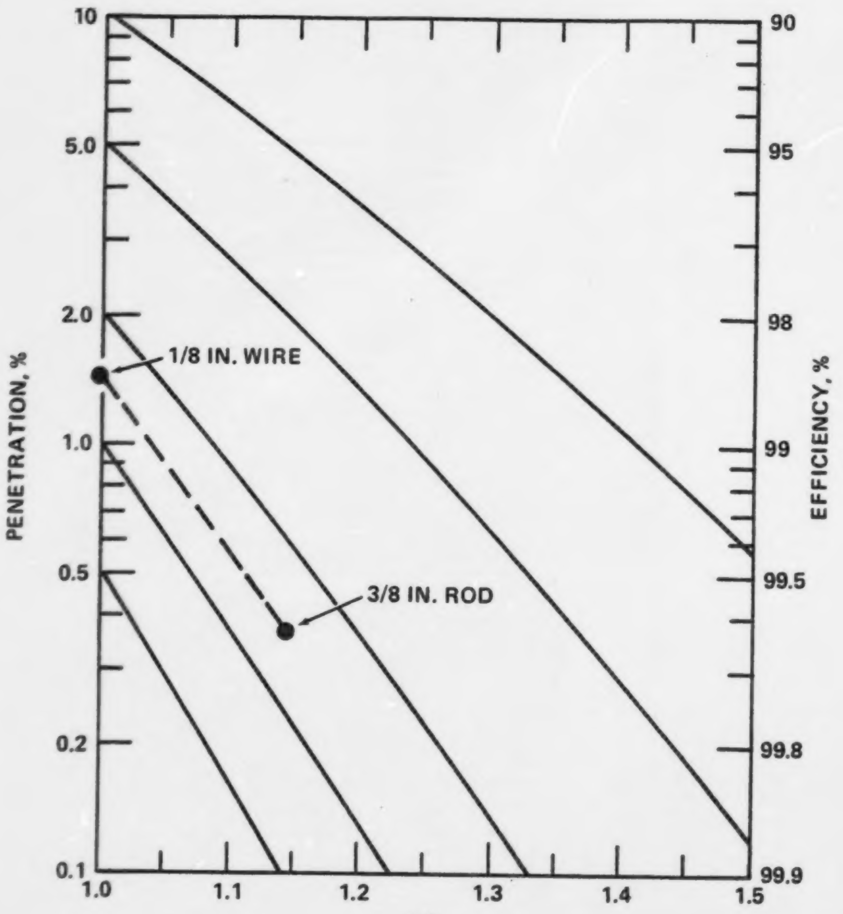

Figure 4. Measured penetrations at two values of electric field strength superimposed on theoretical curves.

LABORATORY CONFIRMING EVIDENCE

Tests were conducted on a 1000 acfm pilot ESP at the EPA Industrial Environmental Research Laboratory in Research Triangle Park, North Carolina. The tests were designed to provide an independent assessment of the performance of the large diameter electrodes versus the conventional discharge electrode design. The pilot ESP was tested with 3/8- and 1/8-inch diameter electrodes installed in a 9-inch wide duct. Wire-to-wire spacing was 9 inches. There are four electrical sections in the single-lane pilot ESP, each with 32 ft^2 collecting surface area. The SCA for the ESP is therefore 128 ft^2/kacfm.

Fly ashes from two sources were used in the tests. The resistivities of the two ashes were $\sim 2x10^{12}$ and $9x10^{10}$ ohm-cm at 300°F. Comparative performance for 3/8- and 1/8-inch diameter discharge electrodes was determined from cascade impactor and Method 17 mass concentration measurements. Operating points for the two electrode configurations were chosen to given the lowest possible outlet emissions as monitored with an opacity meter. In general, both electrodes operated with very limited sparking.

The comparative performance of the discharge electrodes in the presence of high resistivity fly ash (low 10^{12} ohm-cm) was, within the accuracy of the measurements, equivalent to the results from the field measurements on the large pilot ESP at Bull Run Steam Plant. The required low current density operation and the large difference in the electric field strength favored the large diameter discharge electrode. The 3/8-inch diameter wires were approximately four times as effective in reducing penetration as the 1/8-inch wires. These results were anticipated due to the theoretical support as well as the field test results.

The performance benefit of large diameter wires in the case of moderate resistivity fly ash was not as straightforward to predict. The large diameter electrodes operate near the sparking limit with low current emission. The operating current level is constrained by the wire-plate separation and not the precipitated ash. The relatively small diameter electrode has a much broader range of current emission, and the operating level is typically constrained by the ash resistivity. In the limit, reducing the ash resistivity has the effect of reducing the difference in electric field strength between the large and small diameter wires, and increasing the difference in operating current density. In fact, the difference in the electric field strength increases to a maximum value and then decreases as the resistivity of the ash decreases. The trends are illustrated in Figure 5.

Tests were conducted in the laboratory with fly ash having a resistivity of $9x10^{10}$ ohm-cm at 300°F. The average electrical operating values for the pilot ESP (averaged over the four electrical sections and several tests) are presented in Table II. The percent differences between the 1/8-inch diameter electrodes and the 3/8-inch diameter electrodes are also given in the Table. In this case, there were large differences in current and voltage. The measured fractional penetrations are shown in Figure 6 and listed in Table III. The percent difference in penetration as a function of particle diameter is plotted in Figure 7. The mean difference in penetration was ~21%.

TABLE II. LABORATORY ESP OPERATING DATA FOR MODERATE RESISTIVITY FLY ASH

Averages:	3/8-inch	1/8-inch	Units	% Difference
Voltage:	52.510	31.167	kV	-68.48
Current:	0.302	0.899	mA	66.41
Current density:	9.438	28.099	$\mu A/ft^2$	66.41
Power:	0.485	0.877	watts	44.64

TABLE III. PENETRATION VS. DIAMETER MEASURED IN LABORATORY TEST WITH MODERATE RESISTIVITY FLY ASH

Particle diameter	3/8-inch wire average penetration	1/8-inch wire average penetration	% Difference in penetration
0.2	0.406	0.360	-12.778
0.3	0.655	0.535	-22.430
0.4	0.369	0.288	-28.278
0.5	0.255	0.225	-13.497
0.8	0.247	0.285	13.333
1	0.182	0.286	36.510
1.5	0.155	0.301	48.571
2	0.169	0.305	44.479
2.5	0.163	0.288	43.417
4	0.089	0.172	48.245
5	0.058	0.112	47.611
7.5	0.019	0.175	89.413
10	0.029	0.041	27.753
15	0.060	0.052	-14.776
20	0.045	0.048	4.870
Averages:	0.193	0.231	20.830

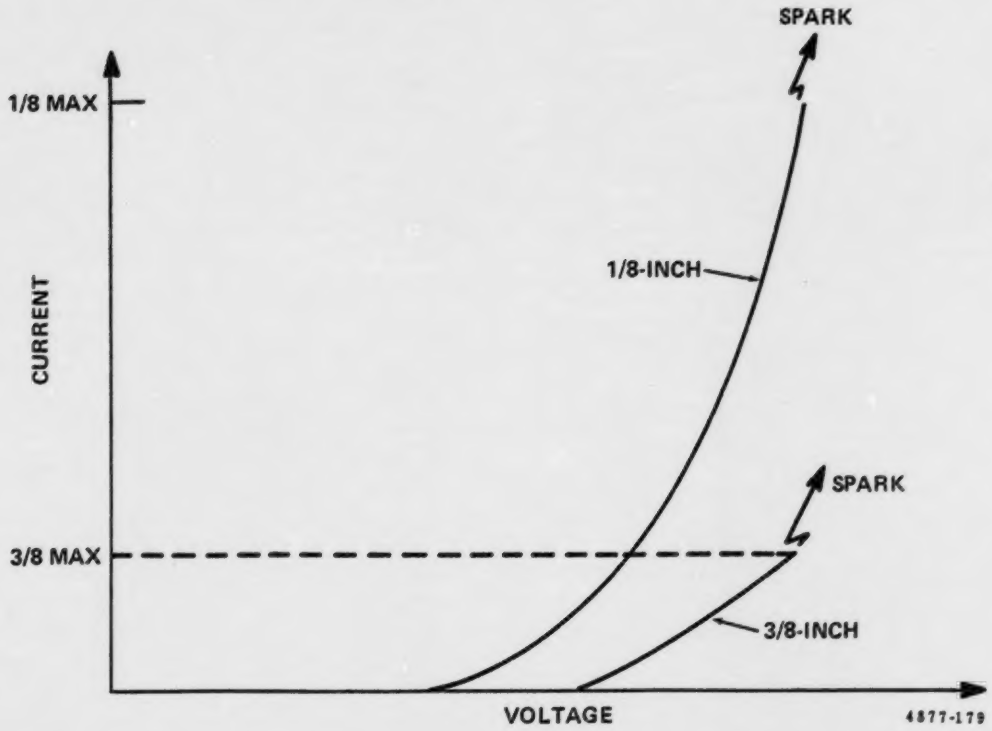

Figure 5. Typical voltage-current characteristics of 3/8-inch and 1/8-inch diameter discharge electrodes.

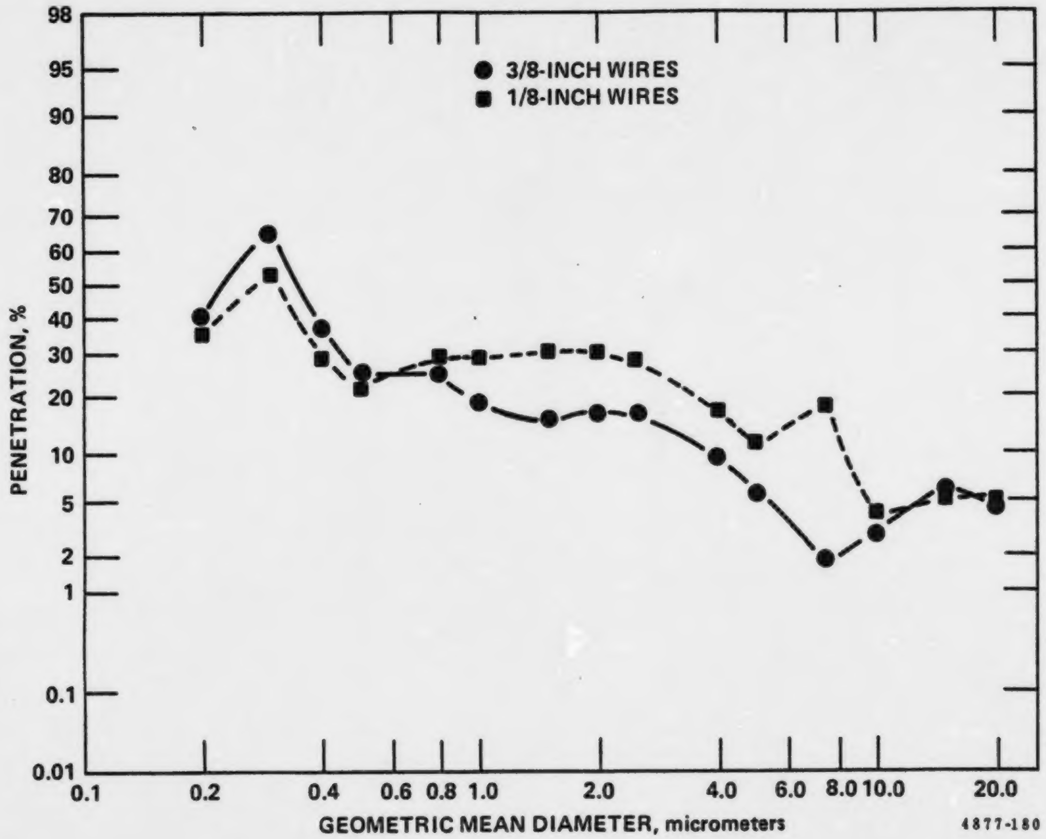

Figure 6. Measured fractional penetration for small pilot ESP with 3/8- and 1/8-inch diameter discharge electrodes. Temperature = 300 °F; ash resistivity = 9 x 10^{10} ohm-cm.

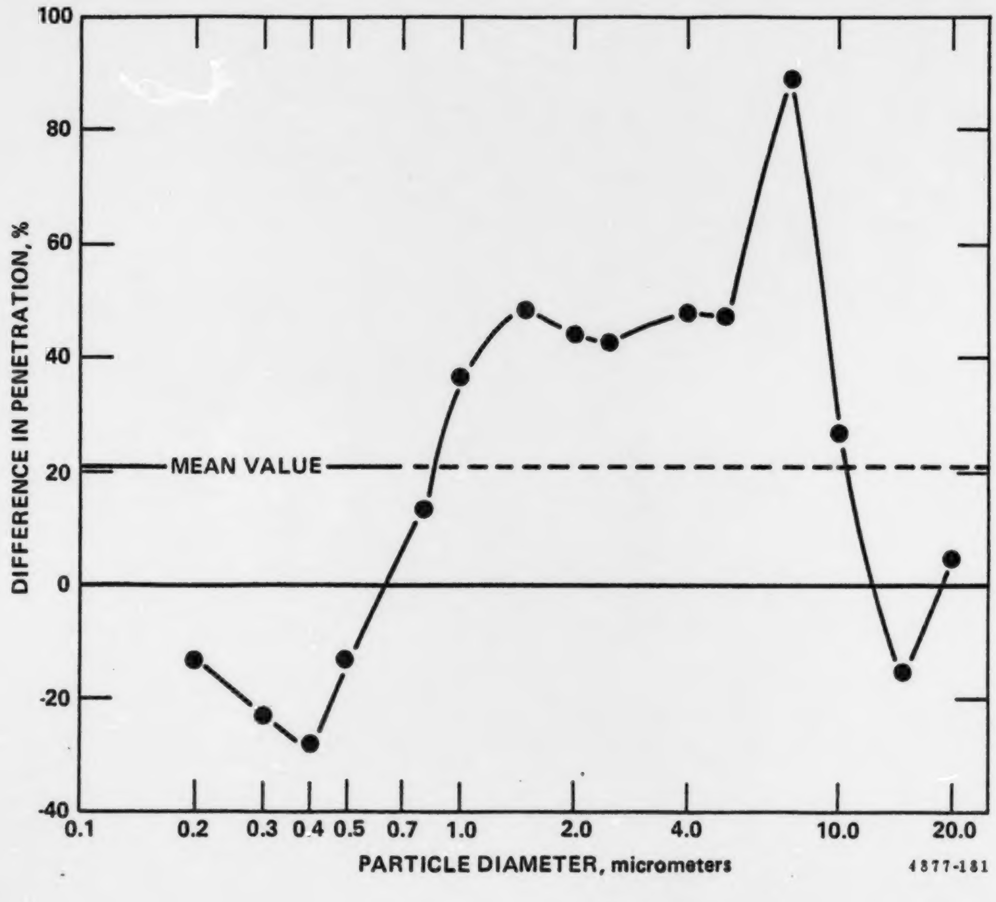

Figure 7. Percent difference in fractional penetration between 1/8- and 3/8-inch diameter discharge electrodes. Temperature = 300 °F; ash resistivity = 9 x 10^{10} ohm-cm.

CONCLUSIONS

Electrodes with emitting surfaces having small radii of curvature have dominated commercial ESP designs. This feature has been preferred because of the uniformity of current emission, high capacity for current emission, and large operating range of voltage between corona onset and sparkover. These characteristics are all desirable. However, in practice the operating current level is restricted to a moderate-to-low level in many cases to prevent back corona formation. Low current levels are adequate to charge particles to saturation within a few feet in the ESP. These facts, combined with the theoretical descriptions of electrostatic precipitation, support the practice of maximizing the electric field strength in the design of electrodes.

Tests in a large pilot ESP have confirmed the accuracy of the theoretical models. Tests with 3/8- and 1/8-inch diameter discharge wires in the same ESP under the same flue gas conditions enabled a direct comparison of the effect of electrical operating conditions on ESP performance. The average electric field strength differed by less than half the difference in current density. The change in the strength of the electric field completely accounted for the very large change in penetration.

Laboratory tests with high resistivity fly ash in a small pilot ESP yielded results in agreement with the field test data. Tests in the laboratory with moderate resistivity indicated a reduced level of performance benefit for the 3/8-inch diameter electrodes.

Conventional practice in the design of corona discharge electrodes has been based on historical precedent and incomplete understanding of the implications of the theoretical models of electrostatic precipitation. Each precipitator installation should be designed in light of the pertinent constraints on performance, such as ash resistivity and loading. In general the bias in the design of electrodes should be toward those which operate at the highest electric field strength. This technology is definitely suited to retrofit applications. Significant performance benefits may result in many instances from the use of large diameter wires as discharge electrodes.

ACKNOWLEDGEMENTS

Much of this work was performed under EPA Contract No. 68-02-2683. The measurements of the performance of the large pilot scale ESP were supervised by Todd Snyder of Southern Research Institute. The laboratory experiments were completed under the direction of Geddes Ramsey of EPA. Their efforts are gratefully acknowledged.

REFERENCES

1. White, H.J. Industrial electrostatic precipitation. Addison-Wesley, Reading, Massachusetts, 1963. pp 363-364.

2. Lagarias, J.S. Discharge electrodes and electrostatic precipitation. J. of APCA 10(4): 271-274, 1960.

3. Bush, P.V. and Snyder, T.R. Laboratory analysis of corona discharge electrodes and back corona phenomena. Paper presented the The Fifth Symposium on the Transfer and Utilization of Particulate Control Technology, U.S. EPA and EPRI, Kansas City, Missouri. August 27-30, 1984.

4. Pontius, D.H., Felix, L.G., McDonald, J.R., and Smith, W.B. Fine particle charging development. EPA-600/2-77-173 (NTIS PB271727). U.S. Environmental Protection Agency, Research Triangle Park, North Carolina, 1977. 240 pp.

5. Bush, P.V. and Pontius, D.H. Pilot demonstration of the precharger-collector system. In: Proceedings of the Third Symposium on the Transfer and Utilization of Particulate Control Technology: Volume I. Control of Emissions from Coal Fired Boilers. EPA-600/9-82-005a (NTIS PB83-149583). U.S. Environmental Protection Agency, Research Triangle Park, North Carolina, 1982. pp 157-164.

6. Bush, P.V. and Pontius, D.H. Pilot demonstration two-stage ESP test results. Presented at the Fourth Symposium on the Transfer and Utilization of Particulate Control Technology, U.S. Environmental Protection Agency, Houston, Texas. October 11-15, 1982.

CONVERSION FACTORS

Readers more familiar with metric units may use the following to convert to that system.

Nonmetric	Times	Yields Metric
°F	5/9(°F-32)	°C
ft	30.48	cm
ft^2	0.093	m^2
ft^3	28.3	liters
gr	0.065	g
in.	2.54	cm

TECHNICAL EVALUATION OF PLATE SPACING EFFECTS ON FLY ASH COLLECTION IN PRECIPITATORS

by: Ralph F. Altman
Electric Power Research Institute
Chattanooga, TN 37411

Gerald W. Driggers, Ronald W. Gray
Combustion Engineering
Birmingham, AL 35243

James L. DuBard
Southern Research Institute
Birmingham, AL 35255

E. C. Landham, Jr.
Southern Research Institute
Denver, CO 80210

ABSTRACT

A joint program between EPRI and C-E is being conducted to evaluate the effects of increasing plate spacing and applied voltage in precipitators collecting coal combustion fly ash. Plate spacings will range from nine (9) inches to twenty-two (22) inches during the experimental program being conducted at the EPRI Arapahoe facility pilot plant. Spacings up to 31.5 inches (800 mm) have been reported on non-fly ash applications and up to 15.7 inches (400 mm) on coal fly ash outside the United States with apparent success. This is the first major experimental program in the U.S. to systematically examine the effects on collection efficiency of various plate spacings, applied voltages, and fly ash resistivities. Total mass and fractional collection efficiencies will be measured under the various operating conditions, and these data will be examined by various analytical techniques to determine the best approach for comparing performance under the varying conditions and to facilitate scale-up to full size precipitators.

This paper reports on the results thus far obtained and their interpretation.

INTRODUCTION

There are more than one thousand electrostatic precipitators in operation at utility plants today; and although few utilities have major construction programs underway, more utility precipitators will undoubtedly be built in the future. Further, the performance of many existing precipitators will have to be improved to comply with changing particulate emission regulations or to cope with changing coal supplies and operating conditions. As a result, the electric utility industry, through the Electric Power Research Institute, is sponsoring a number of research projects to improve electrostatic precipitator performance and reduce cost.

The goal of one of the principal projects in this area is the determination of the effect of plate spacing on precipitator performance. The Environmental Systems Division of Combustion Engineering is a cosponsor and the prime contractor for the work. The interest in this topic derives from international experimental and operating evidence that ESP performance is relatively insensitive to plate spacing and that required total collecting plate area can be reduced due to the higher voltages possible at wider spacings.

A survey of precipitator installations in other countries has identified over 200 industrial or utility units with plate spacings exceeding 305mm (12 inches) either in operation or under construction. Most of these have a spacing of 400 mm (15.7 inches) with some in Japan as great as 800 mm (31.5 inches). Although primarily industrial units, there are also several flyash installations either in operation or under construction. Most data on these units is proprietary and not in the open literature. It is particularly notable, however, that there are twelve (12) 600 MW or larger units on order or under construction in South Africa with 400 mm spacing, reflecting the convincing nature of the available data. This aggressive approach is based on economic considerations since the wide spaced ESP is lighter and less costly to build. In fact, early cost estimates made as a part of this project indicate a potential capital cost reduction of 10-15%. This analysis is illustrated on Figure 1.

Some of the early work on the effect of plate spacing was by G. Heinrich using data supplied by Dr. R. F. Heinrich (1). The work suggested that precipitator performance was related to specific corona power and independent of specific collecting area. This work resulted in a patent on the subject which has since expired (1) (2). In fact, White (3) derived an expression that relates precipitator particle loss, and hence collection efficiency, to corona power and volume flow rate only. Although this approximate expression was not specifically derived to justify increased plate spacings, the statement is made that "the details of the precipitator design do not enter into the basic relation between precipitator loss and corona power."

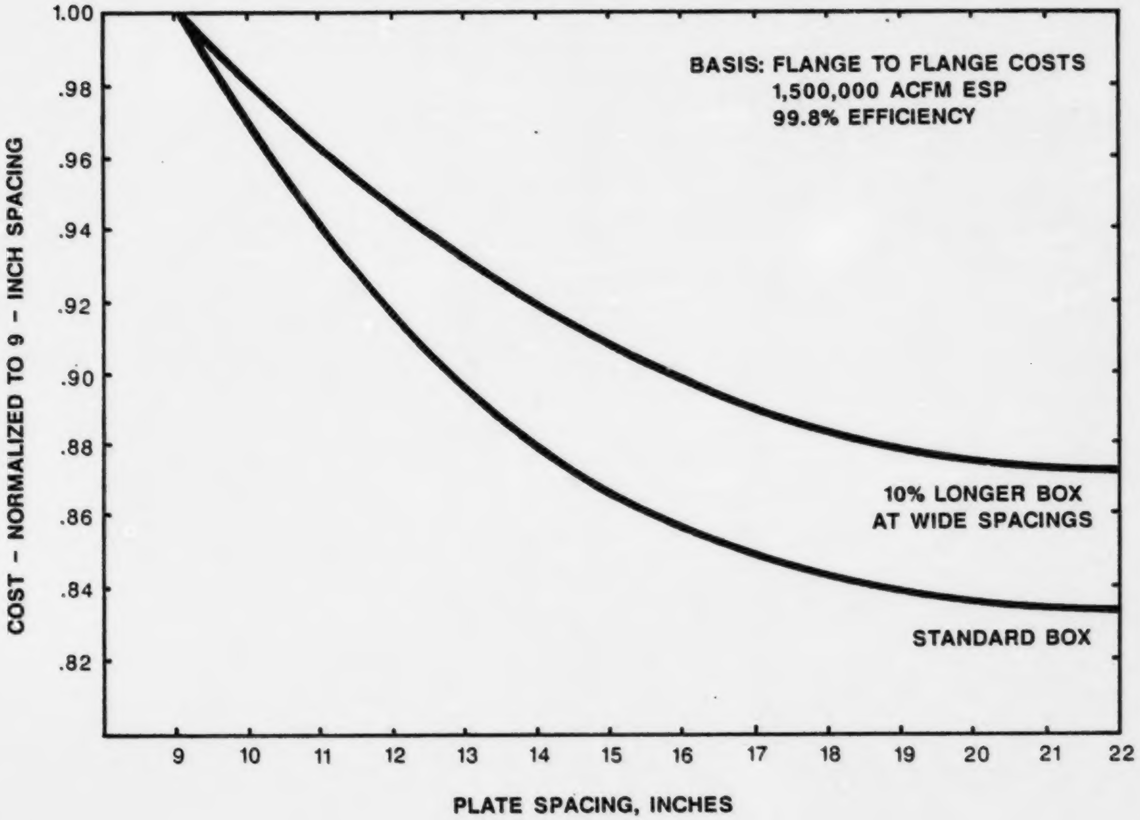

Figure 1. Normalized Cost - vs - Plate Spacing for a Large Precipitator

More recent work conducted in Japan (4) has provided experimental evidence to support the connection between the electric field strength in the vicinity of the collection plate and precipitator collection efficiency. The thrust of this work is that effective migration velocity is proportional to this electric field and that the field near the plate increases as plate spacing increases. However, other work indicates the effect of plate spacing is sensitive to operating parameters (5) or to other details of construction (6). For further background reading on this subject, see reference (1) and references cited therein.

EXPERIMENT PLAN

In view of the potential benefit to be gained from increasing precipitator plate spacing (reduced weight and cost and simplified construction), a project has been initiated to develop a definitive understanding of the effect of plate spacing on the performance of precipitators in utility applications. The first phase of the work is being conducted at the Arapahoe Test Facility where EPRI conducts many of its pilot scale tests of environmental control systems (7). In phase one, a 5000 ACFM pilot precipitator will be operated with plates spaced from 9 to 22 inches. Flue gas will be drawn from unit four of Public Service Company of Colorado's Arapahoe Power Plant for all of these tests. The tests are exploratory in nature; no attempt will be made to optimize precipitator design for each plate spacing. If results from small scale pilot tests are encouraging, then verification tests will be conducted at a much larger scale with more attention paid to details of construction.

The pilot precipitator at Arapahoe has three independent fields in the direction of gas flow. Each field is energized by a transformer-rectifier (TR) set with maximum ratings of 150KV and 40mA. Plates are rapped on the trailing edge and discharge wire frames are rapped at both leading and trailing edges. Before commencing the performance tests, certain modifications were made to the precipitator to ensure a uniform gas velocity profile at the inlet and to minimize electrical section bypassage (sneakage). Other modifications were made to provide the clearances necessary for operation with 22 inch plate spacing. A one-half scale clear acrylic model of the precipitator was constructed, and air flow tests were conducted at Combustion Engineering's model facility in Birmingham, Alabama to select the baffles and inlet and outlet flow control devices. At the conclusion of the flow tests, it was determined that maximum electrical section bypassage should be less than 5% per field and that RMS deviation in the gas flow distribution at the precipitator inlet was less than 10%.

In addition to the flow model study, a limited number of tests were conducted to determine a suitable discharge electrode spacing for different plate spacings. These tests were performed in air at ambient temperature using a simple wire frame and a segmented collecting electrode.

The current distributions at the plate measured with this apparatus indicated that a single wire spacing of 6" would produce reasonable voltage/current curves and a relatively uniform current distribution at the plate for all plate spacings (9 through 22 inches). Although this result was unexpected, performance tests conducted at Arapahoe thus far indicated the decision to use a single wire spacing was justified. The data gathered at 9, 12, and 18 inches (the 22 inch performance tests were not completed in time to be reported in this paper) have yielded relatively high efficiencies under all test conditions. More work must be done to optimize discharge electrode spacing and design; however, the single wire spacing has produced satisfactory data for purposes of comparison.

Following the completion of the flow tests, discharge electrode spacing study, and precipitator modifications, performance testing was begun at Arapahoe in January, 1984. Southern Research Institute is a major subcontractor and their personnel are responsible for these tests and subsequent data analysis. The test conditions are summarized in Table 1. Inlet flue gas temperature was held constant at 300°F, and the precipitator was operated 24 hours a day at constant flow during all performance tests. All three fields were kept energized. Two flue gas flow rates were used to provide variation in gas treatment time and SCA. Sulfur trioxide (SO_3) conditioning is used to adjust fly ash resistivity from its normal level of approximately 10^{12} ohm-cm to about 10^{10} ohm-cm so that data that can be applied to both high and low sulfur coal applications are obtained.

TABLE 1. PLANNED AND TESTED CONDITIONS FOR PILOT SCALE TESTS AT ARAPAHOE

Test Condition	Plate Spacing Inches	SCA (Nominal) ft^2/1000ACFM	Flue Gas Flow Rate ACFM	SO_3 Conditioning
9 - 1	9	370	3,630	not used
12 - 1	12	275	3,690	not used
18 - 1	18	185	3,600	not used
22 - 1	22	185	3,600	not used
9 - 2	9	260	4,900	not used
12 - 2	12	195	5,220	not used
18 - 2	18	130	4,670	not used
22 - 2	22	130	4,900	not used
9 - 3	9	370	3,520	used
12 - 3	12	275	3,630	used
18 - 3	18	185	3,600	used
22 - 3	22	185	3,600	used
9 - 4	9	260	5,000	used
12 - 4	12	195	4,720	used
18 - 4	18	130	4,900	used
22 - 4	22	130	4,900	used

Comprehensive sets of performance data are being gathered at each test condition. These data include total mass collection efficiency measurements made using mass trains (EPA method 17) and particle size efficiency measurements made with impactors. Flue gas composition including H_2O, SO_2, SO_3, and O_2 is determined on a periodic basis. Fly ash resistivity is measured daily using an in-situ probe with a point-to-plane geometry. Ash samples are gathered periodically for chemical analysis. In addition to these performance measurements, a modified back ionization probe developed by Dr. Senichi Masuda (8) in cooperation with Kanomox Corp. of Japan is being used to measure the electric potential near the collection plate for selected operating conditions at each plate spacing. A knowledge of the electric field which can be derived from the potential data should help provide an understanding of the efficiency data since the migration velocity of fly ash particles to the plate should be roughly proportional to this field. At the time of preparation of this paper, the potential probe data are being analyzed, and these results will be reported elsewhere.

EXPERIMENTAL RESULTS

At the beginning of the tests conducted at each plate spacing, voltage-current data are taken at ambient conditions and plotted. These plots, presented in Figures 2 and 3, were used to verify alignment, compare electrical behavior, and to determine the voltage at which sparkover occurs. Optimum ESP performance cannot be achieved if power input to any field is limited by sparking from a discharge element to any grounded surface except the collection plates. Voltage limited by sparking to a support beam or baffle is an indication of inadequate clearance. The clearances needed for 9" and 12" plate spacings are well established and can be incorporated into the design of a small pilot precipitator without difficulty. The clearances needed for operation at 18 and 22 inches were selected at the beginning of the program based on experimental data (provided by Combustion Engineering) for sparkover voltages as a function of high voltage and grounded shapes. It was more difficult to provide the larger clearances without increasing gas sneakage to an unacceptable level in this small pilot, but a satisfactory design was developed; and the pilot ESP was modified to provide the necessary clearances. Observations made at the beginning of the tests at each spacing verified that voltage was limited by sparking to the collection plates, and voltage-current curves demonstrated that sparkover voltage was roughly proportional to the plate spacing.

After the alignment and clearances were verified at each spacing, flue gas flow through the pilot ESP was started, and the precipitator was operated for several days. When the unit reached reasonably stable operating conditions, performance data gathering was begun. As stated earlier, both total mass concentrations and particle size distributions are measured at the inlet and outlet of the precipitator during the performance tests.

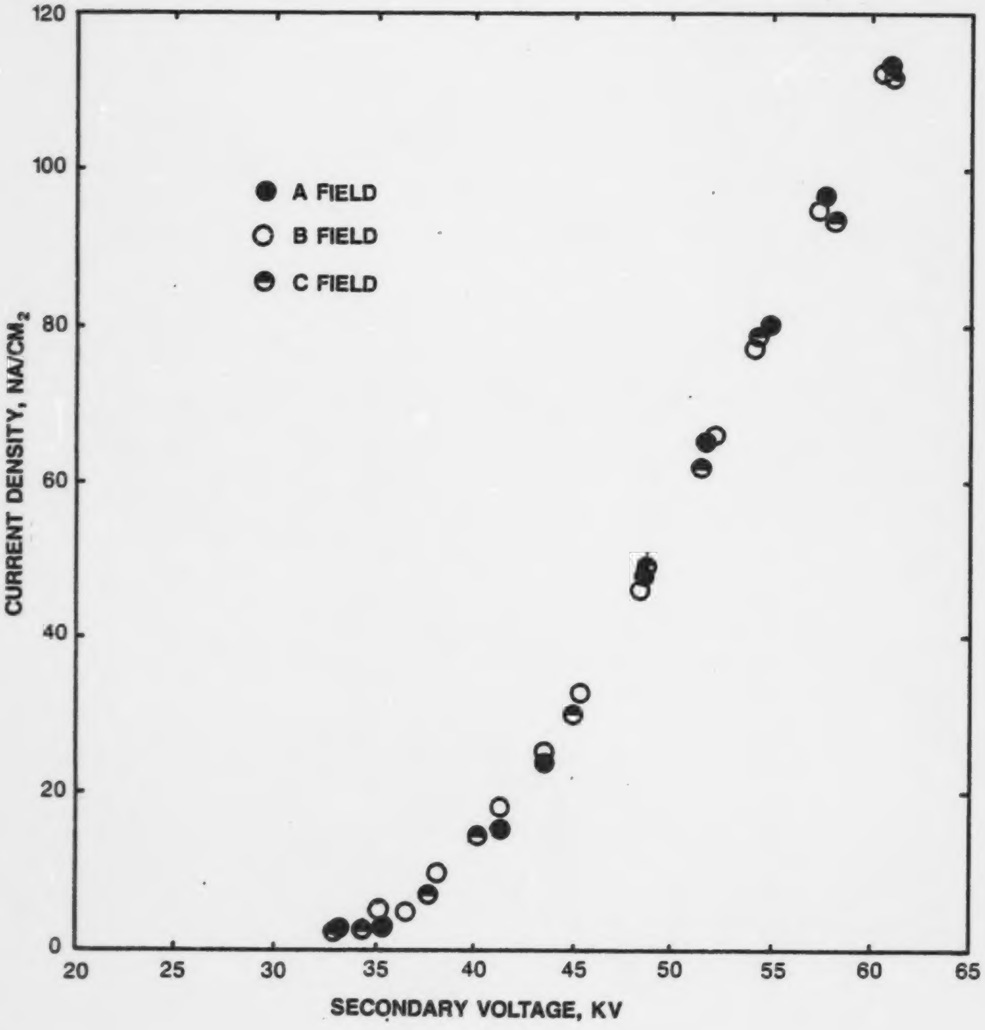

Figure 2. Clean Plate Air Load, V-I Data for the Three Electrical Sections Taken at Ambient Conditions

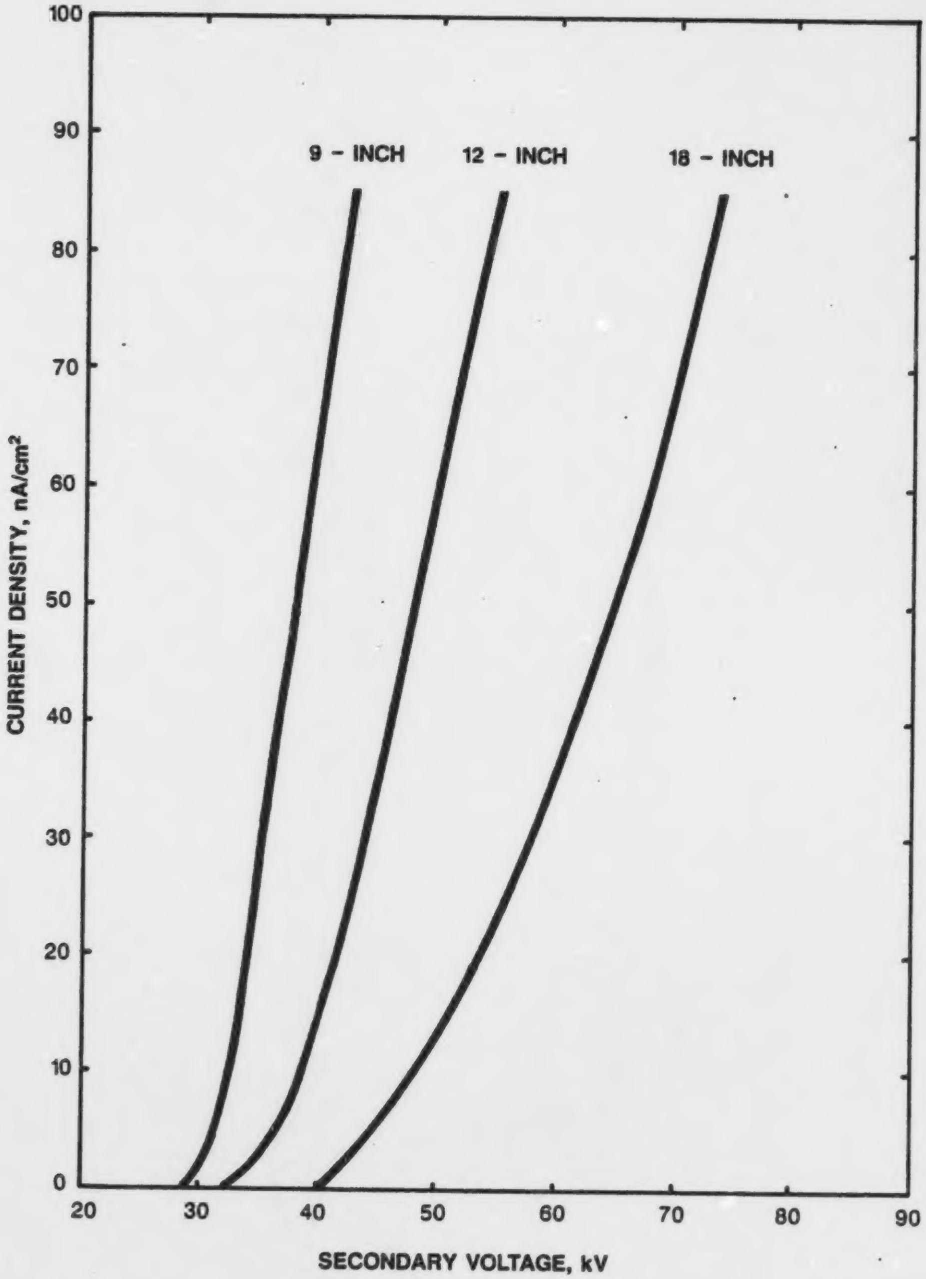

Figure 3. Clean Plate Air Load V-I Curves for the Three Spacings

At the time this paper was prepared, only the mass concentration data had been analyzed, so only these tests with plates spaced at 9 and 12 inches and the high resistivity tests with plates spaced at 18 inches were complete. However, these preliminary data are both interesting and encouraging.

Before presenting the mass efficiency data, it is necessary to discuss the in-situ resistivity data taken during the tests since these data are needed to interpret the performance results. The resistivity data are plotted in Figure 4. The inherent resistivity of the fly ash at Arapahoe is high, usually above $1x10^{12}$ ohm-cm. In fact, the resistivity was greater than this value during all of the tests with no gas conditioning except one. During the low flow, high resistivity test with the plates spaced at 9 inches (condition 9-1 in Table 1), the average resistivity was approximately $6x10^{11}$ ohm-cm, which is one-half order of magnitude lower than the resistivity measured during the other test conducted without flue gas conditioning. This change in resistivity is attributed to a change in the coal supply that took place during the 9 inch tests. During the tests conducted with SO_3 conditioning, it is possible to exercise better control over fly ash resistivity, and the resistivity has stayed in the 3 to $5x10^{10}$ ohm-cm range.

The average collection efficiency data from the tests completed so far are plotted in Figure 5. These data show the expected trends with flue gas flow rate and fly ash resistivity. This fact is apparent if the data collected with the plates spaced at 9 inches is examined. When the resistivity and the gas flow rate were both high, the measured collection efficiency was 98.5%. When the flow rate was low, the efficiency increased to 99.4% (but recall the resistivity was lower than normal during these tests). When the resistivity was lowered to $4x10^{10}$ ohm-cm, the collection efficiency was determined to be 99.7% at the high flow rate and 99.9% at the low flow rate. The same trends are evident in the data gathered with the plates spaced at 12 inches. During the high resistivity tests the collection efficiency was 98.4% at high flow rate and 99.0% at the low flow rate and increased to 99.8% and 99.9% at the high and low flow rates respectively when the resistivity was lowered by SO_3 conditioning.

The most interesting data in Figure 5 are the two average efficiency points for the high resistivity tests with the plates spaced at 18 inches (the only 18 inch tests completed when this paper was being prepared). The efficiencies are unchanged from those measured with the plates spaced at 12 inches, i.e. 98.4% at the high flow rate and 99.0% at the low flow rate. In fact, the collection efficiency changed very little during all of the high flow, high resistivity tests at 9, 12, and 18 inches. The changes that did take place are comparable to the day to day fluctuation in the efficiency data at a fixed spacing. The exception to this trend is the low flow rate, 9 inch efficiency data which was taken during a period of time when the resistivity was lower than usual.

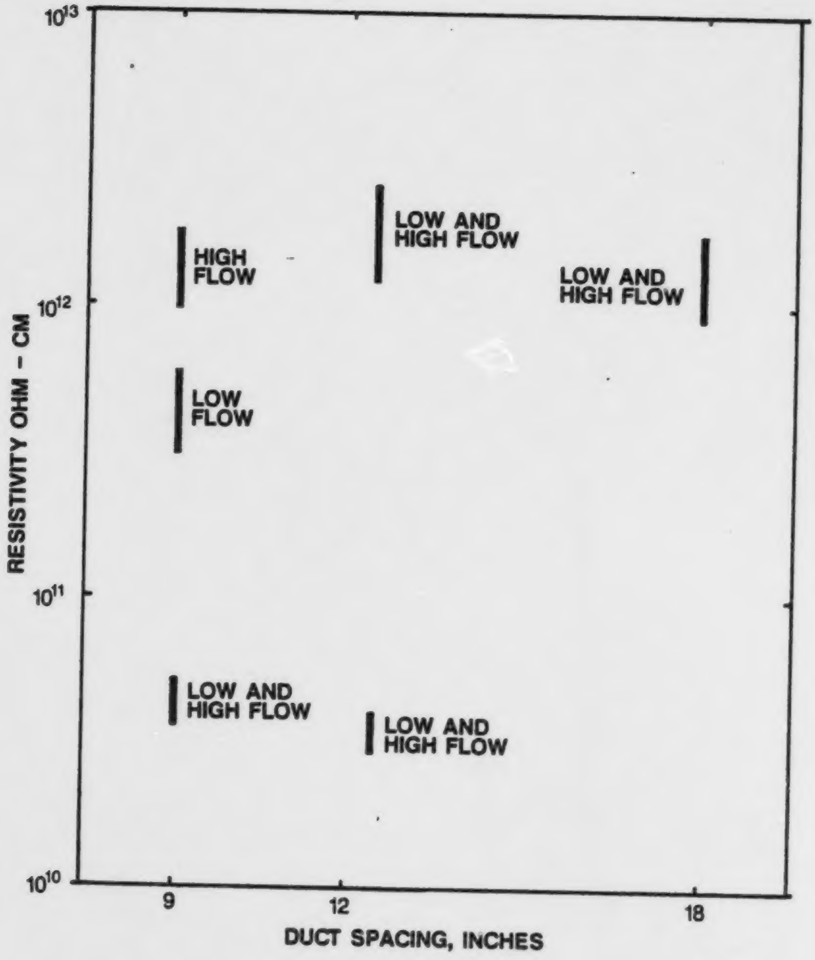

Figure 4.

Resistivity Measured In-Situ During Various Phases of the Test Program

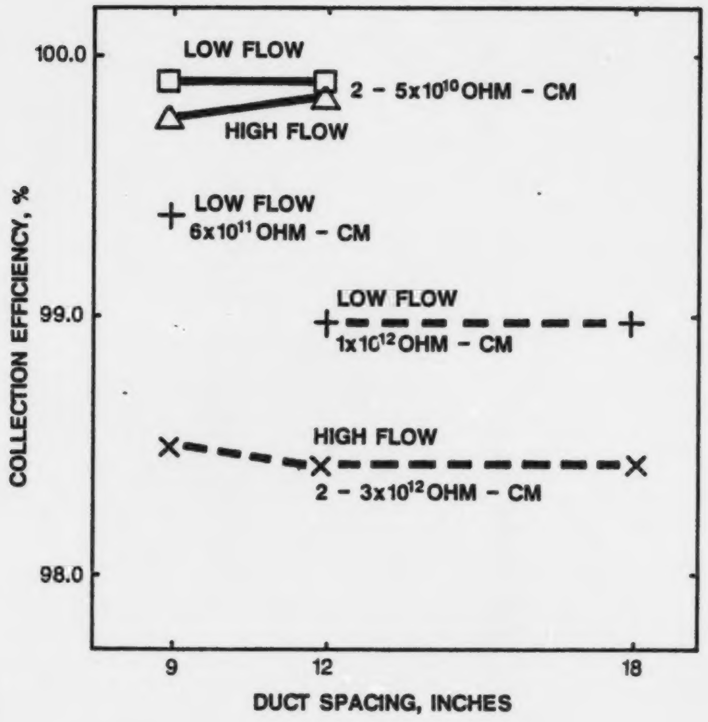

Figure 5.

Comparison of Efficiencies Obtained Under Different Flow and Resistivity Conditions

The efficiency data are compatible with the operating voltages measured during the performance tests. These data, which are summarized in Table 2, show that the average voltage for each field and for the precipitator as a whole was roughly proportional to the plate spacing. This proportionality occurred even though spark rate was used to control the voltage in all fields during all of the tests. These data and the data of others suggest that, for high resistivity applications, operating voltage must be at least proportional to plate spacing if collection efficiency is to be maintained as the plate spacing is increased.

TABLE 2. ELECTRICAL OPERATING VOLTAGES FOR VARIOUS CONDITIONS

Spacing (inches)	Resistivity (ohm-cm)	A FIELD kV	B FIELD kV	C FIELD kV	ESP AVERAGE kV
9	10^{12}	33	32	30	32
	10^{10}	36	36	34	35
12	10^{12}	46	45	38	43
	10^{10}	51	51	50	51
18	10^{12}	64	68	65	66

CONCLUSIONS

Since all of the tests and data analysis from the program have not been completed, the conclusions drawn for the existing data analyses must be considered tentative. However, it is true that, so far, the total mass collection efficiency has shown very little sensitivity to increased plate spacing and reduced SCA. This point is illustrated most clearly by the data gathered with a high flue gas flow rate and high fly ash resistivity with the plates spaced at 9, 12, and 18 inches and by the data gathered with low resistivity with the plates spaced at 9 and 12 inches. The preliminary economic analyses indicate that there is a potential capital cost saving for a new precipitator of from 10 to 20% if the plate spacing is increased to a range of 16 to 20 inches. If the results from the tests that have not been completed continue to show little sensitivity to plate spacing, then further work at a larger scale will be needed to begin to optimize performance at wider plate spacings.

The work described in this paper was not funded by the U.S. Environmental Protection Agency and therefore the contents do not necessarily reflect the views of the Agency and no official endorsement should be inferred.

REFERENCES

1. Heinrich, Dieter O. Review and some practical aspects of wide duct spacing. In: Proceedings of the First International Conference on Electrostatic Precipitation. Air Pollution Control Association, Pittsburgh, PA 15230, 1982. p. 638.

2. Darby, K. The use of pilot precipitators for process and design development. Paper presented at second CSIRO Conference on Electrostatic Precipitation, August, 1983.

3. White, Harry J. Industrial Electrostatic Precipitation , Addison-Wesley Publishing Co., Inc., 1963.

4. Misaka, T., Sugimoto, K., and Yamada, H. Electric field strength and collection efficiency of electrostatic precipitator having wide plate pitches. Paper presented at CSIRO Conference on Electrostatic Precipitation, August, 1978.

5. Weber, E. and Wiggers, H. Investigations in a laboratory precipitator concerning the influence of duct width and gas velocity on the collection efficiency and the dust concentration distribution. Staub-Reinh. Luft 40, 1980. p. 469-502.

6. Pearson, K. and Puttick, D. Operating experience with narrow spaced multi-rapped flat plate precipitators treating fly ash from low sulfur coals, and a reconciliation of wide versus narrow spaced collecting plates. Paper presented at Second CSIRO Conference on Electrostatic Precipitation, August, 1983.

7. Altman, R. and Carr, R. EPRI sponsored research at the Arapahoe Test Facility. DOE/METC/84-13 Vol. 2. U.S. Department of Energy, Grand Forks, ND, February 1984. p. 783.

ELECTRICAL CHARACTERISTICS OF LARGE-DIAMETER DISCHARGE ELECTRODES IN ELECTROSTATIC PRECIPITATORS

by: Kenneth J. McLean
University of Wollongong
Wollongong, NSW, 2500, Australia

Leslie E. Sparks
Industrial Environmental Research Laboratory
U.S. Environmental Protection Agency
Research Triangle Park, North Carolina 27711

ABSTRACT

The paper discusses some of the electrical characteristics that arise in an electrostatic precipitator with large-diameter discharge electrodes collecting high resistivity flyash. These electrodes are effective because, once they are contaminated, corona current flows at voltages well below that which conventional theory predicts. The voltage level however is greater than that of the conventionally sized electrodes, and this produces higher charging and collecting electric fields. The individual tuft discharges that produce this corona current are randomly distributed along the discharge electrode, are often unstable, and produce areas of high current density which can easily charge a particle to saturation. The instability and distribution of these tuft discharges affect the formation of back corona and reduce its deleterious effects. The optimum diameter is about 9.5 mm [3/8-in.] for the test condition.

This paper has been reviewed in accordance with the U.S. Environmental Protection Agency's peer and administrative review policies and approved for presentation and publication.

INTRODUCTION

One of the most interesting recent proposals for improving the performance of conventional electrostatic precipitators collecting high resistivity fly-ash is to use large-diameter discharge electrodes. Their potential advantage was first observed at the EPA/SORI test facility at the TVA station, Bull Run, where the conventional 3.2 mm (1/8-in.) wires were replaced with 9.5 mm

[3/8-in.] diameter wires with the result that both the voltage levels increased and the collection efficiency improved (1).

This effect was further investigated at the EPA in-house Pilot Electrostatic Precipitator at Research Triangle Park, N.C., where it was confirmed that the voltage levels increased and efficiences improved with the larger diameter discharge electrodes.

The purpose of this paper is to identify the special electrical and corona discharge characteristics that occur in electrostatic precipitators with large-diameter electrodes collecting high resistivity flyash and to speculate on how they affect the collection mechanism.

EXPERIMENTAL PROCEDURES

The fundamental mechanisms of corona discharge formed on contaminated discharge wires of different sizes were investigated using the EPA Optical Electrostatic Precipitator. This unit comprises a single gas lane with plates 1.2 m square, made of plexiglass and operated at ambient temperature. The plates are covered with strips of aluminium tape separated from one another by a small gap that provides a means of measuring the current distribution. These strips can be arranged to run parallel or at right angles to the discharge wires. The unit is surrounded by a dark curtain so the nature of the electrical discharges can be observed through the plexiglass frame and panels.

The individual tuft discharges were simulated by a small metal projection on the discharge wire. This produced a stable single discharge which could be easily investigated. For other tests, the discharge wire was covered with flyash, and the characteristics of the naturally produced tuft discharges were identified and measured.

Measurements at elevated temperatures and identification of back corona effects were made on the EPA's Pilot Electrostatic Precipitator. This unit comprises a single pass with four zones comprising collecting plates 1.2 m square. For these tests, gas flow was 0.47 m^3sec at 150 ^oC and the ash injected with an air blast gun to give a dust concentration at the inlet of 2.3 g/m^3. The electrical measurements recorded were made at the inlet zone and current distribution measured by means of a special plate comprising a matrix of isolated 50 mm square segments covering an area of 610 mm by 406 mm.

ELECTRICAL CHARACTERISTICS

VOLTAGE-CURRENT CHARACTERISTICS

The manner in which large diameter electrodes operate can best be understood from the voltage-current curve of a contaminated electrode system as shown in Figure 1.

The perfectly clean electrode characteristic starts at the critical voltage, V_C, and can be modelled using Poisson's Equation. This is possible

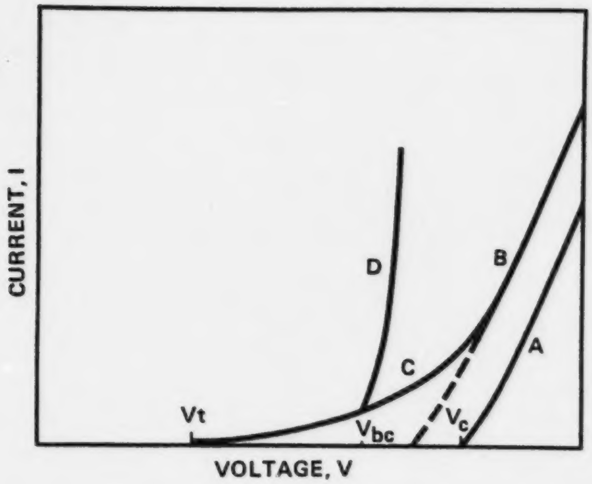

Figure 1. Typical voltage-current characteristics for large diameter-electrodes and high resistivity flyash

A	clean characteristic
B	tuft corona in full corona region, $V > V_c$
C	tuft corona in partial corona region, $V_t < V < V_c$
D	back corona characteristic

because the discharge appears to be evenly distributed along the length of the discharge wire and is mathematically similar to positive corona. The discharge however is much more turbulent, and the physics of the discharge is obviously different.

As the discharge wire becomes contaminated, the visual appearance of the corona discharge changes, and in the steady state, it appears as a number of discrete tufts along the wire's length. The net effect is to,

(i) shift the full corona characteristic to the left, and

(ii) produce a number of randomly located corona tufts between V_c and the tuft corona onset voltage V_t.

This means that corona current flows in this partial corona region at voltage levels well below V_c. The tuft corona onset is approximately 0.6 of V_c, well below the value at which corona current is usually assumed to flow even after taking into account the roughness factor used in the traditional approach. These effects are more obvious with the larger electrodes than with the conventional 3.2 mm electrodes.

The main characteristic of the discharge tufts in this partial corona region is that they switch on at arbitrary points along the discharge wire in such a way that their current fields do not overlap. As the voltage is increased, additional tufts are generated and, at V_c, they are evenly distributed along the full length of the discharge electrode so that their current fields just touch at the plate. Each individual tuft is unstable in this region and often changes its position on the discharge wire.

The equation that reasonably models the average current in this region is given by (2):

$$I = \frac{0.314\ \epsilon o \mu\ V_c^2}{L^2} \left[\frac{V - V_t}{V_c - V_t} \right]^2, \text{ for } V_t \le V \le V_{bc} \qquad (1)$$

$$= 0, \text{ for } V < V_t$$

where
ϵo dielectric constant of air
μ ion mobility
V_c critical voltage
V_t tuft onset voltage
L distance from discharge electrode to plate

If the particulate on the collecting plate is of high resistivity, back corona is formed, and positive ions are injected into the gas space and flow to the discharge electrode. This will occur at some voltage V_{bc} depending on the flyash resistivity. It affects the voltage-current characteristics by causing a rapid increase in current as shown by line D in Figure 1.

The main operating voltage range of the elctrostatic precipitator with large diameter electrodes is from $V = 0.6\ V$ to a voltage just above V_{bc}. Ideally it should be slightly above this voltage.

WIRE DIAMETER VARIATION

A series of measurements were made at 150°C and a range of discharge electrode diameters using the EPA Pilot Electrostatic Precipitator collecting a high resistivity flyash. The results are shown in Figure 2.

Since the voltage waveshapes of the output of the power supply are not steady and vary significantly with the load current, the following voltage measurements were made.

(i) At tuft corona onset.

(ii) At onset of back corona.

(iii) Maximum average voltage.

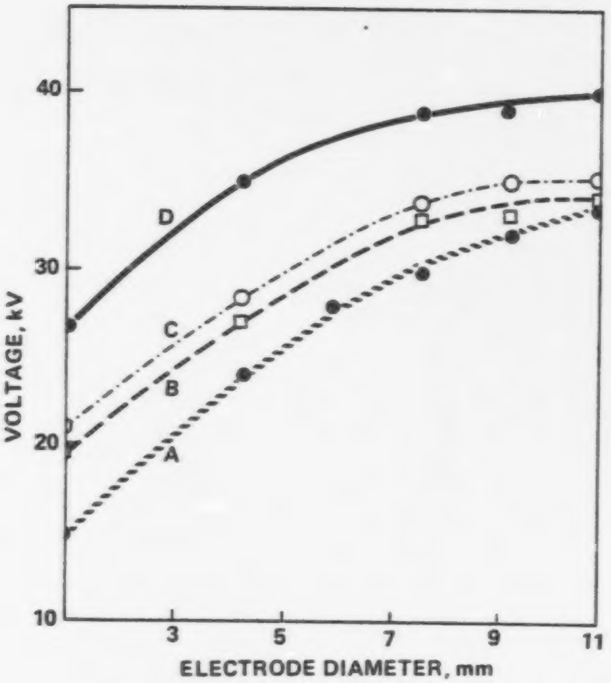

Figure 2. Variation of critical voltages with electrode diameter. Temp = 150°C

A tuft corona onset voltage
B back corona onset voltage
C maximum average voltage
D maximum peak voltage

(iv) Instantaneous peak voltage at maximum average voltage.

For measurements (i) and (ii) the output voltage was approximately constant; but once back corona began to flow, the ripple increased significantly. The main measurements are made at the end of an 8 hour test run by which time the discharge electrode and plates were well contaminated.

The absolute magnitudes are very dependent on the flyash resistivity and to some extent are sensitive to the power supply characteristics. The overall trends and relative values in Figure 2 are probably representative of those in full scale electrostatic precipitators.

INDIVIDUAL TUFT DISCHARGES

The main characteristics of the individual tuft discharges in the partial corona region are discussed in detail elsewhere (2), and only a summary is included in this paper.

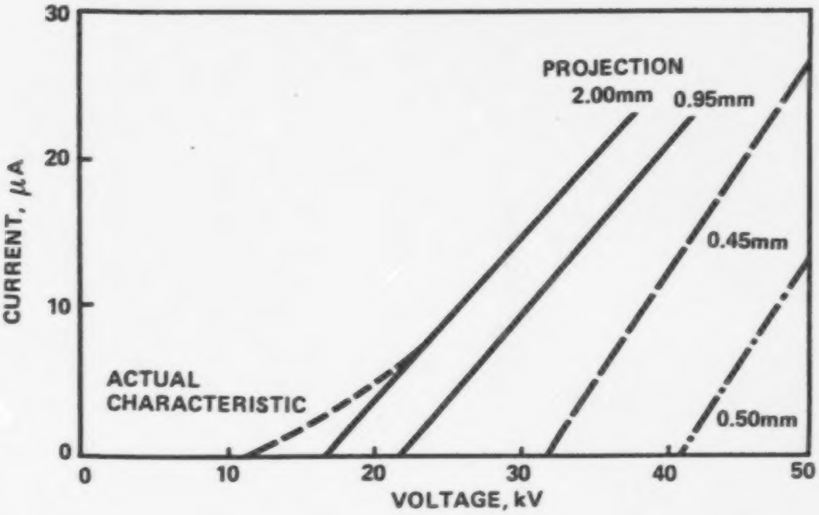

Figure 3. Voltage-current characteristics of micropoints on different diameter wires. Plate spacing = 230mm, ambient temperature

——— Diam. 3.2 mm K = 0.9-1.2 μA/kV
----- Diam. 6.4 mm K = 1.4 μA/kV
—·— Diam. 9.5 mm K = 1.5 μA/kV

Some typical voltage-current characteristics for ambient temperature are shown in Figure 3. These are approximately linear with slopes of 0.9-1.5 μA/kV at ambient temperature which increase to approximately 1.4-2.4 μA/kV at 150^{o}C, for the range of wire diameters from 3.2 mm to 9.5 mm. The approximate expression for the total current from an individual tuft discharge is:

$$I_t = K(V - V_t),\ V_t \le V \le V_{bc} \tag{2}$$

where K slope
V_t tuft corona onset voltage

The pattern of current density distribution on the plate as measured by the parallel aluminium strips on the plates is shown in Figure 4. The distribution at right angles to the discharge electrode is shown in Figure 4(A) and is given by:

$$J/J_o = \cos^n \sigma \tag{3}$$

where J_o is the peak current density and n varies between 5 and 6, and is reasonably independent of electrode diameter, voltage, and current density.

The main variation in the current density distribution occurs in the direction parallel to the discharge electrode as shown in Figure 4(B). As the total current from the tuft discharge increases, the width of the current density curve increases. Tails may extend up to 140 mm either side of the discharge. The maximum current density is determined from the saturated current density equation (3):

$$J_o = \frac{\epsilon \mu V^2}{L^3} \tag{4}$$

This can result in high current densities. At 150°C, the current density is 260 nA/cm^2 for a voltage of 35 kV with a plate spacing of 230 mm.

NUMBER OF TUFT DISCHARGES

If the total current is known either from equation (1) or from measurement, the average spacing between the tufts can be calculated. The basic assumption is that, once the tuft discharges are formed, they are of the same intensity. Hence their number is:

$$N = \frac{I}{K(V-V_t)},\ V_t \le V \le V_{bc} \tag{5}$$

where I is the measured or calculated total current. The average spacing between them, for a total electrode length of L_T, is given by:

$$S = \frac{L_T}{N}$$

In many instances, some of the discharges are intermittent, and this has the effect of reducing the effective value of K and hence of increasing the number of discharge points.

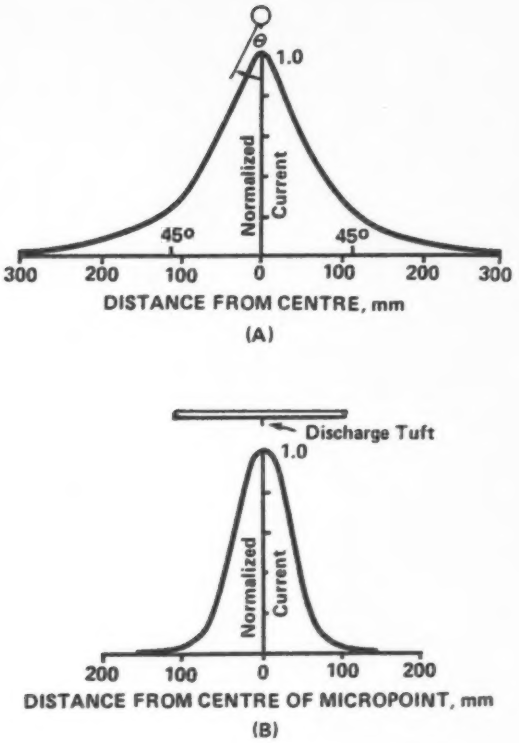

Figure 4. Distribution of current on plate produced from a single micropoint. Plate spacing 230 mm, V = 30 kV, discharge electrode diam. 6.4 mm. Current normalized to peak value.

(A) At right angles to the wire direction
(B) Parallel to the wire direction

BACK CORONA DISCHARGES

Some characteristics of the individual back corona discharges were investigated by means of the special matrix plate located on the collecting electrode which made it possible to isolate individual back corona discharges and to observe and measure their characteristics. The following observations were made:

(i) The individual back corona points on the plate tended to move more frequently from one location to another as the discharge wire diameter increased.

(ii) The number of back corona points in a given area was reduced with increase in discharge wire diameter. In the extreme case, with 12.7 mm diameter, one and sometimes no back corona points could be detected on the measuring plate.

(iii) The intensity of the individual back corona discharge points increased with electrode diameter.

The reason for this is uncertain at this stage but is probably due to the instability of the corona discharge on the wire electrode. One particular streamer may initiate a back corona point, and this is sustained for some time by the reverse flow of positive ions back to the discharge electrode. The process is essentially unstable, and the tuft corona discharge shifts to another location on the discharge electrode; this affects the back corona discharge, causing it to 'jump' from one location to another on the plate, or else to switch off altogether.

EFFECT ON PERFORMANCE

The main electrical factors that affect the operation and performance of electrostatic precipitators with large-diameter discharge electrodes are:

(i) The existence of corona discharges at voltages well below the critical voltage V_c, even after taking into account reasonable values for the roughness factor. The discharges in this partial corona region tend to be unstable and are randomly spaced along the discharge electrode in such a way that their current fields do not overlap.

(ii) Since the tuft corona voltage onset, V_t, is higher for the large diameter wires than for the conventional 3.2 mm diameter wires, the voltage levels for particle charging and collection are correspondingly increased. The 9.5 mm diameter electrodes have an operating voltage about 1.7 times higher than that of the 3.2 mm diameter wire, and the E^2 terms in the Deutsch Efficiency Equation are increased by a factor of 2.8. This can be expected to improve collection performance of the precipitator.

(iii) Each isolated discharge tuft produces a current field that covers a relatively large area. It may extend a maximum of 600 mm in the direction of the gas flow for a single wire; and for a multiwire system, to a distance equal to the wire to wire spacing because of field truncation. The width may vary up to a maximum value of 280 mm. The maximum current density is very high and can be calculated by equation (4). Values of 50 per cent and above this maximum value occupy about a quarter of the total area of the current field.

(iv) The separation between the individual tufts will reduce the probability of particles being charged. However, if there are a sufficient number of wires in series with the gas path, this probability of charging will increase.

(v) Since the current density under an individual tuft is high, if a particle does move into the current field, the $N_o t$ is sufficiently high to charge the particles to saturation.

(vi) As the individual tuft discharges are often intermittent and move about the surface of the discharge electrode, the formation of stable back corona on the collecting plate becomes more difficult. Hence, if back corona is formed and the primary source of negative ions is switched off, and since there are no other tuft discharges sufficiently close by to support the back corona discharge, the discharge decays. This makes it possible for there to be a reasonable working voltage range betwen V_t and V_{bc}.

(vii) If a back corona discharge does become firmly established, and since they are well spaced from other discharges, its volume of influence in the gas stream is small. Providing it does not cause excessive sparking, the back corona will not have a significant detrimental effect on the overall performance.

(viii) There is a rapid improvement in the voltage level as the electrode diameter increases from 3.2 mm; but for values above 7.9 mm, the increase is less significant and the operating voltage range is reduced. This suggests that the optimum diameter is in the range of 7.9 - 9.5 mm [1/8 - 3/8-in.], although this will vary with flyash resistivity and operating conditions.

ACKNOWLEDGEMENTS

The author is grateful to the staff of the Particulate Technology Branch, IERL-RTP, U.S.EPA for their assistance in carrying out the test programs described in this paper.

REFERENCES

1. Bush, P., Pontius, D.H., and Sparks, L.E. Performance of large-diameter wires as discharge electrodes in electrostatic precipitators. Paper presented at The Fifth Symposium on the Transfer and Utilization of Particulate Control Technology, Kansas City, Missouri, August 27-30, 1984.

2. McLean, K.J., Lawless, P.A., Sparks, L.E., and Ramsey, G. Negative corona in wire-plate electrostatic precipitators. To be published.

3. Sigmond, R.S. Simple approximate treatment of unipolar space-charge-dominated coronas: The Warburg law and the saturation current. Jn.App. Phys, 53, 1982, p.891.

LABORATORY ANALYSIS OF CORONA DISCHARGE ELECTRODES AND BACK CORONA PHENOMENA

by: P. Vann Bush and Todd R. Snyder
Southern Research Institute
Birmingham, Alabama 35255-5305

ABSTRACT

An experimental research program was conducted to characterize corona and back corona generation with different geometries in various environments. A wire-parallel plate device and a wire-cylinder apparatus were utilized to monitor the spatial distribution and temporal stability of corona and back corona discharges. Conditions that were varied in the experiments included temperature, diameter of corona electrode wire, corona polarity, and type of corona electrode (smooth versus barbed) and its condition (rough versus polished). Back corona discharges were induced by depositing fly ash on the grounded electrode. Visual observations of corona and back corona phenomena were made with a sensitive video camera. The measured distributions of corona and back corona current and statistical analyses allow a quantitative assessment of the impact of corona electrode design on electrostatic precipitator performance. This paper describes the laboratory apparatus and gives a survey of experimental results. A discussion of the implications of this study for new and retrofit ESP design completes the scope of this paper.

This paper has been reviewed in accordance with the U.S. Environmental Protection Agency's peer and administrative review policies and approved for presentation and publication.

INTRODUCTION

A laboratory research program was conducted to evaluate the character of corona generation from several sources in a variety of environments. Understanding the nature of corona generation, current distribution, and back corona behavior is critical to optimum ESP design and modeling. The program utilized two electrode configurations: wire-plate and wire-cylinder. Conditions that were varied in the experiments included temperature, diameter of corona electrode wire, corona polarity, and type of corona electrode (smooth versus barbed) and its condition (rough versus polished). Back corona phenomena were examined utilizing the wire-plate device with fly ash deposited on the plate.

APPARATUS

The wire-plate corona system incorporated a segmented electrode as one of the two plates. This electrode was made from a high-temperature copper-clad board used for printed circuitry. The plate was segmented into parallel strips by a PC board etching process, with strips 0.50 inches by 6.0 inches, giving each strip an area of approximately 0.02 ft^2. The dimensions of the plate electrodes were 6.0 inches wide by 24.0 inches long. Wire-to-plate spacing for this setup was 4 to 5 inches for all tests. The complete wire-plate apparatus was installed in a convection oven, and the 32 segments were connected to a dual 16-channel electrometer/multiplexer.

Figure 1 shows a diagram of the wire-cylinder apparatus. Components included 32 isolated rings for collecting and measuring the distributed current from a corona electrode positioned along the central axis of the array of rings. The inside diameter of the rings was 9.776 inches, each ring having a surface area of 0.107 square feet. Each ring in the cylinder was connected via shielded cable to the electrometer/multiplexer.

The electrometer was designed to interface with a 16 channel, 12 bit A/D converter installed in a DEC PDP 11/34 minicomputer used for data acquisition, manipulation, storage, and presentation. Data acquisition consisted of 800 passes through the A/D resulting in 400 sequential readings of the current distribution along the 32 plate segments (or rings in the cylinder apparatus). The total elapsed sample time was approximately 66 seconds. This system allowed for rapid acquisition of data showing the current distribution at any given sample time, the change in the current measured on a given segment through time, and statistical quantities describing the current distribution.

The most useful statistical quantity was the Coefficient of Variation (COV), which quantified the corona uniformity. COV was calculated with the expression $COV=(\sigma/\bar{x})\cdot 100$, where σ is the standard deviation of the average value of the current measured on the segment from the mean of the 32 segments, and $\bar{x}$ is the mean value of the distribution. This simply expresses the standard deviation of a distribution as a percentage of its mean.

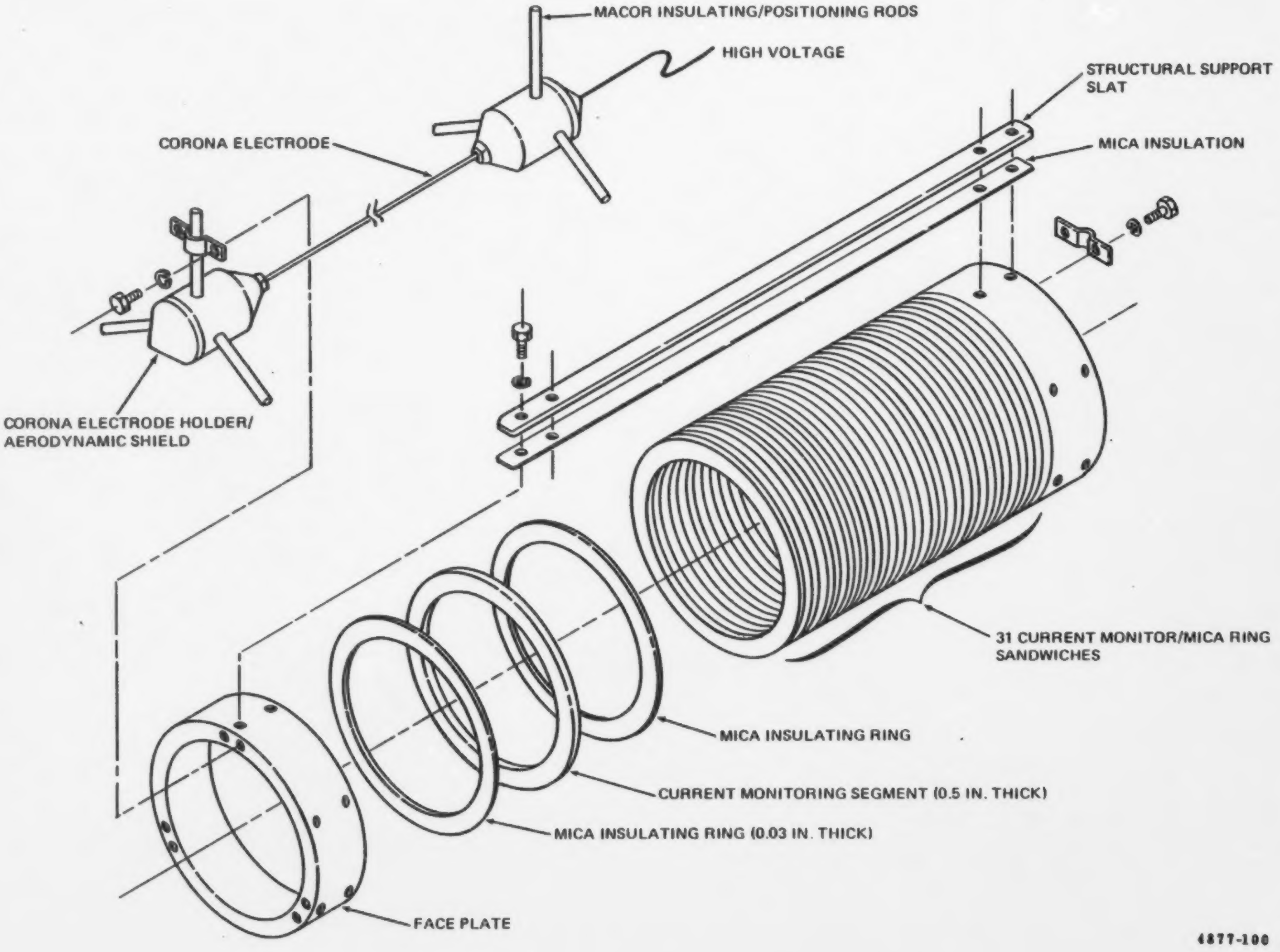
MACOR INSULATING/POSITIONING RODS
HIGH VOLTAGE
STRUCTURAL SUPPORT SLAT
MICA INSULATION
CORONA ELECTRODE
CORONA ELECTRODE HOLDER/ AERODYNAMIC SHIELD
31 CURRENT MONITOR/MICA RING SANDWICHES
MICA INSULATING RING
CURRENT MONITORING SEGMENT (0.5 IN. THICK)
MICA INSULATING RING (0.03 IN. THICK)
FACE PLATE
4877-100

Figure 1. Wire-cylinder current distribution monitor.

CORONA UNIFORMITY

A test plan was designed to cover a broader scope of measurements than the earlier studies of Tassicker (1) and Durham, et al (2). Studies of the corona exhibited by smooth, polished electrodes of different diameters revealed that the uniformity of corona emission increased as the diameter of the corona electrode wire decreased. This effect can be seen in Figure 2. Data in Figure 3 show that increasing the negative polarity corona current emitted by a smooth wire discharge electrode gives a reduction in the value of COV, indicating a more uniform current distribution on the plate. These results are also apparent in the data taken with the wire-cylinder apparatus. Figure 4 shows the distributions of current at two different voltage levels. The end effects caused by the physical design of the wire-cylinder device are clearly visible in the graphs. At typical operating levels the currents read on collectors 7 through 28 were essentially independent of end effects. Also shown in this Figure is the relationship of total current to the COV for channels 7-28 for a 1/8 inch diameter wire at 68°F in the wire-cylinder apparatus.

Another comparison made was between the smooth wire data and data from a barbed electrode. The fundamental difference noted was the way in which corona current was increased with the two electrode designs. For the barbed electrode a corona voltage was reached where each barb tip became a corona source. Raising the voltage from this condition merely intensified the corona activity at each of the barbs but did not raise the number of active corona spots. In the smooth wire case, however, the dominant method for raising the total current was an increase in the number of active corona sites on the wire rather than an amplification in the activity of any given corona spot. The data indicate that more uniform current distribution is reached by providing a higher density of corona points along the electrode.

Negative polarity high voltage excitation generated two very different corona discharge patterns, depending on the condition of the wire surface. One mode of discharge, referred to as Ideal Corona, was achieved by carefully polishing the wire surface. The discharge appeared as a rapidly moving, continuously distributed array of very fine streamers, with the motion traveling along the length of the corona wire. This phenomenon was transient, though it persisted for many minutes. Ideal Corona produced a very low COV, which indicated a very uniform distribution of current. Typical negative corona had the appearance of intense, isolated spots of corona activity which sometimes moved along the wire surface, but were commonly stationary. These discharge spots were persistent and produced much higher total current and local currents than the Ideal Corona. Figure 5 plots COV versus Voltage for the Ideal and typical negative corona. There was a sudden transition from the Ideal Corona mode to typical negative corona which involved the development of individual intense corona spots surrounded by a quiescent zone. The change did not occur over the entire length of the wire simultaneously, though the region affected by local transitions ranged from one inch to the entire length of the wire. After typical corona was observed, Ideal Corona could not be reproduced without resmoothing the wire surface.

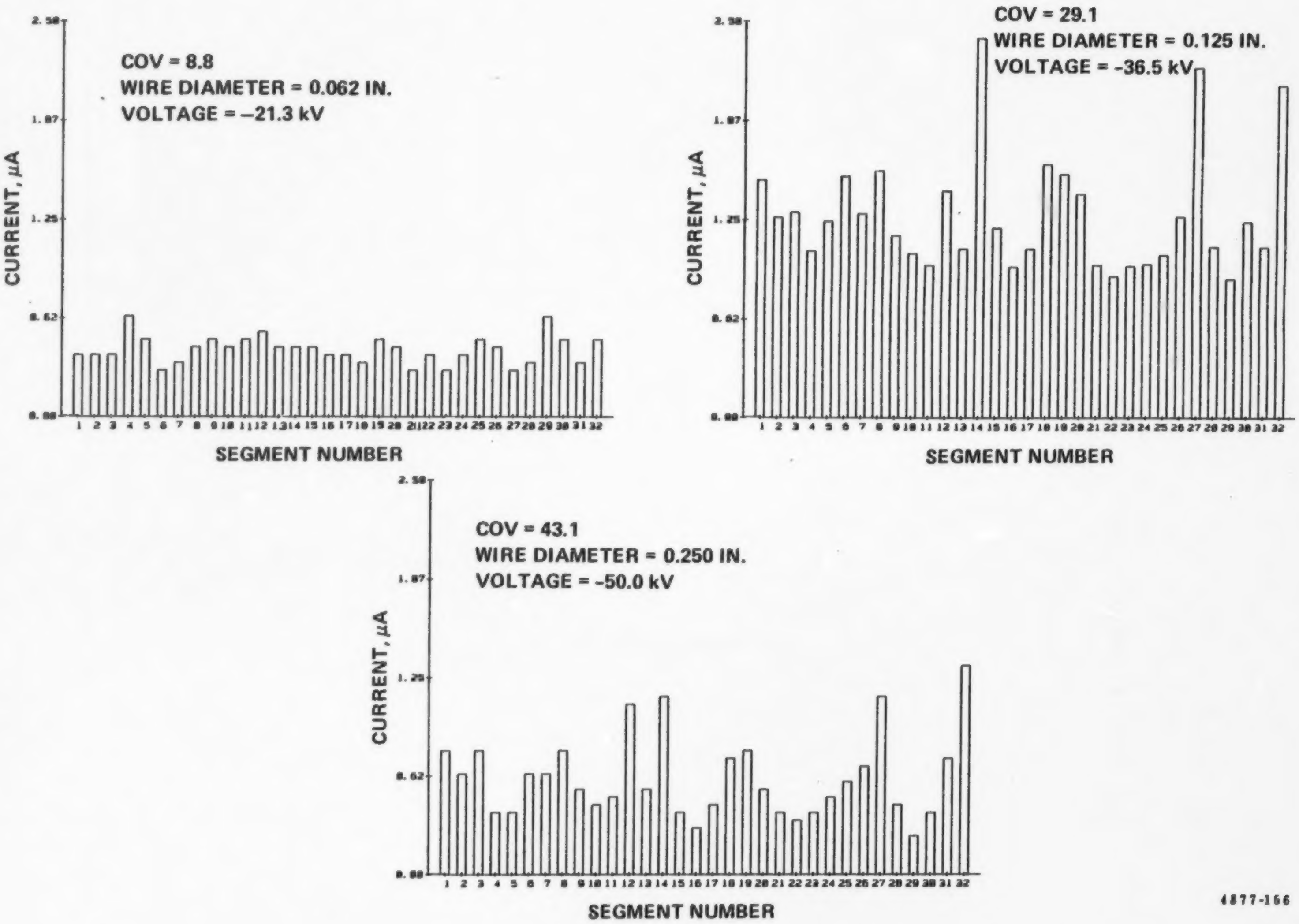

4877-156

Figure 2. The effect of wire diameter on current distribution at negative polarity and 200°F with 100 μA total current.

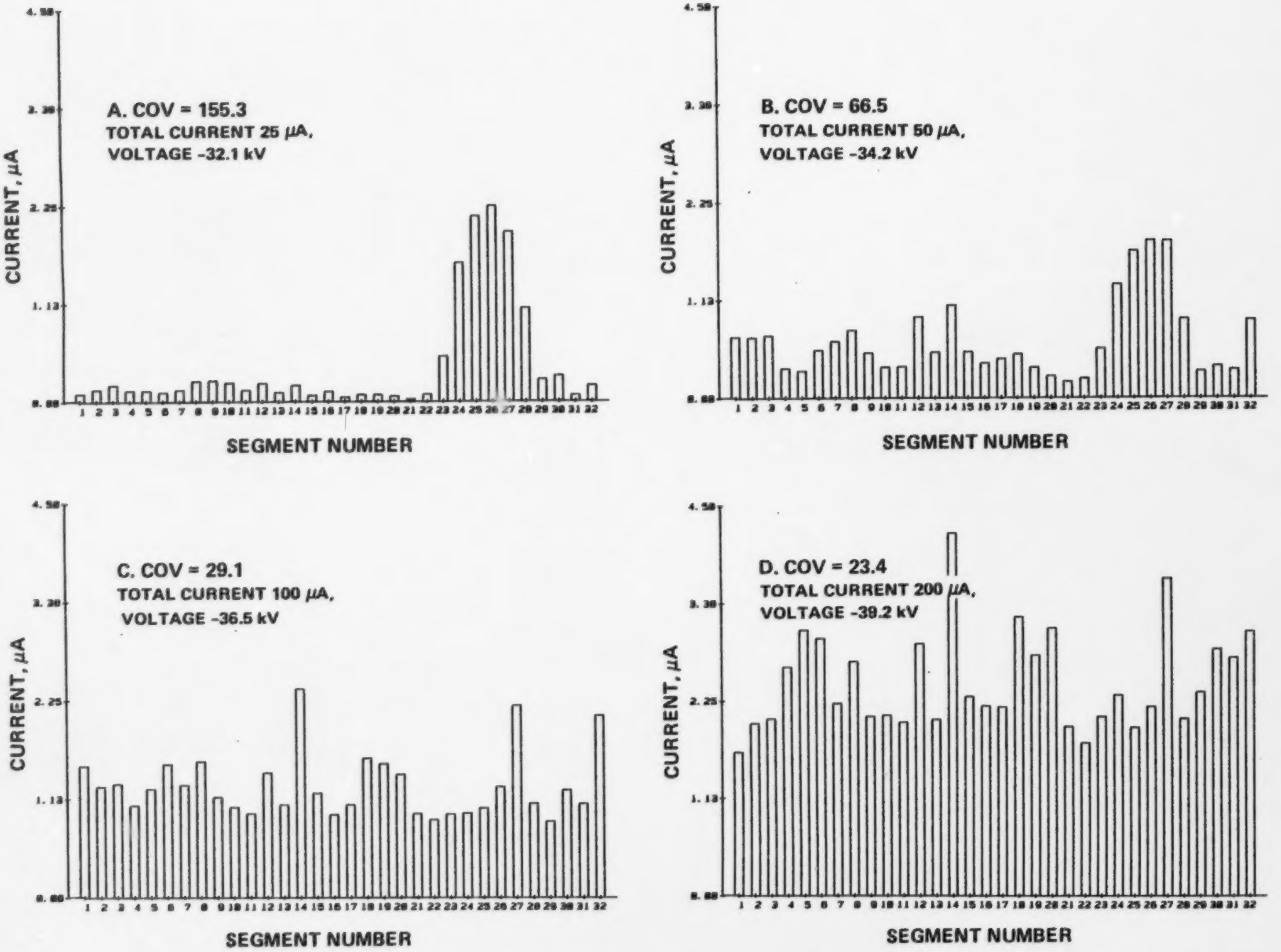

Figure 3. The effect on current distribution of increasing total current from a 1/8-inch diameter wire at negative polarity and 200°F.

4877-157

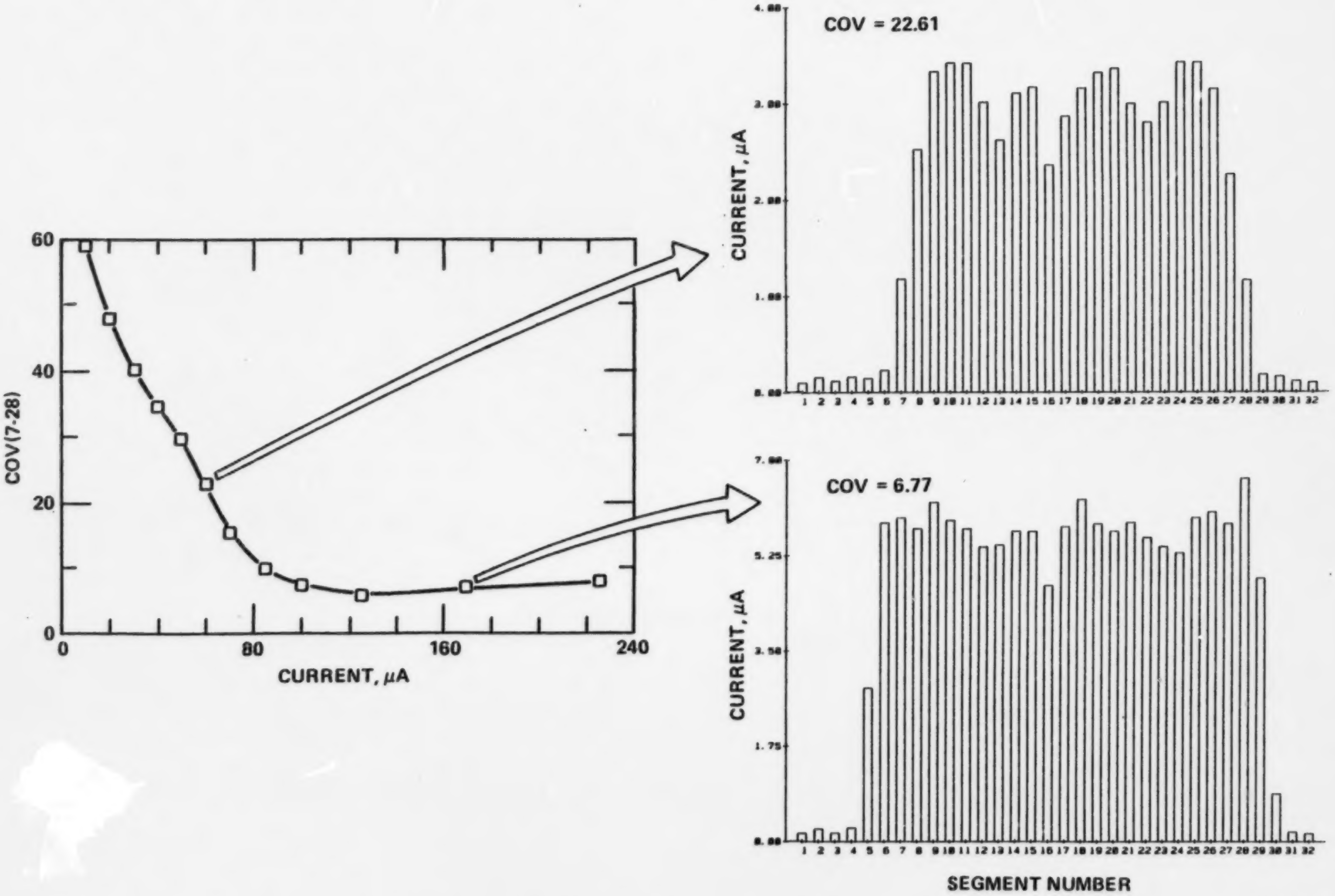

Figure 4. The effect on current distribution of increasing total current from a 1/8-inch diameter wire in the wire-cylinder apparatus at negative polarity and 68°F.

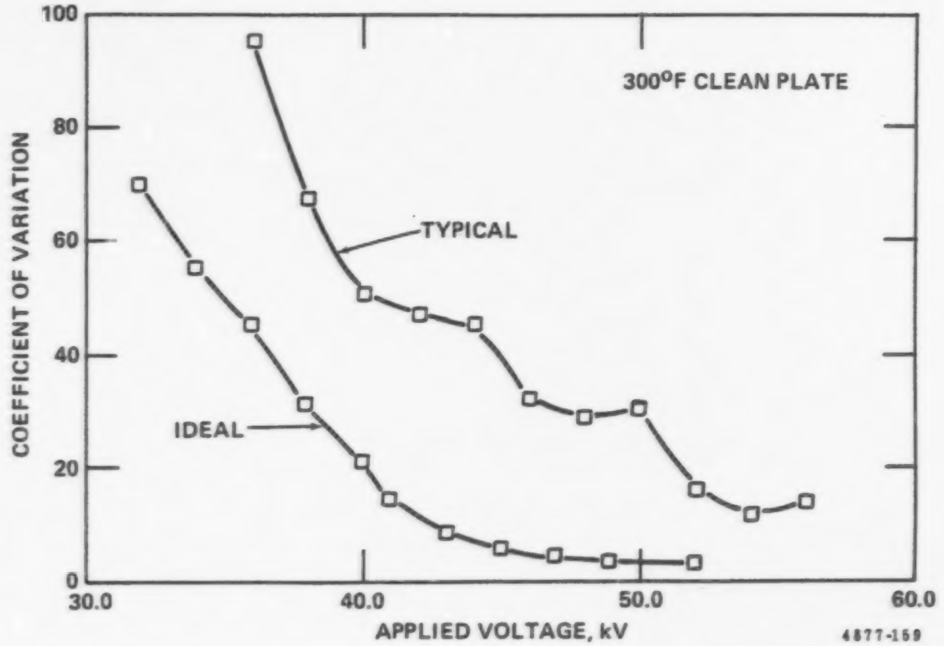

Figure 5. Coefficient of variation vs. voltage for negative corona discharges.

Data from positive polarity experiments consistently showed a more uniform current distribution than negative polarity data. Even at low current densities positive corona produced a very smooth distribution of current on the grounded electrode. A graphic comparison of the current distributions of positive and negative corona is given in Figure 6. The bars indicate the average value of current to each collector.

Raising the temperature in the experimental setups had the effect of shifting the voltage current (V-I) curves to the left. Other trends noted were not substantially altered by the change in temperature. Figure 7 demonstrates the rapid changes that occurred in the amount of current flowing to a specific collector. The change shown here indicates that the corona activity moved from one barb to an adjacent barb.

BACK CORONA

Additional laboratory experiments were performed to gain a qualitative understanding of the nature of back corona and to measure the effect of back corona on the distribution and intensity of current. These studies were designed to expand upon the work done by Spencer (3) and Masuda, et al (4). Back corona was produced by spreading a smooth layer of ash on the plate electrode. The corona electrode used for these observations was a 1/8 inch diameter wire. Conditions varied in these studies included primary current density, polarity of the applied potential, ash resistivity (induced by different operating temperatures), and other ash layer properties, such as

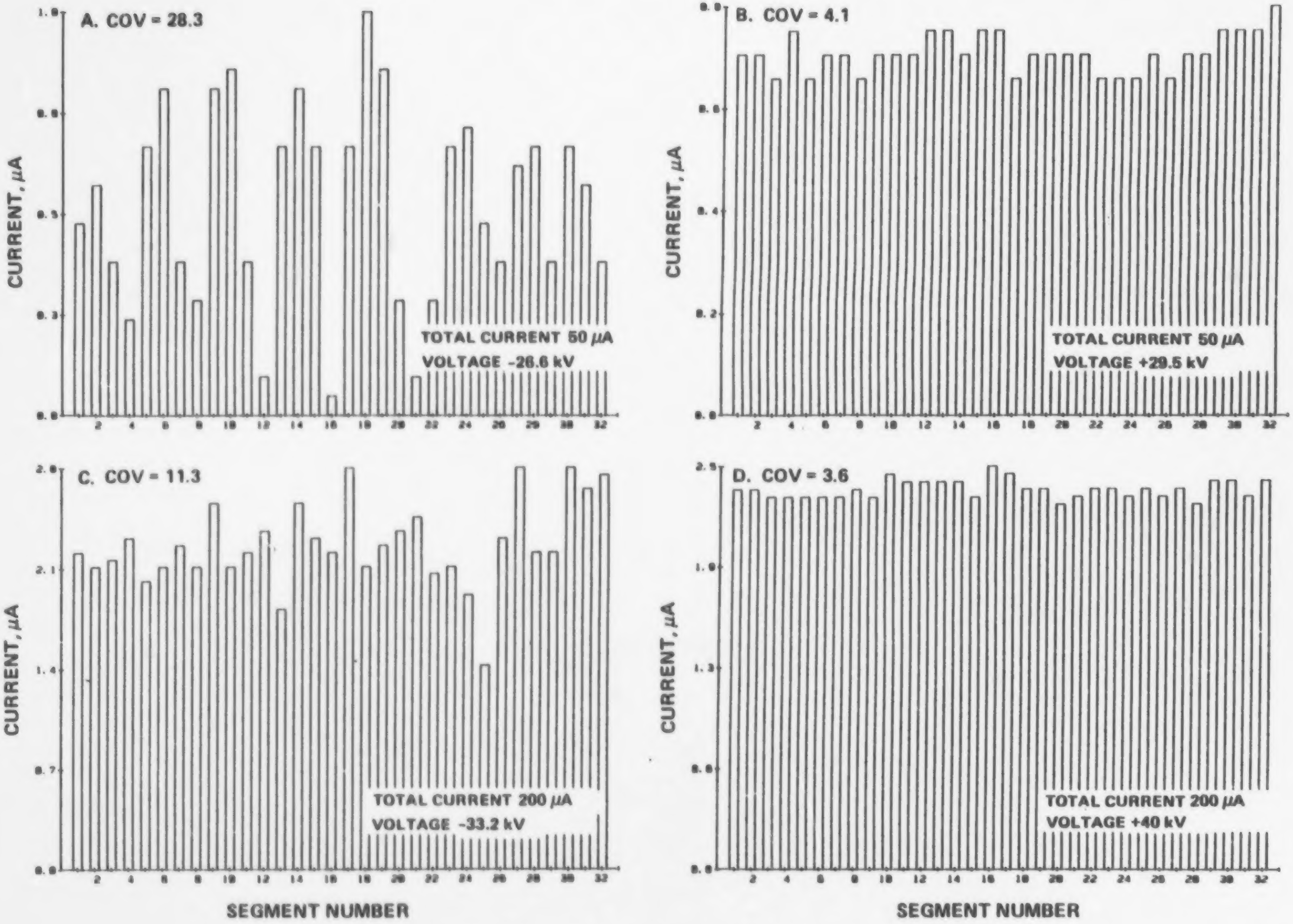

Figure 6. Current distributions generated with positive (B,D) and negative (A,C) polarity corona from a 1/16-inch diameter wire at 200°F.

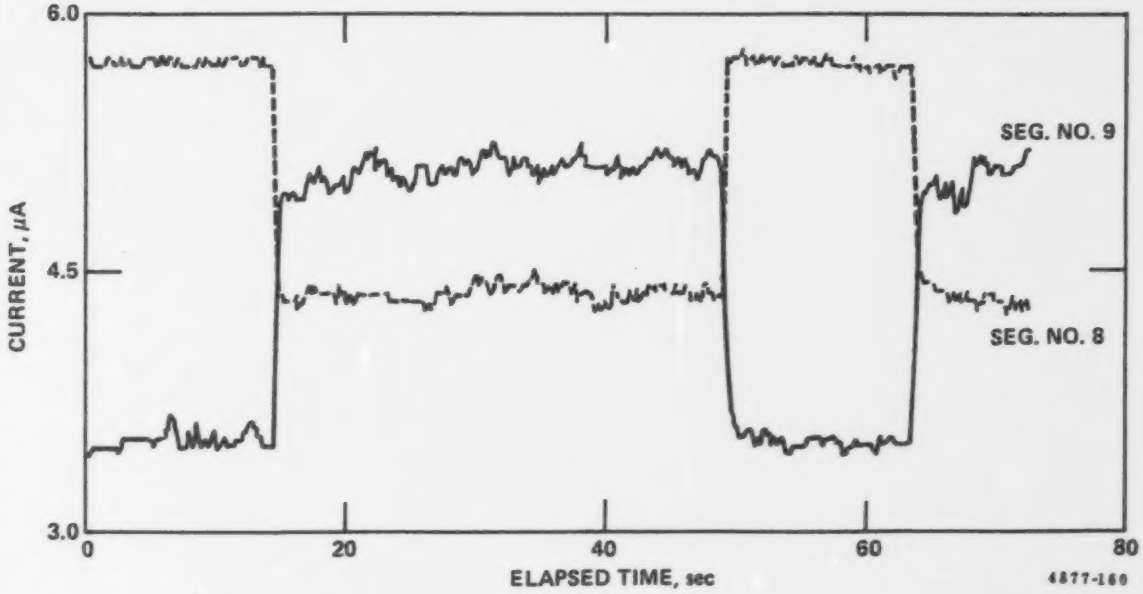

Figure 7. Current measured at two adjacent collector segments vs. time with a barbed corona electrode at negative polarity and 300° F.

thickness and surface roughness. Experiments were performed at temperatures of 200 and 300°F, where ash resistivity was in the low 10^{11} and low 10^{12} ohm-cm range, respectively. All of the measurements of the effects of back corona were made with typical corona discharges as described above.

Measurements of the magnitude of back corona were made by comparing the V-I relationships of clean and dirty systems. The V-I curves are shown in Figure 8. There was a large increase in current due to back corona for all of the measured voltages. Part of this current increase was due to the reduction in the ionic space charge resulting from emissions of corona sources of opposite polarity. Current distribution measurements also showed the relative magnitudes of clean plate current and current with back corona present. Output from a pair of these measurements is shown in Figure 9.

Visual observations of back corona were made with a sensitive video camera. The back corona activity occurred beneath active ionization spots on the wire, indicative of a synergic relationship. Only at very high current densities did the back corona in the layer spread to areas above which there was no observable primary corona.

The back corona which was produced by negative ion bombardment of the ash layer was very active. Centers of back corona moved rapidly in areas which were typically on the order of 4 to 9 in.^{2}, centered beneath a primary corona spot. The back corona features were comparable to Lichtenberg Figures described by Loeb (5), with streamers extending radially along the surface of the ash layer about one inch from the bright core of the back discharge.

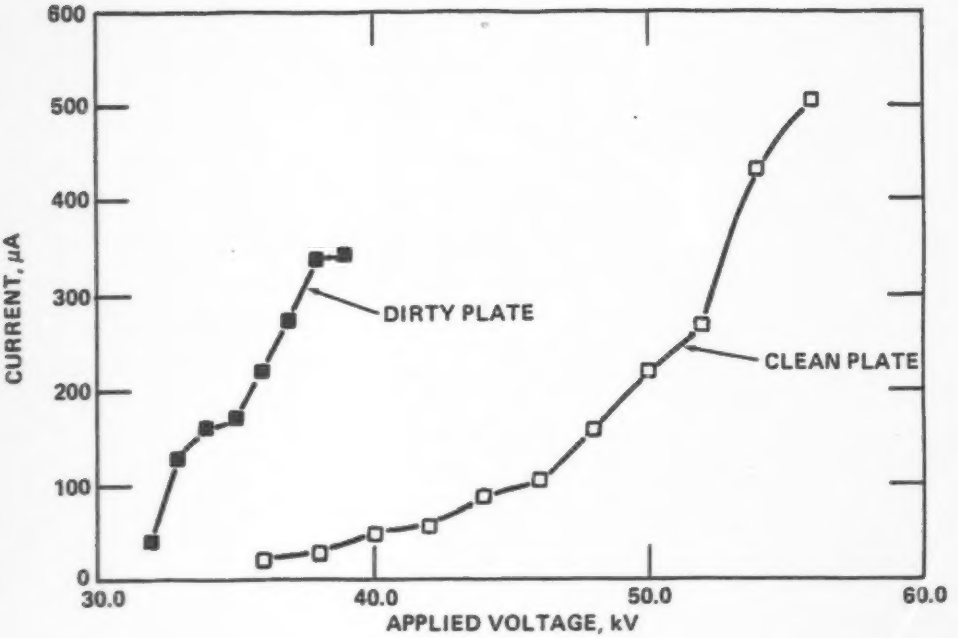

Figure 8. Comparison of clean plate and dirty plate V-I curves with negative polarity and 300°F.

This pattern is shown in the photograph of back corona in Figure 10. Major defects in the ash layer, such as craters formed by arcs, provided stationary sites for back corona. These sites sometimes became very intense, extinguishing nearby activity. Often these intense spots of back corona did not produce radial streamers, but had plate to wire streamer propagation typical of positive corona.

Several ash layer thicknesses between 1/8 and 3/8 inches were studied. There was no observable difference in the distribution or character of the back corona produced in the layers. There was also little difference in the applied voltage at which back corona onset was detected.

The effect of back corona on the current distribution was more pronounced for the positive polarity corona. Figure 11 is a plot of the current distribution of clean-plate and dirty-plate conditions. The current with back corona was an order of magnitude greater than the current generated from the wire in the clean system. The plot of the COV versus Voltage for these measurements (Figure 12) emphasizes the degree to which the back corona degraded the current distribution on the plate. The back corona sites caused corona streamers to develop from the discharge wire, severely limiting the operating voltage range by leading to sparking.

The back corona associated with positive primary corona was different in appearance from the negative corona product, as was expected. The back corona sites typically extended over 1/4 to 1/2 of the area and were more numer-

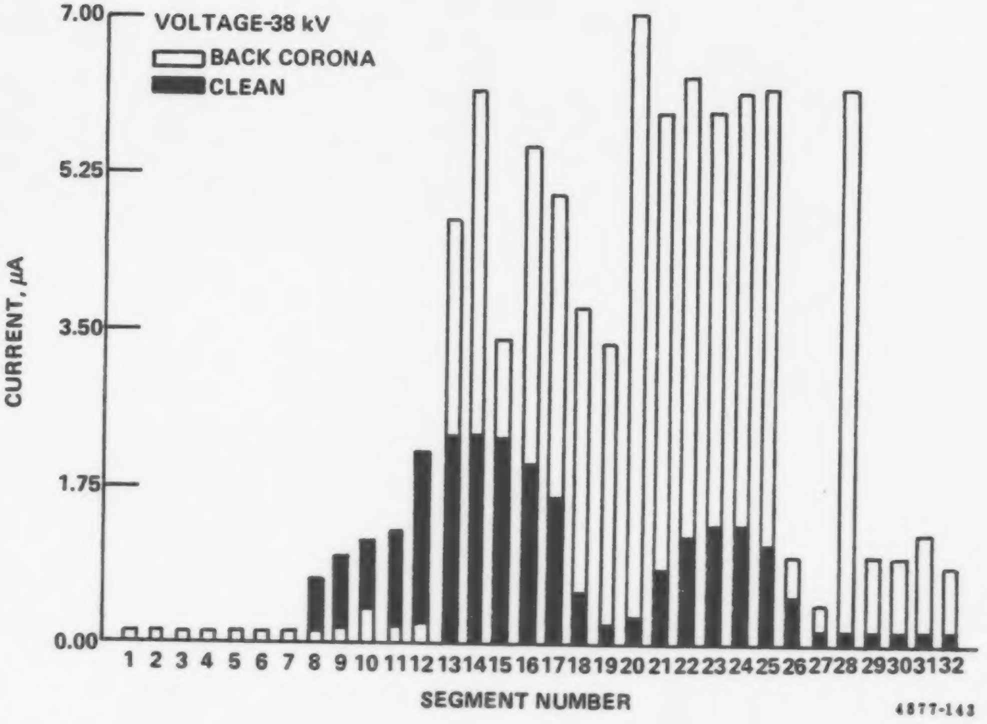

Figure 9. Current distributions for negative corona with and without back corona at 300° F.

ous than the back corona sites induced by negative corona. There were no detectable streamers from each site along the ash layer surface, but rather a cloud of ionization appeared to penetrate within the layer.

IMPLICATIONS FOR ESP DESIGN AND OPERATION

CORONA DISCHARGE ELECTRODES

Utilization of the quantitative data on the relative corona uniformity exhibited by electrodes of various designs and the integrated data contained in the voltage-current curves provide a means to evaluate the impact of discharge electrode design on ESP performance. The electrostatic precipitation process has been effectively modeled as a statistical phenomenon, beginning with the Deutsch equation. The coefficient of variation fits in with the statistical description of the process. It is a measure which is as characteristic of an electrode geometry as is the V-I curve.

The conventional practice of employing a universally applicable electrode design may severely constrain the level of collection efficiency attainable with a given collection surface area. For instance, an applica-

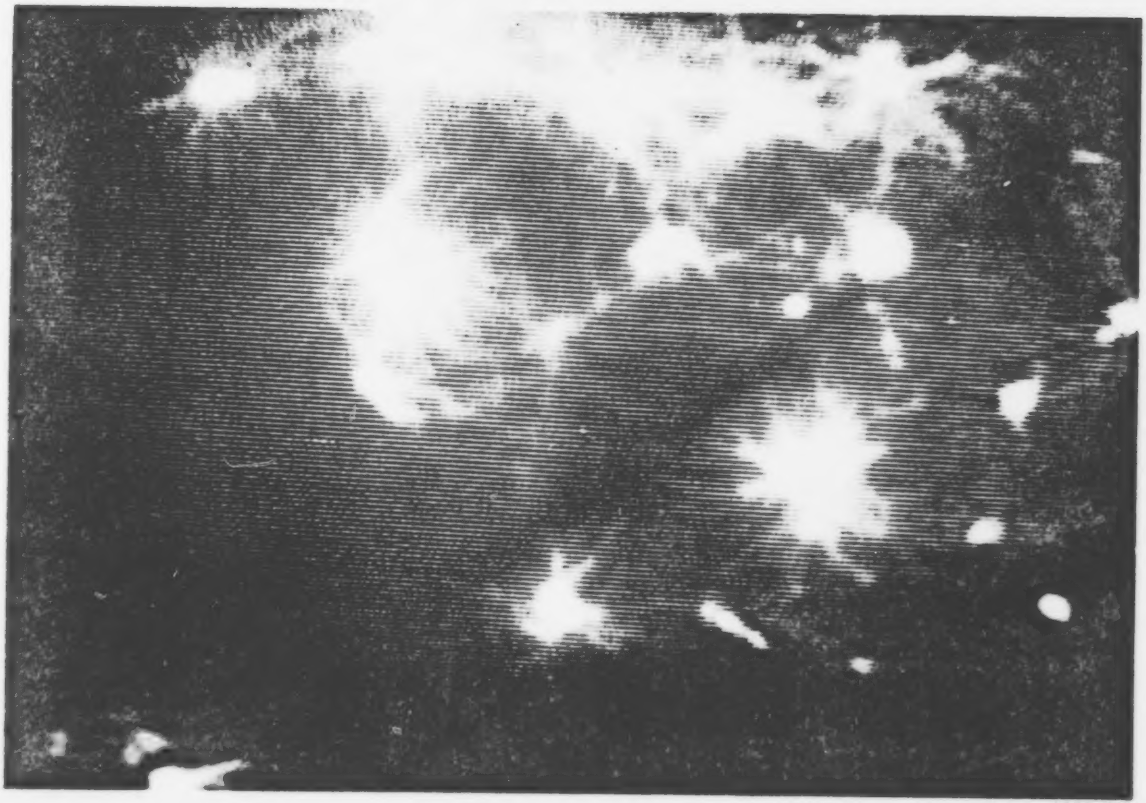

Figure 10. Photograph of back corona on a dust layer (~10^{12} Ω-cm resistivity fly ash) under negative polarity corona wire.

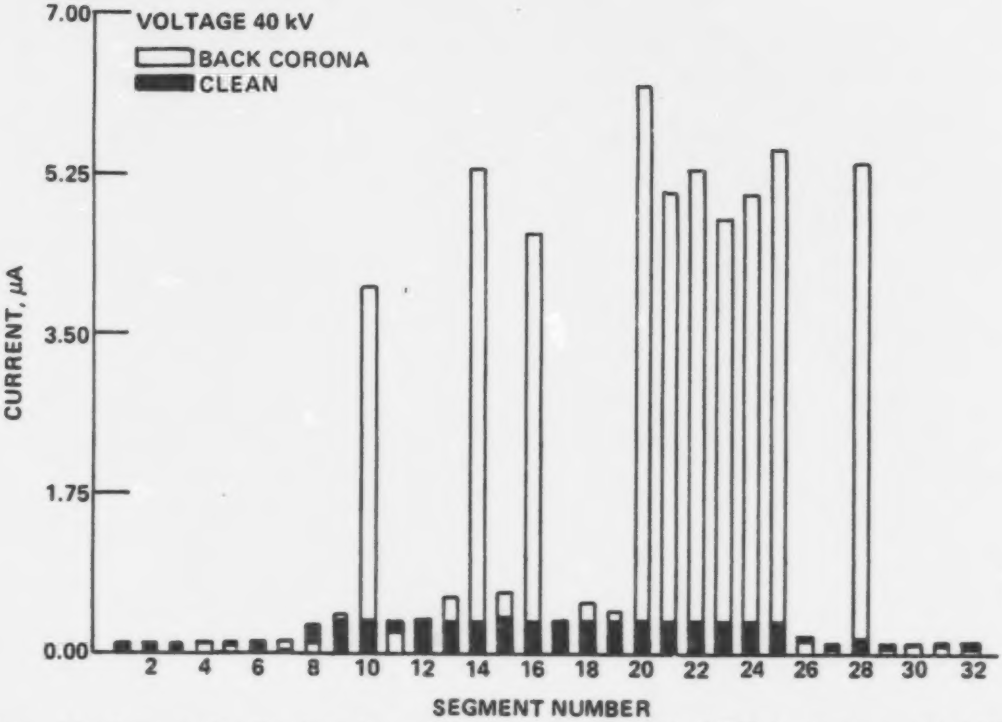

Figure 11. Current distributions for positive corona with and without back corona at 300°F.

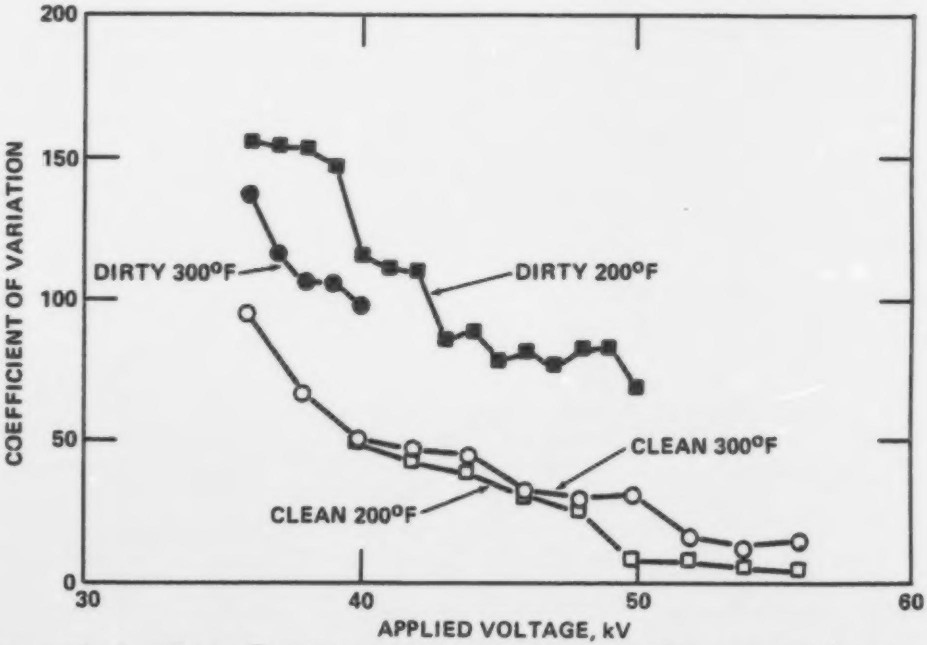

Figure 12. Coefficient of variation vs. voltage for clean and dirty plate with positive polarity corona discharges at 200 and 300°F.

tion with heavy inlet dust loading would call for electrodes with high current emission capacity to overcome the effect of space charge suppression of the corona. For high resistivity ash, a low current level would be selected to prevent back corona formation, yet high electric fields would be desired for good collection performance. This latter case favors large diameter wires. The criteria for choosing an electrode should include the operating voltage level, the corresponding current emission level, and the uniformity of the discharge under the expected conditions.

One reason large diameter wires have been avoided in conventional ESP design is that they provide a less uniform current distribution. This disadvantage is offset by the fact that a few microamps per square foot is adequate corona current to ensure saturation charging of the particles within a small fraction of their residence time in the ESP. The combined effect of having n wires in series is to increase the probability that particles will encounter ions for charging. This is shown in Figure 13 which illustrates the relationship

$$C = COV/(n)^{1/2}$$

where C is the effective coefficient of variation for a lane of n wires and COV is the coefficient of variation of a single wire of the given diameter at the specified operating condition. Since there are typically more than fifty

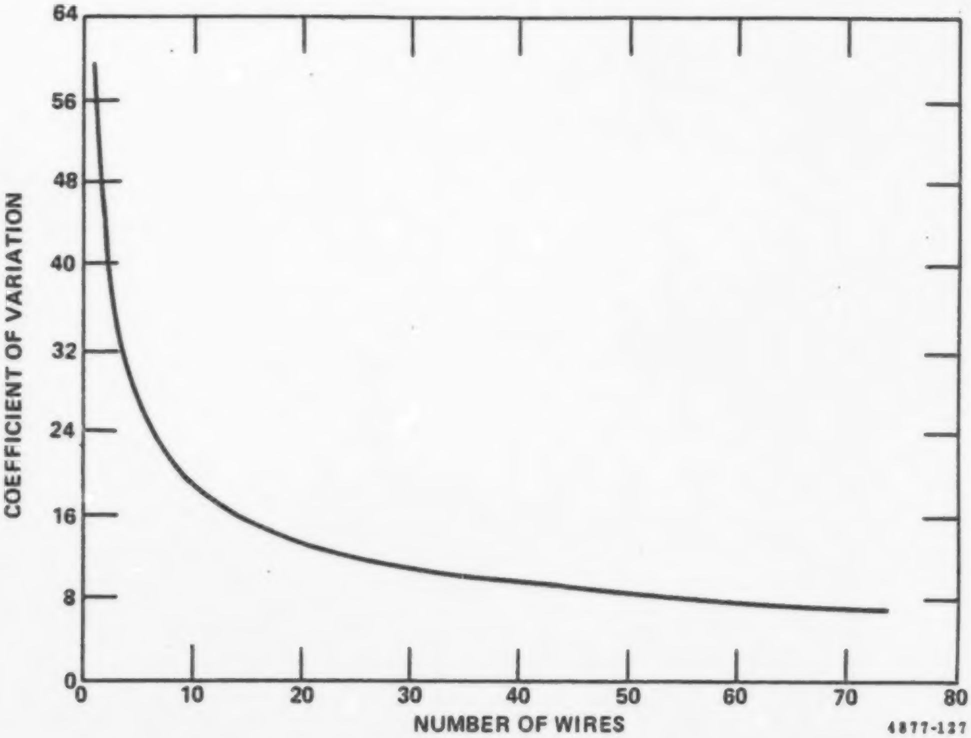

Figure 13. The coefficient of variation versus the number of corona wires.

wires in an ESP lane there is essentially an equal probability with small or large diameter wires that a particle will pass through the required number of charging regions to reach saturation charge levels.

BACK CORONA

The effect of back corona in altering V-I curves and degrading particle charging is well known. It has been assumed that the amount of increase in current evident in V-I curves is equal to the current emitted from back corona on the ash layer. This model neglects the effect of ionic space charge on the primary corona. Back corona activity stimulates primary corona emission by reducing the space charge. The apparatus developed for these experiments has permitted measurement of the effects of back corona on the magnitude and distribution of current. Quantifying the conditions for, and the effects of, back corona will permit proper selection of operating voltage and current levels in ESP's.

CONCLUSIONS

The test apparatus developed for these measurements was extremely versatile for studying various phenomena and conditions found in field applications. The rapid measurement of the distribution of and changes in corona current allowed the calculation of the coefficient of variation, a statistical quantity that describes well the corona uniformity and is therefore useful in the comparison of electrodes for ESP design. Corona uniformity was shown to increase as corona wire diameter decreased and negative polarity corona emission was shown quantitatively to be less uniform than positive polarity corona. These measurements were enhanced by the visual observations of the nature of corona and back corona emissions made with the video camera. Additional measurements quantified the large increases in corona current and changes in current distribution due to the presence of back corona. Further measurements with this test device will allow the determination of conditions for back corona onset and the effect of back corona on precipitator electrical operation.

ACKNOWLEDGEMENTS

This work has been sponsored by the Industrial Environmental Research Laboratory of EPA under the direct guidance of Dr. L.E. Sparks (Cooperative Agreement No. CR-808973-01). The authors appreciate the work of Mr. D.K. Armstrong and Mr. W.G. Kistler in the supporting laboratory experiments and the consulting expertise of Dr. D.H. Pontius.

REFERENCES

1. Tassicker, O.J. Measurement of Corona Current Density at an Electrode Boundary. Electronics Letters. 5 (13): 285-286, 1969.

2. Durham, M., G. Rinard, D. Rugg, and L. Sparks. Measurement and Interpretation of Current Distribution and Charge/Mass Data. In: Third Symposium on the Transfer and Utilization of Particulate Control Technology, Vol. II. EPA-600/9-82-005b (NTIS PB83-149591), 1982. pp. 54-65.

3. Spencer, H.W., III. Electrostatic Precipitators: Relationship Between Resistivity, Particle Size, and Sparkover. EPA-600/2-76-144 (NTIS PB 257130), U.S. Environmental Protection Agency, Research Triangle Park, North Carolina, 1976. 68 pp.

4. Masuda, S. and A. Mizuno. Initiation Condition and Mode of Back Discharge. Journal of Electrostatics, 4: 35-52, 1977.

5. Loeb, L.B. Electrical Coronas: Their Basic Physical Mechanisms. University of California Press, Berkeley, California, 1965. 189 pp.

Session 10: ESP: FUNDAMENTALS I

Grady B. Nichols, Chairman
Southern Research Institute
Birmingham, AL

THE ONSET OF ELECTRICAL BREAKDOWN IN DUST LAYERS

by: R. P. Young
J. L. DuBard
Southern Research Institute
Birmingham, Alabama 35255

L. E. Sparks
Industrial Environmental Research Laboratory
U.S. Environmental Protection Agency
Research Triangle Park, North Carolina 27711

ABSTRACT

The onset of electrical breakdown in 0.5 cm thick layers of fly ash and cement dust has been determined by slowly increasing the applied voltage and observing the oscilloscope trace of the first microspark in the dust layer. The electrical properties of the sample are not altered by this sensitive measurement technique; so multiple experiments can be performed on each sample. Parallel plate electrode geometry is used to define precisely the average electric field in the sample and to permit conventional measurements of the sample resistivity, in addition to the novel measurements of the breakdown voltage, with variations in sample temperature and environmental water vapor. The measured breakdown voltage is systematically influenced by the water vapor concentration, in the temperature region of particle surface conduction, and by the particle size distribution and packing density of the sample.

This paper has been reviewed in accordance with the U.S. Environmental Protection Agency's peer and administrative review policies and approved for presentation and publication.

INTRODUCTION

The negative corona current in an electrostatic precipitator induces a large voltage drop across the dust layer on the collecting electrode. Restricted electrical conduction through this dust layer leads to enhancement of the local electric fields in the gas-filled voids of the layer until these fields become large enough to initiate electrical breakdown across the void. Sustained breakdown within the dust layer then leads to a back discharge of positive ions into the precipitator gas stream, resulting in deterioration of precipitator performance. Thus, an understanding of the factors contributing to the onset of electrical breakdown in these dust layers is important for maintaining and improving the performance of a precipitator.

In this study, a dust layer is hand-deposited between parallel plate electrodes and the applied potential is slowly increased until the first microspark in the dust layer is observed on an oscilloscope. The parallel plate geometry provides a well-defined, uniform average electric field across the dust layer, allows standard resistivity measurements to be performed, and avoids large space charge distortions which can occur with other geometries. In addition, the method used is not destructive to the dust layer, allowing multiple experiments to be performed on each sample.

The onset of breakdown of the dust layers was found to be affected by sample temperature, water vapor in the test environment, dust species, average particle size, degree of mechanical compaction of the surface, and duration of electrical stress across the sample. The breakdown data can be explained by ordinary electron avalanche breakdown across the gas-filled voids in the dust layer.

EXPERIMENT

The components of the apparatus used in these experiments are shown in the schematic diagram of Figure 1. The dust layer was hand-deposited between the parallel plates of the test cell to a uniform depth of 0.5 cm, using a constant surface areal loading of 10 g/cm^2. Negative polarity high voltage was applied to the top electrode and the guarded electrode was connected, by means of a switch (SW), to either the electrometer (A) for resistivity measurements or the oscilloscope (OSC) for electrical breakdown measurements. The loaded test cell was placed into an environmental chamber and baked overnight at 250°C in dried air. The following morning, humid air was introduced, and the system was allowed to equilibrate for at least 1 hour before beginning measurements.

PROCEDURE

The resistivity measurement was made according to procedures listed in the IEEE Standard 548-1981. While increasing the field across the sample from zero to 4 kV/cm, the oscilloscope was monitored to be sure breakdown did not occur. After the current was measured for the resistivity determination, the voltage was immediately removed from the dust layer. In no case did breakdown occur before achieving a field of 4 kV/cm. Moreover, comparison of resistivity measurements made with this test cell and those made with a standard resistivity test cell under equivalent conditions showed no difference between the values measured.

The breakdown measurement was performed by slowly increasing the voltage across the dust layer while observing the trace on the oscilloscope until the breakdown signal (1) appeared as a single pulse. The voltage reading on the power supply meter (the average breakdown voltage, V_{BD}, across the dust layer) was recorded and the applied voltage was immediately removed from the sample. The data obtained were found to be reproducible for different samples of a given dust species under identical conditions. In addition, resistivity measurements made with this test cell on a virgin dust sample were the same as those obtained after breakdown measurements on the same sample. Thus, this procedure for breakdown measurements did not alter the average electrical properties of the dust layer, making possible multiple experiments using the same sample.

The temperature of the environmental chamber was stabilized at a lower temperature and these measurements were repeated. In this way, data were obtained at approximately 15 degree increments from 250°C down to 100°C. If tests for a different level of environmental humidity were to be performed on the same sample, the entire process, beginning with the overnight bake, was repeated. After all tests on a particular sample were completed, the dust layer was removed for chemical analysis and scanning electron microscope (SEM) photographs.

SAMPLES

Three dust species were chosen for this investigation: two coal fly ashes (Sundance and Wabamun) and a Portland cement dust (Lehigh). The two fly ashes are virtually identical in nature except for their sodium content, with Sundance fly ash having five to six times the amount of sodium as Wabamun fly ash. Since sodium is thought to be the dominant conductor of ionic charge in fly ash, data for these two species were compared to provide insight into the role of charge carrier concentration in the breakdown process. The fly ash particles are predominantly spherical in shape and amorphous like a glass, while cement dust is a more crystalline material and has very irregularly shaped particles. Cement dust is very low in sodium and high in $CaCO_3$. Thus, cement dust should present quite different behavior than that of fly ash.

RESULTS

The onset of electrical breakdown was measured with variations in temperature, atmospheric moisture, particle size, degree of compaction, and duration of electrical stress. It was found that, for most test conditions, the three dusts behaved qualitatively the same. Therefore, this discussion will focus on the results of tests with Wabamun fly ash, with any species-dependent characteristics pointed out when appropriate.

BREAKDOWN DATA

The variation of average breakdown voltage, V_{BD} (or average electric field at breakdown, E_{BD}), with temperature and test atmosphere humidity for Wabamun fly ash is shown in Figure 2. V_{BD} is the power supply reading at the occurrence of the first microspark on the oscilloscope and is for negative polarity. E_{BD} is obtained by dividing V_{BD} by the layer thickness, 0.5 cm. The indicated water levels in the atmosphere are in volume percent.

Due to the statistical nature of breakdown, the data are somewhat scattered. However, several features of the breakdown behavior are evident. First, the magnitude of V_{BD} for a given humidity level depends only weakly on temperature, with the greatest variation occurring in the range of 180 to 250°C. This is the volume conduction region of the resistivity curve shown in Figure 3. In the region where surface conduction dominates (100 to 140°C), the magnitude of V_{BD} is relatively constant for a given water level. This is in marked contrast to the rapidly changing resistivity characteristic of the fly ash in this same region, as shown by Figure 3. Generally, increasing the water vapor in the test environment decreases V_{BD}. In addition, there is a much larger difference between the magnitudes of V_{BD} for the dry and moist ash layers than between samples at different levels of moisture in this surface conduction region. Finally, all V_{BD} data, regardless of humidity level, tend to converge at the high temperature (volume conduction) limit.

The greatest variation of the magnitude of V_{BD} at identical test conditions between the three dust species occurs in dry air where differences of 1 to 1.5 kV are sometimes seen. However, the magnitudes of V_{BD} for humid samples are quite similar, as illustrated in Figure 4 for 9% water vapor. In contrast, the resistivity characteristics of the three dust species under the same conditions are shown by Figure 5 to vary by over two orders of magnitude.

SIZE EFFECTS

The influence of particle size on the breakdown behavior of Wabamun fly ash is shown in Figure 6 for 9% water vapor. The results are similar for other humidity levels. "Ordinary distribution" refers to the as-received ash while the two size-fractionated distributions are labeled according to their mass median diameter (MMD). The ordinary distributions of the two fly ashes contain particles which are predominantly spherical in shape with only a few relatively large, irregularly shaped particles. The fine fraction (MMD < 5 μm) samples are almost totally composed of spherical particles while the coarse fraction (MMD > 50 μm) samples have an abundance of the larger, irregularly shaped particles. Both the fine sample and the coarse sample for the two fly ashes exhibited breakdown voltages higher than the ordinary distribution, with the coarse sample producing the largest increase. The corresponding resistivity characteristic for the Wabamun ash is shown in Figure 7. The coarse distribution is about an order of magnitude higher in resistivity than the ordinary distribution; while the fine distribution coincides with the ordinary distribution.

The cement dust is composed of particles having no symmetry. The fine-fraction particles of this dust are relatively uniform in size with only a few larger particles; while the coarse fraction is dominated by the larger particles. Although the resistivity for this dust behaved similarly to that of the fly ashes, essentially no difference in the breakdown behavior of the three distributions was observed for the cement dust at 9% water vapor.

COMPACTION EFFECT

The effect of compaction on the breakdown behavior of the ordinary distribution of the three dusts was studied by increasing the surface areal loading of the samples to about 2500 g/cm^2 in a laboratory press. In the case of fly ash, this had essentially no effect on the breakdown behavior. However, a slight effect was noted in the breakdown of the Lehigh cement dust of Figure 8. Here the increased compression of the dust layer resulted in a lowering of the breakdown potential, with a corresponding lowering of the resistivity curve in Figure 9.

STRESS TEST

A sample of Wabamun fly ash was subjected to continual electrical stress of 4 kV/cm at 152°C and 9% water vapor for many days and its breakdown behavior was monitored. The result is shown in Figure 10. In general, the magnitude of V_{BD} decreased steadily until, after about 20 days of stress, a somewhat abrupt transition to continuous breakdown occurred. The oscillatory behavior discernible in this data seemed to be typical of fly ash since it was also observed in stress tests of other fly ash samples. In contrast, the resistivity of this sample (Figure 11) showed no change corresponding to continuous breakdown at about 20 days, but continued its steady increase.

DISCUSSION

It is generally accepted that electrical breakdown in a precipitated dust layer occurs in the gas-filled voids between particles. (See, for example, Mosley, et al. (2).) The local electric field in such voids must be enhanced over the average value across the sample because the average field values at which breakdown is observed are not large enough to initiate the breakdown process. In the discussion which follows, these two points will be elaborated.

CONDUCTION MECHANISM

A direct relationship between the onset of electrical breakdown in a dust layer and its resistivity is not supported by the data. Figures 2 and 3 show that, in the volume and surface conduction regions, the resistivity changes exponentially with temperature while the breakdown voltage varies only slightly. Figures 4 and 5 illustrate how similar the breakdown behavior can be for dust samples of widely different resistivities. Moreover, the size-fractionated data of Figures 6 and 7 also show different trends. The fine particles appear to control the resistivity of the ordinary sample since the resistivities of the fine and ordinary samples are the same. However, V_{BD} is consistently higher for the fine sample than for the ordinary distribution. Further, the resistivity of the coarse sample is about an order of magnitude higher than the ordinary and fine distributions, but its breakdown voltage is only moderately higher than the other two samples. Therefore, the onset of electrical breakdown in these dust layers and their resistivity are not directly related.

Allowing for the scatter in the data of Figure 2, the addition of water vapor to the test environment results in a large reduction of V_{BD} in the surface conduction region compared to that of a dry sample. However, the actual amount of water vapor has only a small effect on V_{BD} in this region. This suggests that the important parameter is the presence of water vapor rather than the actual humidity level. Furthermore, Figure 4 indicates that when water vapor is present, the breakdown voltage does not depend on dust species. Combining these results with the convergence of all data of Figure 2 at the volume conduction limit, it appears that the electrical breakdown of a dust layer depends very sensitively on the electrical conduction mechanism prior to breakdown.

ELECTRICAL STRESS

The increase of resistivity with time of applied electrical stress shown in Figure 11 is consistent with the gross movement of charge carriers (the alkali metal ions) and the creation of zones depleted of such charge carriers (3,4). Lack of an abrupt change in the resistivity characteristic corresponding to the transition to continuous breakdown (Figure 10) points out the insensitivity of this macroscopic, average measurement to microscopic variations in the dust layer. On the other hand, breakdown measurements are inherently microscopic in nature. Thus, it is not surprising that breakdown and resistivity cannot be directly related.

The oscillating behavior of V_{BD} with time of stress is probably due to the motion of the charge carriers in the bulk, as they change the local values of the electric fields in the voids. It is also possible that this behavior may reflect the existence of a trapping and detrapping mechanism suggested by Mosley, et al. (5). However, the data do not permit conclusions on this matter.

The steady decline in breakdown voltage with increasing duration of electrical stress has obvious implications for electrostatic precipitator operation. If a thin layer of ash remains on the collecting plates and is not effectively removed by rapping, then continual electrical stress of this layer will eventually lead to continuous breakdown in the layer and a degradation in precipitator performance.

BREAKDOWN ACROSS VOIDS

The electron avalanche breakdown of a gas-filled gap is conventionally interpreted using Paschen's law, which states that the breakdown potential applied across the gap is a function of the product of pressure and gap height. Typical data obtained by Earhart (6) for an air gap at different temperatures are shown in Figure 12. In general, the minimum in the curve broadens and shifts to the right as the temperature of the gap is raised, accompanied by a decrease in the slope of the linear portion to the right of the minimum. Earhart also found that when the breakdown potential was plotted as a function of gas density between the electrodes a single curve for all temperatures is obtained.

As previously mentioned, the potential applied across the dust layer at the onset of breakdown, V_{BD}, is too low to initiate the breakdown process. Thus, it is the enhanced local electric potential across the void, V_{loc}, which corresponds to the breakdown potential of Paschen's law. However, the two potentials should be directly related (through an effective dielectric constant) so that Paschen's law can also be applied to V_{BD}. To explain the difference between the breakdown voltage magnitude of this study and that of Earhart, it should be pointed out that Earhart obtained the data of Figure 12 using parallel plate geometry. The void in a dust layer will have nonuniform geometry, and Raju and Hackam (7) and Heisen (8) have shown that the breakdown potential increases dramatically as the geometry departs from that of parallel plates.

By assuming the laboratory pressure to be 1 atmosphere, the gap distance corresponding to the minimum can be calculated from Figure 12 for the three temperatures. This results in distances of about 11, 14, and 17 μm for 22, 155, and 260°C, respectively. Computer simulations for mixtures of spheres (9,10) indicate that the largest void dimensions within the mixture correspond to about 4 mean sphere diameters. Thus, a fly ash layer is likely to have voids of dimension ranging up to several tens of micrometers. As the potential applied across the dust layer is slowly increased, the first microspark will occur at the lowest voltage consistent with the void dimension where breakdown takes place. Since the variation of V_{BD} with temperature is rather slow (Figure 2) the onset of breakdown must correspond to positions on the Paschen curve at or near the minimum and to the right of the minimum.

The general trend of decreasing V_{BD} with increasing levels of humidity (Figure 2) is opposite to the behavior of breakdown in an air-filled gap between two electrodes, where it is observed that breakdown potential increases with increasing water vapor. In the latter case, the increase is attributed to an electron attachment and conversion process which occurs when water vapor is present (11). However, the data for the present work indicate that the primary interaction of water vapor is with the surface of the dust layer particles (and consequently with the conduction mechanism) rather than with the gas molecules in the void. This is in agreement with studies showing the dramatic effect of the presence of water vapor on resistivity.

Paschen's law aids in interpreting the effect of particle size on V_{BD} for the two fly ashes. The coarse-fraction sample consists of particles much larger, on the average, than those of the ordinary distribution, resulting in larger average void dimensions in the coarse sample. Paschen's law then predicts a larger applied potential at breakdown for this coarse sample than for the ordinary distribution. The case for the fine-fraction sample is not as simple because the porosity must be taken into account. Porosity of a dust sample is conventionally expressed as:

$$\% \text{ Porosity} = \frac{V_c - V_d}{V_c} \times 100 \qquad (1)$$

where V_c is the volume of an empty standard cup (known), and V_d is the volume of dust contained in the standard cup when full. The ordinary distribution of Wabamun fly ash has a porosity of about 53%; while the fine distribution has a porosity of about 68%, largely due to the cohesiveness of the smaller particles. This suggests that the fine sample also contains larger, on the average, voids than does the ordinary distribution. Thus, Paschen's law predicts higher breakdown potentials. Finally, the data of Figure 6 indicate that the average void dimension of the fine sample is less than that of the coarse sample. The relative insensitivity of V_{BD} to particle size fractions of the cement dust suggests that the void dimension over which breakdown occurs must be the same for the three distributions.

The mechanical compression used to change the surface areal loading of the Wabamun ash had no effect on its breakdown voltage. Apparently, the predominantly spherical particles of this dust pack so efficiently that the mechanical loading could not further pack the sample and change its void dimensions. The cement dust was affected by the extra compression (Figure 8). In this case, the void dimension of the relatively inefficiently packed sample was decreased and the breakdown voltage was lowered.

APPLICATION OF PASCHEN'S LAW

In this section, the data will be used to justify the application of Paschen's law to breakdown in a gas-filled void, in the volume and surface conduction limits.

One form of the expression for Paschen's law is (12):

$$V_{loc} = \frac{Bpd}{\ln\left(\frac{Apd}{\ln(1+\gamma^{-1})}\right)} , \qquad (2)$$

where V_{loc} is the local enhanced voltage across the void at breakdown; p, the pressure; d, the void dimension; γ, the Townsend secondary ionization coefficient; and A and B, constants related to the gas. Since temperature was the variable in these experiments, it is preferable to write this equation in terms of number density (n, molecules/cm^3) using the ideal gas law:

$$V_{loc} = \frac{Cnd}{\ln\left(\frac{Dnd}{\ln(1+\gamma^{-1})}\right)} , \qquad (3)$$

where C and D are new constants associated with the change in variable. γ and the primary ionization coefficient, α, are related by:

$$\gamma^{-1} = e^{\alpha d} - 1 \quad . \qquad (4)$$

Then

$$V_{loc} = \frac{Cnd}{\ln\left(\frac{Dn}{\alpha}\right)} \quad . \tag{5}$$

$$\ln\left(\frac{Dn}{\alpha}\right) = \left(\frac{Dn}{\alpha} - 1\right) - \frac{1}{2}\left(\frac{Dn}{\alpha} - 1\right)^2 + \frac{1}{3}\left(\frac{Dn}{\alpha} - 1\right)^3 \cdots, \tag{6}$$

$$\text{for } 0 < \frac{Dn}{\alpha} < 2.$$

Neglecting all but the first term, as justified below,

$$V_{loc} \simeq \frac{Cnd}{\frac{Dn}{\alpha} - 1} \tag{7}$$

or

$$V_{loc} \simeq \frac{b}{1 - \frac{m}{n}} \tag{8}$$

where

$$m = \frac{\alpha}{D} \qquad\qquad b = \frac{C\alpha d}{D}$$

Assuming that α and d remain essentially constant for the conditions of this experiment, so that m and b are constants, equation (8) can be put into the form of a straight line:

$$V_{loc} \simeq m\left(\frac{V_{loc}}{n}\right) + b \quad . \tag{9}$$

If the average applied voltage at breakdown is proportionally related to V_{loc} (as through an effective dielectric constant) then the form of equation (9) can be applied to V_{BD} as

$$V_{BD} \simeq m\left(\frac{V_{BD}}{n}\right) + b' \quad , \tag{10}$$

where b′ accounts for the proportional factor. Figure 13 shows the result of plotting equation (10) using the breakdown data of Wabamun fly ash for all moisture levels in the two temperature limits. A straight line for each temperature limit results. Moreover, the slope of these lines results in values of (Dn/α) between 0.8 and 1.1, making the neglect of all but the first term in the logarithmic expansion of equation (6) a valid approximation. Figure 14 shows the same two lines with all available data. The data corresponding to temperatures between the purely volume and surface conduction regions fall between the two limits of equation (10). The data are not complete enough to conclude that the slopes of the two lines are equal, but they are very close. If the slopes were, in fact, equal, then the ionization coefficient would be constant. This would lead to the conclusion that, since the intercepts of the two lines are different, breakdown occurs in voids of different dimensions in the two limits. Before full use of equation (10) is possible, however, reliable values of C and D or A and B are required.

CONCLUSIONS

The foregoing discussion leads to the following conclusions concerning electrical breakdown in dust layers:

1. Electrical breakdown is an ordinary electron avalanche process originating in voids within the dust layer and obeying Paschen's law. The size of voids in the 0.5 cm dust layers used in this work appear to be in the range of 10 to 20 μm.

2. The electrical breakdown mechanism is connected with the conduction mechanism prior to breakdown. Water vapor strongly affects the breakdown voltage by its presence or absence, but only weakly by its abundance.

3. Both a fine (MMD < 5 μm) and a coarse (MMD > 50 μm) distribution of fly ash have void dimensions greater than an as-received distribution and exhibit correspondingly higher breakdown voltages.

4. Moderate mechanical compression (2500 gm/cm^2) has no effect on fly ash, but does decrease the void dimensions in cement dust, resulting in lower breakdown voltages.

REFERENCES

1. Budenstein, P. On the Mechanism of Dielectric Breakdown of Solids. IEEE Trans. Electr. Insul. EI-15:225-40, 1980.

2. Mosley, R., Cavanaugh, P., McDonald, J., and Sparks, L. Measurements of Electrical Properties of Fly Ash Layers. In: Third Symposium on the Transfer and Utilization of Particulate Control Technology: Volume II, EPA-600/9-82-005b (NTIS PB83-149591), July 1982.

3. Bickelhaupt, R. Electrical Volume Conduction in Fly Ash. APCA Journal 24:251-5, 1974.

4. Bickelhaupt, R. Surface Resistivity and the Chemical Composition of Fly Ash. APCA Journal 25:148-52, 1975.

5. Mosley, R., McDonald, J., and Sparks, L. Mathematical Modeling of Ionic Conduction in Fly Ash Layers. In: Third Symposium on the Transfer and Utilization of Particulate Control Technology: Volume II, EPA-600/9-82-005b (NTIS PB83-149591), July 1982.

6. Earhart, R. The Discharge of Electricity Through Gases at Various Temperatures. Phys. Rev. 31:652-61, 1910.

7. Raju, G. and Hackam, R. Note on Paschen Law and the Similarity Theorem at the Minimum Breakdown Voltage. IEEE Trans. Plasma Science PS2:63-6, 1974.

8. Heisen, A. Note on Paschen Law and Similarity Theorem in Gaps with Cylindrical and Plane Geometry. IEEE Trans. Plasma Science PS4:129-33, 1976.

9. Nakano, Y. and Evans, J. The Relationships Between Pore Classes in a Solid Computed by Monte Carlo Technique. Powder Tech. 35:115-8, 1983.

10. Suzuki, M. and Oshima, T. Estimation of the Co-Ordination Number in a Multi-Component Mixture of Spheres. Powder Tech. 35:159-66, 1983.

11. Verhaart, H. and van der Laan, P. The Influence of Water Vapor on Avalanches in Air. J. Appl. Phys. 55:3286-92, 1984.

12. Husain, E. and Nema, R. Analysis of Paschen Curves for Air, N_2 and SF_6 Using the Townsend Breakdown Equation. IEEE Trans. Elect. Insul. EI17:350-3, 1982.

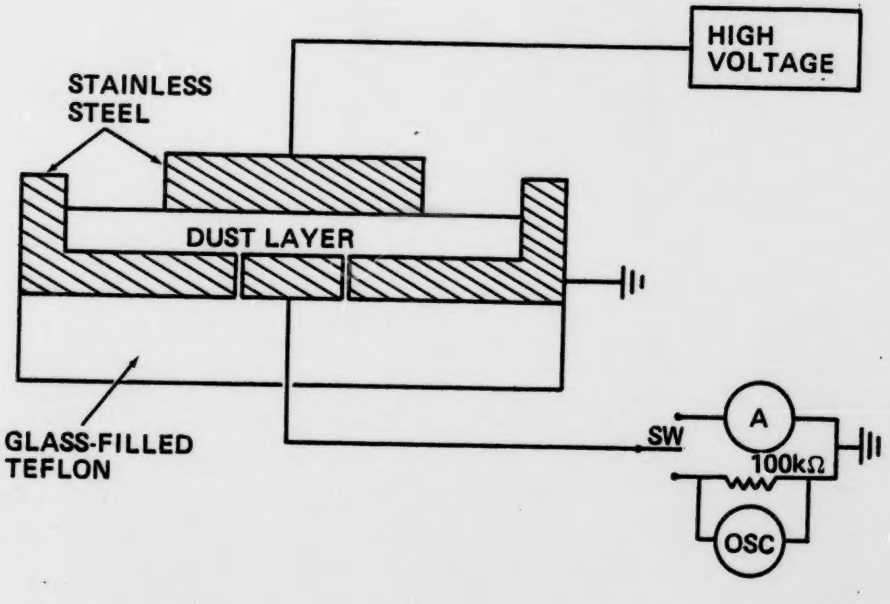

Figure 1. Schematic diagram for electrical breakdown measurements.

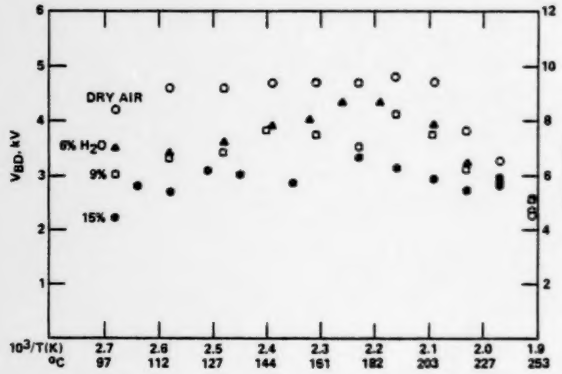

Figure 2. Electrical breakdown of Wabamun fly ash.

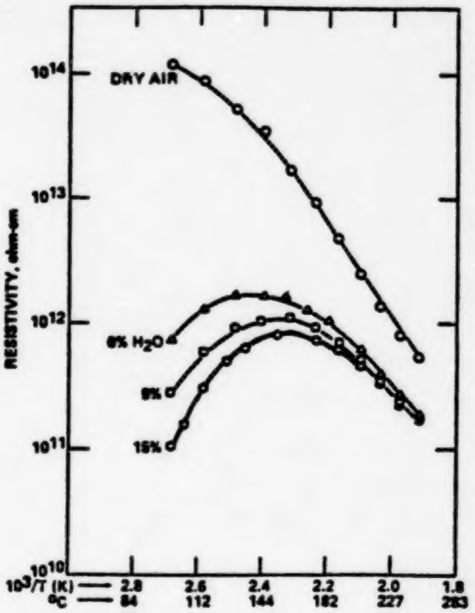

Figure 3. Resistivity of Wabamun fly ash.

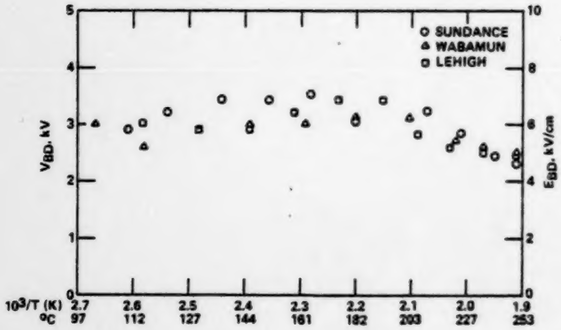

Figure 4. Electrical breakdown of all dust species for 9% water vapor.

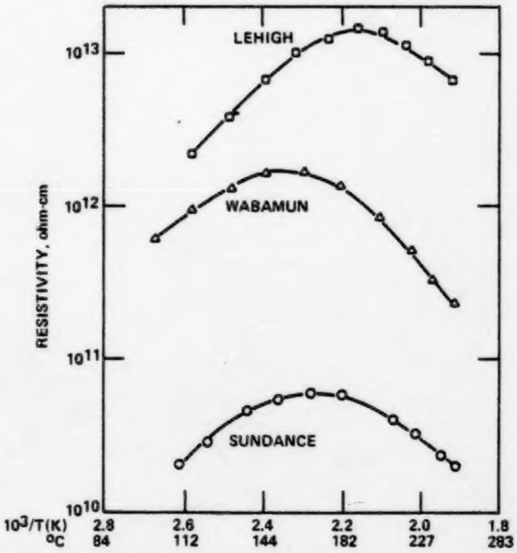

Figure 5. Resistivity of all dust species for 9% water vapor.

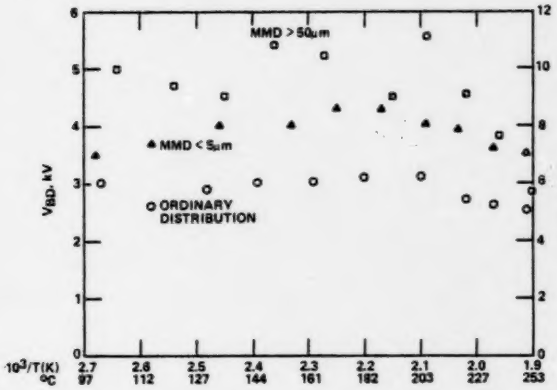

Figure 6. Electrical breakdown of size-fractionated Wabamun fly ash.

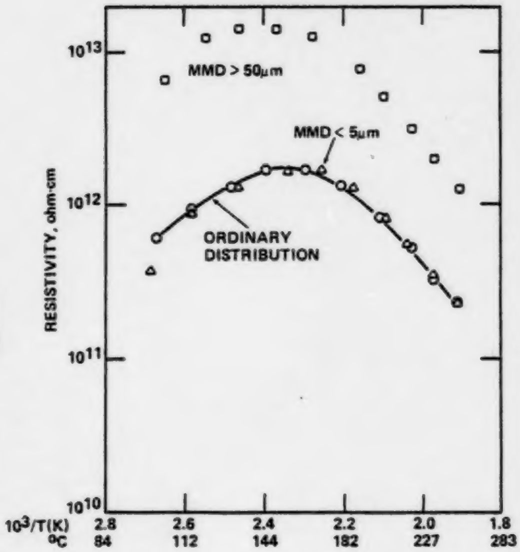

Figure 7. Resistivity of size-fractionated Wabamun fly ash.

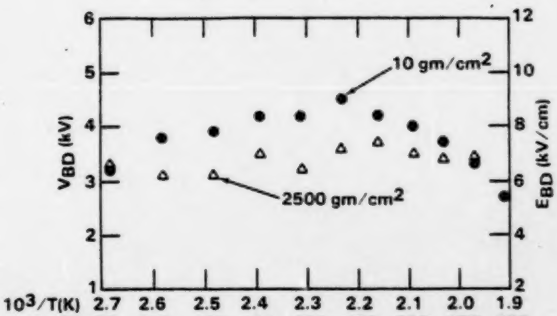

Figure 8. Effect of compaction on the electrical breakdown of Lehigh cement dust.

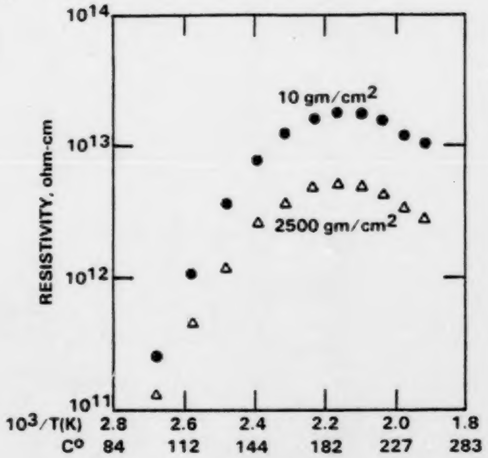

Figure 9. Effect of compaction on the resistivity of Lehigh cement dust.

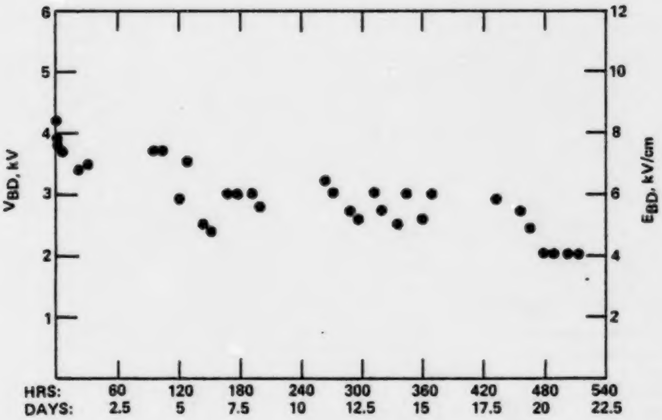

Figure 10. Effect of continual electrical stress on the breakdown behavior of Wabamun fly ash (4 kV/cm stress; 152°C; 9% water vapor).

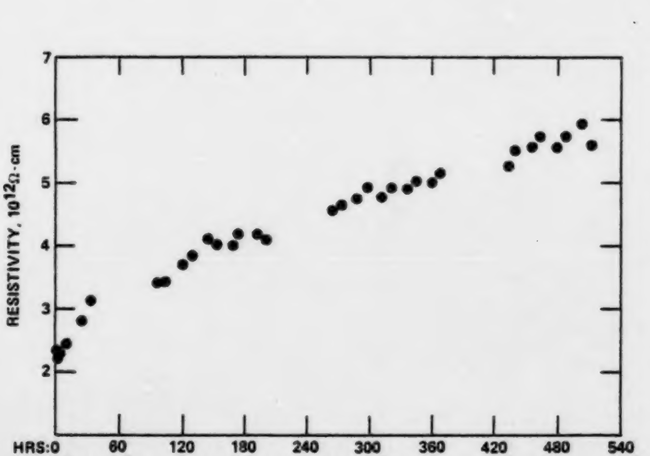

Figure 11. Effect of continual electrical stress on the resistivity of Wabamun fly ash (4 kV/cm stress; 152°C; 9% water vapor).

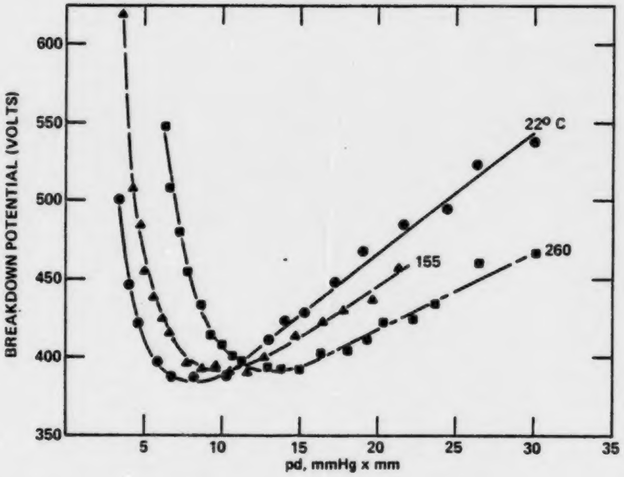

Figure 12. Paschen curves for breakdown in air from Reference 6.

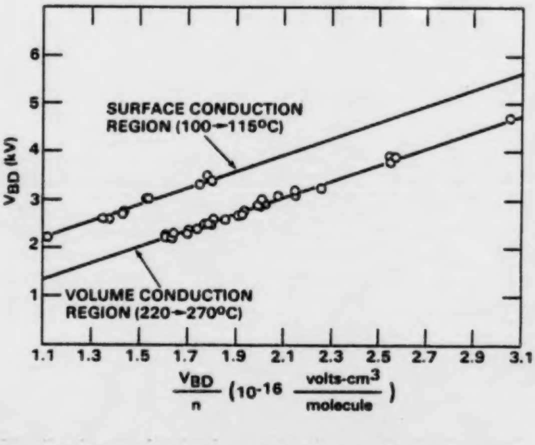

Figure 13. Plot of equation (10) in the volume and surface conduction regions for all humidity levels of Wabamun fly ash.

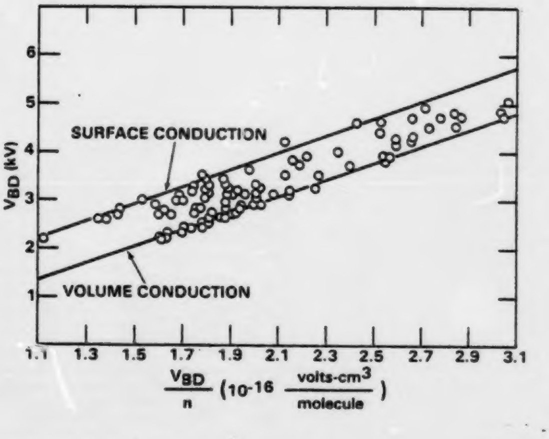

Figure 14. Plot of equation (10) for all Wabamun fly ash data.

BIPOLAR CURRENT PROBE FOR DIAGNOSING FULL-SCALE PRECIPITATORS

by: Senichi Masuda and Toshifumi Itagaki
Department of Electrical Engineering, University of Tokyo
7-3-1, Hongo, Bunkyo-ku, Tokyo, Japan 113

Shigeyuki Nohso and Osamu Tanaka
Sumitomo Heavy Industries, Ltd.
2-1-1, Yato-cho, Tanashi-city, Tokyo, Japan 188

Katsuji Hironaga and Nobuhiko Fukushima
Nihon Kagaku Kogyo Co., Ltd.
2-1, Shimizu, Suita-city, Osaka, Japan 565

ABSTRACT

A bipolar current probe for measuring negative and positive ionic current densities in a back corona field and its space potential distribution is modified so that it can be applied to a full-scale precipitators for their diagnosis. The sensor at a high voltage and the control unit at grounded potential are separated by optical links. Special precautions are made so as to prevent the probe from dust contamination and protect the sensor from sparking damage. Tests are made at a laboratory precipitator and the modified probe is going to be used in a large pilot plant under practical operating conditions. The detailed construction of the modified probe is presented, together with the test results.

1. INTRODUCTION

Measuring current densities of positive and negative ions in a precipitator field is one of the most effective methods for the analysis of the ESP performance under back corona. The ratio of the positive ionic current density, i_+, to the negative one, i_-, in the bi-ionized ESP field theoretically gives the degradation in particle charge, and, hence, the drop of apparent migration velocity of dust and collection efficiency. Therefore, i_+ and i_- should be regarded as key parameters to detect the severity of back corona and to prevent its harmful effects.

The separate measurement of i_+ and i_- is possible with a bipolar ionic current probe developed by the authors (1,2). This probe was tested in a laboratory ESP to confirm its theory and gave a satisfactory result: the decrease in particle charge and dust apparent migration velocity estimated from the measurement of i_+ and i_- agreed with those measured by experiments. Also other important informations concerning back corona were obtained with the probe. In particular, it can be used for measuring the space potential in a bi-ionized field.

Based on these laboratory results, the authors attempted to modify the prove for use in diagnosis of a full-scale ESP under practical operation. The detailed construction of the modified probe and the laboratory test results are presented in the following paragraphs.

2. CONSTRUCTION OF THE PROBE SYSTEM

Figure 1 shows the block diagram of the modified probe system. The system consists of a probe to be inserted into the ESP field, a current measuring unit, optical links for transmission of the current signal, and a control unit where the magnitude of the ionic current is displayed. Each unit has the following features.

2.1 PROBE

Figure 2 shows the configuration of the probe and its supporting pipe. Alumina ceramic is used as the base of the probe. Tungsten electrodes are printed on its surface, and electro-plated with nickel to prevent oxidization. This configuration allows the probe to be used in an elevated temperature. Mechanical strength of the probe is enough with its 6.2 mm diameter.

The probe is attached to the supporting pipe made of stainless steel. When the electrodes are contaminated with dust, the probe is pulled into the supporting pipe through a cleaning head by means of a geared motor which is operated manually. As the probe passes through the cleaning head, the dust on the electrodes is wiped off with ceramic wool packed in the head. The cleaning can be done even if the probe is at high voltage, thus assuring a long term continuous operation.

Figure 3 shows the effect of the probe contamination and its cleaning. The probe is inserted into a laboratory ESP at a point 2.1 m downstream of the inlet. The current I_1 from the probe electrode 1 facing to the discharge electrode drops with time owing to the accumulation of dust. The dust concentration at the inlet of the ESP, the gas temperature and the gas velocity are 7 g/Nm^3, 140 deg.C and 1.1 m/s respectively. The recovery in the magnitude of I_1 by cleaning can be clearly seen.

2.2 CURRENT MEASURING UNIT

In the current measuring unit, one of the I/V converters (operational amplifiers) connected to three probe electrodes is selected by a selection signal from the control unit. The ion current entering the selected electrode is converted into a digital optical signal so as to be transmitted by an optical fiber. Figure 4 shows the terminals of the optical fibers.

Since the current measuring unit is at a high voltage while in operation, solar batteries are used to supply power to its electronic circuit. They are charged through air gap by the light from a halogen lamp at grounded

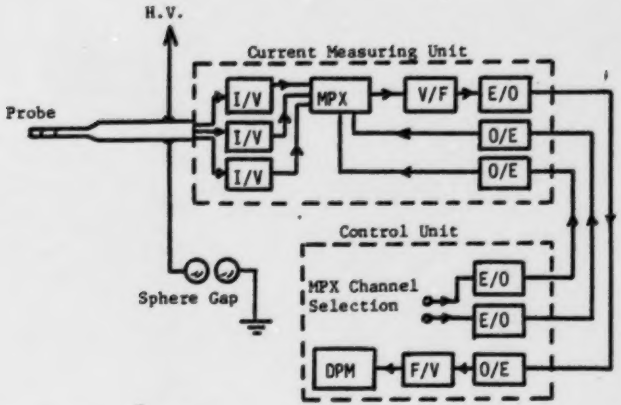

I/V: Current-Voltage Converter

V/F: Voltage-Frequency Converter
F/V: Frequency-Voltage Converter

E/O: Electrical-to-Optical Converter
O/E: Optical-to-Electrical Converter

MPX: Multiplexor

DPM: Digital Panel Meter

H.V.: High Voltage

Figure 1. Block diagram of the modified probe system.

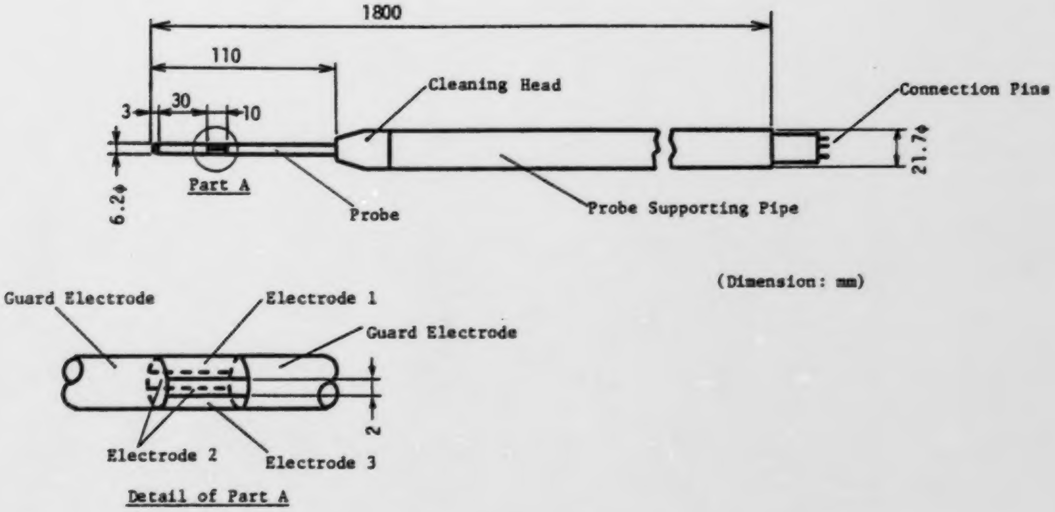

Figure 2. Configuration of the probe and its supporting pipe.

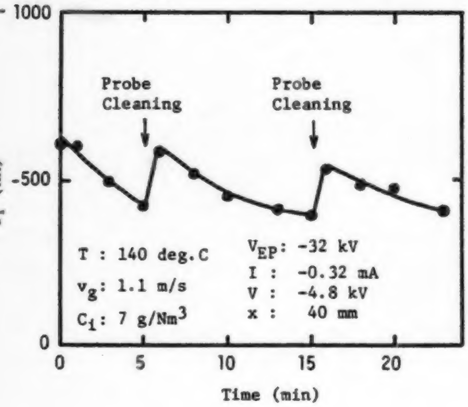

Figure 3. Time-dependent change of the probe current.

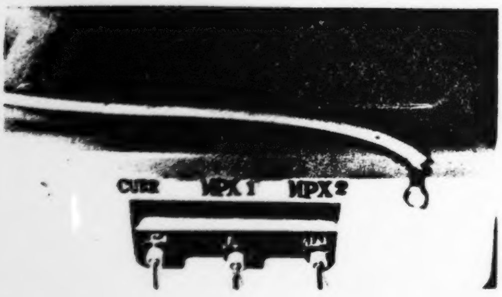

Figure 4. Optical fiber connections to the current measuring unit.

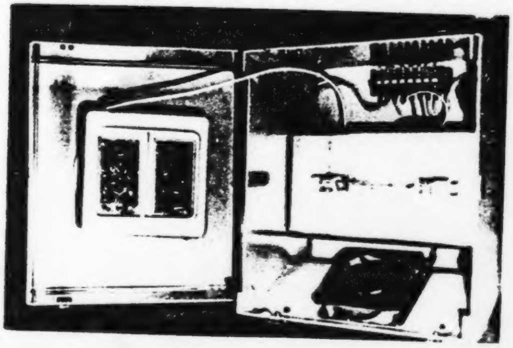

Figure 5. Solar batteries on the current measuring unit and the halogen lamp for their excitation.

potential (Figure 5). Figure 6 and 7 show the photographs of the current measuring unit and the probe supporting pipe.

2.3 OPTICAL LINKS

Three optical fibers are used to separate electrically the current measuring unit at a high voltage from the control unit at the grounded potential in signal transmission. One is for the transmission of the probe current signals, and the others for the transmission of the probe selection signals from the control unit to the current measuring unit.

2.4 CONTROL UNIT

Figure 8 shows the photograph of the control unit. There are two switches, one being to manually select one of the three electrodes of the probe. The selection signal is transmitted to the current measuring unit, and the ionic current entering the selected electrode is optically transmitted to the control unit. Then, it is converted again to the electrical signal and displayed on the front panel.

Another switch is for starting the cleaning of the probe electrodes. By pressing the button, dust on the electrodes begins to be wiped off, and the probe moves back to the initial position to restart measurement.

2.5 SPHERE GAP

The probe is subjected to a sparking caused by two different reasons. One is the sparking between the discharge electrode and the probe occuring in the case when the probe potential is set too much lower than the original local potential of its position, or the probe is located too close to the discharge electrode. The other is the sparking between the probe and the grounded portion of the ESP. The former is much more likely to cause damage to the current measuring unit or high voltage power supply of the probe because of a large capacity of the high voltage power supply of the ESP.

A counter measure is taken by using a sphere gap in parallel to the high voltage power supply, which keeps the voltage of the probe below the gap spark voltage even if the sparking takes place. The spheres used are 20 mm in diameter and the length of the gap is adjusted to a desired value: for example 6 mm gap corresponds to about 20 kV spark voltage. In addition, 100 megohm resistors are connected in series to the electrode wires at the input of the current measuring unit to suppress surge current. The combination of the sphere gap with the resistors can completely prevent the spark damage which would otherwise obstruct the operation of the probe.

3. OPERATION OF THE MODIFIED PROBE SYSTEM

3.1 MEASUREMENT OF LOCAL POTENTIAL AND ION CURRENT DENSITIES

The probe measurement begins with establishing the balanced condition at which the probe voltage becomes equal to the original local potential V_P at

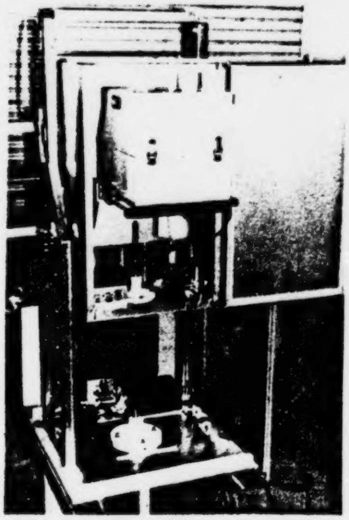

Figure 6. Current measuring unit and probe supporting pipe.

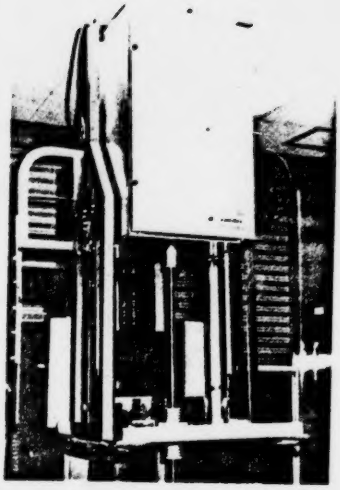

Figure 7. Housing of the current measuring unit and probe supporting pipe.

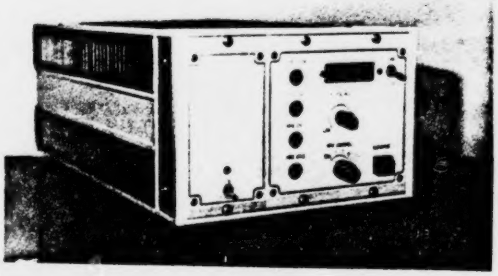

Figure 8. Control unit.

the probe position. The probe potential is varied, and the currents I_1, I_2, I_3 detected by the measuring electrode 1 facing to the corona electrode, the center electrode 2, and the measuring electrode 3 facing to the plate are measured. Then, the ionic current densities i_- and i_+ are calculated from the values of I_1 and I_3 at the balanced potential, I_{1P} and I_{3P} as follows (1):

$$i_- = -I_{1P}/4al \cos(d/2a)$$
$$i_+ = I_{3P}/4al \cos(d/2a)$$

where a = radius of the probe (3.1 mm), l = length of the electrode 2 (10 mm) and d = width of the electrode 2 (2 mm).

The verification of these theoretical equations have already been made by experiments (1), but tests are performed also for this particular modified probe in a mono-ionized corona field of a needle-to-plane system (Figure 9(a)). Figure 9(b) shows the values of I_1, I_2 and I_3 measured as functions of the probe potential V. In the mono-ionized field the balanced potential, V_P, is theoretically given by the crossing point, P, of the extrapolation of the linear region of the I_2-V curve with the horizontal axis. Hence, we get I_{1P} = -70 nA and I_{3P} = 0 nA giving i_- = 60 nA/cm^2 and i_+ = 0 nA/cm^2

3.2 INFLUENCE OF THE RIPPLES IN CORONA VOLTAGE

In a practical ESP the corona voltage always contains more or less ripples to cause fluctuations in the local potential in the field. But even in this case, the probe measurement is possible, so far as the probe potential be supplied through a voltage divider from the corona voltage. In this case, the balanced condition is maintained at every instant, once it has been established. The local potential V_P and the ionic current densities i_- and i_+ thus obtained indicate the averages of the fluctuating values.

If only the measurement of space potential is required, there is no need to use a voltage divider even when the ESP voltage fluctuates. For example Figure 10 shows the comparison between the curves obtained with a voltage divider and with a separate DC high voltage source in a corona system shown in Figure 9(a) now energized by pulsating corona voltage. Although the corona voltage fluctuates between -13 and -25 kV, no difference between the two cases can be seen in the linear regions, giving the same value of V_P.

However, as the probe potential increases (in negative direction), the curves with a DC probe voltage deviate to a higher level, possibly giving rise to the i_-.

3.3 EXTENSION OF THE RANGE OF PROBE POTENTIAL

For accurate measurement of V_P, it is essential to get a linear portion of the I_2-V curve in a wide range of the probe potential. But when a DC power source is used for setting the probe potential, this is sometimes difficult because there exists a lower limit of the probe potential. This is caused by the corona current flowing into the whole surface of the probe and its supporting pipe which increases at a decreased probe potential.

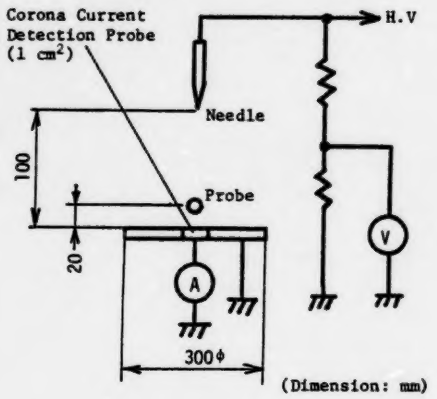

Figure 9(a). Needle-to-plate corona system.

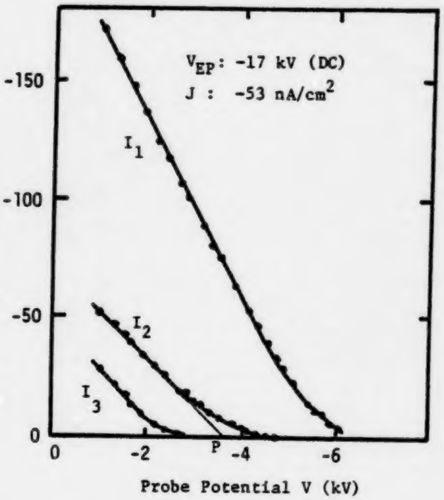

Figure 9(b). Graphical method to determine the original local potential.

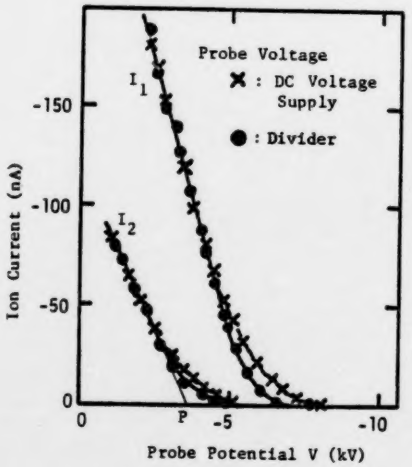

Figure 10. Probe characteristics in a pulsating potential field. (Needle voltage is pulsating between -13 kV and -25 kV. The average corona current density under the needle is about -80 nA/cm^2.)

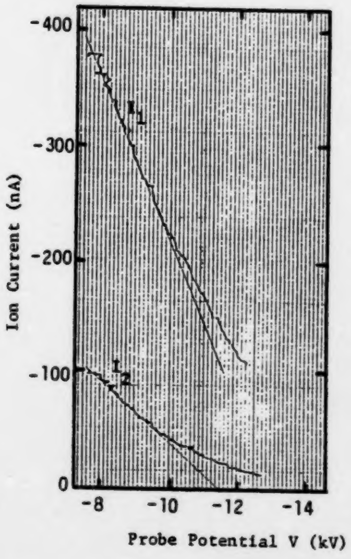

Figure 11. Probe characteristics in EPRI-Alapahoe pilot ESP. V_{EP}: -43 kV, I: -38.5 mA, x: 30 mm, T: 150 deg.C at the inlet (by the courtesy of EPRI, CE and SRI)

This current flows across the high internal resistance of the probe DC power supply to produce a substantial voltage drop. The probe potential cannot be lowered below this level of voltage drop.

In this case, connecting a resistance in parallel to the probe DC voltage source helps extend the range of the probe potential. Of course the magnitude of the resistance should be determined in accordance with the type of the DC power supply, ionic current densities to be measured, probe position in the field, etc., but the use of a 120 megohm resistance doubled the range of the linear portion in the measurement made at a pilot ESP.

3.4 CORONA STABILIZATION

In a clean wire-to-plate system corona points usually move around along the corona wires and cause irregular changes in corona current in time and space when smooth wires are used. This makes the probe measurement difficult, requiring a means of stabilizing corona current. Making notches or attaching small needles on the wires is effective for this purpose, so far as the attention be paid to keep the changes in the current-voltage characteristics and the space potential distribution negligibly small.

But with an ESP in practical operation, no such movement of corona points occur because the wires are covered with dust. Figure 11 shows an example of the result obtained with a pilot ESP in the EPRI-Alapahoe Test Station collecting fly ash. It has 9 inch plate-to-plate spacing and 6 inch wire-to-wire spacing. The probe is inserted in parallel to the wire from the top of the ESP. The center of the probe is 30 mm away from the collection plate. A DC high voltage power supply is used to apply voltage to the probe. The 2.6 mm thick discharge wires without notches or needles but covered with dust provide stable corona current, so very smooth current-voltage curves are obtained.

3.5 AUTOMATIC MEASUREMENT WITH A PERSONAL COMPUTER

Although no computer is used so far in the operation of the modified probe system, it is furnished with terminals to process signals with a personal computer for determination of V_P, calculation of i_- and i_+, and control of the probe cleaning. The DC high voltage power supply or the voltage divider for adjusting the probe potential is also to be controled by the computer.

4. MEASUREMENT OF SPACE POTENTIAL IN A LABORATORY ESP

The space potential is also measured by the present probe in a laboratory ESP which has 250 mm plate-to-plate spacing and 150 mm wire-to-wire spacing (Figure 12(a)). There are 16 discharge wires each with 3.2 mm in diameter. Each of the three neighboring discharge wires out of 16 has a small metal ring wound on it to stabilize a corona point. As shown in Figure 13(a) the rings are made of a 0.6 mm thick copper wire wound in two turns around a notch on the discharge wires and covered with soft solder. Before the experiments, the influence of the ring on the discharge character-

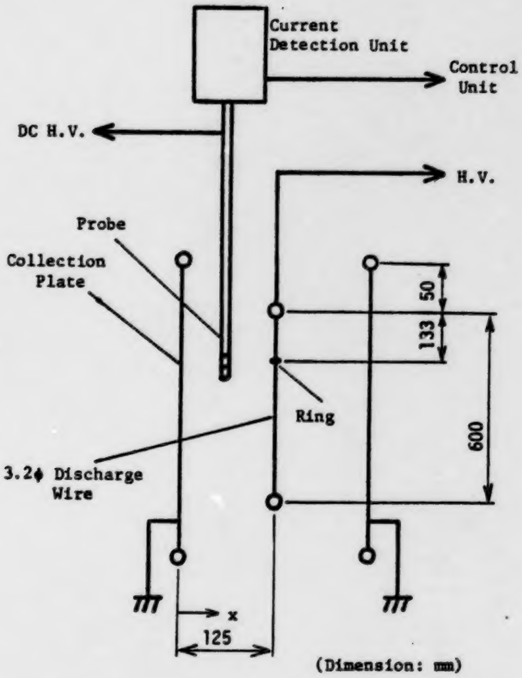

Figure 12(a). Experimental set up of the probe in a laboratory ESP.

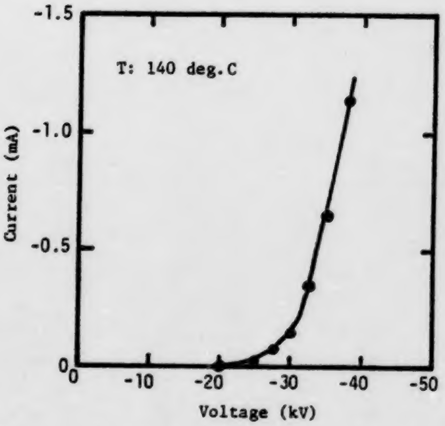

Figure 12(b). Current-voltage characteristic of the laboratory ESP.

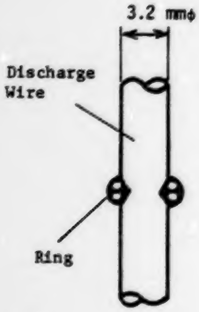

Figure 13(a). Ring around the discharge wire to stabilize the corona.

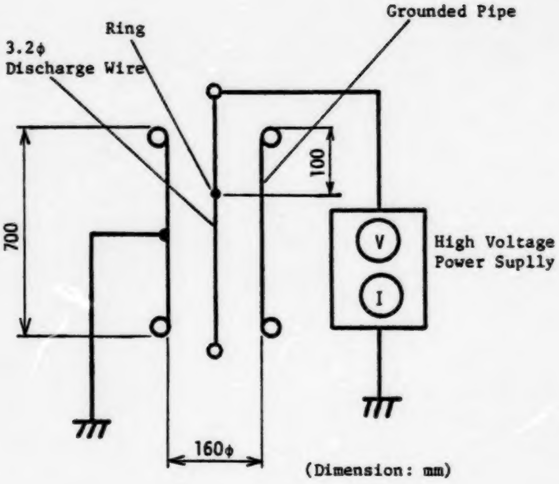

Figure 13(b). Wire-to-cylinder corona system.

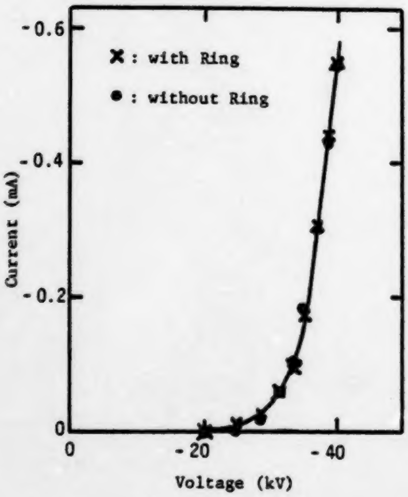

Figure 13(c). Discharge characteristics of the wire with and without the corona-stabilizing ring.

istics of the wire is checked at room temperature with a wire-to-cylinder corona system shown in Figure 13(b), and it is almost negligible as shown in Figure 13(c).

The probe is inserted in front of the middle of the three discharge wires attached with the ring at a position that the electrode 1 faces to the ring. Figure 12(b) shows the current-voltage characteristic of the ESP at the gas temperature T = ca. 140 deg.C and without dust loading. Figures 14(a),(b),(c) and (d) show the probe characteristics measured at this temperature under dust-loaded condition with $C_i = 5$ g/Nm^3 at the ESP inlet. The resistivity of the dust is about 1.9×10^{11} ohm-cm. The original local potential V_p can be easily obtained from these figures. Plotting V_p against the distance x from the collection plate we get Figure 15.

All the results described above are very satisfactory, providing a firm bases for the application of the modified probe in full-scale ESP's.

5. CONCLUSIONS

The bipolar current probe to determine the severity of back corona through separate measurement of i_+ and i_- in a back corona field has been modified so as to be applied to a full-scale ESP in practical operation. The probe can be also used for the measurement of space potential distribution in the bi-ionized field of the ESP.

The modified probe system is fabricated with a heat-resistant alumina ceramic, and comprizes a dust cleaning mechanism. It is powered with solar batteries to drive the current measuring electronics at a high potential position. The signal transmission is made through optical links and the spark protection of the system by a sphere spark gap.

The operation under a pulsating corona voltage is possible, so far as the probe voltage be supplied from the corona voltage source through a voltage divider. In addition, the space potential can be measured also with a DC probe power supply even in this case. However, the use of the DC probe power supply may produce error in i_+ and i_-.

The stabilization of corona points is necessary if the probe is used in a clean wire-to-plate corona system, but no such precautions are necessary when used in a practical ESP field.

The results of performance tests made on the modified probe are very encouraging, suggesting that it could be used in a practical ESP for diagnosis and monitoring of back corona. It also provides a method of laboratory evaluation of dust precipitability.

ACKNOWLEDGMENTS

The authors wish to express their sincere gratitude to Dr. R. Altman and Mr. R. Ritlenmeyer of EPRI, and Mr. G. W. Driggers of CE for their

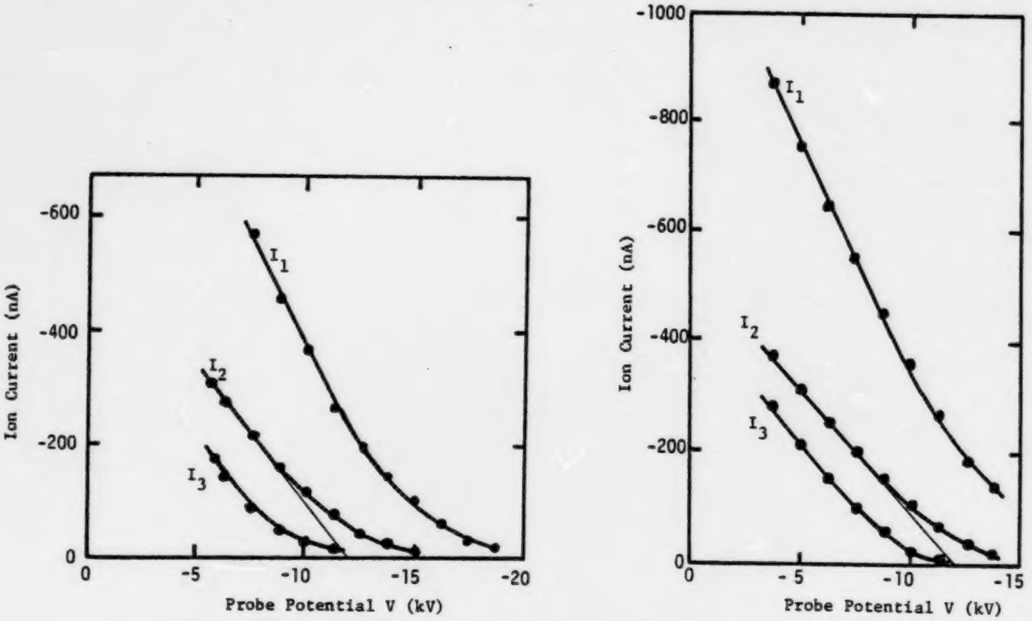

Figure 14(a). x = 40 mm, without dust.

Figure 14(b). x = 35 mm, with dust.

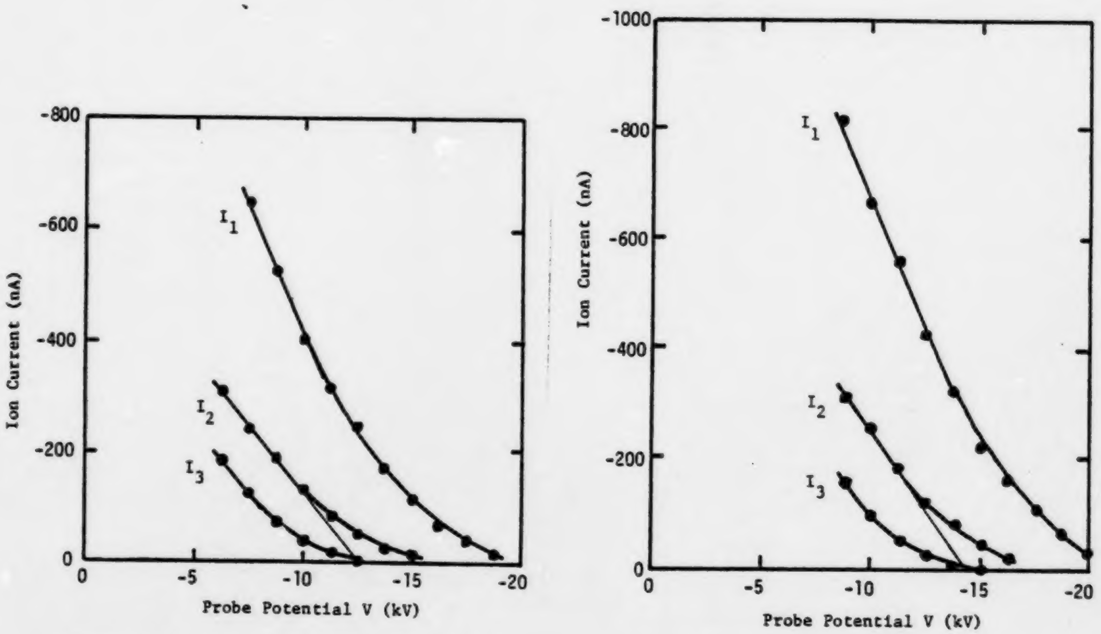

Figure 14(c). x = 40 mm, with dust.

Figure 14(d). x = 45 mm, with dust.

Figure 14. Probe characteristics. V_{EP}: -35 kV, J: -0.25 mA/m^2, T: 140 °C.

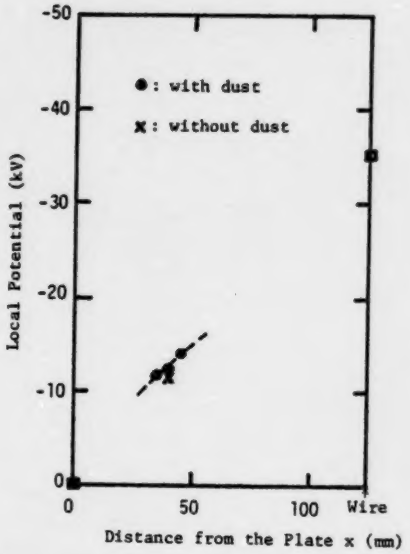

Figure 15. Probe-measured potential in a laboratory ESP field.

support given to this research. The authors are also indebted to Dr. J. L. DuBard, Mr. C. Landham and Mr. C. Lindsey of Southern Research Institute for their help and discussions. Finally, the authors wish to thank Mr. T. Noda and Mr. H. Terai of Sumitomo Heavy Industries for their competent help and advice.

The work described in this paper was not funded by the U.S. Environmental Protection Agency and therefore the contents do not necessarily reflect the views of the Agency and no official endorsement should be inferred.

REFERENCES

1. Masuda, S. and Nonogaki, Y. Sensing of Back Discharge and Bipolar Ionic Current. Journal of Electrostatics. Vol. 10. Elsevier, Amsterdam, Netherlands, 1981. 73 pp.

2. Masuda, S. and Nonogaki, Y. Bi-Ionized Structure of Back Discharge Field in an Electrostatic Precipitator. Record of IEEE/IAS 1981 Annual Meeting in Philadelphia, Pennsylvania. October 1981. 1111 pp.

NOMENCLATURE

a : radius of the probe.
C_i : dust concentration at the inlet of the ESP.
d : width of the probe electrode 2.
i_+ : positive ionic current density.
i_- : negative ionic current density.
I : corona current.
I_1 : ionic current detected by the probe electrode 1.
I_2 : ionic current detected by the probe electrode 2.
I_3 : ionic current detected by the probe electrode 3.
I_{1P}: I_1 at $V = V_P$.
I_{3P}: I_3 at $V = V_P$.
J : corona current density.
l : length of the probe electrode 2.
T : gas temperature.
v_g : gas velocity.
V : probe potential.
V_{EP}: corona voltage.
V_P : original local potential at the center of the probe.
x : distance from the collection plate to the probe.

A METHOD FOR PREDICTING THE EFFECTIVE VOLUME RESISTIVITY OF A SODIUM DEPLETED FLY ASH LAYER

By: Roy E. Bickelhaupt
Bickelhaupt Associates, Inc.
Meadowood Subdivision, Box 54N
P.O. Box 3532
Carbondale, IL 62901

Ralph F. Altman
Electric Power Research Institute
3412 Hillview Avenue
Palo Alto, CA 94303

ABSTRACT

Research has been conducted to develop a technique for predicting the effective volume resistivity of a fly ash layer that has been exposed to circumstances leading to a hot-side precipitator problem known as sodium depletion. Eight fly ashes, representing a major portion of U.S. coals, were evaluated by subjecting 0.5 cm ash layers to a continuously applied voltage gradient of 4 kV/cm for periods of time up to 35 days at a temperature of 350°C (662°F). Resistivity was determined at 350°C before the test started and after the long period of applied voltage used to create the sodium depleted situation. In this condition, resistivity was also determined at 280°C (536°F) for an average electric field intensity of 4 kV/cm and immediately prior to breakdown. This experimental method can be used with any ash sample to estimate resistivity in a sodium depleted condition. But in addition, a correlation resulting from these resistivity data has been developed. This correlation is combined with an existing technique for predicting resistivity to produce a method for calculating the expected fly ash layer resistivity after sodium depletion has occurred.

A METHOD FOR PREDICTING THE EFFECTIVE VOLUME RESISTIVITY OF A SODIUM DEPLETED FLY ASH LAYER

INTRODUCTION

Several years ago when electrostatic precipitators located on the hot side of the air preheater were coming into extensive use, several serious problems were observed including mechanical difficulties such as poor plate alignment and other attendant effects which resulted from faulty design, excessive temperatures, and thermal cycling. These mechanical problems not only caused poor precipitator performance, they masked and contributed to other problems. Precipitator fouling has also been a significant problem. This problem is principally related to ash chemistry, fine particles and inadvertent incursions of excessive moisture and is also influenced by poor gas distribution, poor rapping and excessive grain loading. A third major problem, subsequently called "sodium depletion", was also observed. While this problem is aggravated by fouling and mechanical problems, sodium depletion can have a devastating effect on the performance of a mechanically sound, "clean" precipitator. This article is concerned with the latter problem and gives a method for measuring and predicting the resistivity of an ash layer in a sodium depleted condition.

The sodium depletion problem is characterized by a time-dependent degradation of precipitator performance. It has been observed that performance can be substantially restored by thorough sand blasting or washing the precipitator collection plates only to have the deleterious effect occur again with time. A most interesting observation was that after a period of operation the precipitator electrical characteristics demonstrated back corona suggesting very high resistivity, while in situ and laboratory measurements indicated the resistivity was in a desirable range for ash collection. These observations were made with both "clean" and fouled precipitators.

A generally accepted explanation (1) of the time dependent hot-side precipitator performance deterioration referred to as sodium depletion has been given. Briefly, the argument states that a thin layer of fly ash becomes permanently attached to the collection plates. This occurrence is promoted by high inherent ash resistivity, cementitious ash, and frequent incursions of moisture. It can also be influenced by collection plate material, surface finish, and ineffective rapping. However, the layer can be present in a precipitator with no operational problems and cannot be completely removed by either normal or power-off rapping.

After a long period of time, weeks to months, under electrical stress, the effective resistivity of this thin layer increases greatly, and the precipitator responds as if it were collecting a very high resistivity ash even though the measured inherent ash resistivity is not high. The explanation states that the positive charge-carrying alkali metal ions present in the tenaciously adherent ash layer migrate away from the collection plate leaving a glassy matrix that must depend on another conduction mechanism to transport charge. It has been suggested that this mechanism is controlled by oxygen ion migration and that this change in rate-controlling mechanisms leaves the thin ash layer with a significantly higher resistivity.

Remedial procedures have been discussed (2) and several techniques have been tried with mixed results. Thorough plate cleaning by washing and/or sand blasting gives relief; however, the success of this procedure depends on the length of time until it has to be repeated. A specific sodium conditioning technique has been reported (3) as a suitable procedure. In this case, it is important to uniformly distribute the sodium compound throughout all of the coal to be burned and to make sure the sodium addition is compatible with the boiler operation. The judicious selection (4) of coals can also solve the sodium depletion problem. Ash from select coals can either serve as a form of sodium conditioning or develop an adherent layer that has a resistivity level that can be tolerated by the particular precipitator. Other forms of conditioning with sodium compounds or proprietary compounds have also been reported (5). Finally, the effect of pulse energization devices for controlling the electrical characteristics of the precipitator to combat the back corona resulting from sodium depletion have been described (6).

For several reasons it would be desirable to be able to predict the effective resistivity of an ash layer after sodium depletion has occurred. The data would be useful for: a) selecting coals for compatibility with specific existing precipitators, b) trouble shooting poorly performing precipitators, c) sizing new hot-side precipitators, and d) estimating the lowest tolerable operating temperature for a given coal/precipitator combination. A technique (7) is available for predicting the inherent fly ash resistivity before sodium depletion has occurred as a function of temperature and field strength from the composition of the fly ash or properly prepared coal ash. This report discusses additional work conducted to develop an experimental method for determining the resistivity of depleted ash and to expand the resistivity predictive model to include the prediction of the resistivity of ash layers in the sodium depleted condition.

EXPERIMENTAL APPROACH

As described in reference 7, fly ash resistivity at 350°C (662°F) can be predicted using experimental results correlating resistivity with ash composition and with electric field intensity. From these predicted data and Equation 1 below, resistivity as a function of temperature in the hot side range, 250°C to 500°C (482°F to 932°F) can be computed.

$$\log \rho_v = \log \rho_0 + \log e \, (S/T) \qquad (1)$$

where:

ρ_v = volume resistivity of fly ash at any temperature,

ρ_0 = complex ash parameter involving the number of mobile charge carriers,

S = slope of the high-temperature, linear portion of the log ρ vs (1/T) relationship in °K,

e = natural logarithm base,

T = absolute temperature, °K.

To expand this approach for the prediction of the resistivity of a sodium depleted ash layer, additional data were required as follows:

- the amount of resistivity increase that will occur due to the development of a stable, rate-controlling, sodium-depleted layer,
- the effect of electric field intensity on the resistivity of a stable, rate-controlling, sodium-depleted layer, and
- the effect of the sodium-depleted layer on the slope of the resistivity/temperature relationship.

A stable layer is one that has attained a quasi-equilibrium condition of thickness and composition as a result of competing mechanisms. It exhibits little additional attenuation of current density with time.

To be able to evaluate the required data with respect to inherent ash resistivity and ash composition, a matrix of eight fly ashes was selected. The chemical compositions are shown in Table 1. Ashes 304, 305, and 306 are typical of those ashes produced from bituminous coals from the eastern U.S. The main difference in chemical composition among these ashes is the variation in iron concentration which normally increases with an increase in sulfur in the coal. Ashes 301, 302, 303, 307, and 308 are typical of those ashes produced from lignites and sub-bituminous coals from the western U.S. The principal variations among these ashes are the alkaline earth concentration (calcium plus magnesium) and the sodium concentration. These eight ash compositions represent a large fraction of the coals mined for steam generation. It was anticipated that this collection of ashes would allow data interpretation either in terms of composition or magnitude of inherent resistivity. The predicted inherent resistivity values as well as the measured initial resistivity values at the start of the experimentation are also given in Table 1. From these data it can be seen that a two order of magnitude variation in resistivity was represented by the selected ashes.

To satisfy the objective of the experiment, it was necessary to evaluate the resistivity/temperature relationship after the ash layers had demonstrated that they had attained a stable sodium depleted condition. To achieve this goal, it was decided to apply a constant voltage for a long period of time until current density showed only a minor rate of degradation. The constant voltage, 2 kV, was applied to ash layers 0.5 cm thick yielding a 4 kV/cm electric field intensity in a parallel plate resistivity cell. Furthermore, it was arbitrarily decided that the test would continue until the current density was decreasing at a rate of $<$ 10% in 100 hours. The constant voltage technique was used because it allowed four ashes to be evaluated simultaneously. An electrometer was periodically inserted into the circuit to determine the current passing through a given sample. This was done without interrupting the voltage to the other samples. The apparatus used to conduct these experiments has been previously described (8).

After the current density of the four samples simultaneously under test has reached a degradation rate of <10%/100 hours at 350°C (662°F) and 4 kV/cm, resistivity was determined, and the temperature was lowered to 280°C (536°F). When thermal equilibrium was reached, resistivity was determined again, and resistivity as a function of electric field intensity was determined until dielectric failure occurred. The test environment during the entire program was air containing 4% water.

Table 1.

CHEMICAL COMPOSITION AND RESISTIVITY VALUES FOR THE EIGHT FLY ASHES EVALUATED

Fly Ash	Chemical Composition, Weight Percent after Ignition at 750°C											Resistivity, ohm cm	
												Predicted	Start of test
No.	Li_2O	Na_2O	K_2O	MgO	CaO	Fe_2O_3	Al_2O_3	SiO_2	TiO_2	P_2O_3	SO_3	352°C, 4 kV/cm	350°C, 4 kV/cm
301	0.03	0.51	1.7	1.3	4.4	5.0	25.8	59.0	1.7	0.31	0.35	7 E 9	6 E 9
302	0.01	0.29	0.71	1.8	12.6	4.1	24.6	52.9	1.0	0.13	0.24	9 E 10	8 E 10
303	0.05	0.34	0.42	6.3	19.5	4.3	24.1	41.2	1.5	0.31	0.94	1 E 11	2 E 11
304	0.04	0.19	2.7	0.85	0.56	4.1	32.2	56.4	2.3	0.15	0.18	8 E 9	6 E 9
305	0.05	0.34	3.1	1.1	2.2	12.5	27.1	50.5	1.8	0.33	0.57	2 E 9	1 E 9
306	0.03	0.46	2.4	0.91	3.8	21.4	20.7	46.9	1.5	0.29	1.2	1 E 9	1 E 9
307	0.01	2.8	0.62	1.1	12.8	4.1	25.6	50.4	0.8	0.19	0.41	1 E 9	1 E 9
308	0.02	1.8	0.32	6.2	30.9	5.5	19.8	30.8	1.7	1.1	4.1	8 E 9	6 E 9

Although the eight ashes used in this work collectively represent a very high percentage of all fly ashes produced from U.S. coals, the following test procedure is suggested for the reader who is concerned with an atypical ash or unusual precipitator conditions. A procedure identical to that described above for this research is suitable with the exception of test temperatures. For a specific ash or installation, the depleted layer should be developed at the temperature encountered or expected under normal full-load conditions and the lower temperature used should be the lowest expected under reduced-load conditions.

RESULTS AND DISCUSSION

CURRENT DENSITY/TIME RELATIONSHIP

Using the apparatus described in Reference 8, current passing through each test cell was periodically recorded. Calculated current density plotted as a function of time is shown in Figure 1 for all eight ash samples. The tests were done in groups of four ashes: 301, 304, 305, and 306 in the first group and 302, 303, 307, and 308 in the second group. The test was terminated when the current density for every ash in a given group was decreasing at a rate of <10% per 100 hours. In each group, the current density was decreasing at a rate lower than this for one or more of the ashes when the test was terminated.

This data acquisition method has been used extensively in the past with many different types of ash. The test has been conducted with parallel-plate resistivity cells, as in this case, and with a wire-plate corona discharge apparatus. All results have been similar in that current density as a function of time shows a rapid attenuation in the early part of the test followed by an additional slow decay as the test continues into hundreds of hours. This time-dependent decrease in current density is the result of the development of a stable sodium-depleted layer contiguous with the positive electrode and reflects the time-dependent performance loss by a precipitator.

For the chosen test conditions, ashes 302 and 303 are good examples of fly ashes that will produce the sodium-depletion problem in a hot-side precipitator. After 840 hours (35 days), the current density of ash 303 was <2 nanoamps/cm^2 under the ideal conditions of a laboratory test. Past experience indicates that the average current density could be less for the imperfect situation in a precipitator.

RESISTIVITY/TEMPERATURE RELATIONSHIP

Figure 2 shows the effect of the sodium-depletion phenomenon on the resistivity/temperature relationship for two of the eight ashes evaluated. Current density data and average electric field intensity data were used to calculate resistivity at various stages of the test. Point A indicates the inherent resistivity of ash 302 at 350°C and E = 4 kV/cm. This is the resistivity value before the sodium-depletion test was started. Point B is the resistivity value for ash 302 at 350°C and E = 4 kV/cm after the voltage had been applied for 840 hours. Without removing or changing the voltage gradient, the sample was cooled to 280°C. Point C shows the resistivity of ash 302 under these conditions. Finally at 280°C as a function of average electric field intensity, resistivity was determined for the sample

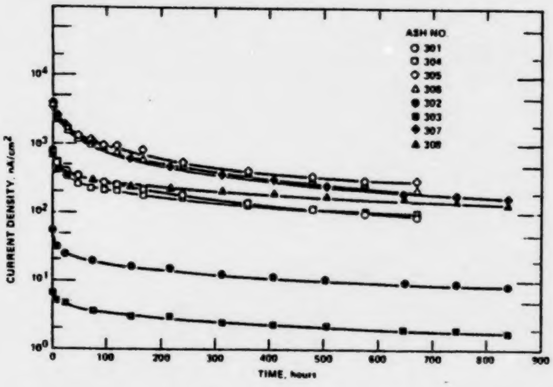

FIGURE 1. Current Density versus time of applied voltage, E = 4 kV/cm.

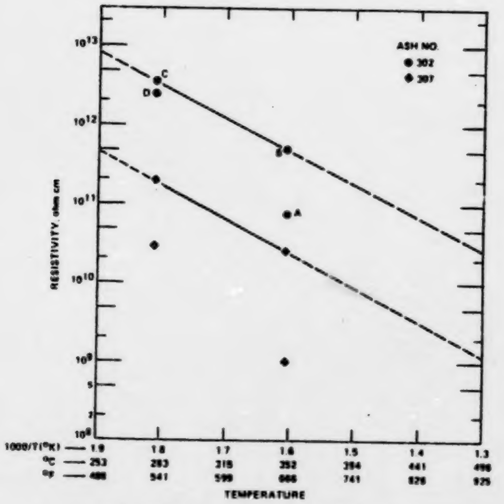

FIGURE 2. Typical resistivity/temperature relationships after 840 hours of applied voltage.

with a sodium-depleted ash layer. Point D is the resistivity value determined just prior to electrical breakdown. All ashes in the depleted condition showed a tendency for arcing at about 8 kV/cm and electrically failed at an average voltage gradient of 9 to 10 kV/cm using a 0.5 cm ash layer.

Although not readily discernible, the slopes of the resistivity versus reciprocal absolute temperature lines in Figure 2 are not identical. Comparison of these slopes with similar data generated for Reference 7 indicates that the slopes associated with sodium-depleted ash layers are slightly greater than the slopes calculated from inherent volume resistivity data. Resistivity predictions, taking into account surface conduction due to adsorbed moisture, indicate that the resistivity values for ashes 307 and 308 at 280°C probably have been slightly lowered by the presence of moisture in the test environment. Thus, the slopes for these two samples have not been used in this work. For the required computations, an average slope of 4788°K was used (S_1 in equation 2). This value ±7% includes the slopes for all ashes except 307 and 308.

Continuing with ash 302 as an example, this ash would probably be successfully collected at the full load temperature of 350°C with a new precipitator sized for ash 302 with a resistivity of 8×10^{10} ohm cm. After operating several weeks or months, a thin, tenaciously held, sodium-depleted ash layer would coat the collection plates producing an effective resistivity of about 5×10^{11} ohm cm. When the unit is operated at reduced load and a much lower precipitator temperature prevails, the resistivity increases to a value $>1 \times 10^{12}$ ohm cm. This sequence of events leading to unacceptable precipitator performance has been observed by many coal-burning power generating stations with hot-side precipitators.

EFFECTIVE RESISTIVITY/INHERENT RESISTIVITY RELATIONSHIP

Previously, miscellaneous tests conducted with respect to the sodium-depletion problem had indicated that one could expect about an order of magnitude increase in resistivity as sodium depletion occurred. The present information allows one to examine a correlation between the inherent resistivity and the resistivity determined after a stable sodium-depleted layer has been produced. Figure 3 shows a plot of resistivity values for all ashes at 350°C and E = 4 kV/cm in which the y axis denotes the values determined after the test to establish the sodium-depleted layer and the x axis denotes the values obtained before the test was started. The data point for ash 302 in Figure 3 is simply point B of Figure 2 (y axis) plotted versus point A of Figure 2 (x axis).

In the upper right corner of Figure 3 is the equation of the line computed from a least squares analysis of the data. The coefficient of correlation R = 0.97 indicates a good fit between the data and the computed line. Using this equation, one can determine that ashes having inherent (before-depletion) resistivities of 1×10^9 ohm cm and 1×10^{12} ohm cm will increase by factors of 12.6 and 5.8, respectively, due to sodium depletion. This agrees reasonably well with the aforementioned rule of thumb which used a factor of 10.

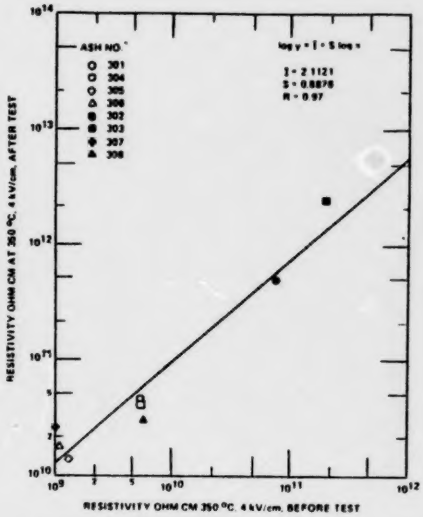

FIGURE 3. Effect of long-time applied voltage on fly ash resistivity at 350°C.

Although additional data could alter the intercept and slope of the line shown in Figure 3, it is interesting to note that the magnitude of the effect of sodium depletion on resistivity apparently decreases as the inherent resistivity increases. Intuitively this relationship seems reasonable. Assume that within the sodium-depleted region conduction is controlled by the migration of unbridged and unassociated oxygen ions in the glassy ash matrix in a manner analogous to that of a soda-lime-silica glass subjected to electrode polarization (9). Because the number of mobile oxygen ions and/or the mobility of these ions are lower than the equivalent characteristics of the alkali metal ions, the resistivity of the sodium depleted zone is greater than the inherent ash resistivity. Alkali metal ions destroy oxygen ion bridging in the silicon-oxygen network and leave the oxygen ion unassociated when the alkali metal ion drifts away under the influence of the electric field. Therefore, a large concentration of alkali metal ions produces a low inherent resistivity and yields a large concentration of mobile oxygen ions in the sodium or alkali depleted region. For this reason, one would not expect all the current-density/time curves shown in Figure 1 to asymptotically approach a single limiting value. As the alkali metal concentration decreases, the inherent resistivity and the effective resistivity of the sodium depleted ash both increase. It can be rationalized that the difference between these two resistivity values should become smaller as the alkali content becomes smaller because as the alkali content approaches zero, the ash resistivity should become a very high value similar to that for pure vitreous silica and show less effect due to electrode polarization.

Obviously the phenomenon is more complex than described above. Volume resistivity is also influenced by the presence of iron and calcium in the ash structure. In addition it is believed that the chemical diffusion of sodium toward the anode due to the sodium concentration gradient established by the electric field affects the ultimate current density/time relationship.

RESISTIVITY/ELECTRIC FIELD INTENSITY RELATIONSHIP

In Figure 4, resistivities measured just prior to electrical breakdown have been plotted versus resistivity values determined for E = 4 kV/cm. The ash layers were in the sodium depleted condition at 280°C. The line represents a linear regression least squares analysis of these data, and the included equation defines the line. This equation is subsequently used to incorporate the effect of electric field intensity into the prediction of resistivity for ash layers subjected to sodium depletion.

From Figure 4 it can be seen that at high levels of resistivity, e.g., 1×10^{13} ohm cm, there is only an attenuation of about 20% due to an increase in field strength from 4 kV/cm to values approaching electrical breakdown. At a moderate resistivity level of 1×10^{11} ohm cm, the resistivity is reduced by a factor of 3 as the field strength increases from 4 kV/cm to breakdown. One can speculate that the glassy structure of the ashes containing the higher concentrations of alkali metal ions are more susceptible to distortion due to electrical stress.

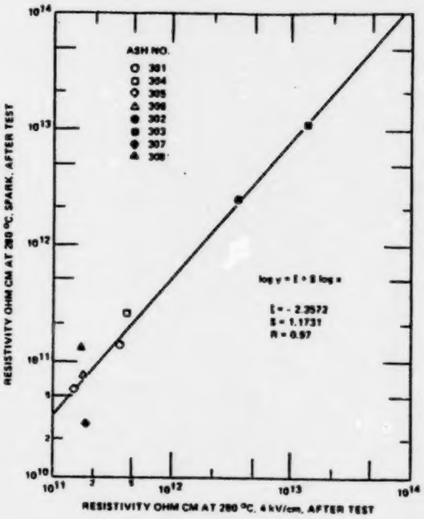

FIGURE 4. Effect of spark voltage on fly ash resistivity after long-time applied voltage.

DETERMINATION OF THE VOLUME RESISTIVITY OF A SODIUM DEPLETED ASH LAYER

Volume resistivity as a function of temperature can be determined experimentally as described above, or it can be determined by computation using the expressions shown in Figures 3 and 4. The requisite information for computing the resistivity is the chemical composition of the fly ash or coal ash. It is recommended that ignited (750°C) fly ash samples should be used and that the coal ash samples should be prepared as stated below. Coal samples should be converted to ash using the ASTM D271 procedure followed by a second ignition at 1050°C ± 10°C in still air for 12 to 16 hours (overnight). It is emphasized that all the research done in this laboratory has utilized this ashing procedure.

The ash samples are analyzed for their major elemental constituents according to the following general outline. Three methods of attack are used to place the ash in solution: a) a sodium carbonate fusion for sulfur determination, b) a sodium hydroxide fusion for aluminum and silicon determination, and c) a sulfuric, hydrofluoric and nitric acid digestion for the elements lithium, sodium, potassium, magnesium, calcium, iron, titanium, and phosphorus. Sulfur is determined by ion chromatography. Phosphorus, silicon, and aluminum are determined by colorimetry. The remaining elements are determined by atomic absorption. The elemental analysis is reported in weight percent as oxides.

Having a chemical analysis from a qualified laboratory, the following calculation is performed to obtain the atomic percentages of lithium plus sodium, magnesium plus calcium, and iron. After normalizing the reported weight percentages to sum 100%, each oxide percentage is divided by the respective oxide molecular weight to obtain the mole fraction. Each mole fraction is divided by the sum of the mole fractions and multiplied by 100 to get the molecular percentage as oxides. Each molecular percentage is multiplied by the fraction of cations in the given oxide to obtain the atomic percentage of the cation. The results of such a calculation are shown in Table 2. In this example, the sum of the lithium plus sodium atomic concentrations is 0.53%, the sum of the magnesium plus calcium atomic concentrations is 15.9%, and the iron atomic concentration is 0.7%.

Using the equations shown in Figures 3 and 4 and the Arrhenius-type expression given in equation 1, the volume resistivity of a sodium depleted ash layer can be computed as a function of temperature. Elsewhere (10), the detailed step-by-step procedure for the development of equation 2 below is given.

$$\log \rho_{vd} = - 7.3759 + 1.0412 \log \rho_{via} + S_1/T \qquad (2)$$

where:

ρ_{vd} = volume resistivity of the sodium depleted ash layer at electrical failure and any temperature T,

ρ_{via} = inherent volume resistivity of the fly ash at 625°K and E = 4 kV/cm,

S_1 = 4788.1°K = average slope of log ρ vs 1/T experimentally determined from curves of the type shown in Figure 2, and

T = temperature in °K.

The inherent volume resistivity as a function of the fly ash composition at 625°K and E = 4 kV/cm can be obtained from equation 3. This equation was developed from reference 7.

Table 2.

TABULATION OF DATA FOR THE CALCULATION OF THE ATOMIC CONCENTRATION OF CATIONS IN COAL ASH

Oxide	Determined Wt %	Normalized Wt %	Molecular Weight	Mole Fraction	Molecular Percentage	Cationic Fraction	% Atomic Concentration of Cation
Li_2O	0.02	0.02	29.88	0.00067	0.044	2/3	0.029
Na_2O	0.70	0.70	61.98	0.01129	0.747	2/3	0.498
K_2O	1.00	1.00	94.20	0.01062	0.703	2/3	0.469
MgO	5.0	5.00	40.31	0.12404	8.208	1/2	4.104
CaO	20.0	20.00	56.08	0.35663	23.598	1/2	11.799
Fe_2O_3	4.0	4.00	159.70	0.02505	1.658	2/5	0.663
Al_2O_3	23.0	23.00	101.96	0.22558	14.927	2/5	5.971
SiO_2	44.0	43.98	60.09	0.73190	48.429	1/3	16.143
TiO_2	1.0	1.00	79.90	0.01252	0.828	1/3	0.276
P_2O_5	0.60	0.60	141.94	0.00423	0.280	2/7	0.080
SO_3	0.70	0.70	80.06	0.00874	0.578	1/4	0.144
Sum	100.02	100.00	---	1.51127	100.000		40.176

$$\log \rho_{via} = 8.3911 - 1.8916 \log x - 0.9696 \log y + 1.2370 \log z \qquad (3)$$

where:

ρ_{via} = defined above,

x = atomic percentage of lithium plus sodium,

y = atomic percentage of iron, and

z = atomic percentage of magnesium plus calcium.

Substituting the expression for ρ_{via}, equation 3, into equation 2 and simplifying, the sodium-depleted volume resistivity can be calculated from the fly ash composition and temperature.

$$\log \rho_{vd} = 1.3609 - 1.9695 \log x - 1.0095 \log y + 1.2880 \log z + 4788.1/T°K. \qquad (4)$$

Combining and simplifying equations from reference 7, an expression similar to equation 4 can be given to calculate the inherent volume resistivity from the fly ash composition and temperature.

$$\log \rho_{vi} = 1.2159 - 1.8916 \log x - 0.9696 \log y + 1.2370 \log z + 4334.5/T°K \qquad (5)$$

where:

ρ_{vi} = inherent volume resistivity for a given fly ash composition, E = 12 kV/cm, and any temperature T°K.

Equations 4 and 5 can be used to manually calculate the predicted resistivity of a fly ash layer before and after the sodium depletion phenomenon has occurred. Computer programs in FORTRAN and BASIC are given in reference 10 to execute these computations. Using the ash composition given in Table 2, the output of the computer program is shown in tabular and graphical form, Table 3 and Figure 5, respectively. In the upper part of Table 3 the fly ash compositional data are given. The atomic concentrations were calculated as described above and illustrated in Table 2. The columns of resistivity data labeled RHO(VI) and RHO(VD) were computed from equations 5 and 4, respectively. These two columns of data are plotted as a function of temperature in Figure 5.

The chosen example illustrates the pronounced effect of sodium depletion and temperature on the effective resistivity of an ash layer. At the typical hot-side precipitator temperature of 352°C for full-load steam generating conditions, the inherent fly ash resistivity is 2.0×10^{10} ohm cm, a desirable level in the absence of the sodium depletion phenomenon. However, after sodium depletion has occurred in the adherent ash layer and low-load steam generating conditions are in effect, the precipitator temperature can be 315°C and the effective resistivity is 5.5×10^{11} ohm cm, a most undesirable level. This situation is additionally aggravated when the boiler load is being increased. The particulate concentration increases rapidly while the precipitator temperature lags.

Table 3. Computer Program, FORTRAN Data Printout

```
THE PREDICTION OF THE EFFECTIVE RESISTIVITY OF A
SODIUM DEPLETED ASH LAYER IS BASED ON WORK DONE BY
DR, ROY BICKELHAUPT OF SOUTHERN RESEARCH INSTITUTE.
THE RESEARCH WAS SPONSORED BY THE ELECTRIC POWER
RESEARCH INSTITUTE, DR, RALPH ALTMAN, PROJECT MANAGER,


FLY ASH 1



                          CORRECTED
               ASH           ASH            ATOMIC
            ANALYSIS      ANALYSIS      CONCENTRATION
            --------      ---------     -------------
LI2O           0,02          0.02            0,030
NA2O           0.70          0.70            0,496
K2O            1,00          1.00            0,468
MGO            5,00          5,00            4.103
CAO           20,00         20.00           11,797
FE2O3          4,00          4.00            0,663
AL2O3         23,00         23.00            5,969
SIO2          44,00         43,99           16,145
TIO2           1.00          1,00            0,276
P2O5           0.60          0,60            0,080
SO3            0,70          0,70            0,145

SUM          100,02        100,00           40,173


SUM OF LITHIUM AND SODIUM ATOMIC CONCENTRATIONS          0.53
SUM OF MAGNESIUM AND CALCIUM ATOMIC CONCENTRATIONS       15,9
IRON ATOMIC CONCENTRATION                                 0.7


1000/T(K)  DEG K  DEG C  DEG F  RHO(VI)  RHO(VD)
---------  -----  -----  -----  -------  -------
   1.30     769    496    925   1,0E+09  6.8E+09
   1.40     714    441    826   2,8E+09  2.1E+10
   1,50     667    394    740   7,5E+09  6.1E+10
   1.60     625    352    665   2,0E+10  1.9E+11
   1.70     588    315    599   5,6E+10  5.6E+11
   1.80     556    282    540   1,5E+11  1.7E+12
   1.90     526    253    488   4.1E+11  5.1E+12

NOTE: BECAUSE THE PREDICTED RESISTIVITY VALUES ARE VERY
SENSITIVE TO SEVERAL ASH COMPOSITIONAL FACTORS, ONE MUST
EXERCISE GREAT CARE IN THE SELECTION AND PREPARATION OF
COAL AND ASH SAMPLES. FURTHERMORE, THE QUALITY OF THE
QUANTITATIVE CHEMICAL ANALYSIS WORK IS OF GREAT IMPORTANCE.
WHEN USING THIS PROGRAM, THE COAL ASH SHOULD BE PRODUCED
USING ASTM D271 PROCEDURE FOLLOWED BY A SECOND IGNITION AT
1050 DEGREES C + OR - 10 DEGREES C IN STILL AIR FOR AT
LEAST 10 HOURS.
```

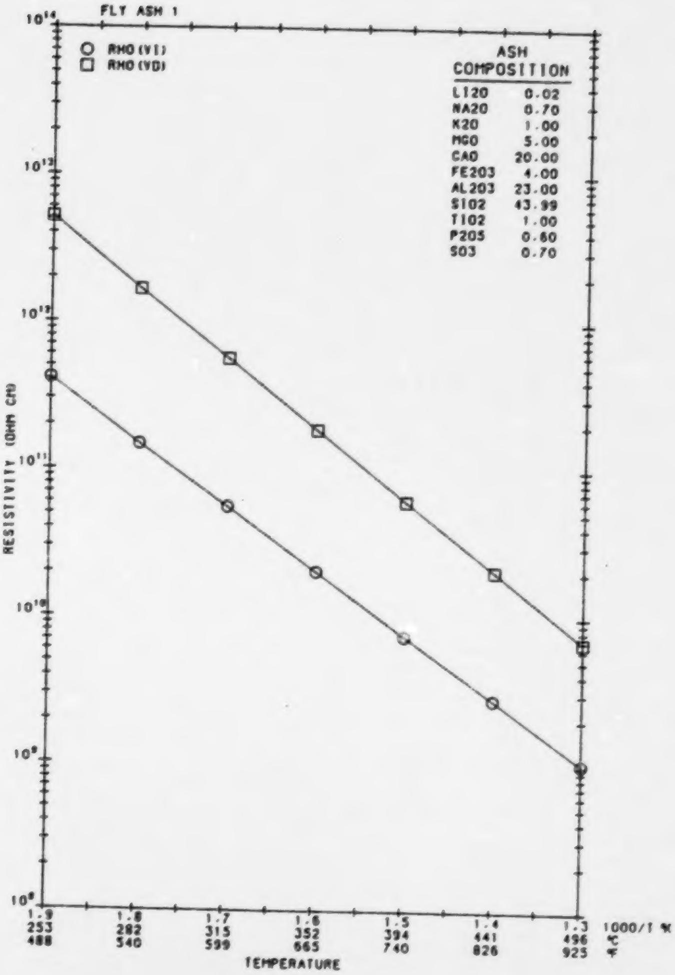

FIGURE 5. Computer plot of inherent and sodium-depleted volume resistivities versus temperature.

SUMMARY

The work reported in this paper has resulted in the development of two new tools, one analytical and one experimental in nature. The analytical correlation developed from data for eight fly ashes can be used to estimate the effective (sodium depleted) resistivity of fly ash in hot-side precipitators for the temperature range that is typical for the operation of these units. This procedure makes it possible to assess the effect of a large number of coal supplies on hot-side precipitator performance quickly and at very little expense. The experimental method that was used to develop the correlation can be used to determine the exact resistivity of sodium-depleted fly ash under conditions that realistically represent the operation of a hot-side precipitator. The use of either approach will make possible a more logical selection of the coal supply for a plant with a hot-side precipitator.

ACKNOWLEDGMENT

This research was made possible by the financial support of the Electric Power Research Institute, Coal Combustion Systems Division.

At the time this research was conducted, Dr. Bickelhaupt was a member of the staff of Southern Research Institute, Birmingham, AL 35255.

REFERENCES

1. R.E. Bickelhaupt, "An Interpretation of the Deteriorative Performance of Hot-Side Precipitators," JAPCA 30:812 (1980).

2. R.E. Bickelhaupt and L.E. Sparks, "Remedial Treatments for Deteriorated Hot-Side Precipitator Performance," EPA-600/9-82-005a 1:165 (1982).

3. J.P. Gooch, et al, "Improvement of Hot-Side Precipitator Performance with Sodium Conditioning - An Interim Report," JAPCA 31:291 (1981).

4. Private communications.

5. a) P.B. Lederman, et al, "Chemical Conditioning of Fly Ash for Hot-Side Precipitation," EPA-600/7-79-044a 1:79 (1979).

   b) R.P. Bennett and A.E. Kober, "Chemical Enhancement of Electrostatic Precipitator Efficiency," EPA-600/7-79-044a 1:113 (1979).

6. a) W.V. Piulle, et al, "Evaluation of Performance Enhancement Obtained with Pulse Energization Systems on a Hot-Side Electrostatic Precipitator," EPA-600/9-82-005a 1:253 (1982).

   b) J.P. Gooch, et al, "An Evaluation of Pulse Energization on a Hot-Side Electrostatic Precipitator," Electric Power Research Institute Final Report CS-2634, November 1982.

7. R.E. Bickelhaupt, "A Technique for Predicting Fly Ash Resistivity," EPA-600/7-79/204 (1979).

8. R.E. Bickelhaupt, "Measurement of Fly Ash Resistivity Using Simulated Flue Gas Environments," EPA-600/7-78-035 (1978).

9. D.E. Carlson, et al, "Electrode Polarization in Alkali-Containing Glasses," J. Am. Cer. S., 55:337 (1972).

10. R.E. Bickelhaupt, "Method for Predicting the Effective Volume Resistivity of Sodium-Depleted Fly Ash Layers in Hot-Side Electrostatic Precipitators," Electric Power Research Institute, CS-3421, Final Report.

ANALYSIS OF AIR HEATER - FLY ASH - SULFURIC ACID VAPOR INTERACTIONS

by: Norman W. Frisch
N.W. FRISCH ASSOCIATES, INC.
Kingston, New Jersey 08528

ABSTRACT

Estimation of ash resistivity level for cold-side precipitator design requires knowledge of SO_3 concentrations at the ESP entrance. Unfortunately, a number of these measurements have indicated a highly variable SO_3/SO_2 ratio. Sources and mechanisms involved in this variable factor are discussed. In particular, this analysis focuses on the air heater as a contributor to SO_3 concentration changes.

An analysis of possible interactions between H_2SO_4 vapor, fly ash and regenerative air heater surfaces was made using a numerical finite-difference method. Situations considered included a fly ash-free system and coal-firing cases involving either a clean or dirty air heater. Equations representative of condensation and adsorption mechanisms were integrated into the finite-difference equations to account for the removal of acid from the flue gas.

This unique Heater Interaction Model (HIM) approach provides an excellent problem solving tool for such complex issues as:

- optimization of gas mixing downstream of air heaters for the elimination of high resistivity ash zones
- investigation of likely causes of malperformance of precipitators and
- cost-effective injection of conditioning agents into various chambers of an ESP system.

Our basic approach is also of interest for non-SO_3 containing agents which condense from the vapor state to a particulate form. Air heater fouling problems which may occur in NH_3-based NO_x control processes can be simulated by our models.

ANALYSIS OF AIR HEATER-FLY ASH-SULFURIC ACID VAPOR INTERACTIONS

INTRODUCTION

Sulfur trioxide and its hydration product, sulfuric acid, exert important effects in fossil fuel combustion systems. These include dew point elevation (1), participation in high temperature metal attack (2), low temperature acid condensation with resulting corrosion (3, 4, 5) possible precipitator performance enhancement (6, 7, 8, 9) as well as plume opacity effects (10). The state of the art fly ash resistivity prediction method (8) relies on knowledge of SO_3 concentrations at the cold-side ESP inlet. Unfortunately, measurements at a number of coal-fired installations have shown that this value, relative to SO_2 concentrations, nearly covers a five-fold ratio range (0.0015 to 0.0070) (11).

This paper first reviews the literature on the major SO_3-generating mechanisms operating in fossil fuel combustion processes. The variability of the several contributing processes is emphasized. Sinks for SO_3 are also noted.

Attention is then focused on the often neglected but important interactive effects which occur in the regenerative air heater feeding cold-side ESP's. The paper discusses the development of a series of computer-based approaches which describe temperature distributions (gas, air, metal) in air heaters, local rates of acid condensation with related acid concentrations, and especially the extent of competitive acid adsorption on both suspended and deposited ashes within the air heater. The inefficiency of sulfuric acid conditioning in certain situations is discussed, as well as suitable remedial approaches. Specific ash types prone to this difficulty are characterized.

ORIGIN OF SULFUR TRIOXIDE

SOURCES OF SULFUR

All fossil fuels contain sulfur. Natural gas in its raw state may contain more than 50% hydrogen sulfide. In petroleum, sulfur occurs as sulfides, mercaptans, polysulfides and thiophenes. In coal, sulfur occurrence is of sufficient interest to warrant a classification - Forms of Sulfur, ASTM D2492-79; included are the three predominant forms - organic, pyritic and sulfate sulfur. In coals, organic sulfur exists mainly as sulfides, disulfides, mercaptans and thiophenes (12). The most widely studied group, pyritic sulfur, consists of FeS_2, largely as the cubic form pyrites, as well as the less common orthorhombic marcasite (13). Other important inorganic sulfides which occur are sphalerite (ZnS), chalcopyrite ($CuFeS_2$), pyrrhotite ($Fe_{1-x}S$) and arsenopyrite (FeAsS) (14). Sulfate sulfur arises in many cases from weathering of sulfides; varieties of iron or alkali metal iron sulfates are believed to be of this origin. Important calcium-containing sulfates found in some U.S. Western coals are gypsum ($CaSO_4 \cdot 2H_2O$), anhydrite ($CaSO_4$) and bassanite ($CaSO_4 \cdot 1/2H_2O$) (14). Another frequently occurring sulfate is barite ($BaSO_4$). Elemental sulfur occurs on occasion.

Oxidizable sulfur compounds in the fuel are converted predominantly to sulfur dioxide during high temperature combustion. Very low levels of SO_3 can be formed by direct oxidation of SO_2 because the equilibrium for the reaction

$$SO_2 + 1/2\ O_2 \rightleftharpoons SO_3$$

is far to the left at flame temperatures (16). Thus, with 4% residual oxygen in the gas, levels of SO_3/SO_2 on the order of 0.002 are the theoretical limit. In practice, considerably higher levels are found; at the air heater entrance, SO_3/SO_2 are typically 0.01-0.03 in situations involving coals with non-alkaline ashes.

There are three likely sources for the observed sulfur trioxide: direct high temperature reaction of SO_2 with atomic oxygen, decomposition of sulfate minerals and catalytic production from $SO_2 + O_2$ at intermediate temperature levels.

DIRECT REACTION OF SO_2 WITH ATOMIC OXYGEN

At flame temperatures, molecular oxygen undergoes a slight dissociation producing active oxygen atoms. Levels observed in experiments involving gas flames are on the order of 50 to 500 ppm, depending upon fuel gas composition and especially excess oxygen and flame temperature. Higher values of the latter two variables result in increased levels of atomic oxygen. The direct reaction

$$SO_2 + O \rightarrow SO_3^*$$

results in the production of an activated SO_3 molecule which can radiate its excess energy or lose it by contact to a third body, producing sulfur trioxide (17).

$$SO_3^* \rightarrow SO_3 + h\nu$$

$$SO_3^* \rightarrow SO_3 + M$$

Support for this theory includes the observation of high levels of SO_3 produced when burning SO_2 - spiked carbon monoxide and also the observed effect of adding compounds which are capable of preferentially reacting with atomic oxygen.

In the case of carbon monoxide oxidation, atomic oxygen may be produced by

$$CO + O_2 \longrightarrow CO_2 + O$$

leading to levels as high as 20% oxidation of SO_2 to SO_3 in dilute SO_2-containing gases. Inhibitors such as pyridine or carbon tetrachloride present at the 3% level can reduce SO_3 formation by 50% (18).

Further support for this theory is shown by the absence of SO_3 production from the 870°C burning of high-sulfur coal. This is a condition at which no atomic oxygen is produced.

Once SO_2, SO_3 and O_2 co-exist, they react to establish the equilibrium levels defined by the equilibrium constant

$$K_P = \frac{P_{SO_3}}{P_{SO_2} \times P_{O_2}^{0.5}}$$

where K_P depends solely on temperature at atmospheric pressure and
P designates the partial pressure of the indicated species.

At flame temperature, the kinetics of the SO_3 dissociation reaction is sufficiently fast to permit some decomposition of the thermodynamically excess SO_3 to form SO_2 and O_2. Even in short cooling periods (0.1-0.2 s), serious reductions in SO_3 concentrations are observed. The data of Hedley (19), shown in Figure 1, support the following series reaction scheme

$$SO_2 + O \xrightarrow{k_1} SO_3 \xrightarrow{k_2} SO_2 + 1/2\ O_2$$

If k_1 and k_2 are taken to be independent of temperature, i.e., activation energies for the reactions are low, the series kinetics yields the following dependence of SO_3 concentration on time

$$SO_3 = [O] \frac{k_1}{(k_2-k_1)} [EXP\ (-k_1 t) - EXP\ (-k_2 t)]$$

where [O] represents the initial concentration of atomic oxygen. Thus, SO_3 peak concentrations are expected at $t = \ln (k_1/k_2)/(k_1-k_2)$ with subsequent decay.

Experimentally, k_2/k_1 has been found to be about 8, and relatively insensitive to temperature. Similar patterns of peak SO_3 concentrations followed by decay have been reported by others.

Moisieeva and Podolyak (20) report peak SO_3 concentrations which are about 3% of the SO_2 level in the case of 11% excess air firing; their corresponding value is 6% for 24% excess air. (These data refer to oil firing.) These peak SO_3 concentrations were reported to be 4 to 5 times higher than the long exposure levels. Ahmed and Zaczek (21) report a similar pattern of peak SO_3 conversions.

A corollary of these observations is that boiler size influences the SO_3 level produced because gas cooling rates are significantly dependent on boiler size. Large utility boilers have rates on the order of 500 to 1000 K/s while industrial units may have rates of 2000 K/s or more.

The role of excess air has been clearly demonstrated in oil-firing situations. SO_3 concentrations in full-scale plants can be controlled by operation at low excess air levels. Figure 2 shows the results of laboratory experiments, demonstrating the role of oxygen concentrations and fuel sulfur content (22). The effect of increased oxygen here is likely to be the sum of two effects: (1) increased atomic oxygen content, and (2) higher catalytic rate of conversion of SO_2 (see below). These data suggest that at least 6% of the sulfur in the gas phase was SO_3.

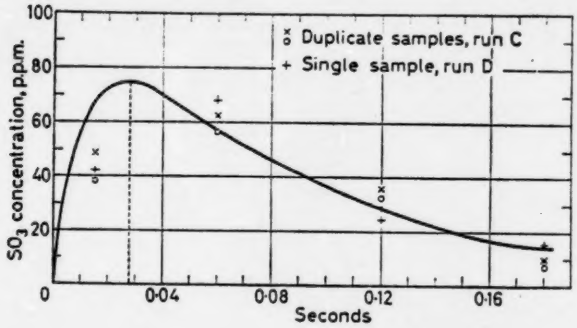

Figure 1. Decay of flame temperature-produced SO_3 (19)

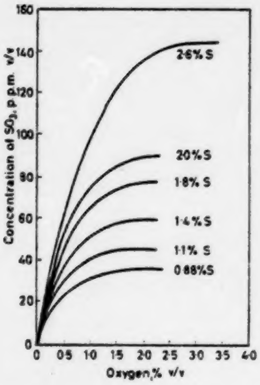

Figure 2. Role of Excess Air on Sulfur Trioxide Yield (22)

It should be noted that operation at extremely high levels of excess air may result in lowered SO_3 levels as a consequence of much reduced flame temperatures in spite of the presence of high oxygen concentrations.

DECOMPOSITION OF MINERAL MATTER

Sulfate minerals exposed to flame temperatures are potential sources of SO_3. Johnstone (1) discussed the direct decomposition of $CaSO_4$. This reaction has been extensively studied. Jakisch (23) considered the reaction of Fe_2O_3 with $CaSO_4$ to yield SO_3. Kinjiro (24) reported the direct decomposition in a neutral or oxidizing atmosphere at 1020-1050°C. Wickert (25) demonstrated the enhanced decomposition of $CaSO_4$ at 1000°C when admixed with SiO_2 or NaCl + SiO_2. These data suggest that at high temperature, SiO_2 acts as a strong acid, competing with SO_3 for reaction with CaO. Similarly, kaolin enhances the decomposition pressure of $CaSO_4$. $MgSO_4$ is appreciably less stable than $CaSO_4$. Barite, of course, retains SO_3 tenaciously.

It is interesting that potassium-containing minerals (illite or K-exchanged muscovite), when admixed with $CaSO_4$, strongly accelerate the decomposition of the latter many-fold at 1020°C (26).

Iron (ferrous) sulfate, which occurs as a result of weathering in some coals is readily decomposed thermally. Ostroff (27) reported a decomposition temperature of 537°C vs. 895 for $MgSO_4$ and 1149 for $CaSO_4$. In Argon, $FeSO_4$ begins to decompose at 500-550°C, yielding Fe_2O_3, SO_2 and SO_3 (28). In air, the decomposition sequence is complicated by the catalysis of SO_2 oxidation by Fe_2O_3.

In general, it is believed that mineral decomposition provides a minor source of SO_3 compared to reaction with atomic oxygen or catalysis. This is in direct contrast to the early view (1) that mineral decomposition could entirely explain the presence of SO_3 in boiler flue gases.

CATALYSIS OF SO_2 OXIDATION

Sulfur dioxide oxidation over heterogeneous catalysts has been extensively studied. Commercially, V_2O_5 is an active material resistant to poisons. While vanadium probably plays little role in coal firing situations, high V oils have exhibited high [$\sim 9\%$ $SO_3/(SO_2 + SO_3)$] levels in the combustion gas, especially at high excess air levels (29).

Iron oxide, Fe_2O_3, is a moderately active catalyst with peak activity about 625°C. It is the prevalent catalytic species involved in coal firing situations; its moderate activity is balanced by the high concentration of iron oxide typically present in boiler systems. Barrett (30) has demonstrated the sharp increase (Fig. 3) in SO_3 concentrations downstream of Fe_2O_3-coated tubular specimens. While MgO-coated specimens were relatively inactive, bare steel samples developed appreciable activity after several hours.

Ash deposited on convective section tube banks can substantially accelerate the catalytic production of SO_3; distinct difference in SO_3 levels are seen at a plant with clean and dirty tube surfaces. (31)

It is generally agreed the Fe_2O_3 can be an active catalyst when present on fly ash surfaces. Fe_3O_4 is known to be inactive; presumably iron can also be inactivated by reaction with acidic species in the ash (silica, alumina).

With moderate to high sulfur coals the potential exists for the production of substantially higher SO_3 levels by catalysis than by direct reaction with atomic oxygen at flame temperatures. Substantial effort has been directed towards suppressing the catalytic activity of tube bank surfaces. Emphasis has been on the use of additives (31), especially alkaline earth oxides. It was concluded that the equilibrium between the metal oxide and SO_3 controls the extent of suppression of SO_3 formation. MgO could suppress SO_3 beyond stoichiometric equivalence, possibly by adsorbing SO_2 from the gas stream.

IMPORTANT SO_3 SINKS

CORROSION

High-Temperature Attack

At temperatures as low as 550-600°C, wastage of tube metal may occur due to liquid-phase attack by complex low melting alkali iron trisulfates (2,33) of the form $M_3Fe(SO_4)_3$, where M represents K, Na or combinations thereof. The formation of the trisulfates may proceed through the reaction of normal alkali metal sulfates (from the fly ash), iron oxide on the tube surface and SO_3 in the gas. The iron oxide may originate in the fly ash or from the tube surface. Substantial concentrations of SO_3 have been shown (34) to be necessary to sustain the alkali trisulfates at high temperatures.

Low-Temperature (Cold-End) Corrosion

Sulfuric acid vapor-containing gas exposed to surfaces below the dew point undergo formation of a liquid phase rich in sulfuric acid. The condensation rate observed (3, 5) with the metal surface near or at the dew point is generally quite low compared to the peak rates observed with surfaces 30 to 50°C below the dewpoint (oil firing case). The data of Rylands and Jenkinson are shown in Figure 4.

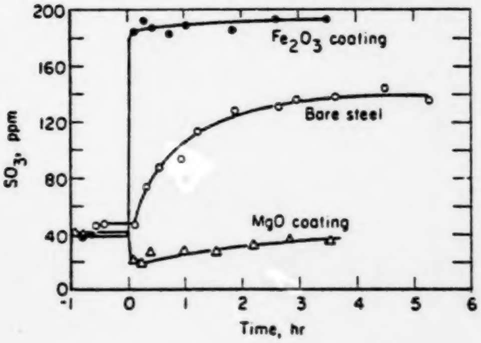

Figure 3. SO_3 concentration downstream of bare and coated steel specimens (30)

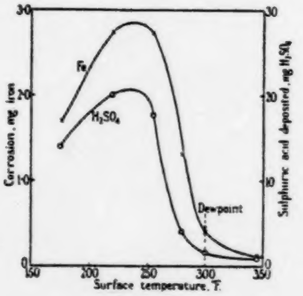

Figure 4. Dependence of condensation and corrosion rate on surface temperature (3)

Condensation rates in coal-firing situations have been reported by Lee, et al (35); their data show similar peak rate behavior with respect to surface temperature. They also report the effect of low excess air firing in a combustion research boiler. With 0.6% residual oxygen, acid dew point was only about 130°F compared to the normal dewpoint for 3-4% oxygen of 280°F. Coal sulfur in this case was 6.2%, ash 13.5%.

The rates of condensation are generally characterized by the rate of conductivity buildup (RBU) using dew point meters and especially by the peak rate (PR) at the peak rate temperature (PRT). Below about a RBU of 100 μamp/min corrosion rates are generally modest. An alternate approach for measuring condensation rates is the acid deposition probe; these are constant temperature probes which permit collection of condensate associated with a specific temperature.

Corrosion of steel surfaces which occur at condensation are largely related to the condensation rates, and relatively insensitive to acid condensate concentration (36) (Under typical conditions, the acid condensate is in the range of 65-85% (w) H_2SO_4). When conditions prevail in which quite dilute acid is deposited, strongly accelerated corrosion rates are observed.

The fact that peak condensation rates occur at surface temperature 30-50°C below the dew point has been explained by Land (37) as follows: with relatively high surface temperatures, condensation rate is dependent upon the difference between the partial pressure of SO_3 in the gas phase and the equilibrium value corresponding to the surface temperature; however, when the surface temperature is sufficiently low, fog formation occurs and the rate of removal from the gas suffers. The equations reported by Land are used in the analysis of cold-end condensation in the air heater section of this paper.

Dew Point Relationships

Data, both experimental as well as thermodynamic, have been developed to predict the effect of SO_3 vapor concentrations and moisture content of a gas on the dew point and resulting acid condensate concentration (38,39,40,41). Banchero and Verhoff (42) have analyzed several sets of data and produced an equation which relates acid dew point, SO_3 and H_2O content of the gas.

The use of the data of Abel which gives the partial pressure of H_2SO_4 over known acid solutions as a function of temperature in conjunction with that of Greenewalt (41) provide a convenient methodology for our problem. Greenewalt provides equations for the partial pressure of water vapor over sulfuric acid solutions as a function of temperatures. Figure 5 is our representation of the combined data over the acid concentration range of 65-85%, for water vapor content of the gas from 5 to 20%.

In our use of these data we use a cubic spline fit to retrieve an equilibrium SO_3 partial pressure value, and the corresponding acid condensate composition for an input of dew point temperature and gas phase moisture content. When equilibrium values were needed outside the range of the Abel-Greenewalt data, we fitted spline-derived values via regression analysis to an equation of the form

$$P^* = \mathrm{EXP}\ (\alpha + \beta/T + \gamma \ell n(T) + \delta T)$$

where P* is the equilibrium partial pressure of H_2SO_4 at temperature T K. The coefficients are functions of gas phase moisture content.

ADSORPTION ON FLY ASH

The beneficial effect of high coal sulfur content on ash resistivity of many U.S. coal has been known for many years (43). The conditioning benefits of H_2SO_4 were recognized as early as 1912 (44). The effect of adsorbed SO_3 on fly ash surfaces of various character was first quantified by Bickelhaupt.

The use of supplemental SO_3 or H_2SO_4 for high resistivity fly ash situations has been practiced for forty years in the U.S. Vaporized sulfuric acid and SO_3 produced by high temperature catalytic oxidation over V_2O_5 are the standard approaches used by conditioning system manufacturers. The claims of some manufacturers notwithstanding, it is recognized that minimal benefits have been achieved with some ashes under some conditions. With some Australian ashes, benefit of sulfuric acid conditioning has been both variable and too limited to warrant continued plant use. Alternate agents are preferred. (45)

The work of Bickelhaupt and the author's exposure to several performance situations prompted his interest in the areas to be discussed in the analysis section. We mainly concern ourselves with the phenomena which occur in a regenerative air heater with gases containing sulfuric acid vapor.

THE ANALYSIS

We analyze the operation of a series of rotary air heaters with respect to average outlet gas temperature and also effectiveness. We then estimate the condensation rates of sulfuric acid in an ash-free environment. The behavior of sulfuric acid vapor in an ash-containing gaseous environment as it passes through the air heater is also presented. The dependence of the extent of acid adsorption is shown to depend on a number of variables. The behavior of a dirty air heater is also analyzed with respect to competing adsorption of acid by the stagnant ash layer on the rotor heat exchange surface.

THE ROTARY REGENERATIVE AIR HEATER

Air heaters serve to transfer sensible heat from combustion gas to combustion air. The rotary regenerative (Ljungstrom) type accomplishes this by periodic contact of the rotor surface with the hot gas, and then releasing the heat to the combustion air. Figure 6 shows the heat exchange surface arranged in baskets.

Typical inlet gas temperatures are in the range of 600-800°F; average gas outlet temperature for utility installations is about 250 to 375°F. The outlet temperature levels are generally based on such considerations as the temperature required to dry the fuel, the cost of coal energy, the cost of heat recovery equipment and the acid dew point range.

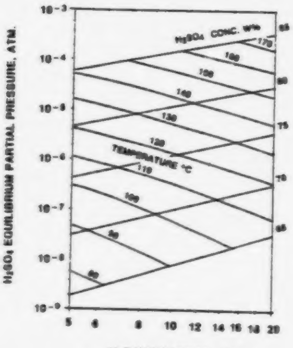

Figure 5. Equilibrium data for the system $H_2SO_4 - H_2O$ - Air (Total pressure = 1 atm.)

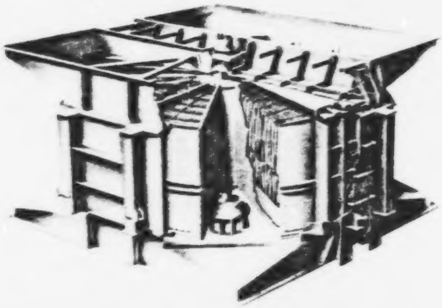

Figure 6. Rotary Regenerative Air Heater

AIR HEATER TEMPERATURES

We require gas and metal temperatures at points within the air heater on the gas side since the extent of the pertinent phenomena (condensation, adsorption, etc.) is influenced by these levels.

There have been a number of approaches (46, 47, 48, 49, 50, 51) to this problem. These include numerical graphical methods, algebraic solution (high rotative speed case), characteristic solutions and finite-difference methods. The latter is convenient and especially useful for the subsequent situations to be considered.

For the case of the periodic-flow heat exchanger, without leakage or longitudinal conduction, four dimensionless parameters serve to define the solution (Figure 7).

$$\text{CMNCMX} = \frac{(\text{MASS FLOW RATE} \times \text{THERMAL CAPACITY})_{\text{AIR}}}{(\text{MASS FLOW RATE} \times \text{THERMAL CAPACITY})_{\text{GAS}}}$$

$$\text{CRCMN} = \frac{\text{ROTOR MASS} \times \text{RPH} \times \text{ROTOR THERMAL CAPACITY}}{(\text{MASS FLOW RATE} \times \text{THERMAL CAPACITY})_{\text{AIR}}}$$

$$\text{SYMM} = \frac{(\text{HEAT TRANS. COEFF} \times \text{HEAT TRANS. AREA})_{\text{AIR}}}{(\text{HEAT TRANS. COEFF} \times \text{HEAT TRANS. AREA})_{\text{GAS}}}$$

$$\text{NTUO} = \frac{1}{\text{CMN}} \frac{1}{\sum_{\text{I = AIR, GAS}} [1/(\text{HEAT TRANS. COEFF} \times \text{HEAT TRANS. AREA})_{\text{I}}]}$$

Figure 7. Four Basic Air Heater Parameters

Figure 8 shows the elementary cells into which both the gas and air streams are subdivided. Heat transfer occurs in cross-flow (Figure 9) as the cooled surface moves (from left to right) contacting the combustion gas (flowing from top to bottom). The heat exchange equations which define the outlet gas and surface temperature for a cell based on the inlet temperatures are linear for a reasonable number of subdivisions in the gas and rotor surface streams.

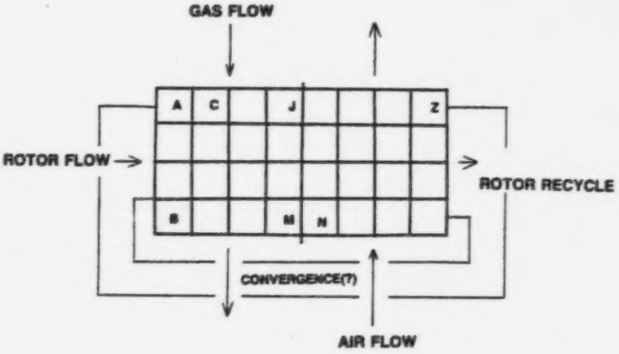

Figure 8. Air Heater Cells For Finite-Difference Approach

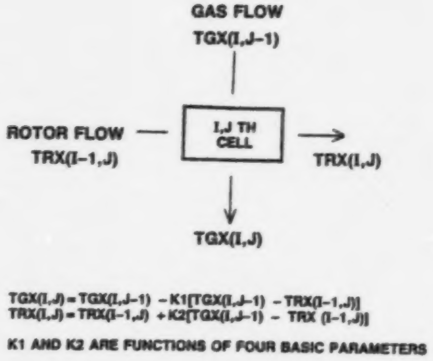
GAS FLOW
TGX(I,J-1)
ROTOR FLOW
TRX(I-1,J)
I,J TH CELL
TRX(I,J)
TGX(I,J)
TGX(I,J) = TGX(I,J-1) - K1[TGX(I,J-1) - TRX(I-1,J)]
TRX(I,J) = TRX(I-1,J) + K2[TGX(I,J-1) - TRX (I-1,J)]
K1 AND K2 ARE FUNCTIONS OF FOUR BASIC PARAMETERS

Figure 9. Heat Exchange Equations For Air Heater Gas Side

An iterative approach is required to achieve convergence of the metal outlet temperature from the air side with the assumed metal inlet temperature to the gas side. Heat balances (as well as mass balances in the other modules) were always well within 1 part in 10,000.

Specific Cases

The basis for subsequent analyses were specific cases using fixed gas and air flows and air heater inlet temperatures. The outlet temperatures were varied by "redesign" of the regenerator. This was accomplished by changing the mass of the heat exchange surface, each time reconfiguring the diameter and depth of the exchanger packing to maintain the pressure drop at a constant value.

Figure 10 presents the effect of relative rotor mass on outlet gas temperature for an inlet gas temperature of 680°F. Also shown is the effectiveness. Air heater operation is characterized thermodynamically by an effectiveness equal to $[(t_{air})_{out} - (t_{air})_{in}]/[t_{gas})_{in} - (t_{air})_{in}]$. In commercial practice this value ranges from 0.7 to 0.9. The number of overall transfer units ranged from 1.8 to 4.9.

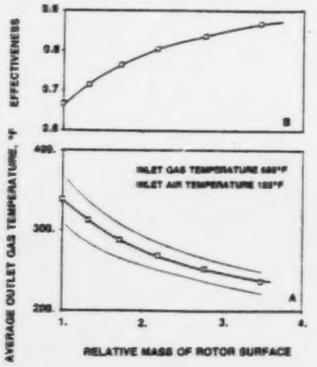

Figure 10. Air Heater Design Parameters (Six Cases)

The gas temperature spread at the air heater outlet ranged from 59°F down to about 16°F at the lowest gas outlet temperature of 237°F. Even higher spreads are observed in some installations.

ACID CONDENSATION RATES

A clean hot gas containing sulfuric acid and water vapor when cooled by passage through an air heater will lose H_2SO_4 from the vapor if the local air heater surface is below the acid dew point temperature.

The rate of condensation is often expressed as being proportional to the difference of the partial pressure of sulfuric acid in the gas, and the equilibrium partial pressure. Thus, the rate, for dilute gases at 1 atmosphere, may be expressed as kg moles of acid/($h\text{-}m^2$) and is given by

$$R = \frac{\alpha H}{C}\ (P_A - P^*) \qquad \text{Mechanism I}$$

where α is the a constant $(\rho_A/\rho)\ (D_A/D_U)^{2/3}$
ρ_A is density of sulfuric acid vapor
ρ is density of gas
D_A is the diffusion coefficient for sulfuric acid vapor
D_U is the thermal diffusivity of the gas
H is the convective heat transfer coefficient
C is the thermal capacity of the gas
(Note D_A/D_U is the Lewis number.)

This condensation rate is applicable provided the gas temperature in any region does not fall below the dew point. If the latter occurs and fog formation results, then the rate of condensation falls (37). In that case, it is given by

$$R = (D_A/D_U)^{1/3}\ (\alpha H/C) \left[\frac{dP_A}{dT}\right]_S (T_G - T_S) \qquad \text{Mechanism II}$$

where T_G is the temperature of the gas, and
T_S is the surface temperature.

Calculations were made using the condensation program for the six air heater designs. Figure 11 shows the results expressed as the fraction of acid condensed versus gas outlet temperature. The dotted line represents the prediction based on Mechanism I (no fog formation); the curve for Mechanism II shows the extent of condensation when fogging occurs. In practice, intermediate rates may occur.

The local rate of condensation in the air heater is shown versus rotor surface temperature in Figure 12 (average gas outlet temperature is 269°F). Mechanism I over-predicts the condensation rate; Mechanism II predicts a condensation rate equal to that of Mechanism II at the inlet to the condensation zone; subsequently, the rate drops markedly as fog formation occurs. (Peak rate corresponds to 22 $\mu g\ SO_3/h/cm^2$). The program also predicts acid condensate composition.

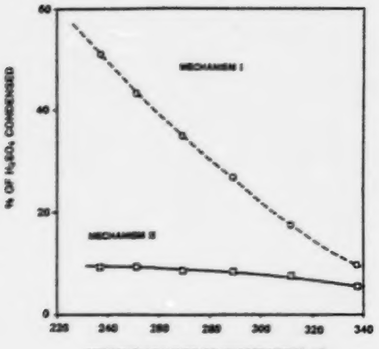

Figure 11. Predicted % H_2SO_4 Condensation Level

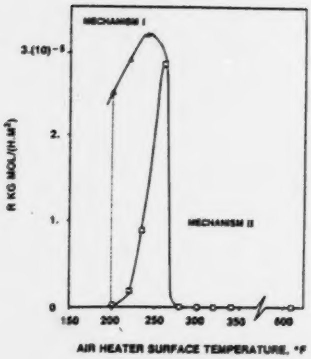

Figure 12. Local H_2SO_4 Condensation Rates

This program can provide an estimate of the extent of condensation, as well as to the location of the condensation zone under various load conditions, thus defining the region in which corrosion-resistant materials are required.

ACID ADSORPTION ON FLY ASH

Natural Conditioning

Gaseous species in contact with particulate are adsorbed on the particulate surface as described by an equilibrium isotherm; the extent depends upon the degree of saturation of the gas with the solute. The degree of saturation is expressed as the ratio of the partial pressure of the solute to its equilibrium saturation pressure.

While there are many types of isotherms reported (Langmuir, Freundlich, Henry, Temkin, etc.), the generalized expression due to Brunauer, Emmett and Teller (BET) (52, 53, 54, 55) is most convenient because it can represent the five main isotherm types observed in practice, involves only two constants, and the constant C_A which describes the affinity level is, in theory, dependent upon a single enthalpy difference. The form of the equation which is most useful for our purposes is

$$N_A = \frac{C_A X_A}{[1-X_A]\,[1+(C_A-1)X_A]}$$

where N_A is the number of adsorbed monolayers of solute on the ash surface

C_A is a constant which describes the affinity between solute and adsorbent

X_A is the degree of saturation

Sulfuric acid is adsorbed on fly ash according to a Type II isotherm (56) (Fig. 13). This is the most common BET isotherm and is characteristic of a solid of low porosity for which there is at least a moderate affinity between the solute and the adsorbent. It is apparent that high values of C_A

imply a significant extent of adsorption at low degrees of saturation.

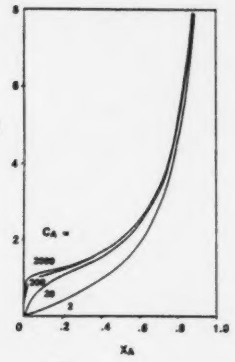

Figure 13. Examples of BET Isotherms

Ashes with strongly basic surfaces are characterized by large C_A values; C_A, according to the BET theory, is given by

$$C_A = \mathrm{EXP}\ (\Delta H/RT)$$

where ΔH is the enthalpy difference between the heat of adsorption between the solute and the ash surface and the heat of condensation of the solute,
R is the universal gas constant and
T is the absolute temperature of sorption.

Thus, for C=2000, a monolayer forms on the ash with relative saturation of only 0.02. This corresponds to an H_2SO_4 concentration of only 0.2 ppm, at 275°F with 8% (v) H_2O in the gas With C=2, the monolayer requirement would correspond to an acid concentration of nearly 5 ppm.

Characterization of surface acidity can be accomplished by a variety of approaches, including titration with bases (n-butylamine, pyridine) with suitable indicators, use of a series of Hammett indicators, and adsorption isotherms. Surface acidity depends largely upon detailed surface composition which may differ substantially from bulk composition. Thermal exposure can be an important influencing parameter.

Bickelhaupt (8) has proposed the use of the following criteria to distinguish "normal" ashes from those which are less responsive to SO_3 conditioning namely, that they contain less than 1 atomic % iron and less than 5 atomic % (Ca + Mg).

In the U.S. low sulfur East Kentucky (and some W. Virginia) coals produce such ashes. A typical bulk ash composition of the former might be 55% SiO_2, 33% Al_2O_3, <4% Fe_2O_3, 1%(CaO + MgO)and < 0.25% Na_2O. Such an ash will be quite refractory with fusion temperatures in excess of 1600° C. When derived from strip-mined coal, contamination with aluminum-containing clays can aggravate SO_3 responsiveness considerably.

A large number of Australian coals yield quite acidic ashes which is probably one of the reasons that some Australian investigators decry the role of sulfur trioxide in influencing ESP performance. One notorious example is derived from Tarong coal (Nanango district of Queensland); its ash composition is 61% SiO_2, 34% Al_2O_3, 3.4% Fe_2O_3, 0.2% (CaO +MgO) and 0.1% Na_2O. Further, the coal sulfur's content is about 0.3% with 28% ash. Many Indian coals also yield acidic ashes.

The adsorption model, in the clean rotor situation, postulates adsorption equilibrium at the outlet of every air heater cell. Obviously, the extent of acid adsorption in the air heater based on this model does not require investigation of interior points; the conditions at the outlet will define the extent of H_2SO_4 removal, as well as the number of monolayers of acid adsorbed on the ash particles. Our module was developed to give information concerning adsorption in the interior region of the air heater, as the module served as a stepping stone to more complex modules.

The application of the finite-difference approach to the adsorption situations (on fly ash, or on both fly ash and ash deposits) is considerably more complicated mathematically than the simple temperature situation of figure 9. In the adsorption case we require the highly accurate solution, for each cell, of 3 or 5 simultaneous equations, some of which are non-linear.

Using the six cases previous noted, we calculated the average number of layers of sulfuric acid adsorbed on the fly ash. Figure 14 shows the extent of SO_3 removal (inlet gas-8 ppm H_2SO_4) with acidic and basic ashes. Below about 250°F, the acidic and basic ashes behave similarly with respect to the average uptake of acid. At higher gas outlet temperatures we see a large difference in behavior of the two types of ashes; there is strongly reduced uptake of acid, especially for the acidic ash. Figure 14 refers to a coal with a 10% ash level.

Ash loading and ash size distribution also exert important effects with respect to acid uptake.

Calculations reveal that with outlet temperature spreads as small as 40°F, resistivities of acidic ashes can range from $2.5\ (10)^9$ ohm cm in the cold part of the air heater duct to more than $4\ (10)^{11}$ ohm cm in the hot part due to the difference in adsorption of acid.

Induced Conditioning

With respect to conditioning, the predicted effect of added SO_3 is shown for a gas outlet temperature of 289°F with acidic and basic ashes. From Figure 15 one might deduce that there is only about 5 ppm SO_3 additional requirement for achieving useful acid uptake levels with the acidic ash compared to the basic ash. This is not generally so for several reasons. The basic ash may have a lower resistivity level when compared at equal average levels of acid uptake. This could follow from the higher conductivity of the basic ash constituents without conditioning as well as from the better uniformity of conditioning achievable with the basic ash.

Also, as expected, some segments of the acidic ash are predicted to undergo little uptake of acid. If the air heater flow stratification persists into the precipitator, some precipitators cells may operate under poor electrical conditions and yield low collection efficiencies.

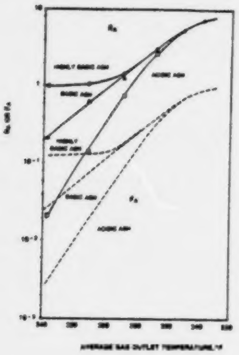

Figure 14. N_A and F_A Values For Three Fly Ash Samples

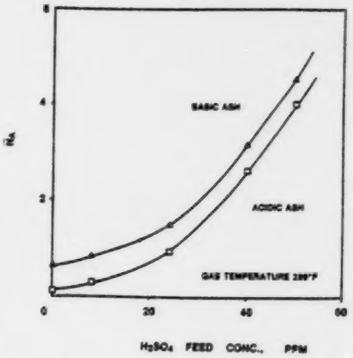

Figure 15. Predicted H_2SO_4 Conditioning Effect For Two Fly Ash Samples

The use of the adsorption model for such situations can provide insight into the cause of malperformance as well as guidance for obtaining optimal conditioning levels with a minimal expenditure of acid. The model also enables one to anticipate leakage of unadsorbed acid into the atmosphere where operation is not conducted at proper conditions.

COMPETITIVE ADSORPTION - FLY ASH VS. ASH DEPOSITS

This specific analysis was prompted by a situation in which H_2SO_4 concentrations in the inlet gas to various chambers of an ESP system were found to vary nearly fivefold (0.6 to 2.9 ppm; at a sister unit the value was 4 ppm). Air heater inlet concentrations averaged about 6 ppm. Measurement of water-soluble sulfate on the ashes did not indicate that the differential quantity of H_2SO_4 lost from the gas was adsorbed on the corresponding fly ash. Further, the 0.6 ppm H_2SO_4 zone produced the highest resistivity ash ($\sim 4(10)^{12}$ ohm cm) and exhibited the poorest electrical operating parameters.

It was postulated that the losses of acid were occurring by adsorption on stagnant ash deposits on the air heater surface or by condensation on the cold metal surface. The lower temperature of the deposits compared to that of the fly ash would favor adsorption on the former.

In our analysis we considered the competitive adsorption of H_2SO_4 on the two categories of ash in each air heater cell with some subsequent stripping of H_2SO_4 from the ash on the air side. It was necessary to involve the boiler system since now some SO_3 was being recycled to the boiler in the combustion air. Figure 16 shows the boiler system with its SO_3 sources and sinks. In the system we considered the SO_3-atomic oxygen reaction, the prompt partial reversion of excess SO_3 to SO_2 and the low temperature heterogeneous catalysis of SO_2 to SO_3.

Figure 17 shows that in the acidic ash situation the stagnant ash deposits compete (in this equilibrium analysis) much more successfully for H_2SO_4 adsorption than does the fly ash. With basic ashes, the competition is less one-sided. The low sulfur content of many coals with acidic ashes further aggravates the competitive adsorption situation.

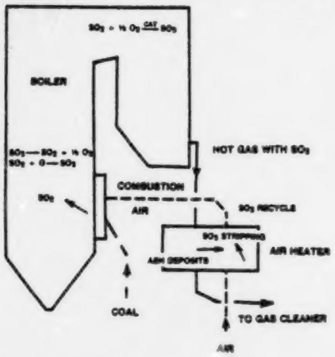

Figure 16. Boiler System SO_3 Sources and Sinks

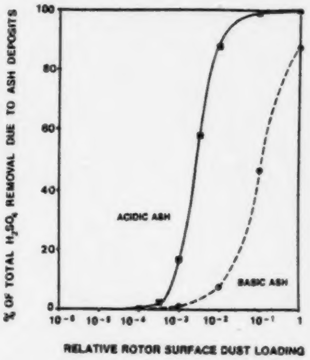

Figure 17. Loss of H_2SO_4 Due To Competitive Adsorption on Ash Deposits

There are several more complex aspects which were not introduced into this limited analysis. First, fly ash surfaces are notoriously heterogeneous and a simple BET isotherm with C_A=constant=f(T) only should be replaced with one which better describes this heterogeniety by expressing a dependence of C_A on X_A, the degree of saturation. While we neglected kinetics aspects of the adsorption process, it is imperative to note that adsorption kinetics with basic ashes are likely to be appreciable faster than with acidic ashes. The latter appears to be a significant factor involved in induced conditioning of various fly ashes.

CONCLUSIONS

Complex phenomena occur in air heaters treating gas streams containing H_2SO_4 vapor. Cold end corrosion results as acid condenses on cold metal surfaces; when the gas temperature falls below the acid dew point, fog may form.

With respect to ESP performance, adsorption of H_2SO_4 on the ash surface can serve to supply a sufficiency of conducting ions to facilitate current flow across a deposited ash layer. A simple equilibrium model (BET) provides guidance as to the adsorptive behavior of ash surfaces of various acidities with H_2SO_4 vapor in the range of air heater temperatures. Under some conditions fly ash exiting the air heater can exhibit a wide distribution of acid loadings, largely dependent upon local temperature levels, and the availability of H_2SO_4. In these cases insufficient gas mixing downstream of the air heater can lead to marginal performance in some zones of the ESP when other conductive ash species are lacking.

Competitive adsorption of acid between fly ash and air heater ash deposits tends to favor the ash deposits since they are at a lower temperature. In situations in which acidic ashes are involved, the adsorbed H_2SO_4 on the stagnant ash layer is more readily stripped on the air side (than in the case of more basic ashes). It was shown that the competition for H_2SO_4 adsorption between fly ash and rotor ash deposits is less favorable from the standpoint of the fly ash in acidic ash cases. Thus normally less attractive situations involving acidic ashes can be appreciably penalized when air heater ash deposits occur. Modeling of this situation involved, in addition to the air heater interactions, boiler system generation of SO_3 by atomic oxygen attack of SO_2, as well as catalytic oxidation of SO_2.

These unique **HIM** computer models have proved themselves useful in a number of situations. Among them are the ability to

- anticipate poor local (natural) conditioning of fly ash and suggest more suitable operating conditions
- provide guidance as to an optional gas mixing approach to eliminate high resistivity ash zones
- define details of a cost-effective SO_3 conditioning scheme which provides proper local SO_3 injection concentrations.

Our basic approach is also of interest for non-SO_3 containing agents which condense from the vapor state to a particulate form. Air heater fouling problems which may occur in NH_3-based NO_x control processes can be simulated by our models.

The work described in this paper was not funded by the U.S. Environmental Protection Agency and therefore the contents do not necessarily reflect the views of the Agency and no official endorsement should be inferred.

REFERENCES

1. Johnstone, H.F. An electrical method for the determination of the dew point of flue gases. Univ. Illinois Eng. Exp. Sta. Circ. No. 20, 1929.

2. Borio, R.W., Hensel, R.P., Wilson, E.B., and J.W. Leonard. The control of high-temperature fire-side corrosion in utility coal-fired boilers. Office of Coal Research, Dept. of the Interior, Research and Development Report No. 41, Apr. 1969, Washington.

3. Rylands, J.R. and J.R. Jenkinson. The acid dew point. J. Inst. Fuel 27: 299-318, 1954.

4. Harlow, W.F. Causes of flue gas deposits and corrosion in modern boiler plants. Proc. Inst. Mech. Engr. (London) 160: 359-368, 1949.

5. Mittelbach, G. Kondensation von Schwelfelsäure aus Rauchgasen und der Meßvorgang auf electrischen Taupunktfuhlern. VGB Kraftuerkstechnik 53: 675-682, 1973.

6. Bickelhaupt, R.E. Measurement of Fly Ash Resistivity Using Simulated Flue Gas Environments, EPA-600/7-78-635 U.S. Environmental Protection Agency, Research Triangle Park, NC, 1978, 23 pp.

7. Bickelhaupt, R.E. The effect of sulfuric acid vapor on fly ash resistivity, presented at Fourth Symposium on the Transfer and Utilization of Particulate Control Technology, Oct. 11-15, 1982, Houston, TX.

8. Bickelhaupt, R.E. A Study to Improve a Technique for Predicting Fly Ash Resistivity with Emphasis on the Effect of Sulfur Trioxide (Draft Report to U.S. Environmental Protection Agency, Mar. 1983).

9. Potter, E.C. and C.A.J. Paulson. Does sulphur dominate fly ash collection in electrostatic precipitators? In EPA-600/9-80-639a. Second Symposium on the Transfer and Utilization of Particulate Control Technology, Vol. I, 184, 1980.

10. Pilat, M.J. and J. M. Wilder. Opacity of monodisperse sulfuric acid aerosols, Atmospheric Environment 17: 1825-1835, 1983.

11. Southern Research Institute measurements supplemented by data from the author.

12. Attar, A. and W.H. Corcoran. Sulfur compounds in coal. Ind. Eng. Chem. Prod. Res. Dev. 16: 168-170, 1977.

13. O'Gorman, J.V. and P.L. Walker, Jr. Mineral Matter and Trace Elements in U.S. Coals. Research and Development Report No. 61 Prepared for Office of Coal Research, U.S. Department of the Interior, 1972.

14. Montano, P.A., Granoff, B. and T.D. Padrick. Role of impurities In: B.R. Cooper and W.A. Ellingson (Eds.), The Science and Technology of Coal and Coal Utilization. Plenum Press, NY, 1984.

15. Mitchell, R.S. and H.J. Gluskoter. Mineralogy of ash of some American coals: Variations with temperature and source. Fuel 55: 90-96, 1976.

16. Bodenstein, M. and W. Pohl. Gleichgewichtsmessungen an der Kontaktschwefelsäure Z. Electrochem. 11: 373, 1905.

17. Dooley, A. and G. Whittingham. The oxidation of sulphur dioxide in gas flames. Trans. Faraday Soc. 42: 354-362, 1946.

18. Whittingham, G. The oxidation of sulphur dioxide in slow cmbustion processes. Trans. Faraday Soc. 44: 141-151, 1948.

19. Hedley, A.B. A kinetic study of sulphur trioxide formation in a pilot scale furnace In H.R. Johnson and D.J. Littler (Eds) The Mechanism of Corrosion by Fuel Impurities. Butterworths, London 1963, p 204-215.

20. Moisieeva, T.A. and V.E. Podolyak. The effect of the rate of cooling of combustion products in the furnace on the formation of sulphur trioxide. Teploenergetika 20: 14-17, 1973.

21. Ahmed, S.H. and B.J. Zaczek. A kinetic study of factors influencing SO_3 formation in a premixed laminar flame. J. Inst. Fuel. 50: 107-110, 1977.

22. Laxton, J.W. Influences of excess oxygen and metallic additives, In H.R. Johnson and D. J. Littler (Eds) The Mechanism of Corrosion by Fuel Impurities, Butterworths 1963, p 232-237.

23. Jakisch, H. Clinkering in the combustion chamber below the softening temperature of the ash. Arch Wärmewirt 23: 211-214, 1942.

24. Kinjiro, F. Decomposition of calcium sulphate at high temperature. Sekko to sekkai No. 7, 2-5, 1952.

25. Wickert, K. Fouling of heating surfaces in steam generator boilers. Part I Composition, physical behaviour and sintering of combustion chamber dust. Brennstoffe, Wärme, Kraft 10: 1, 1958. Part II Chemical reactions in the combustion chamber and measures to counteract the resulting damage, Brennstoffe, Wärme, Kraft 10: 101, 1958.

26. Baker, D.C. and A. Attar. Sulfur pollution from coal combustion. Effect of the mineral components of coal on the thermal stabilities of sulfated ash and calcium sulfate. Environ. Sci. Technol. 15: 288-293, 1981.

27. Ostroff, A.G. and R.T. Sanderson. Thermal stability of some metal sulfates, J. Inorg. & Nuclear Chem. 9: 45, 1958.

28. Pechkovskii, V.V. Formation of metal sulfides and oxides in the thermal decomposition of manganese and iron sulfates. Zhur. Priklad Khim 32: 2613-2618, 1959.

29. Homolya, J.B., Barnes, H.M. and C.R. Fortune. A characterization of the gaseous sulfur emissions from coal and oil-fired boilers, In Proc. 4th National Conference on Energy and Environment, Cincinnati, OH, 1976, p 490-494.

30. Barrett, R.E. High temperature corrosion studies in an oil-fired laboratory combustor, Trans. ASME, J.Eng. Power, Ser. A 89: 288-296, 1967.

31. Reidick, H. and R. Reifenhäuser. Catalytic SO_3 Formation as Function of Boiler Fouling Combusion 52: 17-21, 1980.

32. Zetlmelsl, M.J., McCarthy, K.J. and D.F. Laurence. Investigation of some factors affecting nonflame generation and suppression of SO_3. Ind. Eng. Chem. Prod. Res. Dev. 22: 710-716, 1983.

33. Levy, A. and E.L. Merryman, Interactions in sulphur oxide-iron oxide systems, Trans. ASME J.Eng. Power, Ser. A, 89: 297-303, 1967.

34. Anderson, C.H., and C.W. Goddard, Equilibrium SO_3 pressures of inner layers of fireside deposits from coal boilers. J. Inst. Fuel. 41: 357-363, 1968.

35. Lee, G.K., Friedrich, F.D. and E.R. Mitchell. Paper 4. Effect of fuel characteristics and excess combustion air on sulphuric acid formation in a pulverized-coal-fired boiler. Dept. of Energy, Mines and Resources, Mines Branch (Canada) 1967. 9 pp.

36. Fontana, M.G. and N.D. Greene. Corrosion Engineering (2nd ed.). McGraw-Hill Book Co., NY, 1978, p 225.

37. Land, T. The theory of acid deposition and its application to the dew-point meter. J. Inst. 50: 68-75, 1977.

38. Müller, P. Study of the influence of sulfuric acid on the dew point temperature of the flue gas. Chemie-Ing.-Tech. 31: 345-351, 1959.

39. Abel, E. The vapor phase above the system sulfuric acid-water. J. Phys. Chem. 50: 260-283, 1946.

40. Gmitro, J.I. and Vermuelen, T. Vapor-liquid equilibria for aqueous sulfuric acid. AIChE Journal 10: 740-746, 1964.

41. Greenewalt, C.H. Partial pressure of water out of aqueous solutions of sulfuric acid. Ind. and Eng. Chem. 17: 522-523, 1925.

42. Banchero, J.T. and F.H. Verhoff. Evaluation and interpretation of the vapour pressure data for sulfuric acid aqueous solutions with application to flue gas dewpoints. J. Inst. Fuel 50: 76-80, 1975.

43. White, H.J. Electrical resistivity of fly ash. Air Repair 3: 79-87, 1953.

44. White, H.J. Fifty years of electrostatic precipitation. J. Air Poll. Control Assoc. 7: 167-177, 1957.

45. Tassicker, O.J., Some aspects of electrostatic precipitation research in Australia. J. Air Pollution Control Assoc. 25: 122-127, 1975.

46. Hahnemann, H.W. Approximate calculation of thermal ratios in heat exchangers including heat conduction in direction of flow, National Gas Turbine Establishment Memorandum No. M36, 1948.

47. B. H. Schultz. Regenerators with longitudinal heat conduction, IME-ASME General Discussion on Heat Transfer, London, England, 1951, p 440-443.

48. Coppage, J.E. and A.L. London. The periodic flow regenerator, Trans

ASME 75: 779-787, 1953.

49. Lambertson, T.L. Performance factors of a periodic flow heat exchanger, Trans ASME 80: 586-592, 1958.

50. Bahnke, G.D. Effect of longitudinal heat conduction on rotary regenerators, MS thesis, U.S. Naval Postgraduate School, Monterey, CA, 1962.

51. Mondt, J.R. Heat exchanger solid and fluid temperature distributions, J. Engr. for Power, Trans ASME, Series A, 86: 121-126, 1964.

52. Brunauer, S. and P.H. Emmett. The use of low temperature van de Waals adsorption isotherms in determining the surface areas of various adsorbents, J. Amer. Chem. Soc. 59: 2682-2689, 1937.

53. Brunauer, S., Emmett, P.H. and E. Teller. Adsorption of gases in multimolecular layers, J. Amer. Chem. Soc. 60: 309-319, 1938.

54. Brunauer, S., Deming, L.S., Deming, W.E. and E. Teller. On a theory of the van der Waals adsorption of gases, J. Amer. Chem. Soc. 62: 1723-1732, 1940.

55. Brunauer, S., Skalny, J and E.E. Bodor. J. Colloid Interface Sci. 30: 546-552, 1969.

56. Ditl, P. and R.W. Coughlin. Sorption and diffusion interactions with fly ash of SO_2 in air, SO_3 in air, $SO_2 + H_2O$ in air and SO_3+H_2O in air, Environ. Sci Technol. 11: 701-706, 1977.

Session 11: ESP: FUNDAMENTALS II

Philip A. Lawless, Chairman
Research Triangle Institute
Research Triangle Park, NC

EXPERIMENTAL STUDIES OF SPACE CHARGE EFFECTS IN AN ESP

by: D.H. Pontius and P.V. Bush
Southern Research Institute
Birmingham, Alabama 35255-5305

ABSTRACT

As particles become charged in an electrostatic precipitator they interfere with the normal corona discharge by establishing relatively immobile, local electric field effects. These effects, often referred to as space charge, were demonstrated in a wire-pipe ESP by injecting resuspended fly ash into the system. A simple mathematical model was derived for this ESP configuration to verify the behavior of the system in the presence of substantial space charge effects.

This paper has been reviewed in accordance with the U.S. Environmental Protection Agency's peer and administrative review policies and approved for presentation and publication.

I. INTRODUCTION

The fundamental concept of electrostatic precipitation is elegantly simple. Particles suspended in a gas may be captured by charging them with ions in an electrical corona discharge and forcing them to impact on a solid surface by the effect of an electric field. Given this basic principle, along with the knowledge of what is required to produce a corona discharge, the development of specific configurations of electrodes to perform the operation is straightforward. This information is not, however, enough to define how large the device should be for a specific application.

Among the early attempts to develop a quantitative description of electrostatic precipitation was that of W. Deutsch (1). He derived an expression for the rate of precipitation, based upon certain broad assumptions and approximations. Since that expression is independent of the concentration of suspended dust in the gas to be cleaned, it integrates very neatly into an exponential model for a precipitator of arbitrary size. The Deutsch model has been modified and refined in a number of different ways to suit specific needs, but the fundamental ideas remain useful and effective (2,3).

A model is a representation of an object, a system, or a concept. The utility of a model depends upon the nature of the correspondence, or isomorphism, between the subject and the model; the fidelity is determined by both the accuracy and the consistency of the details. Within the general definition of a model, the operative correspondence can take on any of a great variety of forms, including those of a simple physical transformation of scale, a qualitative description, or a set of abstract mathematical statements. The validity of a model depends entirely upon its intended use. The present discussion concerns an experimental investigation and the development of a mathematical model designed to evaluate the effect of particulate space charge on the behavior of an electrostatic precipitator.

II. PRELIMINARY EXPERIMENTS

The effects of the ionic space charge can be demonstrated by a pair of simple experiments as described in the following part of this discussion and illustrated in Figure 1. First a pair of identical, isolated, parallel wires are energized at equal values of voltage but opposite polarity. If the voltage is high enough, a bipolar corona discharge will occur between the two wires, and if the experiment is done in air at room temperature, the ionic currents due to the positive and negative ions will be nearly the same. The symmetry of the apparatus results in almost identical distributions of positive and negative charge, so that on the macroscopic scale the net space charge in the system is essentially zero.

The plane of symmetry midway between the two wires is an equipotential surface at ground potential. If a grounded metal plate is now inserted on the location of that surface, the electrostatic description remains practically unchanged, but the distribution of space charge is radically altered. The positive and negative ions remain separated until they effectively recom-

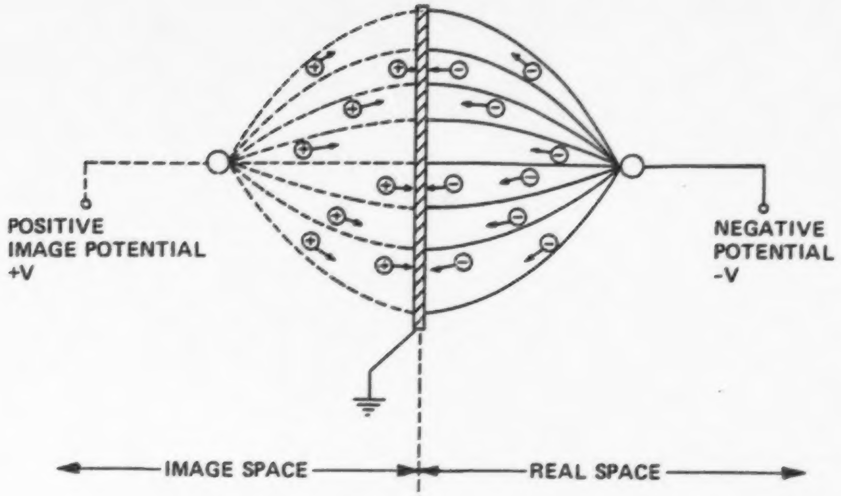

A. WIRE-PLANE APPARATUS

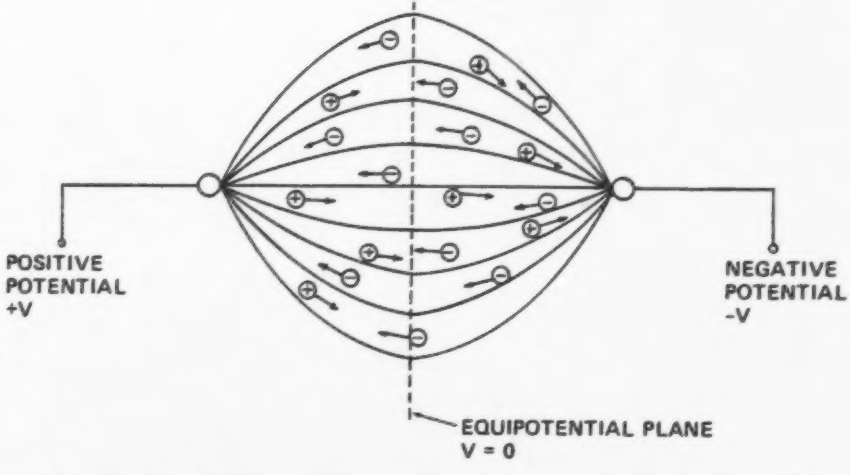

B. WIRE-WIRE APPARATUS

Figure 1. Bipolar corona, space charge neutralized (a). Twin unipolar corona (b).

bine on the grounded plane, Thus, in the space on either side of the plate there is a monopolar distribution of ions--a space charge--similar to that found in an electrostatic precipitator.

If the ionic space charge were, in general, ineffective at suppressing corona discharge, the following results should be observed. At any given value of the applied potential, the sum of the currents measured for each of the two wires with the grounded plate present (i.e., the total ionic current intercepted by the plate) would be the same as the current measured at either wire in the other configuration. But from the experimental results shown in Figure 2 it is clear that the neutralization of the space charge in the mixed bipolar experiment permits a much more vigorous corona discharge than occurs in the other experiment.

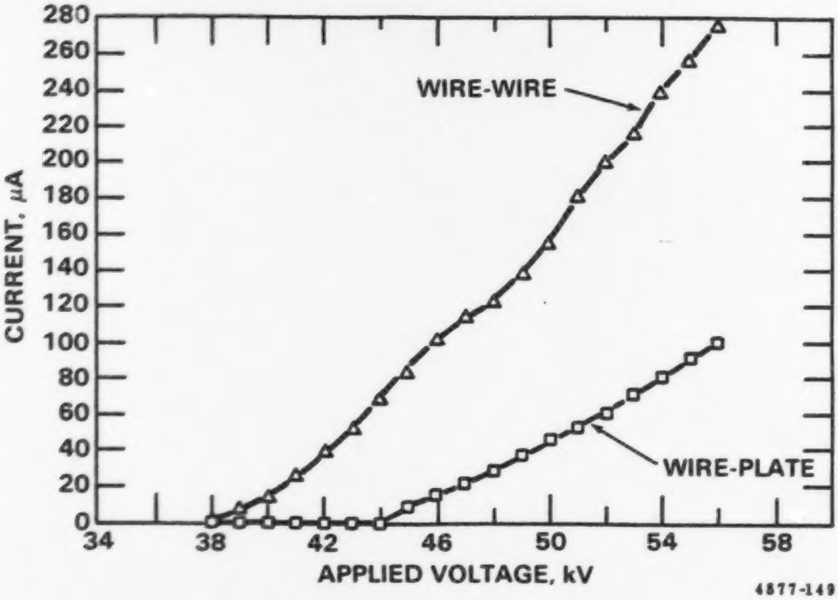

Figure 2. Comparison of conduction characteristics of bipolar and mirror-twin unipolar corona discharges.

The point of the previous discussion is to demonstrate the extent to which a corona discharge is dominated by the distribution of space charge in the system. In the experiment described, only an ionic space charge was present, but additional suppression of the corona discharge results from a particulate space charge. It is that phenomenon which will be addressed in the present discussion.

III. SPACE CHARGE EXPERIMENTS IN THE LABORATORY

Elementary experiments involving space charge associated with particulate loading in a precipitator were carried out in a cylindrical device with a segmented collecting electrode. This system is equipped with a 32-channel electrometer so that accurate measurements of current density as a function of position can be made rapidly. The data are accumulated in computer storage, and statistical analyses are carried out. Typically, 400 measurements are acquired in a period of about one minute. The internal diameter of the cylinder is 24.8 cm, and the active length is 40.6 cm. It is mounted in a wind tunnel which can provide a gas flow of controllable velocity, temperature and dust loading.

Experiments were carried out using both positive and negative corona polarity. Fly ash was injected into the gas by sandblaster. In each experiment, the principal measurements included determination of V-I characteristics, particle size distribution, and electrical charge on the particles. It is notoriously difficult to resuspend the finer fraction of fly ash particles by mechanical means; however, the results were adequate to provide a useful demonstration of the effects of space charge.

Figure 3 shows voltage-current characteristics for the device with positive energization. Clearly, there is a nearly linear shift of the curve to the right when ash is injected into the system. This is just the behavior expected when particulate space charge exists in a precipitator. The other data tend to support this conclusion. In Figure 4 a reasonably uniform distribution of current is indicated in the presence of clean air, and Figure 5, corresponding to approximately the same applied voltage but in the presence of dust in the gas stream, shows a similar distribution, slightly reduced in magnitude. It is significant, however, that the current density is reduced

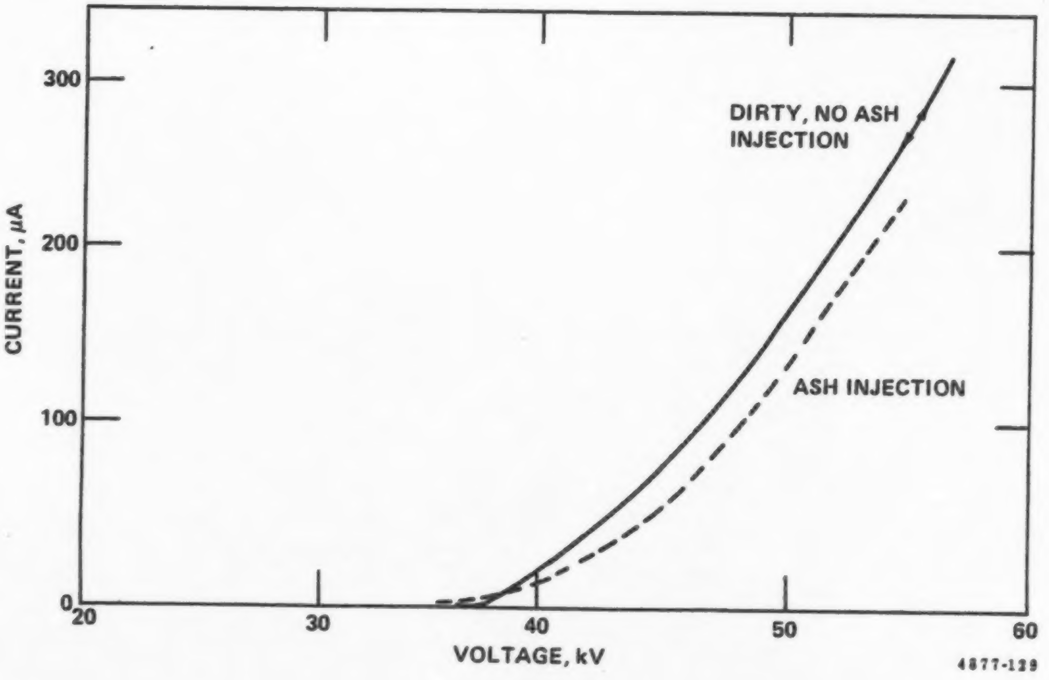

Figure 3. Conduction characteristics of the cylindrical system with positive energization.

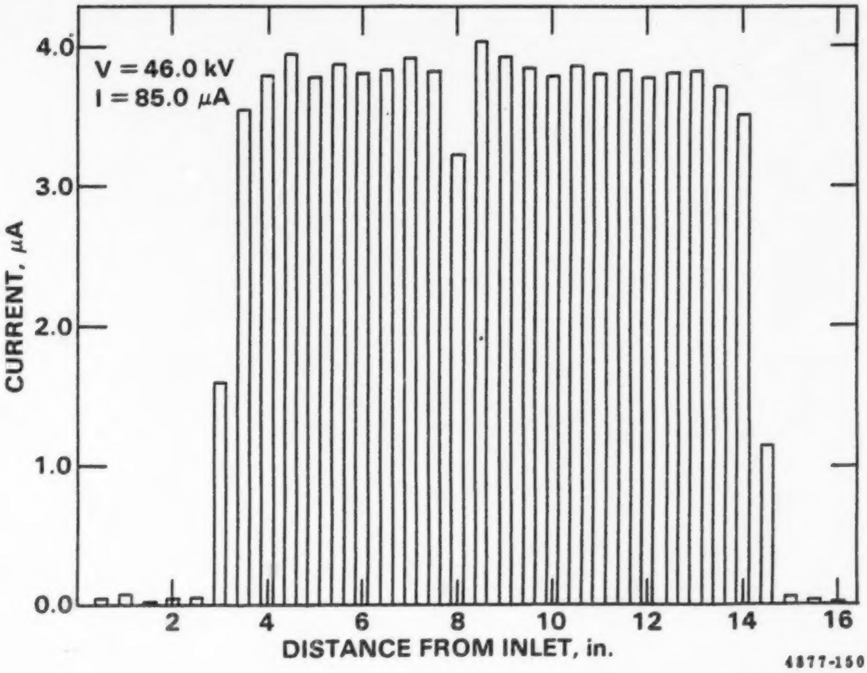

Figure 4. Current distribution for positive corona, clean air.

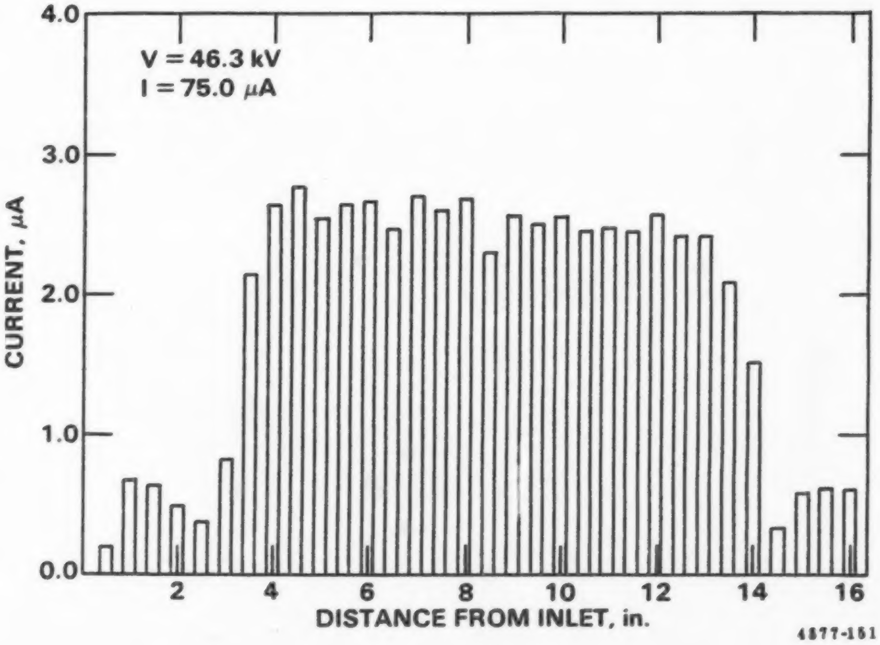

Figure 5. Current distribution for positive corona, dirty air.

even at the closest point to the inlet. This phenomenon implies that essentially complete charging had occurred in an interval of time too small to be resolved by the apparatus, or that the particles were already charged to a relatively high level before they were introduced into the precipitator. Triboelectric charging in the ash dispersion system can account for such an effect. The latter explanation was confirmed by a series of measurements with a Millikan apparatus. Figure 6 shows the distribution of charge as a function of particle diameter at the inlet of the device, and Figure 7 gives the same information at the outlet. They are practically identical. Since no significant change in the status of particulate charge occurred in the precipitator, a uniform effect of space charge is to be expected.

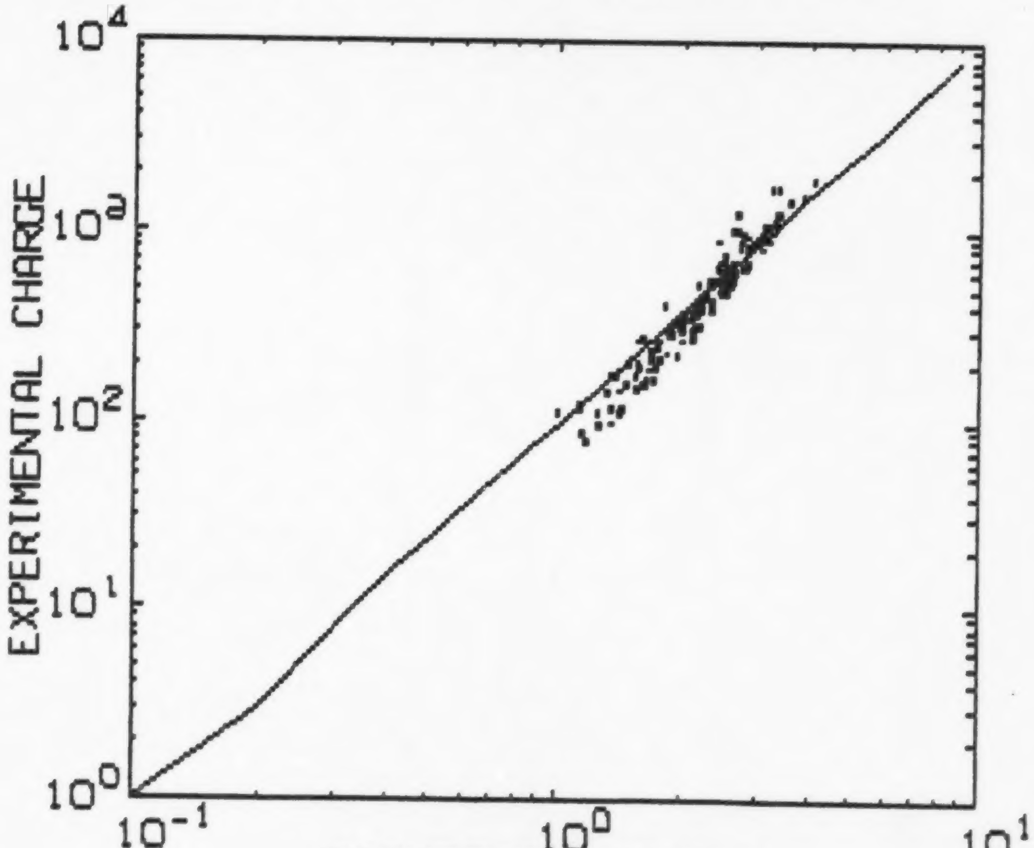

Figure 6. Particle charge as a function of diameter, measured at the inlet of the ESP.

Energizing the system with negative polarity led to somewhat more interesting results in terms of the evolution of the particulate space charge with time. Since the entrant space charge in this instance is opposite in polar-

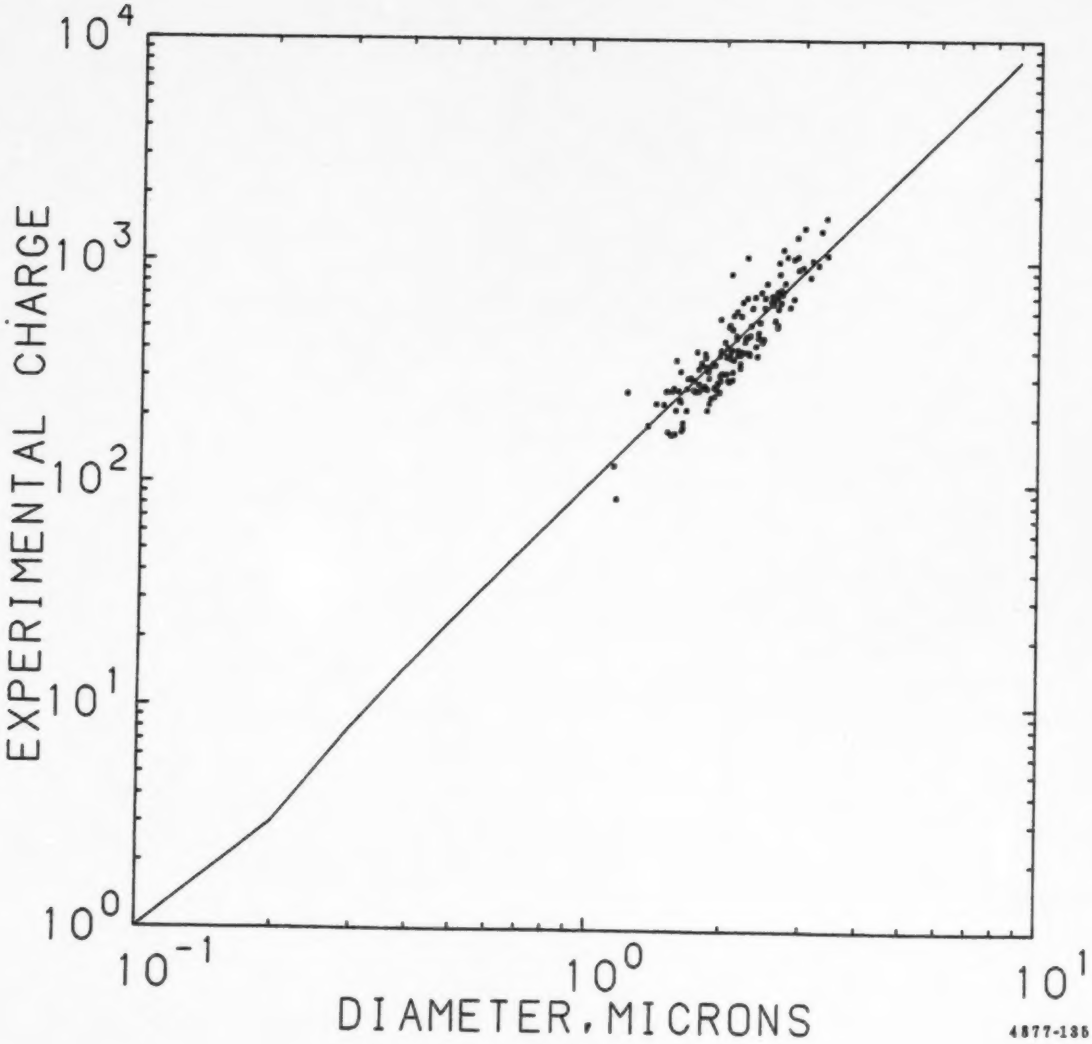

Figure 7. Particle charge as a function of diameter, measured at the outlet of the ESP; positive corona.

ity to the ionic space charge, the current density is increased at the inlet end of the precipitator, as can be observed by comparing Figures 8 and 9. The charge is quickly neutralized and negative charge begins to accumulate on the particles, resulting in progressively greater suppression of corona current toward the outlet end of the device. The measurements of charge distribution by particle charge, shown in Figure 10, indicated that the magnitude of the charge at the outlet was approximately the same as was achieved in the experiment done with positive polarity. In the negative experiment, however, the charge on the particles underwent a complete reversal of polarity, which was graphically traced by the variation of current density with distance down the length of the precipitator.

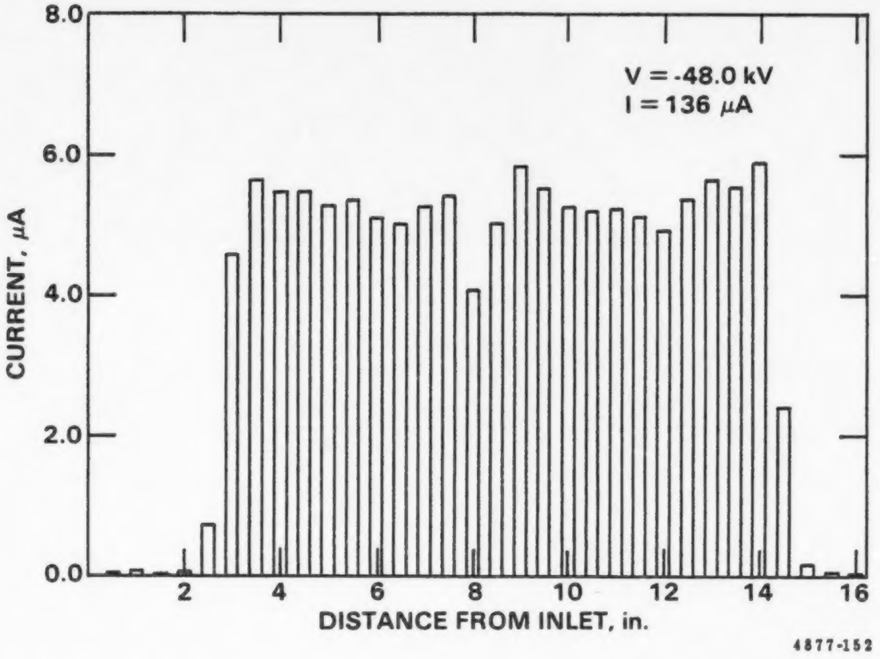

Figure 8. Current distribution for negative corona, clean air.

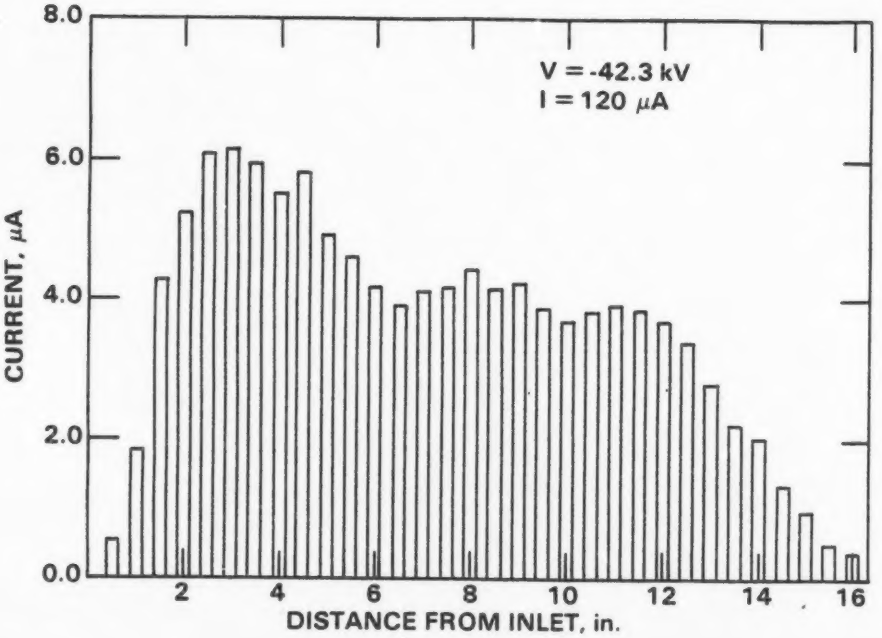

Figure 9. Current distribution for negative corona, dirty air.

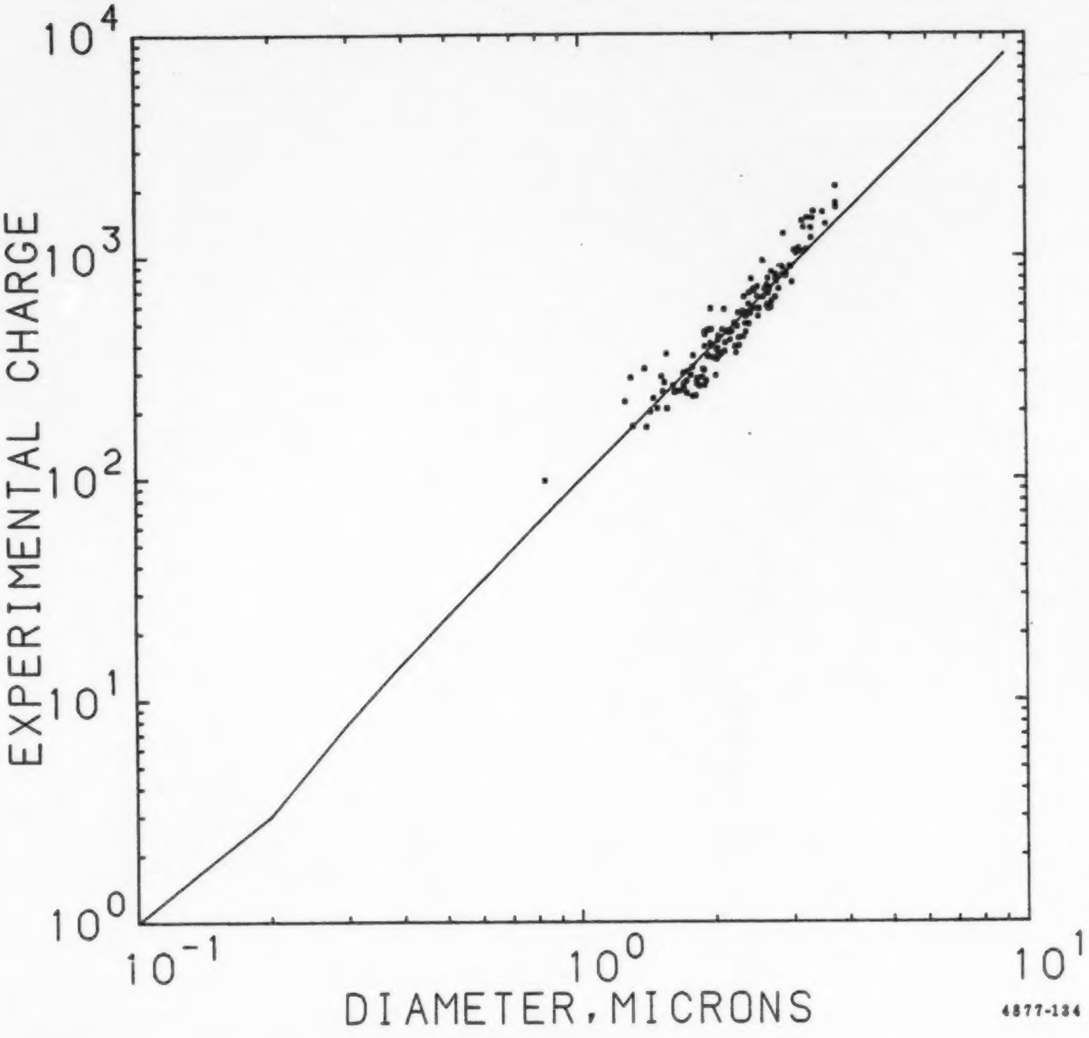

Figure 10. Particle charge as a function of diameter, measured at the outlet of the ESP; negative corona.

IV. THEORETICAL MODEL

The model to be discussed in the following paragraphs shares many of its basic assumptions with the Deutsch model. The most significant area of departure is that in the present model it cannot be assumed that the rate of precipitation is independent of the concentration of dust. This is a deliberate complication, brought about by the inclusion of the charge on the particles in the overall charge distribution. As a result, the rate of precipitation becomes dependent upon the concentration of particles and the charging conditions to which they have been subjected. The simple exponential behavior no longer applies, and a single algebraic expression for the overall collection efficiency of a precipitator cannot be derived. Assumptions and approximations retained from the Deutsch model include the following: (1) Turbulent mixing of the aerosol maintains the distribution of suspended particles uniform over any section of the precipitator normal to the direction of gas flow. (2) Effects of electrostatic forces and turbulence produce no net transfer of particles in a direction parallel to the general flow of the gas. (3) The electric field will be assumed to be a function of position, applied potential and space charge; no discontinuities, instabilities or incongruities will be admitted.

If the constraints upon the model seem overly stringent and perhaps unrealistic, it should be borne in mind that the specific parameter under investigation is the distribution of the particulate space charge. The goal is to provide a quantitative assessment of the extent to which the operation of an electrostatic precipitator is modified by that space charge, given a description of the particle concentration and distribution by size at the inlet of the control device. Provisions will also be made for the possibility that the entrant particles already possess some specified level of charge, due to triboelectric or other effects, before arriving at the inlet of the precipitator.

The set of assumptions upon which this model is based are chosen to minimize the number and length of computational procedures while dealing quantitatively with the presence of particulate space charge in an electrostatic precipitator. This approach results in a smoothed-out model in which the finer details are treated statistically. In the limit, as the particulate space charge is reduced toward zero, the result converges to that of the Deutsch model.

In most instances electrical coronas are controlled, or limited, by the distribution of charge in the space between the electrodes. The effect of ionic space charge is treated in the fundamental theory of corona discharges. In an electrostatic precipitator, however, there is an additional component to the space charge resulting from the capture of ions by dust particles suspended in the gas. The electrical mobility of the charged particles is much smaller than that of the ions, so the resulting particulate space charge tends to build up until a significant redistribution of the electric field occurs. The field near the corona discharge electrode becomes reduced, causing a reduction in the ionic current injected into the system. But at the passive electrode the strength of the electric field increases. The result of the former effect is to diminish the charging rate, and the latter produces an increase in the migration velocity of the particles. The presence of a strong particulate space charge may therefore be either beneficial or detrimental, depending upon which of the two competing effects dominates.

The general concept of space charge as outlined above is well known, but it is a difficult mechanism to build into a mathematical model. The rate of particle charging depends upon the ion current density and the local strength of the electric field, among other things. The current density and field strength, in turn, are strongly affected by the charge distribution in the system, including both the ions and the charge on the particles. (For completeness, the contribution of free electrons to the charge distribution can be included, but this effect will be considered negligible for the purposes of this discussion.)

The working geometry for developing the fundamental solutions will be that of coaxial cylinders. The solutions will be, as implied in our introductory remarks, essentially two-dimensional; the axial components of all quantities will be considered negligible. The configuration is advantageous from both theoretical and experimental grounds.

Because of the relationships between the mechanisms of particulate charging and the effect of the resulting space charge on the charging rate, an iterative method has been developed. The calculation begins with a value of zero for the particulate space charge. Given parameters for the distribution of particles by size, the procedure computes the charge accumulated by the particles during a small increment of time. The calculation is then repeated with the inclusion of the small increase in space charge. Depletion of particles from the system, and the concomitant removal of charge are computed in terms of the values of electrical mobility calculated for the particles and the electric field strength at the collecting surface, as in the model of Deutsch.

V. MATHEMATICAL DEVELOPMENT

If end effects are neglected in a cylindrical system containing only equipotential surfaces that coincide with coaxial cylinders, then the electric field is entirely radial, and from basic electrostatic theory, the magnitude of the electric field E(r) can be expressed in the form

$$E(r) = \frac{\lambda(r)}{2\pi\varepsilon r} \tag{1}$$

where $\lambda(r)$ is the (cylindrically symmetric) charge per unit length of the system within a cylinder defined by radius r, and ε is the permittivity of the medium.

The quantity $\lambda(r)$ can be separated into one part λ_a representing the linear charge density on the center conductor of radius a, and the space charge contribution $\rho(r)$ per unit length of the system;

$$\lambda(r) = \lambda_a + \int_a^r 2\pi\xi\rho(\xi)d\xi \quad . \tag{2}$$

The expression for the electric field strength thus becomes

$$E(r) = \frac{\lambda_a}{2\pi\varepsilon r} + \frac{1}{\varepsilon r}\int_a^r \xi\rho(\xi)d\xi \quad , \tag{3}$$

and the potential V(r) is

$$V(r) = {}_b{-\int}^{r}_{\varepsilon\nu} \frac{1}{2\pi} \left[\frac{\lambda_a}{\varepsilon r} + {}_0\int^{\nu} \xi\rho(\xi)d\xi\right]d\nu \tag{4}$$

assuming that we choose the surface r=b as the reference for zero potential. Application of this method thus consists of specifying or calculating a distribution of space charge, carrying out the integration in Equations (3) and (4), and then evaluating λ_a in terms of the boundary conditions V(a)=V, the applied potential, and V(b)=0.

UNIFORM DISTRIBUTION OF SPACE CHARGE

The simplest nontrivial problem in the geometry in question is that in which a uniform distribution of space charge exists. Cooperman (4) has explained that a uniform distribution of ionic space charge is a very good approximation if the current density is small. Because of the normally turbulent behavior of the gas in a precipitator, an assumption of uniform particulate space charge is also a good first-order approximation. Therefore, taking $\rho(r)=\rho$, a constant, Equation (3) becomes

$$E(r) = \frac{\lambda_a}{2\pi\varepsilon r} + \frac{\rho(r^2 - a^2)}{2\varepsilon r} \quad , \tag{5}$$

and the potential function calculated from Equation (4) is

$$V(r) = \frac{\lambda_a}{2\pi\varepsilon}\,\ell n(b/r) + \frac{\rho}{2\varepsilon}\left[\frac{b^2 - r^2}{2} - a^2\ell n(b/r)\right] \quad . \tag{6}$$

Now, setting V(a)=V and solving for λ_a yields

$$\lambda_a = \frac{2\pi\varepsilon}{\ell n(b/a)}\left\{V - \frac{\rho}{4\varepsilon}\left[b^2 - a^2(1+2\ell n(b/a))\right]\right\} \quad . \tag{7}$$

The first term on the right-hand side of Equation (7) represents the electrostatic contribution, and the second term indicates the reduction in linear charge density on the corona wire required to maintain the imposed potential on the wire in the presence of the space charge.

Inserting the value of λ_a from Equation (7) into Equations (5) and (6) provides the following expressions for E(r) and V(r):

$$E(r) = \frac{V}{r\,\ell n(b/a)} + \frac{\rho}{2\varepsilon r}\left[r^2 - \frac{b^2 - a^2}{2\,\ell n(b/a)}\right] \quad , \tag{8}$$

$$V(r) = \left[V - \frac{\rho(b^2 - d^2)}{4\varepsilon}\right]\frac{\ell n(b/r)}{\ell n(b/a)} + \frac{\rho}{4\varepsilon}(b^2 - r^2) \quad . \tag{9}$$

CORRESPONDENCE WITH TOWNSEND'S THEORY

Up to this point in the discussion, no distinction has been made between ionic and particulate contributions to the space charge. The results expressed in Equations (7) through (9) are static.

Townsend's theory expresses corona current as a quadratic function of the applied potential. In Cooperman's notation (but in MKS units)

$$I = \frac{8\pi\varepsilon_0 k}{b^2 \ell n(b/a)} V(V-V_0) \quad , \tag{10}$$

where I is the current per unit length of corona wire, and k is the ion mobility. The quantity V_0 is the corona inception voltage, defined by the relationship

$$V_0 = aE_0 \ell n(b/a) \tag{11}$$

E_0 is the critical field strength, or the minimum value of the field required to sustain ionization. Then the corona inception voltage is the applied potential required to produce an electric field strength E_0 at the surface of the discharge electrode.

Now, as evidenced by Equation (8), the presence of a space charge will decrease the electric field strength at the surface of the corona wire for a given value of applied voltage. In any event, no corona discharge can occur until the value of E(a) reaches E_0. So, from Equation (8), expressing this condition where $\tilde{V}_0$ is the inception voltage in the presence of the space charge,

$$E_0 = \frac{\tilde{V}_0}{a\ell n(b/a)} + \frac{\rho}{2\varepsilon a}\left[a^2 - \frac{b^2 - a^2}{2\ell n(b/a)}\right] \quad , \tag{12}$$

which yields

$$\tilde{V}_0 = aE_0 \ell n(b/a) + \frac{\rho}{4\varepsilon}\left[b^2 - a^2(1 + 2\ell n(b/a))\right] \quad ,$$

or

$$\tilde{V}_0 = V_0 + \frac{\rho}{4\varepsilon}\left[b^2 - a^2(1 + 2\ell n(b/a))\right] \quad . \tag{13}$$

The corona inception voltage therefore shifts upward by an amount proportional to the space charge. Clearly, the value of ρ in Equations (12) and (13) includes only particulate space charge, since there is no ionic current at the point of corona inception.

Because the general effect of the particulate space charge, under any conditions, is to reduce the linear charge density on the corona wire by an amount proportional to the density of the space charge, the presence of a given distribution of particulate space charge causes a shift in the entire voltage-current characteristic curve. The magnitude of the displacement must be the same as the change in the inception voltage derived above. Consequently, the perturbed expression relating the current to the applied potential takes the form

$$I = \frac{8\pi\varepsilon_0 k}{b^2 \ell n(b/a)} V\left\{V - V_0 - \frac{\rho}{4\varepsilon}\left[b^2 - a^2(1 + 2\,\ell n(b/a))\right]\right\} \quad . \tag{14}$$

VI. RESULTS AND CONCLUSIONS

Equation (14) can be used as it is to describe the effects of space charge in a system where there is a uniform and constant distribution of charge, as in the example presented in connection with Figures 4 and 5. The predicted shift in the V-I characteristic agrees with that indicated in Figure 3. At the time of this writing the modeling of the dynamic behavior, as exemplified by the reversal of the space charge illustrated in Figures 8 and 9, is still in progress. The model includes a charging routine based upon the sum of field and diffusion charging (5); it also accounts for the collection of particles and the concomitant removal of their contribution to the space charge by the collection process developed in the Deutsch-Anderson model.

The experiments described in this paper have shown the extent to which a corona discharge is dominated by the effects of space charge. When the normal ionic space charge in a corona system is augmented by a particulate contribution, the electric field becomes redistributed, resulting in a change in the local field in the zone of the active corona and thus a modification of the overall conduction characteristics of the system. Since the particulate charge can be determined by application of established charging theories, a straightforward linear superposition of all charges results in a complete expression for the behavior of a system where the distribution of charge agrees with the geometrical symmetry of the system.

REFERENCES

1. Deutsch, W. Bewegung und ladung der elektrizitatstrager im zylinderkondensator, Ann. Phys. 68, 1922. 335 pp.

2. Cooperman, P. A new theory of precipitator efficiency. Atmos. Envir. 5:541, 1971.

3. Gooch, J.P. and Francis, N.L. A theoretically based mathematical model for calculation of electrostatic precipitator performance. J. APCA 25:2:108, 1975.

4. Cooperman, P. A theory for space-charge-limited currents with application to electrical precipitation. AIEE Trans., March 1960, p. 47.

5. White, H.J. Particle charging for electrostatic precipitation. AIEE Trans. 70: 1, 1951).

AN ELECTROSTATIC PRECIPITATOR FACILITY FOR TURBULENCE RESEARCH

by: J. H. Davidson
Department of Mechanical and
Aerospace Engineering
University of Delaware
Newark, Delaware 19716

and

E. J. Shaughnessy
Department of Mechanical Engineering
and Materials Science
Duke University
Durham, North Carolina 27706

ABSTRACT

Turbulence is generally accepted to be detrimental to precipitator particle collection efficiency, yet the magnitude and character of electrically induced secondary flow and turbulence in full scale precipitators is not thoroughly understood. Prior laboratory scale experimental studies indicate that negative corona discharge generates turbulence but are restricted to precipitator flow aspect ratios (height to width) much less than those of interest in industrial design. This paper describes a large scale laboratory precipitator aerodynamic research facility. The electrical characteristics of negative corona operation are presented along with hot-film anemometer measurements of the electrically induced turbulence. Measurements include streamwise mean velocities, turbulence intensities, and one-dimensional energy spectra for gas speeds from 0.5 to 2.0 m/sec and electric current densities as high as 0.84 mA/m^2 of plate area. It was found that turbulence was generated throughout the precipitator. The level of turbulence production increases with increasing current but is not sensitive to increases in current density above approximately 0.3 mA/m^2. At a primary gas speed of 1.0 m/sec, a current density of 0.3 mA/m^2 causes a threefold increase in turbulence intensity over that of the background aerodynamic turbulence (from 5 to 15 percent). The implications of these results are discussed in terms of particle transport and precipitator collection efficiency.

This paper has been reviewed in accordance with the U.S. Environmental Protection Agency's peer and administrative review policies and approved for presentation and publication.

INTRODUCTION

During the past decade, expanding research efforts aimed at understanding the fundamental processes of the wire-plate electrostatic precipitator have been directed toward increasing particle collection efficiency without corresponding increases in specific collector area and capital cost. While much of the research has focused on electrical and mechanical characteristics, the impact of fluid forces on the particle collection process must also be considered. Of all the phenomena affecting precipitator performance, the effect of the electric body force associated with a negative corona discharge on secondary flows and turbulence levels, and thus particle motion, is one of the least understood and perhaps one of the most significant. The dispersion and mixing of particles resulting from any electrically induced turbulence and secondary flows may be a dominant effect and is certainly not conducive to the precipitation process in which there is a preferred direction of particle motion. In addition to an initial reduction in particle collection efficiency resulting from the disruption of particle motion toward the collector plates, any turbulent scouring action at the plates causes reentrainment of collected particles into the gas stream and thus further reduces the collection efficiency.

While it is well known that in the case of a uniform discharge along the wire electrodes, the electric body force on the gas produces a secondary flow, referred to as the corona wind, the questions surrounding secondary flow and turbulence generation by the electric field in a negative corona discharge have not been adequately addressed. Research on this subject in the past several years has generated much discussion on the deleterious effects of electrically induced turbulence on precipitator performance, but the fundamental mechanism responsible for turbulence creation is not fully understood. Nor is there any quantitative information on this phenomenon in full scale precipitators.

A theoretical analysis of the governing electrohydrodynamic equations (1,2) points out that the extent to which precipitator gas flows are modified by the corona discharge is determined by the magnitude and distribution of current density J_i. The current density in turn is determined primarily by the electrode geometry and also the discharge polarity. The situation in the case of the wire-plate precipitator is dominated by the structure of the corona discharge along the wires. The majority of what is known about the current density distribution and electrically induced flow modifications in the wire-plate precipitator is restricted to a positive uniform discharge in a laminar flow. The pioneering studies of uniform positive corona by Ramadan and Soo (3), Robinson (4), Yabe et al (5), and Yamamoto and Velkoff (6) indicate that electrically induced secondary flows of a circulatory nature are possible. But because of the inherent differences in negative and positive corona discharge, it is reasonable to assume that the character of the corona induced flow modifications is polarity dependent. Thus these prior studies are of limited use in understanding the flows induced by a negative discharge. Recent laboratory small scale experimental investigations of negative corona discharge by Leonard et al (7,8), Ushimaru et al (9), and Kumaran (10) confirm that turbubulence is generated by a negative discharge. It is not clear that these results are applicable to actual precipitators which have large flow aspect ratios (height to width ratio) and essentially two dimensional flows.

To address these inadequacies, a large scale laboratory electrostatic precipitator was built to study the aerodynamic effects of corona discharge in a facility more representative of commercial practice. In this paper, the facility is described and selected results of an extensive experimental study of flow modifications caused by a negative corona discharge are discussed. Hot film anemometry measurements of mean streamwise velocities, turbulence intensities, and energy spectra are presented for nominal gas speeds of 0.5 to 2.0 m/sec and negative corona discharge currents as high as 0.84 mA/m^2 of plate area. Experiments were conducted at room temperature with no particle loading of the precipitator gas stream. No conclusive evidence of an organized secondary flow was found, but substantial increases in turbulence intensity were seen even at relatively low current levels. The spectral analysis indicates that the electrically induced turbulence is highly diffusive. The implications of these results to the particle collection process and precipitator design are significant.

EXPERIMENTAL FACILITY

THE LABORATORY PRECIPITATOR

The experimental precipitator used in this study was specifically designed to study corona wind and turbulence as they occur in full scale precipitators and is unique among experimental facilities in its size and range of operating conditions. A schematic diagram of the precipitator is shown in Figure 1. The flow channel is 10 m long, 4.88 m high, and 24 cm wide providing an aspect ratio of 20. Room air is drawn through the tunnel past metal inlet scrolls, a foam air filter to remove dust and large particles, and a corrugated paper flow straightener. The inlet scrolls provide a smooth turn into the rectangular duct thus preventing flow separation and a large pressure drop. The straightener eliminates any disruptive flow patterns generated at the entrance by forcing the air stream through 8 mm corrugations 30 cm long. Flow rate is controlled by a variable speed tube-axial blower capable of mean flow speeds up to 2.5 m/sec.

The active precipitator test section, located 5.2 m from the entrance, is 1.83 m in the streamwise direction. Plate to plate spacing is 24 cm. Six 3.2 mm diameter corona discharge wires on 30.5 cm spacings are located midway between the grounded flat metal walls. The steel wires are mounted at the floor and ceiling of the test section to aluminum bus bars electrically isolated from the test section and exterior of the tunnel by 1.3 cm thick plexiglass. Instrumentation ports are located 30.5 cm and 46 cm upstream and downstream of the test section along the entire 4.88 m height. A Del Electronics low ripple power supply rated at 75 kV and 30 mA provides

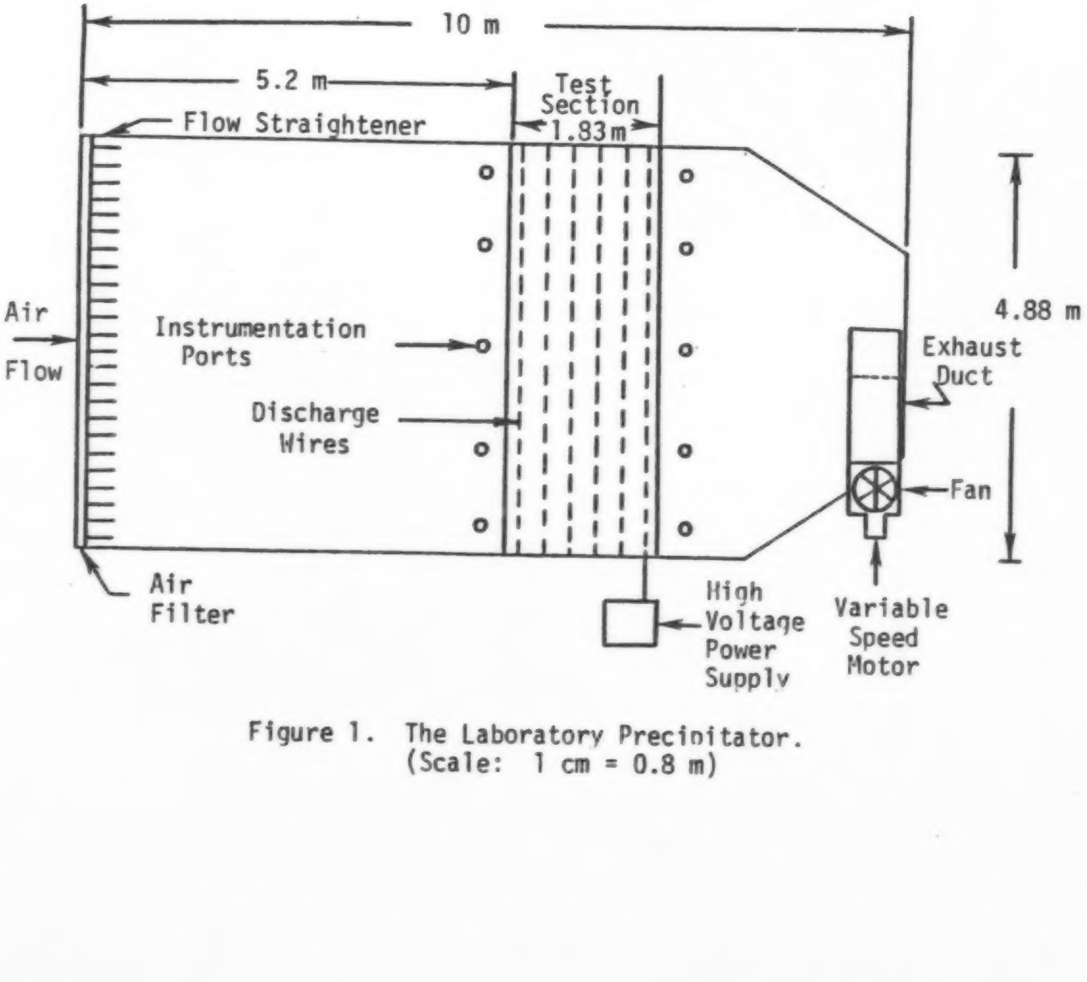

Figure 1. The Laboratory Precipitator.
(Scale: 1 cm = 0.8 m)

the capability of negative and positive corona discharge. Only negative corona is considered in this paper. Wire diameter, wire to wire spacing, and duct width are common to industrial precipitators. The tunnel height, though less than some industrial precipitators, provides a very large experimental aspect ratio and the flow is two dimensional over more than 90% of the precipitator height.

Downstream of the test section a 25 degree contraction reduces the duct height to 2.44 m. The airstream exits the tunnel through a right angle semicircular turn. The blower, mounted at the base of the exit turn, is attached to a removable nylon duct leading outdoors.

INSTRUMENTATION AND PROCEDURES

The difficulties presented in measuring gas velocities inside the active section of a precipitator are immense. Because of these difficulties, the approach taken was to use hot-film anemometry to measure the flow 46 cm downstream of the discharge wires. The basic concept is to view the active precipitator as a black box which transforms the input flow into an output flow. Measurements taken in the absence of a corona discharge are compared to those obtained for a range of electrical current levels. A great deal of effort was taken to insure against the possibility of anomalous velocity measurements attributable to current flow to the hot-film probe itself. Kumaran et al (11) studied this phenomenon in a small model precipitator. A similar study of this problem was carried out in the present facility at the corona current levels and gas speeds of interest (1,12). The results indicate that placing the probe 46 cm from the corona discharge wires prevents measurement errors.

Flow measurements were made with a TSI 1050 linearized anemometer system using 1210-20 film sensors. The hot films were calibrated with the known steady flow provided by a TSI 1125 calibrator. Streamwise mean velocity ($\overline{u}$) and turbulence intensity ($u_{rms}/\overline{u}$) transverse profiles were obtained by traversing the hot-film probe in 20 cm increments across the flow channel at five vertical locations: the centerline, and 1.2 m and 2.1 m above and below the center. The linearized voltage output was signal conditioned to remove most of the DC component and then low pass filtered at 100 Hz with a Kron-Hite 3202R filter. The signal conditioner DC component was retained to restore the mean value to its correct level during data analysis. The output of the low pass filter was connected to a Honeywell SAI-48 correlator linked with a Radio Shack TRS-80 microcomputer. The correlator constructed the probability distribution of velocity using 32,768 samples at 5 millisecond intervals. The 400 point probability density function obtained in this manner was stored and analyzed with the microcomputer to obtain the mean and centered root mean square (rms) voltages which were then converted to velocity using the linearizer gain.

The one dimensional energy spectrum is the cosine transform of the autocorrelation function. To record the autocorrelation function, the hot-film signal is bandpass filtered at 0.1 and 100 Hz and then fed into the correlator which constructs the autocorrelation function. Incremental sampling time is 5 milliseconds and the total number of samples is 131,072.

The total observation time is thus 11 minutes. The autocorrelation data is transformed from the time domain to the frequency domain by means of a cosine transformation algorithm of Bendat and Piersol (13) on the Triangle University Computation Center's mainframe IBM 370.

RESULTS

ELECTRICAL CHARACTERISTICS

The negative corona current-voltage characteristics are shown in Figure 2. The corona onset voltage is approximately 25 kV and sparkover occurs at voltage and current levels of 60 kV and 20 mA respectively. Visual observation of the discharge in the large scale laboratory precipitator confirms the nonuniformity of the current distribution on the discharge wires. At the onset of the discharge, a few discrete corona discharge tufts or spots (on the order of 2 to 5 mm in length) appear along the wires. These spots occur at random positions about 15 cm apart along the length of the wires but tend to predominate on the "sides" of the wires closest to the collector plates. Once established the discharge tufts do not move about on the wires since imperfections on the oxidized wires tend to stabilize the tuft locations. As the voltage is increased, more corona spots are produced and the distribution of the spots along the wires is more uniform. In other words, the spacing between adjacent tufts is relatively constant along the total wire length. The number of discharge spots tends to reach a maximum at current levels of about 5 mA (0.28 mA/m^2) which is twenty five percent of the sparkover current. The minimum tuft spacing is on the order of 3 cm. The tufts appear along the entire length of the six discharge wires.

FLOW MEASUREMENTS

The precipitator flow is uniform over 90 percent of the duct height as shown by the upstream and downstream zero current mean velocity profiles of Figures 3 and 4. The number noted on each curve is the vertical distance from the duct centerline. The profiles indicate a fully developed flow with a slight dip in the downstream profile due to the wakes of the unenergized wires. The overall shape of these curves is representative of those obtained at gas speeds of 0.5 and 2.0 m/sec.

The two-dimensional nature of the flow is maintained with corona discharge and thus to avoid redundancy only the centerline profiles are discussed. Figures 5, 6 and 7 are mean velocity profiles, for nominal gas speeds of 0.5, 1.0 and 2.0 m/sec respectively, at current density levels of 0.0, 0.28, 0.56, and 0.84 mA/m^2 (corresponding to currents of 0, 5, 10, and 15 mA). Clearly there is no significant current effect on the mean flow at gas speeds of 1.0 and 2.0 m/sec. A slight flattening of the profiles suggests increased turbulent mixing. The scatter in the mean velocity data of Figure 5 for the low gas speed of 0.5 m/sec is due to the character of the flow itself. The current off flow is laminar but unsteady whereas with a corona discharge, the flow is intermittently turbulent. Thus repeatable measurements are difficult to obtain using reasonable averaging times.

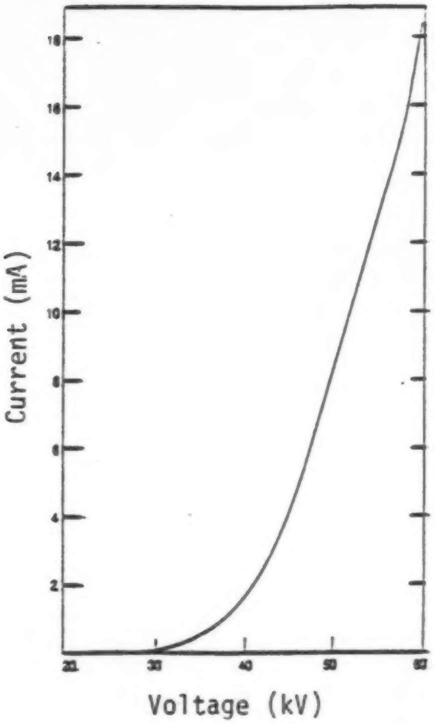

Figure 2. Voltage-Current Characteristics for a Negative Corona Discharge.

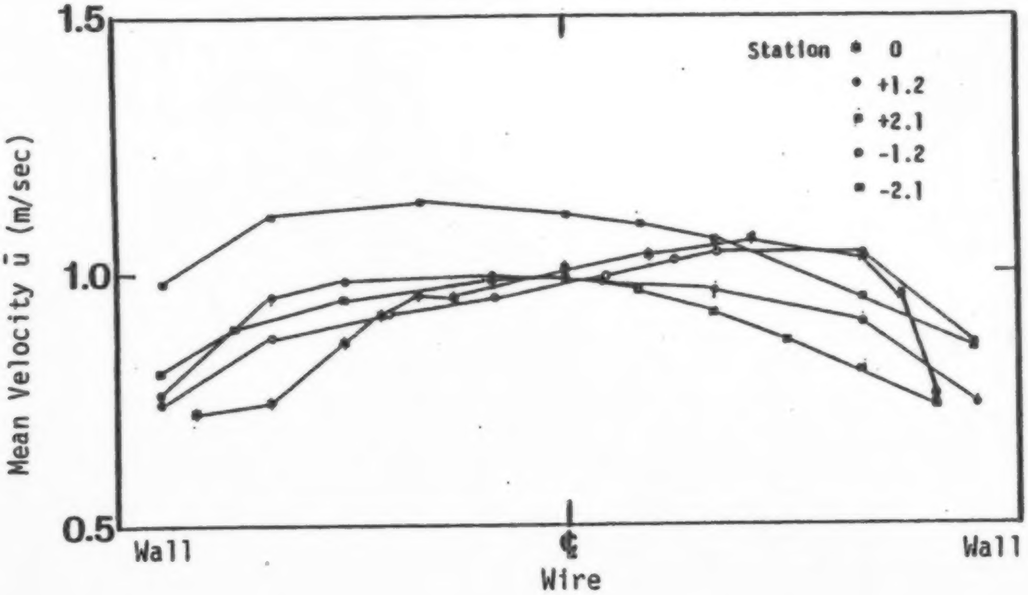

Figure 3. Upstream No Current Mean Velocity Profiles, Gas Speed = 1.0 m/sec.

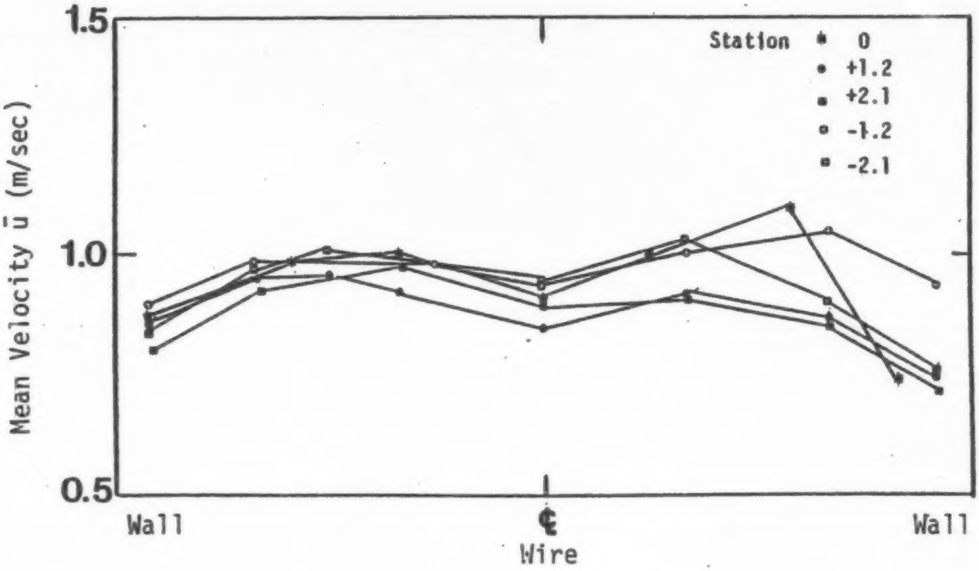

Figure 4. Downstream No Current Mean Velocity Profiles, Gas Speed = 1.0 m/sec.

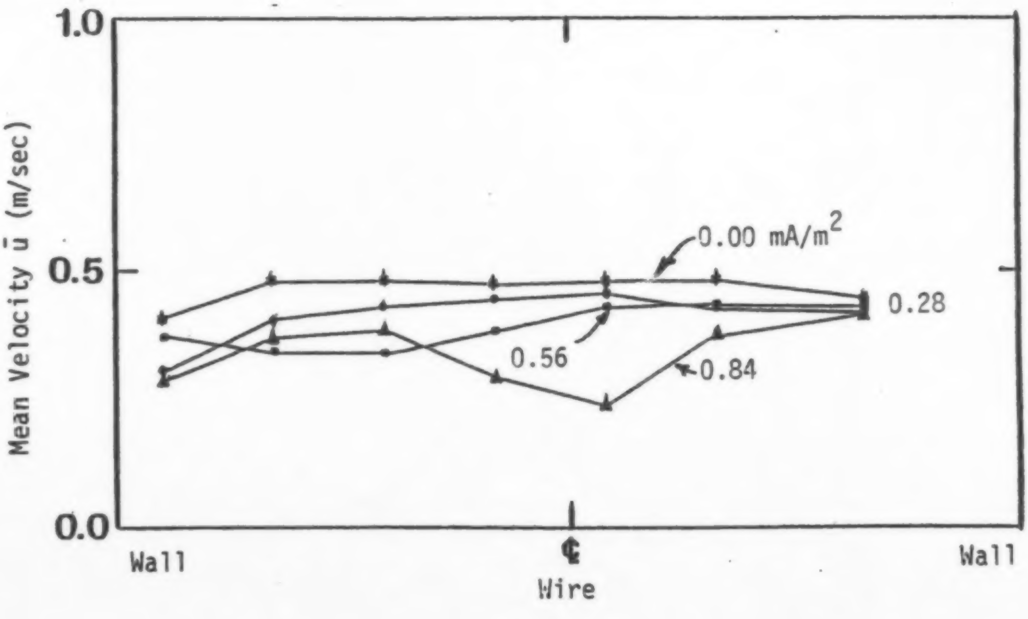

Figure 5. Centerline Mean Velocity Profiles, Gas Speed = 0.5 m/sec.

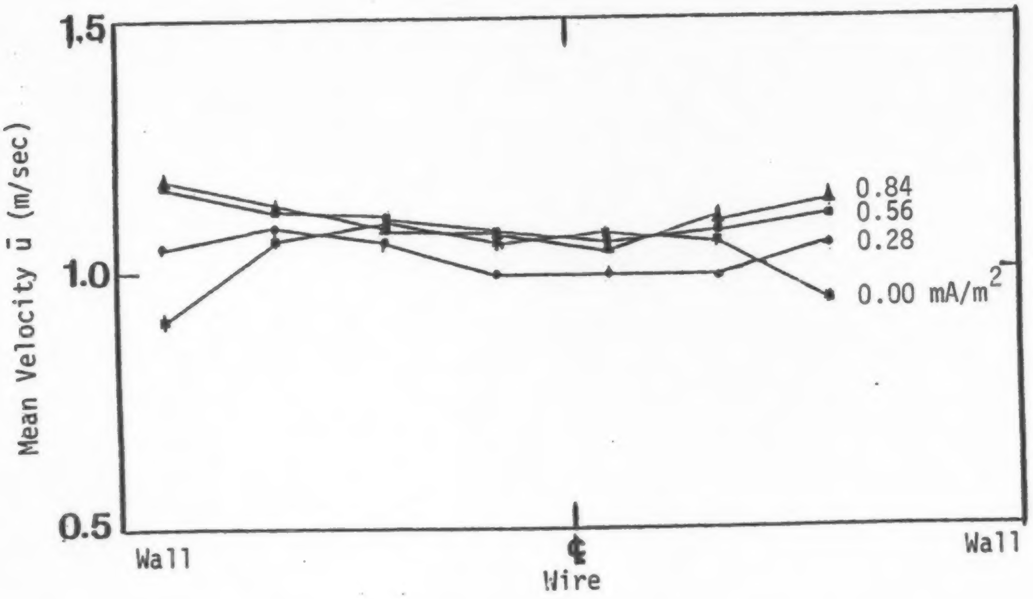

Figure 6. Centerline Mean Velocity Profiles, Gas Speed = 1.0 m/sec.

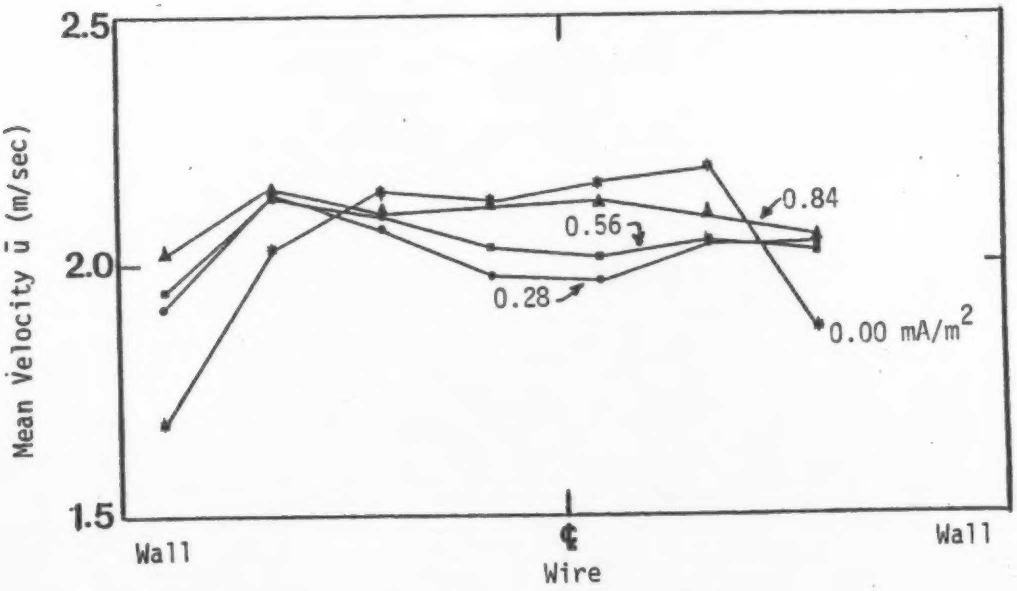

Figure 7. Centerline Mean Velocity Profiles, Gas Speed = 2.0 m/sec.

The turbulence intensity profiles of Figures 8, 9, and 10 indicate that turbulence intensity increases significantly due to the corona discharge at gas speeds of interest for industrial precipitators. The irregularity of the 0.5 m/sec current on profiles is once again a reflection of the intermittent nature of the turbulence. This problem aside, the increase in intensity caused by the discharge is striking. The intermittent behavior of the low speed flow does not persist at gas speeds of 1.0 and 2.0 m/sec. At a flow speed of 1.0 m/sec the intensity increases from 5 to 14% at the duct midpoint. Nearer the walls, the increase in intensity is of less consequence. This can be explained by intense turbulence production in the vicinity of the discharge tufts on the wires. The effect is less dramatic at a gas speed of 2.0 m/sec as shown in Figure 10. Here intensity values are doubled by the corona discharge. Noteworthy in these results is the insensitivity of the data to increasing the current density above 0.28 mA/m^2 of plate area (5 mA).

Some of the more interesting results of this study appear in Figure 11. Centerline turbulence intensities are plotted as a function of current density. This figure highlights the roles of gas speed and current density in determining the magnitude of the electric body force effect on turbulence levels. The data indicate that the effect of the corona discharge becomes more significant as the primary gas speed is reduced and the current density is increased up to a certain point. A remarkable feature of the data is the insensitivity of the turbulence intensity to increasing the current density above 0.3 mA/m^2. The rate of increase of intensity with current level decreases dramatically at this point. This is particularly evident at gas speeds of 0.5 and 1.0 m/sec. This leveling off of intensity occurs at approximately the current density for which the number of discharge tufts is the maximum and the distribution of tufts is most uniform. As the corona current is increased and the discharge tufts become more numerous, the current density distribution becomes more uniform. It is speculated that once the corona discharge becomes more coherent along the wires, any additional electrical energy input results in a more organized secondary flow in the region between the wires and the plates much like that predicted by Yamamoto and Velkoff (6) for a positive uniform discharge. The inability to operate the hot-film probe in the active section of the precipitator is a severe limitation to characterizing the exact nature of any organized secondary flows.

The energy spectra of Figure 12 are those obtained at the tunnel centerline for a nominal gas speed of 1.0 m/sec. The energy spectra indicate the distributions of the turbulent energy among the various frequencies and provide a means of identifying any preferred frequency of the corona generated turbulence. The spectra provide dramatic evidence of the electrical turbulence generation. Like the turbulence intensity results, the spectra do not show any marked differences due to increasing the current density above 0.28 mA/m^2. Compared to the zero current spectrum, the current-on spectra do not indicate a favored frequency but contain additional amounts of energy at all frequencies. Most of the additional energy input is in the lower frequencies corresponding to the large scale turbulent motions. Since turbulent diffusion is a process dominated by large eddies, the spectra suggest that the corona discharge is responsible for increases

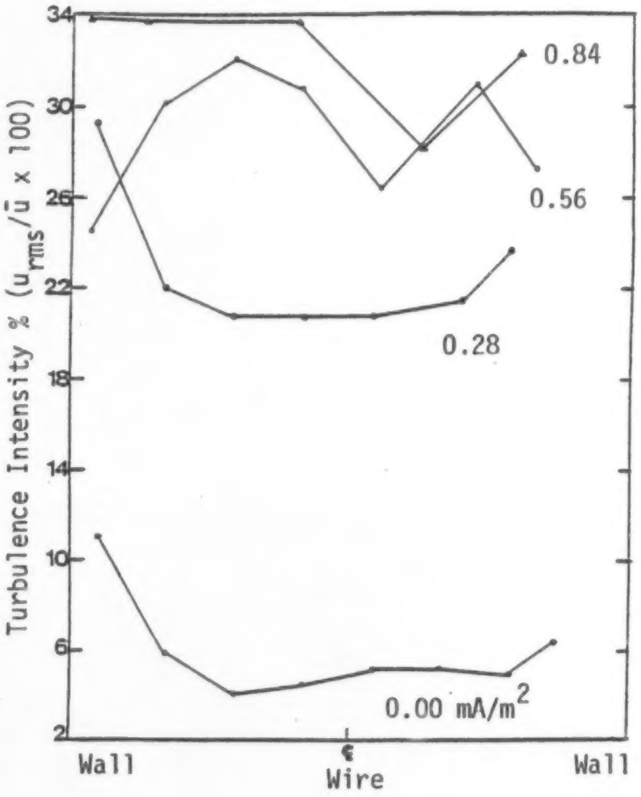

Figure 8. Centerline Turbulence Intensity Profiles, Gas Speed = 0.5 m/sec.

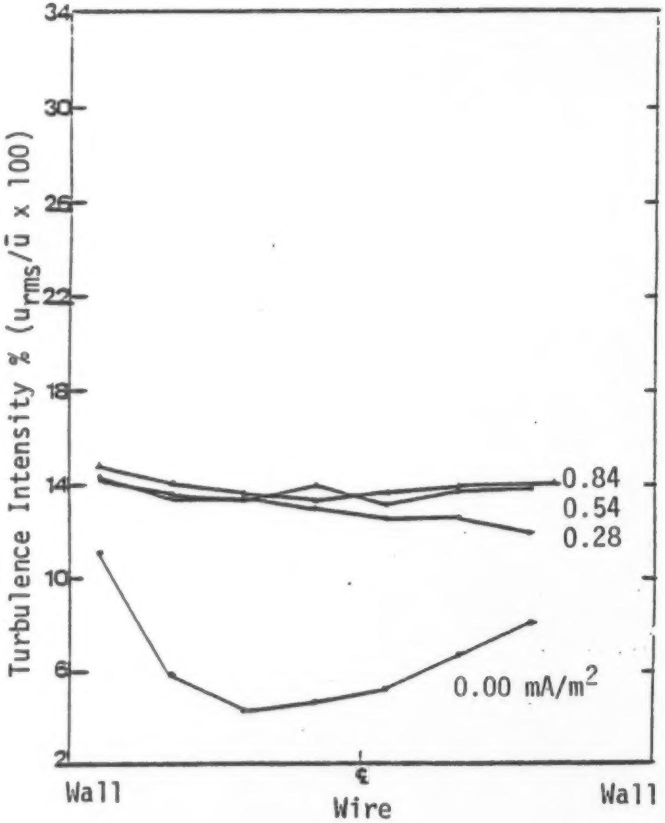

Figure 9. Centerline Turbulence Intensity Profiles, Gas Speed = 1.0 m/sec.

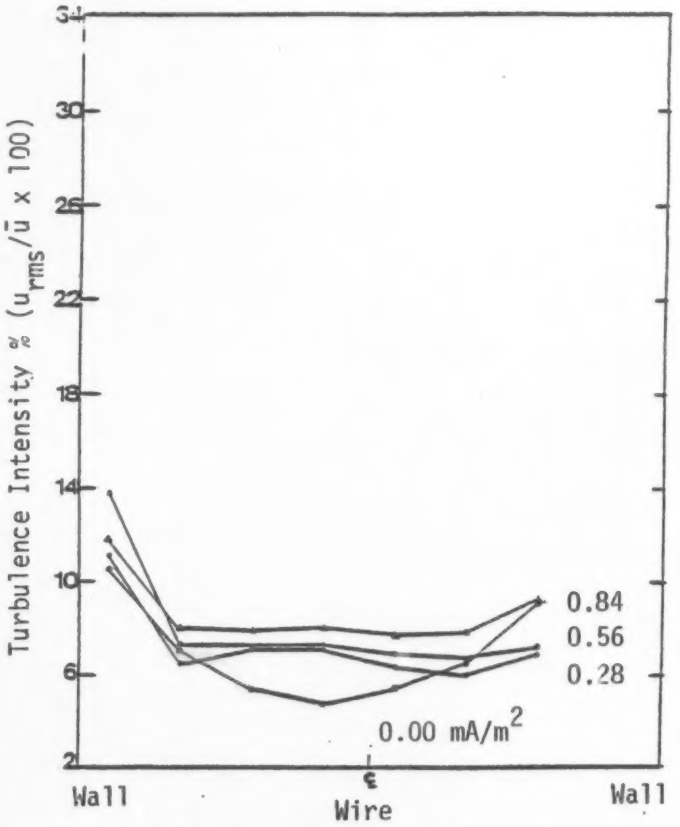

Figure 10. Centerline Turbulence Intensity Profiles, Gas Speed = 2.0 m/sec.

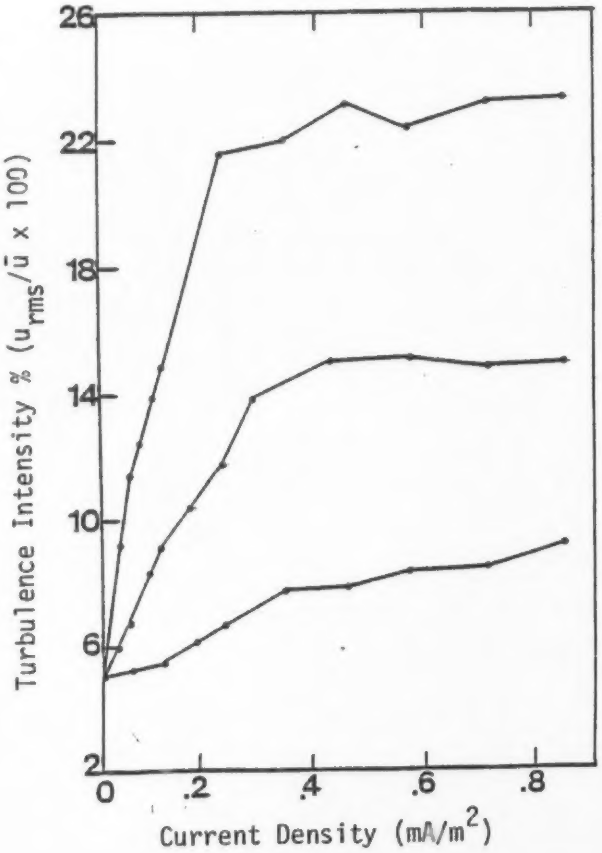

Figure 11. Effect of Corona Discharge Current Density on Centerline Turbulence Intensity.

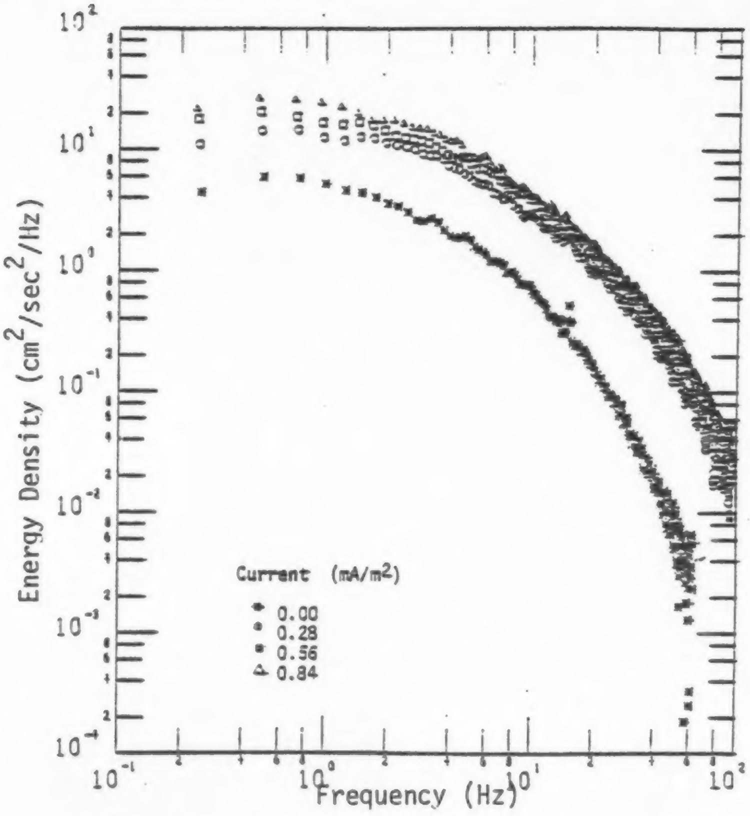

Figure 12. Centerline Energy Spectra,
Gas Speed = 1.0 m/sec.

in turbulent diffusivity. Eulerian length scales (L), which are an estimate of the average turbulent eddy size, were computed from the spectral analysis. With no corona discharge, the length scale is 10.3 cm and with a current density of 0.28 mA/m^2 the length scale is 8.0 cm. An estimate of the increase in particle diffusion can be made from a dimensional estimate of the eddy diffusivity, κ, as u_{rms} L where u_{rms} is the root mean square velocity and L is the integral length scale determined from the spectral analysis. The purely aerodynamic diffusivity is 53 cm^2/sec. At a corona current density of 0.28 mA/m^2, the diffusivity is increased to 79 cm^2/sec.

SUMMARY AND CONCLUSIONS

Measurements of the turbulent flow field in a large scale laboratory precipitator confirm that the inhomogeneous negative corona discharge is responsible for marked increases in turbulence levels over that of the background aerodynamic turbulence. It was found that turbulence was generated throughout the precipitator. The results confirm the experimental results of corona induced turbulence obtained in bench scale model precipitators by Ushimaru et al (9), Leonard et al (7,8), and Kumaran (10) but extend the experimental data to a more realistic geometry and a wider range of operating conditions. The laboratory precipitator has a flow aspect ratio (height/width) of 20. Test conditions included gas speeds from 0.5 to 2.0 m/sec and electrical corona discharge current densities as high as 0.84 mA/m^2 of plate area. The level of turbulence production increases with decreasing gas speed and increasing current density but is not sensitive to increases in current density above 0.28 mA/m^2. The latter result is at first glance quite surprising; however, when viewed in terms of the physical appearance of the discharge is very reasonable. At low current densities the discharge tufts are widely spaced in an irregular pattern on the wires. As the current density is increased, the number of discharge tufts grows and the spacing between tufts decreases and finally stabilizes at a current density of approximately 0.3 mA/m^2. At this point, the electric body force is more uniformly distributed along the length of the wire. In this case the corona discharge may cause a circulating motion on the scale of the wire to wire spacing in addition to increasing turbulence levels.

The implications of these results to the particle collection process in industrial precipitators are significant. At typical operating conditions, a gas speed of 1.0 m/sec and current density of 0.3 to 0.84 mA/m^2, the corona discharge is responsible for a threefold increase in turbulence intensity (from 5 to 15 percent). In addition to the resulting increased turbulent diffusion, any ordered vortical secondary flow which exists at high current densities can significantly disrupt the particle collection process.

Since the turbulent flow in a precipitator arises from both aerodynamic and electric forces, the relative importance of the electrically induced secondary flows and turbulence in commercial precipitators will depend upon the magnitude of other non-ideal effects including poor aerodynamic design. Wire-plate precipitators are used in many applications and are operated over a wide range of conditions. Thus it is nearly impossible to project in a general way the significance of corona induced secondary flows and turbulence. But it is important to realize that the turbulence created by the electric body force is in addition to whatever aerodynamic turbulence is present and will increase turbulent diffusion. Recognizing that turbulent diffusion and secondary vortical motions will always oppose the migration of charged particles to the collection plates, a reduction in these effects will increase precipitator efficiency.

REFERENCES

1. Davidson, J. H., Secondary Flows and Turbulence in Electrostatic Precipitators. Ph.D. Dissertation, Duke University, Durham, N.C., 1984.

2. Shaughnessy, E. J., Davidson, J. H., and Hay, J. C., The Fluid Dynamics of Electrostatic Precipitators: Effects of Electrode Geometry. Fifth Symposium on the Transfer and Utilization of Particulate Control Technology, Kansas City, Missouri. August 27-30, 1984.

3. Ramadan, O. E., and Soo, S. L., Electrohydrodynamic Secondary Flow. Phys. Fluids 12: 1943, 1969.

4. Robinson, M., Effects of the Corona Discharge on Electric-Wind Convection and Eddy Diffusion in an Electrostatic Precipitator. ERDA Health and Safety Laboratory Report, HASL-301, 1976.

5. Yabe, A., Mori, Y., and Nijikate, K., EHD Study of the Corona Wind Between Wire and Plate Electrodes. AIAA Journal 16: 340, 1978.

6. Yamamoto, T., and Velkoff, H. R., Electrohydrodynamics in an Electrostatic Precipitator. J. Fluid Mech. 108: 1, 1981.

7. Leonard, G. L., Mitchner, M., and Self, S. A., Precipitation from Turbulent Flows. Proc. of the Intl. Conf. on Elec. Precip., Monterey, California, 208, 1981.

8. Leonard, G. L., Mitchner, M., and Self, S. A., An Experimental Study of the Electrohydrodynamic Flow in Electrostatic Precipitators. J. Fluid Mech. 127: 123, 1983.

9. Ushimaru, K., Butler, G. W., and Milov soroff, P., An Experimental and Theoretical Investigation of Electrostatic Precipitators. Flow Research Report #219, Flow Industries, Kent, Washington, 1982.

10. Kumaran, A. R., Aspects of the Fluid Mechanics of Electrostatic Precipitators. HTGL Report No. 15-83-TR, 1983.

11. Kumaran, A. R., Leach, R., and Self, S. A., Anomalous Readings from Hot-Wire Anemometers in Strong Electric Fields, TSI Quarterly, July-Sept., 9, 1983.

12. Davidson, J. H., and Shaughnessy, E. J., Mean Velocity and Turbulence Intensity Profiles in a Large Scale Laboratory Precipitator. ASME Joint Power Generation Conference, Toronto, Canada, September, 1984.

13. Bendat, J. S., and Piersol, A. G., Random Data: Analysis and Measurement Procedures, (New York: Wiley-Interscience, 1971), p. 317.

ON THE STATIC FIELD STRENGTH IN WIRE-PLATE ELECTROSTATIC PRECIPITATORS WITH PROFILED COLLECTING ELECTRODES BY AN EXPERIMENTAL METHOD

by: C. E. Akerlund
Flakt AB
Vaxjo, Sweden

ABSTRACT

To introduce the highest possible energy input in an electrostatic precipitator, the field distribution at the collecting plate must be as even as possible. It must be realized, however, that there are peaks in the field distribution at such exposed points as stiffening elements. Sparkover is most probable to occur from these points.

In this report the static field at profiled collecting electrodes has been analyzed using a combined conductive paper - computer aided design technique. The presented results verify that the field strength rises significantly in local areas.

Therefore investigations of the field distribution at collecting electrodes of new design are of great importance, if sparking at too low a voltage is to be avoided.

INTRODUCTION

In an electrostatic precipitator the transformer/rectifier sets are normally current-regulated. To obtain maximum charging and precipitation of the dust, the current is gradually increased up to a level where sparkover starts. However, it is the field strength at the sparkover point - not the current level - which is of importance for the initiation of the sparkover.

The critical field strength is highly dependent on the properties of the gas and the dust - for example, the gas composition, gas temperature, gas velocity and the resistivity of the dust. But if the mechanical design of the collecting electrodes and the discharge electrodes with their frame is unfavorable, sparkovers occur in exposed points even at low charging current and during dust-free operations. Uniform field distribution over the collecting electrode must be secured to avoid sparking at too low a voltage.

The calculation of current-voltage characteristics and the electric field in wire-plate precipitators has been dealt with by many authors (1), (2), (3), (4). These methods are presented under the presumption that the collecting plates are plane.

A light and inexpensive design of the discharge and collecting system always includes stiffening elements in the form of beads or other projecting parts. A stiffener with an inexpedient shape can cause local magnification of the electric field well above the sparkover limit.

A numerical calculation of the field in the region close to earthed profiled collecting electrodes where the potential is sufficiently high for the initiation of sparkovers is consuming considerable time. A practical method will more easily provide a solution with sufficiently reliable accuracy.

Vitkovitch (5) has presented different numerical, graphical and experimental methods in an extensive survey. Among numerical techniques, the method of finite elements is the most important. It requires, however, comprehensive computer programming. Graphical field plotting requires a minimum of equipment but the work can be very laborious if the object has a complex geometrical shape and if high accuracy is required. The electrolytic tank can be used for two-and three-dimensional cases of Laplacian as well as Poissonian fields but requires extensive laboratory resources. In addition, the method is not very flexible, if changes in the object's configuration are desired.

The combined conductive sheet - computer aided design technique proposed in this paper is very attractive, due to its simplicity, although it is limited to two-dimensional cases. It can be used for both static and space-charge fields. This investigation covers fields without space charge.

EQUIPMENT

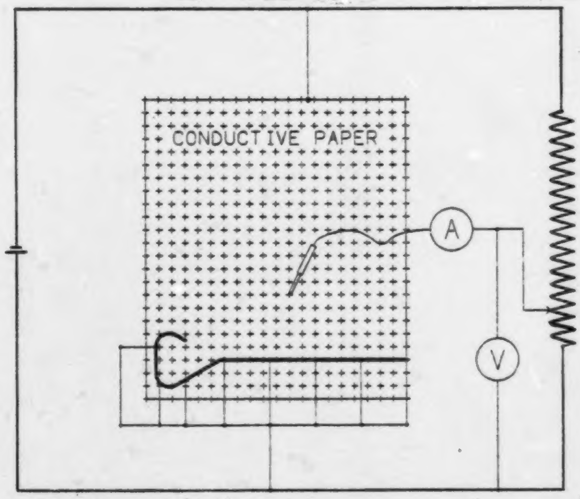

Figure 1. Equipment

Figure 1 shows the equipment used. The conductive paper has a graphite coating. The resistivity of the paper is about 1250 ohms per square. A variation of 3 % has been found from paper to paper. The paper is slightly anisotropic but the anisotropy is so slight - about 1 % - that it can be overlooked.

The model is painted on the paper with a conducting paint containing a high percentage of finely divided silver. After 24 hours curing in ambient temperature, the resistivity is 0.11 ohms per square. Several contacts were attached to the collecting electrode. No further action is required to ensure that the full length of the collecting plate has the same potential.

TECHNIQUE

Equipotentials can be plotted in two different ways. One method is to find a number of points having the same potential and to draw a curve through these points. In areas where the shape of the equipotential is more difficult to predict, many points must be tested with the probe until the equipotential point is determined. The searching takes much time. It was also discovered that the field was disturbed by a large number of closely placed holes made with the probe.

These negative experiences led to the use of another procedure. A grid of points was drawn on the paper. The spacing of the grid was adapted to the complexity of the equipotential's shape. The potential was then measured at every point of the grid. Assuming that the potential varies from a measured value in direct proportion to the distance from the measuring point, the coordinates of the equipotential line were calculated. These coordinates were fed into a computer-aided design system and the lines were drawn using a spline function. The function is a parametric spline fitting through all given points that maintains continuity up to the second derivative. Each segment is described as a cubic function.

The field strength increases rapidly in the vicinity of corners and sharp edges. Consequently, the measuring grid must be very fine in this area and the measurements have to be made in several steps.

As shown in figure 1, a complete model was first painted in such a scale that the silver-painted electrode was given a minimum width of 2.5 mm to ensure an equal potential along the silver string. In this model equipotential lines were drawn; one of these, 4 kV, was drawn using a very fine grid in order to obtain a high degree of accuracy. (See figure 2.)

A second model was painted in much larger scale. (See figure 3.) A large scale was used not only because the grid must be fine at certain areas. It was also discovered that it is most difficult to accurately measure the very low voltage close to the silver string. Consequently, no measurements were made closer to the silver string than about 4 mm in actual scale.

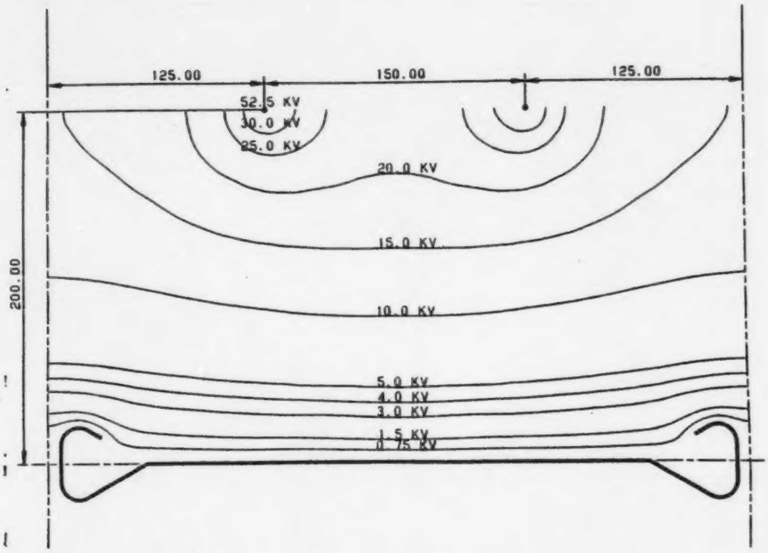

Figure 2. Emitting and collecting electrodes with equipotential lines.

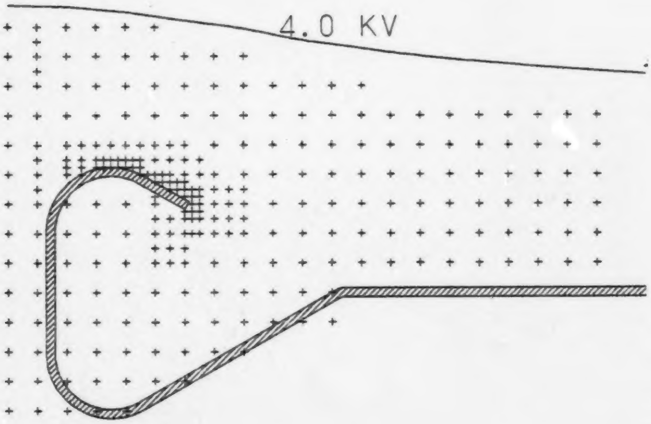

Figure 3. Enlarged section of figure 2.

A voltage difference of about 28 V was used between emitting and collecting electrodes in the models. Since the feed point of current was a silver paint with a diameter of only about 5 mm, the voltage had to be limited to about 30 V to prevent burn in the paper.

The use of a computer-aided design system for the drawing work is a prerequisite for a successful outcome. The technique to make the measurements in several steps in gradually increased scale requires an exact reproduction of the model and the equipotentials, the latter being defined by a great number of coordinates in the spline function.

An error calculation shows that the true value of the field strength with 95 % probability lies within a range of ± 3 % from the mean value.

APPLICATION

Two profiled collecting electrodes were analyzed at different voltage distances, i.e. the distances between emitting and collecting electrodes. The field strengths refer to the corona starting voltages shown in table 1.

TABLE 1. CORONA STARTING VOLTAGES IN KV AT DIFFERENT DISTANCES BETWEEN EMITTING AND COLLECTING ELECTRODES.

Voltage distance mm	Corona starting voltage kV
150	43.0
200	52.5
250	61.0

Let us first revert to figure 2. In the region from the emitting electrodes, and down to about 20 kV, the equipotentials are scarcely affected by the geometrical form of the plate's end profile. Close to the plate the equipotentials follow the profile and "sneak" around its edge. This is further illustrated in figure 4.

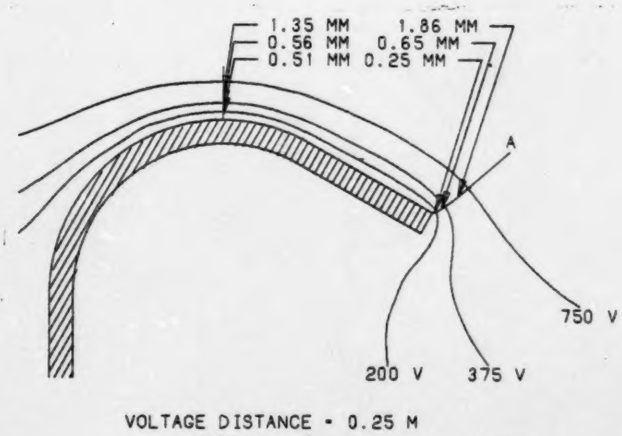

Figure 4. Electric field at profiled collecting electrode.

The field strength at the center of the profiled plate midway between two emitting electrodes (figure 2) is about 137 kV/m for the three voltage distances of 150 mm, 200 mm and 250 mm. Values calculated using both references (1) and (3) agree with this value.

Totally different conditions will be found at the end profile. Table 2 shows the measured field strength along two field lines, one at the top and one at the edge of the profile. (See figure 4.) The field strengths are calculated using reference (6) and the voltages and distances shown in figure 4.

TABLE 2. FIELD STRENGTH KV/M AT TOP AND EDGE OF END PROFILE.

Voltage distance mm	Field strength kV/m					
	at top of profile, calculated as average between			at edge of profile, calculated as average between		
	0-200 V	0-375 V	0-750 V	0-200 V	0-375 V	0-750 V
150	320	290	290	400	220	140
250	410	380	370	530	280	180
Magnification with increased voltage distance	1.3	1.3	1.3	1.3	1.3	1.3

As shown in table 2, the field strength at the top of the profile increases very moderately, about 10 %, if calculated as an average up to the 200 V potential line, compared with a calculation up to the 750 V line. Totally different conditions will be found at the edge. Since the profile has an open part, the 750 V line will not follow the plate profile but directs itself towards the plane part of the plate and moves away from the edge.

Contrary to the 750 V line, the 200 V line "sneaks" around the edge and the field calculated up to the 200 V line is three times higher than the field calculated up to the 750 V line. This illustrates the necessity to base the field strength calculation on potential lines very close to the critical point.

Higher field-strength values would undoubtedly result if an equipotential line had been drawn still closer to the plate than the 200 V line. However, it should be noted that, according to Paschen's law, the minimum voltage is 300 V for discharge in air between two plane electrodes. Thus, in this case as well, large fields for voltages less than 200 V may not initiate breakdown.

If the voltage distance is increased to 250 mm, the field at the top and edge is 30 % higher than the field at the 150 mm voltage distance. (See table 2 and figure 5.) As mentioned above, no corresponding increase is found at the center of the plate.

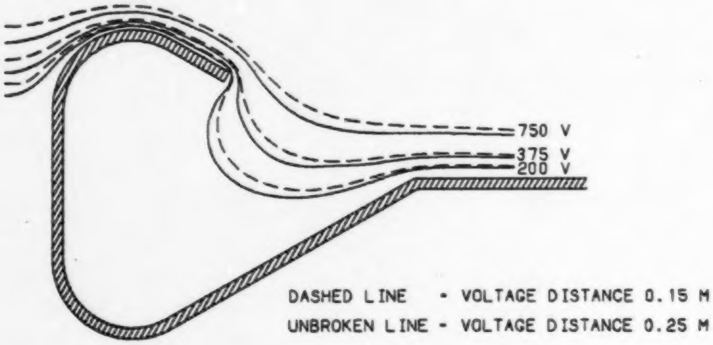
750 V
375 V
200 V
DASHED LINE • VOLTAGE DISTANCE 0.15 M
UNBROKEN LINE - VOLTAGE DISTANCE 0.25 M

Figure 5. Electric field at 150 mm and 250 mm voltage distance.

Table 3 shows the relation between the field strength at the edge of the profile, point A, figure 4, and the center of the plate. The field strength at the edge of the profile is almost four times the field at the center of the plate for a voltage distance of 250 mm.

TABLE 3. RELATION BETWEEN FIELD STRENGTH AT EDGE OF PROFILE AND CENTER OF PLATE.

Voltage distance mm	Relation between field strength at edge of profile and center of the plate, calculated as average between		
	0-200 V	0-375 V	0-750 V
150	3.0	1.6	1.0
250	3.9	2.0	1.3

Another collecting electrode design is shown in figure 6. The trend in precipitator design development is towards wider collecting plates and this design is available in large widths. A fairly wide plate needs one or more stiffeners when a small plate thickness is used. Such stiffeners can be inexpensive and made easily in the roll-forming operation. A typical stiffener design is shown in the middle section of the plate.

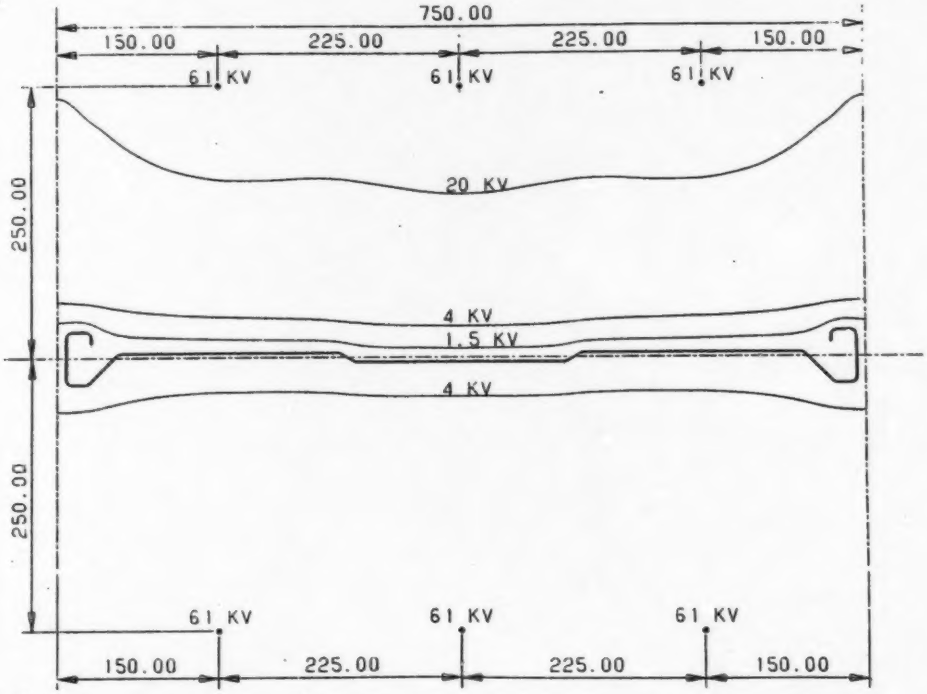

Figure 6. Emitting and collecting electrode with equipotential lines.

As figure 7 shows, equipotentials close to the end profile are affected by the profile but they do not go around the edge of the profile as shown in figure 5.

The field strength along the four different lines A, B, C and D of the collecting electrode have been calculated using reference (6). (See figure 7 and 8.) Line A is on the open side of the end profile, while lines B and C are on the closed side. Line D is at the stiffening bend.

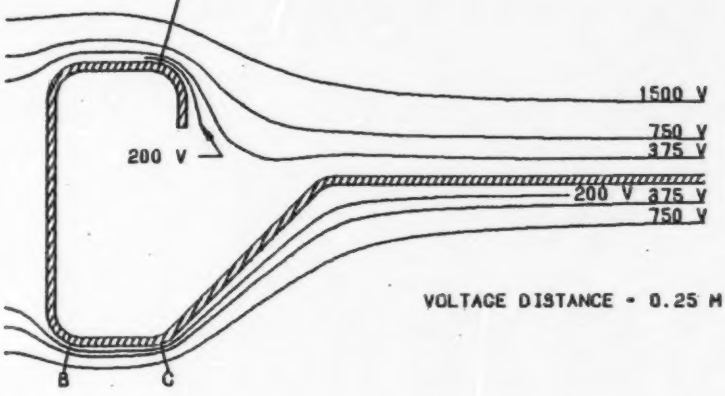

Figure 7. Enlargement of the end section in figure 6.

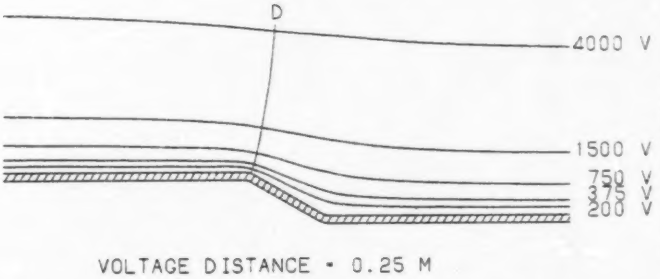

Figure 8. Enlargement of the middle section in figure 6.

TABLE 4. FIELD STRENGTH AT POINTS A, B, C AND D IN FIGURE 7 AND 8.

Voltage distance mm	Field strength kV/m, calculated as average between 0-200 V at the lines				Relation between field strength at different points and center of plate			
	A	B	C	D	A	B	C	D
150	220				1.8			
250	300	260	320	250	2.4	2.1	2.5	1.9
Magnification with increased voltage distance	1.4							

As seen in table 4, the field strength is higher at point C than at point A. A close look at the equipotential lines verifies this observation. At the closed side of the profile, the lines follow the plate profile and come closest to the plate at the bend. On the open side of the profile, the lines leave the upper corner and cross obliquely down to the plane part of the plate, while the plate at the upper corner is bent 90 degrees.

The stiffening bend represents a very moderate change in the collecting electrode's topography and may appear to be fairly harmless from the point of view of field magnification. It should be noted, however, that the field strength at the bend is nearly twice as high as that at the center of the plate.

SUMMARY

The proposed method of investigation has been applied to collecting electrodes which have been used for many years in electrostatic precipitators with high collecting efficiency. The results confirm, however, that a not negligible rise in the field distribution exists in local areas of the collecting electrode. Thus, thorough investigations of the field distribution along collecting electrodes of new design are of great importance if sparking at too low a voltage is to be avoided. The combined conductive paper - computer aided design technique used in this investigation is recommended because of its simplicity.

The work described in this paper was not funded by the U.S. Environmental Protection Agency and therefore the contents do not necessarily reflect the view of the Agency and no official endorsement should be inferred.

ACKNOWLEDGEMENTS

The author wants to thank Professor Stig Lundquist, head of the Institute of High Voltage Research, Uppsala, Sweden, for his most valuable discussions and guidance. I am greatly indebted to many colleagues in the Electrostatic Precipitator and Data Processing Departments of Flakt Industri AB who have contributed their experience.

REFERENCES

1. J. R. Mc Donald et. al. A mathematical model for calculating electrical conditions in wire-duct electrostatic precipitation devices. Journal of Applied Physics, Vol 48, No. 6, June, 1977, pp. 2231 - 2243.

2. P. Cooperman. A theory for space-charge-limited currents with application to electrical precipitation. AIEE, (1960) pp. 47 - 50.

3. S. Sekar et. al. On the prediction of current-voltage characteristics for wire-plate precipitators. Journal of Electrostatics, 10, (1981). pp. 35 - 43.

4. J. L. Davis and J. F. Hoburg. Wire-duct precipitator field and charge computation using finite element and characteristics methods. Journal of Electrostatics, 14, 1983, pp 187 - 199.

5. D. Vitkovitch. Field Analysis. D. Van Nostrand Company Ltd., London, 1966.

6. H. Prinz. Hochspannungsfelder. R. Oldenbourg, München, 1969.

THE FLUID DYNAMICS OF ELECTROSTATIC PRECIPITATORS: EFFECTS OF ELECTRODE GEOMETRY

by: E. J. Shaughnessy, J. H. Davidson,† and J. C. Hay
Department of Mechanical Engineering and
Materials Science
Duke University
Durham, North Carolina 27706

ABSTRACT

The role of the electric body force in the generation of secondary flows and turbulence in precipitators is poorly understood at present, despite the fact that these disturbances are thought to be detrimental to precipitator performance. This paper undertakes a fundamental analysis of the problem using the Navier-Stokes and reduced Maxwell equations. It is shown that the rotational component of the current density causes vorticity production in the gas and is therefore the source of secondary flows and turbulence. When the current density is irrotational, as in a cylindrical precipitator, the electric body force causes a change in the pressure distribution but has no effect on the velocity field. Since the current density distribution is determined by the electrode geometry alone, the electrodes should be designed to minimize the rotational component of the current density and thus reduce gas flow disturbances.

This paper has been reviewed in accordance with the U.S. Environmental Protection Agency's peer and administrative review policies and approved for presentation and publication.

I. INTRODUCTION

There is increasing evidence that secondary flows and turbulence generated by corona discharge influence particle transport and lower the efficiency of precipitators (Williams and Jackson (1); Robinson (2,3); Cooperman (4); Soo and Rogers (5); Feldman *et al* (6); Pyle *et al* (7,8); and Leonard *et al* (9,10,11)). While secondary flows have been described by Ramadan and Soo (12), Yamamoto *et al* (13), Robinson (14), and Ushimaru *et al*

---

†Current address: Mechanical and Aerospace Engineering, University of Delaware.

(15) for the wire-plate precipitator with positive corona, it appears that negative discharge produces turbulence. The recent experimental studies by Ushimaru et al (15), Leonard et al (10,16), Kumaran (17) and Davidson (18) show that the discharge increases the turbulence intensity substantially at gas speeds of 1 m/sec. Perhaps more intriguing is the suggestion (18) that higher current levels generate both turbulence and secondary flows.

Since there is little doubt that both of these processes limit the maximum collection efficiency, identifying the source of these disturbances is the first step towards their elimination. The goal of this paper is to provide a more complete understanding of the electrohydrodynamic interactions in particle free precipitator gas flows. By examining the governing electrohydrodynamic equations, it is shown that the rotational component of the current density causes the vorticity production which generates secondary flows and turbulence. Flippen's (19) study of irrotational electrode geometries and Hay's (20) perturbation solution for the wire-plate precipitator are particularly helpful in revealing the role of electrode geometry in electrical vorticity production.

In turbulent flow the mean and fluctuating rotational components of current density are both capable of generating turbulence. Current density fluctuations, which are probably insignificant with DC energization, may be a very significant source of turbulence when the discharge is pulsed. These results suggest that a uniform planar discharge electrode would cause less flow disturbance than wires.

II. ELECTROHYDRODYNAMIC THEORY

The equations describing the electrohydrodynamics of a precipitator gas flow in the absence of particles are Ohm's law, a set of reduced Maxwell's equations, and the classical fluid mechanics equations. The applicable electrodynamic equations are:

$$J_i = \beta|\rho_c|E_i \qquad (2.1)$$

$$\epsilon \frac{\partial E_i}{\partial x_i} = \rho_c \qquad (2.2)$$

$$E_i = -\frac{\partial \phi}{\partial x_i} \qquad (2.3)$$

$$\frac{\partial J_i}{\partial x_i} = 0 \qquad (2.4)$$

where J_i is the current density, β is the ion mobility, ρ_c is the ionic space charge density, ϵ is a constant gas permittivity, E_i is the electric field, and ϕ is the electric potential. The basic equations for the incompressible flow field are continuity:

$$\frac{\partial u_i}{\partial x_i} = 0 \tag{2.5}$$

and the Navier-Stokes equation with an electric body force term:

$$\rho\left[\frac{\partial u_i}{\partial t} + u_j \frac{\partial u_i}{\partial x_j}\right] = - \frac{\partial p}{\partial x_i} + \mu \frac{\partial^2 u_i}{\partial x_j{}^2} + \rho_c E_i \tag{2.6}$$

where ρ is the fluid density, u_i is the velocity, p is the pressure, and μ is the absolute viscosity. The electric body force per unit volume on gases exposed to corona discharge may be represented as J_i/β for positive corona discharge and as $-J_i/\beta$ for the case of negative corona discharge. In the theoretical development that follows, the discharge is assumed to be negative.

An important feature of this theoretical formulation of the problem is that the electrical equations may be solved independently of the equations governing the flow. The reverse is not true. As a consequence of the partial uncoupling of the equations, an expression for the electric body force can be obtained without regard to the flow conditions. Once the electric body force is known, equations (2.5) and (2.6) may then be solved for the velocity u_i and pressure p.

It is useful to express the body force $-J_i/\beta$ in terms of its scalar and vector potentials ψ and R_i respectively by

$$-J_i/\beta = - \frac{1}{\beta} \left(\frac{\partial \psi}{\partial x_i} + \epsilon_{ijk} \frac{\partial R_k}{\partial x_j}\right). \tag{2.7}$$

Substituting this expression into the Navier-Stokes equation (2.6) yields

$$\rho\left[\frac{\partial u_i}{\partial t} + u_j \frac{\partial u_i}{\partial x_j}\right] = - \frac{\partial P}{\partial x_i} + \mu \frac{\partial^2 u_i}{\partial x_j{}^2} - \frac{1}{\beta} \epsilon_{ijk} \frac{\partial R_k}{\partial x_j}. \tag{2.8}$$

The first term in expression (2.7) for the electric body force has been absorbed into a modified pressure P where $P = (p - p_0) + (\psi - \psi_0)/\beta$. The constants p_0 and ψ_0 are datum values and $p + (\psi_0 - \psi)/\beta$ is the pressure distribution which would exist if the fluid was at rest in the electric body force field. The irrotational component of the body force, $-\frac{1}{\beta}\frac{\partial \psi}{\partial x_i}$, no longer appears in the equation of motion except as a modified pressure. Thus the irrotational component of the electric body force has no effect on the velocity field but merely affects the pressure distribution in the gas.

Very little is known of the exact nature of the current density in most geometries and in particular for a negative corona discharge. Numerical solutions for uniform discharge in the wire-plate geometry (Leutert and Bohlen (21); McDonald et al (22); Lawless and Sparks (23); Yamamoto and Velkoff (24); and Hoburg and Davis (25)) provide no information as to how the current density is divided among its rotational and irrotational components. However, the recent work of Hay (20) on the single wire with positive corona discharge does provide some insight into the composition of the electric body force in the wire-plate geometry. His perturbation solution of the governing electrodynamic equations confirms that J_i is always rotational. The solution shows that at very low current levels the rotational component of J_i is small compared to the irrotational component. At corona current levels comparable to those of electrostatic precipitators, however, the rotational component of the current density dominates the solution.

An examination of the vorticity equations provides further insight into the role of the rotational current density in affecting the gas flow. The vorticity equations are obtained by taking the curl of the continuity and Navier-Stokes equations (2.5 and 2.6). The equations are

$$\frac{\partial \omega_i}{\partial x_i} = 0 \tag{2.9}$$

and

$$\rho\left[\frac{\partial \omega_i}{\partial t} + u_j \frac{\partial \omega_i}{\partial x_j}\right] = \mu \frac{\partial^2 \omega_i}{\partial x_j{}^2} + \omega_j \frac{\partial u_i}{\partial x_j} - \frac{1}{\beta} \varepsilon_{ijk} \frac{\partial J_k}{\partial x_j} \tag{2.10}$$

where $\omega_i = \varepsilon_{ijk} \frac{\partial u_k}{\partial x_j}$ is the vorticity. This is the classical vorticity equation with an added vorticity production term involving the current density. Since the current density term is the curl of J_i, an electric field with a rotational current density component produces vorticity in the interior of the fluid. This vorticity production is the source of the secondary flows described by Yamamoto and Velkoff (13) and Ramadan and Soo (12) for a uniform discharge.

The electric vorticity production term may be decomposed by taking the curl of equation (2.1). The result is

$$- \frac{1}{\beta} \varepsilon_{ijk} \frac{\partial J_k}{\partial x_j} = \varepsilon_{ijk} \left(\frac{\partial \rho_c}{\partial x_j} E_k + \rho_c \frac{\partial E_k}{\partial x_j}\right). \tag{2.11}$$

The second term on the right hand side of this expression is zero by equation (2.3). Thus the curl of the electric body force may be written as

$$- \frac{1}{\beta} \varepsilon_{ijk} \frac{\partial J_k}{\partial x_j} = \varepsilon_{ijk} \frac{\partial \rho_c}{\partial x_j} E_k. \tag{2.12}$$

This expression is zero in two circumstances. The first is whenever the space charge density is uniform, which is physically unrealistic. The second situation for which there is no electrical vorticity production is when the electric field lines are everywhere normal to contours of constant space charge density. Flippen (19) has shown that this is possible for three geometries provided the corona discharge is uniform on one electrode. These geometries are concentric spheres, concentric cylinders, and parallel plates. For all other geometries, and these three if the discharge is nonuniform, the current density has a rotational component. Thus the electrode geometry and uniformity of the discharge completely define the degree to which the electric body force perturbs the gas flow.

Before discussing the mechanisms by which the electric body force produces turbulence in precipitators, it is useful to nondimensionalize the Navier-Stokes equation using the scales I, A, U, and L for current, plate area, velocity, and plate-to-plate spacing. The result is

$$\frac{\partial u_i}{\partial t} + u_j \frac{\partial u_i}{\partial x_j} = - \frac{\partial p}{\partial x_i} + \frac{1}{Re} \frac{\partial^2 u_i}{\partial x_j^2} - \frac{1}{F^2} J_i \qquad (2.13)$$

where $Re = \rho UL/\mu$ is the Reynolds number and $F = [\frac{\rho U^2 \beta A}{IL}]^{1/2}$ is the electric Froude number. The parameter $1/F^2$ is a measure of the ratio of the electric body force to the inertial force. Using values representative of fly ash precipitators ($U = 1$ m/sec, $\rho = 0.55$ kg/m^3, $\mu/\rho = 0.58$ cm^2/sec, $\beta = 2.1 \times 10^4$ m^2/volt-sec, $I/A = 4 \times 10^{-4}$ Amp/m^2 of plate area, $L = 0.25$ m) leads to estimates for the Reynolds and electric Froude numbers of $Re = 4310$, $F = 1.07$ for a precipitator operating at 375°C: at 27°C, $Re = 15,000$ and $F = 1.58$.

These estimates allow us to draw several conclusions regarding the fluid dynamics of wire-plate precipitators. Since Hay (20) has shown that the body force is predominantly rotational in the wire-plate geometry, a ratio of rotational electric body force to inertial force of order one indicates that there is a significant perturbation of the gas flow by the electric body force. It is worth noting that parallel plate flow at these Reynolds numbers exhibits relatively low values of eddy viscosity and diffusivity in the absence of corona discharge, (26). Moreover, at these speeds the flow is just above the Reynolds number at which transition occurs from laminar to turbulent flow (18). Two conclusions may be drawn from this. First, mechanical devices in the precipitator inlet are relatively ineffective in smoothing out nonuniform inlet velocity profiles. And second, particle transport by electrically generated secondary flows and turbulence may be more significant than the transport due to aerodynamic sources of turbulence.

III. TURBULENCE

The interaction of the electric body force with turbulent flow is described by the pertinent turbulence equations. The first step in the analysis is to decompose the instantaneous flow variables into their mean and fluctuating components:

$$u_i = \bar{u}_i + u'_i \qquad (2.14)$$

$$p = \bar{p} + p'$$

and

$$J_i = \bar{J}_i + J'_i$$

where mean and fluctuating values are denoted by an overbar and a prime respectively. Since EHD theory assumes that the instantaneous electric body force and current density are completely independent of the fluid flow, the source of a fluctuating current density must be electric in origin. With DC energization there are a number of possible causes of current density fluctuations. Among the most obvious of these are Trichel pulses and the instabilities often noted with negative corona discharge. Although positive corona discharge on a wire may produce a uniform discharge, negative corona is usually characterized by a series of localized discharge tufts which in some circumstances may move about the wire. Sparkover is another source of current fluctuations as are vibrations and galloping motions of the discharge wires themselves. With pulsed energization, there is obviously a substantial current density fluctuation which cannot be neglected. The turbulence equations to follow are developed assuming that fluctuations in the current density exist.

Following the normal procedure, the decomposed quantities of equation (2.14) are substituted into the continuity (2.5) and Navier-Stokes equations (2.6) and time averaged to yield the classical Reynolds equations for the mean motion:

$$\frac{\partial \bar{u}_i}{\partial x_i} = 0 \qquad (2.15)$$

and

$$\rho\left[\frac{\partial \bar{u}_i}{\partial t} + \bar{u}_j \frac{\partial \bar{u}_i}{\partial x_j}\right] = - \frac{\partial \bar{p}}{\partial x_i} + \mu \frac{\partial^2 \bar{u}_i}{\partial x_j^2} - \rho \frac{\partial}{\partial x_j} (\overline{u'_i u'_j}) - \frac{1}{\beta} \bar{J}_i. \qquad (2.16)$$

From the previous discussion, it can be seen that a mean current density with a non-zero rotational component will perturb the mean velocity field. The earlier discussion on the significance of geometry in determining whether or not J_i is rotational also apply to the mean current density J_i.

An electrical modification of the mean flow is normally referred to as a corona wind. The magnitude of the corona wind will depend on the magnitude of a mean electric Froude number appropriately defined. There is also a more subtle effect on the mean flow due to changes in the Reynolds stress $\overline{u'_i u'_j}$. The equation governing the Reynolds stress contains the additional term $-\frac{1}{\beta}\,[\overline{u'_i J'_j} + \overline{u'_j J'_i}]$ which shows that current fluctuations which are correlated with velocity fluctuations contribute to the Reynolds stresses acting on the gas. Thus turbulence models which assume the Reynolds stress to be only aerodynamic in origin may not be applicable, particularly with a pulsed discharge.

A final insight into the role of the electric body force in generating turbulence may be gained by an examination of the energy balance equation for the mean and fluctuating motion. The mean kinetic energy per unit volume $E_m = 1/2\ \rho u_i^2$ is obtained by multiplying equation (2.16) by u_i. The result in divergence form is

$$\frac{\partial E_m}{\partial t} + \frac{\partial}{\partial x_j}\left(E_m \bar{u}_j + \rho\, \overline{u'_i u'_j}\, \overline{u_i} + \bar{p}\, \bar{u}_j - \mu\, \bar{u}_i \left(\frac{\partial \bar{u}_i}{\partial x_j} + \frac{\partial \bar{u}_j}{\partial x_i}\right)\right)$$

$$= -\frac{\mu}{2}\left(\frac{\partial \bar{u}_i}{\partial x_j} + \frac{\partial \bar{u}_j}{\partial x_i}\right)^2 + \rho\, \overline{u'_i u'_j}\, \frac{\partial \bar{u}_i}{\partial x_j} - \frac{1}{\beta}\, \overline{u_i}\, \overline{J_i}. \qquad (2.17)$$

Each term in this equation represents a physical mechanism which affects the balance of mean flow kinetic energy. The divergence terms on the left hand side reflect the usual fluxes of energy. The terms on the right hand side are the viscous decay term, the transfer term $\rho\, \overline{u'_i u'_j}\, \frac{\partial \bar{u}_i}{\partial x_j}$ which represents the energy transfer from the mean motion to the turbulence, and a term describing the interaction between the mean velocity and mean current density. The transfer term is almost always negative indicating that mean flow kinetic energy is continually being transformed into turbulent kinetic energy. The interaction term $\frac{1}{\beta}\, \overline{u_i}\, \overline{J_i}$ represents the rate at which the mean electric body force contributes energy to the mean velocity field. Thus the energy provided by the mean electric field to the mean flow is ultimately made available to the turbulence via the transfer term.

The equation governing the fluctuating kinetic energy per unit volume $E_t = 1/2\ \rho\, \overline{u_i'^2}$ is obtained by subtracting the Reynolds equation (2.16) from the instantaneous form of the Navier-Stokes equation (2.8) and then multiplying the resultant expression by u'_i and averaging. The turbulent energy balance is then

$$\frac{\partial E_t}{\partial t} + \frac{\partial}{\partial x_i}\left(E_t \bar{u}_i + \frac{1}{2}\rho\, \overline{u'_i u'_j u'_j} + \overline{p' u'_i} - \mu\, \overline{u'_j \left(\frac{\partial u'_i}{\partial x_j} + \frac{\partial u'_j}{\partial x_i}\right)}\right)$$

$$= -\frac{\mu}{2}\, \overline{\left(\frac{\partial u'_i}{\partial x_j} + \frac{\partial u'_j}{\partial x_i}\right)^2} - \rho\, \overline{u'_i u'_j}\, \frac{\partial \bar{u}_i}{\partial x_j} - \frac{1}{\beta}\, \overline{u'_i J'_i}. \qquad (2.18)$$

Once again each term with the exception of the electric body force contribution $\frac{1}{\beta}\overline{u'_i J'_i}$ may be given its usual interpretation. The divergence terms on the left are energy fluxes. The right hand side terms are the fluctuating viscous dissipation, the transfer term describing the exchange of energy between the mean and fluctuating motion, and the interaction term $\frac{1}{\beta}\overline{u'_i J'_i}$ which represents the mean rate at which the fluctuating electric body force contributes energy to the turbulence. Since the current density vector is directed primarily towards the collection plates, it can be shown (18) that the energy transfer is to the transverse velocity fluctuations which transport particles away from the collection plates.

IV. SUMMARY

It has been shown that the degree to which a precipitator gas flow is modified by corona discharge is completely determined by the current density. If the current density has a rotational component there will be electrical vorticity production in the gas resulting in secondary flows and turbulence. In turbulent flow, the mean and fluctuating components of current density cause indirect and direct energy transfer to the turbulence from the electric field. With DC energization it does not appear that current density fluctuations are significant except possibly during sparkover. In pulsed energization, however, this mechanism is likely to be a more significant source of turbulence.

Since turbulence and secondary flows in precipitators cause particle transport away from the collection plates, these effects are detrimental to the particle collection process and must be avoided. The theory demonstrates that the electrode geometry and discharge structure are the critical factors controlling flow perturbations of all types. In three geometries it is possible to avoid these disturbances entirely with a uniform discharge. In the wire-plate geometry the current density always perturbs the flow, but there is presumably an electrode design which delivers a desired total current while causing minimal flow disturbances. An exciting prospect is a planar electrode design to replace the wires. Obtaining a uniform discharge with this geometry is an area of current research.

REFERENCES

1. Williams, J. C., and R. Jackson. The Motion of Solid Particles in an Electrostatic Precipitator, Third Congress of the European Federation of Chemical Engineering, Symposium on the Interaction Between Fluids and Particles, 282-288 (1962).

2. Robinson, M. A Modified Deutsch Efficiency Equation for Electrostatic Precipitation, Atmos. Environment 1, 193-204 (1967).

3. Robinson, M. Turbulent Gas Flow and Electrostatic Precipitation, J. of Air Pollut. Control Assn. 18(4), 235-239 (1968).

4. Cooperman, P. A New Theory of Precipitator Efficiency, Atmos. Environment 5, 541-551 (1971).

5. Soo, S. L., and L. W. Rodgers. Further Studies of the Electroaerodynamic Precipitator, Powder Technology 5, 43-49 (1971).

6. Feldman, P. L., K. S. Kumar, and G. D. Cooperman. Turbulent Diffusion in Electrostatic Precipitators, AIChE Symposium Series 165, 73, 129-130 (1977).

7. Pyle, B. E., D. H. Pontius, T. R. Snyder, and L. E. Sparks. Particle Trajectory Studies in a Scale Model Electrostatic Precipitator, 73rd Annual Meeting of the Air Pollution Control Assn., 80-49.2 (1980).

8. Pyle, B. E., J. R. McDonald, W. B. Smith, and L. E. Sparks. The Relationship Between Gas Steam Turbulence and Collection Efficiency in a Lab-Scaled Electrostatic Precipitator, Third Symposium on the Transfer and Utilization of Particulate Control Technology, Orlando, Fla. (1981).

9. Leonard, G. L., M. Mitchner, and S. A. Self. Particle Transport in Electrostatic Precipitators, Atmos. Environment 14, 1289-1299 (1980).

10. Leonard, G. L., M. Mitchner, and S. A. Self. Precipitation from Turbulent Flows, Proc. Intl. Conf. on Electrostatic Precipitation, Monterey, California, 208-256 (1981).

11. Leonard, G. L., M. Mitchner, and S. A. Self. Experimental Study of the Effect of Turbulent Diffusion on Precipitator Efficiency, J. of Aerosol Science 13(4), 271-284 (1982).

12. Ramadan, O. E., and S. L. Soo. Electrohydrodynamic Secondary Flow, Phys. Fluids 12, 1943 (1969).

13. Yamamoto, T., S. Nakamura, and H. R. Velkoff. Numerical Study of Secondary Flow Interaction in an Electrostatic Precipitator, in _Innovative Numerical Analysis for the Engineering Science_, University Press of Virginia, 3-12 (1980).

14. Robinson, M. Effects of the Corona Discharge on Electric-Wind Convection and Eddy Diffusion in an Electrostatic Precipitator, ERDA-HASL-301 (1976).

15. Ushimaru, K., G. W. Butler, and P. Milovsoroff. An Experimental and Theoretical Investigation of Electrostatic Precipitators, Flow Research Report 219, Flow Industries, Kent, Washington (1982).

16. Leonard, G. L., M. Mitchner, and S. A. Self. An Experimental Study of the Electrohydrodynamic Flow in Electrostatic Precipitators, J. of Fluid Mech. 127, 123-140 (1983).

17. Kumaran, A. R. Aspects of the Fluid Mechanics of Electrostatic Precipitators, HTGL Report No. 15-83-TR (1983).

18. Davidson, J. H. Secondary Flows and Turbulence in Electrostatic Precipitators, Ph.D. Dissertation, Duke University, Durham, N.C. (1984).

19. Flippen, L. D. Electrohydrodynamics, Ph.D. Dissertation, Duke University, Durham, N.C. (1982).

20. Hay, J. C. The Electric Field and Vorticity Production in a Wire-Plate Precipitator with Uniform Discharge, M.S. Thesis, Duke University, Durham, N.C. (1984).

21. Leutert, G., and B. Bohlen. The Spatial Trend of Electric Field Strength and Space Charge Density in Plate-Type Electrostatic Precipitators, Staub-Reinholt. Luft 32(7), 27-33 (1972).

22. McDonald, J. R., W. B. Smith, and H. W. Spencer III. A Mathematical Model for Calculating Electrical Conditions in Wire-Duct Electrostatic Precipitation Devices, J. of Applied Physics 48(6), 2231-2243 (1977).

23. Lawless, P. A., and L. E. Sparks. A Mathematical Model for Calculating Effects of Back Corona in Wire-Duct Electrostatic Precipitators, J. of Applied Physics 51(1), 242-256 (1980).

24. Yamamoto, T., and H. R. Velkoff. Electrohydrodynamics in an Electrostatic Precipitator, J. of Fluid Mech. 108, 1-8 (1981).

25. Hoburg, J. F., and J. L. Davis. Wire-Duct Precipitator Field and Charge Computation Using Finite Element and Characteristics Methods, J. of Electrostatics 14(2), 187-199 (1983).

26. Page, F., W. G. Schlinger, D. K. Breaux, and B. H. Sage. Point Values of Eddy Conductivity and Viscosity in Uniform Flow Between Parallel Plates, Indus. and Engineering Chem. 44(2), 424-430 (1952).